Mechanistic Insight into Heterogeneous Oxidation Catalysts using Combined Operando and Transient Spectroscopies Supported by DFT

Mechanistische Einblicke in heterogene Oxidationskatalysatoren durch die Kombination von Operando- und transienten Spektroskopien unterstützt durch DFT
Zur Erlangung des Grades eines Doktors der Naturwissenschaften (Dr. rer. nat.)
Genehmigte Dissertation von Leon Schumacher aus Frankfurt a.M.
Tag der Einreichung: 17. Oktober 2023, Tag der Prüfung: 30. November 2023

1. Gutachten: Prof. Dr. Christian Hess
2. Gutachten: Prof. Dr. Bastian J. M. Etzold
3. Gutachten: Prof. Dr. Reinhard Schomäcker
Darmstadt, Technische Universität Darmstadt

TECHNISCHE
UNIVERSITÄT
DARMSTADT

Chemistry Department

Eduard-Zintl-Institut für Anorganische und Physikalische Chemie

Prof. Dr. Christian Hess

Mechanistic Insight into Heterogeneous Oxidation Catalysts using Combined Operando and Transient Spectroscopies Supported by DFT
Mechanistische Einblicke in heterogene Oxidationskatalysatoren durch die Kombination von Operando- und transienten Spektroskopien unterstützt durch DFT

Accepted doctoral thesis by Leon Schumacher

Date of submission: 17. Oktober 2023
Date of thesis defense: 30. November 2023

Darmstadt, Technische Universität Darmstadt

Erklärungen laut Promotionsordnung

§ 8 Abs. 1 lit. c PromO

Ich versichere hiermit, dass die elektronische Version meiner Dissertation mit der schriftlichen Version übereinstimmt.

§ 8 Abs. 1 lit. d PromO

Ich versichere hiermit, dass zu einem vorherigen Zeitpunkt noch keine Promotion versucht wurde. In diesem Fall sind nähere Angaben über Zeitpunkt, Hochschule, Dissertationsthema und Ergebnis dieses Versuchs mitzuteilen.

§ 9 Abs. 1 PromO

Ich versichere hiermit, dass die vorliegende Dissertation selbstständig und nur unter Verwendung der angegebenen Quellen verfasst wurde.

§ 9 Abs. 2 PromO

Die Arbeit hat bisher noch nicht zu Prüfungszwecken gedient.

Darmstadt, 17. Oktober 2023

_____

Leon Schumacher

Zusammenfassung

In dieser Arbeit wurden verschieden geträgerte (CeO_2, TiO_2, TiO_x/CeO_2) Vanadiumoxidkatalysatoren und ein bulk Oxid-Katalysator ($Fe_2(MoO_4)_3$) untersucht, um ihre grundlegenden Eigenschaften zu verstehen und die Reaktionsmechanismen während der oxidativen Dehydrierung (ODH) von Propan aufzuklären. Die verwendeten Katalysatoren basieren auf reduziblen Materialien, welche sich dadurch auszeichnen, dass sie durch die Bereitstellung von Sauerstoff aktiv an der Reaktion teilnehmen und dadurch die Performance des Katalysators signifikant beeinflussen können. Dies eröffnet neue Möglichkeiten eines rationalen Katalysatordesigns für neue Materialien mit verbesserter katalytischer Leistung. ODH-Reaktionen ermöglichen durch signifikante Energie- und Ressourceneinsparung eine Route zur umweltfreundlicheren Synthese von Basischemikalien, die durch die Nutzung von CO_2 als ubiquitäres Treibhausgas sogar klimaneutral gestaltet werden kann. Daher wurde der Einfluss der Verwendung von O_2 und CO_2 als Oxidationsmittel untersucht. Das Ziel dieser Arbeit ist es, den Einfluss verschiedener Trägermaterialien, Nuklearitäten und Oxidationsmittel auf den Reaktionsmechanismus zu verstehen und dieses Wissen am Ende für ein rationales Design von geträgerten Katalysatoren zu nutzen und auf das analytisch schwerer zugängliche Verhalten von bulk Oxiden zu übertragen. Für die mechanistische Analyse wurde eine Kombination von in situ und operando Methoden eingesetzt. Multi-Wellenlängen-Raman-Spektroskopie in Kombination mit UV-Vis-Spektroskopie ermöglicht die Untersuchung der Sauerstoffdynamik in der aktiven Phase und dem Träger. Die transiente Modulations-Anregungs-(ME-)IR-Spektroskopie wurde zur Identifizierung aktiv an der Reaktion beteiligter Adsorbat- und Vanadiumoxid-Spezies sowie des schnellen Wasserstofftransfers an der Oberfläche verwendet. Letzterer ist dabei besonders wichtig, da der initiale C-H Bindungsbruch oft als geschwindigkeitsbestimmender Schritt identifiziert wird. Diese Spektroskopien bilden den Kern der meisten mechanistischen Untersuchungen in dieser Arbeit, doch wurden je nach System und spezifischer Fragestellung weitere Methoden eingesetzt. Dazu gehören die Röntgenbeugung (XRD) zur Überwachung verschiedener Kristallstrukturen, die Röntgen-Photoelektronenspektroskopie (XPS) zur Überwachung der Oxidationszustände auf der Katalysatoroberfläche, die ^{51}V Festkörper-Kernspinresonanzspektroskopie (ssNMR), um die nuk-

learitätsabhängige Analyse von Vanadiumoxid zu ermöglichen und die elektrische Impedanzspektroskopie (EIS) zur direkten Überwachung von Massentransportphänomenen in bulk Oxiden. Zusätzlich wurden dichtefunktionaltheoretische Rechnungen (DFT) als unterstützende Methode eingesetzt.

In einem ersten Schritt wurden grundlegende Eigenschaften des VO_x/CeO_2 Systems untersucht. In theoretischen Untersuchungen zur Schwingungsstruktur des Materials mittels DFT wurden Raman-Spektren in Abhängigkeit von der Nuklearität simuliert und das beladungsabhängige Verhalten charakterisiert. Weiterhin wurde die Reduzierbarkeit der VO_x/CeO_2-Katalysatoren mittels der Reduktion in H_2 und das Reoxidationsverhalten unter Verwendung von CO_2, ausgehend von einem teilreduzierten Zustand, untersucht. Das Reduktionsverhalten an der Oberfläche und im Volumen wird stark von der Nuklearitätsverteilung von Vanadiumoxid beeinflusst, die wiederum die Sauerstoffmobilität in Ceroxid beeinflusst. Ein ähnliches nuklearitätsabhängiges Verhalten tritt bei der Regeneration mit CO_2 auf, bei der Ceroxid über Karbonatspezies reoxidiert wird. Vanadium-oxidspezies blockieren diese Regenerationsstellen, da sie über Oberflächensauerstoff verankert sind. Kurzkettige Vanadiumoxidspezies können aufgrund ihrer niedrigeren thermodynamischen Stabilität im Vergleich zu länger kettigen Vanadiumoxidspezies nur teilweise reoxidiert werden, wohingegen letztere aufgrund ihrer erhöhten Stabilität vollständig reoxidiert werden können.

Als nächstes wurde der Reaktionsmechanismus der Propan ODH mit O_2 als Oxidationsmittel über VO_x/CeO_2 Katalysatoren in Abhängigkeit von der Vanadiumoxid-Beladung untersucht. Dieser ist relevant, um die nachhaltigere Synthese der Basischemikalie Propylen zu optimieren und die Propan-ODH industriell relevanter zu machen. Hierbei wurde der Oberflächensauerstoff des Ceroxidgitters als aktive Stelle identifiziert. Dimere und oligomere Vanadiumoxidspezies fungieren als Transferstelle für die Übertragung von Wasserstoff auf den Oberflächensauerstoff des Ceroxidgitters und für die Koordination von Propan. Monomere Spezies nehmen nicht aktiv an der Reaktion teil, interagieren aber mit den Sauerstofffehlstellen von Ceroxid und blockieren diese. Im Vergleich dazu zeigt sich bei der Verwendung von CO_2 als Oxidationsmittel ein komplexeres Reaktionsnetzwerk, bei dem die Dehydrierung von Propan eine Rolle spielt, aber die Totaloxidationsreaktion aufgrund der hohen Sauerstoffmobilität in Ceroxid immer noch sehr ausgeprägt ist. Das Reaktivitätsverhalten hängt dabei stark von den Vorbehandlungsbedingungen ab. Vanadiumoxid vermindert die Prävalenz der Totaloxidationsreaktion und erhöht die Gesamtaktivität des Katalysators. Die Oberfläche wird durch die Bildung stabiler Karbonatspezies unter Reaktionsbedingungen teilweise deaktiviert.

Um den Einfluss des Trägermaterials auf den Reaktionsmechanismus der Propan ODH zu verstehen, wurden VO_x/TiO_2-Katalysatoren unter Verwendung von TiO_2 P25 als Trägermaterial

untersucht. In diesen Katalysatoren fungieren die V=O- und V-O-V-Gruppen des Vanadiumoxids als die wichtigste aktive Spezies. Das Titandioxid sorgt für die Übertragung des Wasserstoffs auf das Vanadiumoxid und beeinflusst ebenfalls dessen Nuklearität über das Anatas/Rutil-Verhältnis im Träger. Im Vergleich zur Verwendung von CeO_2-Trägern ist das VO_x/TiO_2-System bei der Benutzung von CO_2 als Oxidationsmittel hochselektiv für die Dehydrierung von Propan und zeigt Aktivitäten, die mit CrO_x-Katalysatoren vergleichbar sind. Die einzige Nebenreaktion ist die Propantrockenreformierung. Die katalytische Leistung ist jedoch nicht stabil. Die Deaktivierung des Katalysators wird durch die vollständige Reduktion und zu langsame Regeneration des Katalysators verursacht. Die Regenerationsrate des Katalysators wird durch die Gegenwart des Vanadiumoxids erhöht, das die Bildung von Rutil katalysiert und aktiv am Redoxzyklus teilnimmt, wodurch die Regenerationsrate des Katalysators erhöht und die Gesamtselektivität gesteigert wird.

Auf Grundlage des zuvor beschriebenen mechanistischen Wissens zur Propan ODH über VO_x/CeO_2- und VO_x/TiO_2-Katalysatoren wurde der Versuch eines Katalysatordesigns unternommen, indem mittels Atomlagenabscheidung (*atomic layer deposition*, ALD) zunächst ein TiO_x/CeO_2-Trägersystem mit variabler TiO_x-Beladung synthetisiert und anschließend mit Vanadiumoxid beladen wurde. Dadurch wird einerseits eine aktive Beteiligung der Sauerstoffatome aller drei Oxide ermöglicht, andererseits aber ein Großteil der unselektiven Oberflächensauerstoffatome auf der Ceroxidoberfläche mit Titandioxid bedeckt, welches zudem Vanadiumoxid koordiniert. Insgesamt wird durch diesen Ansatz eine höhere Selektivität als bei den Zweikomponentenoxiden erreicht.

Abschließend wurde als kommerzieller bulk Oxid-Katalysator $Fe_2(MoO_4)_3$ untersucht. Dieser unterscheidet sich von einem geträgerten Katalysator dadurch, dass es sich um kein homogenes Material handelt, sondern ein gradueller Übergang von der stöchiometrischen bulk Struktur hin zu einer veränderten Struktur an der Oberfläche erfolgt, welche alle an der Reaktion beteiligt sind und individuelle Rollen übernehmen. Dies macht ein solches Katalysatorsystem komplexer als ein geträgertes, da nicht nur an der Katalysatoroberfläche, sondern auch im Volumen relevante Prozesse stattfinden können. In Vorarbeiten wurde zunächst ein Einfluss der Synthesebedingungen auf die Struktur, Phasenzusammensetzung und das Mo/Fe Verhältnis von $Fe_2(MoO_4)_3$ u.a. mittels Raman- und XP-Spektroskopie festgestellt. Mechanistische Untersuchungen während der Propan-ODH mittels operando- und transienter Spektroskopie ergaben, dass der Gittersauerstoff für die Reaktion von großer Bedeutung ist. Wasserstoff kann durch eine Schicht aus amorphem MoO_x, die sich auf der Katalysatoroberfläche ausbildet, auf das Gitter übertragen werden, wodurch die Selektivität gesteigert werden kann. Hier kann eine Diffusion des Wasserstoffs in den oberflächennahen Bereich des Katalysators stattfinden, wo es zur Bildung von Wasser kommen kann

und eine Fehlstelle direkt im Gitter induziert werden kann. Die Regeneration des Gitters erfolgt durch Diffusion aus dem bulk oder durch einen Phasenübergang zu $FeMoO_4$. Die Mobilität des Sauerstoffs im Katalysator hängt dabei stark vom Eisengehalt des Materials ab.

Diese Arbeit zeigt, dass die Kombination von operando- und transienter Spektroskopie, unterstützt durch DFT, eine detaillierte Beschreibung des Mechanismus von ODH Reaktionen über geträgerten und bulk Oxid-katalysatoren ermöglicht. Dies ist von großer Bedeutung für das rationale Design neuer Katalysatormaterialien, um neue Prozesse zu entwickeln bzw. um den aktuellen Stand bestehender katalytischer Prozesse zu verbessern und damit die Nachhaltigkeitstransformation in der chemischen Industrie voranzutreiben. In diesem Zusammenhang wurde anhand des erfolgreichen rationalen Designs eines Trägermaterials demonstriert, dass die Propan-ODH-Selektivitäten (im Vergleich zu anderen Materialien) durch ein detailliertes Verständnis des Reaktionsmechanismus signifikant erhöht werden können. Insgesamt zeigt sich die große Bedeutung der Kombination komplementärer spektroskopischer Methoden unter Reaktionsbedingungen, um ein vollständiges Bild der Wirkungsweise von Katalysatoren zu erhalten und eine Unterscheidung zwischen Oberflächen-, Untergrund- und Bulk-Prozessen sowie deren Wechselspiel zu ermöglichen.

Abstract

In this work, various supported (CeO_2, TiO_2, TiO_x/CeO_2) vanadium oxide catalysts and a bulk oxide catalyst ($Fe_2(MoO_4)_3$) were investigated in order to understand their fundamental properties and to elucidate the reaction mechanisms during the oxidative dehydrogenation (ODH) of propane. The catalysts used in this work are supported on reducible oxides, which are characterized by the fact that they actively participate in the reaction by providing oxygen, thus significantly influencing the performance of the catalyst. This opens up new avenues towards a rational catalyst design to obtain new materials with improved catalytic performance. ODH reactions enable a route to a more environmentally friendly synthesis of basic chemicals through significant energy and resource savings, which can even be made carbon neutral by using the ubiquitous greenhouse gas CO_2 as the oxidizing agent. Therefore, the influence of using O_2 and CO_2 as oxidants was investigated. The aim of this work is to investigate the influence of different support materials, vanadia nuclearities, and oxidizing agents on the propane ODH reaction mechanism and to use this knowledge for the rational design of supported catalysts and to finally transfer it to the analytically more challenging behavior of bulk oxides. For the mechanistic analysis a combination of in situ and operando methods was used. Multi-wavelength Raman spectroscopy in combination with UV-Vis spectroscopy allows the investigation of the catalysts oxygen dynamics in the active phase and in the support. Transient modulation-excitation (ME-)IR spectroscopy was used to identify actively participating adsorbate and vanadium oxide species as well as the rapid hydrogen transfer from propane to the catalyst surface. The latter is particularly important, as the initial C-H bond break is often described as the rate-limiting step. The combination of these spectroscopies forms the core of most of the mechanistic studies in this work, but depending on the system and the specific question, other methods were used. These include X-ray diffraction (XRD) for monitoring crystal structures, X-ray photoelectron spectroscopy (XPS) to monitor oxidation states on the catalyst surface, ^{51}V solid-state nuclear magnetic resonance spectroscopy (ssNMR) to enable the nuclear-dependent analysis of vanadium oxide and electrical impedance spectroscopy (EIS) for direct monitoring of mass transport phenomena in bulk oxides. In addition, density functional theory (DFT) calculations were used as a supporting method.

In a first step, basic properties of the VO_x/CeO_2 system were investigated. As part of theoretical investigations of the material by DFT, vibrational Raman spectra were simulated as a function of the vanadia nuclearity and the loading-density dependent behavior was characterized. Furthermore, the reducibility by means of temperature-programmed reduction (TPR) in H_2 and the reoxidation behavior in CO_2, starting from a partially reduced state, was investigated. The reduction behavior at the surface and in the subsurface was strongly influenced by the nuclearity distribution of vanadia, which in turn affects the oxygen mobility in ceria. A similar nuclearity-dependent behavior occurs during reoxidation with CO_2, in which ceria is reoxidized via the formation of carbonate species. Vanadia species block these regeneration sites because they are anchored to ceria via surface oxygen. Short nuclearities can only be partially reoxidized due to their lesser thermodynamic stability compared to longer-chain nuclearities, which are fully reoxidized due to their increased stability.

Next, the propane ODH reaction mechanism over VO_x/CeO_2 catalysts as a function of the vanadia loading was investigated using O_2 as the oxidizing agent. This is highly relevant to optimize the more sustainable synthesis of the basis chemical propylene compared to traditional production processes like stam cracking, making the propane-ODH process industrially more relevant. Here, surface oxygen of the ceria lattice was identified as the active site. Dimeric and oligomeric vanadia species act as the transfer site for hydrogen to surface oxygen of the ceria lattice and for the coordination of propane. Monomeric species do not actively participate in the reaction but are able to interact with and block oxygen vacancies of ceria. In comparison, the use of CO_2 as the oxidizing agent leads to a more complex reaction network, in which the dehydrogenation of propane plays a significant role, but total oxidation is still very pronounced due to the high oxygen mobility in ceria. The reactivity behavior also depends strongly on the pretreatment conditions. Vanadia reduces the prevalence of the total oxidation reaction and increases the overall activity of the catalyst. The surface is partially deactivated by the formation of stable carbonate species under reaction conditions.

To investigate the influence of the support material on the propane ODH reaction mechanism, the VO_x/TiO_2 system was investigated in detail using TiO_2 P25 as the support material. Here, the V=O and V-O-V groups of vanadia act as the main active sites, while titania provides the transfer site of hydrogen to the vanadium oxide via lattice oxygen and influences the vanadia nuclearity via the anatase/rutile ratio in the support. In comparison, the VO_x/TiO_2 system is highly selective for the dehydrogenation of propane when using CO_2 as the oxidizing agent and exhibits catalytic activities comparable to CrO_x catalysts. The only side reaction is propane dry reforming. However, the catalytic performance is not stable. The deactivation of the catalyst is caused by the complete reduction and an insufficient regeneration rate of the catalyst by CO_2. The regeneration rate of

the catalyst is increased by the presence of vanadia, which catalyzes the formation of rutile and actively participates in the redox cycle, increasing the regeneration rate of the catalyst and its overall selectivity.

Based on the obtained mechanistic knowledge on propane ODH over VO_x/CeO_2 and VO_x/TiO_2 catalysts, a rational design attempt was made by synthesizing a TiO_x/CeO_2 support system with variable TiO_x loading using atomic layer deposition (ALD) and subsequent loading with vanadia. This allows for the active participation of oxygen atoms of all three oxides, while concurrently, titania covers most of the unselective surface oxygen atoms of the ceria surface and coordinates the vanadia, which results in a higher selectivity than that observed for the two-component oxides.

Finally, $Fe_2(MoO_4)_3$ was investigated as a commercial bulk oxide catalyst. Bulk oxides differ from supported catalysts in the fact that they are not a homogeneous material but gradually transition from the stoichiometric bulk structure to a modified surface structure. All of these parts can be involved in the reaction and take on individual roles. This makes such a system more complex than a supported one, since the reaction takes place not only at the catalyst surface, but relevant processes can also take place in the bulk. First, the influence of the synthesis conditions on the structure, phase composition and Mo/Fe ratio of $Fe_2(MoO_4)_3$ by means of Raman and XP spectroscopy was investigated. Mechanistic studies during propane ODH by means of operando and transient spectroscopy reveal that lattice oxygen is of great importance for the reaction. Hydrogen can be transfered from the propane to the lattice by a layer of amorphous MoO_x, which forms on the catalyst surface and increases its selectivity. Here, diffusion of the hydrogen to the subsurface of the catalyst can occur, leading to water and subsequent vacancy formation. The regeneration of the lattice takes place by diffusion from the bulk or by a phase transition to $FeMoO_4$. The oxygen mobility in the catalyst is highly relevant for the reactivity and strongly depends on the iron content.

This work demonstrates that the combination of operando and transient spectroscopy, supported by DFT, allows for a detailed description of the mechanism of ODH reactions over supported and bulk oxide catalysts. This is of great importance for the rational design of new catalyst materials, aiding in developing new processes, or to improve the current state of existing catalytic processes, thus driving the transformation in the chemical industry towards sustainability. In this context, the successful rational design of a support material shows that the propane ODH selectivities can be enhanced (in comparison to other materials) by a detailed understanding of the reaction mechanism. Overall, this demonstrates the importance of combining complementary spectroscopic methods under reaction conditions in order to obtain a complete picture of the mode of operation of catalysts and to distinguish between surface, subsurface and bulk processes

and their interplay.

Contents

1 Introduction

The field of catalysis is of extraordinary importance to the chemical industry as most of the industrial processes are catalyzed by heterogeneous catalysts.[1] Since the transformation of natural resources by the chemical industry is the basis for our modern life, catalysis is essential to maintain and improve our standard of living.[2] Furthermore, the use of catalysis is essential to the solution of current problems, including the climate change, by supporting the necessary green transformation of our industry.[3] For example, many reactions can be performed using significantly less resources with lower energy expenditure when a catalyst is employed. In addition, CO_2 can be catalytically activated and used in chemical industry to obtain value-added products from this undesired green house gas.[4,5] An important example of these reactions is the ODH of propane, which is a highly promising (additional) way to produce propylene and close the propylene gap, which is caused by an excess of demand for propylene that cannot be satisfied by conventional production processes like steam and fluid catalytic cracking.[6,7] It can significantly lower the required energy for propylene production and reduces waste from deactivated catalysts making it more ecological. However, the challenge to make this reaction viable is that propylene can be more easily oxidized to CO_x than propane. Therefore, the reaction needs to be stopped at the selective oxidation product. One approach towards higher selectivities would be to use CO_2 as a soft-oxidant. Its use as a feed gas instead of O_2 can even make the reaction climate neutral. The main barrier to use CO_2 is its high thermodynamic stability, which requires a high energy input. Furthermore, a plethora of additional side reactions becomes possible compared to O_2. To emphasize this point, the possible ODH reaction networks for both the use of O_2 and CO_2 as oxidizing agents are shown in Figure 1.1.
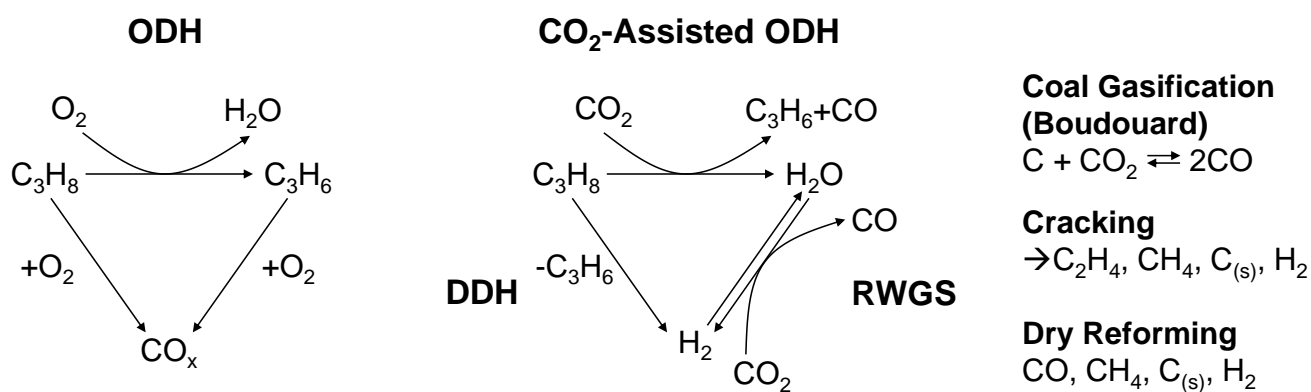
Figure 1.1: Comparison between the reaction network for propane ODH (left) and CO_2-assisted propane ODH (right).

During the propane ODH using O_2, propane can react with O_2 to form propylene and water. From there, two routes towards the total oxidation product CO_x are possible, either directly from propane or from propylene. Since propylene is more easily oxidized than propane, this route is more likely.[8]

For the CO_2-assisted propane ODH, the reaction network becomes more complex. Ascoop et al.[9] proposed, that the dehydrogenation of propane can occur via two pathways. First, the oxidative dehydrogenation can occur in a similar way to the reaction with O_2. Second, direct dehydrogenation (DDH) can lead to propylene and hydrogen formation, which can then react via the RWGSr to CO and H_2O, leading to the same reaction products as the direct pathway. In addition, due to the high temperatures involved, cracking can occur, which can be accompanied by the formation of ethylene, methane, solid carbon and hydrogen.[10] Furthermore, propane dry reforming (PDR) can occur, which convertes propane mainly to CO, but different reaction pathways to methane, solid carbon and hydrogen are also possible.[11] The solid carbon can then be gasified by CO_2 to CO. Due to the plethora of reactions involved, the discrimination between the different reaction pathways is very challenging.

Due to the challenges in both reactions, a suitable catalyst needs to be employed. In general, catalytic conversions occur over active phases, which can be noble metals (Cu, Au, Pt) or oxides (VO_x, MoO_x, CrO_x). To increase the surface area of the catalyst and reduce the required amount of the (often expensive) active phase, they are commonly supported on an oxide material. The support material itself can strongly influence the reaction behaviour of the catalyst.[12,13] This depends on wether or not the catalyst support actively participates in the reaction. Typical inactive supports are SiO_2 and Al_2O_3, while active supports include TiO_2, CeO_2 and In_2O_3. The latter can participate in the reaction (e.g. by providing lattice oxygen). Besides these interactions,

the support can further change the catalytic properties by coordinating the active phase in a different way than in the pure phase, i.e. via strong metal-oxide support interactions (SMOSI).[14] In addition, the exact composition of the support is of importance. For example, TiO_2 supports show different properties depending on their crystal structure.[15,16]

For the propane ODH reaction, supported amorphous vanadium oxide (VO_x) is often used as a catalyst due to its good selectivity and its increased activity when actively supported.[17] Active supports are often characterized by their reducibility, allowing them to participate in the redox cycle of an oxidation reaction. For example, ceria was shown to act as an oxygen buffer[18] that can be reduced and form oxygen vacancies as well as Ce^{3+} states. These can be regenerated by gas phase oxygen or by diffusion from ceria's bulk.[19,20] Similarly, TiO_2 is often described as an oxygen buffer, as it forms vacancies as well. Additionally, it was demonstrated that titania coordinates its active phase in a way that increases the catalytic performance.[21–23] To fully understand the reaction behavior of these catalysts, their oxygen dynamics and interactions with the active phase need to be understood.

To optimize the catalytic performance of supported VO_x catalysts and make the propane ODH reaction viable the reaction mechanism needs to be understood. Many studies report that titania is the most active support, closely followed by zirconia and ceria, while silica and alumina supports are significantly less active.[12,13] In this work, focus was put on the use of ceria and titania, which are both very promising active support materials. The current state of knowledge of VO_x/CeO_2 and VO_X/TiO_2 catalysts, will be briefly summarized. For an extensive literature overview of each reaction and catalyst material, please refer to the introductions of the publications in Section 4. For the VO_x/CeO_2 system, preliminary studies revealed unique interactions between vanadia and ceria, including the formation of a $CeVO_4$ vanadate phase[24] and the presence of different vanadia chain lenghts (nuclearities) on the catalyst surface. The latter results in a vibrational fine structure of the V=O stretching region (Raman and IR spectroscopy) that allows for their discrimination.[25] Further characterization of the interplay between vanadia and ceria was done in a DFT study performed by Penschke et al.[26] revealing a distinct interaction between monomeric vanadia and ceria surface oxygen vacancies, which can irreversibly block the vacancies. Furthermore, it was proposed that vanadia species strongly influence the reducibility of ceria surface oxygen in their proximity. Wether the C_3 species are oxidized to CO_x during the ODH reaction or wether the oxidation can be stopped at the selective oxidation product will strongly depend on the choice of the support material.[12,13,17] Detailed mechanistic studies based on the use of in situ/operando spectroscopy during propane ODH conditions are scarce but the structure of VO_x/CeO_2 samples was extensively characterized by in situ multi-wavelength Raman spectroscopy under O_2.[27–29] Additionally, DFT studies were conducted to calculate the reaction pathway over a VO_3/CeO_2

catalyst. Huang et al.[30] proposed that propyl adsorption to surface vanadia follows the initial hydrogen abstraction from propane to ceria lattice oxygen. Further possibilities included the adsorption of propyl to the ceria surface and hydrogen abstraction to V-O-Ce or V=O bonds. However, these were energetically very similar and a differentiation via DFT was not possbile. On the experimental side, operando X-ray absorption near edge spectroscopy (XANES) was used to observe the structural relaxation of vanadia monomers into ceria oxygen vacancies during ethane ODH, which is the most relevant experimental study.[31,32]

In contrast, in the VO_x/TiO_2 system, titania is often described to coordinate the vanadia structure and possibly participate in the ODH reaction via lattice oxygen and subsequent vacancy formation.[23] The rutile amount within the TiO_2 support is of particular importance for the vanadia structure on the surface.[33] Mechanistic studies by Safonova et al.[34] and Zabliska et al.[35] established that, during ethanol ODH, the redox cycle occurs over vanadia instead of titania, which does not change its oxidation state. Under propane ODH conditions, despite the large number of kinetic studies, no operando/transient spectroscopic studies were available in the literature prior to this work. Therefore, the exact structure of the surface vanadia, due to the lack of a V=O fine structure in Raman spectra, and the influence of the titania on the reaction were not knwon on a molecular level during propane ODH. In addition, there were no mechanistic investigations of three or more oxide component catalysts in the literature.

At last, understanding the support participation during the CO_2-assisted propane ODH is of great importance to develop a full mechanistic picture. This reaction is highly promising for technical applications, using for captured CO_2 in a large scale process to propylene, one of the most important basis chemicals. To this day, highly toxic CrO_x supported on SiO_2 is by far the most active catalyst for the CO_2-assisted propane ODH.[36,37] However, supprted VO_x has newly emerged as a possible alternative.[9,38,39] To that end, Jiang et al.[40,41] published two studies on VO_x supported on In_2O_3, showing that vanadia reduces the prominent PDR reaction rate and stabilizes the catalytic performance of In_2O_3. Furthermore, a nuclearity-dependent behavior was proposed where monomeric species appeared to be more active. In contrast, no literature is available for the VO_x/CeO_2 and VO_X/TiO_2 systems under propane ODH conditions. Therefore, understanding their catalytic performances and reaction mechanisms is an important aspect of this work.

The intimate interaction between the oxides with different properties might lead to different catalytic results and reaction mechanisms, which makes this comparison interesting. In addition, two oxidzing agents, O_2 and CO_2 were compared for these reactions to understand their influence on the reaction. The use of these oxidizing agents leads to different reaction networks and requires different reaction temperatures (caused by the high barrier of CO_2 activation). Besides, after

investigating the propane ODH over the afforementioned catalysts, the mechanistic knowledge obtained from these systems was transferred to a rational design approach based on a TiO_x/CeO_2 support. In addition, $Fe_2(MoO_4)_3$ bulk catalysts were investigated during alkane and also alcohol ODH to elucidate its properties. This material is of great relevance due to its high activity and selectivity during methanol ODH.[42] The activity has been attributed to the good availability of surface lattice oxygen, that can easily be regenerated by bulk oxygen due to the high oxygen mobility in the catalyst, attributed to the presence of iron.[43,44] The molybdenum is proposed to be responsible for the good selectivity and is present in high amounts in promximity to the surface of the material.[45] However, a detailed mechanistic understanding of this catalyst during ODH reactions has not yet been obtained. To investigate the materials properties and understand the reaction mechanism in detail, a full mechanistic study under propane ODH conditions was performed. As an additional activity, spectroscopic investigations during the ethanol ODH over V_4C_3 MXenes and to the reverse water-gas shift reaction (RWGSr) over In_2O_3 were contributed. In summary, the goal of this work is to understand the reaction mechanisms of all reactions and materials mentioned above on a molecular level by combining multiple operando and transient spectroscopies with DFT and further enable rational catalyst design. This contributes to improved catalytic performance leaping propane ODH towards industrial application as a greener alternative to e.g. steam cracking.

2 Theoretical Background

2.1 Spectroscopic Background

2.1.1 In Situ/Operando Spectroscopic Approach

Spectroscopy is an important tool for the investigation of solid catalytic materials. It is often used for the structural characterization of materials before and after a reaction to identify structural changes relevant to the catalytic performance. However, these are not necessarily representative of the involved surface species during the reaction, as the catalyst structure and the species involved are heavily dependent on the employed conditions.[46] To tackle this problem, in situ spectroscopy is performed. Therein, spectroscopic measurements under working conditions are used to unambiguously identify relevant active sites and species. To expand the level of understanding obtained by spectroscopic experiments, operando spectroscopy was introduced. It simultaneously records spectroscopic measurements under catalytically relevant conditions as well as the catalytic activity (e.g. via gas phase analysis of the reaction products). Based on this data, structure-activity relationships can be deduced, which can directly correlate structural changes to catalytic data. Therefore, operando spectroscopy is the only spectroscopic approach that fully enables a mechanistic investigation.

The term operando spectroscopy was first introduced by the Banares group,[47,48] but operando measurements were already published early without utilizing the new term.[49] An overview of all the established operando measurements was published by Wachs et al.[50] It shows that the combination of operando methods is essential to fully understand the interaction of a complex catalytic material such as an oxide-supported system.

To enable detailed insights into reaction mechanisms, multiple operando and in situ spectroscopic methods are combined in this work. Their fundamentals are discussed in the following sections. The experimental set-up used for these measurements is described in more detail in Chapter 3 and the experimental sections of the individual publications in Chapter 4. In addition to the operando and in situ spectroscopies, transient modulation-excitation spectroscopic measurements (IR) were

performed to investigate actively participating surface adsorbates and species (especially the V=O vibrational fine structure) on a fast time scale, allowing for the determination of their temporal evolution.

2.1.2 Resonance Raman Spectroscopy

Since Raman spectroscopy and especially multi-wavelength resonance Raman spectroscopy are highly important for all publications in this work, its fundamental theory will be discussed in this section. It is an important method for the investigation of solid-state catalysts. Many possible applications were summarized in a review by Hess.[51] It allows for the detection of bulk phonons as well as vibrations of the active phase like M=O, anchoring support-O-M, and bridging M-O-M bonds. This is especially important for the understanding of supported vanadia catalysts. Through the usage of resonance effects, the intensity of these vibrations can be selectively enhanced by the choice of the excitation wavelength based on the absorption at the chosen wavelength. This enables the dedicated investigation of the support and active oxides and is a powerful tool for mechanistic insights under operando conditions.[52,53] It is, in many cases, the most important experimental basis for the mechanistic interpretation in this work.

The Raman effect, which describes the inelastic scattering of light by matter, was theoretically predicted by Adolf Smekal[54] and was later experimentally observed by Sir Chandrasekhara Venkata Raman.[55] In general, the interaction between a photon and a molecule/ a solid can occur in different ways. These interactions, relevant to vibrational spectroscopy, are shown schematically in Figure 2.1. A detailed description of the basic theory of Raman spectroscopy is not given in this work and can be found commonly in the literature.[56–58]
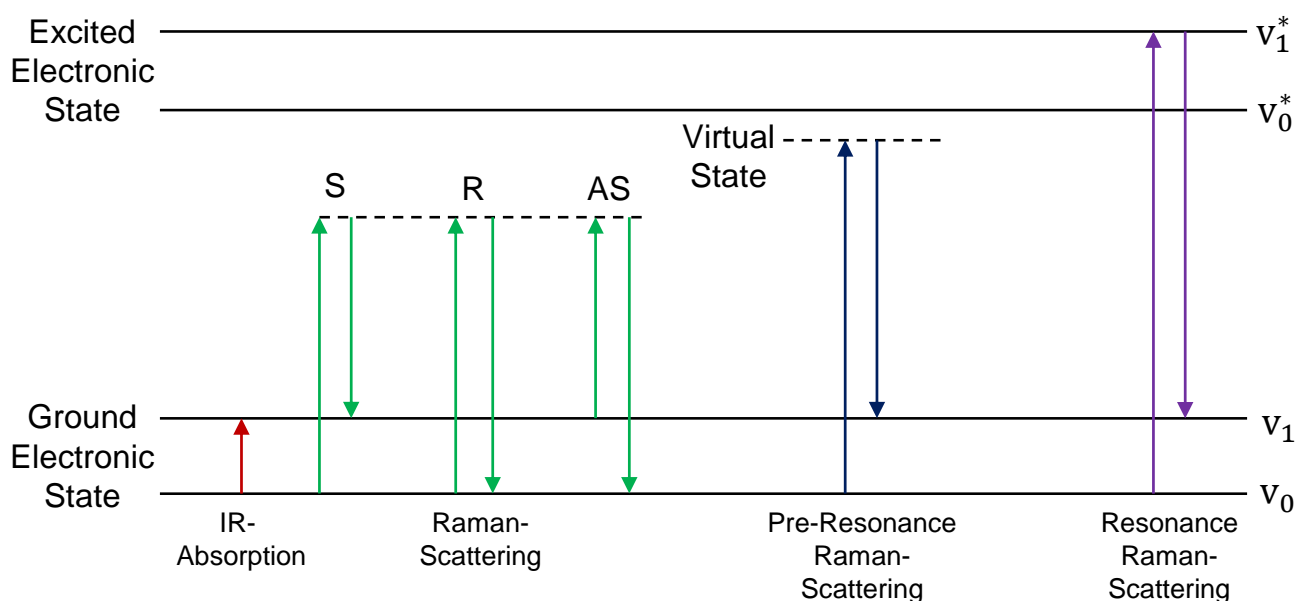
Figure 2.1: Absorption and scattering processes of a photon by matter. The scattering processes include regular (Rayleigh, Stokes, and Anti-Stokes, green), pre-resonance (blue) and resonance (purple) scattering.

The simple absorption of the photon by the molecule induces a transition from the vibrational ground state into a vibrationally excited state, which is the basis of IR spectroscopy. In comparison, the Raman process is fundamentally different, since the photon is scattered and not absorbed, which leads to different optical selection rules. This scattering can occur in three ways and for each a virtual state arises for the moment the photon is scattered. Due to Heisenberg's uncertainty principle this state has a very short lifetime and is not a stationary state of the system. The elastic scattering is called Rayleigh scattering and occurs in 99.9999 % of cases compared to inelastic scattering. However, Rayleigh scattering is not of interest for Raman spectroscopy, since the photons energy is conserved and no information about the energy levels is aquired. To achieve high quality Raman spectra, a laser is therefore required to maximize the photon flux and the Rayleigh scattered light needs to be removed from the resulting Raman spectra afterwards.
The inelastic scattering processes include Stokes and Anti-Sokes scattering. During these processes, energy is exchanged between the photon and the system and information about the energy levels can be aquired by measuring the photon energies after scattering. Stokes scattering starts at the vibrational ground state and ends in a vibrationally excited state, while Anti-Stokes scattering starts in an excited and ends in the ground state. Due to the temperature-dependent Boltzmann distribution, the vibrationally excited state is less populated, resulting in less Anti-Stokes than Stokes scattering.[56–58]

Besides the regular scattering processes via a virtual state, pre-resonance and resonance scattering can occur. Pre-resonance scattering occurs when the excitation wavelength is close to an electronic state, leading to the virtual state overlapping with some of the residual density of states of the electronically excited state. In contrast, resonance scattering occurs when the excitation wavelength is equal to the energy required for an electronic transition. These scattering processes can significantly increase the intensity of the Raman process.[58,59]

To describe the intensities in a Raman spectrum mathematically, the approximation of the harmonic oscillator is used in the following.

In general, the intensity I of a transition observed using spectroscopy is proportional to the square of the transition dipole moment R. This can be calculated acording to Equation 2.1 assuming the wavefunctions Ψ are known.[56–58]

$$R = \int \Psi_{\mathrm{v}} \hat{\mu} \Psi_{\mathrm{v}^\star} d\tau \tag{2.1}$$

The transition dipole moment can be correlated to the electric field (caused by the incident radiation) by employing the transition polarizability α, which is described by the Kramers-Heisenberg-Dirac (KHD) formula given in Equation 2.2.[58]

$$(a_{\rho\sigma})_{\mathrm{IF}} = \frac{1}{\hbar} \cdot \sum_{r \neq \mathrm{I,F}} \left\{ \frac{\langle F | \hat{\mu}_\rho | r \rangle \langle r | \hat{\mu}_\sigma | I \rangle}{\omega_{\mathrm{rI}} - \omega_{\mathrm{L}} - i\Gamma} + \frac{\langle r | \hat{\mu}_\sigma | I \rangle \langle F | \hat{\mu}_\rho | r \rangle}{\omega_{\mathrm{rI}} + \omega_{\mathrm{L}} + i\Gamma} \right\} \tag{2.2}$$

Here, I and F are the initial and final states before and after scattering, while r represents a virtual state. Due to the non-specific nature of the states, the sum over r describes them as a superposition of eigenstates. Furthermore, ρ and σ describe the polarization of the incident and scattered light, respectively. ω_{rI} describes the frequency difference between the virtual and the initial state, ω_{L} is the laser frequency, and $i\Gamma$ is a damping term.

If the excitation wavelength is close to or equal to the corresponding energy of an electronic transition, the resonance leads to a significant increase in the Raman scattering intensity. There, the denominator in the first term of Equation 2.2 becomes much larger than the second term, which can be neglected. In addition, the integrals in the first term of Equation 2.2 can be evaluated. In the Born-Oppenheimer approximation, the electronic (θ) and vibrational (ψ) components of the vibronic wavefunction can be evaluated separately under the assumption that the movement of the nuclei during the scattering process is small. The operator of the dipole moment $\hat{\mu}$ then only applies to the electronic wave function and can be evaluated by employing a Taylor expansion. This is shown in Equations 2.3-2.5.[58,59]

$$\langle r \,|\hat{\mu}_\rho|\, I \rangle = \langle \theta_r \cdot \psi_r \,|\hat{\mu}_\rho|\, \theta_I \cdot \psi_I \rangle = \langle \psi_r \,|\langle \theta_r \,|\hat{\mu}_\rho|\, \theta_I \rangle|\, \psi_I \rangle \tag{2.3}$$

$$\langle \theta_r \,|\hat{\mu}_\rho|\, \theta_I \rangle = M_{rI}(R) \tag{2.4}$$

$$M_{rI}(R) = M_{rI}(R_0) + \left[\frac{\partial M_{rI}}{\partial R}\right]_{R_0} \cdot R_\epsilon + \left[\frac{\partial^2 M_{rI}}{\partial R^2}\right]_{R_0} \cdot \frac{R_\epsilon^2}{2} + \text{ higher order terms} \tag{2.5}$$

Here, M_{rI} is a component of the pure electronic transition electric dipole moment associated with the transition $r \rightarrow F$. Applying the results of the expansion to the KHD expression in Equation 2.2 results in Equation 2.6.[58,59]

$$
\begin{aligned}
(\alpha_{\rho\sigma})_{IF} = &\underbrace{\frac{1}{\hbar} \cdot M_{rI}^2(R_0) \cdot \sum_{r \neq I,F} \frac{\langle \psi_F \,|\, \psi_r \rangle \langle \psi_r \,|\, \psi_I \rangle}{\omega_{rI} - \omega_L - i\Gamma}}_{A-\text{Term}} \\
&+ \underbrace{\frac{1}{\hbar} \cdot M_{rI}(R_0) \cdot \left[\frac{\partial M_{rI}}{\partial R}\right]_{R_0} \cdot \sum_{r \neq I,F} \frac{\langle \psi_F \,|R_\epsilon|\, \psi_r \rangle \langle \psi_r \,|\, \psi_I \rangle + \langle \psi_F \,|\, \psi_r \rangle \langle \psi_r \,|R_\epsilon|\, \psi_I \rangle}{\omega_{rI} - \omega_L - i\Gamma}}_{B-\text{Term}}
\end{aligned}
\tag{2.6}
$$

If α_{IF} is zero or very close to zero, the intensity also approaches zero. Since the effect of the denominator has already been discussed under resonance conditions, the enumerator is now of importance. For its evaluation, the wavefunctions ψ must be considered. Under the assumption of a harmonic oscillator, four possible relations between the electronic ground and the excited state are possible, depending on the change of the force constant k and/or the nuclear distance q. The influence of these different possibilites on the potential energy curves of the ground and excited electronic states are shown in Figure 2.2.[58,59]
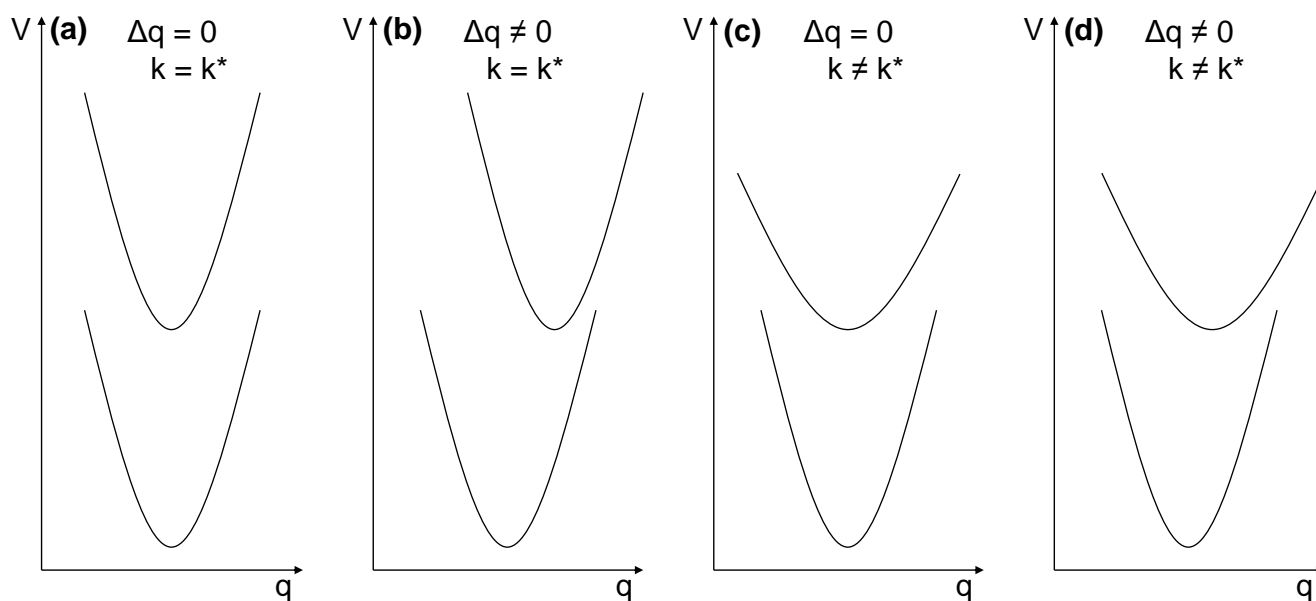
Figure 2.2: Possible relationships between the potential curves of the electronic ground and excited states depending on *q* and *k*.

In 2.2a, no changes in *q* or *k* occur, leading to identical vibrational wave functions for the same vibrational quantum number within different electronic states. Since the eigenfunctions ψ are orthonormal, the integrals in the enumerator of the A-term become zero for all inelastic scattering processes. The integrals in the B-term contain the displacement operator and become $\neq 0$ if the vibrational wavefunctions correspond to $\Delta \nu = \pm 1$.

In the other three cases, at least one parameter changes between the two states, leading to different wavefunctions, which are not orthogonal. This leads to the possibility of A-Term scattering, which also includes overtones. *q* will only differ for totally symmetric modes or a changed symmetry of the mode in the electronically excited state. Commonly, a change in *q* will also result in a change in *k*, which makes the case in 2.2d the most common.[58,59]

Besides the *A*- and *B*-terms, the *C*- and *D*-term can also contribute to the resonance enhancement. The total enhancement is given by the sum of all four terms, which is shown in Equation 2.7.[58,59]

$$(\alpha_{\rho\sigma})_{\text{e}^g\text{v}^f:\text{e}^g\text{v}^i} = A + B + C + D \tag{2.7}$$

The C- and D-term are given in the Equations 2.8 and 2.9.[58,59]

$$C = \frac{1}{\hbar^2} \frac{h^k_{e^g e^t}}{\omega_{e^g} - \omega_{e^t}} (p_\rho)^0_{e^t e^r} (p_\sigma)^0_{e^r e^g} \sum_{v^r_k} \frac{\left\langle v^{f(g)}_k \left| Q_k \right| v^{r(r)}_k \right\rangle \left\langle v^{r(r)}_k \mid v^{i(g)}_k \right\rangle}{\omega_{e^r v^r_k \cdot e^g v^i_k} - \omega_1 - i\Gamma^r_{e^r v^r_k}}$$
$$+ \frac{1}{\hbar^2} (p_\rho)^0_{e^g e^r} (p_\sigma)^0_{e^r e^r} \frac{h^k_{e^t e^g}}{\omega_{e^g} - \omega_{e^t}} \sum_{v^r_k} \frac{\left\langle v^{f(g)}_k \mid v^{r(r)}_k \right\rangle \left\langle\!\left\langle v^{r(r)}_k \left| Q_k \right| v^{i(g)}_k \right\rangle\right.}{\omega_{e^r v^r_k : e^g v^g_k} - \omega_1 - i\Gamma^r_{e^r v^r_k}} \tag{2.8}$$

$$D = \frac{1}{\hbar^3} (p_\rho)^0_{e^g e^s} \frac{h^k_{e^s e^r} h^k_{e^r e^{s'}}}{(\omega_{e^r} - \omega_{e^s})(\omega_{e^r} - \omega_{e^{s'}})} (p_\sigma)^0_{e^{s'} e^g} \sum_{v^r_k, v^r_{k^\star}} \frac{\left\langle v^{f(g)}_k \left| Q_k \right| v^{r(r)}_k \right\rangle \left\langle v^{r(r)}_{k'} \left| Q_{k'} \right| v^{i(g)}_{k'} \right\rangle}{\omega_{e^r v^r_k : e^g v^i_k} - \omega_1 - i\Gamma^r_{e^r v^r_k}} \tag{2.9}$$

The *C*-term only contributes when vibronic coupling between the ground and excited electronic state exists and the *D*-term when vibronic coupling between three excited electronic states occurs. These conditions are rarely met in molecules and are therefore negliable in these cases. However in solids,[52,53] these can regularly occur and even become dominant, giving rise to overtones and combination vibrations.[58,59]

In this work, the combination of two wavelengths (385 nm, 514 nm) for the selective intensity enhancement of supported vanadia catalysts were especially favorable. First, a near-UV wavelength at 385 nm was used for ceria and titania resonance enhancements due to their band gap absorptions in this region.[60–63] This leads to a pronounced intensity increase in the surface lattice oxygen and defect region for ceria and rutile signals, and allows to observe the phase transitions from anatase to nanodispersive rutile in titania, which is usually dominated by anatase. Furthermore, short-chain vanadia species, especially monomers and dimers, are also resonance enhanced at this wavelength.[29] This increases the intensity of anchoring vibrations. Secondly, 514 nm excitation is useful for the resonance enhancement of long-chain vanadia species and is located outside of the band gap absorption of the supports. It gives rise to the vanadyl fine structure caused by dipole-dipole interactions between the V=O groups.[25] This feature is most pronounced for VO_x/CeO_2 catalysts but is also somewhat observable in the TiO_2 system. To gain insight into the absorption behavior of the used materials and their potential resonance conditions, UV-Vis spectroscopy is employed.

2.1.3 Diffuse-Reflectance UV-Vis Spectroscopy

UV-Vis absorption spectroscopy is an important complementary method for resonance Raman spectroscopy, since it measures the wavelgenth-dependent absorption of a sample. The absorption is caused by electronic transitions in the material, which are often located in the UV-Vis section of the electromagnetic spectrum. Changes in the electronic structure, e.g. the creation of lattice defects such as oxygen vacancies in oxide materials, or a change in the oxidation state can therefore influence the UV-Vis spectrum significantly, allowing to follow changes in the material. To that end, the combination of UV-Vis and Raman spectroscopy was previously of great use for understanding materials and reaction mechanisms.[60,64]

UV-Vis spectroscopy is important for the investigation of the materials in this work, which are mainly VO_x/CeO_2 and VO_x/TiO_2. The support materials exhibit band gap transitions arising from O 2p $\rightarrow$ Ce 4f[60,61] and O 2p $\rightarrow$ Ti 3d transitions.[62,63] Since both supports are dynamic systems that can be reduced during the reaction, lattice oxygen vacancies may occur under reaction conditions. These lead to the creation of new states in the band gap that lower the energy of band gap transitions, resulting in a red-shift, and create reduced states (Ce^{3+} and Ti^{3+}), which leads to the charge transfers $Ce^{3+} \rightarrow Ce^{4+}$ and $Ti^{3+} \rightarrow Ti^{4+}$.[60,65] In addition, the absorption of V^{5+} can be monitored via ligand-to-metal-charge transfers (LMCT) and the presence of reduced vanadia by d-d transitions $V^{3+/4+} \rightarrow V^{5+}$.[66]

The obtained information about the materials intrinsic absorption properties and the ability to monitor changes in its electronic structure makes operando UV-Vis spectroscopy a core part of this work.

2.1.4 Electrical Impedance Spectroscopy

Electrical impedance spectroscopy measures the frequency-dependent resistance of a sample. For this, a sine wave voltage is applied to the sample while the current is measured to determine the resistance (potentiostatic electrical impedance spectroscopy, PEIS). For a single excitation sine wave, the frequency is constantly varied to achieve the full frequency range required for the PEIS spectrum. To decrease the measurement time, a multi-sine excitation can be performed, which was done to record the impedance spectra in this work. Due to different processes answering at different frequencies, PEIS is especially well equipped to observe mass transport processes through a material. This method was already applied in various contexts, like battery material research,[67–69] but has not yet been used as an operando method during thermal catalysis on powder samples. However, as it enables the observation of e.g. oxygen transport through the bulk

it is especially viable for bulk materials like $Fe_2(MoO_4)_3$ and In_2O_3, which were investigated in this work.[70] In addition, if the sample is very conductive, hydrogen transport processes and phase transitions can be observed. A detailed equivalent-circuit analysis for this new application can further enable significant new and detailed insights into the reaction mechanism in bulk materials.

2.1.5 Modulation-Excitation Diffuse-Reflectance Infrared Fourier Transform Spectroscopy

To investigate surface species, especially adsorbates, diffuse-reflectance IR Fourier transform spectroscopy (DRIFTS) can be used. It is based on the absorption of a photon in the IR region of the electromagnetic spectrum that leads to a vibrational transition between the ground and first excited state (see Figure 2.1). However, on catalysts with multiple actively participating oxide species, a plethora of adsorbate species is possible. For CeO_2, the carbonate region (between 1200 and 1800 cm^{-1}) is especially important due to surface oxygen defects, which can lead to the formation of many different cabon containing adsorbates.[71] The corresponding signals are often broad and can overlap, which makes the interpretation of operando DRIFT spectra difficult. However, the information that can be extracted from DRIFT spectra is often highly relevant to the mechanistic understanding of a catalyst.

To address the DRIFTS related problems mentioned above, modulation-excitation (ME)-DRIFTS can be employed. For performing ME-DRIFTS experiments, two gases A and B as well as an inert gas are required. Then, one gas flow is kept constant (A in this example) and the second gas B is pulsed periodically, while time-resolved DRIFT spectra are measured to follow the changes on the surface of the catalyst. Due to the different chemical potential, depending on the gas phase, the adsorbate signals behave differently. Adsorbate peaks that participate under reaction conditions (presence of gases A+B) exhibit a modulation of intensity/position that follows the concentration modulation with a certain phase-shift. Observer species (that do not participate in the reaction) are accumulated, their signals do not modulate in intensity/position. Therefore, the active species can be isolated by a Fourier transformation over all phase-shifts. This removes significant amounts of noise, background, and spectator species, which allows for a much easier interpretation of the spectra and assignment of active species. In addition, the fast time-scale at which the spectra are recorded allows for the determination of the time-evolution of the adsorbates. This strongly facilitates the mechanistic interpretation of the observed surface species.[72–74]

Different gas-switching patterns can be employed, e.g. the flow of gas B can be kept constant over the sample, while gas A is pulsed. In this work, isotopic ME-DRIFTS was introduced (publication

four in Chapter 4), which switches between h8-propane and d8-propane, while the oxygen gas flow remains constant to ensure propane ODH conditions. This allows for the dedicated investigation of hydrogen transfer paths, as only the signal positions of the species involved in the h/d exchange modulate their position and are isolated by Fourier transformation. This was shown to be highly relevant to the mechanistic investigation of alkane ODH reactions, since it allowed for the identification of transient hydrogen transfer sites that are only present on a short time scale but catalyze the rate-limiting step in this reaction.

Overall, the ME-DRIFTS greatly contributes to the mechanistic analysis in this work as it can identify active adsorbates in the carbonate region, which are important for the identification of CO_x formation routes, hydrogen transfer sites in the M-OH region, and the nuclearity-dependent analysis of the V=O region. The latter was especially important for the VO_x/CeO_2 system, which exhibits a pronounced V=O fine structure, where the assignement of catalytic functions to different vanadia chain lengths was performed.

2.1.6 Quasi In Situ X-Ray Photoelectron Spectroscopy

Photoelectron spectroscopy is based on the excitation and removal of core electrons from an atom using X-ray radiation. When the energy of the X-ray radiation is constant (monochromatic), the measurement of the kinetic energy of the released electrons allows for the determination of the element from which the electron was removed. When multiple elements are present in a solid, the determination of the elemental composition of the material is possible. The depth of penetration using XPS is small, which limits the information obtained to the surface of the sample. Since electrons are detected, XPS is performed under ultra-high vacuum (often $<0.5 \cdot 10^{-8}$ mbar). Therefore, it cannot be performed as an in situ/operando method due to the pressure gap. However, pre-treatments under catalytically relevant conditions can be performed in a reaction cell, after which the sample is cooled under an inert gas to room temperature and is subsequently transferred inertly into the XPS measurement chamber. This is referred to as a quasi in situ measurement. However, it needs to be taken into account that structural changes on the sample surface may occur, which are caused by the removal of the gas phase. In this work, quasi in situ XPS measurements were of great use for the investigation of the surface vanadium oxidation states after exposure to different gas feeds.

2.1.7 Further Methods

Further methods for characterization were applied in this work, including X-ray diffraction (XRD), ^{51}V solid-state nuclear magnetic resonance spectroscopy (ssNMR), H_2 temperature-programmed reduction (TPR), and N_2 physisorption. Their theoretical background is covered by the literature,[75–77] while the more complex ^{51}V ssNMR experiments will be explained in Chapter 4.

2.2 Density Functional Theory

As a basis for the interpretation of Raman spectra of VO_x/CeO_2 obtained under catalytically relevant conditions, density functional theory (DFT) was employed to simulate Raman spectra of VO_x/CeO_2 with different vanadia nuclearity distributions.[78,79] Therefore, in the following chapter, a brief description of the basics of DFT and the calculation of Raman intensities, based on the normal modes obtained by density functional pertubation theory (DFPT), is given.

2.2.1 Fundamentals of Density Functional Theory

DFT is based on the usage of the electron density as the central descriptor of properties. This density is defined in Equation 2.10.

$$\rho(\vec{r}) = N \int \dots \int \left| \Psi \left(\vec{x}_1, \vec{x}_2, \dots, \vec{x}_N \right) \right|^2 d\vec{x}_1 \, d\vec{x}_2 \dots d\vec{x}_N \qquad (2.10)$$

Here, $\vec{x}_N$ is the position of an electron n, ρ gives the propability for an electron in a given volume, while the remaining electrons are at any position, which is described by their wavefunction ψ. This functional's energy is only minimial if the exact electron density is known.[80]
The energy functional is comprised of different contributions, including the kinetic energy of the electrons as well as the electron-electron and core-electron interactions. The electron-electron interaction can be split into the contribution from the Coulomb and the Exchange functional. The expressions for the Coulomb functional and the electron-core interaction are given by Equations 2.11 and 2.12, respectively.[81,82]

$$J[\rho] = \frac{1}{2} \iint \frac{\rho \left(\vec{r}_1 \right) \rho \left(\vec{r}_2 \right)}{\left| \vec{r}_1 - \vec{r}_2 \right|} d^3 \vec{r}_1 d^3 \vec{r}_2 \qquad (2.11)$$

$$E_{\text{eC}}[\rho] = \sum_{I=1}^{N_{\text{C}}} \int \frac{Z_{\text{I}}\rho(\vec{r})}{\left|\vec{R}_{\text{I}} - \vec{r}\right|} d^3\vec{r} \tag{2.12}$$

However, the expressions for the electrons kinetic energy and the exchange functional are not known. The kinetic energy can be calculated based on the introduction of orbitals into the calculation, which was first done by Kohn and Sham. This splits the kinetic energy into two parts. The first can be calculated exactly, while the second is a correction term. Equation 2.13 gives the expression for the kinetic energy based on non-interacting electrons.

$$T_{\text{S}} = \sum_{i=1}^{N} \left\langle \varphi_{\text{i}} \left| -\frac{1}{2}\nabla^2 \right| \varphi_{\text{i}} \right\rangle \tag{2.13}$$

The expression for the total energy of a given system obtained via DFT using the expressions mentioned above is given in Equation 2.14.[80–82]

$$E_{\text{DFT}}[\rho] = T_{\text{S}}[\rho] + E_{\text{eK}}[\rho] + J[\rho] + E_{\text{XC}}[\rho] \tag{2.14}$$

The exchange-correlation functional relevant to obtain a more exact total energy is given in Equation 2.15 and summarizes the electron-electron interactions, the correction term for the kinetic energy of the electrons, and the exchange energy.[80–82]

$$E_{\text{XC}}[\rho] = (T[\rho] - T_{\text{S}}[\rho]) + (E_{\text{ee}}[\rho] - J[\rho]) \tag{2.15}$$

Since the exchange-correlation functional cannot be calculated accurately, approximations, such as the local density approximation, are required. The local density approximation (LDA) provides a framework within DFT for the exchange and correlation functionals.[80–82] Herein, ϵ_{XC} describes an inhomogeneous electron density based on the correlation and exchange functionals for a homogeneous electron gas. However, it delivers poor results for most molecules and only gives sufficient results for some metals due to the electron gas assumption. The LDA approximation is shown in Equation 2.16.[80–82]

$$E_{\text{XC}}^{LDA}[n(\vec{r})] = \int n(\vec{r}) \cdot \epsilon_{\text{XC}}(n(\vec{r}))d\vec{r} \tag{2.16}$$

However, it is often not sufficient for molecules and solids. Therefore, the generalized gradient approximation (GGA) is used.[80–82] It can be parameterized based on the Perdew, Burke and Ernzerhof (PBE) functional.[83] For the materials used in this work, the PBE+U approach was used. The U parameter aids with the localization of Ce 4f electrons.[84] Most commonly, a value of 4.5 eV is used in the literature.[85] To construct the electron density, orthonormal Kohn-Sham orbitals (KSO) are introduced, which are shown in Equation 2.17. Their energy needs to be minimized.[80–82]

$$n(\vec{r}) = \sum_{i}^{N} \phi_i^*(\vec{r}) \cdot \phi_i(\vec{r}) \tag{2.17}$$

By introducing Lagrangian multipliers, the Kohn-Sham equation, central to calculate material properties in the DFT framework, is obtained as shown in Equation 2.18.[80–82]

$$\left[-\frac{1}{2}\nabla^2 + \int \frac{n(\vec{r}_2)}{r_{12}} d\vec{r}_2 + V_{XC}(\vec{r}_1) - \sum_{A=1}^{N} \frac{Z_A}{r_{1A}} \right] \cdot \phi_i = \epsilon_i \cdot \phi_i \tag{2.18}$$

To solve this equation numerically, a basis set expansion is performed, reducing the set of differential equations to a matrix eigenvalue problem. A plane wave basis set is used, as it is advantageous for solid materials as used in this work. To avoid the use of infinite basis functions the plane waves are truncated at a cutoff energy of 400 eV. The basis set expansion and the plane wave function are shown in Equations 2.19 and 2.20, respectively.[80–82]

$$\phi_i(\vec{r}) = \sum_{\mu=1}^{N} c_{\mu i} \eta_\mu(\vec{r}) \tag{2.19}$$

$$\eta^{PW}(\vec{r}) = e^{(i\vec{k}\vec{r})} \tag{2.20}$$

To reduce the numerical demand of the calculations, the core electrons of the atoms are summarized in a pseudo-potential. Only the valence electrons are taken into account. For that, projector augmented wave (PAW) potentials are used.[86]

At last, due to the periodicity of the solids investigated, the Kohn-Sham equation needs to be solved at every k-point in the Brillouin zone. The total density is obtained from the sum over all k-points. To sample the k-points, the Monkhorst-Pack is used, which generates equally distributed k-points in the irreducible representation of the Brillouin zone.[87]

A detailed description of the calculations performed in this work can be found in the experimental section of the first publication in Chapter 4.

2.2.2 Calculation of Raman Intensities

The Raman intensities were calculated using the Vienna Ab initio Simulation package (VASP, Version 5.4.4, https://www.vasp.at/) using the PBE+U approach with a U_{eff} value of 4.5 eV. The plane wave cutoff was 400 eV and the Kohn-Sham equation was solved using the PAW method. For more details, please refer to the first publication in Chapter 4. The Raman intensities are calculated based on an already published approach by Porezag and Pederson that calculates the differential cross section according to Equation 2.21.[88] This requires the normal modes, which were obtained by DFPT as implemented in VASP.

$$\frac{d\sigma_{\text{i}}}{d\Omega} = \frac{(2\pi v_{\text{s}})^4 \cdot h \left(n_{\text{i}}^b + 1\right) \cdot I_{\text{Raman}}}{45 \cdot c^4 \cdot 8\pi^2 \cdot v_{\text{i}}} \tag{2.21}$$

Here, ν_{s} is the frequency of the scattered light, n_{b}^i is the statistical Bose-Einstein factor, I_{Raman} is the Raman scattering intensity, and ν_{i} the frequency of the ith vibrational mode. The Raman scattering intensity required to obtain the cross section is calculated from the derivatives of the polarizability with respect to the atomic coordinates, as shown in Equation 2.22.

$$I_{\text{Raman}} = 45 \left(\frac{d\alpha}{dQ}\right)^2 + 7 \left(\frac{d\beta}{dQ}\right)^2 = 45\alpha'^2 + 7\beta'^2 \tag{2.22}$$

The calculation of the derivatives of the polarizabilities for α and β was already described previously and can be performed according to Equations 2.23 and 2.24.

$$\alpha' = \frac{1}{3} \left(\bar{\alpha}'_{\text{xx}} + \bar{\alpha}'_{\text{yy}} + \bar{\alpha}'_{\text{zz}}\right) \tag{2.23}$$

$$\beta'^2 = \frac{1}{2} \left[\left(\bar{\alpha}'_{\text{xx}} - \bar{\alpha}'_{\text{yy}}\right)^2 + \left(\bar{\alpha}'_{\text{yy}} - \bar{\alpha}'_{\text{zz}}\right)^2 + \left(\bar{\alpha}'_{\text{zz}} - \bar{\alpha}'_{\text{xx}}\right)^2 + 6 \left(\bar{\alpha}'^2_{\text{xx}} + \bar{\alpha}'^2_{\text{yy}} + \bar{\alpha}'^2_{\text{zz}}\right) \right] \tag{2.24}$$

An external electric field, which is the incident radiation, causes this change of the polarizability $\bar{\text{a}}_{\text{ij}}$ with respect to the atomic coordinates R_{k}, as shown in Equation 2.25.

$$\frac{\partial \bar{\alpha}_{ij}}{\partial R_k} = -\frac{\partial^3 E^{el}}{\partial E_i \partial E_j \partial R_k} \tag{2.25}$$

Here, E^{el} is the electronic energy of the system. To express the direct response of the molecule to the external electric field, the dielectric tensor can be used, according to Equation 2.26.[89]

$$\epsilon_{ij}^{\infty} = \delta_{ij} - \frac{4\pi}{\Omega_{cell}} \cdot \frac{\partial^2 E^{el}}{\partial E_i \partial E_j} \leftrightarrow \frac{\partial^2 E^{el}}{\partial E_i \partial E_j} = -\frac{\Omega_{cell}}{4\pi} \epsilon_{ij}^{\infty} + \frac{\Omega_{cell}}{4\pi} \delta_{ij} \tag{2.26}$$

Here, δ_{ij} corresponds to the Kronecker delta, Ω_{Cell} is the volume of the unit cell for which the Raman spectrum is calculated and ϵ_{ij}^{∞} describes the components of the dielectric tensor. With this definition, the response to an external electric field can be expressed as a finite difference, as shown in Equation 2.27.

$$\frac{\partial \bar{\alpha}_{ij}}{\partial R_k} = -\left[\left(\frac{\partial^2 E^{el}}{\partial E_i \partial E_j} \right)_+ - \left(\frac{\partial^2 E^{el}}{\partial E_i \partial E_j} \right)_- \right]_{\frac{1}{R_k}} = \frac{\Omega_{cell}}{4\pi} \left[\left(\epsilon_{ij}^{\infty} \right)_+ - \left(\epsilon_{ij}^{\infty} \right)_- \right] \frac{1}{\Delta R_k} \tag{2.27}$$

The elements of the dielectric tensor $(\epsilon_{ij}^{\infty})_+$ and $(\epsilon_{ij}^{\infty})_-$ are obtained when the atoms are displaced by +0.005 and -0.005 along the normal mode vector. ΔR_k stands for the total displacement of the atoms along the normal mode vector and is therefore 0.01 Å. Since the full dielectric matrix is calculated for each run, the time needed to calculate Raman intensities using DFT is vastly greater than that needed to calculate infrared intensities.

3 Instrumentation

The following chapter aims to provide a brief overview of the instrumental set-up used during this work. The experimental set-up is shown schematically in Figure 3.1.
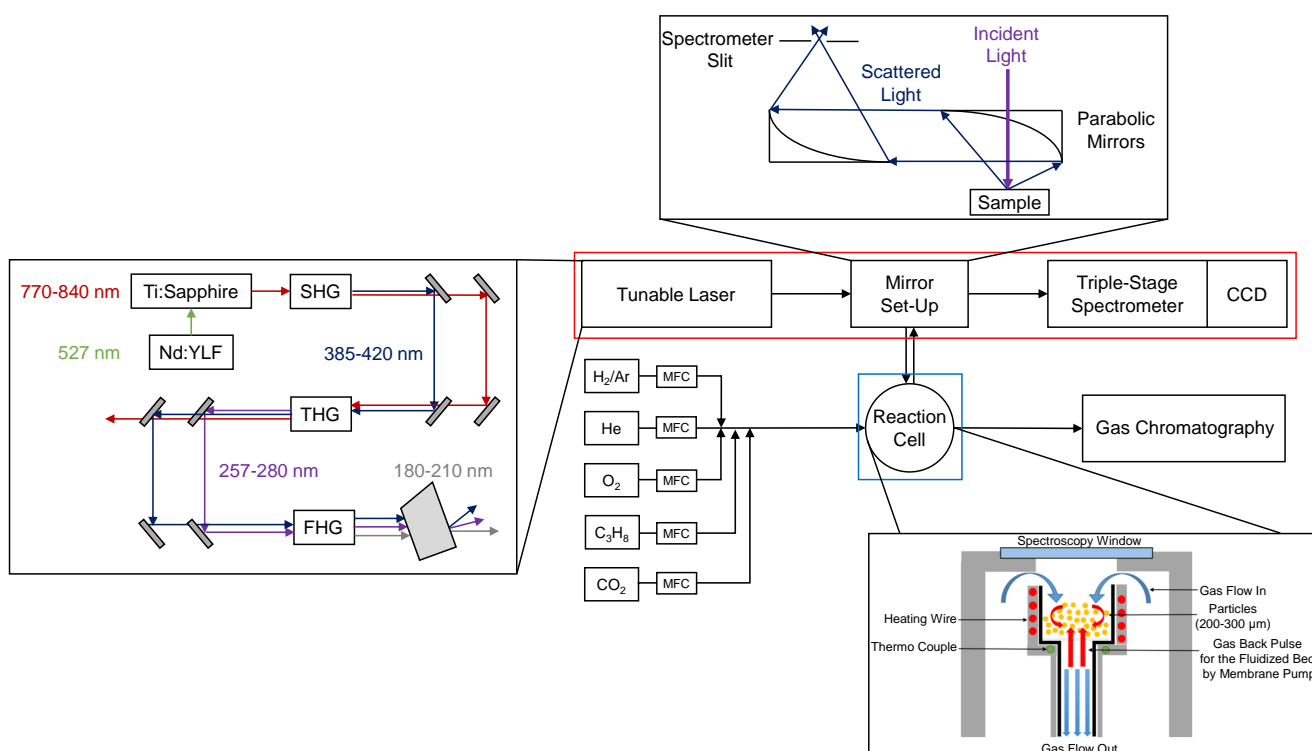
Figure 3.1: Schematic overview of the experimental set-up used for UV-Raman spectroscopy. The tuneable UV-Laser, the optical set-up and the reaction cell are shown in detail. The red and blue rectangles indicate that a different spectroscopic set-up or reaction cell can be used, respectively.

The core of the set-up is the reaction cell where the catalyst is located. A commercially available Linkam CCR 1000 reactor was used. Different gases can be dosed via mass-flow controllers (MFCs), including diluted hydrogen (7 % H_2/Ar), helium, oxygen, propane and CO_2. The gases

flow over the catalyst and can be analyzed by gas chromatography after leaving the reactor. The chromatograph is an Agilent 7890B equipped with two columns, a PoraPlotQ for the separation of hydrocarbons, and a molesieve for the remaining gases. The separated gases are analyzed by a thermal conductivity detector (TCD) and a flame ionization detector (FID) in series.

To analyze the catalyst during the reaction and obtain structure-activity relationships, in situ/operando spectroscopy is applied. In Figure 3.1, the schematic set-up during UV-Raman spectroscopy is shown, since it is the most complex. For the generation of the UV-radiation, a tuneable UV-solid state laser (Coherent) is used. To this end, a Q-switched, intracavity Nd:YLF laser is frequency-doubled and pumps a continuously tuneable Ti:Sapphire laser, which can generate near infrared (NIR) laser radiation between 770 and 900 nm. However, due to the set of mirrors used, only the wavelength region between 770 and 840 nm is accessible in our case. The 770 nm wavelength is used as the basis for the UV-Raman experiments performed in this work. Barium borate (BBO) and lithium triborate (LBO) are used to generate the second (385 nm), and third (257 nm) harmonic (SHG and THG). In theory, fourth harmonic generation is also possible with this set-up but was not used in this work. To achieve such a nonlinear frequency conversion, both input polarizations are required to be collinear. Therefore, the fundamental and second harmonic generation are separated via a dichroic mirror and have to travel different path lengths before reaching the second nonlinear crystal for the THG. Each of the wavelengths (770, 385 and 257 nm) can be used for catalyst measurements.[52,53]

The generated laser radiation is focused onto the sample and the scattered radiation is collected and focused onto the spectrometer entrance slit using a parabolic mirror set-up. This maximizes the signal due to the best collection of the scattered light. For details, please refer to the literature.[28] It also increases the laser spot-size to decrease the energy input into the sample and reduces the risk of laser-induced damages to the sample. This is especially powerful in combination with the employed fluidized-bed reactor, resulting in a significant reduction of UV-radiation induced damage to the sample during UV-Raman spectroscopy. The radiation is then separated in a TriVista 555 triple-stage spectrometer (Princeton Instruments) with an attached Spec 10:2kBUV CCD camera (Princeton Instruments). The camera is cooled with liquid nitrogen to -120 °C and employs 2048x512 pixels, achieving a spectral resolution of 0.3 cm^{-1}. To minimize the intense background caused by Rayleigh radiation, the spectrometer is used in the subtractive mode, which uses the first two stages as Notch filters to remove the Rayleigh scattered light, while the third stage disperses the light onto the CCD camera.

The red and blue boxes in Figure 3.1 indicate that these components can be exchanged to perform different spectroscopies. The spectroscopic set-up can be modified to perform Vis-Raman (514, 532, and 633 nm), UV-Vis, DRIFT and electrical impedance spectroscopy. For UV-Raman,

Vis-Raman, and EI spectroscopy, the Linkam cell can be employed, while for the DRIFT-based spectroscopies, the Linkam cell was replaced by the commercially available Praying Mantis reaction chamber (Harrick Scientific). For details on the set-up of the mentioned methods, please refer to the publications in chapter 4.

To ensure that the spectroscopies in both reaction cells are performed at identical temperatures, calibrations were performed using a thermocouple. The results are shown in Equations 3.1 and 3.2 for the Linkam and the Harrick cell, respectively. The temperatures in both cells were set to a value where the temperature at the sample is identical for both set-ups.

$$T_{\text{act}} = 0.91 \cdot T_{\text{set}} + 1.75°\text{C} \tag{3.1}$$

$$T_{\text{act}} = 0.65 \cdot T_{\text{set}} - 2°\text{C} \tag{3.2}$$

Besides the methods mentioned above, further characterization including the use of in situ methods was performed outside of the set-up shown, including nitrogen physisorption, XRD, H_2 temperature programmed reduction (H_2-TPR), XPS and ^{51}V ssNMR. Details on the used set-ups and on the experimental procedures are given in the experimental sections of Chapter 4 and in the literature.[90,91]

4 Results and Discussion

Using the methods described in Chapter 2 and 3, supported vanadia catalysts were investigated in regard to their fundamental properties and during the ODH of propane. Hereby, the combination of different operando and in situ spectroscopies was of particular importance to understand the reaction mechanism and the complex interplay between the support, the active vanadia, and the gas phase. Especially multi-wavelength resonance Raman in combination with UV-Vis spectroscopy was used to understand the oxygen transport in the samples and to differentiate between vanadia structures. In addition, ME-DRIFT spectroscopy was used to understand quick hydrogen transfers and adsorbate dynamics during the reaction. Different reducible materials, that is, ceria and titania, were used to investigate the influence of the support on the vanadia structure and reactivity, as well as the support participation in the reaction. For the ceria-based system, DFT was employed to understand the vibrational structure of the different nuclearities of vanadia and to facilitate the assignment signals of important features. In addition, different oxidizing agents, namely O_2 and CO_2, and their influence on the catalytic performance and the reaction mechanism in dependence of the support material were investigated. Furthermore, bulk oxides were investigated during reaction conditions and operando impedance spectroscopy, developed in our group, was used for mechanistic elucidation. Lastly, based on the obtained knowledge, the rational design of a support material for vanadia was used to enhance its catalytic performance during propane ODH. The results of this work are summarized by the following articles. Their contents are categorized by topic into five sections. For articles which have not been fully published yet, the supporting information is also attached, while for the published articles, the supporting information is freely available online.

4.1 Fundamental Properties of Propane ODH over VO_x/CeO_2 Catalysts Using O_2 and CO_2 as the Oxidizing Agents

The first part of this work is concerned with the fundamental properties of VO_x/CeO_2 catalysts, including their vibrational structure and reducibility. Afterwards, focus is put on the elucidation of the reaction mechanism of propane ODH over VO_x/CeO_2 catalysts employing O_2 and CO_2 as the oxidizing agents.

4.1.1 Detailed Analysis of the Raman Vibrational Structure of Vanadia in VO_x/CeO_2: A Periodic Density Functional Theory Study

The first publication is concerned with the simulation and analysis of Raman spectra of vanadia monomers and oligomers using DFT on a clean ceria surface. The structures of these oligomers were already established in literature.[26,92,93] Based on these structures, the vibrational frequencies and Raman intensities of monomeric structures were determined for different cell sizes, varying the effective distance between them. A $Ce_{48}O_{96}$-cell was necessary to minimize the interactions between the clusters beyond the periodic boundary conditions (PBC) and obtain the isolated vibrational structure of the monomer. Based on this cell size, different V_nO_{2n} (n=1-7) oligomers were simulated and their vibrational structure was determined. Using the experimentally determined vanadyl fine structure and the thermodynamic stability of the different vanadia nuclearities, coefficients were determined to combine the Raman spectra of isolated clusters towards a real spectrum with a distribution of nuclearities. The simulated spectra are in agreement with the experimental Raman spectra, allowing for a detailed understanding of experimentally very broad vanadia features. The variation of vanadia loadings could be simulated with good accuracy by variation of these coefficients, resulting in a loading-dependent understanding of experimental Raman spectra, serving as a foundation for the understanding of these catalysts in many applications.

1. Leon Schumacher, Christian Hess, Detailed Analysis of the Raman Vibrational Structure of Vanadia in VO_x/CeO_2: A Periodic Density Functional Theory Study, Manuscript.

Detailed Analysis of the Raman Vibrational Structure of Vanadia in VO_x/CeO_2: A Periodic Density Functional Theory Study

Leon Schumacher and Christian Hess*

Technical University of Darmstadt, Department of Chemistry, Eduard-Zintl-Institut für Anorganische und Physikalische Chemie, Peter-Grünberg-Str. 8, 64287 Darmstadt, Germany.

*Corresponding Author (E-Mail: christian.hess@tu-darmstadt.de)

Abstract

Supported vanadia is an important catalyst for oxidation reactions but its properties and catalytic activity heavily depend on the support material. Ceria is a promising support, due to its reducibility and active participation in many oxidation reactions. To understand these catalysts at work, operando spectroscopy is required, which can be difficult to interpret. To obtain a fundamental understanding of the Raman vibrational structure of VO_x/CeO_2, density functional theory (DFT) calculations was employed in this study. For that, structures established in the literature were used to calculate the vibrational frequencies and Raman intensities. First, the support size was optimized resulting in a $Ce_{48}O_{96}$ (111) cell. Monomeric and oligomeric structures were simulated based on VO and VO_2 clusters, resulting in V_nO_n (n=1-3) and V_nO_{2n} (n=1-7) oligomers. The latter were combined based on weighting factors determined from the experimental Raman vanadyl vibrational fine structure (measured by 514 nm excitation) and data on the thermodynamic stability of the clusters, yielding a simulated spectrum of a nuclearity distribution. By changing these weighting factors, vanadium coverage effects were simulated, which resulted in an overall agreement between experimental and theoretical spectra, giving detailed insight into the origin of the broad interface vibration regions and the vanadyl fine structure. Our study highlights the importance of DFT calculations to facilitate the assignment of spectral results and to obtain a detailed understanding of catalytic materials.

1. Introduction

Supported vanadia is already employed as a commercial catalyst in the synthesis of sulfuric acid and phthalic anhydride,[1] but also of great interest for the use in oxidation reactions, such as the oxidative dehydrogenation of alcohols and alkanes.[2–4] One of the most important aspects regarding its performance is the structure and nuclearity in which the vanadia is present on the surface. These properties have been a matter of great debate in the literature and depend heavily on the support that is used.[1,5] One of the more promising support materials is ceria, which has been used in many applications like the combustion of volatile organic compounds,[6,7] the low-temperature NH_3-selective catalytic reduction (SCR),[8,9] the oxidative dehydrogenation (ODH) of alcohols (methanol and ethanol),[3,10] and the ODH of short alkanes (propane, butane, cyclohexane).[4,11–13] Its favorable catalytic properties are often attributed to its reducibility and ability to regenerate vanadium (+V).[4,14–16]

Multiple approaches have been used, including in situ/operando spectroscopic methods and density functional theory (DFT) in an attempt to understand the complex behavior of vanadia supported on ceria (VO_x/CeO_2).[17–20]

On the experimental side, vibrational spectroscopy, especially Raman spectroscopy, is a useful and non-destructive tool to investigate the structure and nuclearity of VO_x/CeO_2 catalysts. The vibrational spectra exhibit broad contributions from V-O-Ce and V-O-V bonds, as well as a fine structure of the vanadyl bond (V=O), which allows to obtain information about the nuclearity of vanadia surface species.[4,11,17] However, the V-O-Ce and V-O-V regions are quite broad and a detailed understanding of their spectral shape is still missing. The fine structure of the vanadyl region is explained by the blue-shift caused by dipole-dipole coupling of V=O groups in vanadia aggregates.[21,22] This is a unique effect only observed for VO_x/CeO_2 as there is a much less detailed or even no fine structure of the vanadyl peak on other support materials,[23–25] which may suggest that the vanadyl groups are highly aligned in their geometry on ceria as to maximize the dipole-dipole coupling. Nevertheless, DFT calculations of different vanadia clusters supported on ceria show that the V=O bonds are not aligned,[14,26] leaving the question about the unique fine structure of vanadia on ceria up to debate.

On the theoretical side, multiple studies have investigated the structure and the properties of ceria and VO_x/CeO_2 systems.[14,18,26–30] Different monomeric clusters supported on ceria were previously investigated, showing different structural and

catalytic properties, depending on the amount of oxygen introduced with the vanadium atom.[27,29,30] Based on these calculations, the VO and VO_2 clusters were identified to be suitable for structure optimization of oligomeric species. Penschke et al.[14,26] calculated the structures and reactivities as well as the infrared (IR) frequencies of different clusters ranging from monomeric VO/VO_2 to V_8O_{16} clusters. It was shown that the symmetric ring structures like V_3O_6 and V_6O_{12} are especially stable while asymmetric chain and ring structures like V_2O_4, V_4O_8, V_5O_{10}, V_7O_{14}, and V_8O_{16} are characterized by lower stabilities and reducibilities. Due to the extensive amount of computing time used for the calculation of Raman intensities, Raman spectra of the VO_x/CeO_2 surface based on DFT calculations are distinctly missing from the literature. This is caused by the large necessary ceria cells, the fact that vanadia clusters introduce copious amounts of Ce^{3+} defects onto the ceria surface, as well as the variety of different vanadia structures present on the ceria surface at catalytically relevant temperatures.

In this study, we aim to develop a method to facilitate the calculation of Raman spectra based on established VO_x/CeO_2 structures[14,26,29] in order to enable the spectral assignments on a molecular level. First, the effect of the periodicity of the CeO_2 support on the monomeric structure is investigated for VO, VO_2, VO_3, and VO_4 monomers on CeO_2 (111) supports with p(2x2) ($Ce_{12}O_{24}$), p(3x3) ($Ce_{27}O_{54}$), and p(4x4) ($Ce_{48}O_{96}$) cell sizes, followed by a calculation of the Raman spectra of the VO_2 monomer and different oligomers (V_nO_{2n}; n=1-7) are calculated. Based on experimental Raman spectra and information on the thermodynamic stabilities of the nuclearities, DFT calculated spectra are then combined to simulate realistic spectra of a VO_x/CeO_2 catalyst at different vanadium surface densities (0.57, 1.36, and 2.83 V/nm^2). We show that this method allows for detailed understanding of Raman spectra of VO_x/CeO_2 catalysts and increases the level of information obtained by operando spectroscopic methods.

2. Computational and Experimental Section

Models and Structure Optimization. For the calculations of the VO_x/CeO_2 models, spin-polarized DFT in the DFT+U approach together with the projector-augmented-wave (PAW) method was used as implemented in the vienna ab initio simulation package (VASP version 5.4.4).[31–33] To correct for onsite Coulomb interaction of Ce 4f states, the Perdew-Burke-Ernzerhof (PBE)[34] exchange-correlation functional with a U value of 4.5 eV was used as previously demonstrated.[14,26,27,29,35] Hybrid functionals, like HSE06, were not used as the computation time for Raman intensities of larger structures used in this study (e.g. $V_7O_{14}/Ce_{48}O_{96}$) was already quite demanding. The PAW potentials used to describe the interactions between core and valence electrons regarded the Ce 4f, 5s, 5p, 5d, and 6s, the O 2s and 2p, as well as the V 3p, 3d, and 4s electrons as valence states with a plane-wave cut-off energy of 400 eV. The ceria surface was modeled using a periodic slab consisting of three O-Ce-O trilayers, employing the equilibrium bulk lattice constant[36] with a p(2x2), and p(3x3) periodicity (resulting in $Ce_{12}O_{24}$ and $Ce_{27}O_{54}$)[36,37] for the comparison between different monomers and periodicities, as well as p(4x4) (resulting in $Ce_{48}O_{96}$) for the oligomeric vanadia structures, each with a (111) surface termination, which is thermodynamically most stable.[38,39] The (4x4), (3x3), and (2x2) periodicities used (2x2x1), (3x3x1), and (3x3x1) Monkhorst grids, respectively.[40] The bottom ceria layer positions were fixed while the top two ceria layers and all V_nO_n and V_nO_{2n} clusters were allowed to fully relax. Monomeric vanadia was introduced as VO, VO_2, VO_3, and VO_4 clusters, as previously described in the literature,[27,29] while for vanadia oligomers, VO and VO_2 clusters were oligomerized. Since the VO cluster introduces three Ce^{3+} states per vanadium atom into the ceria lattice, the VO clusters were only oligomerized to V_2O_2 and V_3O_3. As a VO_2 cluster introduces only one Ce^{3+} state per vanadium atom into the ceria lattice, it was used for the oligomerization.[14,26] Therefore, the obtained oligomers were a V_2O_4 chain, a V_2O_4 ring, as well as V_3O_6, V_4O_8, V_5O_{10}, V_6O_{12}, and V_7O_{14} on $Ce_{48}O_{96}$. All VO_x/CeO_2 structures were calculated in their high-spin state for better comparability. The spin state was previously described to have a small influence on the overall structure and vibrational frequencies.[26] The positions of the Ce^{3+} ions were fixed to the positions reported in the literature.[14,26] The atoms were moved until the residual forces were <0.05 eV/Å. All structures were calculated from various initial positions until they closely resembled the established literature structures (identical bond lengths for the vanadia) for the best comparability.

Vibrational Analysis. Density functional perturbation theory (DFPT)[41] as implemented in VASP 5.4.4 was used to calculate the necessary force constants for the mass-weighted Hessian matrix required for vibrational analysis.[42] All atomic positions, except for those of the introduced VO_x cluster, were fixed in place for the vibrational analysis. It was previously shown by Penschke et al.[14,26], that this leads to slight shifts of the absolute vibrational frequencies, but that the positional difference between the peaks stays constant, allowing to shift the entire spectrum to obtain similar results. No imaginary frequencies were found for the investigated structures. The Raman scattering intensity was calculated from the resulting normal modes and the change in the dielectric tensor, resulting in the need for the third derivative of the energy with respect to the electric field and atomic positions.[43] The exact mathematical approach to calculate the change based on finite differences was previously published.[37] For the calculation of Raman intensities, a python script from Fornari and Stauffer was used.[44] Due to the large computational demand required for the calculation of Raman intensities (scaling with 36 N_{atom}), only the modes between 200 and 1100 cm^{-1} were calculated. To account for spectral line broadening, the resulting Raman intensities were multiplied with a Lorentzian function with a full width at half maximum (FWHM) of 10 cm^{-1} and a resolution of 0.1 cm^{-1}. The Raman spectra of each $V_nO_{2n}/Ce_{48}O_{96}$ structure were then convoluted using the nuclearity distribution obtained from experimental Raman spectra and their published thermodynamic stabilities based on DFT results.[14,26]

Experimental Raman Measurements. Using experimental Raman spectra the calculated Raman spectra of different vanadia clusters were combined to represent loading-dependent Raman spectra. Experimental Raman spectra were measured with Vis- (514 nm) and UV (385 nm) laser excitation, as described below. The preparation of the samples was based on the thermal decomposition of cerium nitrate to obtain CeO_2, which was subsequently loaded with different amounts of vanadium by incipient wetness impregnation, resulting in surface densities of 0.57, 1.36 and 2.83 V/nm². The detailed description of the synthesis can be found elsewhere.[4,11,15]

UV-Raman Spectroscopy. UV-Raman spectroscopy was performed at an excitation wavelength of 385 nm generated by a laser system based on a Ti:Sa solid state laser pumped by a frequency-doubled Nd:YAG laser (Coherent, Indigo). The fundamental wavelength is frequency doubled to 385 nm using a LiB_3O_5 crystal. The light is focused

onto the sample, and the scattered light is collected by a confocal mirror setup and focused into a triple stage spectrometer (Princeton Instruments, TriVista 555), as described previously.[45] Finally, the Raman contribution is detected by a charge-coupled device (CCD, 2048×512 pixels) cooled to –120 °C. The spectral resolution of the spectrometer is 1 cm^{-1}. For Raman measurements, 50 mg of the sample was placed in a CCR 1000 reactor (Linkam Scientific Instruments) equipped with a CaF$_2$ window (Korth Kristalle GmbH). The samples was then heated up to 365 °C and dehydrated for 1 h in a flow of 12.5% O$_2$/He (total flow: 40 ml$_n$/min) and was subsequently cooled to room temperature. A fluidized-bed reactor was employed to avoid laser-induced damage, allowing the use of a laser power of 9 mW at the location of the sample. Data processing included a cosmic ray removal and a background subtraction.

Visible Raman Spectroscopy. Vis-Raman spectroscopy was performed at 514 nm excitation, emitted from an argon ion gas laser (Melles Griot). The light was focused onto the sample, gathered by an optical fibre and dispersed by a transmission spectrometer (Kaiser Optical, HL5R). The dispersed Raman radiation was subsequently detected by an electronically cooled CCD detector (–40 °C, 1024×256 pixels). The spectral resolution was 5 cm^{-1} with a wavelength stability of better than 0.5 cm^{-1}. For Raman measurements, 50 mg of catalyst was filled into a CCR 1000 reactor (Linkam Scientific Instruments), equipped with a quartz window (Linkam Scientific Instruments). The samples was then heated up to 365 °C and dehydrated for 1 h in a flow of 12.5% O$_2$/He (total flow: 40 ml$_n$/min) and was subsequently cooled to room temperature. A fluidized-bed reactor was employed to avoid laser-induced damage, allowing the use of a laser power of 6 mW at the location of the sample. Data analysis of the Raman spectra included a cosmic ray removal and an auto new dark correction. The vanadyl peak was fitted with five Lorentzian functions at fixed positions after a previous background subtraction, using a least-square approach.

3. Results and Discussions

Raman spectra of individual V_nO_{2n} clusters. The detailed discussion of the periodicity-dependent structure of the monomeric clusters is given in the SI (see Figures and Tables S1-S3). Based on these structures, the Raman spectra were calculated (see Figure S4), showing that the p(4x4) cell ($Ce_{48}O_{96}$) is required to calculate an isolated monomer, which will therefore also be used in the oligomerization of the VO_2 cluster and the discussion of their spectra. Since the VO_3 and the VO_4 cluster show different electronic and geometric properties, leading to a vastly different vanadyl signature than those observed in experimental Raman spectra of VO_x/CeO_2 samples, these clusters are not suitable for the oligomerization.[27,29,30] The VO_2 cluster was preferred to the VO cluster for the oligomerization, as the oligomers based on the VO cluster are less stable and the high density of Ce^{3+} ions does not allow the VO unit to be oligomerized up to higher chain lengths than V_3O_3.[14] Such nuclearities are however observed in experimental Raman spectra, and therefore need to be taken into account. Nevertheless, the V_2O_2 and V_3O_3 oligomeric structures and Raman spectra based on the VO unit were also calculated for completeness and are shown in the SI (see Figures S5 and S6).

Figure 1 shows the structures of the short chain vanadia clusters supported on $Ce_{48}O_{96}(111)$ based on the oligomerization of VO_2 units. The V_2O_4 cluster was realized as a chain and a ring structure, since the energies of both clusters are similar. The averaged bond lengths of the structures are summarized in Table 1. The V-O-Ce bond refers to the bond distance between the vanadium atom and an oxygen atom introduced with the cluster (e.g. the angled V-O-Ce bond in VO_2 and the two angled V-O-Ce bonds in VO_3), while the interface bond refers to the bond distance of the vanadium atom and an oxygen atom of the topmost ceria lattice forming a V-O-Ce bond. This definition is also used throughout the rest of the manuscript and is relevant due to the different geometry of the interface bond based on the origin of the oxygen atom.
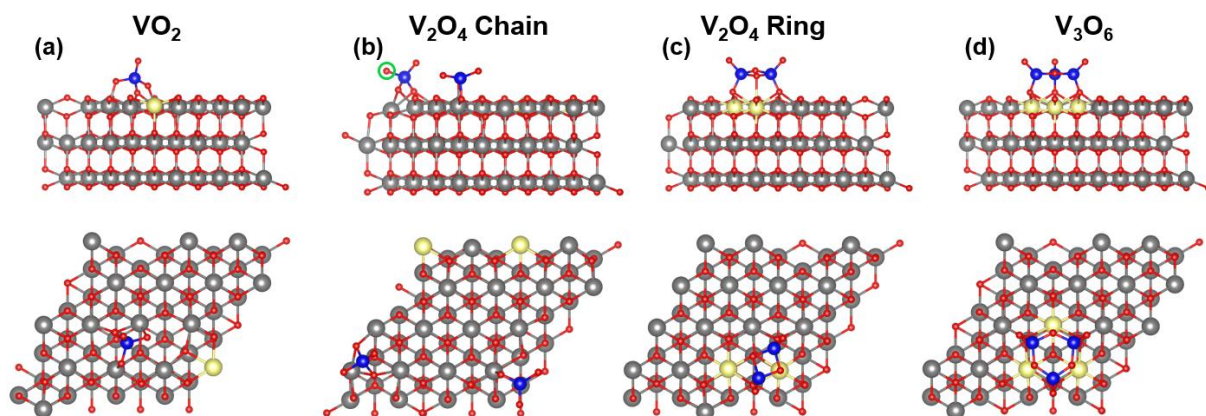
Figure 1: Structures of short-chain oligomeric V_nO_{2n} clusters: **(a)** monomeric VO_2, **(b)** a dimeric V_2O_4 chain, **(c)** a dimeric V_2O_4 ring, and **(d)** a V_3O_6 ring cluster supported on the CeO_2 (111) surface with a p(4x4) periodicity viewed from the side (top) and from above (bottom). Ce^{4+} and Ce^{3+} are shown in grey and light-yellow, respectively. V^{5+} and O^{2-} are shown in blue and red, respectively. This color-code is used throughout the rest of the manuscript. The V-O-V bridging atom of the V_2O_4 chain is highlighted with a green circle.

Table 1: Bond lengths (in pm) of different vanadium containing bonds in different short chain V_nO_{2n} (n=1-3) clusters supported on a CeO_2 (111) surface with a p(4x4) periodicity.

Cluster	V=O	V-O-V	V-O-Ce	Interface
VO_2	163	-	181	174
V_2O_4 Ring	162	183	-	175
V_2O_4 Chain	164	182	169	178
V_3O_6	162	182	-	174

In Figure 1a, the structure of the fully relaxed VO_2 is shown. The exact procedure of the monomeric calculations is given in the SI. The VO_2 cluster is introduced with two additional oxygen atoms, leading to an isolated oxidation state +IV. As vanadia is kept in oxidation state +V by ceria, one Ce^{3+} ion is created due to an electron transfer from vanadium to Ce^{4+}.[14,27,29] The introduced oxygen atoms are used for the vanadyl group and a V-O-Ce bond, which is angled in comparison to the other two interface bonds. These are formed by surface ceria lattice oxygen atoms binding to the vanadium atom. The whole cluster is tilted compared to the surface normal.

Figure 1b shows the fully relaxed V_2O_4 chain, which is similar to the isolated VO_2 cluster. The chain is placed on the border of the $Ce_{48}O_{96}$ (111) support cell, so

that the full chain is only present under periodic boundary conditions (PBC). However, to help with the clarity, the V-O-V bridging atom is highlighted (green circle in Figure 1b). Both Ce^{3+} ions introduced by the vanadia dimer are located next to the chain under PBC. Two of the introduced oxygen atoms are located in the V=O bonds of each vanadium atom. These are tilted in different directions in comparison to the surface normal, making the cluster asymmetric in this regard. One further oxygen atom is in the V-O-V bond, and the fourth oxygen forms an angled V-O-Ce bond on one side of the chain, compared to the interface bond formed using ceria surface lattice oxygen on the other side. This breaks the symmetry of the cluster further, as both chain ends are bound to the surface differently. This also explains the non-aligned V=O bonds. The V_2O_4 ring, on the other hand, includes two oxygen atoms in the V=O groups and the remaining two oxygen atoms in V-O-V bonds, leading to two interface bonds and no V-O-Ce bonds, increasing the symmetry of the cluster. The V=O bonds are also aligned in the same angle in regard to the cluster center. Additionally, the Ce^{3+} ions are located right next to the cluster, but due to the small size of the cluster, they have different distances from the interface bonds, leading to slightly shifted bond lengths (~1 pm). This is due to the fact that Ce^{3+} ions have larger radii than Ce^{4+} ions, slightly changing the bond geometry of their surroundings due to lattice expansion.[37,46,47]

The V_3O_6 cluster also forms a highly symmetrical ring, where three oxygen atoms are located in the V=O groups and the remaining three are bound in V-O-V bridges connecting the ring, whereas three interface bonds are formed by anchoring the cluster to the ceria surface via lattice oxygen. For the V_3O_6 ring, the location of the Ce^{3+} states is highly symmetrical in contrast to both V_2O_4 clusters, leading to highly identical bond lengths for all present bonds (<0.1 pm). This high degree of symmetry makes this cluster one of the most stable VO_2-based oligomers on the ceria surface. The results obtained for the clusters discussed above strongly resemble those published in the literature regarding structure and bond length.[14,27,29] The positions of the Ce^{3+} ions upon cluster deposition were replicated based on previously established models and were only allowed to deviate if the total energy of the system was lower than that reported before.[14] However, as the total energy is only weakly affected (by meV) by the position of the Ce^{3+} ions the overall structure of the models (bond lengths, angles, etc.) is not changed by a significant amount.

Figure 2 shows the Raman spectra of the short chain oligomers based on the structures shown in Figure 1. The spectra were not normalized due to the identical

support structures used. The Raman spectra of the VO, VO_3, and VO_4 clusters are discussed in dependence of the supports periodicity in the SI (see Figure S4). Only clusters supported on the p(4x4) support, resulting in $Ce_{48}O_{96}$ (111), will be discussed here, as this is the most suitable support for the calculation of isolated clusters not interacting with other clusters due to PBC.
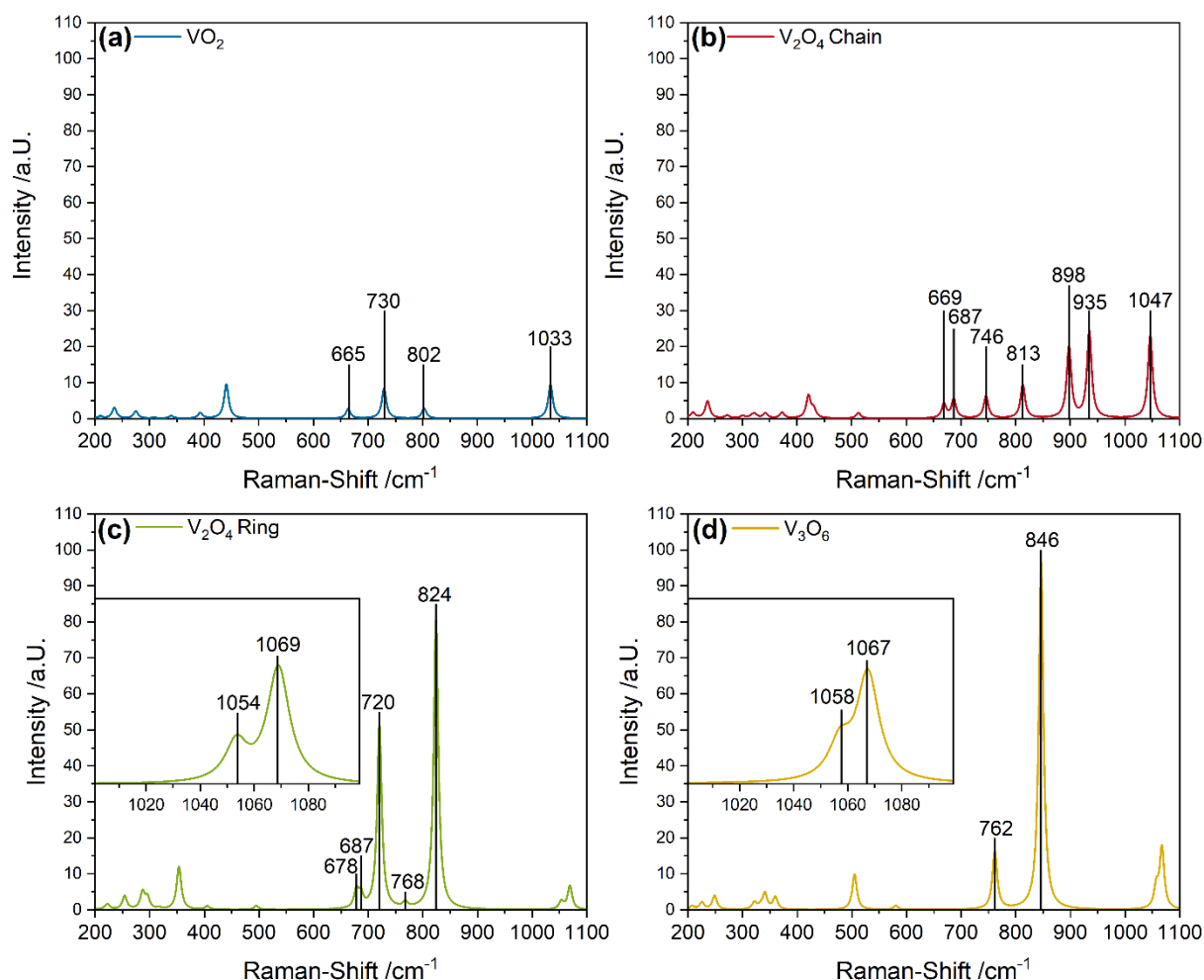
Figure 2: Raman spectra of **(a)** monomeric VO_2, **(b)** the V_2O_4 chain, **(c)** a V_2O_4 ring, and **(d)** a V_3O_6 ring cluster supported on the CeO_2 (111) surface with a p(4x4) periodicity. The insets provide an enlarged view of the vanadyl fine structure.

Since the peaks below 650 cm^{-1} are caused by the deformation vibrations of the same bonds that exhibit stretching vibrations with higher intensities above 650 cm^{-1}, they are not mentioned again in the discussion below.

Figure 2a shows the Raman spectrum of the VO_2 cluster, which shows more Raman active peaks compared to e.g. the VO cluster (see Figure S4), due to the angled V-O-Ce bond breaking the cluster symmetry. The V=O peak position is red-

shifted by 7 cm^{-1} to 1033 cm^{-1} in comparison to VO, while the symmetric stretching vibration of the V-O-Ce bond is added to the interface vibrations that were already observed for the VO cluster, resulting in the peaks within 600-850 cm^{-1}. The peaks below 600 cm^{-1} are caused by the deformation vibrations of the interface and V-O-Ce bonds. The intensity of the monomeric spectrum is low compared to those of the other clusters.

Figure 2b depicts the Raman spectrum of the V_2O_4 chain cluster and consists of seven relevant peaks above 650 cm^{-1}. The peak at 1047 cm^{-1} is caused by the stretching vibration of the vanadyl group on the side of the chain with an interface bond only, while the vibration of the vanadyl bond located on the side of the chain where the additional oxygen atom is used to form an angled V-O-Ce bond is located at 935 cm^{-1}, which is a shift of 112 cm^{-1} compared to the other vanadyl bond. This is caused by the introduction of asymmetry into the chain and the high degree of tilt towards the ceria surface, thus creating an interaction with the surface leading to the shift. The pair of peaks located at 898 and 813 cm^{-1}, as well as at 746 and 687 cm^{-1} originates from the symmetric and antisymmetric stretching vibrations of the V-O-Ce and the interface bonds, respectively, while the final peak at 669 cm^{-1} is caused by the V-O-V vibration of the chain. The V_2O_4 chain gives rise to a higher intensity than the VO_2 monomer, but, a lower intensity compared to the symmetric rings of V_2O_4 and V_3O_6. The Raman spectrum of the V_2O_4 ring, is characterized by seven intense peaks above 650 cm^{-1} including the vanadyl fine structure consisting of two vibrations located at 1069 and 1054 cm^{-1} (see inset). These are caused by the (more intense) symmetric and the antisymmetric stretching vibrations of the vanadyl bonds, which are much more symmetric in this cluster and do not interact with the ceria surface, resulting in similar Raman shifts. The V_2O_4 ring is more symmetric than the chain due to the fourth oxygen atom being bound in an additional bridging V-O-V bond, leading to the formation of interface bonds which use lattice oxygen only. The very intense peak at 824 cm^{-1} and the small peak at 768 cm^{-1} originate from by the symmetric and antisymmetric stretching vibrations of the interface bonds, while the very intense peak at 720 cm^{-1} is caused by the symmetric stretching vibration of both V-O-V bonds (ring breathing vibration). The additional smaller peaks at 687 and 678 cm^{-1} originate from antisymmetric stretching vibrations of the two V-O-V bonds (parallel and perpendicular to the V-V axis).

At last, the Raman spectrum of the V_3O_6 ring cluster exhibits four vibrations with a significant intensity above 650 cm^{-1}. The vanadyl peak shows a fine structure (see inset), including two V=O vibrations at 1067 and 1058 cm^{-1} caused by the symmetric and antisymmetric stretching vibrations of the three V=O oxygen atoms. The antisymmetric stretching vibration is degenerate and consists of two vibrations located at 1058 and 1057.8 cm^{-1}, representing the antisymmetric stretching vibration of two of the three V=O oxygen atoms each. Two Raman inactive vibrations at 855 cm^{-1} (degenerate) are caused by antisymmetric combination vibrations of interface and V-O-V bonds, leading to no significant change in polarization caused by the vibration. At 846 cm^{-1}, a characteristic symmetric stretching vibration of the entire interface is observed, which moves the whole V_3O_6 ring, thus resulting in a high intensity of the vibration. The last intense peak is located at 762 cm^{-1} and is caused by two degenerate symmetric interface and V-O-V combination vibrations.

The high degree of symmetry in the V_3O_6 ring cluster leads to a significant reduction in the amount of peaks compared to the other clusters, as many of the vibrations become degenerate. In contrast, these vibrations all have different energies if the cluster is asymmetric, leading to a larger amount of observable peaks. Hereby, the position of the Ce^{3+} ions is also important, which can change bond lengths slightly due to lattice expansion if they are not arranged symmetrically around the cluster. Additionally, the interface vibrations are much more intense and located at higher wavenumbers than the V-O-V vibrations, which are barely relevant for the Raman spectra of the above clusters. This seems to contradict experimental observations, where the V-O-V vibration is located at much higher Raman shifts than the interface/V-O-Ce vibrations.[11,21,48–50] However, experimental spectra do not only contain monomeric, dimeric and trimeric species, but rather a plethora of different nuclearities, including clusters with higher chain lengths.

Therefore, Figure 3 shows the structures of the long chain vanadia clusters (V_nO_{2n} with n=4-7) supported on the $Ce_{48}O_{96}$ (111) cell based on the oligomerization of VO_2 units. The bond lengths of the structures are summarized in Table 2 and are averaged. For deviations of the bond lengths by more than ±2 pm, the range is given in parentheses.
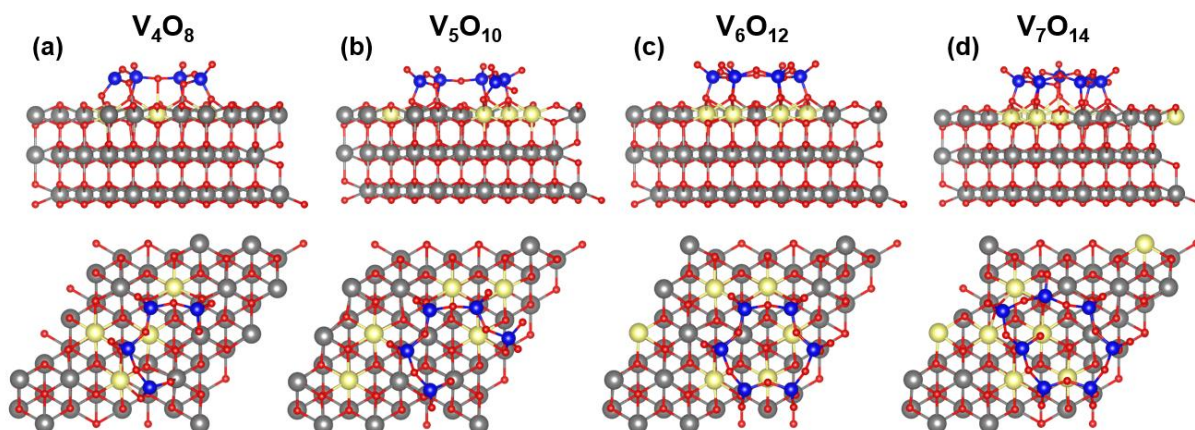
Figure 3: Structures of long chain oligomeric V_nO_{2n} clusters: **(a)** V_4O_8, **(b)** V_5O_{10}, **(c)** a V_6O_{12} ring, and **(d)** a V_7O_{14} ring cluster supported on the CeO_2 (111) surface with a p(4x4) periodicity viewed from the side (top) and above (bottom).

Table 2: Bond lengths (in pm) of different vanadia containing bonds in long chain V_nO_{2n} clusters supported on a CeO_2 (111) surface with a p(4x4) periodicity.

Cluster	V=O	V-O-V	V-O-Ce	Interface
V_4O_8	162	181 (177-186)	168	176
V_5O_{10}	162	181 (177-186)	172	178
V_6O_{12}	162	181	-	175
V_7O_{14}	162	181 (177-184)	-	175

The structures show similar Ce^{3+} positions compared to those published in the literature,[14,26] leading to very similar total energies and bond lengths. No imaginary frequencies were observed, verifying the calculation of the Raman spectra of the supported clusters. Similar to the structures already published, the bond lengths in the V_4O_8, V_5O_{10} and V_7O_{14} cluster vary in a range of ~10 pm, which is explained below.

In the V_4O_8 structure in Figure 3a, by adding another VO_2 unit, the ring structure observed the trimer is broken up and a chain is formed on the surface as the energetically most preferred structure. Of the eight oxygen atoms that are introduced together with the cluster, four constitute the vanadyl bonds while three are bound in V-O-V bonds bridging the vanadium atoms. The additional oxygen atom forms an angled V-O-Ce bond and the remaining four bonds anchoring the cluster to the ceria surface are interface bonds, leading to an asymmetric chain similar to the V_2O_4 chain.

14

Interestingly, the terminal vanadyl bond of the vanadium atom on the opposite side of the asymmetric V-O-Ce bond does not fully form a V=O bond, but rather a mix of a V=O and an additional V-O-Ce bond as the electron density in the bond is ~1.5. This leads to a more symmetric structure compared to other chains since both chain ends exhibit an angled bond, which leads to comparably harmonized V-O-Ce and interface bond lengths. The Ce^{3+} atoms are all positioned close to the cluster and three of them form a line below the vanadium atoms, while an additional defect is next to one of the two center vanadium atoms, slightly changing its interface bond length (<1 pm).

As shown in Figure 3b, the V_5O_{10} cluster exhibits a similar structure, where an open chain of five vanadium atoms is formed on the surface, containing five V=O bonds and four V-O-V bonds. Here, five V=O bonds with a binding order of 2 are present and only one additional asymmetric V-O-Ce bond is observed. The lack of an additional V-O-Ce/V=O bond, as observed for the V_4O_8 structure, might be caused by the higher chain length, which might decrease the influence of the introduced structural asymmetry. Overall, the open chains of the V_4O_8 and V_5O_{10} clusters show a higher degree of asymmetry than the ring structures, showing variations in the V-O-V, interface and V-O-Ce bond lengths. As a result, richer Raman spectra are expected.

The additional vanadium atom introduced by the V_6O_{12} ring leads to the formation of a highly symmetric ring (see Figure 3c), similar to the V_3O_6 structure, which exhibits a high degree of stability in agreement with the already established model.[26] For the V_6O_{12} ring, six of the oxygen atoms of introduced VO_2 create the V=O bonds, while the remaining six atoms constitute the V-O-V bonds. Due to the ring structure leading to an additional V-O-V bond, no additional oxygen atom is contained in V-O-Ce bonds and the cluster is anchored to the ceria surface by interface bonds only. Only the distribution of the Ce^{3+} ions is less symmetric, compared to the V_3O_6 ring, less symmetric, leading to slightly varying bond lengths for the interface bonds (1 pm).

In contrast, the V_7O_{14} cluster shown in Figure 3d, introduces an additional vanadium atom, which breaks the symmetry of the hexamer, forming an asymmetric ring. No additional asymmetry is introduced by V-O-Ce bonds and the ring is bound to the ceria surface by interface bonds only. Contrary to all other structures, the additional V=O bond introduced is oriented towards the inside of the ring structure. Overall, the structures for the long-chain oligomers strongly resemble those previously reported in the literature.[26]

Figure 4 shows the Raman spectra of the long-chain oligomers based on the structures discussed above (see Figure 3). Please note, that the intensity axis is scaled differently than in Figure 2 and changes for the V_7O_{14} cluster.
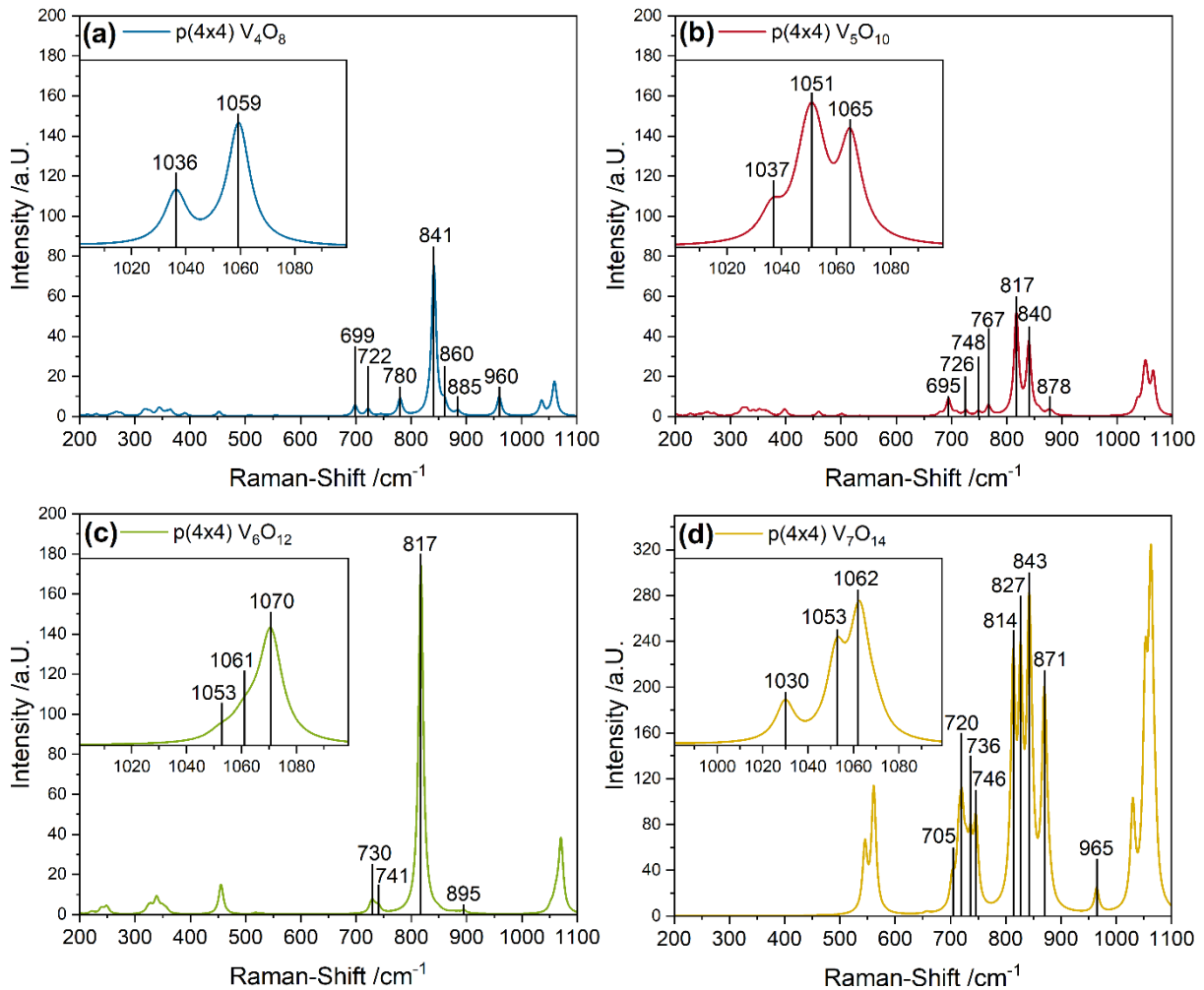
Figure 4: Raman spectra of **(a)** V_4O_8, **(b)** V_5O_{10}, **(c)** a V_6O_{12} ring, and **(d)** a V_7O_{14} ring cluster supported on the CeO_2 (111) surface with a p(4x4) periodicity. The V_7O_{14} Raman bands were calculated only starting at 500 cm^{-1} due to the low intensity of the peaks below 650 cm^{-1}. The insets show the vanadyl fine structure of each cluster.

In the following discussion, we focus on the peaks located above 650 cm^{-1}, for the same reasons as described above. The V_4O_8 cluster shows a spectrum, which contains nine peaks of relevant intensity above 650 cm^{-1} (see Figure 4a), and which due to the asymmetry is more complex than that of the short chain rings. As can be seen in the inset, the vanadyl fine structure contains two Raman active vibrations, at 1059 and 1036 cm^{-1}, originating from the simultaneous symmetric stretching vibrations of all V=O groups simultaneously and the symmetric stretching vibration of the terminal

V=O group, respectively. Another (Raman inactive) vanadyl mode is caused by the asymmetric stretching vibrations of the two middle V=O bonds. Additionally, the V=O/V-O-Ce bond that was formed during relaxation exhibits a stretching vibration at 960 cm^{-1}, red-shifted by ~80 cm^{-1} compared to the other V=O positions. The other vibrations observed are not isolated but include V-O-V, V-O-Ce, and interface combination vibrations. The feature at 885 cm^{-1} results from the symmetric stretching vibrations of V-O-V, V-O-Ce, and the interface bond of both terminal vanadium atoms, leading to an umbrella-like vibration. At 860 cm^{-1}, the vibration of the center V-O-V bond is located, which is almost a pure V-O-V vibration, while the most intense vibration at 841 cm^{-1} is a combination vibration, including the symmetric vibration of both outer V-O-V bonds as well as the symmetric stretching vibration of the two center interface bonds. These show a higher degree of symmetry, as they are more distant to the asymmetric edges of the V_4O_8 chain. The peak at 780 cm^{-1} is caused by the simultaneous symmetric stretching vibration of all four interface bonds, while the peak at 722 cm^{-1} is caused by the antisymmetric vibration of the two center interface bonds together with the stretching vibration of the center V-O-V bond. The last peak at 698 cm^{-1} is caused by the symmetric stretching vibration of all V-O-V bonds.

Similarly, due to its asymmetry, the V_5O_{10} structure gives rise to a rich Raman spectrum (see Figure 4b), including three distinct peaks as part of the vanadyl fine structure (see inset). The peak at 1065 cm^{-1} is caused by the stretching vibration of the center V=O bond, the peak at 1051 cm^{-1}, by the three center V=O bonds, exhibiting a degenerate vibration, and the peak at 1037 cm^{-1}, by the symmetric stretching vibration of the terminal V=O bonds. Due to the absence of a mixed V=O/V-O-Ce bond, there are no peaks in the region between 900 and 1000 cm^{-1}. The remaining peaks are combination vibrations of multiple bonds. At 878 cm^{-1} a doubly degenerate V-O-V vibration, containing antisymmetric and symmetric contributions from interface bonds, is observed. The more intense peaks at 840 and 817 cm^{-1} are caused by the combination vibration of the outer V-O-V bonds and the symmetric stretching vibration of interface bonds, as well as an umbrella-like vibration of terminal VO_4 on the opposite chain end of the terminal V-O-Ce bond. The remaining peaks between 767 and 695 cm^{-1} are caused by different antisymmetric combination vibrations of V-O-V and interface bonds, explaining the low intensities of the vibrations.

In comparison to the more asymmetric long-chain clusters, the highly symmetric V_6O_{12} ring cluster exhibits significantly less peaks compared, further reinforcing that

the degree of symmetry is important for the overall appearance of the Raman spectrum.[51–53] The vanadyl region of the V_6O_{12} structure is characterized by a single peak with a pronounced asymmetry towards lower wavenumbers. It consists of six different peaks, with the maximum peak intensity being located at 1070 cm^{-1}, representing the simultaneous symmetric stretching vibration of all six V=O groups, as well as five less intense peaks between 1064 and 1052 cm^{-1}, originating from different combinations of antisymmetric stretching vibrations of different vanadyl groups. The symmetry of the V_6O_{12} ring leads to the absence of any terminal V=O vibrations or vibrations close to angled V-O-Ce bonds. Besides the peak at 895 cm^{-1}, there are five additional peaks with low intensities between 885 and 845 cm^{-1} that are caused by different combinations of antisymmetric V-O-V stretching vibrations. The most intense peak in the spectrum, located at 817 cm^{-1}, is caused by the symmetric stretching vibration of all interface bonds, moving the whole ring up and down, similar to the most intense peaks observed for the V_2O_4 ring and V_3O_6 cluster (see Figure 2). Thus, this peak appears to be a unique feature of ring structures. The remaining peaks at 741 and 730 cm^{-1} are the asymmetric vibrations of the interface modes, which also consist of multiple peaks with low intensities, comparable to the region between 895 and 845 cm^{-1}. Summarizing the overall spectrum of the V_6O_{12} ring is dominated by two vibrations, the vanadyl and the interface stretching vibrations.

The V_7O_{14} ring, on the other hand, is less symmetric due to the additional vanadium atom, resulting in 12 clearly defined peaks. The vanadyl fine structure consists of seven peaks, three of which are Raman inactive and one of which is shifted to below 1000 cm^{-1}. The three intense peaks above 1000 cm^{-1} are located at 1062, 1053, and 1030 cm^{-1} and are caused by the symmetric stretching vibration of the two V=O bonds neighboring the tilted one, of the next two and of the two opposite bonds, respectively. The peak at 965 cm^{-1} is caused by the tilted vanadyl bond itself. The peak at 871 cm^{-1} consists of multiple peaks that are almost degenerate and are caused by different combinations of symmetric V-O-V vibrations of the ring, while the remaining peaks between 843 and 817 cm^{-1} are all caused by combinations of symmetric interface stretching vibrations. The peaks at 827 and 814 cm^{-1} originate from an interface stretching vibration similar to those in V_2O_4, V_3O_6, and V_6O_{12}, but split into two vibrations due to the asymmetry in the ring. Finally, the peaks between 746 and 705 cm^{-1} result from the asymmetric component of the same vibrations causing the vibrations between 843 and 817 cm^{-1}.

Overall, the symmetry of the cluster strongly determines the Raman vibrational signature as asymmetries introduce additional peaks. The most intense vibrations are caused by symmetric interface vibrations of vanadia rings, while V-O-V bonds do not significantly contribute to the Raman spectrum up to the V_6O_{12} ring. The remaining features in the spectra of the smaller clusters between 900 and 1000 cm^{-1} show small intensities and originate from vanadyl groups that are located close to the surface with a lowered electron density in the V=O double bond, leading to a binding order of ~1.3-1.8, which can be described as a V-O-Ce/V=O mixed bond. However, these have small intensities. The spectra of the long-chain clusters underlines that the observed vibrational structure cannot be assigned to individual vibrations, but rather a combination of vibrations.

Simulation of Experimental Spectra. Real supported VO_x/CeO_2 samples consist of a combination of different surface structures with different nuclearities.[4,21,22] Thus, to approximate an experimental spectrum the calculated spectra were combined, starting with the vanadyl fine structure as a basis. Figure 5 shows the Raman spectra of the vanadyl region of VO_x/CeO_2 samples loaded with 0.57, 1.36, and 2.83 V/nm² recorded at 514 nm excitation after dehydration at 365 °C for 1 h in a 12.5% O_2/He flow and subsequent cooling to room temperature. The vanadyl regions show a fine structure that is commonly explained by nuclearity-dependent dipole-dipole coupling of the V=O oscillators[4,21,22,45,54,55] and which was deconvoluted by using five Lorentzian functions, representing the monomeric, dimeric, trimeric, tetrameric, and oligomeric contributions, respectively, as described previously.[4,11]
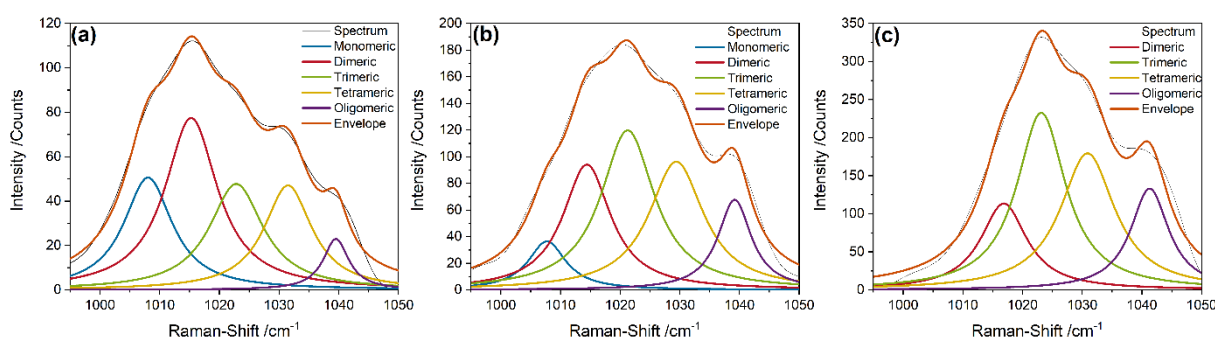

Figure 5: Experimental vanadyl regions of ceria-supported vanadia samples with surface densities of **(a)** 0.57, **(b)** 1.36, and **(c)** 2.83 V/nm² from Raman spectra recorded at 514 nm excitation after dehydration of the sample in 12.5% O_2/He for 1 h at 365 °C and subsequent cooling to room temperature. The peak fit analysis is described in detail in the experimental section.

The areas for the monomeric, dimeric, trimeric, tetrameric, and oligomeric contributions, resulting from the above fit analysis, were converted into relative contributions to the overall vanadyl peak, which are summarized in the SI (see Table S5). As the experimental spectrum only shows one contribution for the dimeric and oligomeric peaks, while there are two (V_2O_4 chain and ring) and three (V_5O_{10}, V_6O_{12}, and V_7O_{14}) different DFT-based spectra for these contributions, respectively, the calculated spectra were weighted based on their DFT-based thermodynamic stability (see Table S6) and summarized as one dimeric and one oligomeric DFT-based contribution (see Table S5).[14,26] Based on these values, the DFT spectra can then be combined into an experimental spectrum and the effect of the coverage is introduced by the different weighting factors. Table 3 summarizes the weighting factors for the different DFT spectra, based on the experimental vanadyl peak and the relative thermodynamic stabilities for dimeric and oligomeric peaks.

Table 3: Relative intensity contribution of each V_nO_{2n} cluster on a CeO_2 (111) surface with a p(4x4) periodicity based on the relative amounts of the respective nuclearity determined from the experimental vanadyl peak (see Table S5). For peaks in which multiple clusters (dimeric and oligomeric) are contained, the individual clusters are scaled by their relative stabilities (compare Table S6).

Experimental Nuclearity	Vanadia Cluster	Cluster Contribution to the Spectrum		
		0.57 V/nm²	1.36 V/nm²	2.83 V/nm²
Monomeric	VO_2	0.206	0.070	0
Dimeric	V_2O_4 Ring	0.171	0.114	0.083
	V_2O_4 Chain	0.171	0.114	0.083
Trimeric	V_3O_6	0.215	0.324	0.361
Tetrameric	V_4O_8	0.189	0.264	0.311
Oligomeric	V_5O_{10}	0.006	0.013	0.018
	V_6O_{12}	0.035	0.080	0.114
	V_7O_{14}	0.009	0.021	0.030

Figure 6 shows the Raman spectrum as a combination of contributions from the V_nO_{2n} clusters (n=1-7), using the determined weighting factors for the VO_x/CeO_2 sample loaded with a vanadia surface density of 1.36 V/nm². The spectrum was added to the Raman spectrum of a clean surface $Ce_{48}O_{96}$ (111) cell for best comparability. The Raman shift for the bare ceria calculated by DFT was shifted to the experimental F_{2g} peak before adding it to the vanadia spectrum, resulting in a shift factor of 1.075.

The vanadia contribution was also shifted before the addition so that the monomeric contribution was at the same positions (i.e. at 1008 cm^{-1}) for DFT and experimental spectra, resulting in a shift factor of 0.973. The individual weighted contributions from the DFT-based Raman spectra are highlighted for each cluster in different colors. The combined spectra based on the experimental vanadyl peak of the 0.57 and 2.83 V/nm² sample are shown in the SI (see Figure S7).
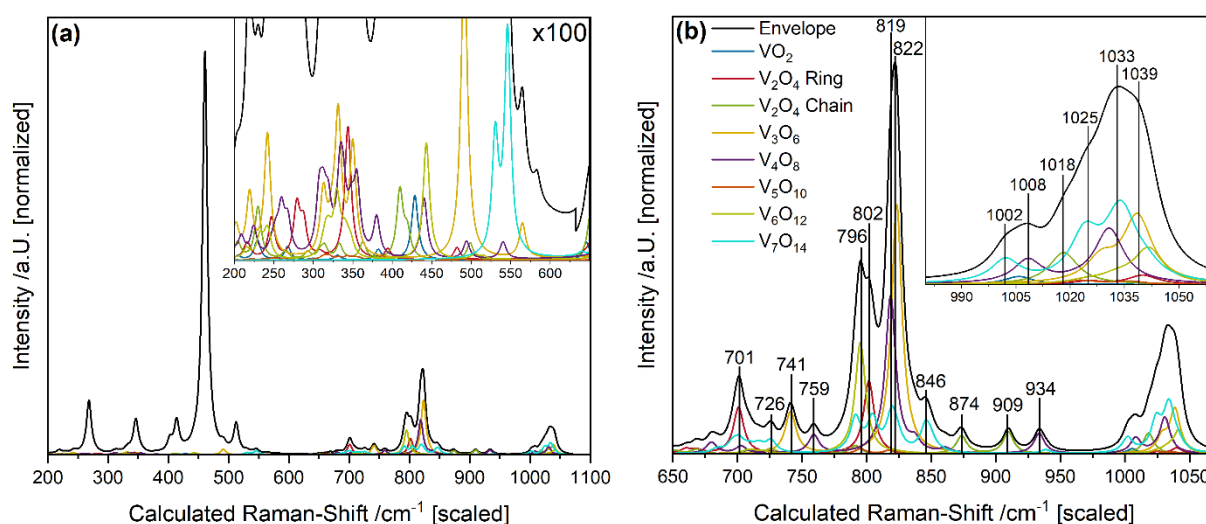

Figure 6: (a) Combined Raman spectrum of a CeO$_2$ (111) trilayer with a p(4x4) periodicity and the Raman spectra of the individual V$_n$O$_{2n}$ vanadia clusters based on the vanadyl fine structure of an experimental Raman spectrum of CeO$_2$ loaded with 1.36 V/nm². The inset shows the region between 200 and 650 cm^{-1} zoomed in by a factor of x100. **(b)** Enlarged view of the vanadia-related region of the spectrum. The contributions of the individual clusters to the overall spectrum are highlighted in different colors and the most relevant peaks in the combined spectrum are marked. The inset shows the vanadyl fine structure.

The spectrum below 650 cm^{-1} is dominated by ceria, while vanadia contributions are negliable. Focusing the discussion on the spectral region above 650 cm^{-1}, shown in Figure 6b, the two most significant regions are located within 990-1060 cm^{-1} (mostly vanadyl vibrations) and within 775-875 cm^{-1} (mostly interface, ring and V-O-V vibrations), which includes contributions from dimeric to septameric clusters. In detail, the four low intensity peaks at 701, 726, 741, and 759 cm^{-1} originate from antisymmetric stretching vibrations of interface bonds of the indicated clusters (V$_2$O$_4$ ring, V$_3$O$_6$, V$_4$O$_8$, V$_7$O$_{14}$). In the region within 775-875 cm^{-1}, four main peaks are observed at 796, 802, 819, and 822 cm^{-1}, which originate from contributions of the V$_2$O$_4$ ring, the V$_3$O$_6$ ring, V$_4$O$_8$, the V$_6$O$_{12}$ ring and the V$_7$O$_{14}$ ring, highlighting that the

most intense region is dominated mostly by ring structures. Due to its thermodynamic stability, trimeric vanadia has the largest contribution to the spectrum, but also the V_4O_8 chain contributes significantly to the most intense peak. All of the features shown in this region originate from, at least in part, by symmetric stretching vibrations of the interface bonds, which are the most intense vibrations for ring strutures, and as the rings are very stable, these vibrations have significant relative contributions to the combined spectrum. Some of these vibrations also contain smaller contributions of V-O-V stretching as they are all combination vibrations. The features observed above 875 cm^{-1} are mainly caused by the asymmetrically oriented V=O bonds of the V_2O_4 chain, the V_4O_8 chain, and the V_7O_{14} ring, resulting in the peaks at 874, 909, and 934 cm^{-1}, respectively. The vanadyl region shows a defined fine structure (see inset), which has six distinct contributions, separated by 6 to 10 cm^{-1}, consistent with the experimental results.[11,21,48,55] The fine structure is dominated by the contributions of oligomeric species even at lower Raman shifts, where the V_7O_{14} ring exhibits the lowest contribution at 1002 cm^{-1}. However, following the assignments of the experimental vanadyl peak, contributions from monomers at 1008 cm^{-1}, from dimers at 1018 cm^{-1}, from trimers at 1029 cm^{-1}, from tetramers at 1031 cm^{-1} and mutliple ones from oligomers above 1033 cm^{-1} can be observed, which is consistent with the observed shifts in the experiment. Nevertheless, it is important to consider that these assignments are somewhat simplified, as the regions of traditionally assigned nuclearities also exhibit additional (mostly antisymmetric) vibrations from higher nuclearities.

Regarding the combined DFT spectra as a function of vanadium loading, a loading-dependent behavior consistent with the expectations is observed. The intensity of the vanadyl peak (especially above 1020 cm^{-1}) and of vibrational features within 775-875 cm^{-1} increases with increasing vanadia coverage, as the contributions shift from mainly mono- and dimeric contributions at low vanadium loadings to mainly tri- to oligomeric contributions at higher vanadium loadings.

To evaluate the importance of the DFT-based Raman spectra simulating a nuclearity distribution, Figure 7 shows a comparison between theoretical and experimental Raman spectra of VO_x/CeO_2 samples with vanadia surface densities of 0.57, 1.36 and 2.83 V/nm² recorded at 385 and 514 nm excitation, the contributions and structures of the individual clusters are shown as line spectra. Calculated spectra were shifted as described above (see Figure 6). The excitation wavelengths of the

experimental spectra were chosen based on the best comparability with the DFT spectra. A comparison between all excitation wavelengths and DFT spectra is given in the SI (see Figure S8).
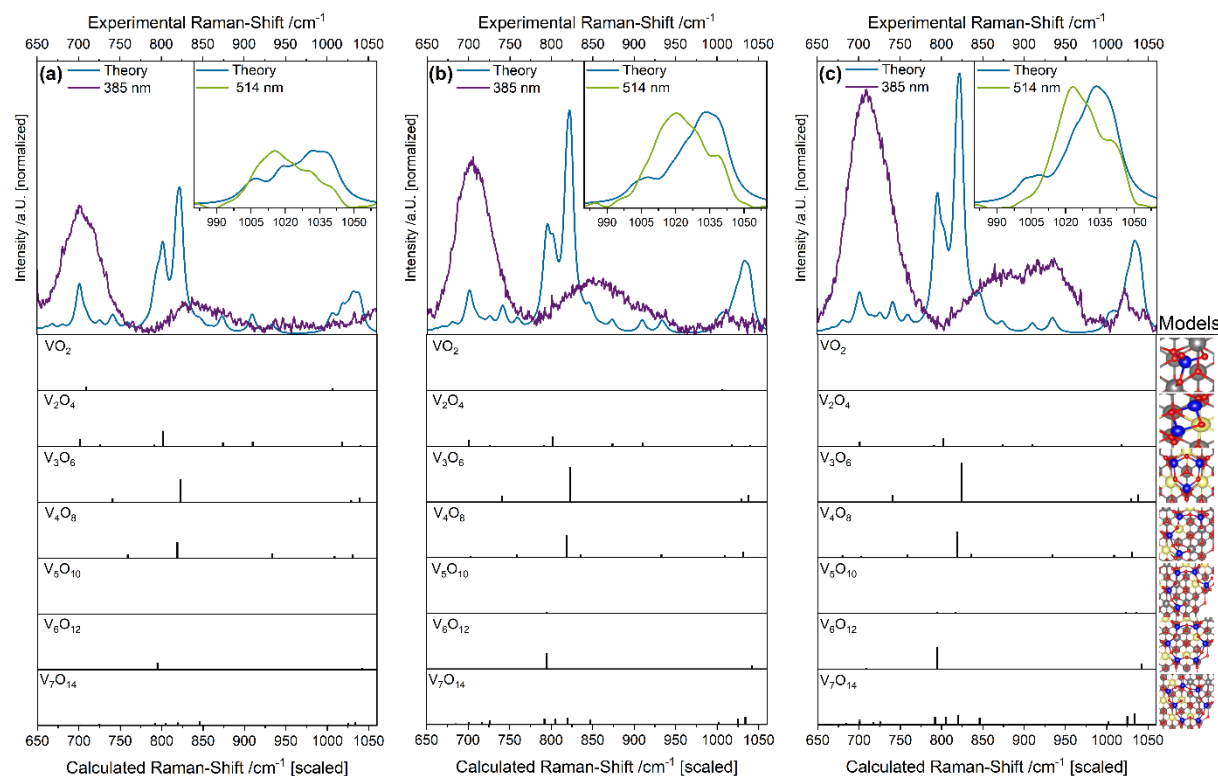
Figure 7: Comparison between experimental Raman spectra (385 nm, 514 nm) and calculated Raman spectra based on individual Raman spectra of vanadia clusters for vanadium densities of **(a)** 0.57, **(b)** 1.36, and **(c)** 2.83 V/nm². Below the spectra, calculated contributions from the individual vanadia clusters to the overall spectra as well as the underlying cluster are shown. For the dimeric cluster, the V_2O_4 ring is shown as the model structure, but the V_2O_4 chain was also used. For details, see text.

Figure 7 shows an overall agreement between the experimental and the theoretical spectra in regard to the peak positions. The agreement between the spectra with respect to the intensity ratios is moderate, but can be explained by multiple effects that were not included in the calculations (resonance enhancement, temperature, absorption behavior). Starting with a vanadium surface density of 0.57 V/nm², Figure 7a shows the comparison of the DFT-based spectrum with the UV-Raman spectrum recorded at 385 nm excitation in the V-O-Ce and V-O-V regions, while the inset compares the vanadyl region with the 514 nm experimental Raman spectrum. This was done to account for the respective resonance enhancements to achieve the best

comparability, which were described in detail in the previous literature.[4,11] Apparently, at this loading, there is good agreement in position within the region 650-750 cm^{-1}, originating from short-chain V-O-Ce/interface modes, which are resonance enhanced at this wavelength, explaining the discrepancy in intensity.[4,55] The highest intensities in the DFT-based spectrum are observed within 750-850 cm^{-1} and originate from symmetric interface stretching vibrations of ring species, in particular V_3O_6, V_4O_8 and V_6O_{12} which fits very well with the V-O-Ce assignment of the experimental spectrum at 820 cm^{-1}.[21] This assignment also explains the lower intensity, as this region is dominated by interface vibrations originating from higher chain length species than those resonance enhanced at this wavelength. At 385 nm, only short-chain vanadia is enhanced, which is most prominent within 650-750 cm^{-1}, while longer chains would be enhanced at higher wavelengths, leading to the lower spectral intensity in the UV-Raman spectrum.[55]

The peak at 920 cm^{-1} only increases significantly in intensity for the highest loading of 2.83 V/nm². As the loading is increased from 0.57 V/nm² to 2.83 V/nm², the distribution of the clusters strongly shifts towards oligomeric structures, but the peaks in the region around 920 cm^{-1} do not significantly increase in intensity and are still mainly caused by the asymmetric vanadyl peaks of the V_2O_4 and V_4O_8 chains, with an additional small contribution from the asymmetric, inwards facing V=O group of the V_7O_{14} ring. As the experimental vanadyl peak does not resolve oligomeric structures above the tetrameric nuclearity, it is possibly also that structures with higher nuclearities contribute to the experimental spectrum (e.g. V_8O_{16}, V_9O_{18}, $V_{10}O_{20}$, etc.) that were not considered in this study due to limitations in the computation time, as they would necessitate even larger ceria supports (p(5x5)). However, due to the significant contribution of the asymmetric V_7O_{14} ring, it seems likely that species with even higher nuclearities would increase the intensities in this region as they are also asymmetric rings, as shown before.[26] Therefore, this region can be assigned to stretching vibrations of V=O groups in an asymmetric environment of high chain lengths. This is in agreement with the high loading required for this peak to become clearly visible in the experimental Raman spectrum. V-O-V based vibrations are mostly irrelevant for the DFT-based spectra, as they are mostly Raman inactive, due to their antisymmetry, especially at higher nuclearities. In the experimental spectra, V-O-V species are assigned to the position at 920 cm^{-1},[21] which shows a small intensity at the lowest and an increasing intensity with an increasing loading. The position of some

calculated peaks are also at this position and originate from the shifted V=O vibrations of asymmetric V_2O_4 and V_4O_8 clusters, which were already discussed above (see Figures 1-4).

Regarding the vanadyl fine structures, the position of the monomeric peak was shifted to its experimental value of 1008 cm^{-1}, resulting in a good agreement with the experimental positions for all nuclearities. With increasing vanadium loading, there are more significant contributions from oligomeric species, as manifested by the overall blue-shift of the vanadyl peak both in experiment and theory, as evidenced by the fit analysis (see Figure 5 and Table 3).[21,22] However, the classic assignment of larger nuclearities to higher wavenumbers is only partly correct, as discussed above (see Figure 6). The intensity distribution of the experimental spectra is also influenced by resonance effects, which are not accounted for in the DFT-based spectra, and therefore, a divergence in their intensity is observed.

Coverage-based effects are also portrayed by the DFT-based spectra, as the intensity increase in the region within 650-850 cm^{-1}. The intensity increase and overall blue-shift in the vanadyl region is also well reflected. Both effects can be explained by a shift towards larger structures (e.g. V_4O_8, V_6O_{12}, and V_7O_{14}) when the loading density is increased from 0.57 to 2.83 V/nm².

In general, the approach described above appears suitable to obtain a more detailed understanding of the Raman spectra of VO_x/CeO_2. It also strongly facilitates the interpretation of spectra on a molecular level by combining the spectra of singular clusters.

4. Conclusion

In this study, we calculated Raman spectra of VO_x/CeO_2 based on multiple literature-known structures of VO_x clusters supported on CeO_2 (111), enabling molecular-level interpretation of the VO_x/CeO_2 vibrational structure of experimental spectra, which is of high relevance for a detailed fundamental understanding but also regarding catalytic applications of VO_x/CeO_2 systems.[3,4,6–13,15,16] The spectra of single clusters were combined by using experimental data allowing to define weighting factors for the different nuclearities allowing to simulate nuclearity distributions and analyze loading-dependent effects.

The calculation of monomeric clusters was performed on ceria cell sizes of different periodicity, which resulted in similar structures but shifts in the peak positions. Especially the vanadyl stretching vibration showed a red-shift with increasing support cell size, which correlates well with the increased distance between the monomeric structures, indicating that monomeric clusters show interactions beyond the boundaries of the p(2x2) and p(3x3) support cells. This is caused by dipole-dipole interactions with the next monomeric cluster due to periodic boundary conditions, which leads to a red-shift for larger cells, reflecting the decreasing intermolecular distance. Therefore, the largest cell size of $Ce_{48}O_{96}$ (111) p(4x4) is the most suitable to investigate isolated monomeric clusters and oligomers.

Based on this analysis, short-chain V_nO_{2n} (n=1-3) and long-chain oligomeric (n=4-7) structures were established and their Raman spectra were calculated.[14,18,26,27,29] The Raman spectra are dominated by the vanadyl stretching vibration and combination vibrations with significant contributions of symmetric interface vibrations, which were especially intense for symmetric rings like V_3O_6 and V_6O_{12}. Overall, the degree of symmetry of the V_nO_{2n} cluster was highly important for the appearance of the Raman spectrum.

To interpret experimental spectra, the obtained spectra for the single clusters were combined after weighting their contributions based on the experimental vanadyl fine structure of VO_x/CeO_2 samples with vanadium loadings of 0.57, 1.36, and 2.83 V/nm². The dimeric and oligomeric contributions were weighted by their thermodynamic stabilities, as there were more individual cluster spectra than resolvable contributions in the experimental vanadyl region. The combined spectra show contributions from different clusters, depending on the simulated surface density and show an overall good agreement with the experimental spectra, recorded at two

different excitation wavelengths. The spectra exhibit a vanadyl fine structure, consisting of many V=O stretching vibrations, which are generally located at higher wavenumbers for higher nuclearities, in agreement with the experimental interpretation.[22] However, the asymmetric V=O stretching vibration of higher nuclearities was also located at lower positions, which overlaps e.g. monomeric contributions in the vanadyl region. The experimentally broad V-O-Ce and V-O-V regions were resolved in detail and the V-O-Ce regions at ~710 and 820 cm^{-1} were assigned to short-chain and long-chain contributions, respectively. The V-O-V area at 920 cm^{-1} originates from V=O bonds of asymmetric vanadia chains (V_2O_4 and V_4O_8) with a low electron density in the double bond. In addition, it seems likely that additional contributions from long nuclearities with ≥8 vanadium atoms might occur but these structures were not calculated here. It would also be in agreement with the high loading necessary to obtain an intensity increase at this position in the experimental spectra.

To further increase the quality of the calculated spectra, multiple approaches are available. First, higher nuclearities like V_8O_{16}, and even vanadia monolayers based on literature results can be considered,[26] which might be relevant to the spectral shape, especially in the 900-950 cm^{-1} region. Furthermore, the introduction of oxygen vacancies into the system might significantly change the vibrational structure of some of the clusters, as was already shown for monomeric structures, which are able to structurally relax into those vacancies. These can also be regarded in the weighting factors by quantifying the defect peak and F_{2g} position of ceria. Resonance effects are also important to calculated precise intensities and might be regarded. At last a temperature can be introduced to account for temperature-dependent behavior, which might be relevant due to the differing thermodynamic stabilities of certain clusters, which might additionally influence the nuclearity distribution.

In summary, the calculation of Raman spectra of VO_x/CeO_2 based on established DFT structures of V_nO_{2n} was successful. By combination of individual clusters' spectra, experimental spectra of different vanadia coverages were simulated with overall agreement, enabling a molecular-level interpretation of vibrational Raman spectra. VO_x/CeO_2 catalysts are of great interest to academic research and are applied in many catalytic reactions. Their functioning is commonly investigated by operando methods and for vanadia systems, Raman spectroscopy has been shown to be one of the most important techniques. Therefore, the spectra obtained in this study are of great importance for an improved understanding of their mode of operation under

working conditions and the rational design of better catalysts. The outlined approach is readily transferable to other relevant systems, such as VO_x/TiO_2 or MoO_x-based catalysts, which also exhibit some form of vanadyl nuclearity distribution.[56,57]

Declaration of Competing Interest

The authors declare that they have no known competing financial interests or personal relationships that could have appeared to influence the work reported in this paper.

Supporting Information

The supporting information contains the periodicity-dependent structures and Raman spectra of monomeric vanadia clusters, structures and Raman spectra of V_nO_n clusters (n=1-3) and additional information about the combination of individual spectra into an overall spectrum and the combined DFT spectra at different surface densities.

References

(1) Wachs, I. E. Catalysis science of supported vanadium oxide catalysts. *Dalton Trans.* **2013**, *42* (33), 11762–11769. DOI: 10.1039/c3dt50692d.

(2) Rogg, S.; Hess, C. CO_2 as a soft oxidant for propane oxidative dehydrogenation: A mechanistic study using operando UV Raman spectroscopy. *J. CO2 Util.* **2021**, *50* (9), 101604. DOI: 10.1016/j.jcou.2021.101604.

(3) Ober, P.; Rogg, S.; Hess, C. Direct Evidence for Active Support Participation in Oxide Catalysis: Multiple Operando Spectroscopy of VO_x/Ceria. *ACS Catal.* **2020**, *10* (5), 2999–3008. DOI: 10.1021/acscatal.9b05174.

(4) Schumacher, L.; Hess, C. The active role of the support in propane ODH over VO_x/CeO_2 catalysts studied using multiple operando spectroscopies. *J. Catal.* **2021**, *398* (13), 29–43. DOI: 10.1016/j.jcat.2021.04.006.

(5) Weckhuysen, B. M.; Keller, D. E. Chemistry, spectroscopy and the role of supported vanadium oxides in heterogeneous catalysis. *Catal. Today* **2003**, *78* (1-4), 25–46. DOI: 10.1016/S0920-5861(02)00323-1.

(6) Guan, Y.; Li, C. Effect of CeO_2 Redox Behavior on the Catalytic Activity of a VO_x/CeO_2 Catalyst for Chlorobenzene Oxidation. *Chin. J. Catal.* **2007**, *28* (5), 392–394. DOI: 10.1016/S1872-2067(07)60033-3.

(7) Dai, Q.; Yin, L.-L.; Bai, S.; Wang, W.; Wang, X.; Gong, X.-Q.; Lu, G. Catalytic total oxidation of 1,2-dichloroethane over VO_x/CeO_2 catalysts: Further insights via isotopic tracer techniques. *Appl. Catal. B: Environ.* **2016**, *182*, 598–610. DOI: 10.1016/j.apcatb.2015.10.016.

(8) Peng, Y.; Wang, C.; Li, J. Structure–activity relationship of VO_x/CeO_2 nanorod for NO removal with ammonia. *Appl. Catal. B: Environ.* **2014**, *144*, 538–546. DOI: 10.1016/j.apcatb.2013.07.059.

(9) Zhang, T.; Chang, H.; Li, K.; Peng, Y.; Li, X.; Li, J. Different exposed facets VO_x/CeO_2 catalysts for the selective catalytic reduction of NO with NH_3. *Chem. Eng. J.* **2018**, *349*, 184–191. DOI: 10.1016/j.cej.2018.05.049.

(10) Vining, W. C.; Strunk, J.; Bell, A. T. Investigation of the structure and activity of VO_x/CeO_2/SiO_2 catalysts for methanol oxidation to formaldehyde. *J. Catal.* **2012**, *285* (1), 160–167. DOI: 10.1016/j.jcat.2011.09.024.

(11) Schumacher, L.; Weyel, J.; Hess, C. Unraveling the Active Vanadium Sites and Adsorbate Dynamics in VO_x/CeO_2 Oxidation Catalysts Using Transient IR Spectroscopy. *J. Am. Chem. Soc.* **2022**, *144* (32), 14874–14887. DOI: 10.1021/jacs.2c06303. Published Online: Aug. 2, 2022.

(12) Sánchez-García, J.-L.; Handy, B. E.; Rodríguez, Á. G.; González-Chávez, M. M.; García de León, R.; Cardenas-Galindo, M.-G. Relating the Synthesis Method of VO_x/CeO_2/SiO_2 Catalysts to Red-Ox Properties, Acid Sites, and Catalytic Activity for the Oxidative Dehydrogenation of Propane and n-Butane. *Top. Catal.* **2022**, *65* (13-16), 1408–1418. DOI: 10.1007/s11244-022-01661-y.

(13) Samek, I. A.; Bobbitt, N. S.; Snurr, R. Q.; Stair, P. C. Structure and activity of mixed VO_x-CeO_2 domains supported on alumina in cyclohexane oxidative dehydrogenation. *J. Catal.* **2020**, *384*, 147–158. DOI: 10.1016/j.jcat.2020.02.017.

(14) Penschke, C.; Paier, J.; Sauer, J. Oligomeric Vanadium Oxide Species Supported on the CeO_2(111) Surface: Structure and Reactivity Studied by Density Functional Theory. *J. Phys. Chem. C* **2013**, *117* (10), 5274–5285. DOI: 10.1021/jp400520j.

(15) Schumacher, L.; Ziemba, M.; Brunnengräber, K.; Totzauer, L.; Hofmann, K.; Etzold, B. J. M.; Albert, B.; Hess, C. Understanding the Reduction Behavior of VO_x/CeO_2 on a Molecular Level: Combining Temperature-Programmed Reduction with Multiple In-Situ Spectroscopies and X-ray Diffraction. *J. Phys. Chem. C* **2023**, *127* (12), 5810–5824. DOI: 10.1021/acs.jpcc.3c00622.

(16) Duchoň, T.; Hackl, J.; Mueller, D. N.; Kullgren, J.; Du, D.; Senanayake, S. D.; Mouls, C.; Gottlob, D. M.; Khan, M. I.; Cramm, S.; Veltruská, K.; Matolín, V.; Nemšák, S.; Schneider, C. M. Establishing structure-sensitivity of ceria reducibility: real-time observations of surface-hydrogen interactions. *J. Mater. Chem. A* **2020**, *8* (11), 5501–5507. DOI: 10.1039/C9TA11784A.

(17) Hess, C. New advances in using Raman spectroscopy for the characterization of catalysts and catalytic reactions. *Chem. Soc. Rev.* **2021**, *50* (5), 3519–3564. DOI: 10.1039/D0CS01059F.

(18) Ganduglia-Pirovano, M. V. The non-innocent role of cerium oxide in heterogeneous catalysis: A theoretical perspective. *Catal. Today* **2015**, *253*, 20–32. DOI: 10.1016/j.cattod.2015.01.049.

(19) Fan, H.-X.; Zhen, L.-F.; Rajendran, A.; Feng, J.; Li, W.-Y. Crucial role of H and O spillover in VO_x/CeO_2 catalysts reduction and re-oxidation during the ODH reaction. *Appl. Surf. Sci.* **2023**, *626*, 157250. DOI: 10.1016/j.apsusc.2023.157250.

(20) Zabilska, A.; Zabilskiy, M.; Nuguid, R. J. G.; Clark, A. H.; Sadykov, I. I.; Nachtegaal, M.; Kröcher, O.; Safonova, O. V. Origin of the Activity Trend in the Oxidative Dehydrogenation of Ethanol over VO_x/CeO_2. *Angew. Chem. Int. Ed.* **2023**, *135* (18), 321. DOI: 10.1002/ange.202301297.

(21) Wu, Z.; Rondinone, A. J.; Ivanov, I. N.; Overbury, S. H. Structure of Vanadium Oxide Supported on Ceria by Multiwavelength Raman Spectroscopy. *J. Phys. Chem. C* **2011**, *115* (51), 25368–25378. DOI: 10.1021/jp2084605.

(22) Baron, M.; Abbott, H.; Bondarchuk, O.; Stacchiola, D.; Uhl, A.; Shaikhutdinov, S.; Freund, H.-J.; Popa, C.; Ganduglia-Pirovano, M. V.; Sauer, J. Resolving the Atomic Structure of Vanadia Monolayer Catalysts: Monomers, Trimers, and Oligomers on Ceria. *Angew. Chem. Int. Ed.* **2009**, *121* (43), 8150–8153. DOI: 10.1002/ange.200903085.

(23) Wang, C.-B.; Deo, G.; Wachs, I. E. Characterization of Vanadia Sites in V-Silicalite, Vanadia-Silica Cogel, and Silica-Supported Vanadia Catalysts: X-Ray Powder Diffraction, Raman Spectroscopy, Solid-State ^{51}V NMR, Temperature-Programmed Reduction, and Methanol Oxidation Studies. *J. Catal.* **1998**, *178* (2), 640–648. DOI: 10.1006/jcat.1998.2193.

(24) Topsøe, N.-Y.; Anstrom, M.; Dumesic, J. A. Raman, FTIR and Theoretical Evidence for Dynamic Structural Rearrangements of Vanadia/Titania $DeNO_x$ Catalysts. *Catal. Lett.* **2001**, *76* (1/2), 11–20. DOI: 10.1023/A:1016715823630.

(25) Cortez, G. G.; Bañares, M. A. A Raman Spectroscopy Study of Alumina-Supported Vanadium Oxide Catalyst during Propane Oxidative Dehydrogenation with Online Activity Measurement. *J. Catal.* **2002**, *209* (1), 197–201. DOI: 10.1006/jcat.2002.3600.

(26) Penschke, C.; Paier, J.; Sauer, J. Vanadium Oxide Oligomers and Ordered Monolayers Supported on CeO$_2$ (111): Structure and Stability Studied by Density Functional Theory. *J. Phys. Chem. C* **2018**, *122* (16), 9101–9110. DOI: 10.1021/acs.jpcc.8b01998.

(27) Ganduglia-Pirovano, M. V.; Popa, C.; Sauer, J.; Abbott, H.; Uhl, A.; Baron, M.; Stacchiola, D.; Bondarchuk, O.; Shaikhutdinov, S.; Freund, H.-J. Role of ceria in oxidative dehydrogenation on supported vanadia catalysts. *J. Am. Chem. Soc.* **2010**, *132* (7), 2345–2349. DOI: 10.1021/ja910574h.

(28) Kropp, T.; Paier, J.; Sauer, J. Support effect in oxide catalysis: methanol oxidation on vanadia/ceria. *J. Am. Chem. Soc.* **2014**, *136* (41), 14616–14625. DOI: 10.1021/ja508657c. Published Online: Oct. 2, 2014.

(29) Popa, C.; Ganduglia-Pirovano, M. V.; Sauer, J. Periodic Density Functional Theory Study of VO$_n$ Species Supported on the CeO$_2$ (111) Surface. *J. Phys. Chem. C* **2011**, *115* (15), 7399–7410. DOI: 10.1021/jp108185y.

(30) Wu, X.-P.; Gong, X.-Q. Unique Electronic and Structural Effects in Vanadia/Ceria-Catalyzed Reactions. *J. Am. Chem. Soc.* **2015**, *137* (41), 13228–13231. DOI: 10.1021/jacs.5b07939. Published Online: Oct. 9, 2015.

(31) Kresse, G.; Joubert, D. From ultrasoft pseudopotentials to the projector augmented-wave method. *Phys. Rev. B Condens. Matter* **1999**, *59* (3), 1758–1775. DOI: 10.1103/PhysRevB.59.1758.

(32) Kresse, G.; Furthmüller, J. Efficiency of ab-initio total energy calculations for metals and semiconductors using a plane-wave basis set. *Comput. Mater. Sci.* **1996**, *6* (1), 15–50. DOI: 10.1016/0927-0256(96)00008-0.

(33) Blöchl, P. E. Projector augmented-wave method. *Phys. Rev. B Condens. Matter* **1994**, *50* (24), 17953–17979. DOI: 10.1103/physrevb.50.17953.

(34) Perdew, J. P.; Burke, K.; Ernzerhof, M. Generalized Gradient Approximation Made Simple. *Phys. Rev. Lett.* **1996**, *77* (18), 3865–3868. DOI: 10.1103/PhysRevLett.77.3865.

(35) Fabris, S.; Gironcoli, S. de; Baroni, S.; Vicario, G.; Balducci, G. Reply to "Comment on 'Taming multiple valency with density functionals: A case study of defective ceria' ". *Phys. Rev. B* **2005**, *72* (23). DOI: 10.1103/PhysRevB.72.237102.

(36) Da Silva, J. L. F.; Ganduglia-Pirovano, M. V.; Sauer, J.; Bayer, V.; Kresse, G. Hybrid functionals applied to rare-earth oxides: The example of ceria. *Phys. Rev. B* **2007**, *75* (4). DOI: 10.1103/PhysRevB.75.045121.

(37) Schilling, C.; Hofmann, A.; Hess, C.; Ganduglia-Pirovano, M. V. Raman Spectra of Polycrystalline CeO_2 : A Density Functional Theory Study. *J. Phys. Chem. C* **2017**, *121* (38), 20834–20849. DOI: 10.1021/acs.jpcc.7b06643.

(38) Wu, L.; Wiesmann, H. J.; Moodenbaugh, A. R.; Klie, R. F.; Zhu, Y.; Welch, D. O.; Suenaga, M. Oxidation state and lattice expansion of CeO_{2-x} nanoparticles as a function of particle size. *Phys. Rev. B* **2004**, *69* (12), 649. DOI: 10.1103/PhysRevB.69.125415.

(39) Zhang, F.; Chan, S.-W.; Spanier, J. E.; Apak, E.; Jin, Q.; Robinson, R. D.; Herman, I. P. Cerium oxide nanoparticles: Size-selective formation and structure analysis. *Appl. Phys. Lett.* **2002**, *80* (1), 127–129. DOI: 10.1063/1.1430502.

(40) Monkhorst, H. J.; Pack, J. D. Special points for Brillouin-zone integrations. *Phys. Rev. B* **1976**, *13* (12), 5188–5192. DOI: 10.1103/PhysRevB.13.5188.

(41) Baroni, S.; Gironcoli, S. de; Dal Corso, A.; Giannozzi, P. Phonons and related crystal properties from density-functional perturbation theory. *Rev. Mod. Phys.* **2001**, *73* (2), 515–562. DOI: 10.1103/RevModPhys.73.515.

(42) Gajdoš, M.; Hummer, K.; Kresse, G.; Furthmüller, J.; Bechstedt, F. Linear optical properties in the projector-augmented wave methodology. *Phys. Rev. B* **2006**, *73* (4). DOI: 10.1103/PhysRevB.73.045112.

(43) Porezag, D.; Pederson. Infrared intensities and Raman-scattering activities within density-functional theory. *Phys. Rev. B Condens. Matter* **1996**, *54* (11), 7830–7836. DOI: 10.1103/physrevb.54.7830.

(44) Fonari, A.; Stauffer, S. *vasp_raman.py*, 2013. https://github.com/raman-sc/VASP.

(45) Waleska, P. S.; Hess, C. Oligomerization of Supported Vanadia: Structural Insight Using Surface-Science Models with Chemical Complexity. *J. Phys. Chem. C* **2016**, *120* (33), 18510–18519. DOI: 10.1021/acs.jpcc.6b01672.

(46) Nolan, M. Charge Compensation and Ce^{3+} Formation in Trivalent Doping of the CeO_2 (110) Surface: The Key Role of Dopant Ionic Radius. *J. Phys. Chem. C* **2011**, *115* (14), 6671–6681. DOI: 10.1021/jp112112u.

(47) Filtschew, A.; Hofmann, K.; Hess, C. Ceria and Its Defect Structure: New Insights from a Combined Spectroscopic Approach. *J. Phys. Chem. C* **2016**, *120* (12), 6694–6703. DOI: 10.1021/acs.jpcc.6b00959.

(48) Bosco, M. V.; Bañares, M. A.; Martínez-Huerta, M. V.; Bonivardi, A. L.; Collins, S. E. In situ FTIR and Raman study on the distribution and reactivity of surface vanadia species in V_2O_5/CeO_2 catalysts. *J. Mol. Catal. A: Chem.* **2015**, *408*, 75–84. DOI: 10.1016/j.molcata.2015.07.012.

(49) Iglesias-Juez, A.; Martínez-Huerta, M. V.; Rojas-García, E.; Jehng, J.-M.; Bañares, M. A. On the Nature of the Unusual Redox Cycle at the Vanadia Ceria Interface. *J. Phys. Chem. C* **2018**, *122* (2), 1197–1205. DOI: 10.1021/acs.jpcc.7b09832.

(50) Martínez-Huerta, M.; Coronado, J. M.; Fernández-García, M.; Iglesias-Juez, A.; Deo, G.; Fierro, J.L.G.; Banares, M.A. Nature of the vanadia-ceria interface in V^{5+}/CeO_2 catalysts and its relevance for the solid-state reaction toward $CeVO_4$ and catalytic properties. *J. Catal.* **2004**, *225* (1), 240–248. DOI: 10.1016/j.jcat.2004.04.005.

(51) Griffith, W. P. Raman Spectroscopy of Minerals. *Nature* **1969**, *224* (5216), 264–266. DOI: 10.1038/224264a0.

(52) Yin, Z.; Xu, K.; Jiang, S.; Luo, D.; Chen, R.; Xu, C.; Shum, P.; Liu, Y. J. Recent progress on two-dimensional layered materials for surface enhanced Raman spectroscopy and their applications. *Mater. Today Phys.* **2021**, *18* (1), 100378. DOI: 10.1016/j.mtphys.2021.100378.

(53) Abrashev, M. V.; Bäckström, J.; Börjesson, L.; Popov, V. N.; Chakalov, R. A.; Kolev, N.; Meng, R.-L.; Iliev, M. N. Raman spectroscopy of $CaMnO_3$: Mode assignment and relationship between Raman line intensities and structural distortions. *Phys. Rev. B* **2002**, *65* (18). DOI: 10.1103/PhysRevB.65.184301.

(54) Bulánek, R.; Čičmanec, P.; Setnička, M. Possibility of VO_x/SiO_2 Complexes Speciation: Comparative Multi-wavelength Raman and DR UV-vis Study. *Phys. Procedia* **2013**, *44*, 195–205. DOI: 10.1016/j.phpro.2013.04.024.

(55) Nitsche, D.; Hess, C. Structure of Isolated Vanadia and Titania: A Deep UV Raman, UV–Vis, and IR Spectroscopic Study. *J. Phys. Chem. C* **2016**, *120* (2), 1025–1037. DOI: 10.1021/acs.jpcc.5b10317.

(56) Jaegers, N. R.; Lai, J.-K.; He, Y.; Walter, E.; Dixon, D. A.; Vasiliu, M.; Chen, Y.; Wang, C.; Hu, M. Y.; Mueller, K. T.; Wachs, I. E.; Wang, Y.; Hu, J. Z. Mechanism by which Tungsten Oxide Promotes the Activity of Supported V_2O_5/TiO_2 Catalysts for NO_x Abatement: Structural Effects Revealed by [51]V MAS NMR Spectroscopy. *Angew. Chem. Int. Ed.* **2019**, *58* (36), 12609–12616. DOI: 10.1002/anie.201904503.

(57) Hu, J. Z.; Xu, S.; Li, W.-Z.; Hu, M. Y.; Deng, X.; Dixon, D. A.; Vasiliu, M.; Craciun, R.; Wang, Y.; Bao, X.; Peden, C. H. F. Investigation of the Structure and Active Sites of TiO_2 Nanorod Supported VO_x Catalysts by High-Field and Fast-Spinning [51]V MAS NMR. *ACS Catal.* **2015**, *5* (7), 3945–3952. DOI: 10.1021/acscatal.5b00286.

Supporting Information

Detailed Analysis of the Raman Vibrational Structure of Vanadia in VO_x/CeO_2: A Periodic Density Functional Theory Study

Leon Schumacher and Christian Hess*

Technical University of Darmstadt, Department of Chemistry, Eduard-Zintl-Institut für Anorganische und Physikalische Chemie, Peter-Grünberg-Str. 8, 64287 Darmstadt, Germany.

*Corresponding Author (E-Mail: christian.hess@tu-darmstadt.de)

Comparison of CeO$_2$ (111) support sizes for monomeric vanadia. Figures S1-S3 show the optimized structures of a VO, a VO$_2$, a VO$_3$, and a VO$_4$ cluster supported on Ce$_{12}$O$_{24}$(111), Ce$_{27}$O$_{54}$(111) and Ce$_{48}$O$_{96}$(111) from the side and the top view. Tables S1-S3 summarize the bond distances of the different bonds in the clusters. For bonds that occur more than once, the bond lengths were averaged and, if the bond distance deviate by more than ±2 pm, the range of distances is given in parentheses.
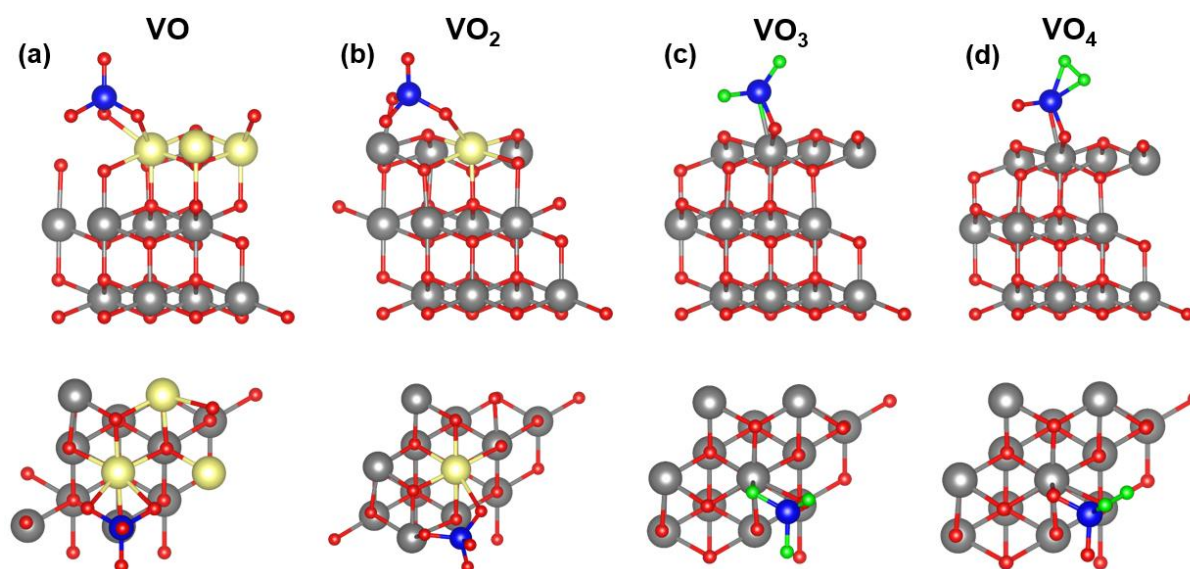
Figure S1: Structures of **(a)** VO, **(b)** VO$_2$, **(c)** VO$_3$ and **(d)** VO$_4$ cluster supported on the CeO$_2$ (111) surface with a p(2x2) periodicity viewed from the side (top) and above (bottom). Ce^{4+} and Ce^{3+} are shown in grey and light-yellow, respectively. V^{5+} and O^{2-} are shown in blue and red, respectively. O$^-$ is shown in green. This color-code is used throughout the rest of the manuscript.

Table S1: Bond lengths of different vanadia bonds (in ppm) in different monomeric clusters supported on a CeO$_2$ (111) surface with a p(2x2) periodicity.

Cluster	V=O	V-O-Ce	Interface	O-O
VO	162	-	180	-
VO$_2$	162	173	183	-
VO$_3$	167	173	180	-
VO$_4$	199	168	181	134
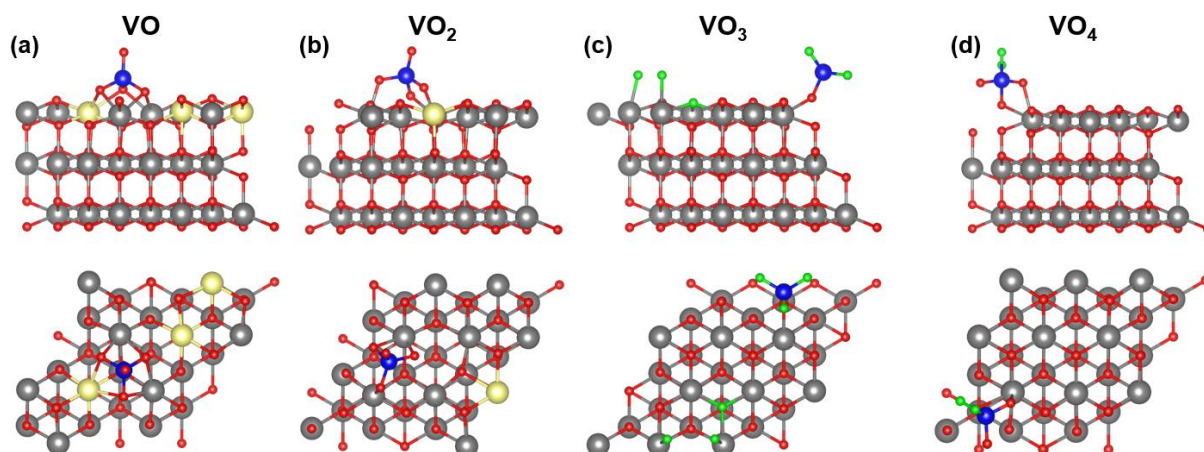
Figure S2: Structures of **(a)** VO, **(b)** VO_2, **(c)** VO_3 and **(d)** VO_4 cluster supported on the CeO_2 (111) surface with a p(3x3) periodicity viewed from the side (top) and above (bottom).

Table S2: Bond lengths of different vanadia bonds (in ppm) in different monomeric clusters supported on a CeO_2 (111) surface with a p(3x3) periodicity.

Cluster	V=O	V-O-Ce	Interface	O-O
VO	163	-	180	-
VO_2	163	174	181	-
VO_3	166	174	180	-
VO_4	200	168	180	134
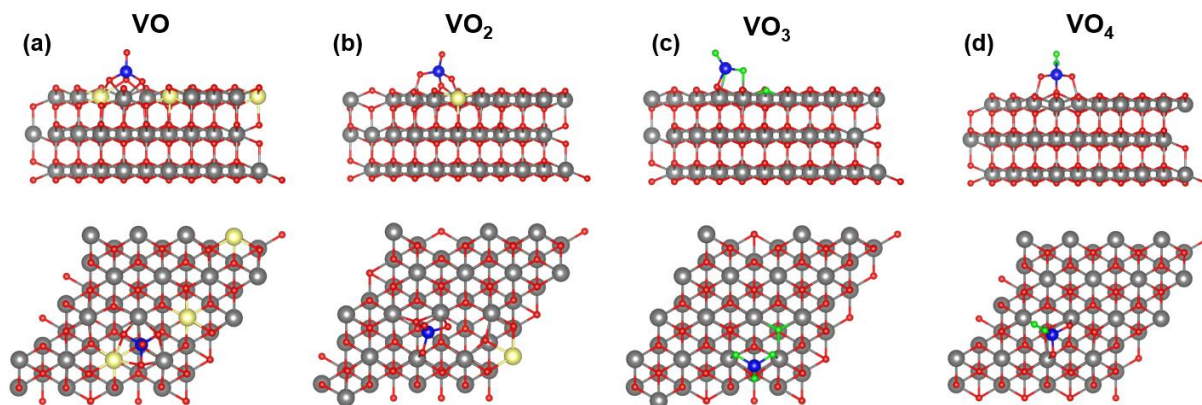
Figure S3: Structures of **(a)** VO, **(b)** VO_2, **(c)** VO_3 and **(d)** VO_4 cluster supported on the CeO_2 (111) surface with a p(4x4) periodicity viewed from the side (top) and above (bottom).

Table S3: Bond lengths of different vanadia bonds (in ppm) in different monomeric clusters supported on a CeO_2 (111) surface with a p(4x4) periodicity.

Cluster	V=O	V-O-Ce	Interface	O-O
VO	163	-	180	-
VO_2	163	174	181	-
VO_3	166	175	180	-
VO_4	200	168	180	134

The VO cluster is introduced onto the ceria surface with one oxygen atom, leading to an initial vanadium oxidation state of +II. As vanadium is always in oxidation state +V, three electrons are transferred from vanadium to Ce^{4+} ions, creating three Ce^{3+} ions which are located in the surface ceria layer.[1–5] The oxygen atom introduced with the vanadium forms the vanadyl group while the vanadium is bound to the ceria surface via lattice oxygen, leading to three interface bonds in which the ceria lattice oxygen atoms are involved. Thereby, they move slightly towards the vanadium.

In the VO_3 cluster, vanadium is present in oxidation state +VI, which necessitates the transfer of one electron from ceria to the vanadia cluster, introducing partially oxidized and highly reactive oxygen 2p states, which were previously described.[5] The electron is delocalized over multiple oxygen atoms close to vanadium and on the ceria surface, slightly lowering the average electron density of those atoms.[5] Due to the additional oxygen atom, only one interface bond is formed with surface ceria

lattice oxygen while two angled V-O-Ce bonds are introduced, which leads to a cluster that is more tilted than the VO_2 cluster.[3] The most stable configuration of a VO_4 cluster introduces a peroxidic bond instead of a vanadyl bond in addition to the two angled V-O-Ce bonds. The peroxidic vanadyl bond contains two oxygen atoms, which are partially oxidized to result in the vanadium oxidation state +V.[3]

The differences in structure of the clusters between the different ceria cell sizes of the vanadium support are negligible. The bond lengths are very similar and vary by ±2 pm at most. The geometries are also similar and the location of the Ce^{3+} ions is in the top ceria layer for all periodicities. The largest difference can observed for the VO_3 cluster, where the amount of oxygen atoms, from which the electron is transferred to the vanadium atom, varies between those introduced with the cluster on a p(2x2) periodicity support and one additional ceria surface lattice oxygen atom on p(3x3) and p(4x4) periodicity supports. The two additional oxygen atoms colored in green in the p(3x3) model of the VO_3 cluster (see Figure S2) are caused by the periodic boundary conditions and originate from the next VO_3 cluster. Overall, the results are comparable to previous results obtained for monomeric vanadia supported on CeO_2 (111), which were mostly performed on $Ce_{12}O_{24}$, which seems to be sufficient for structural investigations.[3,4]

Figure S4 shows the Raman spectra corresponding to the structures of the VO, VO_2, VO_3, and VO_4 clusters supported on $Ce_{12}O_{24}(111)$, $Ce_{27}O_{54}(111)$, and $Ce_{48}O_{96}(111)$ that are depicted in Figures S1-S3. The Raman spectra were normalized for better comparability since the relative amount of vanadium in the entire model is lower the larger the support cell is, changing the intensity between the models by default. The spectrum of the VO_2 cluster is discussed in the main text.
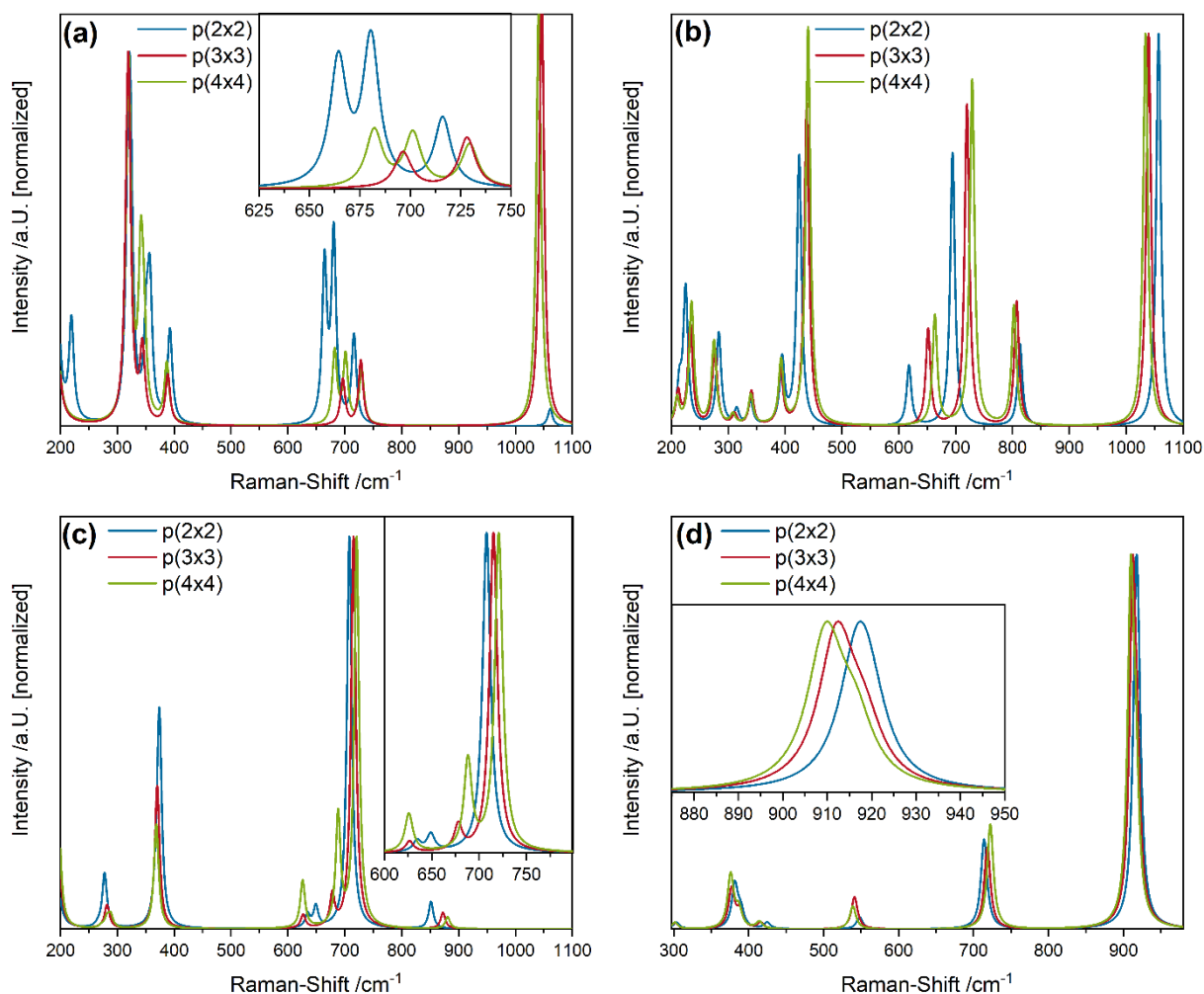
Figure S4: Raman spectra of **(a)** VO, **(b)** VO_2, **(c)** VO_3 and **(d)** VO_4 monomers supported on a CeO_2 (111) surface with a p(2x2), p(3x3), and p(4x4) periodicity. The spectra were normalized to their most intense peaks and the insets show regions where peaks are crowded.

The Raman spectra of the monomeric structures show similar peaks despite the different ceria cell sizes on which they are supported. However, the intensities and positions of the Raman peaks depend on the ceria supports' cell size. The peak positions shift when the size of the support cell is varied. Hereby, the shifts follow the trend that the positional shift between the p(2x2) and p(3x3) cell is large and between the p(3x3) and p(4x4) cell is smaller, indicating that the effect scales with the distances between the vanadia clusters. The best example for this behavior is the position of the vanadyl bond of the VO, VO_2, and VO_4 clusters, which is located above 1000 cm^{-1}. With increasing ceria cell size, the vanadyl peak shows a red-shift. Since the geometry (especially the bond length) of the vanadyl bond is identical for all three cell sizes, the shift needs to be caused by the interaction of vanadia monomers with each other due to periodic boundary conditions. When the cell size is increased, the vanadia

monomers become more distant from each other and the dipole-dipole coupling between vanadyl bonds decreases, leading to a red-shift.[6,7] This indicates that a p(4x4) cell is required for the investigation of the Raman spectrum of an isolated vanadia monomer, even though a p(2x2) cell is sufficient to investigate the structure. Therefore, the monomers supported on the p(4x4) cell will be discussed.

In the Raman spectrum of the highly symmetrical VO cluster the symmetric stretching vibration of the V=O bond is observed at 1040 cm^{-1}. This is followed by three peaks between 650 and 750 cm^{-1}, which are caused by the symmetric and antisymmetric stretching vibrations of the interface bonds, while the remaining peaks between 250 and 400 cm^{-1} are caused by the deformation vibrations of the interface bonds. The VO_3 and VO_4 clusters differ from the aforementioned clusters, since the symmetric V=O stretching vibrations are shifted to 882 and 1179 cm^{-1}, respectively. The V=O bond of the VO_3 cluster is significantly red-shifted due the reduced electron density, which was transferred to the three oxygen atoms introduced with the cluster (see Figure S3).[5] The very intense peak at 720 cm^{-1} is caused by the symmetric stretching vibration of the single interface bond, while the two peaks 685 and 625 cm^{-1} are caused by the symmetric and antisymmetric stretching vibrations of the two V-O-Ce bonds, respectively. The remaining peaks are also caused by the deformation vibrations of the vanadia cluster. In the VO_4 cluster, the vanadyl shift is caused by the peroxidic vanadyl group with a reduced electron density at the oxygen atoms involved in the vibration. The peak at 912 cm^{-1} is caused by the symmetric and antisymmetric stretching vibrations of V-O-Ce, which are degenerate for this cluster. The additional peak at 722 cm^{-1} is the symmetric stretching vibration of the interface bond and the remaining peaks are caused by the deformation vibrations of the cluster. Overall, the spectra of the clusters are rather comparable and a similar vibrational structure is found, while the biggest differences can be observed in the vanadyl region due to the different electronic structures of the clusters.

VO   **V_2O_2**   **V_3O_3**

(a)   **(b)**   **(c)**
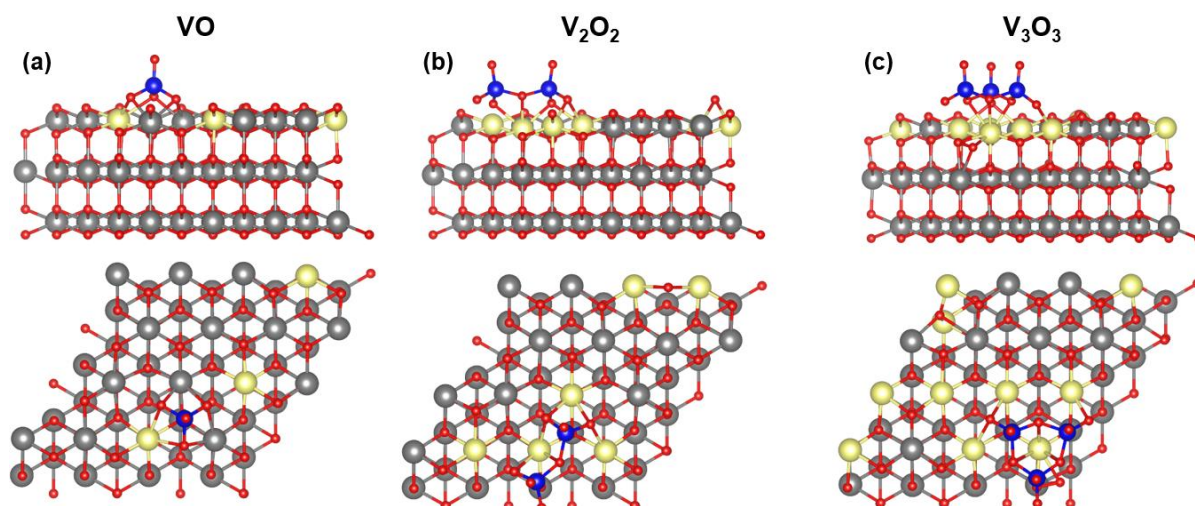
S5: Structures of short chain oligomeric V_nO_n clusters: **(a)** Monomeric VO, **(b)** dimeric V_2O_2 and **(c)** a V_3O_3 ring cluster supported on the CeO_2(111) surface with a p(4x4) periodicity viewed from the side (top) and above (bottom).

Table S4: Bond lengths of different vanadia bonds (in ppm) in different short chain V_nO_n clusters supported on a CeO_2(111) surface with a p(4x4) periodicity.

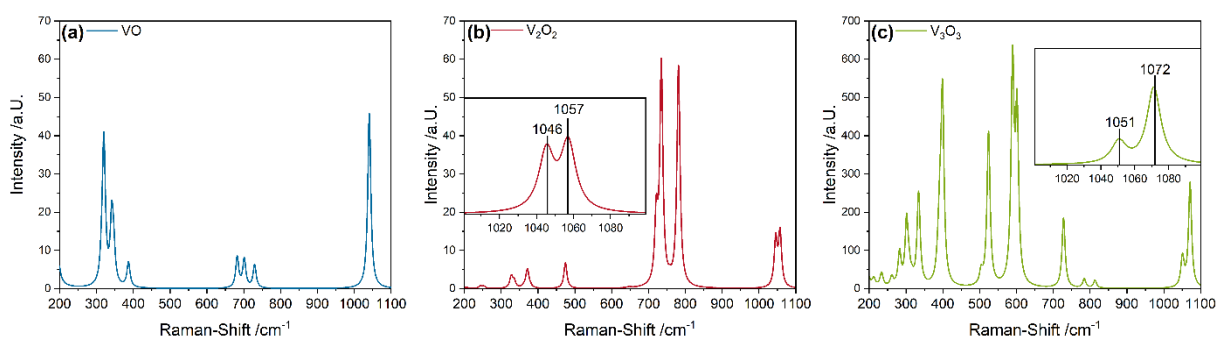| Cluster	V=O	V-O-V	Interface
VO	163	-	180
V_2O_2	162	190	177
V_3O_3	162	191 (184-198)	175

Figure S6: Raman spectra of **(a)** monomeric VO, **(b)** dimeric V_2O_2, and **(c)** a V_3O_3 ring cluster supported on the CeO_2(111) surface with a p(4x4) periodicity. The insets show the vanadyl fine structure of each cluster.

Table S5: Relative amount of different nuclearities contributing to the overall vanadyl fine structure from 514 nm excitation Raman spectra (see Figure 7).

Nuclearity	0.57 V/nm²	1.36 V/nm²	2.83 V/nm²
Monomeric	0.206	0.070	0
Dimeric	0.341	0.228	0.166
Trimeric	0.215	0.324	0.361
Tetrameric	0.189	0.264	0.311
Oligomeric	0.049	0.114	0.162

Table S6: Relative stability of dimeric and oligomeric vanadia clusters on a $CeO_2(111)$ surface with a p(4x4) periodicity used to scale the individual cluster contributions to the experimentally determined dimeric and oligomeric peaks from the vanadyl fine structure.

	Cluster	Stability /eV	Dimeric/Oligomeric Contributions
Dimers	V_2O_4 Ring	-0.99	0.5
	V_2O_4 Chain	-0.99	0.5
Oligomers	V_5O_{10}	-0.18	0.112
	V_6O_{12}	-1.13	0.702
	V_7O_{14}	-0.30	0.186
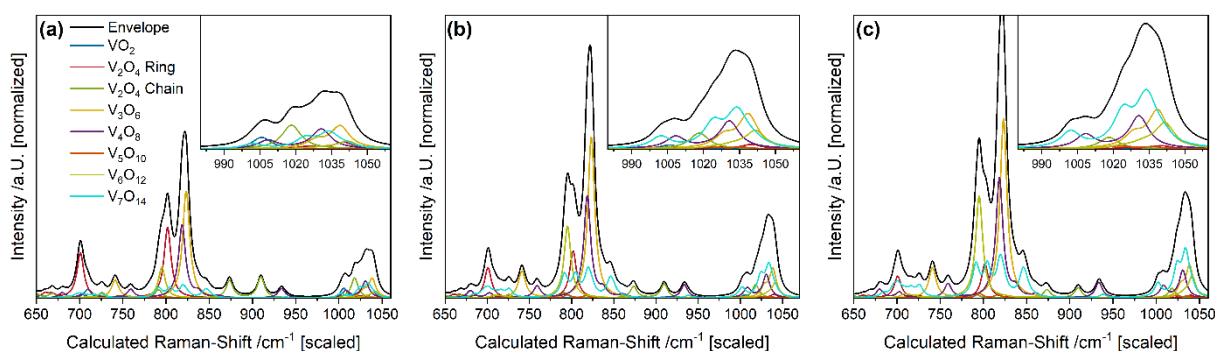
Figure S7: Combined Raman spectrum of a CeO_2 (111) trilayer with a p(4x4) periodicity and the Raman spectra of the individual V_nO_{2n} vanadia clusters between 650 and 1060 cm^{-1} based on the vanadyl fine structure of an experimental Raman spectrum of a CeO_2 sample loaded with **(a)** 0.57, **(b)** 1.36, and **(c)** 2.83 V/nm². The insets show the vanadyl fine structures at each loading.
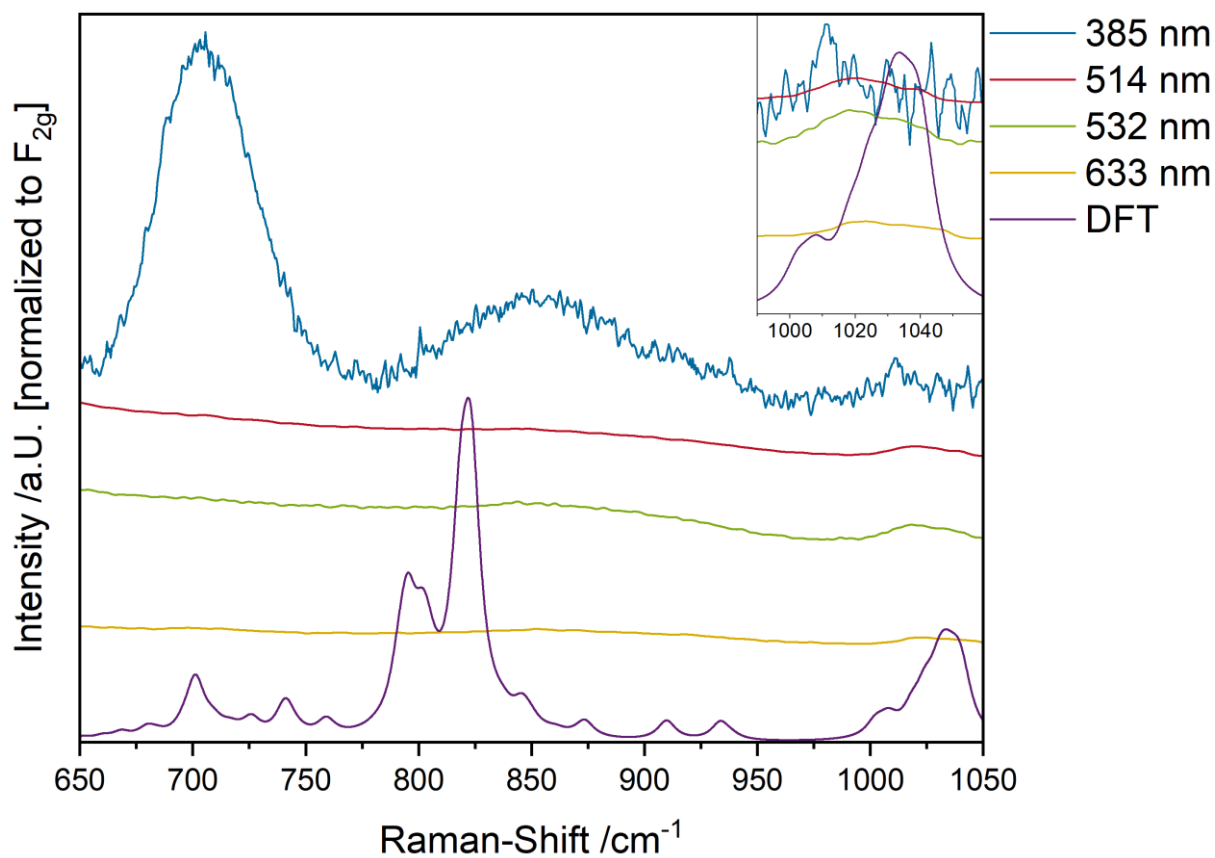
Figure S8: Comparison of Raman spectra in the region within 650-1050 cm^{-1} at different excitation wavelengths.

References

(1) Popa, C.; Ganduglia-Pirovano, M. V.; Sauer, J. Periodic Density Functional Theory Study of VO_n Species Supported on the CeO_2 (111) Surface. *J. Phys. Chem. C* **2011**, *115* (15), 7399–7410. DOI: 10.1021/jp108185y.

(2) Penschke, C.; Paier, J.; Sauer, J. Oligomeric Vanadium Oxide Species Supported on the CeO_2(111) Surface: Structure and Reactivity Studied by Density Functional Theory. *J. Phys. Chem. C* **2013**, *117* (10), 5274–5285. DOI: 10.1021/jp400520j.

(3) Ganduglia-Pirovano, M. V.; Popa, C.; Sauer, J.; Abbott, H.; Uhl, A.; Baron, M.; Stacchiola, D.; Bondarchuk, O.; Shaikhutdinov, S.; Freund, H.-J. Role of ceria in oxidative dehydrogenation on supported vanadia catalysts. *J. Am. Chem. Soc.* **2010**, *132* (7), 2345–2349. DOI: 10.1021/ja910574h.

(4) Ganduglia-Pirovano, M. V. The non-innocent role of cerium oxide in heterogeneous catalysis: A theoretical perspective. *Catal. Today* **2015**, *253*, 20–32. DOI: 10.1016/j.cattod.2015.01.049.

(5) Huang, C.; Wang, Z.-Q.; Gong, X.-Q. Activity and selectivity of propane oxidative dehydrogenation over VO_3/CeO_2 (111) catalysts: A density functional theory study. *Chin. J. Catal.* **2018**, *39* (9), 1520–1526. DOI: 10.1016/S1872-2067(18)63072-4.

(6) Baron, M.; Abbott, H.; Bondarchuk, O.; Stacchiola, D.; Uhl, A.; Shaikhutdinov, S.; Freund, H.-J.; Popa, C.; Ganduglia-Pirovano, M. V.; Sauer, J. Resolving the Atomic Structure of Vanadia Monolayer Catalysts: Monomers, Trimers, and Oligomers on Ceria. *Angew. Chem. Int. Ed.* **2009**, *121* (43), 8150–8153. DOI: 10.1002/ange.200903085.

(7) Wu, Z.; Rondinone, A. J.; Ivanov, I. N.; Overbury, S. H. Structure of Vanadium Oxide Supported on Ceria by Multiwavelength Raman Spectroscopy. *J. Phys. Chem. C* **2011**, *115* (51), 25368–25378. DOI: 10.1021/jp2084605.

4.1.2 Understanding the Reduction Behavior of VO_x/CeO_2 on a Molecular Level: Combining Temperature-Programmed Reduction with Multiple In-Situ Spectroscopies and X-Ray Diffraction

The second publication investigates the loading-dependent reduction behavior of VO_x/CeO_2 samples by combining H_2 TPR with multiple in situ and quasi in situ spectroscopies to understand the reduction on a molecular level. These findings may serve as an experimental basis for applications where the reducibility is important. The TPR revealed a high and a low temperature region, where only the low temperature region is affected by the presence of vanadia. The high temperature region is caused by the phase transition of CeO_2 into a nanodispersive substochiometric phase. The low temperature region is caused by the surface/subsurface chemistry of the samples, where vanadia plays a significant role. First, surface Ce-OH species are reduced, while the oxygen depletion in the ceria surface and vacancy formation follow at higher temperatures. Concurrently, vanadia is reduced and accompanied by disproportionation of V^{4+} into V^{3+} and V^{5+}. Both processes in combination lead to an overall decrease of oxidation state. The temperatures at which these processes occur, and therefore the overall reduction behavior, is largely influenced by the nuclearity distribution of vanadia, which can be determined via the vanadyl fine structure from Vis-Raman spectroscopy. At even higher temperatures, subsurface and bulk oxygen can diffuse to the surface, forming bulk vacancies, while vanadia is strongly reduced to V^{3+}. Before the phase transition, bulk hydrides are formed. The combined usage of TPR and in situ spectroscopies shows great potential to understand reduction behaviors of catalytic materials, which is often important for their performance, allowing to gain insight into their mode of operation.

Article

Understanding the Reduction Behavior of VO$_x$/CeO$_2$ on a Molecular Level: Combining Temperature-Programmed Reduction with Multiple In-Situ Spectroscopies and X-ray Diffraction

Leon Schumacher, Marc Ziemba, Kai Brunnengräber, Lea Totzauer, Kathrin Hofmann, Bastian J. M. Etzold, Barbara Albert, and Christian Hess*

Read Online

ACCESS | 📊 Metrics & More | 📄 Article Recommendations | 📑 Supporting Information

ABSTRACT: As catalytic processes become more important in academic and industrial applications, an intimate understanding is highly desirable to improve their efficiency on a rational basis. Because thorough mechanistic investigations require an elaborate and expensive spectroscopic and theoretical analysis, it is a major goal to link mechanistic insights to simple descriptors, such as the reducibility, that are accessible by temperature-programmed reduction (TPR) experiments, to bridge the gap between fundamental understanding and application of catalysts. In this work, we present a detailed in-situ spectroscopic analysis of TPR results from loading-dependent VO$_x$/CeO$_2$ catalysts, using in-situ multiwavelength Raman, IR, UV−vis, and quasi-in-situ X-ray photoelectron spectroscopy as well as in-situ X-ray diffraction. The catalyst reduction shows a complex network of different processes, contributing to the overall reducibility, which are controlled by the unique interaction at the vanadia−ceria interface. The temperatures at which they occur depend significantly on the nuclearity of the surface vanadia species. By elucidating the temperature- and vanadia loading-dependent behavior, we provide a fundamental understanding of the underlying molecular processes, thus developing an important basis for interpretation of the reduction behavior of other oxide catalysts.
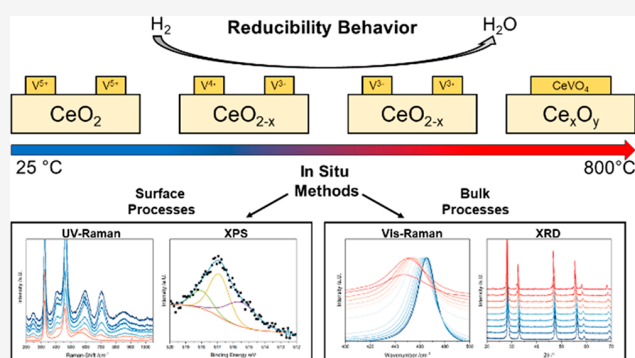
INTRODUCTION

Catalytic processes are a significant part of both the chemical industry and academic research, whereby the choice of the catalyst material is of great importance to the overall process performance. For many applications, supported materials are the best option due to their high activity, stability, and separability,[1] but the choice of the support is crucial, as different supports can change the catalytic activity significantly.[2−4] A commonly used support in oxidation reactions is ceria due to its outstanding redox properties. These are often attributed to ceria's ability to form oxygen vacancies, where a lattice oxygen atom is consumed in the reaction and an oxygen vacancy is created along with two Ce^{3+} ions. The latter can then be regenerated using either oxygen from the gas-phase or subsurface oxygen, which is transported to the surface by diffusion.[5,6] Therefore, due to its redox properties, ceria is an excellent support material and has been employed in a variety of reactions, such as NO$_2$ storage,[7] NH$_3$ selective catalytic reduction (SCR),[8] CO oxidation,[9] reverse water-gas shift reaction,[10] and CO$_2$ hydrogenation[11] as well as alcohol[12] and alkane[13] oxidative dehydrogenations (ODHs). The corresponding active phases are very diverse and can typically be either a metal (e.g., gold,[10] copper,[14] platinum[15]) or an oxide (e.g., MnO$_x$,[16] VO$_x$,[13] MoO$_x$[17]), depending on the application.

A catalyst commonly used in the oxidation of alcohols and short chain alkanes is ceria-supported vanadia (VO$_x$/CeO$_2$).[12,13,18] The reducibility of CeO$_2$ in this system is often cited as the reason for the good catalytic performance in oxidation reactions and is accessible by H$_2$ temperature-programmed reduction (TPR) measurements. However, a detailed understanding of the catalyst reduction on a molecular level through spectroscopic means is still lacking.[3,19−23] Furthermore, the intimate interaction between vanadia and ceria has a significant influence on the reduction behavior of the catalyst as it has often been described in the literature that ceria keeps vanadia in its highest oxidation state and vanadia interacts with lattice oxygen as well as oxygen vacancies on the

5810
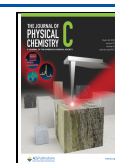
surface.[18,22,24−27] Therefore, the reduction behavior is much more complicated and cannot be fully understood by using TPR only. It would therefore be highly desirable to link the measured TPR data to a molecular understanding of the reduction process, as obtained by spectroscopy, so that the easily available descriptor, the reducibility, could be used for the rational enhancement of catalytic structure and performance. While previous studies have started to explain some aspects of TPR by spectroscopy[28,29] and on ceria during hydrogen treatment,[20,22,30] there have been no reports in the literature that address VO_x/CeO_2 catalysts at different vanadia loadings, although the loading heavily influences the materials' properties, or with multiple supplementary in-situ spectroscopies to cover the TPR's full temperature range.

TPR has been used to characterize catalysts in more applied technical studies (e.g., for VO_x/TiO_2 systems[31]), thus allowing to bridge the gap between detailed molecular investigations by spectroscopy and technical investigations used for catalyst optimization, thereby increasing the amount of knowledge obtainable by measurements, which can be performed with comparable ease. Although technical catalysts have a much more complex composition than their academically used counterparts, there are still based on the properties of the main active part, which are then modified by additional elements. Therefore, understanding the fundamental properties of the main component is of great importance for its further optimization.

In this study, we aim at a fundamental understanding of the reduction behavior of VO_x/CeO_2 catalysts with three different vanadium loadings below vanadia crystal formation to deepen the understanding of ceria's properties in oxidation catalysis as well as the interplay between the ceria support and its active phase. We apply multiple in-situ methods, including multiwavelength Raman, UV−vis, DRIFTS, and XRD, to explain on a molecular level the TPR results obtained over a wide range of temperatures and to gain detailed insight into the catalysts̀ behavior under reducing conditions. Our approach can readily be transferred to other catalytically relevant materials, such as VO_x/TiO_2 catalysts, to explain their reducibility behavior in a comprehensive manner. Furthermore, other methods, such as temperature-programmed oxidation (TPO) and temperature-programmed desorption (TPD), might also be explained in detail in the future by applying similar approaches.

■ EXPERIMENTAL SECTION

Catalyst Preparation. The ceria support was prepared as previously described[6] and loaded with vanadia by incipient wetness impregnation. Three different loadings were prepared by mixing 1 g of ceria with 0.5 mL of differently concentrated precursor solutions (1.07, 0.51, and 0.21 mol/L) containing vanadium(V) oxytriisopropoxide (≥97%, Sigma-Aldrich) and 2-propanol (99.5%, Sigma-Aldrich). The samples were then heated to 600 °C at a heating rate of 1.5 °C/min and calcined for 12 h. The specific surface was determined by analysis of the nitrogen adsorption, and desorption isotherms were recorded on a Surfer analyzer (Thermo Fisher) after drying the samples in a vacuum for 24 h. The isotherms were then analyzed by multipoint Brunauer−Emmett−Teller (BET) analysis, and the specific surface area was determined to be 61.4 m^2/g, yielding vanadium loadings of 2.83 V/nm^2 (2.32 wt % V_2O_5), 1.36 V/nm^2 (1.11 wt % V_2O_5), and 0.57 V/nm^2 (0.47 wt % V_2O_5). Higher vanadium loadings were not considered because vanadia crystallites were shown to be present at loadings

>2.9 V/nm^2.[32] The resulting catalyst powders were subsequently pressed at a pressure of 2000 kg/m^2 for 20 s, ground, and then sieved using a combination of sieves to obtain 200−300 μm sized particles.

Reduction Procedure. The catalyst sample was placed in the reaction chamber (see below) and was dehydrated at 365 °C in 12.5% O_2/He for 1 h. After the samples had cooled to room temperature, the gas phase was switched to 7% H_2/Ar (total flow rate: 40 mL_n/min). The temperature was increased stepwise to 550 °C using 45 °C steps, and a spectrum was recorded at each temperature. This procedure was performed for all methods except for quasi-in-situ XPS, DRIFTS, in-situ XRD, and TPR, which will be described separately in the corresponding sections.

Temperature-Programmed Reduction (TPR). TPR was performed on a Micromeritics 3Flex instrument. The sample was loaded in a quartz reactor and pretreated by oxidation in synthetic air (20% O_2 in N_2, Westfalen) at 400 °C for 1 h, with a flow rate of 50 mL_n/min. The sample was then cooled to 40 °C, while being flushed with 50 mL_n/min argon. After cooling, the gas was switched to 50 mL_n/min 7% H_2/Ar. After waiting for 1.5 h for the reactor and instrument to be fully purged, TPR was performed by heating the sample up to 850 °C with a heating rate of 5 K/min. Consumption of hydrogen was detected using a thermal conductivity detector (TCD). During the measurement, a cold trap cooled to −10 °C was placed between the sensor and the sample. To confirm the accuracy of the temperature calibration, V_2O_5 was measured as a well-known reference sample (see Figure S1).[33] To integrate the TCD signal, a baseline correction was performed, taking the three minima before and after the first hydrogen consumption region as well as before the phase-transition region as anchor points.

UV-Raman Spectroscopy. UV-Raman spectroscopy was performed at an excitation wavelength of 385 nm generated by a laser system based on a Ti:Sa solid-state laser pumped by a frequency-doubled Nd:YAG laser (Coherent, Indigo). The fundamental wavelength is frequency doubled to 385 nm using a LiB_3O_5 crystal. The light is focused onto the sample, and the scattered light is collected by a confocal mirror setup and focused into a triple stage spectrometer (Princeton Instruments, TriVista 555), as described previously.[32] Finally, the Raman contribution is detected by a charge-coupled device (CCD, 2048 × 512 pixels) cooled to −120 °C. The spectral resolution of the spectrometer is 1 cm^{-1}. For Raman experiments, 70 mg of sample was placed in a CCR 1000 reactor (Linkam Scientific Instruments) equipped with a CaF_2 window (Korth Kristalle GmbH). A fluidized bed reactor was employed to avoid laser-induced damage, allowing the use of a laser power of 9 mW at the location of the sample. Data processing included cosmic ray removal and background subtraction.

Visible-Raman Spectroscopy. Visible (vis)-Raman spectroscopy was performed at 514 nm excitation, emitted from an argon ion gas laser (Melles Griot). The light was focused onto the sample, gathered by an optical fiber and dispersed by a transmission spectrometer (Kaiser Optical, HL5R). The dispersed Raman radiation was subsequently detected by an electronically cooled CCD detector (−40 °C, 1024 × 256 pixels). The spectral resolution was 5 cm^{-1} with a wavelength stability of better than 0.5 cm^{-1}. For Raman experiments, 70 mg of catalyst was filled into a CCR 1000 reactor (Linkam Scientific Instruments), equipped with a quartz window
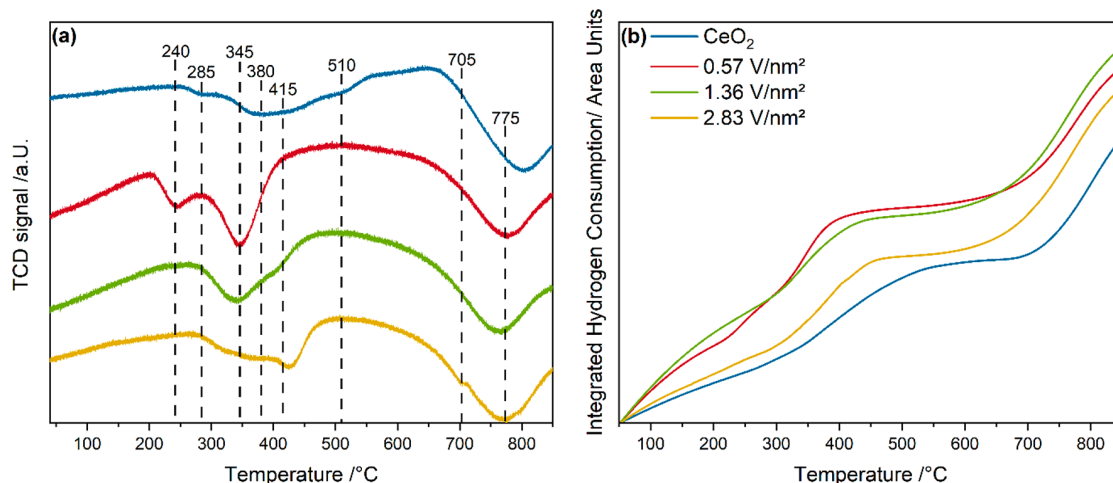
Figure 1. (a) TPR results of bare ceria and vanadia-loaded samples recorded with a heating rate of 5 K/min in 7.5% H_2/Ar between 50 and 850 °C. The temperature axis was calibrated by using V_2O_5 as a reference sample (see Figure S1). Temperatures at which maxima in hydrogen consumption were detected are marked. (b) Integrated hydrogen consumption. The baseline correction is described in the Experimental Section.

(Linkam Scientific Instruments). A fluidized bed reactor was employed to avoid laser-induced damage, allowing the use of a laser power of 6 mW at the location of the sample. Data analysis of the Raman spectra included cosmic ray removal and an auto new dark correction. The F_{2g} mode was fitted using one Lorentzian function without any positional restriction due to the possible occurrence of red-shifts.[34]

Diffuse Reflectance UV–Vis Spectroscopy. Diffuse reflectance (DR) UV–vis spectra were recorded on a Jasco V-770 UV–vis spectrometer. Dehydrated $BaSO_4$ was used as the white standard. For each experiment, 90 mg of catalyst was put in the commercially available reaction cell (Praying Mantis High Temperature Reaction Chamber, Harrick Scientific) equipped with transparent quartz glass windows.

X-ray Photoelectron Spectroscopy (XPS). XP spectra were recorded on a modified LHS/SPECS EA200 MCD system described previously.[35−37] The XPS system was equipped with a Mg Kα source (1253.6 eV, 168 W), and the calibration of the binding energy scale was performed with Au $4f_{7/2}$ = 84.0 eV and Cu $2p_{3/2}$ = 932.67 eV signals from foil samples. The samples were treated in 12.5% O_2/Ar for 1 h before the measurements and with 7.5% H_2/Ar for 30 min after the measurements, both at 300 °C at a total flow rate of 40 mL/min.

The subsequent transfer of the sample to the analysis chamber was performed without exposure to air (quasi-in-situ). Sample charging was taken into account by setting the u‴ peak of the Ce 3d signal to 916.7 eV.[38] Detailed spectra were recorded at a resolution of 0.1 eV. The X-ray satellite peaks due to the use of a nonmonochromatic source were subtracted from the spectra. The deconvolution of the spectra was performed analogously for all measurements using Gauss–Lorentzian product functions (30/70), whereby the background was subtracted by the Shirley method.

V:Ce and O:Ce ratios were obtained from a least-squares fit analysis by integrating the Ce 3d signal and the O 1s or the V $2p_{3/2}$ signal after a Shirley background subtraction from the detailed spectra and by applying the same integration boundaries. The resulting areas were corrected with the corresponding relative sensitivity factors, i.e., 10 for the Ce 3d, 0.66 for the O 1s, and 1.3 for the V $2p_{3/2}$ signal.[39]

Diffuse Reflectance Infrared Fourier Transform Spectroscopy (DRIFTS). DRIFT spectra were recorded on a Vertex 70 spectrometer (Bruker), equipped with a liquid nitrogen-cooled mercury cadmium telluride (MCT) detector, operating at a resolution of 1 cm^{-1}. Dehydrated potassium bromide was employed as an infrared transparent sample for the background spectrum. For each experiment, 90 mg of the catalyst was placed in the reaction cell (Praying Mantis High Temperature Reaction Chamber, Harrick Scientific) equipped with transparent KBr windows.

The sample was dehydrated at 365 °C in 12.5% O_2/He for 1 h, subsequently heated in 7% H_2/Ar to 550 °C and kept at 550 °C for 30 min until a steady state was reached. After the gas phase had been switched to pure He, the sample was rapidly cooled to room temperature (approximately 1 min), and a spectrum was recorded.

Data processing consisted of background removal by subtraction of a baseline formed by 12 anchor points. A background spectrum of the gas phase was recorded using KBr as an infrared-transparent sample. The propane gas phase and the operando spectra were then normalized to the propane gas-phase peak at ~3000 cm^{-1} and subtracted to remove propane gas-phase contributions.

X-ray Diffraction (XRD). X-ray diffraction patterns were recorded on an Empyrean system (Malvern Panalytical) in Bragg–Brentano geometry using Cu Kα radiation and a $PIXcel^{1D}$ detector. For in-situ analysis, 90 mg of catalyst was placed in an XRK 900 (Anton Paar) reaction chamber equipped with a NiCr–NiAl thermocouple to measure the temperature directly next to the sample surface. The samples were first dehydrated in 12.5% O_2/N_2, cooled to room temperature, and subsequently treated in 5% H_2/Ar. The samples were then heated in 100 °C steps up to 900 °C, with an equilibration time of 30 min at each temperature. They were measured for 10 min in a 2θ range from 20° to 70° with a step width of 0.025° for each step. Rietveld analysis was performed between 750 and 900 °C using the TOPAS software together with reference structures from the ICSD database. The background was corrected by using a Chebychev function with ten polynomials.
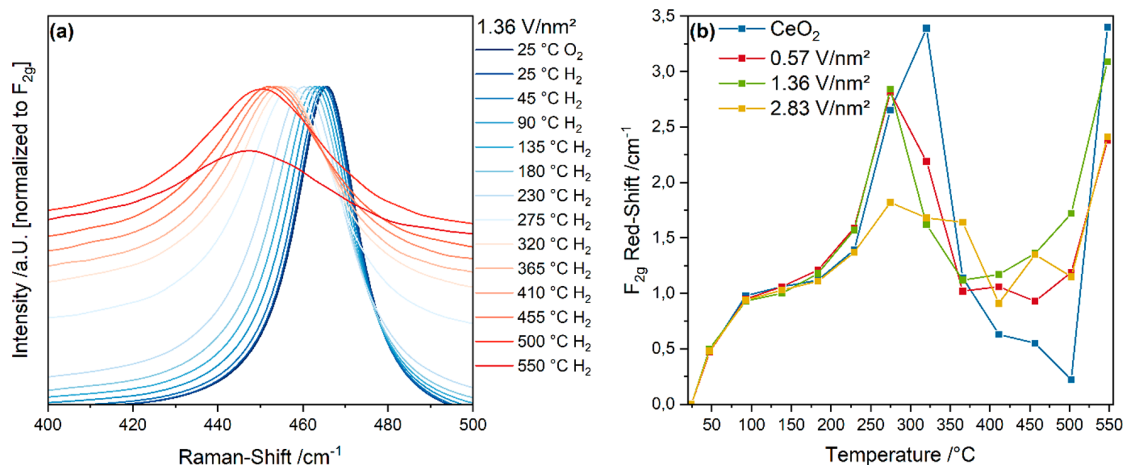
Figure 2. (a) Evolution of the F_{2g} peak for the 1.36 V/nm^2 sample between 25 and 550 °C in 7.5% H_2/Ar. (b) Summary of observed F_{2g} red-shifts between 25 and 550 °C for VO$_x$/CeO$_2$ samples and bare ceria. The positions were determined from in-situ 514 nm Raman spectra. Please refer to the Supporting Information for full-range spectra and F_{2g} peaks.

RESULTS AND DISCUSSION

Figure 1 depicts the reducibility behavior of ceria-supported vanadia and bare ceria from TPR experiments performed between 50 and 850 °C, using a TCD to measure the hydrogen consumption (Figure 1a). Extensive spectroscopic characterization of the samples is given elsewhere.[18] V_2O_5 was employed as a well-known reference to calibrate the temperature axis.[33] For further analysis of the reducibility behavior, the hydrogen consumption during TPR was integrated (see Figure 1b).

As can be seen from Figure 1a, all samples show two distinct regions of hydrogen consumption—a low temperature one and a high temperature one. The low temperature region is located between 200 and 500 °C, and even though the vanadia loading for all samples is relatively low, this region still varies significantly between different loadings. Bare ceria shows a very broad feature with a maximum at 380 °C, with two distinct shoulders at 285 and 510 °C indicating different contributions to the reduction behavior. The sample loaded with 0.57 V/nm^2 reveals a very different low temperature region where the observed hydrogen consumption is shifted to significantly lower temperatures, with two distinct features at 240 and 345 °C, indicating that the sample becomes much more reducible even for small vanadia loadings. For higher-loaded samples with 1.36 and 2.83 V/nm^2, the feature at 240 °C is absent, and the feature at 345 °C decreases in intensity. Interestingly, a new feature appears at 415 °C, which becomes dominant for the sample loaded with 2.83 V/nm^2, indicating that there is a strong dependency on the vanadia loading. Such a splitting between different features within the low temperature region was previously observed in VO$_x$/CeO$_2$ TPR and has been attributed to surface reduction at lower temperatures and subsurface/bulk reduction at higher temperatures.[22,30] The high temperature region starts at around 650 °C and is similar for all vanadia loadings. There is one distinct maximum, which for bare ceria is located at 805 °C but shifts to lower temperatures with increasing vanadia loading. For the sample with the highest loading, an additional shoulder can be observed at 705 °C, indicating additional contributions for the sample with the highest loading.

The integrated hydrogen consumption shown in Figure 1b appears quite similar and indicates that the general reduction behavior of VO$_x$/CeO$_2$ resembles that of bare ceria, but it

reveals significant differences regarding the overall amount of consumption and the temperatures at which some of the processes start to occur. The differences in the amounts of consumed hydrogen are especially large at the temperatures below 230 °C. Even though no distinct peaks are observable in this region, a constant hydrogen consumption is still observed, as can be seen from the different slopes below 230 °C in Figure 1a. A constant reduction process between 45 and 230 °C is therefore expected for all four samples, but different amounts of hydrogen are consumed, which is likely to be caused by a change in reducibility. For bare ceria and the 2.83 V/nm^2 sample there is low hydrogen consumption below 250 °C, whereas for the 0.57 and 1.36 V/nm^2 samples a much steeper increase can be observed, indicating the presence of reduction processes even at temperatures below the first TPR peaks (see Figure 1a). The sample loaded with 0.57 V/nm^2 shows the strongest consumption of hydrogen below 420 °C, which plateaus afterward and stays constant up to ~600 °C. The remaining samples show a similar behavior, but the temperature at which the plateau is reached increases to 460 °C (1.36 V/nm^2), 480 °C (2.83 V/nm^2), and 590 °C (CeO$_2$). Even though ceria continues to consume hydrogen up to much higher temperatures, the overall amount of consumed hydrogen is still lower at 590 °C compared to the vanadia-loaded samples. This indicates that low vanadia loadings increase the reducibility in the low temperature region significantly, which then starts to drop off again for higher vanadia loadings. After the plateau, the samples continue to consume hydrogen at higher temperatures, beginning at ~600 °C for the 0.57 and 1.36 V/nm^2 samples, at 615 °C for the 2.83 V/nm^2 sample, and at 675 °C for bare ceria. The high temperature region is very similar in shape and overall amount of consumed hydrogen for all four samples, indicating that the reduction behavior above 600 °C is much less affected by the vanadia loading than the low temperature region. At 850 °C, the overall amount of consumed hydrogen is lowest for ceria, followed by the 2.83 V/nm^2 sample and the 0.57 V/nm^2 and 1.36 V/nm^2 samples, which show a similar overall consumption.

To gain a detailed understanding of the reduction behavior observed in TPR, we investigated the samples with different spectroscopic methods. A good initial descriptor of the
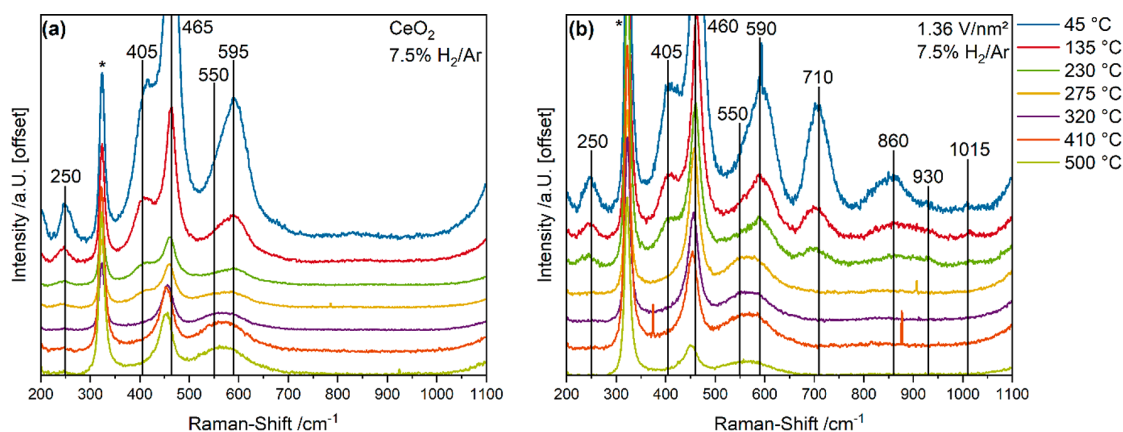
Figure 3. In-situ UV-Raman spectra (385 nm excitation) of bare ceria (a) and the 1.36 V/nm^2 sample (b) recorded in 7.5% H$_2$/Ar flow at selected temperatures between 45 and 500 °C. The asterisk marks the signal from the used CaF$_2$ window.

reduction of ceria is the F$_{2g}$ red-shift, which is determined here from Vis-Raman spectra (at 514 nm) because visible excitation allows a higher depth of penetration[18] in comparison to UV wavelengths and therefore increased sensitivity toward subsurface/bulk contributions. The F$_{2g}$ position is an excellent descriptor for subsurface/bulk reduction due to the ceria lattice expansion upon Ce^{3+} formation during reduction.[34] Figure 2 exemplarily depicts the F$_{2g}$ mode of ceria loaded with 1.36 V/nm^2 at different temperatures in 7.5% H$_2$/Ar (see Figure 2a) and the F$_{2g}$ red-shifts determined by fitting analysis for all samples (see Figure 2b). For the full-range Vis-Raman spectra at each temperature as well as the evolution of the F$_{2g}$ positions, refer to the Supporting Information (see Figures S2 and S3).

As can be seen from Figure 2a, the F$_{2g}$ mode shows a continuous red-shift toward a lower wavenumber with increasing temperature. The observed F$_{2g}$ shifts are significant, considering the degree of bulk reduction needed for a shift of multiple wavenumbers.[5,32] Interestingly, the shifts show a strong variation with temperature, with a maximum between 200 and 350 °C. Such a behavior would not be expected from a pure temperature effect. Furthermore, the full width at half-maximum (FWHM) steadily increases with increasing temperature up to 550 °C, which is also indicative of strongly defective ceria.[40]

Performing a fitting analysis to determine the F$_{2g}$ maximum allowed the shifts to be quantified, as shown in Figure 2b (see the Experimental Section for details). Between 25 and 90 °C rather small shifts between 0 and 1 cm^{-1} are observed, and up to 180 °C the shift stays constant at about 1 cm^{-1} with each temperature step, indicating that these effects are caused by the temperature increase.[41] After that a significant increase of the observed red-shifts occurs, starting at 230 °C with ~1.5 cm^{-1} for all samples, which increases to a maximum of 3.5 cm^{-1} at 320 °C for bare ceria and to slightly smaller maxima of 2−3 cm^{-1} at 275 °C for the vanadia-loaded samples. Only the 2.83 V/nm^2 sample does not show a clearly defined maximum but rather a plateau at 1.5 and 2 cm^{-1} between 275 and 365 °C, indicating a rather constant rate of reduction over a broad temperature range, which is consistent with the observed TPR behavior. This might be caused by the increased variety of surface vanadia species with different nuclearities, which may show differing reduction behavior and interaction with the support, thereby affecting the support reduction properties, as shown previously.[26,27] Thus, the reduction behavior is strongly

altered at temperatures below 450 °C depending on the distribution of vanadia species on the surface, consistent with the TPR results.

After this maximum, bare ceria shows a significant decrease in its red-shift down to almost 0 cm^{-1} at 500 °C, followed by a rapid increase to almost 3 cm^{-1} at 550 °C. This indicates the onset of an additional reduction process discussed below. For the vanadia-loaded samples a similar drop in the F$_{2g}$ red-shift is observed between 400 and 500 °C, but to a lesser extent than for bare ceria, reaching a minimum of ~1 cm^{-1} per temperature step. Consequently, at these temperatures, the VO$_x$/CeO$_2$ samples are more strongly reduced than bare ceria, which may also be related to the changed reduction behavior caused by the presence of surface vanadia and ceria's tendency to reoxidize vanadium.[18,22,24−27,30] Between 500 and 550 °C, the vanadia-loaded samples also show a massive increase in the F$_{2g}$ red-shift, comparable to bare ceria, indicating similar reduction processes. Therefore, similar to the TPR results, two distinct reduction regions at ~300 °C (low temperature region) and 550 °C (high temperature region) can be observed for VO$_x$/CeO$_2$ and bare ceria for the subsurface/bulk of the samples, as indicated by the F$_{2g}$ red-shifts. This leads to the conclusion that the overall reduction behavior of the samples can be separated into surface reduction processes (<275 °C) and subsurface/bulk reduction processes (≥275 °C), both occurring in the low temperature region, as well as additional reduction processes at above 500 °C. The surface reduction is evidenced by a small but significant hydrogen consumption in the TPR below 275 °C (see Figure 1). Such a small amount of consumed hydrogen would be consistent with surface reduction due to its small content of oxygen species in comparison to the overall amount of oxygen present in the catalyst. In the following, the discussion of the reduction behavior will be separated into surface, subsurface, and bulk reduction.

Starting with the investigation of surface reduction processes, Figures 3a and 3b depict UV-Raman spectra (385 nm excitation) at selected temperatures for bare ceria and the 1.36 V/nm^2 sample. The Raman spectra of all samples at all temperatures are shown in Figure S4. The region beyond 1100 cm^{-1} only contains the 2LO peak and is therefore not relevant for the analysis. A summary of the peak assignments is given in Table 1.

The overall intensity of the ceria signals shows a decrease with increasing temperature during the treatment in H$_2$/Ar, as

Table 1. Peak Assignments for the UV-Raman Spectra

position/ cm^{-1}	assignment	ref
250	longitudinal Ce—O surface phonon (2TA contribution)	5
405	transversal Ce—O surface phonon	5
465	F_{2g}	42
550	defects (contribution from $V_{\ddot{O}}$)	6
595	defects (contribution from Ce^{3+})	6
710	V—O—Ce	22
860	V—O—Ce	22
930	V—O—V	22
1015	V=O	22

observed before.[43,44] Therefore, further analysis of the peak intensities discussed below will be in relation to the F_{2g} peak area to ensure better comparability. For bare ceria, phonons are located at 250−600 cm^{-1}, including the longitudinal and transversal surface phonons at 250 and 405 cm^{-1}, respectively, which first stay constant in intensity in comparison to the F_{2g} mode, then start to show a decrease in intensity at 275 °C, and finally disappear completely at 320 °C. As the decrease in surface phonon intensity is observed, the oxygen vacancy contribution in the defect region at 550 cm^{-1} starts to increase in intensity and becomes as intense as the Ce^{3+} contribution at 595 cm^{-1}. From there, both features increase equally, reaching their highest intensity compared to the F_{2g} mode at 500 °C. This behavior indicates that oxygen vacancies on the surface are first created at around 275 °C, when both the surface phonon intensity decreases and the oxygen vacancy contribution in the defect region increases. From there on, oxygen vacancies are continuously produced with increasing temperature, while oxygen is also transported from the ceria bulk to the surface (see F_{2g} shifts in Figure 2), as oxygen becomes quite mobile in ceria at elevated temperatures.

In comparison, the spectra of the 1.36 V/nm^2 sample reveal additional features from surface vanadia species, located between 710 and 1050 cm^{-1} (see Figure 3b). The V=O peak shows only a very small intensity at the chosen excitation wavelength and will therefore be discussed below in the context of the 514 nm Raman data. The V—O—Ce features at 710 and 860 cm^{-1} are reduced significantly in their intensities between 45 and 130 °C, continuing up to 230 °C for the 710 cm^{-1} feature. The transversal Ce—O surface phonon also

decreases in intensity, but to a lesser extent than the vanadia features and slightly changes its line shape between 135 and 230 °C during the strong reduction of V—O—Ce. This smaller decrease in intensity is probably caused by ceria regenerating some of the reduced vanadia back to oxidation state V^{5+}, thereby consuming some of the lattice oxygen. At 275 °C the surface phonon completely disappears, indicating strong reduction of the ceria surface about 45 °C below the temperature at which the phonon fully disappeared on bare ceria. Concurrently, all vanadia-related peaks disappear, as they cannot be kept in oxidation state V^{5+} by ceria's lattice oxygen anymore, and the oxygen vacancy contribution in the defect region increases. Reduced vanadia in oxidation state V$^{3+/4+}$ has a significantly lower Raman scattering cross section than V^{5+}, which results in the disappearance of the V^{5+}-related signals from the UV-Raman spectra.[28,45]

At temperatures above 275 °C, the vanadia-loaded sample appears to behave in the same way as bare ceria. The first maximum in the F_{2g} shifts (see Figure 2b) occurs at the same temperature as the complete disappearance of the Ce—O surface phonon signal and the significant intensity increase in the defect region of the UV-Raman spectra. Therefore, the reduction observed on the surface (see Figure 3a,b) is also observable in the subsurface/bulk of the material due to oxygen diffusion to the catalyst surface. The maxima for the vanadia-loaded samples are also observed at 275 °C instead of 320 °C, supporting the interpretation of indirect ceria reduction mediated by vanadia reduction and subsequent reoxidation by the ceria surface. As vanadia structures can be well reduced below 275 °C and ceria keeps vanadium in the oxidation state V^{5+}, the surface can be reduced at lower temperatures, where it is not as easily regenerated by oxygen from the ceria bulk due to the lower rate of diffusion at lower temperatures. When both samples are in a reduced state at higher temperatures (i.e., ≥320 °C), a balance between the increased rate of reduction by H$_2$ and the increased rate of oxygen diffusion from the bulk seems to be reached. The general trends are the same for the 0.57 and 2.83 V/nm^2 samples. These results provide important first insights into the surface reduction behavior and the interaction between vanadia, the ceria surface, and the subsurface. These reduction processes occur at temperatures that are consistent with the early reduction observed in TPR below 230 °C, where mainly vanadia seems to be reduced, thereby indirectly reducing ceria
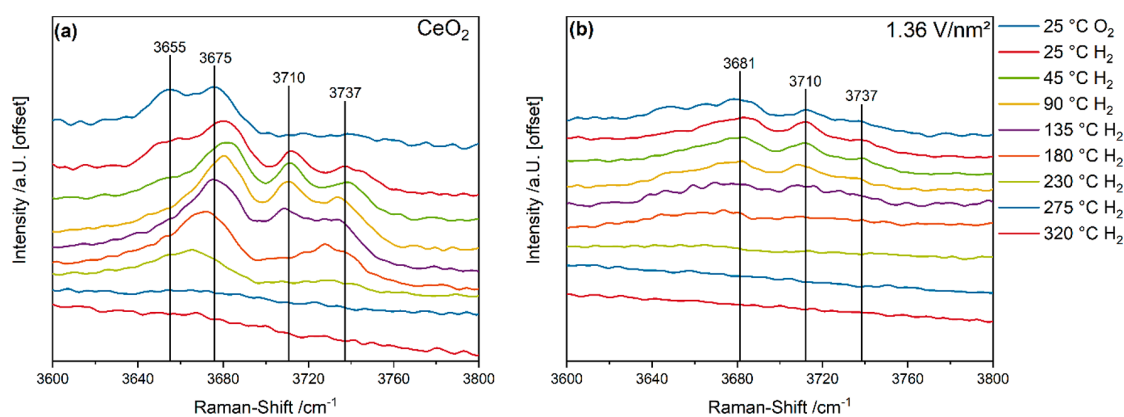

Figure 4. In-situ Vis-Raman spectra (514 nm excitation) of the Ce—OH region between 25 and 320 °C for bare ceria (a) and the 1.36 V/nm^2 sample (b) in 7.5% H$_2$/Ar. Spectra are offset for clarity.
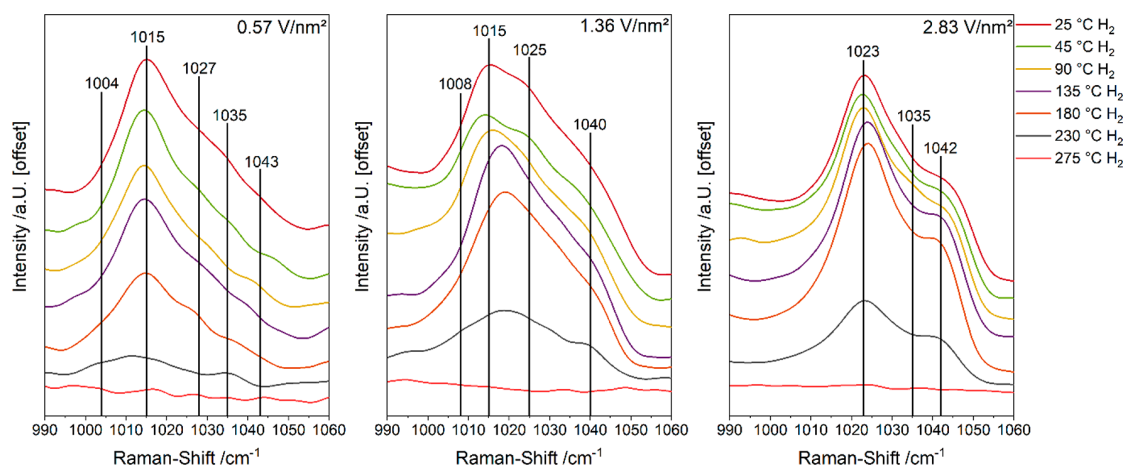
Figure 5. In-situ Vis-Raman spectra (514 nm excitation) of the vanadyl region between 25 and 275 °C for VO_x/CeO_2 samples in 7.5% H_2/Ar. At higher temperatures (>275 °C) no vanadyl peak is observed. Spectra are offset for clarity and normalized to the F_{2g} peak.

via the regeneration process. The intensity decrease cannot be directly correlated to the hydrogen consumption due to the potential presence of resonance Raman effects, which may selectively enhance some of the signal intensities, but qualitative trends can be derived. Between 275 and 320 °C the first strong hydrogen consumption signals can be observed in TPR, which are consistent with the complete reduction of surface lattice oxygen as indicated by the surface phonons in UV-Raman spectra.

To explain the early surface reduction behavior of bare ceria when no vanadia is present, Figure 4 exemplarily shows the Ce−OH region of bare ceria and the 1.36 V/nm^2 sample at temperatures between 25 and 320 °C, as an indicator for ceria surface reduction below the temperatures of vacancy formation.

Compared to the vanadia-loaded sample, bare ceria shows much more pronounced Ce−OH signals, as the vanadia species anchor to ceria Ce−OH groups during the synthesis.[18,22] As discussed in the following, the reduction of Ce−OH can readily explain why ceria shows some hydrogen consumption during TPR (see Figure 1) at <230 °C although no vanadia is present. For bare ceria, at room temperature in 12.5% O_2/He flow, two Ce−OH peaks are observed at 3655 and 3675 cm^{-1}, which have been assigned to bridged Ce−OH bonds on the clean ceria surface (type II-A) and bridged Ce−OH bonds next to an oxygen vacancy (type II*-B), respectively, as some oxygen vacancies are always present on the ceria surface.[46] Upon exposure to 7.5% H_2/Ar at the same temperature, two additional Ce−OH peaks appear at 3710 and 3737 cm^{-1}, which according to the literature can be assigned to type II−B Ce−OH groups and singly bound Ce−OH bonds (type I-A), respectively.[46] The occurrence of additional Ce−OH peaks at 25 °C upon hydrogen exposure indicates the activation of hydrogen at very low temperatures, which is very different to the activation behavior of other reactants such as ethanol or propane, which are only activated at much higher temperatures.[12,13,18] When the temperature is increased, the peak at 3655 cm^{-1} decreases significantly at 45 °C and fully disappears at 90 °C, indicating that Ce−OH groups on the clean ceria surface are rather easily reduced. The peak at 3675 cm^{-1} stays constant in intensity up to 135 °C, starts to decrease at 180 °C, and finally disappears at 275 °C. The type II-B Ce−OH signal located at 3710 cm^{-1} is reduced within the

same temperature range, whereas the singly bound Ce−OH groups first increase in their relative intensity up to 90 °C and then start to decline until their disappearance at 275 °C. At 275 °C and above, the Ce−OH groups are all fully reduced, which is consistent with the TPR results, where ceria shows a small but constant hydrogen consumption up to 285 °C, where it starts to show the first hydrogen consumption peak, explaining the surface reduction behavior at temperatures below oxygen vacancy formation. In comparison, vanadia barely shows any Ce−OH groups, so that their contribution to the overall reduction behavior is expected to be negligible compared to the vanadia contribution.

To understand the different vanadia surface reduction processes as indicated by their different hydrogen consumptions during TPR below 230 °C, the vanadyl region was analyzed in more detail between 25 and 275 °C (see Figure 5).

In the vanadyl region of the VO_x/CeO_2 samples, multiple contributions to the overall peak can be observed at ∼1005, ∼1015, ∼1025, ∼1035, and ∼1040 cm^{-1}, which originate from different vanadia nuclearities as vanadyl groups can exhibit dipole−dipole interactions. As a result, vanadia structures with higher nuclearities show larger blue-shifts, resulting in a fine structure on a ceria support. The above positions can be assigned to monomeric, dimeric, trimeric, tetrameric, and pentameric species, respectively.[13,18,47] In the following, the tetra- and pentameric species will be termed oligomeric vanadia species. In general, only very small changes in the vanadyl fine structure are detected below 230 °C. It needs to be pointed out that very small changes might be caused by noise, as the vanadyl intensity is comparably small (see red curves at 275 °C in Figure 5). Additionally, the reduction of V−O−V (see Figure 3) results in a decrease of the nuclearity, thereby also slightly changing the position before its regeneration by ceria. The overall shape, however, shows only insignificant changes at lower temperatures before it is more significantly reduced. As the vanadia reduction is regenerated by ceria, the reducibility of the different nuclearities should not influence the fine structure for the same sample at different temperatures but still leads to different hydrogen consumptions due to the different ceria reduction rates mediated by the different (nuclearity-dependent) reducibilities. For the 0.57 V/nm^2 sample, the strongest contribution to the vanadyl peak comes from the dimeric
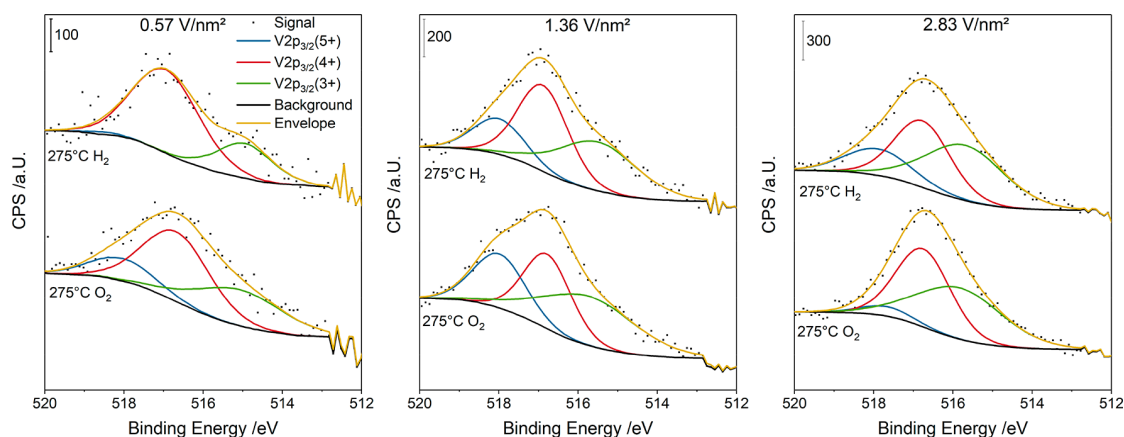
Figure 6. V 2p$_{3/2}$ photoemission of VO$_x$/CeO$_2$ samples at room temperature after oxygen pretreatment (12.5% O$_2$/Ar) at 300 °C (bottom) and after hydrogen pretreatment (7.5% H$_2$/Ar) at 300 °C (top) followed by (air-free) transfer to the analysis chamber, together with the results of a fit analysis.[48] Spectra are offset for clarity.

species, whereas at higher loadings, there is a shift toward increasingly higher contributions from trimeric and oligomeric species. With increasing temperature, the vanadyl peaks appear to stay unchanged up to 230 °C, where a significant decrease in intensity is observed, but the overall line shape still stays unchanged. When the temperature is increased further to 275 °C, the vanadyl peak completely disappears, which is consistent with the other vanadia features detected by UV-Raman spectroscopy (see Figure 3) and indicates the complete reduction of vanadium(V) species on the catalyst surface. This coincides well with the subsequent creation of oxygen vacancies as observed in the UV-Raman spectra as well as the strong increase in hydrogen consumption in TPR at the same temperature.

To explain the difference in the observed hydrogen consumptions between samples with different vanadia loadings at temperatures below 230 °C, the strong shift in the distribution of nuclearities with vanadium loading seems to be of relevance. Previous DFT (density functional theory) studies already showed that there is a significant difference in the reducibility between monomeric, dimeric, and trimeric vanadia species, where the vanadyl oxygen is easily reduced for monomeric and dimeric species, whereas trimeric vanadyl oxygen is not as easily reduced.[26] This finding, in combination with the observed vanadia nuclearity distributions, can explain the difference in reduction behavior, as the two samples with significant monomeric and dimeric contributions show significantly more hydrogen consumption below 230 °C compared to the 2.83 V/nm^2 sample, which contains mostly trimeric and oligomeric species, leading to much less hydrogen consumption at these temperatures.

The difference between the onset temperatures for the first hydrogen consumption peak (see Figure 1) can also be explained by the different distribution of surface vanadia species. Vanadia changes the reducibility of ceria surface oxygen species in close proximity to the vanadia species, whereby ceria lattice oxygen atoms next to monomeric and dimeric species are more easily reduced than those close to trimeric species.[26,27] Due to the decreasing relative amount of monomeric and dimeric species with increasing vanadia loading, the temperature at which the ceria surface lattice oxygen is first reduced is lowest for the 0.57 V/nm^2 sample and steadily increases with increasing loading. The hydrogen

consumption signal for the 0.57 V/nm^2 sample is also sharper than that of the more highly loaded samples, as there is a sharp distribution of different surface species. As the samples with higher vanadia loadings contain a broader distribution of species, the hydrogen consumption signal also broadens, as the different species influence the reducibility differently, resulting in a variety of different vacancy formation energies. Despite this, the initial vacancy formation temperature is lower for all vanadia-loaded samples than for bare ceria, as the reduction of surface lattice oxygen is always easier in proximity to vanadia than on a clean surface.[26]

To investigate in more detail the very significant reduction step at 275 °C, where surface oxygen vacancies start to form and the V^{5+}-related signals disappear, Figure 6 depicts quasi-in-situ XP spectra of the V 2p$_{3/2}$ region for VO$_x$/CeO$_2$ samples after treatment in 7.5% H$_2$/Ar and 12.5% O$_2$/Ar, together with the results of a fit analysis using three components (V^{3+}, V^{4+}, V^{5+}). The resulting areas for the V^{3+}, V^{4+}, and V^{5+} contributions[48] as well as the ratios of O/Ce and V/Ce for VO$_x$/CeO$_2$ and bare ceria in 12.5% O$_2$/Ar and 7.5% H$_2$/Ar are summarized in Table 2.

Starting with bare ceria, the O/Ce ration was determined to decrease from 1.61 to 1.42 for O$_2$/He and H$_2$/Ar treatment, respectively. This is in line with expectation as the reduction of the ceria surface is accompanied by surface oxygen vacancy formation, which is consistent with the TPR results, as a first

Table 2. Results of the Quasi-In-Situ XPS Analysis Focusing on the Vanadium Oxide State^a

sample	O/Ce	V/Ce	% V^{3+}	% V^{4+}	% V^{5+}	oxidation state
CeO$_2$ O$_2$	1.61					
CeO$_2$ H$_2$	1.42					
0.57 V/nm^2 O$_2$	2.13	0.07	0.34	0.50	0.16	3.82
0.57 V/nm^2 H$_2$	2.16	0.06	0.26	0.73	0.01	3.75
1.36 V/nm^2 O$_2$	2.04	0.11	0.42	0.32	0.26	3.84
1.36 V/nm^2 H$_2$	2.60	0.13	0.39	0.43	0.18	3.79
2.83 V/nm^2 O$_2$	2.44	0.25	0.49	0.46	0.05	3.56
2.83 V/nm^2 H$_2$	2.61	0.22	0.44	0.38	0.18	3.74

^{a}Spectra were recorded after pretreatments in 12.5% O$_2$/He and 7.5% H$_2$/Ar at 300 °C. For details of the analysis, refer to the Experimental Section.
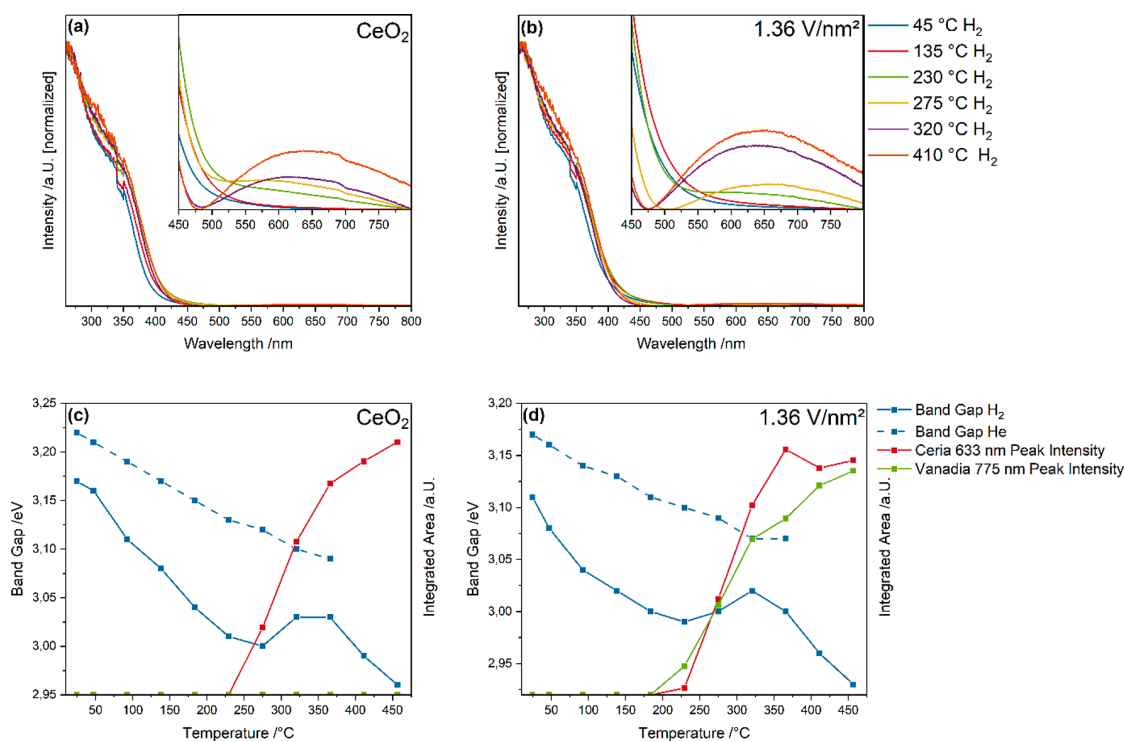
Figure 7. In-situ UV−vis spectra for bare ceria (a) and the 1.36 V/nm^2 sample (b) in 7.5% H$_2$/Ar at selected temperatures between 45 and 410 °C. The insets highlight the absorption behavior between 450 and 800 nm. From the fit analysis (see Figure S7), the areas of the Ce^{3+} → Ce^{4+} charge transfer and vanadia d−d transitions for bare ceria (c) and the 1.36 V/nm^2 sample (d) are obtained and compared to the determined band gaps. To exclude temperature effects, the same spectra were recorded in pure helium at the same temperatures. For details see text and the Supporting Information.

small hydrogen consumption peak is observed at 285 °C. Remarkably, for the vanadia-loaded samples, this trend is reversed. While unexpected at first sight, the observed behavior can be explained when the limited information depth of XPS is taken into account. In fact, as vanadia becomes reduced, it is reoxidized back to oxidation state V^{5+} by ceria, leading to the creation of oxygen vacancies. This increase in the number of charge carriers increases the oxygen mobility, and due to vanadia reoxidation, more oxygen is found in the first few sample layers, even though overall the catalyst is in a more reduced state. This trend is reproducible for all vanadia-loaded samples and is unlikely to be caused by any external effect, such as exposure to air during the transfer because the sample was directly transferred from the gas-pretreatment cell via several pressure stages to the analysis chamber. The increase in the V/Ce ratios is in line with the increase expected due to the increase in vanadia loading from sample to sample and does not vary significantly with the type of pretreatment. This also explains the higher O/Ce ratio for the 2.83 V/nm^2 sample, as more vanadium is detected within the limited information depth of XPS, leading to less detected Ce while the amount of detected oxygen stays similar, as VO$_x$ also contains oxygen. This is also described by the V/Ce ratio that increases much more significantly from 1.36 to 2.83 V/nm^2 compared to the sample with the lowest loading.

Based on the results of the fit analysis shown in Table 2, the distribution of the vanadium oxidation states can be compared as a function of pretreatment and loading. Contributions from all three oxidation states are present in oxidizing as well as reducing conditions where V^{4+} becomes especially dominant. The average oxidation states are lower than for other supports

such as alumina, but the significant presence of V^{4+} has been observed before.[29] For the 0.57 V/nm^2 sample, a decrease in the proportion of V^{5+} and of V^{3+} as well as a significant increase in the amount of V^{4+} can be observed on comparing the spectra after O$_2$/Ar and H$_2$/Ar treatment. This indicates a disproportionation of V^{5+} and V^{3+} species to form additional V^{4+} species on the surface. As more V^{5+} than V^{3+} is consumed during disproportionation, the additional V^{5+} is likely to be reduced directly to V^{4+}, suggesting multiple channels of reduction and regeneration at the interface despite the similar average oxidation state, highlighting the complexity of the system. The increase in V^{4+} species might be caused by the unique interaction between vanadia and ceria and the higher availability of ceria lattice oxygen close to the surface during the reduction processes, before vanadia is further reduced at higher temperatures, as this behavior during initial reduction can not be observed for other supports.[29,49] The complete disappearance of V^{5+} is also in agreement with the Raman results, where no vanadia signals can be observed at 275 °C anymore (see Figures 3 and 5).

The same observations can be made for the 1.36 V/nm^2 sample. However, the sample with the highest vanadia loading diverges from the observed trends and decreases in its V^{3+} and V^{4+} contribution, whereas the V^{5+} contribution to the observed signal increases. This behavior differs significantly from that of the first two samples when the average oxidation state of the samples is considered. In fact, the two lower-loaded samples have similar average oxidation states after oxidizing gas-phase treatments and a slightly decreased oxidation state after hydrogen treatment (see Table 2). Nevertheless, the observed decrease is quite small, indicating that ceria can reoxidize

reduced vanadia as vanadia disproportionates and mostly consists of V^{4+} after reduction at this temperature. This is in good agreement with literature results, where ceria is also described to keep vanadia oxidized in different gas phases.[22,24−26] This measurement is not limited by the precision of XPS, as the average oxidation states are very similar and within the margin of error, but the individual contributions from the vanadium oxidation states vary quite significantly between the gas phases, i.e., outside the margin of error, and the results for the average oxidation state are still similar. This also coincides with the temperature at which the first oxygen vacancies are created in the ceria surfaces, indicating that vanadia is first reduced by hydrogen and then disproportionation occurs, which requires ceria lattice oxygen, leading to vacancy creation and a rather constant oxidation state. In comparison, the oxidation state in the 2.83 V/nm^2 sample increases from an initial value of 3.56 to 3.74, which resembles the averaged oxidation states of the other samples after hydrogen treatment but differs from its initial value under oxidizing conditions. This indicates that the different trend observed for this sample appears to be caused by the low average oxidation state after oxidizing treatment. The difference in the initial state of the sample might be caused by the high vanadia loading, which is very close to the point where three-dimensional VO_x particles form on the surface (2.9 V/nm^2). If such particles were formed, one may expect part of the particles to exhibit a different electronic behavior than the (2-dimensional) surface vanadia aggregates of the other samples, leading to different oxidation states at higher loadings. It appears that upon reduction V−O−V bonds in these particles are broken, leading to the formation of more surface-confined species, which behave similarly to those present in the samples with lower loadings, resulting in a similar average oxidation state. Notably, a loading-dependent difference in behavior can also be observed in the TPR results (see Figure 1b), where the initial reduction of the 2.83 V/nm^2 sample varies significantly from those of the other vanadia-loaded samples and rather resembles that of bare ceria. The change in reduction behavior is unlikely to be caused by the presence of vanadia trimers only as there are significant contributions from higher vanadia nuclearities at this loading (see Figure 5), thus providing a structural rationale for the different characteristics of the highly loaded sample.

So far, the surface processes up to the reduction of V^{5+} and the first formation of surface oxygen vacancies have been analyzed and discussed in detail. To understand the reduction behavior at higher temperatures, bulk methods are necessary to probe subsurface and bulk processes. Furthermore, at 275 °C, most vanadium is not yet fully reduced but mainly present in oxidation state V^{4+}. With increasing temperature, further reduction of vanadium is expected but not accessible by Raman spectroscopy, due to the low scattering cross section of reduced species, or by quasi-in-situ XPS, due to temperature limitations of the experimental setup. Therefore, we have explored the potential of in-situ UV−vis spectroscopy to probe vanadia as well as ceria bulk reduction. Figure 7 shows the UV−vis spectra of CeO_2 and the 1.36 V/nm^2 sample in 7.5% H$_2$/Ar at selected temperatures. As many properties measured in UV−vis spectra are temperature-dependent, the same temperature ramp as for the reduction with hydrogen was performed in pure helium to exclude any temperature effects. The temperature-dependent spectra of all samples in pure helium and 7.5% H$_2$/Ar are given in Figures S5 and S6.

In Figures 7a,b, in-situ UV−vis spectra for bare ceria and the 1.36 V/nm^2 sample are shown. Two types of spectral changes are observed: first, the band gap absorption energy shifts toward higher wavelengths with increasing temperature, and second, a distinct absorption between 500 and 800 nm becomes observable for both samples. The shift in the band gap energy is caused by the formation of oxygen vacancies, which create electronic states closer to the conduction band, thereby decreasing the overall band gap.[50] The shift in band gap energy is therefore a good indicator of the overall ceria reduction. The absorption in the region between 500 and 800 nm is caused by $Ce^{3+} \rightarrow Ce^{4+}$ transitions located at around 633 nm, which is a good second indicator of reduced bulk ceria,[51,52] and by vanadia d−d transitions, which only become allowed transitions upon vanadia reduction ($V^{3+/4+} \rightarrow V^{5+}$), thus representing a good indicator for further vanadia reduction beyond V^{4+}. Because the vanadia d−d transitions are very broad, it is difficult to determine their exact position. We used 775 nm as the position of the vanadium d−d transition as determined by electron energy loss spectroscopy (EELS) on a 2D V_2O_5 material and allowed for divergence between 750 and 800 nm to account for the different material and possibly different vanadia state.[53]

The observed dynamics in the spectra were quantified using Tauc plots for the band gap and fitting analysis (exemplarily shown in Figure S7) for both transitions in the region between 500 and 800 nm. Figures 7c and 7d show the trends obtained for bare ceria and the 1.36 V/nm^2 sample, respectively. In the presence of helium, the band gap energy shows a constant red-shift with increasing temperature. The absorption in the region between 500 and 800 nm is not present in helium (see Figure S5). The observed spectroscopic changes are therefore caused by the reducing hydrogen atmosphere. As shown in Figures 7c,d, the band gap energy shows a linear decrease for both samples, which continues up to 275 °C for ceria and up to 230 °C for the 1.36 V/nm^2 sample. Above these temperatures, the band gap increases again and moves through a maximum, which coincides perfectly with the appearance of the $Ce^{3+} \rightarrow Ce^{4+}$ transition for both samples. The observed blue-shift of the band gap can therefore serve as an indicator of the onset of oxygen vacancy formation, as the blue-shift does not appear to be caused by actual ceria reduction (which would lead to a red-shift), but rather by the influence of the absorption at 633 nm on the Tauc analysis. These temperatures are well in line with the observed structural dynamics and vacancy formation from F_{2g} red-shifts and UV-Raman spectra.

In addition, the ceria reduction can be quantified by UV−vis spectroscopy up to much higher temperatures than by UV-Raman spectroscopy, where the decreasing scattering cross section and the constant shape of the defect region make quantification rather difficult. Figures 7c,d show that ceria is strongly reduced between 250 and 400 °C, whereby the observed 633 nm absorption increases sharply before it starts to drop off at 400 °C for bare ceria but increases more slowly and then plateaus at 400 °C for the 1.36 V/nm^2 sample. This behavior is roughly in line with the observed hydrogen consumptions from TPR (see Figure 1). In addition, the vanadia reduction can be probed further. The observed absorptions for d−d transitions reveal (see Figures 7c,d) that vanadia is strongly reduced when ceria is reduced. However, the absorption does not plateau at around 400 °C, but further increases up to the maximum UV−vis temperature, which is likely to be caused by vanadia reduction down to V^{3+}, thus
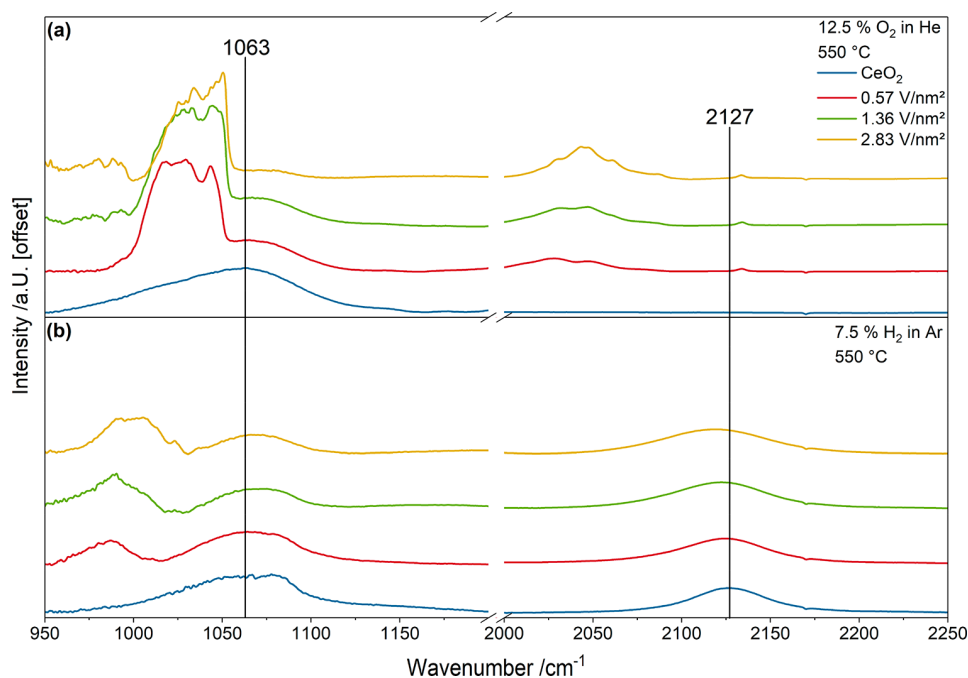
Figure 8. DRIFT spectra of bare ceria and VO_x/CeO_2 samples recorded at 25 °C after pretreatment in (a) 12.5% O_2/He and (b) 7.5% H_2/Ar and subsequent cooling from 550 to 25 °C in He. The resulting spectra are offset for clarity.
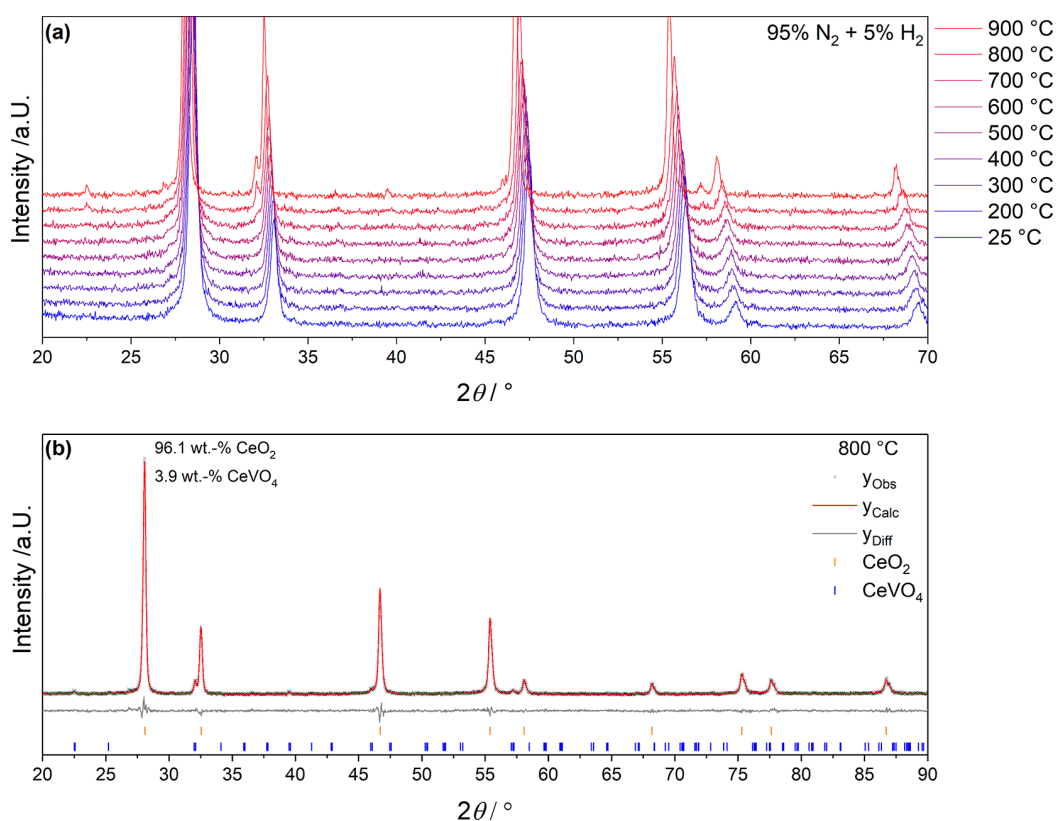
Figure 9. In-situ XRD diffraction patterns for the 2.83 V/nm² sample (a) measured in 5% H_2/N_2 at 25 °C and in 100 °C steps between 200 and 900 °C. (b) Rietveld fit (red) performed on the diffractogram (black) collected at 800 °C.

explaining why the vanadia-loaded samples have a higher overall hydrogen consumption than bare ceria in TPR analysis. The spectra for all four samples at all temperatures are shown in Figure S6, and the obtained trends for the band gap as well

as the obtained areas from the fit analysis are shown in Figures S8 and S9.

The previously performed analysis allowed the complete TPR low-temperature region to be investigated and interpreted

by spectroscopic methods. Above 500 °C, very low amounts of hydrogen are consumed up to the high-temperature region. The small consumptions of hydrogen were investigated by quasi-in-situ DRIFTS analysis. For that the sample was placed in the IR reaction chamber and was pretreated in 12.5% O_2/ He and 7.5% H_2/Ar. After the sample had cooled to room temperature in pure helium, an IR spectrum was measured to avoid thermal noise at the elevated temperatures.

Figure 8 depicts room temperature DRIFT spectra after oxidative (a) and reductive (b) pretreatment, covering the regions 900−1200 and 2000−2400 cm^{-1}, where vanadyl fundamental and overtone vibrations may be expected. After oxidative pretreatment, a vanadyl peak is observed at 1000− 1050 cm^{-1}. Apparently, there is an additional broad (asymmetric) feature, which overlaps with the vanadyl peak. In this wavenumber region, besides Ce−O vibrations of Ce− OH bonds, also Ce−H vibrations of different surface and bulk hydrides may be located.[54] To disentangle the different contributions, we therefore examined the overtone region between 2000 and 2400 cm^{-1}. At 2127 cm^{-1} a peak is observed that would be consistent with a 4-fold coordinated bulk hydride,[54] corresponding to a fundamental vibration located at 1063 cm^{-1}, where analysis is difficult due to overlap. To confirm that this assignment, we performed DRIFTS at different temperatures, as the Ce−O and vanadyl vibrations would be expected to be present at all temperatures whereas Ce−H vibrations should be observable only at high temperatures in hydrogen atmosphere. From the DRIFT spectra it can be seen that this overtone is not present at lower temperatures but begins to appear at above 300 °C (see Figure S10). We therefore conclude bulk hydride formation to occur at above 300 °C up to 550 °C, which offers an explanation for the continuous hydrogen consumption above 400 °C together with the continuous vanadia reduction for the vanadia-loaded samples (see above).

Above 550 °C, our spectroscopies become unviable due to sensitivity issues caused by the high temperature, but large hydrogen consumptions were observed in TPR at temperatures above 700 °C, indicating a phase transition. These occur between 775 and 810 °C and are consistent with the beginning phase transition into substoichiometric structures which first start to appear in nanoparticles, not detected by XRD.[55,56] Only at higher temperatures, a significant change in the diffraction pattern would become apparent.[57] Only the sample with the highest loading (2.83 V/nm^2) shows an additional shoulder at 705 °C (see Figure 1). Besides, the temperatures of the phase transition are shifted toward lower values when vanadia is present. To determine the cause of the shoulder for the 2.83 V/nm^2 sample, in-situ XRD was performed in 5% H_2/ Ar to determine any additional phase transitions besides the one mentioned above.

Figure 9 depicts temperature-dependent diffractograms of the 2.83 V/nm^2 samples together with the results of a Rietveld analysis based on the diffractogram at 800 °C. Up to 600 °C the diffractograms reveal no differences and show only a slight shift of the reflections peaks toward lower angles due to the increased temperatures. At 700 °C, small changes start to become apparent at 22°, 32°, and 57° 2θ where additional reflections appear. When the temperature is further increased, these reflections gain in intensity and coincide well with the positions expected for $CeVO_4$ that has been reported to be formed in the presence of high vanadium loading (starting at 1 V/nm^2 at high temperatures under reducing conditions, but

much more significant amounts are formed at ∼3 V/nm^2) or under reducing conditions.[22,25] To quantify the amount of $CeVO_4$ present under these conditions, Rietveld analysis was performed for the diffractogram at 800 °C, yielding 3.9% $CeVO_4$. This is a significant amount, which is likely to cause some measurable degree of hydrogen consumption, leading to the formation of the shoulder observed for the sample with the highest vanadia loading (2.83 V/nm^2). For the other VO_x/ CeO_2 samples, such a reaction is not observed because the vanadium loading is too low at 0.57 and 1.36 V/nm^2 in the measured temperature range.

Figure 10 summarizes the above findings and bridges the gap between the observed hydrogen consumptions and the
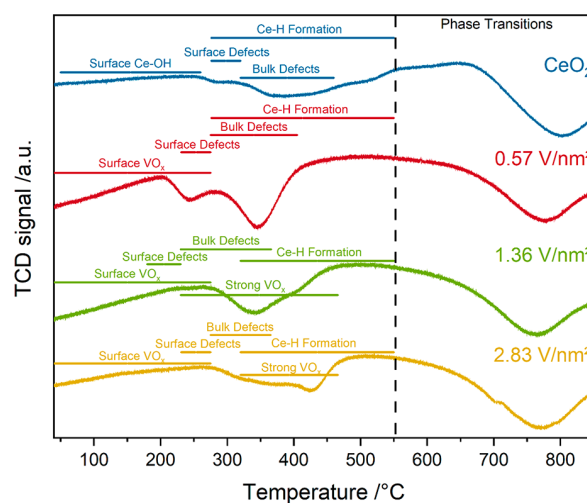

Figure 10. Insight into the structural changes during TPR of bare ceria and vanadia-loaded samples, based on temperature-dependent analysis by multiple in-situ spectroscopy and in-situ diffraction. For details refer to the text.

interpretations on a molecular level, thus allowing the hydrogen consumption behavior in the TPR to be assigned to different structural changes, including the influence of the vanadia loading. The bars indicate the temperature range for each process which was determined exclusively by our spectroscopic findings and show a very good agreement with the observed hydrogen consumptions. The designations of surface Ce−OH and surface vanadia refer to initial Ce−OH and vanadia reduction regenerated by ceria, respectively, determined from UV- and Vis-Raman spectra (see Figures 3−5). Surface defect formation is caused by the depletion of surface oxygen and the permanent formation of oxygen vacancies on the surface as analyzed by UV-Raman spectroscopy (see Figures 3 and S4), and bulk defects are caused by the diffusion of bulk oxygen to the sample surface and subsequent reduction which was determined from Vis-Raman and UV−vis spectra (see Figures 2, 3, 7, and S9). Strong vanadia reduction refers to the continued reduction of vanadia from V^{4+} to V^{3+} and starts after V^{5+}-related signals disappeared from the Raman spectra. The continued reduction was determined by XP and UV−vis spectroscopy (see Figures 6 and 7). For the 0.57 V/ nm^2 sample, there is not enough vanadium present to detect this feature using TPR, as the hydrogen consumption for this reduction process is very small, even for the 1.36 V/nm^2 sample. Hydride formation is tracked by temperature-dependent DRIFTS measurements (Figures 8 and S10), but its

contribution to the overall hydrogen consumption is expected to be comparably small as the TPR shows only small hydrogen consumptions without any maxima in this temperature range. Finally, the phase transitions were determined using in-situ XRD (see Figure 9), but no temperature range is given as no additional processes were determined to occur in this temperature range; therefore, the observed hydrogen consumption is attributed to the occurring phase transitions.

CONCLUSION

In this study we link the reducibility, an important property of metal−oxide catalysts accessible by temperature-programmed reduction (TPR), to molecule-based processes, as developed by the application of multiple in-situ methods. It is shown that a detailed understanding of the surface, subsurface, and bulk dynamics during temperature-dependent reduction is strongly facilitated by complementary analysis using spectroscopy and diffraction.

The TPR of VO_x/CeO_2 catalysts and bare ceria as a reference sample reveals that the hydrogen consumptions can be separated into a high temperature region and a low temperature one, whereby the low temperature region shows multiple contributions and significant variations between different vanadia loadings. In the high temperature region, a rather similar behavior is observed, and the position of the maximum hydrogen consumption is located at temperatures, where first phase transitions into nanodispersive substoichiometric phases can appear. Vis-Raman spectra, employed to further separate the processes in the low temperature region, reveal surface and subsurface/bulk contributions.

Surface contributions at temperatures below 230 °C were determined to be caused by Ce−OH reduction for bare ceria, where bridged Ce−OH groups next to vacancies and singly bound Ce−OH groups were the most important, as well as early vanadia reduction, which is regenerated by ceria to keep vanadium in oxidation state 5+. Further reduction at higher temperatures is caused by oxygen depletion in the ceria surface and surface vacancy formation as well as vanadia reduction by disproportionation of V^{3+} and V^{5+} species to V^{4+} species. All reduction processes occur at different temperatures for different vanadia loadings, and the surface vanadia structures, as determined by the vanadyl fine structure, significantly influence the overall reduction behavior.

Beyond surface reduction ceria subsurface and bulk oxygen atoms diffuse to the surface, where they become reduced and bulk oxygen vacancies are formed. For vanadia-loaded samples, concurrently, strong vanadia reduction to oxidation states lower than V^{4+} occurs and leads to an overall higher hydrogen consumption for vanadia-loaded samples than for bare ceria. These processes are overlapped by the formation of Ce−H bulk hydrides, which add to the overall hydrogen consumption up to 550 °C. At even higher temperatures, the beginning of phase transitions toward substoichiometric nanodispersive phases can be observed for all samples, but for the sample with the highest loading, first a partial phase transition from CeO_2 to $CeVO_4$ is observed. It is demonstrated that the temperature at which the reduction processes occur is strongly determined by the vanadium loading because the changes in vanadia structure with increasing loading and the different structures are characterized by different reducibilities.

In summary, we present the first comprehensive study in which the reduction properties of ceria and different VO_x/CeO_2 samples are investigated with multiple in-situ methods over a temperature range of 800 °C and used for the interpretation of TPR results. With our approach, it is possible to also interpret in detail the TPR results of other important catalytic materials and allow for a molecular interpretation of the easily accessible reducibility behavior, thus facilitating the link between mechanistic research and technical application. This approach can readily be transferred to other important catalytic materials such as TiO_2 or SiO_2, which are already used in technical applications and to different properties accessible by, for example, temperature-programmed oxidation (TPO), temperature-programmed adsorption/desorption (TPD), or temperature-programmed reaction (TPR), making this approach highly and broadly applicable in the field of metal−oxide catalysis.

ASSOCIATED CONTENT

ⓢ Supporting Information

The Supporting Information is available free of charge at https://pubs.acs.org/doi/10.1021/acs.jpcc.3c00622.

> Additional TPR data, in-situ Raman, UV−vis, and DRIFT spectra, and results from further analyses (PDF)

AUTHOR INFORMATION

Corresponding Author

Christian Hess − *Department of Chemistry, Eduard-Zintl-Institut für Anorganische und Physikalische Chemie, Technical University of Darmstadt, 64287 Darmstadt, Germany;* ⓞ orcid.org/0000-0002-4738-7674; Email: christian.hess@tu-darmstadt.de

Authors

Leon Schumacher − *Department of Chemistry, Eduard-Zintl-Institut für Anorganische und Physikalische Chemie, Technical University of Darmstadt, 64287 Darmstadt, Germany*

Marc Ziemba − *Department of Chemistry, Eduard-Zintl-Institut für Anorganische und Physikalische Chemie, Technical University of Darmstadt, 64287 Darmstadt, Germany;* ⓞ orcid.org/0000-0001-8075-2322

Kai Brunnengräber − *Department of Chemistry, Ernst-Berl-Insitut für Technische und Makromolekulare Chemie, Technical University of Darmstadt, 64287 Darmstadt, Germany;* ⓞ orcid.org/0000-0002-0318-1850

Lea Totzauer − *Department of Chemistry, Eduard-Zintl-Institut für Anorganische und Physikalische Chemie, Technical University of Darmstadt, 64287 Darmstadt, Germany*

Kathrin Hofmann − *Department of Chemistry, Eduard-Zintl-Institut für Anorganische und Physikalische Chemie, Technical University of Darmstadt, 64287 Darmstadt, Germany*

Bastian J. M. Etzold − *Department of Chemistry, Ernst-Berl-Insitut für Technische und Makromolekulare Chemie, Technical University of Darmstadt, 64287 Darmstadt, Germany;* ⓞ orcid.org/0000-0001-6530-4978

Barbara Albert − *Department of Chemistry, Eduard-Zintl-Institut für Anorganische und Physikalische Chemie, Technical University of Darmstadt, 64287 Darmstadt, Germany*

Complete contact information is available at:
https://pubs.acs.org/10.1021/acs.jpcc.3c00622

Notes

The authors declare no competing financial interest.

ACKNOWLEDGMENTS

REFERENCES

(1) Bond, G. C. Heterogeneous Catalysis; Oxford University Press: New York, 1987.

(2) Beck, B.; Harth, M.; Hamilton, N. G.; Carrero, C.; Uhlrich, J. J.; Trunschke, A.; Shaikhutdinov, S.; Schubert, H.; Freund, H.-J.; Schlögl, R.; et al. Partial oxidation of ethanol on vanadia catalysts on supporting oxides with different redox properties compared to propane. J. Catal. 2012, 296, 120−131.

(3) Carrero, C. A.; Schloegl, R.; Wachs, I. E.; Schomaecker, R. Critical Literature Review of the Kinetics for the Oxidative Dehydrogenation of Propane over Well-Defined Supported Vanadium Oxide Catalysts. ACS Catal. 2014, 4 (10), 3357−3380.

(4) Luo, Z.; Zhao, G.; Pan, H.; Sun, W. Strong Metal-Support Interaction in Heterogeneous Catalysts. Adv. Energy Mater. 2022, 12 (37), 2201395.

(5) Schilling, C.; Hofmann, A.; Hess, C.; Ganduglia-Pirovano, M. V. Raman Spectra of Polycrystalline CeO_2: A Density Functional Theory Study. J. Phys. Chem. C 2017, 121 (38), 20834−20849.

(6) Filtschew, A.; Hofmann, K.; Hess, C. Ceria and Its Defect Structure: New Insights from a Combined Spectroscopic Approach. J. Phys. Chem. C 2016, 120 (12), 6694−6703.

(7) Filtschew, A.; Hess, C. Unravelling the mechanism of NO and NO_2 storage in ceria: The role of defects and Ce-O surface sites. Appl. Catal. B: Environ. 2018, 237, 1066−1081.

(8) Hu, X.; Chen, J.; Qu, W.; Liu, R.; Xu, D.; Ma, Z.; Tang, X. Sulfur-Resistant Ceria-Based Low-Temperature SCR Catalysts with the Non-bulk Electronic States of Ceria. Environ. Sci. Technol. 2021, 55 (8), 5435−5441.

(9) Ziemba, M.; Hess, C. Influence of gold on the reactivity behaviour of ceria nanorods in CO oxidation: combining operando spectroscopies and DFT calculations. Catal. Sci. Technol. 2020, 10 (11), 3720−3730.

(10) Ziemba, M.; Weyel, J.; Hess, C. Elucidating the mechanism of the reverse water-gas shift reaction over Au/CeO_2 catalysts using operando and transient spectroscopies. Appl. Catal. B: Environ. 2022, 301, 120825.

(11) Lin, L.; Yao, S.; Liu, Z.; Zhang, F.; Li, N.; Vovchok, D.; Martínez-Arias, A.; Castañeda, R.; Lin, J.; Senanayake, S. D.; et al. In Situ Characterization of Cu/CeO_2 Nanocatalysts for CO_2 Hydrogenation: Morphological Effects of Nanostructured Ceria on the Catalytic Activity. J. Phys. Chem. C 2018, 122 (24), 12934−12943.

(12) Ober, P.; Rogg, S.; Hess, C. Direct Evidence for Active Support Participation in Oxide Catalysis: Multiple Operando Spectroscopy of VO_x/Ceria. ACS Catal. 2020, 10 (5), 2999−3008.

(13) Schumacher, L.; Weyel, J.; Hess, C. Unraveling the Active Vanadium Sites and Adsorbate Dynamics in VO_x/CeO_2 Oxidation Catalysts Using Transient IR Spectroscopy. J. Am. Chem. Soc. 2022, 144 (32), 14874−14887.

(14) Chen, J.; Zhu, J.; Zhan, Y.; Lin, X.; Cai, G.; Wei, K.; Zheng, Q. Characterization and catalytic performance of Cu/CeO_2 and $Cu/MgO-CeO_2$ catalysts for NO reduction by CO. Appl. Catal. A: Gen. 2009, 363 (1−2), 208−215.

(15) Salaev, M. A.; Salaeva, A. A.; Kharlamova, T. S.; Mamontov, G. V. $Pt-CeO_2$-based composites in environmental catalysis: A review. Appl. Catal. B: Environ. 2021, 295, 120286.

(16) Zou, Z.-Q.; Meng, M.; Zha, Y.-Q. Surfactant-Assisted Synthesis, Characterizations, and Catalytic Oxidation Mechanisms of the Mesoporous MnO_x-CeO_2 and Pd/MnO_x-CeO_2 Catalysts Used for CO and C_3H_8 Oxidation. J. Phys. Chem. C 2010, 114 (1), 468−477.

(17) Zhang, H.; Gao, X.; Gong, B.; Shao, S.; Tu, C.; Pan, J.; Wang, Y.; Dai, Q.; Guo, Y.; Wang, X. Catalytic combustion of CVOCs over MoO_x/CeO_2 catalysts. Appl. Catal. B: Environ. 2022, 310, 121240.

(18) Schumacher, L.; Hess, C. The active role of the support in propane ODH over VO_x/CeO_2 catalysts studied using multiple operando spectroscopies. J. Catal. 2021, 398, 29−43.

(19) Daniell, W.; Ponchel, A.; Kuba, S.; Anderle, F.; Weingand, T.; Gregory, D. H.; Knözinger, H. Characterization and Catalytic Behavior of VO_x-CeO_2 Catalysts for the Oxidative Dehydrogenation of Propane. Top. Catal. 2002, 20 (1/4), 65−74.

(20) Giordano, F.; Trovarelli, A.; de Leitenburg, C.; Giona, M. A Model for the Temperature-Programmed Reduction of Low and High Surface Area Ceria. J. Catal. 2000, 193 (2), 273−282.

(21) Guan, Y.; LI, C. Effect of CeO_2 Redox Behavior on the Catalytic Activity of a VO_x/CeO_2 Catalyst for Chlorobenzene Oxidation. Chin. J. Catal. 2007, 28 (5), 392−394.

(22) Wu, Z.; Rondinone, A. J.; Ivanov, I. N.; Overbury, S. H. Structure of Vanadium Oxide Supported on Ceria by Multiwavelength Raman Spectroscopy. J. Phys. Chem. C 2011, 115 (51), 25368−25378.

(23) Bruce, L. A.; Hoang, M.; Hughes, A. E.; Turney, T. W. Surface area control during the synthesis and reduction of high area ceria catalyst supports. Appl. Catal. A: Gen. 1996, 134 (2), 351−362.

(24) Iglesias-Juez, A.; Martínez-Huerta, M. V.; Rojas-García, E.; Jehng, J.-M.; Bañares, M. A. On the Nature of the Unusual Redox Cycle at the Vanadia Ceria Interface. J. Phys. Chem. C 2018, 122 (2), 1197−1205.

(25) Martínez-Huerta, M. V.; Coronado, J. M.; Fernández-García, M.; Iglesias-Juez, A.; Deo, G.; Fierro, J. L.G.; Banares, M. A. Nature of the vanadia-ceria interface in V^{5+}/CeO_2 catalysts and its relevance for the solid-state reaction toward $CeVO_4$ and catalytic properties. J. Catal. 2004, 225 (1), 240−248.

(26) Penschke, C.; Paier, J.; Sauer, J. Oligomeric Vanadium Oxide Species Supported on the CeO_2 (111) Surface: Structure and Reactivity Studied by Density Functional Theory. J. Phys. Chem. C 2013, 117 (10), 5274−5285.

(27) Penschke, C.; Paier, J.; Sauer, J. Vanadium Oxide Oligomers and Ordered Monolayers Supported on CeO_2 (111): Structure and Stability Studied by Density Functional Theory. J. Phys. Chem. C 2018, 122 (16), 9101−9110.

(28) Wu, Z.; Kim, H.-S.; Stair, P. C.; Rugmini, S.; Jackson, S. D. On the structure of vanadium oxide supported on aluminas: UV and visible raman spectroscopy, UV-visible diffuse reflectance spectroscopy, and temperature-programmed reduction studies. J. Phys. Chem. B 2005, 109 (7), 2793−2800.

(29) Klose, F.; Wolff, T.; Lorenz, H.; Seidelmorgenstern, A.; Suchorski, Y.; Piorkowska, M.; Weiss, H. Active species on γ-alumina-supported vanadia catalysts: Nature and reducibility. J. Catal. 2007, 247 (2), 176−193.

(30) Martínez-Huerta, M. V.; Deo, G.; Fierro, J. L. G.; Bañares, M. A. Changes in Ceria-Supported Vanadium Oxide Catalysts during the Oxidative Dehydrogenation of Ethane and Temperature-Programmed Treatments. J. Phys. Chem. C 2007, 111 (50), 18708−18714.

(31) Suprun, W. Y.; Machold, T.; Papp, H. Comparison of a VO_x-TiO_2 and a VO_x/SbO_y-TiO_2 Industrial Catalyst in the Oxidative Scission of Methyl Ethyl Ketone and 2-Butanol to Acetic Acid. Z. Phys. Chem. 2008, 222 (1), 129−151.

(32) Waleska, P. S.; Hess, C. Oligomerization of Supported Vanadia: Structural Insight Using Surface-Science Models with Chemical Complexity. J. Phys. Chem. C 2016, 120 (33), 18510−18519.

(33) Briand, L. E.; Gambaro, L.; Thomas, H. Temperature-programmed reduction of V_2O_5 and coprecipitated $V_2O_5-TiO_2$ by hydrogen. J. Therm. Anal. 1995, 44 (4), 803−821.

(34) Schilling, C.; Hess, C. Real-Time Observation of the Defect Dynamics in Working Au/CeO_2 Catalysts by Combined Operando Raman/UV-Vis Spectroscopy. J. Phys. Chem. C 2018, 122 (5), 2909−2917.

(35) Nottbohm, C. T.; Hess, C. Investigation of ceria by combined Raman, UV-vis and X-ray photoelectron spectroscopy. Catal. Comm. 2012, 22, 39−42.

(36) Ziemba, M.; Schumacher, L.; Hess, C. Reduction Behavior of Cubic In_2O_3 Nanoparticles by Combined Multiple In Situ Spectroscopy and DFT. *J. Phys. Chem. Lett.* **2021**, *12* (15), 3749−3754.

(37) Hess, C. Direct correlation of the dispersion and structure in vanadium oxide supported on silica SBA-15. *J. Catal.* **2007**, *248* (1), 120−123.

(38) Laachir, A.; Perrichon, V.; Badri, A.; Lamotte, J.; Catherine, E.; Lavalley, J. C.; El Fallah, J.; Hilaire, L.; Le Normand, F.; Quéméré, E.; et al. Reduction of CeO_2 by hydrogen. Magnetic susceptibility and Fourier-transform infrared, ultraviolet and X-ray photoelectron spectroscopy measurements. *J. Chem. Soc., Faraday Trans.* **1991**, *87* (10), 1601−1609.

(39) Oelhafen, P. Practical surface analysis by auger and X-ray photoelectron spectroscopy. *J. Electron Spectrosc. Relat. Phenom.* **1984**, *34* (2), 203.

(40) Suzuki, T.; Kosacki, I.; Anderson, H. U.; Colomban, P. Electrical Conductivity and Lattice Defects in Nanocrystalline Cerium Oxide Thin Films. *J. Am. Ceram. Soc.* **2001**, *84* (9), 2007−2014.

(41) Kainbayev, N.; Sriubas, M.; Virbukas, D.; Rutkuniene, Z.; Bockute, K.; Bolegenova, S.; Laukaitis, G. Raman Study of Nanocrystalline-Doped Ceria Oxide Thin Films. *Coatings* **2020**, *10* (5), 432.

(42) Weber; Hass; McBride. Raman study of CeO_2: Second-order scattering, lattice dynamics, and particle-size effects. *Phys. Rev. B Condens. Matter* **1993**, *48* (1), 178−185.

(43) Loridant, S. Raman spectroscopy as a powerful tool to characterize ceria-based catalysts. *Catal. Today* **2021**, *373*, 98−111.

(44) Dohčević-Mitrović, Z. D.; Radović, M.; Šćepanović, M.; Grujić-Brojčin, M.; Popović, Z. V.; Matović, B.; Bošković, S. Temperature-dependent Raman study of $Ce_{0.75}Nd_{0.25}O_{2-\delta}$ nanocrystals. *Appl. Phys. Lett.* **2007**, *91* (20), 203118.

(45) Shvets, P.; Dikaya, O.; Maksimova, K.; Goikhman, A. A review of Raman spectroscopy of vanadium oxides. *J. Raman Spectrosc.* **2019**, *50* (8), 1226−1244.

(46) Badri, A.; Binet, C.; Lavalley, J.-C. An FTIR study of surface ceria hydroxy groups during a redox process with H_2. *J. Chem. Soc., Faraday Trans.* **1996**, *92* (23), 4669.

(47) Baron, M.; Abbott, H.; Bondarchuk, O.; Stacchiola, D.; Uhl, A.; Shaikhutdinov, S.; Freund, H.-J.; Popa, C.; Ganduglia-Pirovano, M. V.; Sauer, J. Resolving the Atomic Structure of Vanadia Monolayer Catalysts: Monomers, Trimers, and Oligomers on Ceria. *Angew. Chem., Int. Ed.* **2009**, *121* (43), 8150−8153.

(48) Silversmit, G.; Depla, D.; Poelman, H.; Marin, G. B.; De Gryse, R. Determination of the V2p XPS binding energies for different vanadium oxidation states (V^{5+} to V^{0+}). *J. Electron Spectrosc. Relat. Phenom.* **2004**, *135* (2−3), 167−175.

(49) Eberhardt, M. A.; Proctor, A.; Houalla, M.; Hercules, D. M. Investigation of V Oxidation States in Reduced V/Al2O3 Catalysts by XPS. *J. Catal.* **1996**, *160* (1), 27−34.

(50) Skorodumova, N. V.; Ahuja, R.; Simak, S. I.; Abrikosov, I. A.; Johansson, B.; Lundqvist, B. I. Electronic, bonding, and optical properties of CeO_2 and Ce_2O_3 from first principles. *Phys. Rev. B Condens. Matter* **2001**, *64* (11), 548.

(51) Binet, C.; Badri, A.; Lavalley, J.-C. A Spectroscopic Characterization of the Reduction of Ceria from Electronic Transitions of Intrinsic Point Defects. *J. Phys. Chem.* **1994**, *98* (25), 6392−6398.

(52) Castleton, C. W. M.; Kullgren, J.; Hermansson, K. Tuning LDA +U for electron localization and structure at oxygen vacancies in ceria. *J. Chem. Phys.* **2007**, *127* (24), 244704.

(53) Lamoureux, B.; Singh, V. R.; Jovic, V.; Kuyyalil, J.; Su, T.-Y.; Smith, K. E. Structural and electronic properties of thermally evaporated V_2O_5 epitaxial thin films. *Thin Solid Films* **2016**, *615*, 409−414.

(54) Li, Z.; Werner, K.; Chen, L.; Jia, A.; Qian, K.; Zhong, J.-Q.; You, R.; Wu, L.; Zhang, L.; Pan, H.; et al. Interaction of Hydrogen with Ceria: Hydroxylation, Reduction, and Hydride Formation on the Surface and in the Bulk. *Chemistry* **2021**, *27* (16), 5268−5276.

(55) Höcker, J.; Krisponeit, J.-O.; Schmidt, T.; Falta, J.; Flege, J. I. The cubic-to-hexagonal phase transition of cerium oxide particles: dynamics and structure. *Nanoscale* **2017**, *9* (27), 9352−9358.

(56) Ma, R.; Jahurul Islam, M.; Amaranatha Reddy, D.; Kim, T. K. Transformation of CeO_2 into a mixed phase CeO_2/Ce_2O_3 nanohybrid by liquid phase pulsed laser ablation for enhanced photocatalytic activity through Z-scheme pattern. *Ceram. Int.* **2016**, *42* (16), 18495−18502.

(57) Körner, R.; Ricken, M.; Nölting, J.; Riess, I. Phase transformations in reduced ceria: Determination by thermal expansion measurements. *J. Solid State Chem.* **1989**, *78* (1), 136−147.

4.1.3 The Active Role of the Support in Propane ODH over VO$_x$/CeO$_2$ Catalysts Studied Using Multiple Operando Spectroscopies

The third publication investigates the reaction mechanism of VO$_x$/CeO$_2$ during propane ODH using O$_2$ as the oxidizing agent. Bare ceria and vanadia-loaded samples were investigated by combining multiple operando spectroscopies including multi-wavelength Raman, UV-Vis, and (isotopic-)DRIFT spectroscopy. The usage of multi-wavelength Raman spectroscopy allows for the disentanglement of ceria and vanadia dynamics by the targeted enhancement of either oxide. The corresponding excitation wavelengths were determined by UV-Vis spectroscopy. The usage of 385 nm excitation enables the dedicated investigation of the ceria support, showing that ceria surface lattice oxygen is reduced during the reaction, directly evidencing that the ceria support actively participates in the reaction. However, the intensity of the defects decreases, despite the reducing conditions. Vanadia can be enhanced selectively by the usage of 514 nm excitation, enabling the investigation of its vanadyl fine structure. This allows for the quantification of the nuclearity distribution on the surface and the assignment of catalytic functions to each chain length. Based on the operando spectra, vanadia shows no structural dynamics under reaction conditions. A specific interaction between monomeric vanadia and ceria surface oxygen vacancies was evidenced by the quantification of monomeric species, showing the ireversible blockage of these active sites, reducing the catalytic activity while enhancing the selectivity. Operando DRIFT spectroscopy enabled the investigation of key adsorbates relevant for the formation of either CO$_x$ or propylene. These results demonstrate the potential of combining multiple operando spectroscopies for the mechanistic investigation of complex catalytic reactions, enabling their understaning on a molecular level.

The active role of the support in propane ODH over VO$_x$/CeO$_2$ catalysts studied using multiple *operando* spectroscopies

Leon Schumacher, Christian Hess *

Eduard-Zintl-Institut für Anorganische und Physikalische Chemie, Technical University Darmstadt, Alarich-Weiss-Str. 8, 64287 Darmstadt, Germany

ABSTRACT

Because of the relevance of supported vanadia catalysts for the oxidative dehydrogenation (ODH) of alcohols and short alkanes, a detailed mechanistic understanding, including the role of the support, is of great importance. In this work, we address the ODH of propane over ceria-supported vanadia (VO$_x$/CeO$_2$) catalysts, especially regarding the active participation of ceria and the synergy effect between ceria and vanadia. A combination of *operando* multi-wavelength Raman-, *operando* UV-Vis- and *operando* IR spectroscopy is applied, including the targeted use of different Raman excitation wavelengths to selectively enhance vibrational features through resonance from vanadia (514 nm) and the ceria support (385 nm). Our *operando* results show that surface lattice oxygen from ceria is crucial for the selective oxidation of propane while the structure of vanadia seems to stay unchanged during the reaction. Rather vanadia structures play an indirect role in increasing the overall selectivity of the reaction. The surface oxygen defects of ceria are affected by the interaction with vanadia monomeric species in direct proximity, owing to an irreversible occupancy of the vacancies by vanadia monomers, which slows down the overall oxygen dynamics and thereby decreases the amount of CO$_2$ produced. Dimeric and oligomeric vanadia species weaken the adsorption of propane onto the ceria surface, further increasing the selectivity. Our mechanistic insights demonstrate the synergy effect between vanadia and ceria in oxidation reactions and provide an experimental basis for a detailed understanding of the role of the support in VO$_x$/CeO$_2$ and other supported vanadia catalysts.

© 2021 Elsevier Inc. All rights reserved.

1. Introduction

Vanadia based catalysts have been shown to be active in the oxidative dehydrogenation (ODH) of alcohols and short-chain alkanes [1–5]. The selective oxidation of propane to propylene is of particular importance due to the increasing demand for propylene to produce polypropylene [6]. The ODH of propane is considered as an alternative/additional way to produce propylene in comparison to conventional processes such as steam cracking or fluid catalytic cracking (FCC) [7]. Besides the active phase, the support material also plays an important role with respect to the catalytic activity during propane selective oxidation. Generally, support materials can be classified as inactive (SiO$_2$, Al$_2$O$_3$) or active (TiO$_2$, ZrO$_2$, CeO$_2$), where active materials are proposed to directly participate in the redox cycle [2,8,9]. While vanadia supported on inactive support materials has been studied intensively [8–15], experimental evidence for the participation of active support materials in

selective oxidation reactions is scarce and mostly present for ethane ODH [16,17].

The use of CeO$_2$ as a support material in combination with vanadia for selective oxidation reactions has attracted considerable attention from both the experimental and theoretical points of view [2,5,8,9,16–27]. The reducibility of the catalyst is regarded as an important factor contributing to the overall reactivity of the system, but direct spectroscopy evidence, for example from *in situ* and *operando* spectroscopy, is still scarce for most reactions [5,14,16,28–31], especially propane ODH. Previous experimental [16,17,27,32–35] and theoretical [19,22–24,36–40] studies on VO$_x$/CeO$_2$ catalysts mainly focused on general properties of the system and the synergy between vanadia and ceria. To this end, it was concluded that the ceria support keeps vanadia in an oxidation state of V^{5+} [16,17,19,27,36] and can actively participate in the reaction through its low defect formation energy [22,24,37]. In the context of propane ODH only a few theoretical studies and even less experimental studies with *operando* spectroscopic evidence are available. Using density functional theory (DFT), Huang et al. investigated possible reaction pathways for propane conversion on the catalyst surface [37] and proposed that propyl adsorption

---

* Corresponding author.
  E-mail address: christian.hess@tu-darmstadt.de (C. Hess).

initiated by hydrogen abstraction at ceria surface lattice oxygen (proposed to be the rate-determining step), owing to its low defect formation energy in the proximity of vanadia structures, followed by adsorption of propyl to a V-O-Ce bond. Further possibilities would be a hydrogen abstraction to V-O-Ce or vanadyl bonds and an adsorption of the propane to the ceria surface, since the energy of those structures is very similar [22,37]. In Raman spectroscopic studies on the structural properties of VO_x/CeO_2 by Wu et al. [35] a synergy effect between ceria defects and vanadia structures was reported, as has been proposed previously for the ODH of ethane and later confirmed using *operando* XANES [16,17,27,28,41]. This was supported by a DFT study by Penschke et al. [22], reporting the structural relaxation of monomeric vanadia structures close to oxygen defects.

In this study, we applied a combination of *operando* multi-wavelength Raman, *operando* UV-Vis, and *operando* DRIFTS (diffuse reflectance infrared Fourier transform spectroscopy) to VO_x/CeO_2 catalysts to address specifically the role of the support material during propane ODH as well as the synergy between the active phase and the ceria support. The use of different Raman excitation wavelengths is crucial to selectively enhance vibrational features from ceria and vanadia, enabling us to unravel the structural dynamics of VO_x/CeO_2 catalysts during propane ODH. While the potential of multi-wavelength Raman spectroscopy has been demonstrated previously for ethanol ODH [5,14], to the best of our knowledge, such an approach has not been applied to propane ODH over vanadium-containing catalysts such as supported vanadia, supported V_2O_5 or mixed oxide catalysts such as supported $MoVO_x$ [42,43]. Combining *operando* Raman, UV-Vis and DRIFT spectroscopy in one study allows the structures of (sub)surface ceria and surface vanadia as well as the presence of adsorbates to be monitored under reaction conditions. Additional mechanistic insight is provided by the dependence of structural properties on vanadium loading.

2. Experimental section

2.1. Catalyst preparation

Ceria was synthesized as described previously [44] and loaded with vanadia by incipient wetness impregnation. Three different loadings were achieved by mixing 2 g of ceria with 0.5 mL of differently concentrated precursor solutions (1.07 mol/L, 0.51 mol/L, 0.21 mol/L) containing vanadium(V) oxytriisopropoxide ($\geq$ 97%, Sigma Aldrich) and 2-propanol (99.5%, Sigma Aldrich). The samples were then heated to 600 °C at a heating rate of 1.5 °C min^{-1} and calcined at 600 °C for 12 h. The specific surface area of the ceria was determined before the impregnation with vanadia and was determined to be 57 $m^2 g^{-1}$ by nitrogen physisorption experiments and use of the Brunauer-Emmett-Teller (BET) method, yielding vanadia loadings of 2.83 V nm^{-2} (2,12 wt-% V_2O_5), 1.36 V nm^{-2} (1,02 wt-% V_2O_5), and 0.57 V/nm^{-2} (0.43 wt-% V_2O_5), respectively. Higher vanadia loadings were not considered due to the presence of crystallites burying part of the deposited vanadia [45]. The resulting catalyst powders were subsequently pressed at a pressure of 2000 kg m^{-2} for 20 s, ground and then sieved using a combination of sieves with 200 μm and 300 μm opening to obtain 200–300 μm particles, suitable for use in a fluidized bed reactor.

2.2. UV-Raman spectroscopy

UV-Raman spectroscopy was performed at an excitation wavelength of 385 nm generated by a laser system based on a Ti:Sa solid state laser pumped by a frequency-doubled Nd:YAG laser (Coherent, Indigo). The fundamental wavelength is frequency doubled

to 385 nm using a LiB_3O_5 crystal. The light is focused onto the sample, and the scattered light is collected by a confocal mirror set-up and focused into a triple stage spectrometer (Princeton Instruments, TriVista 555) [45]. Finally, the Raman contribution is detected by a charge-coupled device (CCD, 2048 × 512 pixels) cooled to −120 °C. The spectral resolution of the spectrometer is 1 cm^{-1}. For Raman experiments, 70 mg of catalyst was placed in a CCR 1000 reactor (Linkam Scientific Instruments) equipped with a CaF_2 window (Korth Kristalle GmbH). A fluidized bed reactor was employed to avoid laser-induced damage, allowing the use of a laser power of 9 mW at the location of the sample. Data processing included cosmic ray removal and background subtraction.

2.3. Vis-Raman spectroscopy

Vis-Raman spectroscopy was performed at excitation wavelengths of 514 nm and 532 nm using an argon ion gas laser (Melles Griot) and a frequency-doubled Nd:YAG laser (Cobolt), respectively. The light was focused on to the sample, gathered by an optic fiber and dispersed by a transmission spectrometer (Kaiser Optical, HL5R). The dispersed Raman radiation was subsequently detected by an electronically cooled CCD detector (-40 °C, 1024 × 256 pixels). The spectral resolution was 5 cm^{-1} with a wavelength stability of better than 0.5 cm^{-1}. For Raman experiments, 70 mg of catalyst was filled into a CCR 1000 reactor (Linkam Scientific Instruments) equipped with a quartz window (Linkam Scientific Instruments). A fluidized bed reactor was employed to avoid laser-induced damage, and for both wavelengths a laser power of 2.5 mW at the sample location was applied. Data analysis of the Raman spectra included cosmic ray removal and an auto new dark correction. Peak fitting analysis was performed for the V = O stretching region of VO_x/CeO_2 samples, fitting five Lorentzian functions to the region between 990 and 1060 cm^{-1} using a Levenberg-Marquardt algorithm implementation in OriginLab 2018.

2.4. Diffuse reflectance UV-Vis spectroscopy

Diffuse reflectance (DR) UV-Vis spectroscopy was performed on a Jasco V-770 UV-Vis spectrometer. Dehydrated $BaSO_4$ was used as white standard. For each experiment, 90 mg of catalyst was put in the commercially available reaction cell (Praying Mantis High Temperature Reaction Chamber, Harrick Scientific) equipped with transparent quartz glass windows.

2.5. Diffuse reflectance infrared Fourier transform spectroscopy

Diffuse reflectance infrared Fourier transform spectroscopy (DRIFTS) was performed using a Vertex 70 spectrometer (Bruker). A liquid nitrogen-cooled mercury cadmium telluride (MCT) detector was used, operating at a resolution of 1 cm^{-1}. Dehydrated potassium bromide was employed as an infrared transparent sample for the background spectrum. For each experiment, 90 mg of catalyst was placed in the commercially available reaction cell (Praying Mantis High Temperature Reaction Chamber, Harrick Scientific) equipped with transparent KBr windows.

Data processing consisted of background removal by subtracting a baseline formed by 11 anchor points. A background spectrum of the propane gas-phase was recorded using KBr as an infrared transmitting sample. The propane gas phase and the *operando* spectrum were then normalized to the propane gas phase peak at 3000 cm^{-1} and subtracted to remove gas phase contributions from propane. Afterwards, rotational bands from water, formed during the ODH of propane, were removed. Finally, to quantify the adsorbate peaks in the region between 1120 cm^{-1} and 1920 cm^{-1}, the spectrum recorded under oxidizing conditions was subtracted from that recorded under reaction conditions to

remove signals caused by the sample itself. Six contributions were identified in the region between 1120 cm^{-1} and 1920 cm^{-1} and four contributions were identified for the region between 2640 cm^{-1} and 2980 cm^{-1}. These were fitted using Lorentzian functions employing the Levenberg-Marquardt algorithm implemented in OriginLab 2018. The spectrum recorded under oxidizing conditions has not been subtracted in Fig. 8.

2.6. Catalytic measurements

Catalytic testing was performed by employing a CCR 1000 reaction cell (Linkam Scientific Instruments) in fluidized bed mode using 70 mg of catalyst. Catalyst samples were first dehydrated for 1 h at 366 °C under oxidative conditions (12.5% oxygen (Westfalen, 5.0) and 87.5% helium (Westfalen, 5.0), 40 mL$_n$/min), then cooled to 50 °C, and subsequently exposed to reaction conditions (12.5% oxygen, 12.5% propane (Westfalen, 3.5) and 75% helium, 40mL$_n$/min). Samples were heated in 50 °C steps up to 600 °C keeping each temperature for 1 h, while the gas-phase composition was analyzed using gas chromatography (GC, Agilent Technologies 7890B). The GC system consists of two columns – a PoraPlotQ and a Molesieve – as well as a thermal conductivity detector (TCD) and a flame ionization detector (FID) connected through a twelve-way valve. Recording one chromatogram took 29 min; so for each temperature, two chromatograms were measured. The pressure was monitored before and after the GC apparatus in order to be able to correct the detected areas for pressure fluctuations.

2.7. Operando measurements

Operando experiments were performed by measuring the catalyst samples first under oxidative conditions (12.5% oxygen (Westfalen, 5.0) and 87.5% helium (Westfalen, 5.0), 40 mL$_n$/min) and then under reactive conditions (12.5% oxygen, 12.5% propane (Westfalen, 3.5) and 75% helium, 40mL$_n$/min), each at 275 °C in a fluidized bed reactor. For the isotope experiments using propane-d$_8$, in addition to treatment in oxidative and reactive conditions, measurements in reactive conditions with propane-d$_8$ were performed (12.5% oxygen, 12.5% propane-d$_8$ (Eurisotope, 98%) and 75% helium, 40mL$_n$/min), after the measurements in reactive conditions using regular propane (propane-h$_8$). The reaction cells used for *operando* experiments are described in the experimental section of the respective techniques. We verified that the Linkam CCR 1000 reactor produced activity data comparable to that obtained in a fixed bed reactor, by comparing the values for the conversions and selectivities obtained during *operando* experiments with those reported in the literature [9] for similar temperatures and vanadia loadings. As an example, for the *operando* reactor used here, for a loading of 1.36 V/nm^2, at a conversion of 13% a selectivity of 22% was obtained (at 366 °C), compared to a selectivity of 25% at 10% conversion (at 350 °C and 1.5 V/nm^2 loading) in a fixed bed reactor. A scheme of the experimental set-up has been discussed previously by Waleska et al. [45]. The penetration depth of the 385 nm radiation (~50–100 nm at 385 nm, ~0.5–1 μm at 514 nm for silicon [46] or ZnO [47]; exact values depend on the actual absorption at the respective wavelength, the material, etc. but values for mixed metal oxides can also be roughly determined [48]) is expected to be significantly lower than that of silicon (<50 nm) owing to the strong absorption of ceria at this wavelength. The temperature of the samples at the surface was determined to be 275 °C for reaction conditions. Characterization of the samples was performed after dehydration at 366 °C for 1 h and cooling back to 25 °C.

3. Results and discussion

3.1. Characterization

Fig. 1 presents the DR-UV-Vis spectra of the VO$_x$/CeO$_2$ catalyst samples prepared with different vanadium loadings, together with that for bare ceria as a reference. The strong absorption below 400 nm can be attributed to ceria [35]. The features at 262 nm and 330 nm result from band gap absorption of ceria, that is, O 2p → Ce 4f transitions [49–51], overlapping with the usually observed ligand-to-metal-charge transfer (LMCT) features of vanadia monomers below 300 nm and dimeric species at ~ 350 nm [52]. Above 400 nm, we observe an increase in absorption with increasing vanadia loading, which has been assigned to LMCT features of oligomeric vanadia species [52]. In the depicted spectra, the excitation wavelengths used for the Raman experiments are marked (385, 514, and 532 nm). An excitation wavelength of 385 nm was chosen because of the significantly higher relative contribution of ceria to the absorption as compared to vanadia, enabling a resonance enhancement for ceria vibrational features. Owing to the low penetration depth at 385 nm excitation, the structural dynamics at the catalyst surface will be measured [52]. As described above, oligomeric vanadia species dominate the absorption behavior at 514 nm (in comparison to 385 nm). Thus, with 514 nm excitation, vanadia-related Raman features can be selectively enhanced due to resonance effects. Laser excitation at 532 nm was chosen to increase the sensitivity towards the characteristic F$_{2g}$ mode as a result of a slightly deeper penetration depth in comparison to 514 nm. In general, excitation at 514 and 532 nm gave similar Raman results. Therefore, only data for either 514 nm or 532 nm excitation will be shown in the following. In conclusion, the multi-wavelength Raman approach enables access to complementary information about VO$_x$/CeO$_2$ catalysts.

Fig. 2 shows the Raman spectra of the VO$_x$/CeO$_2$ catalysts and bare CeO$_2$ at 385 and 532 nm excitation, which were recorded after dehydration at 366 °C and cooling down to 25 °C in 40 mL$_n$/min helium. Spectra are normalized to the F$_{2g}$ peak and offset for clarity. As shown at the top of Fig. 2, for 385 nm excitation, Raman features appear at 247, 405, 463, 590, 709, 860, 930, 1023, and 1170 cm^{-1}. Ceria-related features include the longitudinal (247 cm^{-1}) and transversal (405 cm^{-1}) Ce-O surface phonons [53]. No specific loading-dependent changes in their intensity is observed. A contribution of the bulk 2TA mode at 250 cm^{-1} to the longitudinal surface phonon cannot be excluded, as discussed previously in the literature [53].

Furthermore, characteristic ceria bulk features due to F$_{2g}$ (463 cm^{-1}), 2LO (1170 cm^{-1}), and a broad defect peak with a maximum at ~ 590 cm^{-1} are detected. The latter contains contributions from oxygen vacancies (550 cm^{-1}) and reduced ceria ions (Ce^{3+}, 590 cm^{-1}) [44]. With increasing vanadium loading, the position of the F$_{2g}$ peak shows a small shift towards lower wavenumbers (0.3 cm^{-1}). While these changes are very small, they indicate the reduction of ceria when trying to keep vanadium in oxidation state 5+, as has been observed previously for the VO$_x$/CeO$_2$ system [16,17,27,28] and described by DFT calculations [19,22–24,36]. Previously observed peroxide peaks at ~ 830 cm^{-1} are almost absent, due to the oxidative pre-treatment of the catalyst in 12.5% O$_2$/He at 366 °C for 1 h and subsequent cooling in pure helium [54].

Vanadia-related features include V-O-Ce interface vibrations at 709 and 860 cm^{-1} and a feature at 930 cm^{-1}, which is still being discussed in the literature [34] but might be assigned to either a V-O-Ce or a V-O-V vibration of dimeric/oligomeric species by comparison with the spectra of vanadates [28,34,35,55]. This is supported by the fact that this feature is only present for the sample
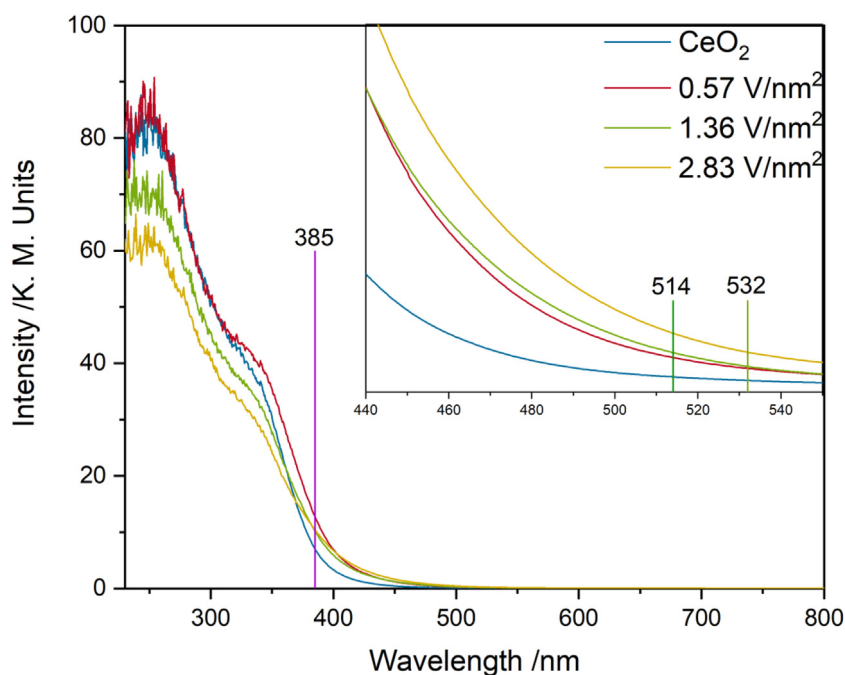
Fig. 1. UV-Vis absorption spectra of VO_x/CeO_2 catalysts and bare CeO_2 at 25 °C recorded in 40 mL_n/min helium after dehydration at 366 °C for 1 h (12.5% O_2 in helium, 40mL_n/min). Excitation wavelengths used for Raman spectroscopy are indicated in purple (385 nm), dark green (514 nm), and light green (532 nm). The inset gives an enlarged view of vanadia absorptions in the region between 440 nm and 550 nm. (For interpretation of the references to colour in this figure legend, the reader is referred to the web version of this article.)
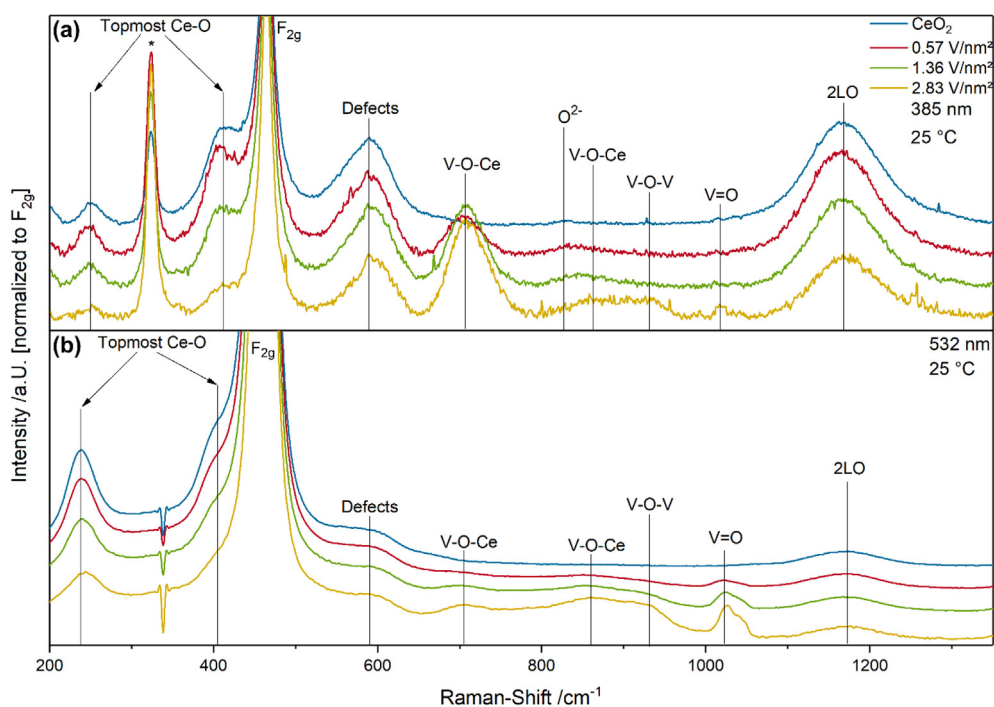
Fig. 2. Raman spectra of VO_x/CeO_2 catalysts and bare CeO_2 at 385 nm (a) and 532 nm (b) excitation, recorded at 25 °C after dehydration at 366 °C in 12.5% O_2/He (40 mL_n/min). Spectra are normalized to the F_{2g} peak. The signal of the CaF_2 window is marked with an asterisk. Spectra are offset for clarity.

with the highest vanadium loading (at 385 nm excitation). Note that at this wavelength, the V = O (vanadyl) stretching vibration at 1023 cm^{-1} is barely visible for samples with low vanadium loading [35].

Raman spectra recorded at 532 nm excitation show in principle the same features as those at 385 nm excitation (see bottom panel of Fig. 2). However, vast differences in the ceria-related peak inten-

sities are observed, owing to the lack of ceria resonance enhancement at 532 nm excitation. The intensity of the V-O-Ce interface peak at 709 cm^{-1} also decreases significantly upon switching from 385 nm to 532 nm, suggesting that this feature might also be resonantly enhanced (also supported by the presence of a small peak at $\sim$ 1400 cm^{-1}, consistent with the first V-O-Ce overtone), for example by excitation of monomeric/dimeric vanadia species

showing UV-Vis absorption below 400 nm. On the other hand, the V-O-Ce and V-O-Ce/V-O-V vibrations at 860 cm^{-1} and 930 cm^{-1}, respectively, become more visible at 532 nm excitation, due to their higher absorption at this wavelength, and increase with vanadium loading, indicating that these features might be assigned to dimeric/oligomeric vanadia [52]. The vanadyl vibration is now clearly visible at all vanadium loadings and shows loading-dependent changes in the profile. In fact, a detailed analysis of the 532 nm spectra (for details refer to the Experimental Section) reveals the presence of (at least) three contributions due to monomeric (~1010 cm^{-1}), dimeric (~1015 cm^{-1}), and oligomeric (>1020 cm^{-1}) species, leading to a broad band in the V = O region [56]. The presence of oligomeric species as indicated by the 532 nm Raman spectra is further confirmed by the band gap energies of the samples (see Tauc plots in Fig. S1 [44]), which were determined to be 2.88, 2.84, and 2.72 eV, corresponding to 2.9, 3.05 and 3.55 V – O–V bonds for loadings of 0.57, 1.36 and 2.83 V/nm^2, respectively [52]. Table 1 summarizes the detected Raman signals for the VO_x/CeO_2 catalysts together with their assignments.

3.2. Catalytic measurements

Fig. 3 shows the results of the catalytic measurements performed for the VO_x/CeO_2 catalysts and bare CeO_2 during propane ODH (feed: 12.5% O_2/12.5% C_3H_8/He) at a flow rate of 40 mL_n/min between 47 °C and 366 °C. The empty reactor shows no activity up to 320 °C, where it starts to show conversions of < 1% with corresponding propylene selectivities of < 5% at 366 °C. In contrast, bare ceria shows catalytic activity with conversions of up to 20%, but with a maximum propylene selectivity of 5.7% at 320 °C. Besides propylene and some CO, mainly CO_2 is produced over bare ceria, indicating high activity for total oxidation of propane, as described in the literature [9,25,57]. A similar behavior was observed for ODH reactions with other alkanes e.g. ethane [16,17,27]. In comparison, upon vanadium deposition, the conversion first significantly decreases for the VO_x/CeO_2 sample with 0.57 V/nm^2 loading and then shows a near-linear decrease with further vanadium loadings (e.g. at 275 °C). This behavior differs from other ODH reactions, for example, the ODH of ethanol [5]. On the other hand, the selectivity of the catalyst increases significantly with vanadium loading, as was reported previously for highly dispersed vanadia on different supports and under different reaction conditions [7,16,17,27,58,59]. Selectivities for conversions > 1% reach up to 46% for 2.83 V/nm^2 at 275 °C, which is 17 times the increase compared to bare ceria, emphasizing the dramatic selectivity increase when ceria is loaded with vanadium. On the whole, the observed conversions and selectivities are of the same order of magnitude as those previously reported in the

literature [9,25,57], however, the absolute values are influenced by different aspects, such as reactor geometry, the catalyst mass, and retention time.

The above results indicate that the presence of vanadia decreases the total oxidation potential and the reaction rate, leading to smaller conversions and higher selectivities. This increase in selectivity cannot be caused just by a decrease in conversion, since the selectivities of the 1.36 and 2.83 V/nm^2 samples at 320 °C are almost equal, whereas the observed conversions differ by ~ 3%. Therefore, further effects need to be considered to explain the observed catalytic behavior in addition to the dependence between conversion and selectivity.

For the *operando* experiments presented in this work, a reaction temperature of 275 °C was chosen. At this temperature, a contribution of homogeneous gas-phase reactions can be excluded. Besides, conversions range between 1.5% and 12.5% (differential conditions), with corresponding propylene selectivities between 46% and 2.8%, allowing relations between structure and activity to be captured. In the following, *operando* spectroscopy is applied to gain mechanistic insight into the structural dynamics of the catalyst under reaction conditions.

3.3. Raman results

The left side of Fig. 4 depicts Raman spectra at 385 nm excitation for bare ceria (top panel) and the VO_x/CeO_2 catalyst with a loading of 1.36 V/nm^2 (bottom panel), both under oxidizing and under reaction conditions (*operando*) at 275 °C. Corresponding spectra recorded for the other catalysts (0.57 and 2.83 V/nm^2) are shown in Fig. S2. In the following, we will focus on the transversal Ce-O surface phonon and the defect area (385 nm spectra), on the vanadyl feature (514 nm spectra), and on the F_{2g} peak (532 nm spectra). Spectra were normalized to the F_{2g} peak. The insets show the shifts of the F_{2g} peaks upon switching from oxidative to reactive conditions, recorded at 532 nm excitation. The right side of Fig. 4 shows the corresponding gas-phase compositions as analyzed by GC, as well as the conversions and selectivities for each sample.

Upon switching from oxidizing to reaction conditions, multiple changes are observable in the recorded spectra. For bare ceria, there is a significant reduction in intensity of the transversal topmost Ce-O surface vibrations, which is indicative of reduction of the ceria surface owing to hydroxyl group formation by hydrogen abstraction from propane and subsequent formation of water, resulting in oxygen defect formation (see Fig. 11). This step may also follow a hydrogen abstraction from propane to the vanadia species and a fast hydrogen transfer to the ceria surface, so that a change in Raman intensity cannot be observed. However, this does not change the overall mechanism described in this study, since either way hydrogen is finally transferred to the ceria surface (see Figs. 8 and 9). The intensity change decreases with increasing vanadium loading (compare Fig. 5), which correlates with the decline in conversion with increase in vanadium loading, further supporting the idea that the reduction in Ce-O intensity originates from propane ODH.

The redshift of the F_{2g} peak (see inset) implies a reduction of the ceria subsurface due to lattice expansion upon oxygen vacancy formation, as previously described in the literature [51]. To work out this effect more clearly, we employed 532 nm laser excitation with its deeper penetration depth compared to 385 nm excitation. Subsurface reduction may be caused by diffusion of surface defects into subsurface layers. As a consequence, diffusion of subsurface oxygen to the catalyst surface is expected, representing a source of ceria surface regeneration besides gas-phase oxygen. The extent of the F_{2g} redshift (see Fig. 5c) also correlates with the observed conversion changes with increasing vanadium loading, whereas

Table 1
Summary of Raman signals in VO_x/CeO_2 catalysts detected at 385 nm/532 nm excitation together with their assignments.

Position / cm^{-1}	Assignment	Reference
250	Longitudinal Ce-O surface phonon (contribution from 2TA)	32
405	Transversal Ce-O surface phonon	32
464	F_{2g}	27
590	Defect peak (contributions from V_O and Ce^{3+})	27
709	V-O-Ce	26
860	V-O-Ce	26
930	V-O-Ce / V-O-V (?)	26
1010	V = O monomer	26
1015	V = O dimer	26
>1025	V = O in different oligomers	26
1170	2LO	27

Fig. 3. Temperature-dependent propane conversion (a) and propylene selectivity (b) of the VO$_x$/CeO2 catalysts and bare CeO$_2$ during propane ODH at a flow rate of 40 mLn/ min (feed: 12.5% O$_2$/12.5% C$_3$H$_8$/He). The surface temperature of the sample is given on the bottom axis. The temperature chosen for the *operando* measurements is indicated by the dotted line. Error bars have been added exemplarily for bare ceria (conversion) and the VO$_x$/CeO$_2$ sample with 2.83 V/nm^2, those of the other samples are of the same order of magnitude.
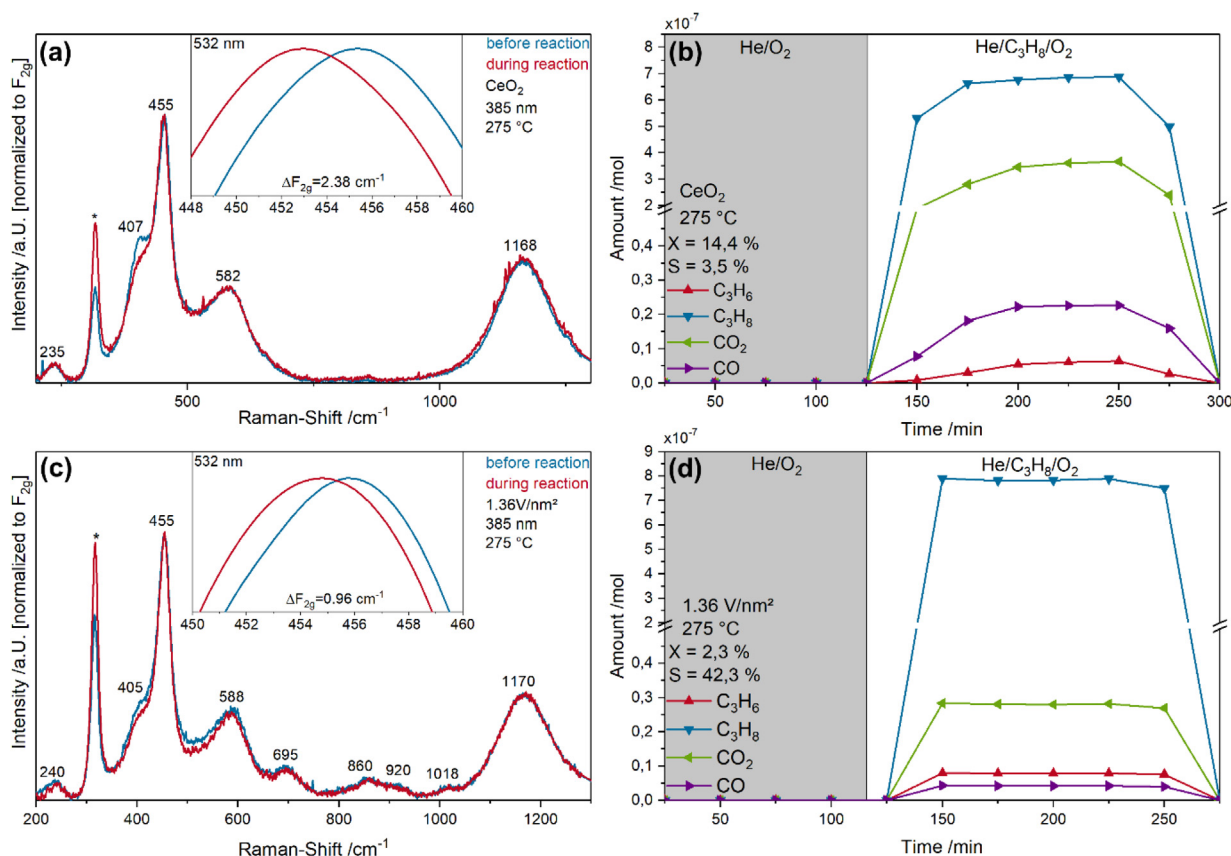
Fig. 4. *Operando* 385 nm Raman spectra (red) of bare ceria (a) and VO$_x$/CeO$_2$ (1.36 V/nm^2) (c) at 275 °C, compared to spectra recorded prior to reaction under oxidative conditions (blue). Spectra have been normalized to the F$_{2g}$ peak. The signal from the CaF$_2$ window is marked with an asterisk. The insets give enlarged views of the F$_{2g}$ maxima recorded at 532 nm excitation. The corresponding gas-phase compositions under oxidizing and reactive conditions are shown on the right for bare ceria (b) and VO$_x$/CeO$_2$ (1.36 V/nm^2) (d) together with the propane conversions and propylene selectivities. Note that the y axis is interrupted between 0.5 and 2 mol for clarity. (For interpretation of the references to colour in this figure legend, the reader is referred to the web version of this article.)

vanadia does not seem to be taking an active part in the reaction since we do not observe any changes in the Raman intensity of vanadia-related features upon switching from oxidizing to reaction conditions.

Besides the dynamics of the surface phonon mode and the F$_{2g}$ peak, we observe significant intensity changes in the defect area

(500–650 cm^{-1}) of the VO$_x$/CeO$_2$ samples, which are not detected for bare ceria. This difference in behavior is attributed to the ability of ceria to act as an oxygen ion conductor, regenerating surface oxygen vacancies fast enough for changes in the surface oxygen defect concentration not to be observed. In contrast, for ceria loaded with vanadium, the defect band decreases under reaction
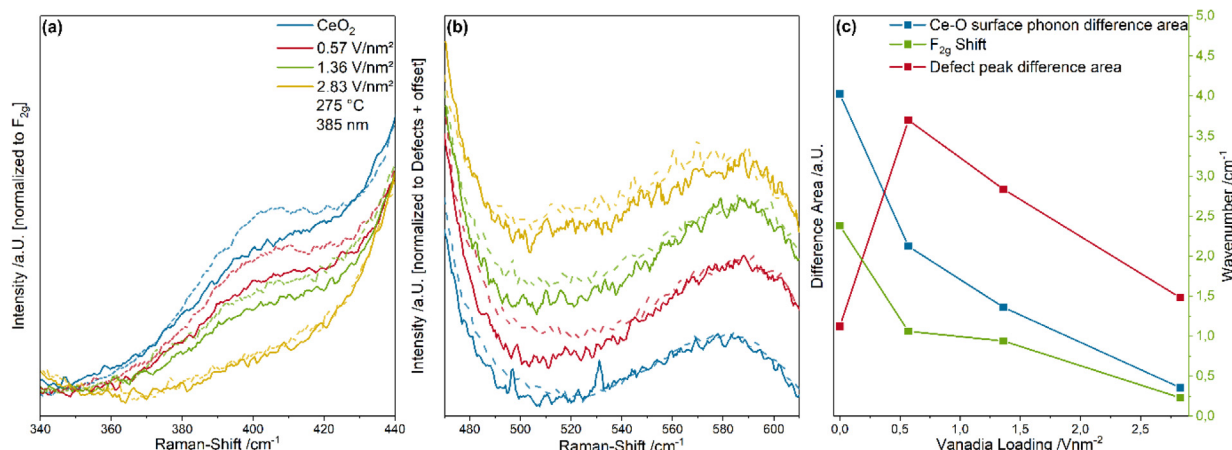
Fig. 5. Raman intensity change of (a) the transversal surface phonon and (b) the ceria defect region (normalized to the defect peak at 590 cm^{-1}) with increasing vanadium loading based on the 385 nm spectra shown in Fig. 4. Dashed lines represent the spectra recorded under oxidizing conditions and solid lines those recorded under reaction conditions. Spectra are offset for clarity. The intensity changes are summarized in (c) together with the F_{2g} shift plotted as a function of vanadium loading.

conditions. Since the oxygen dynamics in the ceria lattice is reduced upon vanadium loading (see F_{2g} shift in Fig. 5c), the surface oxygen defect concentration may be expected to show an increase. This apparent discrepancy might be explained by interactions between vanadia and ceria oxygen defects proposed by Wu et al. [34,35] and further supported by DFT calculations by Penschke et al. showing a structural relaxation of vanadia monomers into ceria surface oxygen defects, thereby blocking defect sites [22] and decreasing their concentration. The defect band region was investigated in more detail by Schilling et al. [53] who conclude that oxygen-vacancy-containing contributions to the overall defect band occur in the same spectral region as the dynamics observed in the Raman spectra (see Fig. 4), which provides additional support for the hypothesis that the observed decrease is caused by surface vanadia after structural relaxation into the vacancy. Since the diffusion barrier of vanadia species on a ceria surface is not overcome at this temperature [23], the sites are irreversibly blocked. As can be seen on the right side of Fig. 4, propane ODH over VO$_x$/CeO$_2$ catalysts does not lead to an increase in the amount of propylene but rather to a significantly reduced CO$_2$ production; based on the above findings, we propose the interaction between vanadia and oxygen vacancies to be responsible for the slowdown in oxygen dynamics during propane ODH resulting in a decreasing CO$_2$ production.

Fig. 5 depicts the changes in Raman intensity of the transversal Ce-O surface phonon (a) and the defect band (b) for VO$_x$/CeO$_2$ samples and bare ceria, based on the 385 nm Raman spectra shown in Fig. 4. Dashed lines represent spectra recorded under oxidizing conditions and solid lines those recorded under reaction conditions. Spectra are offset for clarity. To quantify the observed changes, we calculated difference spectra and integrated the resulting areas (see Fig. 5c). Fig. 5c also contains F_{2g} shifts, which were determined by fitting Lorentzian curves to the F_{2g} peaks under oxidizing and reaction conditions.

Fig. 5a shows that the intensity changes of the transversal Ce-O surface phonon upon switching from oxidizing to reaction conditions decline with increasing vanadium loading. As can be seen in Fig. 5b, changes of the defect band intensity first increase from bare ceria to low-loaded VO$_x$/CeO$_2$ (0.57 V/nm^2), but then decrease almost linearly with a further increase in vanadium loading. This behavior indicates that not all surface vanadia species are capable of interacting with oxygen vacancies but rather only those present at low loadings. According to the DFT study by Penschke et al. [22] monomeric vanadia species are able to relax in to nearby oxygen

defect sites. This was also verified by *operando* XANES [27] and, further supporting the hypothesis of monomeric vanadia species interacting with ceria active sites. Conversely, this means that defect sites further away from monomeric vanadia species should be able to be regenerated by oxygen. The F_{2g} mode also shows a smaller redshift with increasing vanadia loading, indicating less reduced ceria states in the subsurface. This trend correlates with the observed conversion and indicates that ceria reduction is an important feature during the redox cycle of propane ODH. Furthermore, due to blocking of defect sites by vanadia, the defects are not able to diffuse into the subsurface of the catalyst but rather stay at the surface, thus further decreasing the observed F_{2g} shift. This is also shown by the trend of the defect peak difference area where the area differences are large and in a similar order of magnitude for 0.57 and 1.36 V/nm^2, which leads to a reduced F_{2g} redshift in comparison to bare ceria. The area difference of the defect peak of the 2.83 V/nm^2 catalyst is comparable to that of the bare ceria. Therefore, the very small F_{2g} redshift is likely to be influenced mainly by the significantly reduced conversion (see DRIFTS section for an explanation of the reduced conversion at 2.83 V/nm^2).

As a basis for a more detailed structural analysis of the vanadia species present on the ceria surface, Raman spectra were recorded under oxidizing conditions at 275 °C at 514 nm excitation to enhance the vanadia signals (especially the V = O stretching signal) compared to 385 nm excitation. The nuclearity of the vanadia species can be determined from the different frequency positions of the vanadyl peak, as discussed previously in the literature [56]. The full Raman 514 nm spectra (see Fig. S3) do not provide any further mechanistic insight in comparison to those recorded at 385 nm excitation. Hence, the following discussion focuses on the vanadyl stretching region, which is shown in Fig. 6 together with characteristic V = O stretching frequencies of vanadia species with different nuclearities. Slight variations in the V = O positions at different nuclearities are expected due to the influence of dipole interactions of neighboring V = O groups. The V = O stretching contribution with the lowest wavenumber is found to be located at 1008 cm^{-1} in good agreement with the literature, attributed to a monomeric vanadia species [35,36]. Further blueshifted features were then assigned to vanadia species with one more V-O-V bond each. Accordingly, the five contributions at 1008, 1016, 1023, 1030, and 1040 cm^{-1} are assigned to monomeric, dimeric, trimeric, tetrameric, and heptameric species, respectively. These positions are similar to those reported previously in the context of Raman and IR spectra [35,36]. Please note that Raman spectra recorded at
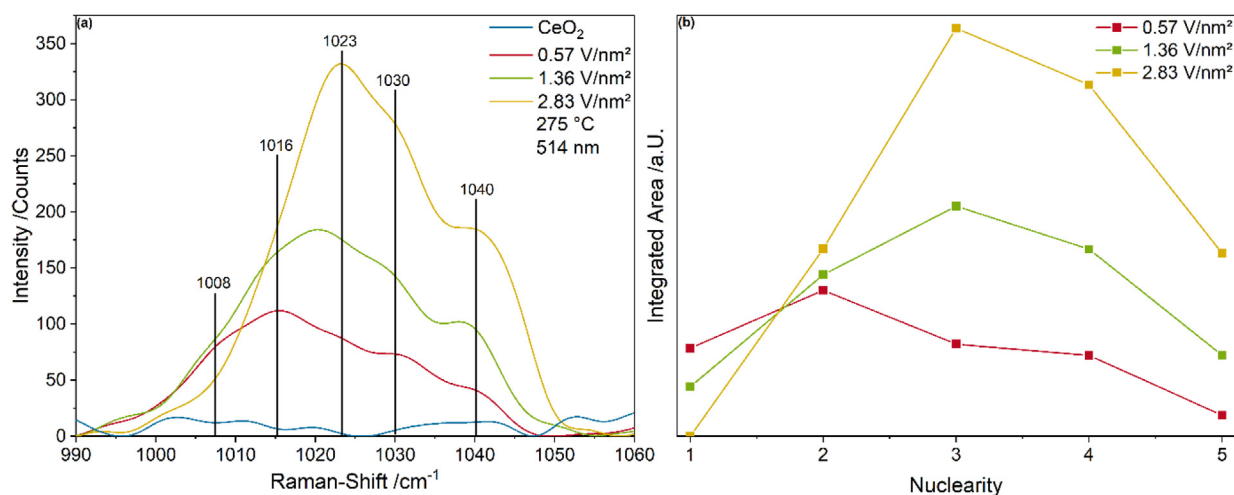
Fig. 6. Vanadyl stretching region of 514 nm Raman spectra (a) recorded under oxidizing conditions at 275 °C for VO_x/CeO_2 and bare ceria. Marked V = O stretching frequencies indicate vanadia species of different nuclearity. From a peak fitting analysis (compare Fig. S4) the areas shown in (b) are obtained.

532 nm and 25 °C gave a slightly higher value for the monomeric species (see Table 1) than that detected at 514 nm and 275 °C (see Fig. 6), consistent with thermal effects.

To quantify the fraction of each surface vanadia species, the vanadyl signal was fitted using five Lorentzian functions, as shown exemplarily in Fig. S4 for a loading of 0.57 V/nm^2. Fig. 6b summarizes the resulting areas as a function of nuclearity. For the lowest vanadium loading (0.57 V/nm^2), dimers are found to be the most common vanadia species on the ceria surface, whereas trimers are most common for higher loadings. According to theoretical calculations, trimeric species are predicted to be the most stable species on a ceria (1 1 1) surface [22]. As discussed before, the observed changes in the defect band intensities (see Fig. 5) may be attributed to the interaction with surface vanadia, most likely monomeric species. In fact, the concentration of monomeric species decreases linearly with the vanadium loading and therefore correlates with the trend observed for the defect intensity changes, whereas the concentration of all other species increases with the vanadium loading. Furthermore, for the sample with a loading of 2.83 V/nm^2, almost no intensity changes in the defect region as well as no monomeric species in the 514 and 532 nm Raman spectra are observed. This behavior is in good agreement with DFT results predicting vanadia monomers to engage in interactions with defects, as mentioned above in the context of Fig. 5 [22].

3.4. DR UV-Vis results

The application of *operando* UV-Vis spectroscopy may provide additional information about the structure of ceria-supported vanadia, but it also allows us to ensure that the dynamics observed in the Raman spectra do not result from changes in sample absorption during reaction, thereby changing the extent of resonance enhancement. Fig. 7 depicts *operando* UV-Vis spectra of bare ceria (a) and VO_x/CeO_2 (1.36 V/nm^2) (b) at 275 °C, compared to spectra recorded under oxidative conditions prior to reaction. The corresponding spectra for the other loadings (0.57 and 2.83 V/nm^2) are shown in Fig. S5. The laser excitation wavelengths (385, 514 and 532 nm) used in this study are indicated, showing no significant changes in absorption between the two conditions. Band gap shifts between spectra measured under oxidizing and reaction conditions were determined using Tauc plots, and the d-d transition intensity caused by reduced vanadium states [60,61] was determined by comparing intensities at 700 nm. Fig. 7c summarizes these results as a function of vanadium loading.

As can be seen from Fig. 7, the absorption changes caused by the exposure to reaction conditions are very small at the excitation wavelengths chosen for Raman spectroscopy. Furthermore, for resonantly enhanced spectra, a change in the ceria, vanadia, or a combination of ceria and vanadia absorption behavior would not be expected to affect only one Raman feature (e.g. the transversal Ce-O surface phonon) but rather multiple features. Based on the *operando* UV-Vis data we therefore conclude that the dynamics in the Raman spectra originates from switching the gas environment from oxidative to reactive rather than changes in the absorption behavior at the excitation wavelengths.

More detailed analysis of the UV-Vis spectra using Tauc plots [44] reveals small but reproducible changes in the band gap energy. The band gap shifts by 0.05 eV between oxidizing and reaction conditions for bare ceria but shows even smaller shifts for the VO_x/CeO_2 samples, i.e., 0.01 eV for the 1.36 V/nm^2 sample. Note that the values determined for the samples loaded with 1.36 V/nm^2 and 2.83 V/nm^2 are within the margin of error. However, the general trend of the band gap shifts indicates the reduction of ceria during propane ODH and the observed band gap shifts also correlate with the conversion observed with increasing vanadium loading. The correlation between the degree of reduction and the band gap has already been proposed by Flitschew et al. [44] based on UV-Vis and Raman spectra at 514 nm excitation and is supported by a first principles DFT study by Skorodumova et al. [62] suggesting that Ce(III) oxide has a smaller band gap than Ce(IV) oxide. This observed band gap shift also correlates with the observed F_{2g} shift from Raman results, indicating that the results from the different methods are consistent. This shows quite clearly, that the bare ceria is reduced most during reaction conditions, whereas an increasing vanadia loading leads to less and less ceria reduction. This is similar to results obtained during ethane ODH [17].

As indicated in the insets of Fig. 7, upon switching from oxidative to reactive conditions, an increase in absorption at higher wavelengths is observed, which originates from d-d transitions of reduced vanadia species (e.g. V^{3+}/V^{4+}) [60,61], and which increases with the vanadium loading. Nevertheless, the relative d-d transition intensities are significantly smaller than those observed for catalyst systems in which vanadia takes part in the reaction or is reduced [63,64]. Therefore, vanadia is either reduced to a very small extent or most of the vanadia is regenerated very fast by ceria to vanadium (V), which would be consistent with previous experimental [16,17,35] and theoretical work [23,37,65]. The
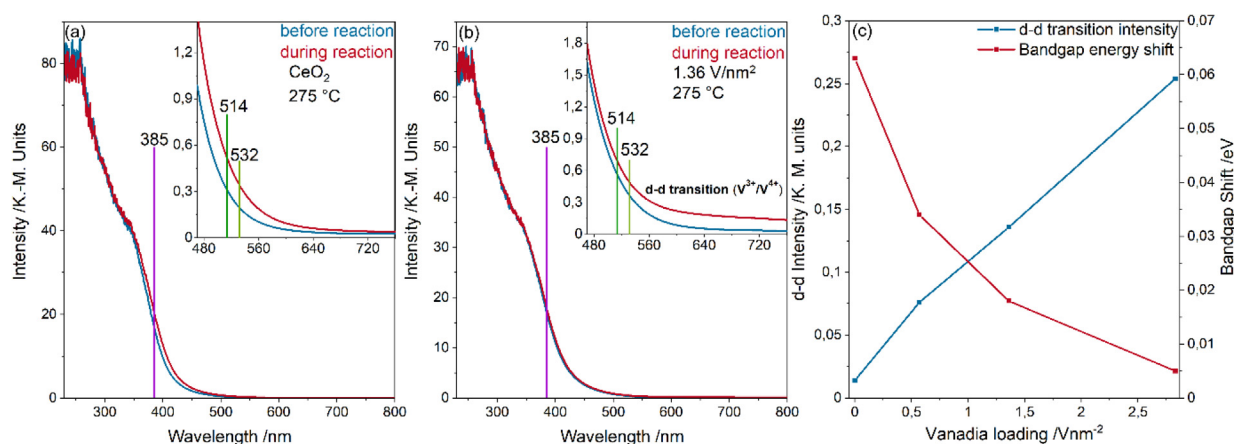
Fig. 7. *Operando* UV-Vis spectra (red) of bare ceria (a) and VO_x/CeO_2 (1.36 V/nm^2) (b) at 275 °C, compared to spectra recorded under oxidative conditions prior to reaction (blue). The laser excitation wavelengths (385, 514, and 532 nm) are indicated. Insets highlight the region between 470 nm and 760 nm. Band gap shifts were determined using Tauc plots and the d-d transition intensity was determined based on intensities measured at 700 nm (c). (For interpretation of the references to colour in this figure legend, the reader is referred to the web version of this article.)

observed d-d intensity increases with vanadium loading (see Fig. 7c) but does not correlate with the observed conversion, indicating that the presence of reduced vanadia species is not linked to the ODH of propane but is rather caused by other effects, such as a generally increased reducibility of the catalyst or a very fast hydrogen transfer from the vanadia to the ceria surface and a very slow further conversion on the ceria surface due to blocked defect sites. This is supported by the fact that there are no observable intensity changes for any vanadia-related features in the Raman spectra on switching to reaction conditions. The small changes in d-d transition intensity and the absence of intensity changes for vanadia related features in 385 nm Raman spectra indicate that vanadia remains largely unchanged during propane ODH or is regenerated very fast after the first C-H hydrogen abstraction to the catalyst surface.

The changes in band gap energy observed in the UV-Vis spectra are indicative of a reduction of the ceria (sub)surface during the reaction. This behavior is fully consistent with the 385 and 532 nm Raman results described above (see Fig. 5c). In fact, the reduction of the ceria surface is indicated by the Ce-O intensity decrease in the 385 nm Raman spectra, whereas the ceria subsurface reduction is evidenced by the F_{2g} redshift at 532 nm excitation.

3.5. DRIFTS results

Based on the results from operando Raman and UV-Vis spectroscopy we propose the ceria support to be actively taking part in the ODH of propane. As discussed for the catalytic measurements, a decrease in conversion cannot be the only reason for the increase in selectivity with increasing vanadium loading, since VO_x/CeO_2 samples with different loadings at the same conversion had different selectivities. The observed decrease in conversion and increase in selectivity of the 0.57 V/nm^2 catalyst (compared to bare ceria) could be rationalized by an interaction between monomeric vanadia species and ceria oxygen defect sites, which is consistent with previous experimental results [16,17,27,28,35] also showing that dispersed vanadia interacted with ceria active sites. However, this effect cannot explain the further selectivity increase when more vanadia is added, since the concentration of monomeric species was shown to decrease at higher vanadium loadings. Therefore, a decrease in selectivity would be expected for higher vanadium loading despite the decrease in conversion. Since this is not detected, other effects not accessible by Raman

and UV-Vis may be responsible for the observed behavior. To gain additional insight, particularly regarding the presence of adsorbates and their role in propane ODH, *operando* DRIFT spectra were measured.

Fig. 8 presents DRIFT spectra of bare ceria (a) and VO_x/CeO_2 loaded with 1.36 V/nm^2 (b) during oxidizing and reaction conditions. Since the formation of hydroxyl groups via hydrogen transfer from propane to the ceria surface has been conjectured as a possible reaction step (see above), isotope experiments using propane-d_8 were performed to verify the formation of Ce-O-D groups. The corresponding spectra for the other VO_x/CeO_2 samples (0.57 and 2.83 V/nm^2) can be found in Fig. S7. For details of the data processing please refer to the Experimental Section; as an example, the processing steps are illustrated in Fig. S6 for the VO_x/CeO_2 sample with 1.36 V/nm^2 loading.

According to Fig. 8, spectral changes upon switching from oxidizing to reaction conditions are mainly detected within the ranges 1200–1800 cm^{-1} and 2700–3000 cm^{-1}. Furthermore, there is an overall intensity increase in the O-H stretching region (3400–3750 cm^{-1}), as well as new features at 3690 cm^{-1} and at 3734 cm^{-1} due to Ce-O-H groups [66]. These will be discussed in more detail below in the context of Figs. 9 and 10. Additional peaks are observed at ∼ 2050 cm^{-1} and within 2250–2400 cm^{-1}, which may originate from the first overtone of the V = O stretching vibration [67] and gas-phase CO_2 produced by the reaction, respectively. When propane-d_8 is used instead of regular propane, new signals appear in the range 2500–2750 cm^{-1} with the same profile as that of the O-H stretching bands, evidencing the presence of O-D stretching vibrations. The peaks at 2720 cm^{-1} and at 2770 cm^{-1} are assigned to be a Ce-O-D vibration since the CH_2 vibration from propane at this position should not be present with a significant intensity for propane-d_8, confirming the abstraction of hydrogen from propane to the ceria surface. Furthermore, the position of the Ce-O-D features at 2720 cm^{-1} and 2770 cm^{-1} is in good agreement with those expected for the Ce-O-H vibrations at 3690 cm^{-1} and 3734 cm^{-1}, when hydrogen is replaced by deuterium. In addition, a peak at ∼ 2150 cm^{-1} is detected. This peak is assigned to a CDH vibration of gas-phase propane-2-d_1, in agreement with the literature [68], formed over the ceria surface via isotope scrambling between regular propane and propane-d_8. In the DRIFT spectra in Fig. 8, this peak is the only detected gas-phase signal, since gas-phase contributions from propane and propane-d_8 have been subtracted and there is no indication of H/D exchange of the CH_3/CD_3 group. For the VO_x/CeO_2 samples, there are no apparent
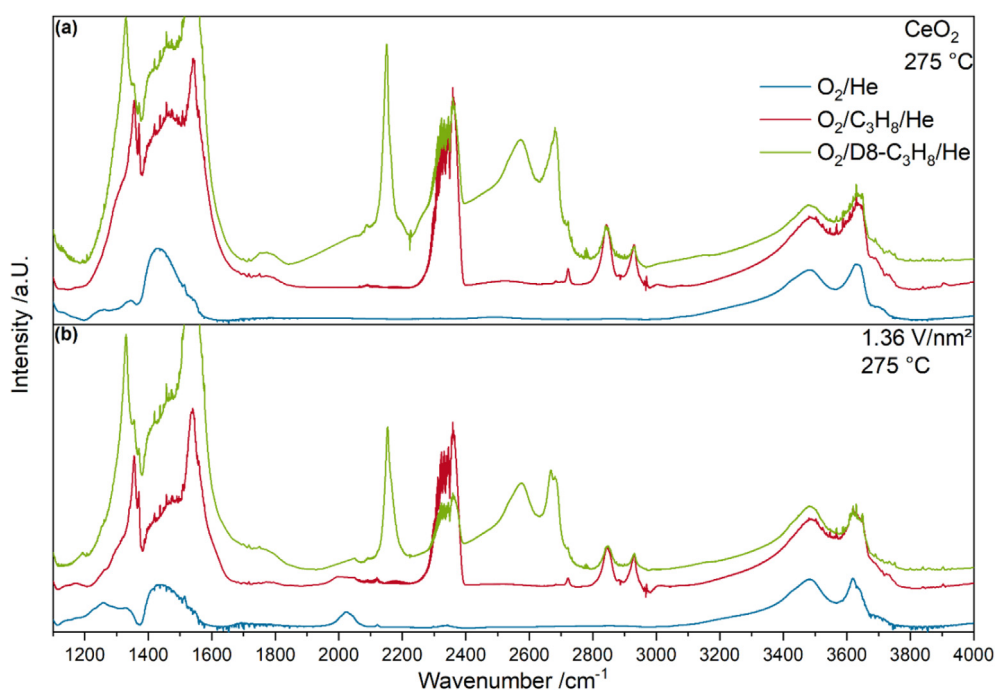
Fig. 8. DRIFT spectra of bare ceria (a) and VO$_x$/CeO$_2$ (1.36 V/nm^2) (b), recorded under oxidizing conditions, reaction conditions, and reaction conditions with propane-d$_8$ at 275 °C.
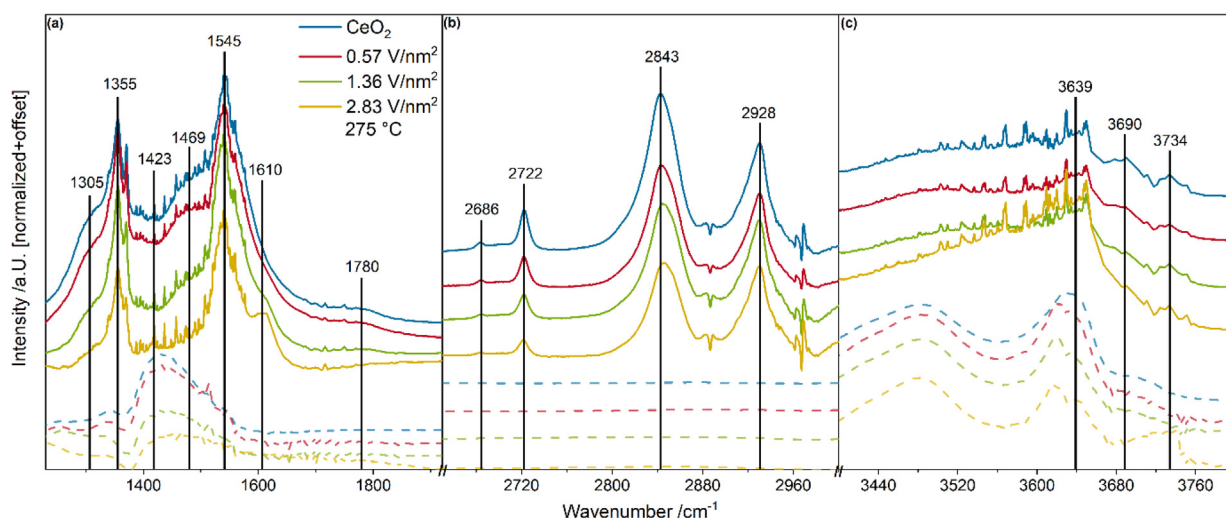
Fig. 9. Enlarged view of the carbonate (a), the carbohydrate (b) and the O-H stretching (c) [65,66,69–72] regions based on the DRIFT spectra shown in Fig. 8. Dashed lines represent spectra under oxidizing conditions and solid lines represent *operando* spectra after subtraction of the spectra under oxidizing conditions. Spectra are offset for clarity.

changes in the nature of the adsorbates observed, neither for regular propane nor for propane-d$_8$. Therefore, we conclude that the observed adsorbates are essentially the same for ceria and VO$_x$/CeO$_2$ samples.

For a more detailed analysis, Fig. 9 gives an enlarged view of the regions 1200–1800 cm^{-1} (a; carbonate), 2650–3000 cm^{-1} (b; carbohydrates), and 3400–3750 cm^{-1} (c; O-H stretching). Dashed lines represent the respective under oxidizing conditions, while solid lines represent *operando* spectra after subtraction of the spectra obtained under oxidizing conditions. Spectra are offset for clarity. The assignments for the features in Fig. 9 are summarized in Table 2. The peaks at 2686 cm^{-1} and 2722 cm^{-1} are assigned to C-H stretching vibrations of propane adsorbed to the ceria surface

(possibly C$_3$H$_7$ species) in different configurations. Note that the latter assignment follows a previous study on Pd/CeO$_2$ [39], which did not report the 2686 cm^{-1} peak, probably for sensitivity reasons.

The Ce-O-H stretching region shows changes in intensity between oxidizing and reaction conditions (see Fig. 9c). Three distinct types of hydroxyl groups are identified in the difference spectra at 3639, 3690, and 3734 cm^{-1}, which have previously been attributed to II-B, II*-A, and I-A Ce-O-H vibrations, respectively [66]. Type I represent mono-coordinated, and type II doubly bridging hydroxyl groups. According to the literature, a II-B hydroxyl corresponds to a doubly bridging hydroxyl group adjacent to a surface oxygen vacancy, whereas a II*-A hydroxyl results from a dou-
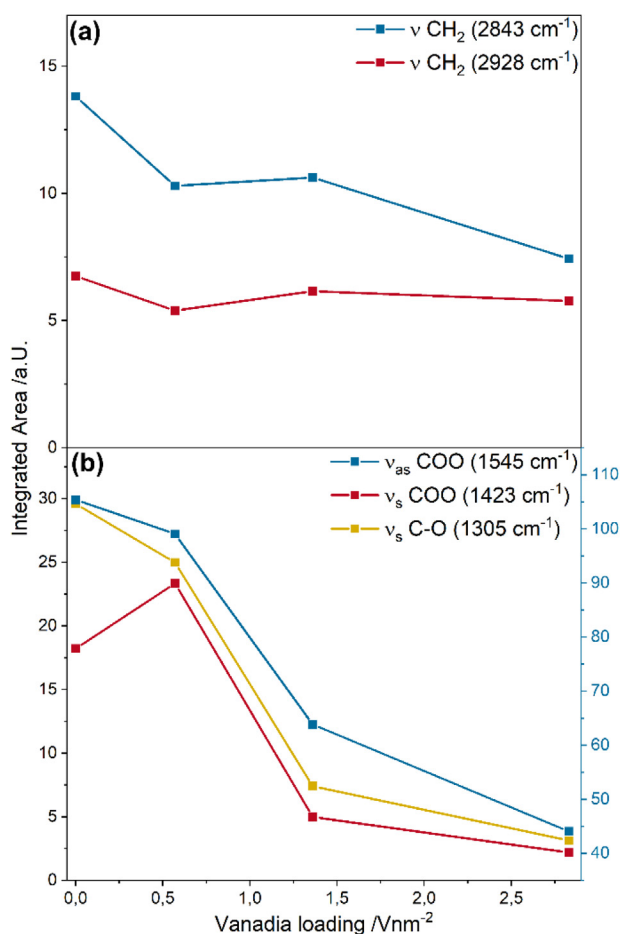
Fig. 10. Selected adsorbate features relevant to the discussion of the mechanism of propane ODH. The areas result from a fit analysis to the *operando* DRIFT spectra shown in Fig. 9a and b. The features in (a) and (b) are related to oxygen-free and oxygen-containing adsorbates, respectively.

Table 2
Assignments of IR features detected for VO_x/CeO_2 catalysts and bare ceria during propane ODH at 275 °C.

Position /cm^{-1}	Assignment	Reference
1305	υ_s C-O	18
1355	υ_s CH$_3$	18
1423	υ_s COO	18
1469	δ_{as} CH$_3$	18
1545	υ_{as} COO	18
1610	υ_{as} O-C-O	58
1780	υ C-O	62
2686	υ C-H (?)	this work
2722	υ C-H	35
2843	υ CH$_2$	18
2928	υ CH$_2$	18
3639	Ce-O-H II-B	57
3690	Ce-O-H II*-A	57
3734	Ce-O-H I-A	57

bly bridging hydroxyl group with cerium reduction.[57] For the hydroxyl group at 3639 cm^{-1} no equivalent Ce-OD feature was observeable since it overlaps heavily with the D_2O region. Since D8-propane was only present during the reaction conditions, no difference spectra are available. The observation of these hydroxyl features further supports the hypothesis that hydrogen is first abstracted from propane and then transferred to the ceria surface (either by ceria directly or via vanadia structures with a subsequent fast transfer to the ceria surface), forming hydroxyl groups.

While Fig. 9 shows that the nature of the adsorbates does not change with increasing vanadium loading, a change in their relative concentrations can be detected. The most common adsorbates, according to Fig. 9, are carbonates characterized by signals at 1305, 1423, 1545, and 1780 cm^{-1} [20,65,69,71,73]. In addition, C-H stretching vibrations of CH$_2$ groups in propane adsorbed to ceria are observed at 2928 and 2843 cm^{-1} [20]. In the following, the peaks within the range 1300–1800 cm^{-1} will be related to oxygen-containing adsorbates due to their high oxygen content, whereas the peaks between 2680 and 2930 cm^{-1} will be related to oxygen-free adsorbates.

The adsorbate features in Fig. 9a and b show changes in intensity with increasing vanadium loading, particularly, those of the oxygen-containing adsorbates, but no completely new features. One exception is the peak at 1610 cm^{-1}, previously assigned to carbonates [71], which first appears for the sample loaded with 0.57 V/nm^2 and then increases in intensity for higher vanadium loadings. There is no indication of this peak on bare ceria, which may be explained by its higher oxygen dynamics facilitating the oxidation of carbonates to CO_2. With increasing vanadium loading, the oxygen dynamics are slowed down (see above); thus carbonates might stay (longer) on the surface, possibly blocking reaction sites.

To quantify the changes in adsorbate intensity, the selected regions from Fig. 9a and b were fit using Lorentzian functions. As an example, this is illustrated in Fig. S8 for VO_x/CeO_2 loaded with 0.57 V/nm^2. Fig. 10 depicts the resulting peak areas of selected adsorbate peaks for (a) oxygen-free adsorbates (represented by the symmetric and asymmetric CH$_2$ stretching vibrations at 2843 and 2928 cm^{-1}) and (b) oxygen-containing adsorbates (represented by the asymmetric COO stretching vibration at 1545 cm^{-1}, the symmetric COO stretching vibration at 1423 cm^{-1}, and the symmetric C-O stretching vibration at 1305 cm^{-1}) as a function of vanadium loading.

As can be seen in Fig. 10, the peaks related to the oxygen-containing adsorbates show a more pronounced intensity decrease with increasing vanadium loading than those related to the oxygen-free adsorbates. In fact, a sharp drop is observed for an increase in vanadium loading from 0.57 V/nm^2 to 1.36 V/nm^2, which may indicate a weaker adsorption of propane, probably caused by changes in the vanadia surface structure. The weaker adsorption may facilitate the transformation of a higher proportion of propane to propylene and its desorption from the catalyst surface before it is fully oxidized to CO_2, thereby decreasing the detectable presence of oxygen-containing adsorbates and increasing the overall selectivity.

3.6. Mechanistic discussion

In the following, we will discuss the findings from Raman, UV-Vis, and IR spectroscopy presented in the previous sections with regard to their mechanistic insights into the ODH of propane over VO_x/CeO_2 catalysts.

The presence of vanadia monomers, dimers, and oligomers on the catalyst surface was evidenced by their contributions to the vanadyl band in the 514/532 nm Raman spectra. Since all detected vanadyl signals were located above 1000 cm^{-1}, we conclude that the VO_x/CeO_2 catalysts do not contain (micro)crystalline V_2O_5. Furthermore, there is no indication of the presence of $CeVO_4$ in the Raman spectra, in agreement with the literature, as these structures would be expected at higher temperatures and vanadia loadings or more reducing conditions than proapne and oxygen such as pure propane or H_2 [35,57]. Thus, in the VO_x/CeO_2 catalysts studied here, vanadia is present exclusively as monomeric, dimeric, and oligomeric surface species.

The first step of the reaction mechanism is the adsorption of propane onto the catalyst surface, which involves the abstraction of a hydrogen atom from propane and its transfer to ceria surface lattice oxygen. This is experimentally confirmed under reaction conditions by the intensity decrease of the transversal Ce-O surface phonon in the UV-Raman spectra and the detection of Ce-O-D stretching vibrations in the propane-D_8 DRIFT spectra. To this end, DFT studies have suggested a hydrogen transfer to surface oxygen located in close proximity to the propane adsorption site [37]. As a result of the first reaction, intermediary $C_3H_7^*$ is formed (see Fig. 11), from which a second hydrogen may either be abstracted to the same ceria site as the first hydrogen, leading to Ce-OH$_2$ formation, or to another surface lattice oxygen atom to yield a second hydroxyl group. Both scenarios result in a decrease of the transversal Ce-O phonon intensity and are therefore consistent with the experimental results (see Figs. 4 and 5). As also DFT studies have considered both as likely, based on their very similar energies [37], it is currently not possible to favor one of the above scenarios.

In the last step, propylene desorbs from the catalyst surface and water is formed from both abstracted hydrogen atoms and one surface lattice oxygen atom, resulting in an oxygen defect site (see Fig. 11). The formed surface oxygen defect may then interact with vanadia monomers in close proximity to the defect site, as suggested by the UV-Raman spectra (see Figs. 4 and 5). Please note that of all detected surface vanadia species only the monomers follow the same trend as the observed decrease in defect intensity. These findings are supported by DFT results [22], showing that the monomeric vanadia species hereby undergoes structural relaxation into the formed vacancy, resulting in an irreversible blocking of the vacancy. As a consequence, the overall oxygen dynamics in the catalyst are slowed down, thereby increasing the selectivity. On the other hand, vacancies located further away from vanadia monomers are not influenced by this interaction [22].

The *operando* DRIFT spectra provide information on the presence of adsorbates on bare ceria and on the VO$_x$/CeO$_2$ catalysts under reaction conditions. With increasing vanadium loading, a continuous decrease in adsorbate intensity but no apparent change in the nature of the adsorbates is observed. On the other hand, the pronounced influence of vanadia on the catalytic performance is expected to influence the propane adsorption/reaction behavior. The detection of higher adsorbate concentrations for bare ceria points to a stronger adsorption compared to VO$_x$/CeO$_2$, thus resulting in more total oxidation products such as CO$_2$ (or CO), for example via formation of different intermediates as proposed previously [74], while the presence of vanadia may increase the selectivity by decreasing the adsorption strength of propane and reaction intermediates to the surface. This hypothesis is supported by the observation that the peaks related to the oxygen-containing adsorbates

strongly decrease with vanadium loading, while those of the oxygen-free features show much smaller variations (see Fig. 10). Regarding the adsorption of propane on VO$_x$/CeO$_2$ catalysts, one may in principle envisage an adsorption onto ceria influenced by the presence of nearby vanadia or the direct adsorption onto vanadia surface structures [12,75]. As switching from oxidative to reactive conditions did not lead to any changes in the vanadia-related Raman features (see Fig. S3), the rate-determining step, which has been proposed to be the first hydrogen abstraction, is proposed to proceed without bond breaking in the vanadia structure (see Fig. 11). While our results do not allow for a further specification of the propane adsorption/reaction site, the exclusive involvement of vanadia monomers appears rather unlikely, as the fraction of monomeric species shows a strong decrease with increasing vanadium loading and even disappears for 2.83 V/nm^2, while the loading-dependent catalyst properties show a different behavior. More detailed information on the interaction between surface vanadia and propane may be accessible by future DRIFTS experiments using other propane isotopes such as CH$_3$CD$_2$CH$_3$, as previously reported by Chen et al. [75].

Besides reduction of the topmost ceria surface layer detected via the transversal Ce-O phonon intensity as discussed above, there is evidence for the reduction of the ceria subsurface accessible by the F$_{2g}$ redshift in the *operando* visible Raman spectra (see Figs. 4 and 5) during reaction conditions, which is consistent with previous experimental data on the VO$_x$/CeO$_2$ system recorded under different conditions [27]. This behavior is fully consistent with the *operando* UV-Vis spectra (see Fig. 7), which monitor both surface and subsurface and show a reduction-induced redshift of the observed band gap. In fact, the extent of the intensity decrease/redshift is correlated to the observed conversion, indicating that these effects are linked to the reaction. From these findings, we conclude that surface oxygen vacancies consumed during propane ODH are replenished by oxygen diffusing from the subsurface to the surface, leading to ceria reduction in the subsurface region. This process is likely to occur in parallel with ceria regeneration by gas-phase oxygen, since the conversion of propane stays constant for 3 h (see Fig. 4), which is unlikely if only ceria bulk oxygen were consumed without regeneration by gas-phase oxygen. This is further supported by the fact that the amount of oxygen present in CO$_2$ formed as a reaction product over 3 h for bare ceria (see Fig. 5b) exceeds the amount of oxygen present in the 70 mg catalyst sample. Therefore, gas-phase oxygen seems to be the oxygen source during propane ODH. Since a subsurface reduction of ceria is observed, (see Fig. 5c and 7c) the regeneration at the active centers is likely due to oxygen diffusion from the subsurface and the gas-phase oxygen probably regenerates the catalyst at a different position. Therefore, ceria acts as an oxygen buffer for the reaction.
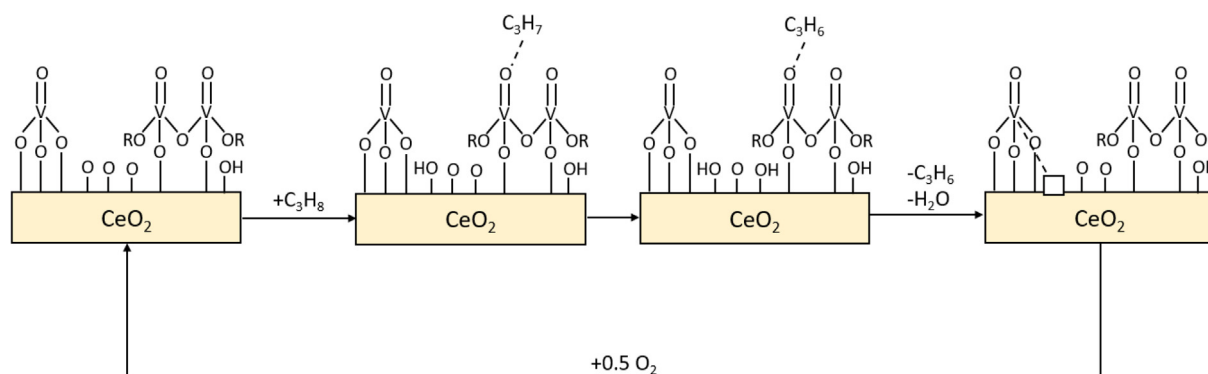

Fig. 11. Proposed mechanism for propane ODH over VO$_x$/CeO$_2$ catalysts. For details see text.

The presence of weak d-d transitions in the *operando* UV-Vis spectra indicates a small degree of vanadium reduction. However, as the d-d transition intensity correlates with the vanadium loading rather than the observed conversion and the overall intensity changes are very small, it is suggested that the observed vanadium reduction is not caused by the reaction but rather by unrelated (thermal) processes.

The proposed reaction mechanism for propane ODH over VO_x/CeO_2 catalysts is summarized in Fig. 11. Our findings differ from those reported for the ODH of small alcohols (MeOH, EtOH) over VO_x/ceria catalysts, according to which ceria has been proposed to act as an oxygen buffer, regenerating the vanadia species on the surface. In these reactions, surface vanadia species actively participate in the reaction, in particular, via V-O-Ce interface bonds, as shown by our previous *operando* work [18], which is in contrast to the passive role of vanadia in propane ODH as elucidated in the present study. The origin of this different behavior can be related to the structure of the substrate molecule. Alcohols form stable surface alkoxy species as an intermediate of the reaction, which are readily accessible by spectroscopy, based on which the rate-determining C-H bond breakage and further reaction to the product occurs. In fact, the presence of alkoxy species modifies the V-O-Ce interface bonds and facilitates the subsequent hydrogen transfer, a scenario which is fully consistent with theory [36]. However, despite the differences in reactivity behavior during alcohol and alkane ODH over VO_x/ceria catalysts, vanadium is not participating as a redox system in these reactions.

For propane ODH over vanadia on other supports (e.g. SiO_2 and Al_2O_3), vanadia-related features such as interface bonds (e.g. V-O-support) or the V = O bond have been proposed to be important for the reaction mechanism [8,76]. For the ODH of ethane on oxide-supported vanadia catalysts, the interface bond, e.g. V-O-Al, was also reported to be crucial for the overall reaction mechanism [41]. Thus the rather passive role of vanadia in combination with direct support participation is in sharp contrast to catalysts with inactive support materials e.g. VO_x/SiO_2 and VO_x/Al_2O_3.

While ethane and propane ODH reactivities are known to be different, a detailed experimental characterization of intermediate species in the course of alkane ODH will require further methodical developments. Once established possible differences in the mechanistic behavior may be accessible. Nevertheless, the present work on propane ODH and previous work on ethane ODH [16,17,27,28] underline the importance of the V-O-Ce bond for the overall reaction mechanism, thus showing mechanistic similarities for VO_x/ceria catalysts during short alkane ODH. To this end, it will be of great interest to apply the detailed nuclearity-dependent *operando* spectroscopic analysis of the (sub)surface dynamics presented in this study also to the ODH of ethane, which will allow to develop a more general mechanistic picture of alkane ODH over VO_x/ceria catalysts.

4. Conclusions

In this work, we present a multiple *operando* spectroscopic study including multi-wavelength Raman, UV-Vis, and DRIFT spectroscopy for the ODH of propane on VO_x/CeO_2 catalysts. We provide direct spectroscopic evidence for the active participation of the CeO_2 support in the reaction. While the ceria surface is shown to be directly involved in the ODH reaction, the surface vanadia species are proposed to be taking part only indirectly, without observable structural changes or bond breaking. As part of the study, we have developed an experimental basis for a detailed understanding of the reaction mechanism and support participation, which may also be applied to other catalyst systems with active support materials.

Our findings show that *operando* techniques are an important tool for unravelling the dynamics in oxide catalysis with regarding to structural and electronic changes. As demonstrated for VO_x/CeO_2 catalysts, our approach allows us to disentangle the dynamics of vanadia and ceria by targeted enhancement using multiwavelength Raman spectroscopy. Using 385 nm excitation, we were able to show that ceria is actively participating in the reaction. Thereby, hydrogen is abstracted to the ceria surface, subsequently leading to the formation of water and surface oxygen vacancies, which can interact with nearby vanadia structures. Using 514 nm excitation, we identified these structures as vanadia monomers, irreversibly blocking the defect sites and slowing down the oxygen dynamics in ceria. In addition, UV-Vis spectra revealed a redshift of the band gap energy, consistent with ceria reduction, that correlated with the conversion, further indicating the participation of ceria. The DRIFTS results provided insight into the relationship between the nature of adsorbates and catalyst selectivity, revealing that the amount of oxygen-containing adsorbates decreased sharply with increasing vanadium loading in contrast to that of oxygen-free adsorbates. This indicates that vanadia structures influence the adsorption/reaction of propane by reducing the total oxidation to CO_2.

Based on our findings, we propose a reaction mechanism for the ODH of propane over VO_x/CeO_2 catalysts. We found experimental evidence for interactions between vanadia and ceria, that had previously been observed for VO_x/CeO_2 systems [17,27,35,66] and had been described by DFT [22] but had not been verified experimentally before for propane ODH and by the applied *operando* multiwavelength Raman, IR, and UV-Vis spectroscopies. These results go beyond previous experimental work in this area by linking the oxygen dynamics in the support material and adsorbate effects to specific vanadia structures present on the catalyst surface (e.g. monomers interacting with oxygen vacancies). The experimental results furthermore allowed a comparison with reaction pathways for propane ODH proposed by DFT calculations, confirming the abstraction of hydrogen atoms from propane to the ceria surface rather than vanadia interface bonds [37].

As exemplified by the VO_x/CeO_2 system, supported oxide catalysts may enable new mechanistic scenarios if active support participation is involved. In fact, in contrast to the support, vanadia is observed to participate only indirectly, i.e., no structural changes during reaction are observed, in addition to largely keeping its oxidation state at V^{5+}. This behavior may not be unique to vanadia/ceria catalysts. In fact, our approach might be expanded to other oxide catalysts with active support materials, including other transition metals (e.g. molybdena, tungstia) and/or other redox active support materials (e.g. titania). Provided the laser excitation wavelengths can be adapted to the UV-Vis properties of the catalyst, no limitations regarding the general applicability of our overall approach to a broad range of materials are expected.

Declaration of Competing Interest

The authors declare that they have no known competing financial interests or personal relationships that could have appeared to influence the work reported in this paper.

Acknowledgements

Appendix A. Supplementary data

Supplementary data to this article can be found online at https://doi.org/10.1016/j.jcat.2021.04.006.

References

[1] A.A. Ayandiran, I.A. Bakare, H. Binous, S. Al-Ghamdi, S.A. Razzak, M.M. Hossain, Oxidative dehydrogenation of propane to propylene over $VO_x/CaO-\gamma-Al_2O_3$ using lattice oxygen, Catal. Sci. Technol. 6 (13) (2016) 5154–5167, https://doi.org/10.1039/C6CY00078A.

[2] C.A. Carrero, R. Schloegl, I.E. Wachs, R. Schomaecker, Critical Literature Review of the Kinetics for the Oxidative Dehydrogenation of Propane over Well-Defined Supported Vanadium Oxide Catalysts, ACS Catal. 4 (10) (2014) 3357–3380, https://doi.org/10.1021/cs5003417.

[3] A.H. Elbadawi, M.S. Ba-Shammakh, S. Al-Ghamdi, S.A. Razzak, M.M. Hossain, Reduction kinetics and catalytic activity of $VO_x/\gamma-Al_2O_3-ZrO_2$ for gas phase oxygen free ODH of ethane, Chem. Eng. J. 284 (2016) 448–457, https://doi.org/10.1016/j.cej.2015.08.048.

[4] P. Hellier, P.P. Wells, D. Gianolio, M. Bowker, VO_x/Fe_2O_3 Shell-Core Catalysts for the Selective Oxidation of Methanol to Formaldehyde, Top. Catal. 61 (5-6) (2018) 357–364, https://doi.org/10.1007/s11244-017-0873-2.

[5] P. Ober, S. Rogg, C. Hess, Direct Evidence for Active Support Participation in Oxide Catalysis: Multiple Operando Spectroscopy of VO_x/Ceria, ACS Catal. 10 (5) (2020) 2999–3008, https://doi.org/10.1021/acscatal.9b0517410.1021/acscatal.9b05174.s001.

[6] I. Amghizar, L.A. Vandewalle, K.M. Van Geem, G.B. Marin, New Trends in Olefin Production, Engineering 3 (2) (2017) 171–178, https://doi.org/10.1016/J.ENG.2017.02.006.

[7] F. Cavani, N. Ballarini, A. Cericola, Oxidative dehydrogenation of ethane and propane: How far from commercial implementation?, Catal. Today 127 (1-4) (2007) 113–131, https://doi.org/10.1016/j.cattod.2007.05.009.

[8] B. Beck, M. Harth, N.G. Hamilton, C. Carrero, J.J. Uhlrich, A. Trunschke, S. Shaikhutdinov, H. Schubert, H.-J. Freund, R. Schlögl, J. Sauer, R. Schomäcker, Partial oxidation of ethanol on vanadia catalysts on supporting oxides with different redox properties compared to propane, J. Catal. 296 (2012) 120–131, https://doi.org/10.1016/j.jcat.2012.09.008.

[9] A. Dinse, B. Frank, C. Hess, D. Habel, R. Schomäcker, Oxidative dehydrogenation of propane over low-loaded vanadia catalysts: Impact of the support material on kinetics and selectivity, J. Mol. Catal. A Chem. 289 (1-2) (2008) 28–37, https://doi.org/10.1016/j.molcata.2008.04.007.

[10] R. Bulánek, P. Čičmanec, M. Setnička, Possibility of VO_x/SiO_2 Complexes Speciation: Comparative Multi-wavelength Raman and DR UV-vis Study, Phys. Procedia 44 (2013) 195–205, https://doi.org/10.1016/j.phpro.2013.04.024.

[11] R. Grabowski, J. Słoczyński, Kinetics of oxidative dehydrogenation of propane and ethane on VO_x/SiO_2 pure and with potassium additive, Chem. Eng. Process. 44 (10) (2005) 1082–1093, https://doi.org/10.1016/j.cep.2005.03.002.

[12] M. Piumetti, M. Armandi, E. Garrone, B. Bonelli, An IR spectroscopy assessment of the surface acidity of mesoporous $VO_x–SiO_2$ catalysts, Micropor. Mesopor. Mat. 164 (2012) 111–119, https://doi.org/10.1016/j.micromeso.2012.05.041.

[13] K. Shimura, T. Fujitani, Effects of promoters on the performance of a VO_x/SiO_2 catalyst for the oxidation of methane to formaldehyde, Appl. Catal. A Gen. 577 (2019) 44–51, https://doi.org/10.1016/j.apcata.2019.03.014.

[14] P. Waleska, S. Rupp, C. Hess, Operando Multiwavelength and Time-Resolved Raman Spectroscopy: Structural Dynamics of a Supported Vanadia Catalyst at Work, J. Phys. Chem. C 122 (6) (2018) 3386–3400, https://doi.org/10.1021/acs.jpcc.7b1051810.1021/acs.jpcc.7b10518.s001.

[15] H. Zhu, S. Ould-Chikh, H. Dong, I. Llorens, Y. Saih, D.H. Anjum, J.-L. Hazemann, J.-M. Basset, VO_x/SiO_2 Catalyst Prepared by Grafting $VOCl_3$ on Silica for Oxidative Dehydrogenation of Propane, ChemCatChem 7 (20) (2015) 3332–3339, https://doi.org/10.1002/cctc.201500607.

[16] M.V. Martinez-Huerta, J.M. Coronado, M. Fernandez-Garcia, A. Iglesias-Juez, G. Deo, J.L.G. Fierro, M.A. Banares, Nature of the vanadia-ceria interface in V^{5+}/CeO_2 catalysts and its relevance for the solid-state reaction toward $CeVO_4$ and catalytic properties, J. Catal. 225 (1) (2004) 240–248, https://doi.org/10.1016/j.jcat.2004.04.005.

[17] M.V. Martínez-Huerta, G. Deo, J.L.G. Fierro, M.A. Bañares, Operando Raman-GC Study on the Structure–Activity Relationships in V^{5+}/CeO_2 Catalyst for Ethane Oxidative Dehydrogenation: The Formation of $CeVO_4$, J. Phys. Chem. C 112 (30) (2008) 11441–11447, https://doi.org/10.1021/jp802827t.

[18] M.A. Bañares, I.E. Wachs, Molecular structures of supported metal oxide catalysts under different environments, J. Raman Spectrosc. 33 (5) (2002) 359–380, https://doi.org/10.1002/jrs.866.

[19] M.V. Ganduglia-Pirovano, C. Popa, J. Sauer, H. Abbott, A. Uhl, M. Baron, D. Stacchiola, O. Bondarchuk, S. Shaikhutdinov, H.-J. Freund, Role of ceria in oxidative dehydrogenation on supported vanadia catalysts, J. Am. Chem. Soc. 132 (7) (2010) 2345–2349, https://doi.org/10.1021/ja910574h.

[20] Z. Hu, Z. Wang, Y. Guo, Li. Wang, Y. Guo, J. Zhang, W. Zhan, Total Oxidation of Propane over a Ru/CeO_2 Catalyst at Low Temperature, Environ. Sci. 52 (16) (2018) 9531–9541, https://doi.org/10.1021/acs.est.8b0344810.1021/acs.est.8b03448.s001.

[21] Y. Li, Z. Wei, F. Gao, L. Kovarik, R.A.L. Baylon, C.H.F. Peden, Y. Wang, Effect of Oxygen Defects on the Catalytic Performance of VO_x/CeO_2 Catalysts for

[22] Oxidative Dehydrogenation of Methanol, ACS Catal. 5 (5) (2015) 3006–3012, https://doi.org/10.1021/cs502084g.

[22] C. Penschke, J. Paier, J. Sauer, Oligomeric Vanadium Oxide Species Supported on the CeO_2 (111) Surface: Structure and Reactivity Studied by Density Functional Theory, J. Phys. Chem. C 117 (10) (2013) 5274–5285, https://doi.org/10.1021/jp400520j.

[23] C. Penschke, J. Paier, J. Sauer, Vanadium Oxide Oligomers and Ordered Monolayers Supported on CeO_2 (111): Structure and Stability Studied by Density Functional Theory, J. Phys. Chem. C 122 (16) (2018) 9101–9110, https://doi.org/10.1021/acs.jpcc.8b0199810.1021/acs.jpcc.8b01998.s001.

[24] C. Popa, M.V. Ganduglia-Pirovano, J. Sauer, Periodic Density Functional Theory Study of VO n Species Supported on the CeO_2 (111) Surface, J. Phys. Chem. C 115 (15) (2011) 7399–7410, https://doi.org/10.1021/jp108185y.

[25] M.N. Taylor, A.F. Carley, T.E. Davies, S.H. Taylor, The Oxidative Dehydrogenation of Propane Using Vanadium Oxide Supported on Nanocrystalline Ceria, Top. Catal. 52 (12) (2009) 1660–1668, https://doi.org/10.1007/s11244-009-9307-0.

[26] X.-P. Wu, J. Liu, J. Fan, X.-Q. Gong, Theoretical studies on the monomeric vanadium oxides supported by ceria: the atomic structures and oxidative dehydrogenation activities, RSC Adv. 5 (64) (2015) 52259–52263, https://doi.org/10.1039/C5RA08962J.

[27] A. Iglesias-Juez, M.V. Martínez-Huerta, E. Rojas-García, J.-M. Jehng, M.A. Bañares, On the Nature of the Unusual Redox Cycle at the Vanadia Ceria Interface, J. Phys. Chem. C 122 (2) (2018) 1197–1205, https://doi.org/10.1021/acs.jpcc.7b09832.

[28] M.V. Martínez-Huerta, G. Deo, J.L.G. Fierro, M.A. Bañares, Changes in Ceria-Supported Vanadium Oxide Catalysts during the Oxidative Dehydrogenation of Ethane and Temperature-Programmed Treatments, J. Phys. Chem. C 111 (50) (2007) 18708–18714, https://doi.org/10.1021/jp0772225.

[29] X. Gao, M.A. Bañares, I.E. Wachs, Ethane and n-Butane Oxidation over Supported Vanadium Oxide Catalysts: An in Situ UV–Visible Diffuse Reflectance Spectroscopic Investigation, J. Catal. 188 (2) (1999) 325–331, https://doi.org/10.1006/jcat.1999.2647.

[30] M.O. Guerrero-Pérez, A.J. McCue, J.A. Anderson, Rapid scan FTIR reveals propane (am)oxidation mechanisms over vanadium based catalysts, J. Catal. 390 (2020) 72–80, https://doi.org/10.1016/j.jcat.2020.07.031.

[31] J.J. Ternero-Hidalgo, M.O. Guerrero-Pérez, J. Rodríguez-Mirasol, T. Cordero, M. A. Bañares, R. Portela, P. Bazin, G. Clet, M. Daturi, Operando Reactor-Cell with Simultaneous Transmission FTIR and Raman Characterization (IRRaman) for the Study of Gas-Phase Reactions with Solid Catalysts, Anal. Chem. 92 (7) (2020) 5100–5106, https://doi.org/10.1021/acs.analchem.9b0547310.1021/acs.analchem.9b05473.s001.

[32] M.A. Bañares, M.V. Martínez-Huerta, X. Gao, J.L.G. Fierro, I.E. Wachs, Dynamic behavior of supported vanadia catalysts in the selective oxidation of ethane, Catal. Today 61 (1-4) (2000) 295–301, https://doi.org/10.1016/S0920-5861(00)00388-6.

[33] M.A. Bañares, M. Martínez-Huerta, X. Gao, I.E. Wachs, J.L.G. Fierro, Identification and roles of the different active sites in supported vanadia catalysts by in situ techniques, in: in: 12th International Congress on Catalysis, Proceedings of the 12th ICC, 2000, pp. 3125–3130.

[34] Z. Wu, Multi-wavelength Raman spectroscopy study of supported vanadia catalysts: Structure identification and quantification, Chin. J. Catal. 35 (2014) 1591–1608, https://doi.org/10.1016/S1872-2067(14)60082-6.

[35] Z. Wu, A.J. Rondinone, I.N. Ivanov, S.H. Overbury, Structure of Vanadium Oxide Supported on Ceria by Multiwavelength Raman Spectroscopy, J. Phys. Chem. C 115 (51) (2011) 25368–25378, https://doi.org/10.1021/jp2084605.

[36] T. Kropp, J. Paier, J. Sauer, Support effect in oxide catalysis: methanol oxidation on vanadia/ceria, J. Am. Chem. Soc. 136 (41) (2014) 14616–14625, https://doi.org/10.1021/ja508657c.

[37] C. Huang, Z.-Q. Wang, X.-Q. Gong, Activity and selectivity of propane oxidative dehydrogenation over VO_3/CeO_2 (111) catalysts: A density functional theory study, Chin. J. Catal. 39 (9) (2018) 1520–1526, https://doi.org/10.1016/S1872-2067(18)63072-4.

[38] X.-P. Wu, X.-Q. Gong, Unique Electronic and Structural Effects in Vanadia/Ceria-Catalyzed Reactions, J. Am. Chem. Soc. 137 (41) (2015) 13228–13231, https://doi.org/10.1021/jacs.5b07939.

[39] Z. Hu, X. Liu, D. Meng, Y. Guo, Y. Guo, G. Lu, Effect of Ceria Crystal Plane on the Physicochemical and Catalytic Properties of Pd/Ceria for CO and Propane Oxidation, ACS Catal. 6 (4) (2016) 2265–2279, https://doi.org/10.1021/acscatal.5b0261710.1021/acscatal.5b02617.s001.

[40] Y. Li, Z. Wei, F. Gao, L. Kovarik, C.H.F. Peden, Y. Wang, Effects of CeO_2 support facets on VO_x/CeO_2 catalysts in oxidative dehydrogenation of methanol, J. Catal. 315 (2014) 15–24, https://doi.org/10.1016/j.jcat.2014.04.013.

[41] M. Martinezhuerta, X. Gao, H. Tian, I. Wachs, J. Fierro, M. Banares, Oxidative dehydrogenation of ethane to ethylene over alumina-supported vanadium oxide catalysts: Relationship between molecular structures and chemical reactivity, Catal. Today 118 (3-4) (2006) 279–287, https://doi.org/10.1016/j.cattod.2006.07.034.

[42] A. Klisińska, K. Samson, I. Gressel, B. Grzybowska, Effect of additives on properties of V_2O_5/SiO_2 and V_2O_5/MgO catalysts, Appl. Catal. A Gen. 309 (1) (2006) 10–16, https://doi.org/10.1016/j.apcata.2006.04.028.

[43] A. Kubas, J. Noak, A. Trunschke, R. Schlögl, F. Neese, D. Maganas, A combined experimental and theoretical spectroscopic protocol for determination of the structure of heterogeneous catalysts: developing the information content of the resonance Raman spectra of M1 $MoVO_x$, Chem. Sci. 8 (9) (2017) 6338–6353, https://doi.org/10.1039/C7SC01771E.

[44] A. Filtschew, K. Hofmann, C. Hess, Ceria and Its Defect Structure: New Insights from a Combined Spectroscopic Approach, J. Phys. Chem. C 120 (12) (2016) 6694–6703, https://doi.org/10.1021/acs.jpcc.6b0095910.1021/acs.jpcc.6b00959.s001.

[45] P.S. Waleska, C. Hess, Oligomerization of Supported Vanadia: Structural Insight Using Surface-Science Models with Chemical Complexity, J. Phys. Chem. C 120 (33) (2016) 18510–18519, https://doi.org/10.1021/acs.jpcc.6b0167210.1021/acs.jpcc.6b01672.s001.

[46] A.A. Vikharev, G.G. Denisov, V.V. Kocharovsky, S.V. Kuzikov, V.V. Parshin, N.Y. Peskov, A.N. Stepanov, D.I. Sobolev, M.Y. Shmelev, Fast quasi-optical phase shifter based on the effect of induced photo conductivity in silicon, Radiophys. Quantum Electr. 50 (10-11) (2007) 786–793, https://doi.org/10.1007/s11141-007-0069-x.

[47] I.E. Paulauskas, G.E. Jellison, L.A. Boatner, G.M. Brown, Photoelectrochemical Stability and Alteration Products of n-Type Single-Crystal ZnO Photoanodes, Intern. J. Electrochem. 2011 (2011) 1–10, https://doi.org/10.4061/2011/563427.

[48] J. Kreisel, M.C. Weber, N. Dix, F. Sánchez, P.A. Thomas, J. Fontcuberta, Probing Individual Layers in Functional Oxide Multilayers by Wavelength-Dependent Raman Scattering, Adv. Funct. Mater. 22 (23) (2012) 5044–5049, https://doi.org/10.1002/adfm.v22.2310.1002/adfm.201201272.

[49] B. Huang, R. Gillen, J. Robertson, Study of CeO₂ and Its Native Defects by Density Functional Theory with Repulsive Potential, J. Phys. Chem. C 118 (42) (2014) 24248–24256, https://doi.org/10.1021/jp506625h.

[50] M. Lohrenscheit, C. Hess, Direct Evidence for the Participation of Oxygen Vacancies in the Oxidation of Carbon Monoxide over Ceria-Supported Gold Catalysts by using Operando Raman Spectroscopy, ChemCatChem 8 (3) (2016) 523–526, https://doi.org/10.1002/cctc.201501129.

[51] C. Schilling, C. Hess, Real-Time Observation of the Defect Dynamics in Working Au/CeO₂ Catalysts by Combined Operando Raman/UV–Vis Spectroscopy, J. Phys. Chem. C 122 (5) (2018) 2909–2917, https://doi.org/10.1021/acs.jpcc.8b0002710.1021/acs.jpcc.8b00027.s001.

[52] D. Nitsche, C. Hess, Structure of Isolated Vanadia and Titania: A Deep UV Raman, UV–Vis, and IR Spectroscopic Study, J. Phys. Chem. C 120 (2) (2016) 1025–1037, https://doi.org/10.1021/acs.jpcc.5b1031710.1021/acs.jpcc.5b10317.s001.

[53] C. Schilling, A. Hofmann, C. Hess, M.V. Ganduglia-Pirovano, Raman Spectra of Polycrystalline CeO₂ A Density Functional Theory Study, J. Phys. Chem. C 121 (38) (2017) 20834–20849, https://doi.org/10.1021/acs.jpcc.7b06643.

[54] Z. Wu, M. Li, J. Howe, H.M. Meyer, S.H. Overbury, Probing defect sites on CeO₂ nanocrystals with well-defined surface planes by Raman spectroscopy and O₂ adsorption, Langmuir 26 (21) (2010) 16595–16606, https://doi.org/10.1021/la101723w.

[55] J.-M. Jehng, G. Deo, B.M. Weckhuysen, I.E. Wachs, Effect of water vapor on the molecular structures of supported vanadium oxide catalysts at elevated temperatures, J. Mol. Catal. A Chem. 110 (1) (1996) 41–54, https://doi.org/10.1016/1381-1169(96)00061-1.

[56] M. Baron, H. Abbott, O. Bondarchuk, D. Stacchiola, A. Uhl, S. Shaikhutdinov, H.-J. Freund, C. Popa, M. Ganduglia-Pirovano, J. Sauer, Resolving the atomic structure of vanadia monolayer catalysts: monomers, trimers, and oligomers on ceria, Angew. Chem. Int. Ed. 48 (43) (2009) 8006–8009, https://doi.org/10.1002/anie.v48:4310.1002/anie.200903085.

[57] W. Daniell, A. Ponchel, S. Kuba, F. Anderle, T. Weingand, D.H. Gregory, H. Knözinger, Characterization and Catalytic Behavior of VOₓ-CeO₂ Catalysts for the Oxidative Dehydrogenation of Propane, Top. Catal. 20 (2002) 65–74, https://doi.org/10.1023/A:1016399315511.

[58] P. Gruene, T. Wolfram, K. Pelzer, R. Schlögl, A. Trunschke, Role of dispersion of vanadia on SBA-15 in the oxidative dehydrogenation of propane, Catal. Today 157 (1-4) (2010) 137–142, https://doi.org/10.1016/j.cattod.2010.03.014.

[59] M.L. Peña, A. Dejoz, V. Fornés, F. Rey, M.I. Vázquez, J.M. López Nieto, V-containing MCM-41 and MCM-48 catalysts for the selective oxidation of propane in gas phase, Appl. Catal. A Gen. 209 (1-2) (2001) 155–164, https://doi.org/10.1016/S0926-860X(00)00761-4.

[60] J. Liu, Z. Zhao, C. Xu, A. Duan, G. Jiang, CeO₂-supported vanadium oxide catalysts for soot oxidation: the roles of molecular structure and nanometer effect, J. Rare Earths 28 (2) (2010) 198–204, https://doi.org/10.1016/S1002-0721(09)60080-6.

[61] R.J. Deeth, Electronic structures and d-d spectra of vanadium(IV) and VO²⁺ complexes: discrete variational Xα calculations, J. Chem. Soc., Dalton Trans. 65 (1991) 1467–1477, https://doi.org/10.1039/DT9910001467.

[62] N.V. Skorodumova, R. Ahuja, S.I. Simak, I.A. Abrikosov, B. Johansson, B.I. Lundqvist, Electronic, bonding, and optical properties of CeO₂ and Ce₂O₃ from first principles, Phys. Rev. B 64 (2001) 548, https://doi.org/10.1103/PhysRevB.64.115108.

[63] X. Gao, J.-M. Jehng, I.E. Wachs, In Situ UV–vis–NIR Diffuse Reflectance and Raman Spectroscopic Studies of Propane Oxidation over ZrO₂-Supported Vanadium Oxide Catalysts, J. Catal. 209 (1) (2002) 43–50, https://doi.org/10.1006/jcat.2002.3635.

[64] Z. Zhao, Y. Yamada, A. Ueda, H. Sakurai, T. Kobayashi, The roles of redox and acid–base properties of silica-supported vanadia catalysts in the selective oxidation of ethane, Catal. Today 93–95 (2004) 163–171, https://doi.org/10.1016/j.cattod.2004.06.130.

[65] A. Abd El-Moemen, A.M. Abdel-Mageed, J. Bansmann, M. Parlinska-Wojtan, R.J. Behm, G. Kučerová, Deactivation of Au/CeO₂ catalysts during CO oxidation: Influence of pretreatment and reaction conditions, J. Catal. 341 (2016) 160–179, https://doi.org/10.1016/j.jcat.2016.07.005.

[66] A. Badri, C. Binet, J.-C. Lavalley, An FTIR study of surface ceria hydroxy groups during a redox process with H₂, Faraday Trans. 92 (23) (1996) 4669, https://doi.org/10.1039/ft9969204669.

[67] M.A. Centeno, I. Carrizosa, J.A. Odriozola, NO–NH₃ coadsorption on vanadia/titania catalysts: determination of the reduction degree of vanadium, Appl. Catal. B 29 (4) (2001) 307–314, https://doi.org/10.1016/S0926-3373(00)00214-9.

[68] L. Friedman, J. Turkevich, The Infra-Red Absorption Spectra of Propane-D-1 and Propane-D-2, Int. J. Chem. Phys. 17 (11) (1949) 1012–1015, https://doi.org/10.1063/1.1747105.

[69] C. Binet, M. Daturi, J.-C. Lavalley, IR study of polycrystalline ceria properties in oxidised and reduced states, Catal. Today 50 (2) (1999) 207–225, https://doi.org/10.1016/S0920-5861(98)00504-5.

[70] C. Li, Y. Sakata, T. Arai, K. Domen, K.-I. Maruya, T. Onishi, Carbon monoxide and carbon dioxide adsorption on cerium oxide studied by Fourier-transform infrared spectroscopy. Part 1. -Formation of carbonate species on dehydroxylated CeO₂, at room temperature, J. Chem. Soc., Faraday Trans. 1 (85) (1989) 929, https://doi.org/10.1039/F19898500929.

[71] C. Schilling, C. Hess, Elucidating the Role of Support Oxygen in the Water-Gas Shift Reaction over Ceria-Supported Gold Catalysts Using Operando Spectroscopy, ACS Catal. 9 (2) (2019) 1159–1171, https://doi.org/10.1021/acscatal.8b0453610.1021/acscatal.8b04536.s001.

[72] G.N. Vayssilov, M. Mihaylov, P. St., Petkov, K.I. Hadjiivanov, K.M. Neyman, Reassignment of the Vibrational Spectra of Carbonates, Formates, and Related Surface Species on Ceria: A Combined Density Functional and Infrared Spectroscopy Investigation, J. Phys. Chem. C 115 (2011) 23435–23454, https://doi.org/10.1021/jp208050a.

[73] A. Badri, C. Binet, J.-C. Lavalley, Surface-Chlorinated Ceria and Chlorine-Containing Reduced Pd/CeO₂ Catalysts. A FTIR Study, J. Phys. Chem. 100 (20) (1996) 8363–8368, https://doi.org/10.1021/jp953023m.

[74] D. Shee, G. Deo, Adsorption and ODH reaction of alkane on sol–gel synthesized TiO₂–WO₃ supported vanadium oxide catalysts: In situ DRIFT and structure–reactivity study, J. Mol. Catal. A Chem. 308 (1-2) (2009) 46–55, https://doi.org/10.1016/j.molcata.2009.03.032.

[75] K. Chen, A.T. Bell, E. Iglesia, Kinetics and Mechanism of Oxidative Dehydrogenation of Propane on Vanadium, Molybdenum, and Tungsten Oxides, J. Phys. Chem. B 104 (6) (2000) 1292–1299, https://doi.org/10.1021/jp9933875.

[76] M.M. Hossain, Kinetics of Oxidative Dehydrogenation of Propane to Propylene Using Lattice Oxygen of VOₓ/CaO/γ-Al₂O₃ Catalysts, Ind. Eng. Chem. Res. 56 (15) (2017) 4309–4318, https://doi.org/10.1021/acs.iecr.7b00759.

4.1.4 Unraveling the Active Vanadium Sites and Adsorbate Dynamics in VO$_x$/CeO$_2$ Oxidation Catalysts Using Transient IR Spectroscopy

The fourth publication applies ME-DRIFT spectroscopy and isotopic ME-DRIFT spectroscopy to VO$_x$/CeO$_2$ under propane ODH conditions, providing important details on the mechanistic picture of the reaction. Due to the fast time-scale on which ME-DRIFTS operates, it allows for the isolation of the signals of active species and the observation of fast hydrogen transfers and adsorbate dynamics. Using ME-DRIFTS on VO$_x$/CeO$_2$ catalysts with different loadings, the vanadyl fine structure was analyzed and actively participating nuclearities were identified. This directly evidences vanadia's role in the ODH reaction for the first time. Furthermore, through different patterns of the pulsed gases, as well as the switching between propane and d8-propane (isotopic ME-DRIFTS), it was possible to assign catalytic functions to each vanadia nuclearity. Monomeric species block ceria surface oxygen vacancies, while trimeric species are very stable and are only present as observer species. In contrast, the vanadyl functionality of dimeric and oligomeric vanadia species facilitates a fast hydrogen transfer from propane to ceria lattice oxygen atoms that catalyzes the rate-limiting step of the initial C-H bond breakage. Through the same switching patterns, the time evolution of adsorbates in the carbonate region was determined and a differentiation between hydrogen and non-hydrogen containing carbonate peaks was achieved, further refining the mechanistic understanding. The initial adsorption geometry and the geometry after the first hydrogen transfer as well as key adsorbates responsible for CO$_x$ formation were identified. This paper highlights the wealth of information obtainable by using different gas switching patterns in ME-DRIFT spectroscopy and the subsequent refinement towards a detailed mechanistic picture.

Unraveling the Active Vanadium Sites and Adsorbate Dynamics in VO$_x$/CeO$_2$ Oxidation Catalysts Using Transient IR Spectroscopy

Leon Schumacher, Jakob Weyel, and Christian Hess*

ACCESS | Metrics & More | Article Recommendations | Supporting Information

ABSTRACT: The oxidative dehydrogenation (ODH) of propane over supported vanadia catalysts is an attractive route toward propene (propylene) with the potential of industrial application and has been extensively studied over decades. Despite numerous mechanistic studies, the active vanadyl site of the reaction has not been elucidated. In this work, we unravel the ODH reaction mechanism, including the nuclearity-dependent vanadyl and surface dynamics, over ceria-supported vanadia (VO$_x$/CeO$_2$) catalysts by applying (isotopic) modulation excitation IR spectroscopy supported by *operando* Raman and UV−vis spectroscopies. Based on our loading-dependent analysis, we were able to identify two different mechanisms leading to propylene, which are characterized by isopropyl- and acrylate-like intermediates. The modulation excitation IR approach also allows for the determination of the time evolution of the vanadia, hydroxyl, and adsorbate dynamics, underlining the intimate interplay between the surface vanadia species and the ceria support. Our results highlight the potential of transient IR spectroscopy to provide a detailed understanding of reaction mechanisms in oxidation catalysis and the dynamics of surface catalytic processes in general.
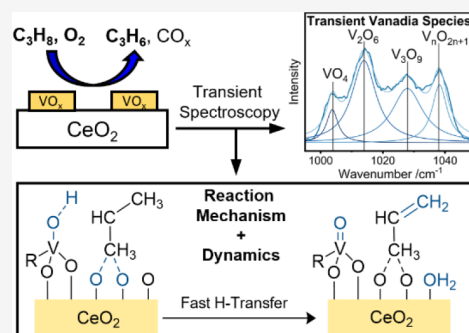
1. INTRODUCTION

Propylene (propene) is among the most important starting materials of the petrochemical industry and used for a variety of products. As the gap between demand and supply is constantly growing, alternative ways of producing propylene are of great interest. One such way is oxidative dehydrogenation (ODH), which shows favorable reaction characteristics in comparison to conventional processes such as steam cracking or fluid catalytic cracking.[1,2] Propane ODH is possible at lower temperatures and is exothermic in nature, thereby reducing energy expenditure, while the addition of oxygen to the reaction feed decreases catalyst deactivation due to coke formation or leaching.[3] However, it has been a challenge to find active and highly selective catalysts to avoid overoxidation to CO$_x$.[4]

For a rational design of better catalysts, a detailed understanding of the mode of operation and identification of the active sites are crucial but remain a tremendous challenge. Despite the extensive success of applying *in situ/operando* approaches to catalysts under steady-state conditions,[5] access to the reaction dynamics requires the use of transient spectroscopy, for example, modulation excitation spectroscopy (MES), which changes one parameter (typically the concentration) over time and measures the system's response.[6] In fact, besides significant noise reduction, such an approach allows discrimination between active and spectator species and, thus, a focus on the crucial aspects of the mechanism. In heterogeneous catalysis, MES has been mostly used to study reactions of small molecules, e.g., CO oxidation,[7−14] NH$_3$−

SCR (selective catalytic reduction),[15−17] and CO$_2$ activation,[18−21] but to the best of our knowledge, there has been no application in the context of the economically important field of alkane oxidation catalysis.

As suitable catalysts for ODH of short alkanes, especially propane, mainly vanadia but also NiO- and boron-oxide-based catalysts have been discussed.[3,22,23] In particular, catalysts with amorphous surface vanadia species (VO$_x$) as the active phase have shown promising performances during propane ODH, but further catalyst optimization is still required.[3,24−29] Besides the active phase, the choice of the support material is of great importance and has been proposed to increase the catalytic performance in the case of active support materials such as CeO$_2$ and TiO$_2$ due to their direct participation in the reaction.[3,25,29] Recently, ceria-supported vanadia (VO$_x$/CeO$_2$) catalysts have attracted increased attention, both theoretically[30−34] and experimentally.[3,25,26,29,35−38] Nevertheless, direct experimental insight into the reaction intermediates and the surface dynamics have not been reported yet.

Previous theoretical studies focused on general properties of VO$_x$/CeO$_2$ catalysts and concluded that the participation of

ceria in oxidation reactions is related to its low defect formation energy,[30,32,33] keeping vanadium in the oxidation state V^{5+}.[34−37,39] Density functional theory (DFT) calculations on propane ODH have proposed multiple pathways toward propylene but were not conclusive due to their small energy differences.[33] Experimental studies using Raman spectroscopy have demonstrated the interaction of vanadia with ceria oxygen vacancies,[40] which was supported by DFT calculations[32] and later by X-ray absorption near-edge structure spectroscopy (XANES) in the context of ethane ODH.[35] Our previous work[27] confirmed the active participation of ceria in the oxidation process and also the structural relaxation of monomeric vanadia sites into surface oxygen vacancies, irreversibly blocking them for propane ODH.

One of the major open questions in oxidation catalysis over supported vanadia catalysts has been the influence of vanadia nuclearity on catalytic performance and the involvement of vanadyl groups in the reaction mechanism. In this mechanistic study, we address these vanadia-related aspects besides the surface and adsorbate dynamics during the ODH of propane over VO_x/CeO_2 catalysts using transient IR spectroscopy supported by steady-state *operando* spectroscopies (diffuse reflectance infrared Fourier transform spectroscopy (DRIFTS), Raman, UV−vis). We highlight the potential of (isotopic) modulation excitation IR spectroscopy to add crucial new information to the mechanistic understanding of oxidation catalysts, thus greatly facilitating their rational design.

2. EXPERIMENTAL SECTION

2.1. Catalyst Preparation. The ceria support was prepared as previously described[41] and loaded with vanadia by incipient wetness impregnation. Three different loadings were prepared by mixing 1 g of ceria with 0.5 mL of different-concentration precursor solutions (1.07, 0.51, and 0.21 mol/L) containing vanadium(V) oxytriisopropoxide (≥97%, Sigma-Aldrich) and 2-propanol (99.5%, Sigma-Aldrich). The samples were then heated to 600 °C at a heating rate of 1.5 C/min and calcined for 12 h. The specific surface area of bare ceria was determined to be 61.4 m^2/g by nitrogen physisorption experiments and the use of the Brunauer−Emmett−Teller (BET) method, yielding vanadium loadings of 2.83 V/nm^2 (2.32 wt % V_2O_5), 1.36 V/nm^2 (1.11 wt % V_2O_5), and 0.57 V/nm^2 (0.47 wt % V_2O_5), respectively. Higher vanadium loadings were not considered, since vanadia crystallites were shown to be present at loadings >2.9 V/nm^2.[42] The resulting catalyst powders were subsequently pressed at a pressure of 2000 kg/m^2 for 20 s, ground, and then sieved using a combination of sieves to obtain 200−300 μm particles.

2.2. X-ray Diffraction. Powder X-ray diffraction (XRD) patterns were recorded on a Stoe Stadi P diffractometer with a Ge(111)-monochromator, Cu Kα radiation (λ = 1.54060 Å), and a MYTHEN-1K Dectris detector, using a flat sample holder in transmission geometry. The powder XRD patterns were recorded after the synthesis of the samples.

2.3. UV−Raman Spectroscopy. UV−Raman spectroscopy was performed at an excitation wavelength of 385 nm generated by a laser system based on a Ti:Sa solid-state laser pumped by a frequency-doubled Nd:YAG laser (Coherent, Indigo). The fundamental wavelength is frequency-doubled to 385 nm using a LiB_3O_5 crystal. The light is focused onto the sample, and the scattered light is collected by a confocal mirror setup and focused into a triple-stage spectrometer (Princeton Instruments, TriVista 555).[42] Finally, the Raman contribution is detected by a charge-coupled device (CCD, 2048 × 512 pixels) cooled to −120 °C. The spectral resolution of the spectrometer is 1 cm^{-1}. For Raman experiments, 70 mg of catalyst was placed in a CCR 1000 reactor (Linkam Scientific Instruments) equipped with a CaF_2 window (Korth Kristalle GmbH). A fluidized bed reactor was employed to avoid laser-induced damage, allowing

the use of a laser power of 9 mW at the location of the sample. Data processing included cosmic ray removal and background subtraction. For structural characterization, spectra were measured at room temperature after dehydration at 366 °C in 12.5% O_2/He for 1 h. *Operando* spectra were measured at 275 °C during exposure to reactive conditions (12.5% C_3H_8/12.5% O_2/He) in comparison to oxidizing conditions (12.5% O_2/He) after 1 h of dehydration in 12.5% O_2/He at 366 °C with a total flow rate of 40 mL_n/min. The spectra were further analyzed by a least-squares fitting analysis using Lorentzian functions.

2.4. Visible Raman Spectroscopy. Visible (Vis) Raman spectroscopy was performed at 514 nm excitation, emitted from an argon ion gas laser (Melles Griot). The light was focused onto the sample, gathered by an optical fiber, and dispersed by a transmission spectrometer (Kaiser Optical, HL5R). The dispersed Raman radiation was subsequently detected by an electronically cooled CCD detector (−40 °C, 1024 × 256 pixels). The spectral resolution was 5 cm^{-1} with a wavelength stability of better than 0.5 cm^{-1}. For Raman experiments, 70 mg of catalyst was filled into a CCR 1000 reactor (Linkam Scientific Instruments) equipped with a quartz window (Linkam Scientific Instruments). The laser power at the sample location was 2.5 mW. Data analysis of the Raman spectra included cosmic ray removal and an auto new dark correction. For structural characterization, spectra were measured at room temperature after dehydration at 366 °C in 12.5% O_2/He for 1 h. *Operando* spectra were measured at 275 °C during exposure to 12.5% C_3H_8/12.5% O_2/He, in comparison to oxidizing conditions (12.5% O_2/He), after 1 h of dehydration in 12.5% O_2/He at 366 °C with a total flow rate of 40 mL_n/min. The vanadyl region was fit using Lorentzian functions at distinct spectral positions representative of the different vanadia nuclearities with a fluctuation of 1 cm^{-1}. The F_{2g} mode was fitted without any positional restrictions due to the possible occurrence of red-shifts.

2.5. Diffuse Reflectance UV−vis Spectroscopy. Diffuse reflectance (DR) UV−vis spectra were recorded on a Jasco V-770 UV−vis spectrometer. Dehydrated $BaSO_4$ was used as the white standard. For each experiment, 90 mg of catalyst was put in the commercially available reaction cell (Praying Mantis High Temperature Reaction Chamber, Harrick Scientific) equipped with transparent quartz glass windows. For structural characterization, spectra were measured at room temperature after dehydration at 366 °C in 12.5% O_2/He for 1 h. *Operando* spectra were measured at 275 °C during exposure to 12.5% C_3H_8/12.5% O_2/He, in comparison to oxidizing conditions (12.5% O_2/He), after 1 h of dehydration in 12.5% O_2/He at 366 °C with a total flow rate of 40 mL_n/min.

2.6. Catalytic Measurements. Catalytic testing was performed in a CCR 1000 reaction cell in a fluidized bed using 90 mg of catalyst. The sample was first dehydrated for 1 h at 366 °C in 12.5% O_2/He. The catalyst was then cooled to 50 °C, exposed to 12.5% O_2/12.5% C_3H_8/He with a total flow rate of 40 mL_n/min, and heated in 45 °C steps up to 500 °C, staying at each temperature for 1 h. The gas-phase composition was analyzed continuously using gas chromatography (GC, Agilent Technologies 7890B). The GC is equipped with a PoraPlotQ and a Molsieve column as well as a thermal conductivity detector (TCD) and a flame ionization detector (FID) in series. The setup is connected through a 12-way valve. One chromatogram is measured every 29 min, resulting in two chromatograms for each temperature, which were averaged. The pressure before and after the GC was monitored to correct the detected areas for pressure fluctuations.

2.7. DRIFTS. DRIFT spectra were recorded on a Vertex 70 spectrometer (Bruker), equipped with a liquid-nitrogen-cooled mercury cadmium telluride (MCT) detector, operating at a resolution of 1 cm^{-1}. Dehydrated potassium bromide was used as an infrared transparent sample for the background spectrum. For each experiment, 90 mg of the catalyst was placed in the reaction cell (Praying Mantis High Temperature Reaction Chamber, Harrick Scientific) equipped with transparent KBr windows. The sample was dehydrated for 1 h in 12.5% O_2/He at 366 °C, cooled to 50 °C, and then exposed to 12.5% O_2/12.5% C_3H_8/He. After 30 min of equilibration, a
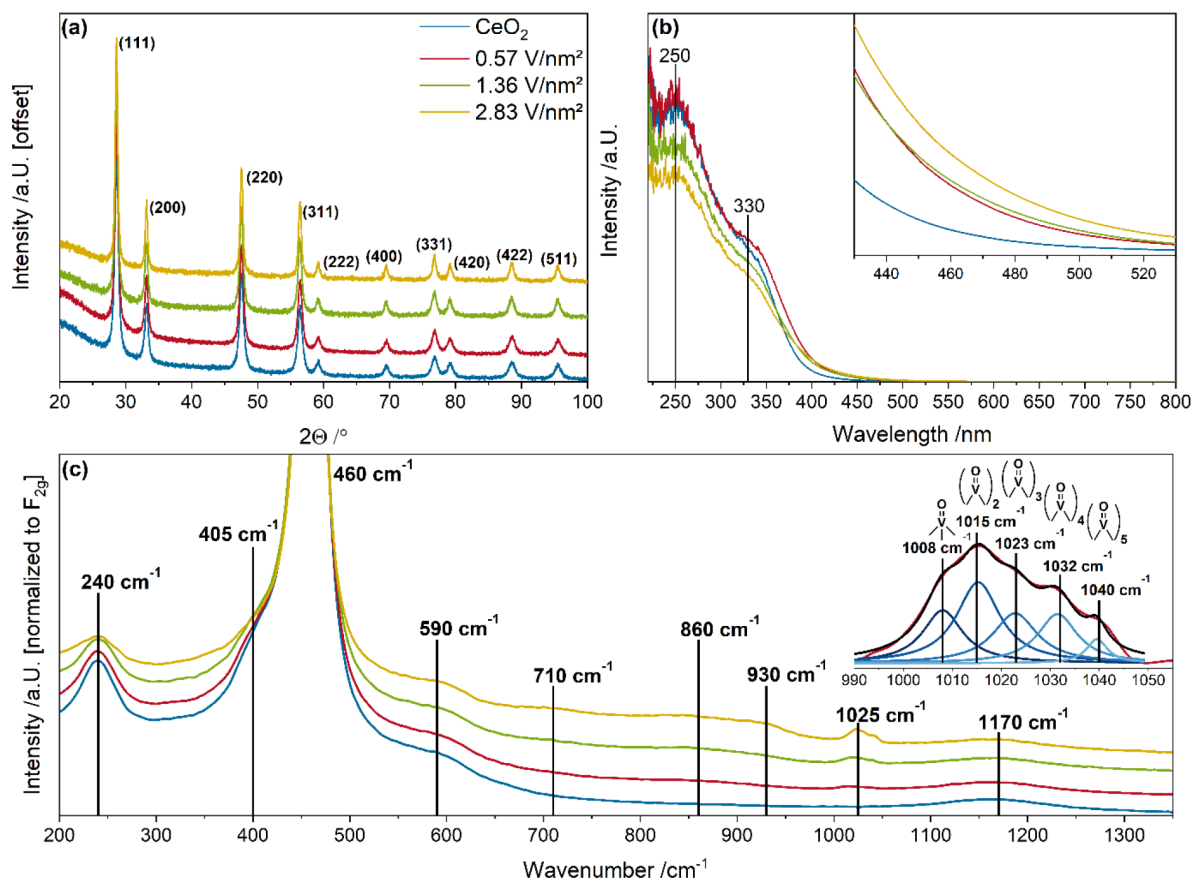
Figure 1. Summary of characterization data of VO_x/CeO_2 catalysts and bare ceria. (a) XRD diffraction patterns and (b) UV−vis spectra. Diffraction peaks and absorption bands characteristic for CeO_2 are highlighted. For clarity, the region within 430−530 nm is enlarged. (c) Raman spectra at 514 nm excitation. The inset shows an example fit to the vanadyl signal of the 0.57 V/nm^2 sample with assigned structural features. All characterization data was measured after dehydration (12.5% O_2/He at 365 °C for 1 h).

spectrum was recorded. The sample was then heated in 45 °C steps to 320 °C, and DRIFT spectra were recorded after 30 min at each temperature. In all measurements, the total flow rate was set to 40 mL_n/min.

Data processing consisted of background removal by subtraction of a baseline formed by 12 anchor points. A background spectrum of the gas phase was recorded using KBr as an infrared transparent sample. The propane gas phase and the *operando* spectra were then normalized to the propane gas-phase peak at ∼3000 cm^{-1} and subtracted to remove propane gas-phase contributions. Example data processing for ceria loaded with 0.57 V/nm^2 is shown in Figure S1.

2.8. Modulation Excitation (ME)-DRIFTS. ME-DRIFT spectroscopy was performed using the same apparatus as for steady-state DRIFTS; a more detailed description of our basic DRIFTS setup and the modifications made for recording ME-DRIFT spectra (see Figure S2) have already been published.[14,43−45] For each experiment, 90 mg of catalyst was used.

We used the rapid scan mode extension of Bruker's spectrometer software OPUS 7.2. Spectra were measured from 850 to 3800 cm^{-1} with a resolution of 0.5 cm^{-1}, an aperture of 8 mm, and a mirror speed of 40 kHz. A Valco Instruments 4/2 valve (Model E2CA, version ED), communicating with the Vertex 70, is used to rapidly switch between different gas feeds, which are controlled via digital mass flow controllers (Bronkhorst).

As gases, we used C_3H_8 (Westfalen, 3.5), C_3D_8 (Eurisotope, 98% isotopic labeling), O_2 (Westfalen, 5.0), and helium (Westfalen, 5.0). One measurement series consisted of 20 periods (20 gas-phase switches), each of which had a duration of 360 s and consisted of 240 spectra. For one spectrum, five consecutive interferograms were averaged, so that a new spectrum was acquired every 1.54 s.

As background, the catalyst spectrum itself was used, after 60 min of dehydration at 366 °C in 12.5% O_2/helium atmosphere and a 10 min treatment at 275 °C in one of the reaction gases for conventional ME-DRIFTS (12.5% O_2 or 12.5% C_3H_8 in helium) or in a reaction gas atmosphere (12.5% C_3H_8/12.5% O_2/75% He) for isotope ME-DRIFTS. The flow was kept constant at 100 mL_n/min during the pretreatment and experiment.

During conventional ME-DRIFTS, a flow of either 12.5% C_3H_8 or 12.5% O_2 in helium was kept constant over the sample, while the other feed gas was pulsed over the sample. In our isotope ME-DRIFTS experiments, the propane-h_8-containing reaction atmosphere was switched to a propane-d_8-containing reaction atmosphere, while the flow of oxygen through the reaction chamber was constant.

The temperature during all modulation excitation experiments was kept at 275 °C. To remove the gas-phase contribution, we subtracted gas-phase spectra over KBr (see Figure S3) from each recorded DRIFT spectrum. To exclude the possibility of intensity fluctuations over multiple periods, we checked the intensity profile at three distinct wavenumbers, representative of the background, an adsorbate peak, and a gas-phase peak, but detected no absolute intensity changes over multiple periods that could influence the Fourier transformation (see Figure S4). Peak-fitting analysis of ME-DRIFT spectra was performed using Lorentzian functions employing the Levenberg− Marquardt algorithm implemented in OriginLab 2018.

To obtain phase-sensitive spectra, the time-resolved 3D spectral data were converted from the time to the phase domain. For an overview, the resolution of phase spectra was chosen to be 30°, whereas mechanistic insights were obtained using a resolution of 1°. The main operation of phase-sensitive detection (PSD) is a Fourier transformation according to[46]
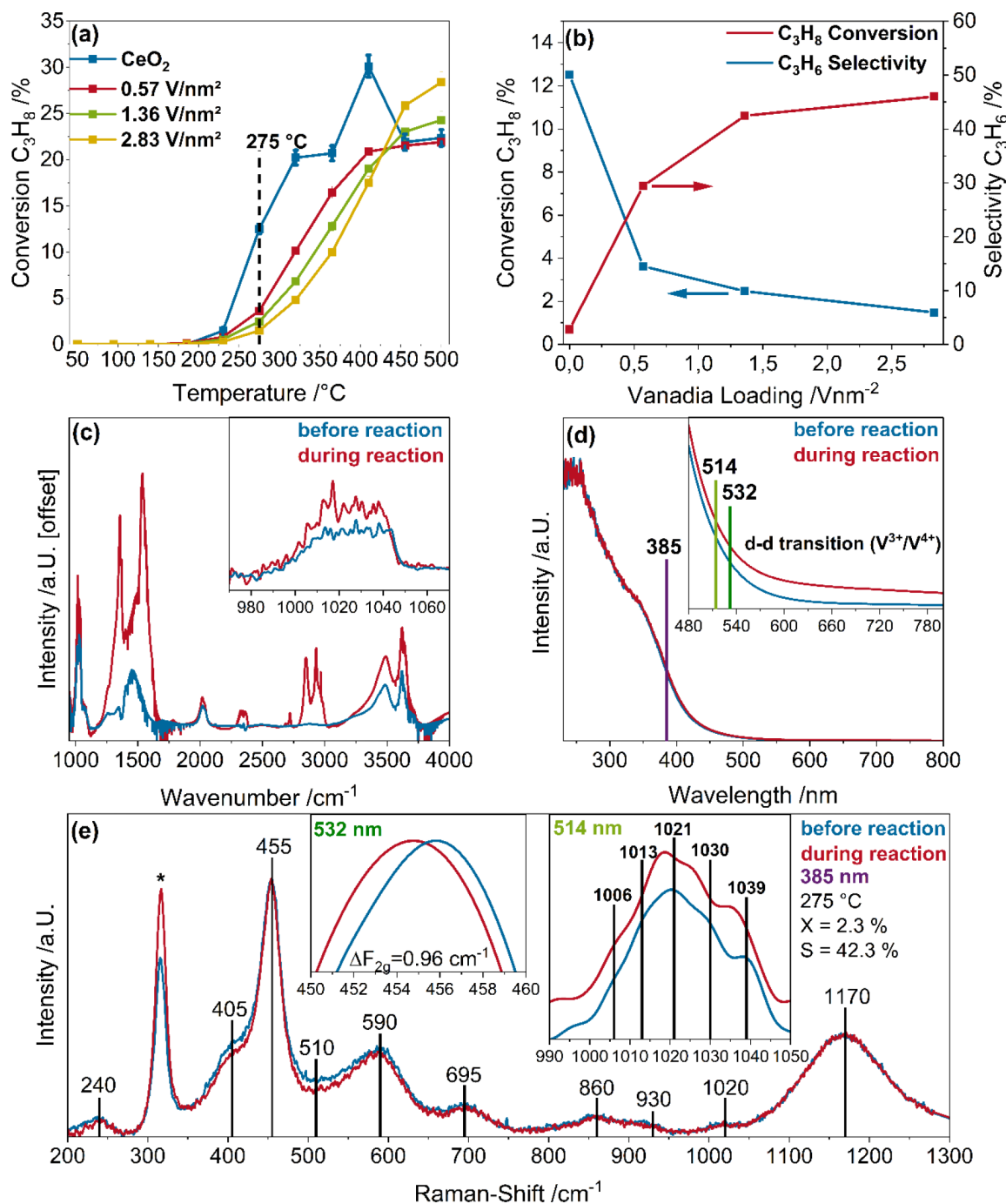
Figure 2. Results from the *operando* analysis of VO$_x$/CeO$_2$ catalysts during propane ODH. (a) Propane conversions compared to bare CeO$_2$ (with error bars). The dotted line marks the temperature of the *operando* experiments. (b) Loading-dependent propane conversions and propylene selectivities at 275 °C. (c−e) Exemplary *operando* spectroscopic results for the 1.36 V/nm^2 sample at 275 °C upon exposure to a feed of 12.5% C$_3$H$_8$/12.5% O$_2$/He (red), compared to oxidative conditions, i.e., 12.5% O$_2$/ He (blue). (c) DRIFT spectra with an enlarged view of the vanadyl region (inset). (d) UV−vis spectra including the three excitation wavelengths used for Raman spectroscopy. The inset shows the region of vanadia d-d transitions. (e) UV−Raman spectra at 385 nm laser excitation. The insets provide enlarged views of the vanadyl (514 nm) and F$_{2g}$ (532 nm) regions.

$$I_{\tilde{\nu}}(\varphi) = \frac{2}{T} \int_{t_0}^{t_e} I_{\tilde{\nu}}(t) \cdot \sin(2\pi f t + \varphi) \, dt$$

where $I(t)$ is the time-dependent intensity at one specified wavenumber ($\tilde{\nu}$) that is convoluted with the sine function, representing the modulation of the external parameter (e.g., the gas-phase concentration), thus forming $I(\varphi)$, the phase-resolved intensity. T denotes the period. The frequency of the external modulation is f,

and t_0 and t_e represent the times at which the considered data set begins and ends, respectively. To obtain a complete phase-resolved spectrum, this procedure is repeated for every wavenumber. By varying φ from 0 to 360° with a chosen resolution and repeating the steps above, the complete phase-resolved data set is created.

To obtain time constants for a particular wavenumber, first the phase angle in the PSD function is determined where $I(t)$ shows the best overlap with the external modulation function. This is done for a

set of chosen peak positions. To this end, the phase angle corresponding to the phase spectrum with the largest signal at the particular wavenumber is extracted by automatically comparing the intensities for spectra of all the different phase angles. The following equation is used to translate this phase angle back into a time value within the interval of one period, in order to make it more interpretable

$$t_{con} = \frac{(360 - \varphi_{max})}{360} \cdot T$$

The experimental error is 1.54 s, which represents the measurement time of one spectrum. Regarding the temporal analysis of the vanadyl peak, the time constants of the overtones were considered due to their much higher accuracy in comparison to the fundamental vibration. A detailed description and discussion of this effect is given in the Supporting Information (see Figure S5 and the attached discussion). Further details regarding the used software and the full code, which is available free of charge at GitHub, can be found elsewhere.[47]

3. RESULTS AND DISCUSSION

3.1. Catalytic Activity and *Operando* Spectroscopy.

The structure of the synthesized VO_x/CeO_2 catalysts was characterized using XRD, UV–vis, and Raman spectroscopy, confirming the presence of polycrystalline ceria and amorphous surface vanadia at all loadings (see Figure 1). Even at the highest loading, there is no indication of crystalline V_2O_5 (Raman, Figure 1c) or $CeVO_4$ (XRD, Figure 1a).[48] Detailed assignments for XRD, UV–vis, and vis–Raman bands are given elsewhere.[27] Besides the ceria and the interface-related Raman features discussed below, the vanadyl (V=O) stretching region is resolved especially well at 514 nm excitation[49] and is characterized by nuclearity-dependent features at 1008, 1015, 1023, 1032, and 1040 cm^{-1}, which are attributed to monomeric, dimeric, trimeric, tetrameric, and pentameric species, respectively (see inset of Figure 1c).[40,50] The loading-dependent nuclearity distribution resulting from a peak-fit analysis, depicted in Figure S6, shows a shift in the maximum of the distribution from dimeric to trimeric species at higher vanadium loadings.

Figure 2 summarizes results from the temperature- and loading-dependent *operando* analysis of VO_x/CeO_2 catalysts during propane ODH, using *operando* DRIFT, UV–vis, and Raman spectroscopies. Figure 2a depicts the temperature-dependent propane conversions in 12.5% O_2/12.5% C_3H_8/He, in comparison to bare ceria. The empty reaction cell has no significant influence on the activity data (conversion <0.1%).[27] The onset of conversion is located at 230 °C for all catalysts and reaches a plateau at around 450 °C. For the following discussion, a temperature of 275 °C was chosen (dashed line), at which gas-phase processes can be excluded and conversions are <15% (differential conditions). Besides, propylene selectivities are maximized to ensure the investigation of the selective oxidation pathway rather than total oxidation. Figure 2b shows the loading-dependent conversions and selectivities at 275 °C (for details, please refer to Figure S7). Even small amounts of vanadia (0.57 V/nm^2) strongly affect the propylene selectivity, but for further additions of vanadia, the increase in selectivity becomes increasingly smaller. Due to the different conversions and selectivities, the oxygen consumption of the catalysts is different, and therefore, the oxygen partial pressure may change differently for the samples. To exclude any significant effects of the different oxygen partial pressures on our observed activities

and structural dynamics, the oxygen concentrations and the corresponding propylene selectivities for all samples during propane ODH at 275 °C are given in Figure S8. The differences in oxygen concentration for all vanadia-loaded samples are very similar, and a change in the vanadium oxidation state due to this small difference appears unlikely. In comparison, the decrease in gas-phase oxygen due to the very high CO_2 production of ceria deviates significantly from the vanadia-loaded samples. As ceria takes 75 min to reach an equilibrium oxygen concentration and the selectivity changes are in the same time frame, it can be assumed that the changes in oxygen concentration from an initial 45% up to a 75% decrease in oxygen concentration correspond to those observed for the propylene selectivity, i.e., a selectivity increase from 2.9 to 4.2%. This reveals a slight effect of the oxygen concentration on the reactivity behavior, which however is significantly lower than the influence of vanadium. In addition, while for ceria the amount of oxygen largely drops under reaction conditions, there is still enough oxygen present during equilibrium concentrations (after 200–250 min, 27% of initial oxygen) to not limit the conversion. Therefore, we can conclude that our measurements represent changes caused by vanadia (see below) and that the observed structural dynamics is not a result of different conversions. The catalytic data produced in our reaction cell are in good agreement with those from a fixed bed reactor at similar vanadium loadings and temperatures.[29]

As a basis for the transient spectra discussed below, Figure 2c–e provides an overview of major results from the *operando* spectroscopic analysis at 275 °C, exemplarily shown for the 1.36 V/nm^2 sample for clarity (see Figures S10–S13 for the other samples). Figure 2c depicts the *operando* DRIFT spectrum during propane ODH (red). In comparison to the spectrum obtained under oxidative conditions (blue), multiple new features and intensity changes are observed in the carbonate (1100–1800 cm^{-1}), C–H stretching (2700–3000 cm^{-1}), and hydroxyl (3500–3900 cm^{-1}) regions (see Table S1 for detailed assignments). The C–H stretch vibrations originate from propane that is adsorbed on the ceria surface.[51] The intensity changes of the hydroxyl groups at 3640, 3690, and 3740 cm^{-1} indicate hydrogen abstraction from propane to the ceria surface, either directly, i.e., without any involvement of surface vanadia species, or by rapid transfer from a vanadia species to the ceria surface. Especially the increase in intensity at 3740 cm^{-1} indicates the formation of an isopropylic state via hydrogen transfer from propane to ceria lattice oxygen.[52,53]

The dramatic changes in the carbonate region during reaction conditions result from the formation of adsorbates, which is related to the presence of propane in comparison to oxidative conditions. These include the appearance of a shoulder at 1610 cm^{-1}, originating from the propylene double bond as well as the features at 1545 and 1567 cm^{-1}, which are usually assigned to O–C–O vibrations of carbonates and may be indicative of propane adsorption in an O–C–O geometry as well as subsequent CO_2 formation from carbonates (see Figure S9 for detailed DRIFT spectra).[27,51,54,55] In this context, it is important to note that the presented DRIFT spectra do not allow one to distinguish between spectator and mechanistically relevant (active) species. Finally, surface vanadia is detected via the V=O stretch vibration at 1020–1040 cm^{-1} and its overtone. However, as can be seen from the inset of Figure 2c, no information about the nuclearity of the
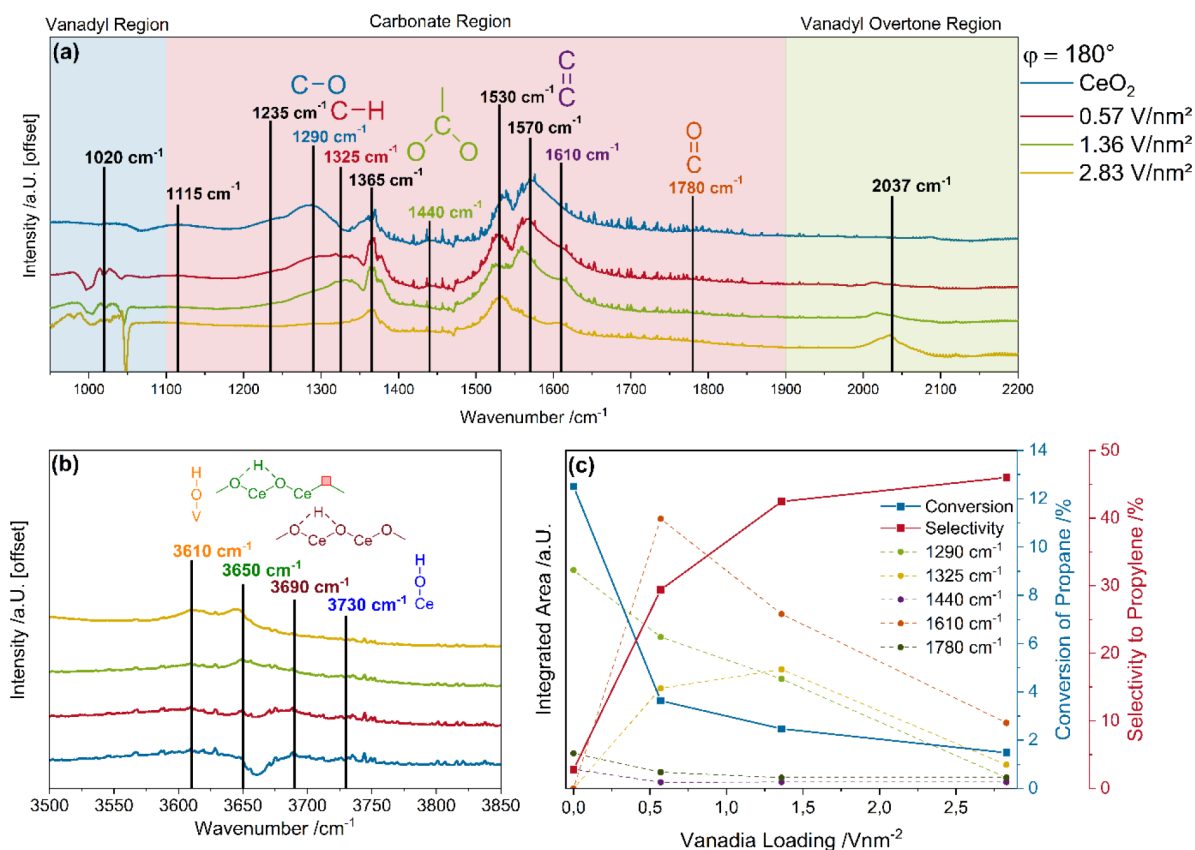
Figure 3. Results from transient IR spectroscopy for VO_x/CeO_2 catalysts compared to bare ceria during propane ODH at 275 °C. (a) PSD spectra ($\varphi = 180°$) at constant propane and pulsed oxygen flow highlighting adsorbate-related features of particular relevance for the mechanistic discussion. (b) PSD spectra of the Ce−OH region. (c) Loading-dependent peak areas of selected IR features related to the catalytic properties. An example fit of the spectrum of the 1.36 V/nm² sample is shown in the SI (see Figure S19).

species and/or reaction-induced changes is revealed, due to the noise level in this region.

Figure 2d shows the UV−vis spectra recorded under oxidative (blue) and reactive (red) atmospheres. Generally, the UV−vis spectra are characterized by the strong absorption of ceria below 400 nm caused by band gap absorption,[56] overlapping with the ligand-to-metal charge transfer (LMCT) features of vanadia between 300 and 550 nm.[57] Upon exposure to ODH conditions, multiple changes are detected. First, the observed absorption increase implies a red-shift of the band gap by 0.02 eV, which is indicative of ceria reduction in the ceria subsurface/bulk, since newly created oxygen vacancies lead to electronic states closer to the conduction band, thereby decreasing the overall band gap.[41,58] Further changes in the absorption behavior at 550−800 nm (see inset of Figure 2d) can be associated with vanadia d−d transitions, indicating the presence of reduced vanadia during reaction.[59,60] This is a remarkable observation, as a number of experimental and theoretical studies have proposed that vanadia prefers an oxidation state of 5+ on the ceria surface.[30,32,34,35,37] In this context, the question arises of whether the reduction of vanadia species is an essential part of the reaction mechanism or a parallel process. Besides the gas-phase-induced changes, the spectra highlight the three Raman excitation wavelengths that have been chosen to allow for the most sensitive analysis of different parts of the catalyst system (385 nm: ceria surface; 514 nm: vanadia; 532 nm: ceria bulk), also exploiting resonance enhancements, as described previously.[26,27]

The corresponding *operando* Raman spectra are shown in Figure 2e, in comparison to those recorded under oxidative conditions, all normalized to the F_{2g} mode. Exposure to ODH conditions leads to an intensity decrease of the Ce−O surface phonon at 405 cm^{-1} as well as the features within the range of 470−600 cm^{-1} assigned to the defect region, containing a contribution of Ce^{3+} at 550 cm^{-1} and oxygen vacancies at 590 cm^{-1}.[41,44] This behavior indicates surface reduction of ceria, whereby lattice oxygen is used to oxidize propane to propylene and CO_x. Note that ceria, as an active support material, clearly participates in the reaction, in contrast to other carriers, such as SiO_2.[61,62] Interestingly, the vanadia structures (V−O−Ce, V−O−V, V=O) seem to remain unchanged during the reaction, as no observable intensity changes are detected between oxidative and reactive conditions, which is consistent with the previously mentioned literature but appears to be at odds with the d−d transitions observed in the UV−vis spectra.

The UV−Raman behavior is supported by the 514 nm spectra, including the V=O profile (see inset of Figure 2e, 514 nm), which shows a defined fine structure (see above), but remains largely unchanged, exhibiting a slight red-shift of the higher nuclearities but no clear trend when all four samples are considered (see Figure S13). The F_{2g} mode is an important probe of the ceria subsurface/bulk properties. Using 532 nm excitation, a red-shift of the F_{2g} mode of 0.96 cm^{-1} was detected when the gas atmosphere was switched to reactive conditions (see inset of Figure 2e, 532 nm), which can be associated with ceria reduction, as the Ce^{3+} ions have a larger
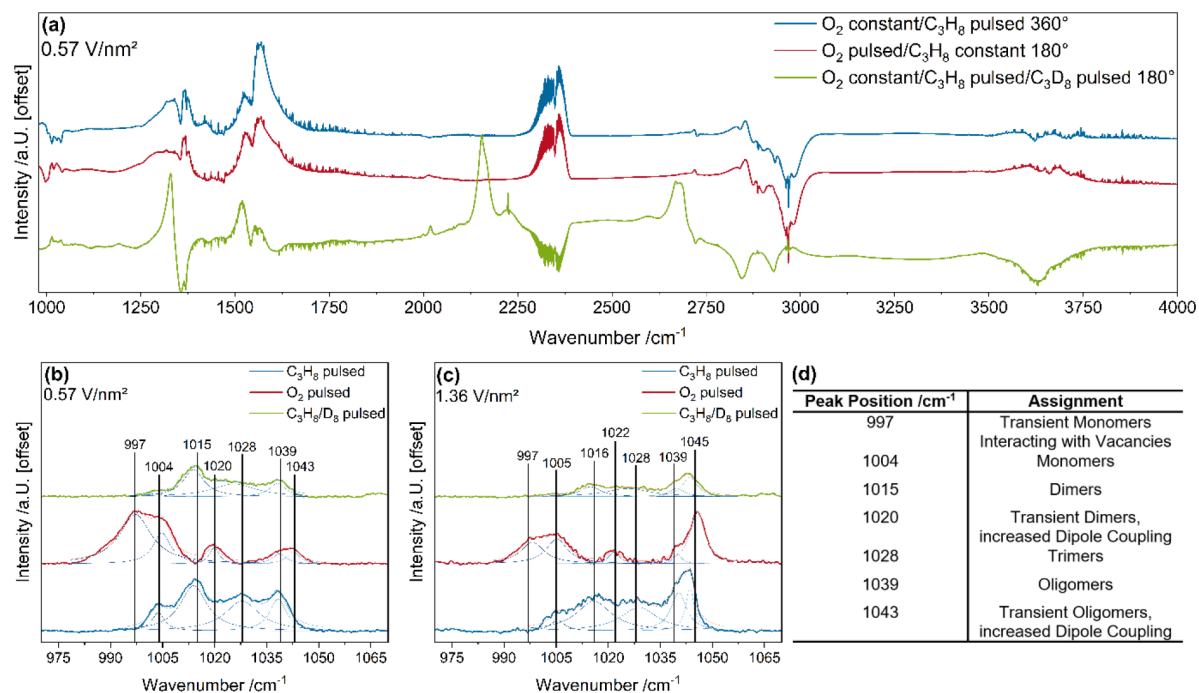
Figure 4. Results from isotopic transient IR spectroscopy during propane ODH at 275 °C. (a) PSD spectra during different ME-DRIFTS experiments. (b,c) Enlarged view of the vanadyl region for two different loadings, together with the result of a fit analysis. (d) Proposed assignments for the different vanadyl (V=O) signals during MES experiments. Please refer to the text for details and to Figure S22 for MES results on the 2.83 V/nm^2 sample.
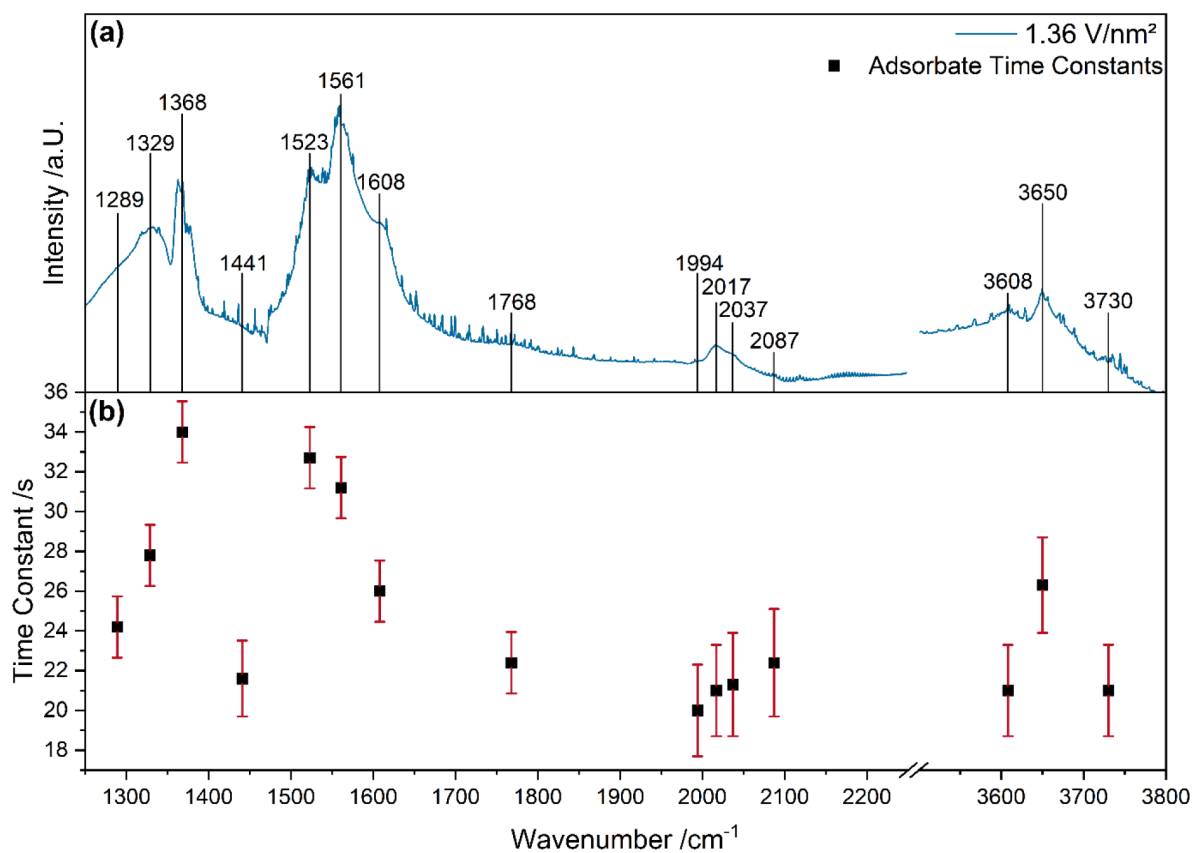
Figure 5. Temporal analysis of propane ODH at 275 °C. (a) ME-DRIFT spectrum of the 1.36 V/nm^2 sample during constant propane/pulsed oxygen flow. (b) Corresponding time constants determined by in-phase angle analysis. Error bars were determined from multiple measurements of the same sample (compare Table S2).

radius, leading to lattice expansion.[63] This is in good agreement with the band gap shift deduced from the UV−vis spectra, also indicating ceria reduction. From the above results, it is apparent that the ceria support actively participates in the reaction mechanism as an oxygen buffer, which provides surface oxygen for the ODH reaction and can be regenerated by either subsurface/bulk or gas-phase oxygen.

To gain further insight into the role of vanadia and to understand the significant activity changes of the catalyst upon vanadia impregnation, a quantitative analysis of the spectroscopic data was performed. The data is presented in Figure S14 and summarizes the loading dependence of the dynamics of the transversal Ce−O surface phonon and the ceria defect region as well as the F_{2g} shift. Both trends are related to the oxygen dynamics within the ceria lattice. The Ce−O dynamics and the F_{2g} red-shift correlate with the observed conversions (see Figure 2b), indicating that the reducibility of the catalyst is important for the conversion and that ceria supplies oxygen for the reaction. With increasing vanadium loading, the oxygen transfer toward the surface is slowed down, as also supported by the decreasing band gap energy shifts (see Figure S14b). Considering the selectivity, the high oxygen dynamics in bare ceria counteract the selective oxidation to propylene, and mostly CO_x is produced. From the above findings, we can deduce that the slowdown of the oxygen dynamics induced by surface vanadia species significantly increases the selectivity. The decrease in Raman intensity in the defect region correlates well with the amount of monomeric vanadia species in the samples (see Figure S6), fully consistent with a DFT study by the Sauer group reporting a structural relaxation of monomeric vanadia species into newly created oxygen vacancies.[32] Therefore, as surface lattice oxygen is regarded as an active center for propane conversion leading to CO_x formation, as previously established,[64] this interaction leads to an overall slowdown of this reaction due to decreased oxygen mobility, thereby increasing the propylene selectivity. This explains the jump in propylene selectivity for 0.57 V/nm^2 and in part for 1.36 V/nm^2 but not for the highest vanadium loading with almost no monomeric species present. Thus, we suspect an additional reason for the selectivity increase at higher vanadium loadings, overlapping with the slowdown in oxygen dynamics induced by monomeric vanadia species.

3.2. Transient IR Spectroscopy. To further investigate the ODH reaction mechanism, we employed ME-DRIFTS, which is introduced in Figure S15a−e. The results of the measurements and the quantitative analysis are shown in Figure 3. In the following discussion, we will focus on the spectra recorded in constant propane and pulsed oxygen at a phase shift of 180° (see Figure 3a), at which the maximum intensities were detected. Corresponding spectra recorded in constant oxygen and pulsed propane show consistent results (see Figures S16 and S18) but do not contain additional information, as discussed in detail in the SI (see Figure S18). For clarity, in Figure 3a the gas-phase contributions from CO, CO_2, and propane at 2100−3500 cm^{-1} have been removed, and the relevant regions have been indicated. For the carbonate region (center), detailed assignments and structures relevant for the quantitative analysis in Figure 3c are depicted. The vanadyl regions (left and right) contain no detailed assignments at this point but will be discussed in detail below (see Figures 4 and 5). Figure 3b highlights the Ce−OH region with its relevant structures. The peak assignments are summarized in Table 1.

Table 1. Peak Assignments for the ME-DRIFT Spectra of Bare Ceria and the Vanadia-Loaded Samples Recorded at 275 °C during Constant Propane and Pulsed Oxygen Flow

position/cm^{-1}	assignment	reference
997	V=O monomeric	40, 50
1004	V=O dimeric	40, 50
1020	V=O trimeric	40, 50
1040	V=O tetrameric	40, 50
1049	V=O pentameric	40, 50
1115	v COO^-	55
1235	v COO^-	55
1290	v_s C−O	51
1325	v C−H	65
1365	v_s CH_3	51
1380	v C−H	65
1440	v_s COO	66
1530	v_{as} COO	51
1570	v_{as} COO	51
1610	v_{as} C=C	51
1780	v C=O	67
1994	V=O overtone	68
2017	V=O overtone	68
2037	V=O overtone	68
2087	V=O overtone	68
3610	V−O−H	69
3650	Ce−O−H II-B	70
3690	Ce−O−H II*-A	70
3730	Ce−O−H I-A	70

It is apparent that the transient spectra in Figure 3a show smaller and more clearly defined peaks in the carbonate and hydroxyl region compared to Figure 2c, underlining that some of the features in regular DRIFTS originate from spectator species. In addition, the presence of vanadyl peaks within 1000−1060 cm^{-1} as well as their overtones in the PSD spectra now evidence the active participation of the vanadyl group in the ODH reaction. Moreover, in contrast to Figure 2c (inset), the vanadyl feature shows a clearly defined fine structure (see below), allowing a nuclearity-dependent analysis, which is of great importance considering the ongoing debate on the role of V=O in ODH reactions.[27,29,35,36,38] The participation of vanadia is also supported by the 3610 cm^{-1} peak in the OH stretching region, which is only detected for V-loaded samples, fully consistent with V−OH.[69] The Ce−OH peak located at 3730 cm^{-1}, which is commonly associated with an isopropylic adsorbate,[52,53] declines with increasing vanadium loading and is most pronounced for ceria, indicating that isopropyl adsorbate results from the first hydrogen abstraction from propane. The intensity decrease also correlates with the decrease in conversion, strongly suggesting that most, if not all, of the converted propane on ceria passes through an isopropyl adsorbate, as has been proposed in the literature.[51] The peaks at 3690 and 3650 cm^{-1} have been associated with bridged Ce−OH groups located either on clean ceria or next to an oxygen vacancy, respectively.[41,70] With increasing vanadium loading, the 3650 cm^{-1} signal gains intensity, while the 3690 cm^{-1} peak declines and is not observable anymore at higher loadings. This behavior highlights the importance of defects at higher vanadium loadings but also points to the relevance of other (V-related) surface processes besides the ceria oxygen dynamics discussed above, which is most pronounced at low loadings and becomes less relevant for higher loadings.

Owing to its significance for the interpretation of the ME-DRIFT spectra, a detailed analysis of the carbonate region was performed (see Figure 3a). Species with significant intensity changes were analyzed quantitatively (dashed lines) and compared to the loading-dependent conversions and selectivities (solid lines). Starting with the region between 1200 and 1400 cm^{-1}, with increasing loading, the features at 1235 and 1290 cm^{-1} decrease, while the peak at 1325 cm^{-1} increases in relative intensity. The features at 1235 and 1290 cm^{-1} originate from adsorbates that contain C−O bonds,[51,55] which are likely to be strongly bound to the surface and, hence, to be overoxidized to CO_x, decreasing the propylene selectivity. The peak at 1325 cm^{-1} is attributed to a C−H bond from a single hydrogen bound to carbon,[65] which is only possible at the middle carbon atom of propane after double bond formation. Therefore, the presence of this peak is associated with selective oxidation to propylene rather than total oxidation.[65] The 0.57 V/nm^2 sample shows all three peaks, indicating that at low vanadium loadings both reaction pathways appear simultaneously. Also, the feature at 1440 cm^{-1}, associated with an O−C−O-containing adsorbate,[51,66] shows a decrease in intensity with increasing vanadium loading, representing the state in which the propane adsorbs to the catalyst surface, as can be verified by in-phase angle analysis (see below).

At higher wavenumbers, the peaks at 1610 and 1780 cm^{-1} are of interest, which originate from C=C and C=O stretching modes, respectively. The latter feature has been associated with CO_2 formation on MnO_x-ceria catalysts,[52] whereas the 1610 cm^{-1} peak, which increases with vanadium loading, was previously identified as part of an acrylate-based state in the context of Ru/CeO_2 catalysts used for propane combustion.[51] Therefore, the above findings suggest the presence of two different pathways toward propylene formation. One operates on the bare ceria and is based on an isopropyl transition state, as indicated by the presence of the corresponding Ce−OH groups, while the other one is based on an acrylic transition state, as evidenced by the C=C peak at 1610 cm^{-1}, and is formed by participation of vanadia.

These scenarios are corroborated by the loading-dependent correlations of structure with activity/selectivity in Figure 3c. First, the peaks at 1290 and 1780 cm^{-1}, associated with adsorbates related to CO_x formation, follow the trend of the conversion, which is in line with the Raman results on the decreased oxygen dynamics (see above), as does the peak at 1440 cm^{-1}, associated with the initial adsorbate after the first hydrogen abstraction. As the first hydrogen abstraction is considered the rate-determining step of the ODH reaction, less adsorbed propane would lead to smaller conversions. Finally, the features at 1325 and 1610 cm^{-1}, related to propylene formation, show trends that at first sight appear to correlate with neither the conversion nor the selectivity. This is because catalysts with higher vanadium loadings have lower conversions, while the propylene yield stays almost constant. Therefore, the peak intensities at 1325 and 1610 cm^{-1} need to be regarded in relation to other peak intensities, such as those at 1290 and 1780 cm^{-1}. Indeed, for these relative intensities, a similar loading dependence as for the selectivities is observed.

For further insight into the dynamics, we performed isotopic exchange experiments, in which the propane-h_8-containing reaction atmosphere was switched to a propane-d_8-containing reaction atmosphere, while the flow of oxygen through the reaction chamber was constant. This experiment allows features to be identified that are associated with a hydrogen transfer during the reaction mechanism, as the only way of introducing hydrogen/deuterium is through propane. Figure 4a depicts an example spectrum for the 0.57 V/nm^2 catalyst, together with the results from the two modulation settings used above, while the spectra of the other samples are discussed in the SI (see Figures S20 and S21). The results largely confirm those obtained for the OH and carbonate regions (see Figure 3a). In the carbonate region, besides the major peaks at 1325 and 1360 cm^{-1}, small contributions due to COO modes are detected at 1440 and 1530 cm^{-1}, which are attributed to a kinetic isotope effect, showing its relevance for the first hydrogen abstraction to the catalyst's surface. Remarkably, the isotopic ME-DRIFT spectra provide important new insight into the vanadia dynamics, which goes beyond the *operando* Raman and DRIFTS results shown in Figure 2. In fact, closer inspection of the vanadyl region reveals a gas-phase-dependent fine structure, which is shown in an enlarged view in Figure 4b,c together with results of a fit analysis. Figure 4d summarizes the proposed assignments for the transient vanadyl features.

Considering the (static) Raman results, the active participation of vanadyl in the ODH reaction can be rationalized on the basis of a fast regeneration process, which prevents the structural dynamics from being resolved by the *operando* Raman experiments. While the vanadyl fine structure is resolved for all loadings (see Figure 4), it is most clearly visible for the 0.57 V/nm^2 sample. This behavior can be explained by the fact that the MES signals are based on intensity changes triggered by the modulation, which in this context is the conversion of propane. As can be seen in Figure 4a, the 0.57 V/nm^2 sample shows a distinct signature for each gas phase. For constant oxygen and pulsed propane flow, the PSD spectrum is dominated by four peaks, at 1004, 1015, 1028, and 1039 cm^{-1}, that coincide with monomeric, dimeric, tetrameric, and pentameric vanadia species, respectively, consistent with the Raman results (see Figure 2e).

Comparison of the different gas phases, i.e., constant oxygen/pulsed propane to constant propane/pulsed oxygen, reveals significant shifts in the peak positions. Interestingly, for all three samples, peaks at around 997, 1005, 1020, 1040, and 1045 cm^{-1} are observed. A vanadyl peak at 997 cm^{-1} is typically associated with crystalline V_2O_5, which is expected at high vanadium loadings. Based on the characterization data, including the visible Raman data discussed above, the presence of crystalline V_2O_5 can be safely ruled out. Furthermore, the peak at 997 cm^{-1} decreases in intensity with increasing vanadium loading, contradicting the current knowledge about V_2O_5 formation on supported VO_x systems.[36−38,42] Since the constant propane mode leads to more reducing conditions, the formation of reduced states appears to be a reasonable explanation. To this end, the reduction of the ceria support may lead to the creation of surface oxygen vacancies, which can subsequently be occupied by vanadia monomers through structural relaxation. Other reasons for the red-shift, such as the binding of water to the vanadyl bond, which were previously described,[26] seem unlikely due to the high temperature at which the reaction takes place. Therefore, it is proposed that the unique interaction between surface oxygen vacancies and monomeric species induces a vanadyl red-shift. This interaction is only observed for monomeric species, as described in previous DFT studies.[32] Such a red-shift of monomers was also observed in our preliminary DFT

calculations on defective ceria loaded with monomeric VO$_x$ in the form of VO and VO$_2$ clusters.[31,32] Such a scenario would also be in good agreement with the changes in the Ce−OH region (see Figure 3a), where, with increasing vanadium loading, Ce−OH groups are formed close to surface vacancies, indicating that hydrogen from propane is first transferred to VO$_x$ and then to a nearby ceria lattice oxygen before a subsequent reaction to water accompanied by the formation of a surface vacancy (see below), located in proximity to a vanadia species. While ceria keeps vanadium in oxidation state +5, the time resolution of MES is sufficient to detect the brief phase in which vanadia is reduced by the reaction before it is quickly reoxidized by ceria.

Comparison of spectra recorded in constant oxygen (blue) and constant propane (red) mode reveals that monomeric, dimeric, tetrameric, and pentameric vanadia structures are present for both gas phases, confirming that all of those species are active during the ODH reaction, whereas the trimeric vanadia species is only observable in constant oxygen mode, which is likely to also show observer species for the same reasons as mentioned above and described in detail in the SI (see Figure S18). This makes it likely that trimeric species do not participate in the ODH of propane, which would be consistent with previous DFT results,[32] which have identified trimers as the energetically most stable species on a ceria surface. Therefore, the trimeric species seems to undergo an initial reduction step, which makes it detectable in the constant oxygen mode, but does not continue to react further toward propylene from this reduced state, which leads to its absence in the spectrum in the constant propane mode and the presence of a permanently reduced trimeric species, explaining the observed d-d transitions from the *operando* UV−vis spectra (see Figure 2d).

To distinguish the roles of the remaining dimeric, tetrameric, and pentameric species, the vanadyl region of the isotopic MES data is considered (see Figures 4b,c and S22, green). In these spectra, only the V=O peaks at 1015 and 1040 cm^{-1} for the 0.57 and 1.36 V/nm^2 samples and the V=O peak at ∼1040 cm^{-1} for the 2.83 V/nm^2 sample are clearly observable, indicating that dimeric and (with higher loading increasingly) pentameric vanadia species are involved in the reaction. A broad signal at the trimeric position is also present, which is in agreement with the aforementioned discussion about the reduced trimeric state. Interestingly, comparison of the blue and red spectra reveals that the V=O peaks of the dimeric and oligomeric species show blue-shifts under more reducing conditions. While DFT calculations of surface vanadia species under such transient conditions are not available in the literature, the detected spectral behavior may be explained by structural changes in vanadia upon hydrogen abstraction, which is, for example, induced by oxygen vacancies, hydrogen bound to the ceria surface, or V=O⋯H formation. No complete relaxation into nearby vacancies as for monomeric species is observed for dimers and oligomers, probably due to the structural constraints of vanadia chains. The detected blue-shifts in the transient spectra rather imply more condensed vanadia structures, which are subject to increased dipole coupling between neighboring V=O groups.[31,32] Bond-length changes of the vanadyl group, explaining the blue-shift, depending on its interaction with propane/hydrogen atoms and its chemical surroundings, were also previously predicted on silica using DFT calculations.[71] Furthermore, it has already been shown by DFT calculations[32] that for monomeric

structures hydrogen that was abstracted to the ceria surface can form hydrogen bonds with V−O−Ce interface oxygen, which may introduce changes in vanadia bond lengths and may also be possible for dimeric and oligomeric species. Since oxygen vacancies are preferably formed in proximity to vanadia and hydrogen that is transferred from a V=O bond to the ceria surface is also in close proximity to vanadia (thereby creating hydrogen bonds), only vanadia species that actively participate in the ODH reaction should be subject to such ceria- and/or interface-induced structural changes.[32] Therefore, dimeric and oligomeric vanadia can be identified as key structures for hydrogen abstraction from propane toward the ceria surface. These effects can only be observed using transient spectroscopy, as vanadia is regenerated very fast to oxidation state +5 by ceria, making the detection of those species impossible with static spectroscopies. For the samples with higher loadings, the vanadia surface species are shifted toward higher nuclearities. For example, for the 2.83 V/nm^2 sample, mostly the oligomeric species is detected, which can be explained by the relatively smaller proportion of species with lower nuclearity as well as the even smaller propane conversion of the 2.83 V/nm^2 sample, both of which decrease the intensity of those contributions below the detection limit of MES. In summary, different vanadia nuclearities fulfill different roles during propane ODH, which leads to different spectroscopic behavior, where different species might red-shift, blue-shift, or not change their position in the PSD spectra, depending on their reaction behavior.

Finally, the time evolution of the surface processes, i.e., the adsorbate dynamics, will be discussed, based on the in-phase angle analysis of the spectra (see Experimental Section). The top of Figure 5 depicts the ME-DRIFT spectrum recorded at constant propane/pulsed oxygen flow for the 1.36 V/nm^2 sample, while the bottom shows the time constants determined for important vibrational features (marked in the top panel), allowing the temporal evolution of the relevant surface processes during the ODH reaction to be visualized. The values of the time constants referring to the 1.36 V/nm^2 sample are summarized in Table 2, and those for the remaining samples in Table S2.

Table 2. Temporal Evolution of IR Modes Involved in Propane ODH at 275 °C[a]

wavenumber/cm^{-1}	time/s	assignment
1994	20 ± 2.3	V=O overtone
2017	21 ± 2.3	V=O overtone
3608	21 ± 2.3	V−O−H
3730	21 ± 2.3	Ce−OH I-A
2037	21.3 ± 2.6	V=O overtone
1441	21.6 ± 1.54	v_s O−C−O
1768	24.2 ± 1.54	v C=O
2087	22.4 ± 2.7	V=O overtone
1289	22.4 ± 1.54	v_s C−O
1608	26 ± 1.54	v_{as} C=C
3650	26.3 ± 2.4	Ce−OH II-B
1329	27.8 ± 1.54	v C−H
1561	31.2 ± 1.54	v_{as} COO
1523	32.7 ± 1.54	v_{as} COO
1368	34 ± 1.54	v_s CH$_3$

[a]Example result for the 1.36 V/nm^2 sample.
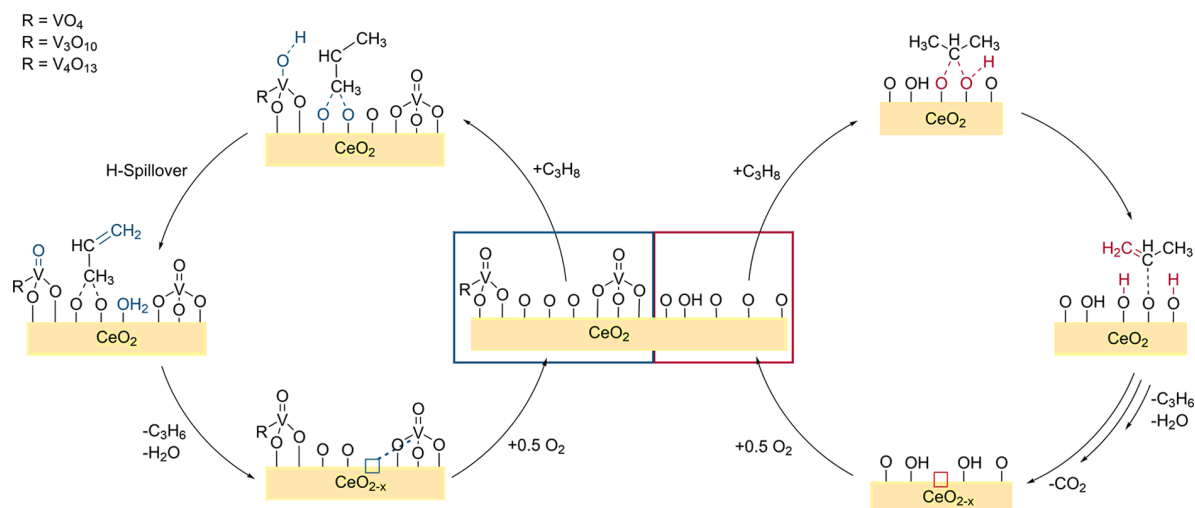
Figure 6. Proposed reaction mechanism for propane ODH over VO_x/CeO_2 catalysts. As shown on the left, in the vicinity of surface vanadia, the reaction proceeds via an acrylate intermediate. On ceria (i.e., at a large distance from surface vanadia), the reaction is proposed to proceed via an isopropyl intermediate (on the right).

From the values of the time constants, it can be seen that vanadyl signals, Ce−OH signals from singly bound hydroxyl groups, and V−OH signal groups are the first to be detected. For the following discussion, only the time constant of the overtone will be considered, which is explained in the SI (see Figure S5). As there is no evidence from static *operando* spectroscopy for the permanent reduction of vanadia, but only from transient results, V−O−H formation is likely to occur very fast and to be followed by a hydrogen transfer to the ceria surface, thereby regenerating the vanadia structure.[33] Such a scenario is supported by DFT results, which propose the reduction of ceria lattice oxygen to be energetically more favorable than vanadia reduction.[31−34,39] Continuing with the discussion of Figure 3a, within the time frame of the initial processes, also the feature at ∼1440 cm^{-1} (O−C−O) appears. The temporal evolution suggests that the corresponding adsorbate represents the state in which propane is initially adsorbed, either during or after the first hydrogen abstraction. In parallel to the 1440 cm^{-1} feature, the peak at ∼1780 cm^{-1} is detected, which is correlated with CO_2 formation,[51,52] indicating that CO_2 formation may occur in parallel to propylene formation and not exclusively as a follow-up reaction to propylene formation, as suggested in the literature. Such a scenario is supported by the fact that, with increasing vanadium loading, the peak at 1780 cm^{-1} declines, whereas the 1440 cm^{-1} feature stays largely constant, resembling the CO_x and propylene yields, respectively.

The observed behavior supports the proposal of two distinct reaction pathways: one, which proceeds close to vanadia structures, leading mostly to propylene, and another, which proceeds on the CeO_2 surface, yielding mostly CO_2. This also explains the smaller increases in selectivity upon doubling the vanadium loading, as 3D structures begin to form and the CO_x pathway is still accessible on the remaining ceria surface. These processes occur in addition to the observed interaction between vanadia monomers and oxygen vacancies. In this context, it seems likely that the blockage of vacancies by vanadia monomers might not only slow down the ceria lattice oxygen dynamics but also block the sites on the ceria surface that play an important role in the reaction pathway toward CO_x, further increasing the complexity of interactions among

vanadia, ceria, and propane. Based on the MES data, the two different routes toward CO_2 and propylene, as well as the further reaction of the abstracted hydrogen, can be followed separately. We start with the abstracted hydrogen, which is first transferred to the V=O group and then to the ceria surface, forming singly bound Ce−OH (I-A) and continuing to react toward bridged hydroxyl (II-B) close to an oxygen surface vacancy.[41,70] While no additional signals for this route are observed, it stands to reason that bridged hydroxyls recombine to form singly bound Ce−OH$_2$ and finally water on a time scale not accessible by MES.[33] For the route toward CO_2 the first adsorption state is followed by structures characterized by features at 1289 cm^{-1} (C−O) and finally 1523 and 1561 cm^{-1} (COO). These were assigned by their late appearance in the temporal evolution as well as their high oxygen content, which is commonly associated with carbonate formation. The latter features are among the last to be detected and exhibit comparably high intensities, indicating that they represent important intermediates toward CO_2 formation.

For the propylene route, after the initial adsorption state, the appearance of the features at 1608 (C=C) and 1329 cm^{-1} (C−H) is in good agreement with a propylene-like intermediate state. In fact, the double bond at 1608 cm^{-1} was previously described in the context of an acrylic coordination of propane.[51] Also, the peak intensities of the features at 1608 and 1329 cm^{-1} are in agreement with the observed propylene selectivities. The feature at 1368 cm^{-1} (CH$_3$), which is observed last in the temporal analysis, is likely to originate from the CH$_3$ group of propylene, which is either adsorbed or about to be desorbed. Based on the detailed mechanistic insights discussed above, we propose a reaction mechanism for propane ODH over VO_x/CeO_2 catalysts (see Figure 6) containing two pathways, one that occurs close to vanadia and leads to propylene and another that occurs on ceria and leads to CO_x.

4. CONCLUSION

We present the first application of conventional *operando* spectroscopies, ME-DRIFTS, and isotopic ME-DRIFTS to ODH reactions of alkanes, focusing on the mechanistic investigation of propane ODH, which is of great interest for

commercial applications. Previously established, commonly applied *operando* spectroscopy provides significant insights into the reaction mechanism; however, the surface dynamics and the role of vanadia have not been clarified yet.[27] By applying modulation excitation spectroscopy in combination with multiple *operando* spectroscopies, we were able to greatly enhance the level of understanding of propane ODH over supported vanadia catalysts.

We were able to demonstrate that ceria actively participates in the reaction, providing surface oxygen for the oxidation of propane and acting as an oxygen buffer with the possibility of reoxidizing the surface via bulk oxygen, mainly producing CO_x. The introduction of vanadia leads to multiple interactions, which change the activity of the catalyst. First, monomeric vanadia species are shown to slow down the oxygen dynamics in the catalyst by irreversibly blocking surface vacancies required for CO_x production, resulting in a decreased conversion and CO_x production. The addition of vanadia enables a second reaction pathway, which leads to the formation of propylene. The route to CO_x passes through an isopropylic structure on ceria, whereas propylene is formed from an acrylic structure strongly facilitated by proximity to vanadia. Both routes proceed in parallel but at different locations on the surface.

For vanadia-loaded catalysts, the specific roles of different vanadia nuclearities for the reaction mechanism were elucidated, i.e., monomeric species block oxygen vacancies, the V=O bonds of dimeric and oligomeric species are involved in the initial hydrogen abstraction, while trimers were too stable for active participation. Hydrogen is then transferred to the ceria surface, regenerating V^{5+} and forming Ce—OH on a very fast time scale, before leading to water and oxygen vacancy formation. These vanadia dynamics were accessible for the first time by MES on VO_x/CeO_2 due to the detected vanadyl fine structure, which allows the structural changes in the vanadia species to be temporally resolved. The observed structural changes shed new light on the role of vanadia in ODH reactions, which both experimentally and theoretically has been proposed to stay in the +5 oxidation state during propane ODH over ceria-based catalysts.[3,29−39]

Based on our findings,[27] we propose a detailed reaction mechanism for the ODH of propane over VO_x/CeO_2, directly linking the catalytic activity to solid-state properties (including defects), adsorbate structures, and the roles of different vanadia nuclearities. Our results highlight the potential of (isotopic) modulation excitation IR spectroscopy for elucidating the surface dynamics of propane ODH over supported vanadia. The combination of IR-MES with *operando* spectroscopies provides a powerful methodical approach readily applicable to other catalysts and reactions in the context of oxidation catalysis. Due to the importance of IR spectroscopy in catalysis, we expect widespread adoption of the MES approach for performing detailed mechanistic investigations and for resolving the catalysts' dynamics.

ASSOCIATED CONTENT

ⓈⒾ Supporting Information

The Supporting Information is available free of charge at https://pubs.acs.org/doi/10.1021/jacs.2c06303.

> Information on the experimental setup; additional data on sample characterization and reactivity behavior; additional *operando* data (DRIFTS, UV−vis, Raman);

additional ME-DRIFTS data, PSD spectra, and temporal analysis (PDF)

AUTHOR INFORMATION

Corresponding Author

Christian Hess − *Eduard Zintl Institute of Inorganic and Physical Chemistry, Technical University of Darmstadt, 64287 Darmstadt, Germany;* ⓞ orcid.org/0000-0002-4738-7674; Email: christian.hess@tu-darmstadt.de

Authors

Leon Schumacher − *Eduard Zintl Institute of Inorganic and Physical Chemistry, Technical University of Darmstadt, 64287 Darmstadt, Germany*

Jakob Weyel − *Eduard Zintl Institute of Inorganic and Physical Chemistry, Technical University of Darmstadt, 64287 Darmstadt, Germany*

Complete contact information is available at:
https://pubs.acs.org/10.1021/jacs.2c06303

Notes

The authors declare no competing financial interest.

REFERENCES

(1) Amghizar, I.; Vandewalle, L. A.; van Geem, K. M.; Marin, G. B. New Trends in Olefin Production. *Engineering* **2017**, *3* (2), 171−178.

(2) Cavani, F.; Ballarini, N.; Cericola, A. Oxidative dehydrogenation of ethane and propane: How far from commercial implementation? *Catal. Today* **2007**, *127* (1−4), 113−131.

(3) Carrero, C. A.; Schloegl, R.; Wachs, I. E.; Schomaecker, R. Critical Literature Review of the Kinetics for the Oxidative Dehydrogenation of Propane over Well-Defined Supported Vanadium Oxide Catalysts. *ACS Catal.* **2014**, *4* (10), 3357−3380.

(4) Chen, K.; Bell, A. T.; Iglesia, E. Kinetics and Mechanism of Oxidative Dehydrogenation of Propane on Vanadium, Molybdenum, and Tungsten Oxides. *J. Phys. Chem. B* **2000**, *104* (6), 1292−1299.

(5) Kim, H.; Kosuda, K. M.; van Duyne, R. P.; Stair, P. C. Resonance Raman and surface- and tip-enhanced Raman spectroscopy methods to study solid catalysts and heterogeneous catalytic reactions. *Chem. Soc. Rev.* **2010**, *39* (12), 4820−4844.

(6) Zabilska, A.; Clark, A. H.; Moskowitz, B. M.; Wachs, I. E.; Kakiuchi, Y.; Copéret, C.; Nachtegaal, M.; Kröcher, O.; Safonova, O. V. Redox Dynamics of Active VO x Sites Promoted by TiO x during Oxidative Dehydrogenation of Ethanol Detected by Operando Quick XAS. *JACS Au* **2022**, *2* (3), 762−776.

(7) Chiarello, G. L.; Lu, Y.; Agote-Arán, M.; Pellegrini, R.; Ferri, D. Changes of Pd Oxidation State in Pd/Al2O3 Catalysts Using Modulated Excitation DRIFTS. *Catalysts* **2021**, *11* (1), 116.

(8) Vecchietti, J.; Bonivardi, A. L.; Xu, W.; Stacchiola, D.; Delgado, J. J.; Calatayud, M.; Collins, S. E. Understanding the Role of Oxygen Vacancies in the Water Gas Shift Reaction on Ceria-Supported Platinum Catalysts. *ACS Catal.* **2014**, *4* (4), 2088−2096.

(9) Aguirre, A.; Barrios, C. E.; Aguilar-Tapia, A.; Zanella, R.; Baltanás, M. A.; Collins, S. E. In-Situ DRIFT Study of Au-Ir/Ceria Catalysts: Activity and Stability for CO Oxidation. *Top. Catal.* **2016**, *59* (2−4), 347−356.

Journal of the American Chemical Society
pubs.acs.org/JACS
Article

(10) Aguirre, A.; Zanella, R.; Barrios, C.; Hernández, S.; Bonivardi, A.; Collins, S. E. Gold Stabilized with Iridium on Ceria-Niobia Catalyst: Activity and Stability for CO Oxidation. *Top. Catal.* **2019**, *62* (12), 977–988.

(11) del Río, E.; Collins, S. E.; Aguirre, A.; Chen, X.; Delgado, J. J.; Calvino, J. J.; Bernal, S. Reversible deactivation of a Au/Ce$_{0.62}$Zr$_{0.38}$O$_2$ catalyst in CO oxidation: A systematic study of CO$_2$-triggered carbonate inhibition. *J. Catal.* **2014**, *316*, 210–218.

(12) Fernández-García, S.; Collins, S. E.; Tinoco, M.; Hungría, A. B.; Calvino, J. J.; Cauqui, M. A.; Chen, X. Influence of {111} nanofaceting on the dynamics of CO adsorption and oxidation over Au supported on CeO$_2$ nanocubes: An operando DRIFT insight. *Catal. Today* **2019**, *336*, 90–98.

(13) Ferri, D.; Newton, M. A.; Di Michiel, M.; Chiarello, G. L.; Yoon, S.; Lu, Y.; Andrieux, J. Revealing the Dynamic Structure of Complex Solid Catalysts Using Modulated Excitation X-ray Diffraction. *Angew. Chem., Int. Ed.* **2014**, *126* (34), 9036–9040.

(14) Weyel, J.; Ziemba, M.; Hess, C. Elucidating Active CO-Au Species on Au/CeO$_2$(111): A Combined Modulation Excitation DRIFTS and Density Functional Theory Study. *Top. Catal.* **2022**, *65*, 779.

(15) Greenaway, A. G.; Marberger, A.; Thetford, A.; Lezcano-González, I.; Agote-Arán, M.; Nachtegaal, M.; Ferri, D.; Kröcher, O.; Catlow, C. R. A.; Beale, A. M. Detection of key transient Cu intermediates in SSZ-13 during NH$_3$ -SCR deNO$_x$ by modulation excitation IR spectroscopy. *Chem. Sci.* **2020**, *11* (2), 447–455.

(16) Nuguid, R. J. G.; Ferri, D.; Kröcher, O. Design of a Reactor Cell for Modulated Excitation Raman and Diffuse Reflectance Studies of Selective Catalytic Reduction Catalysts. *Emiss. Control Sci. Technol.* **2019**, *5* (4), 307–316.

(17) Nuguid, R. J. G.; Ferri, D.; Marberger, A.; Nachtegaal, M.; Kröcher, O. Modulated Excitation Raman Spectroscopy of V$_2$O$_5$/TiO$_2$: Mechanistic Insights into the Selective Catalytic Reduction of NO with NH$_3$. *ACS Catal.* **2019**, *9* (8), 6814–6820.

(18) Aguirre, A.; Collins, S. E. Selective detection of reaction intermediates using concentration-modulation excitation DRIFT spectroscopy. *Catal. Today* **2013**, *205*, 34–40.

(19) Hemmingsson, F.; Schaefer, A.; Skoglundh, M.; Carlsson, P.-A. CO$_2$ Methanation over Rh/CeO$_2$ Studied with Infrared Modulation Excitation Spectroscopy and Phase Sensitive Detection. *Catalysts* **2020**, *10* (6), 601.

(20) König, C. F.J.; Schildhauer, T. J.; Nachtegaal, M. Methane Synthesis and Sulfur Removal over a Ru Catalyst Probed In Situ with High Sensitivity X-Ray Absorption Spectroscopy. *J. Catal.* **2013**, *305*, 92–100.

(21) Serrer, M.-A.; Gaur, A.; Jelic, J.; Weber, S.; Fritsch, C.; Clark, A. H.; Saraçi, E.; Studt, F.; Grunwaldt, J.-D. Structural dynamics in Ni-Fe catalysts during CO$_2$ methanation - role of iron oxide clusters. *Catal. Sci. Technol.* **2020**, *10* (22), 7542–7554.

(22) Delgado, D.; Sanchis, R.; Solsona, B.; Concepción, P.; López Nieto, J. M. Influence of the Nature of the Promoter in NiO Catalysts on the Selectivity to Olefin During the Oxidative Dehydrogenation of Propane and Ethane. *Top. Catal.* **2020**, *63* (19–20), 1731–1742.

(23) Lu, W.-D.; Wang, D.; Zhao, Z.; Song, W.; Li, W.-C.; Lu, A.-H. Supported Boron Oxide Catalysts for Selective and Low-Temperature Oxidative Dehydrogenation of Propane. *ACS Catal.* **2019**, *9* (9), 8263–8270.

(24) Daniell, W.; Ponchel, A.; Kuba, S.; Anderle, F.; Weingand, T.; Gregory, D. H.; Knözinger, H. Characterization and Catalytic Behavior of VO$_x$-CeO$_2$ Catalysts for the Oxidative Dehydrogenation of Propane. *Top. Catal.* **2002**, *20* (1), 65–74.

(25) Beck, B.; Harth, M.; Hamilton, N. G.; Carrero, C.; Uhlrich, J. J.; Trunschke, A.; Shaikhutdinov, S.; Schubert, H.; Freund, H.-J.; Schlögl, R.; Sauer, J.; Schomäcker, R. Partial oxidation of ethanol on vanadia catalysts on supporting oxides with different redox properties compared to propane. *J. Catal.* **2012**, *296*, 120–131.

(26) Ober, P.; Rogg, S.; Hess, C. Direct Evidence for Active Support Participation in Oxide Catalysis: Multiple Operando Spectroscopy of VO$_x$/Ceria. *ACS Catal.* **2020**, *10* (5), 2999–3008.

(27) Schumacher, L.; Hess, C. The active role of the support in propane ODH over VO$_x$/CeO$_2$ catalysts studied using multiple operando spectroscopies. *J. Catal.* **2021**, *398* (13), 29–43.

(28) Taylor, M. N.; Carley, A. F.; Davies, T. E.; Taylor, S. H. The Oxidative Dehydrogenation of Propane Using Vanadium Oxide Supported on Nanocrystalline Ceria. *Top. Catal.* **2009**, *52* (12), 1660–1668.

(29) Dinse, A.; Frank, B.; Hess, C.; Habel, D.; Schomäcker, R. Oxidative dehydrogenation of propane over low-loaded vanadia catalysts: Impact of the support material on kinetics and selectivity. *J. Mol. Catal. A: Chemical* **2008**, *289* (1–2), 28–37.

(30) Popa, C.; Ganduglia-Pirovano, M. V.; Sauer, J. Periodic Density Functional Theory Study of VO$_n$ Species Supported on the CeO$_2$ (111) Surface. *J. Phys. Chem. C* **2011**, *115* (15), 7399–7410.

(31) Penschke, C.; Paier, J.; Sauer, J. Vanadium Oxide Oligomers and Ordered Monolayers Supported on CeO$_2$ (111): Structure and Stability Studied by Density Functional Theory. *J. Phys. Chem. C* **2018**, *122* (16), 9101–9110.

(32) Penschke, C.; Paier, J.; Sauer, J. Oligomeric Vanadium Oxide Species Supported on the CeO$_2$ (111) Surface: Structure and Reactivity Studied by Density Functional Theory. *J. Phys. Chem. C* **2013**, *117* (10), 5274–5285.

(33) Huang, C.; Wang, Z.-Q.; Gong, X.-Q. Activity and selectivity of propane oxidative dehydrogenation over VO$_3$/CeO$_2$ (111) catalysts: A density functional theory study. *Chin. J. Catal.* **2018**, *39* (9), 1520–1526.

(34) Ganduglia-Pirovano, M. V.; Popa, C.; Sauer, J.; Abbott, H.; Uhl, A.; Baron, M.; Stacchiola, D.; Bondarchuk, O.; Shaikhutdinov, S.; Freund, H.-J. Role of ceria in oxidative dehydrogenation on supported vanadia catalysts. *J. Am. Chem. Soc.* **2010**, *132* (7), 2345–2349.

(35) Iglesias-Juez, A.; Martínez-Huerta, M. V.; Rojas-García, E.; Jehng, J.-M.; Bañares, M. A. On the Nature of the Unusual Redox Cycle at the Vanadia Ceria Interface. *J. Phys. Chem. C* **2018**, *122* (2), 1197–1205.

(36) Martínez-Huerta, M. V.; Deo, G.; Fierro, J. L. G.; Bañares, M. A. Operando Raman-GC Study on the Structure-Activity Relationships in V^{5+}/CeO$_2$ Catalyst for Ethane Oxidative Dehydrogenation: The Formation of CeVO 4. *J. Phys. Chem. C* **2008**, *112* (30), 11441–11447.

(37) Martínez-Huerta, M. Nature of the vanadia-ceria interface in V^{5+}/CeO$_2$ catalysts and its relevance for the solid-state reaction toward CeVO4 and catalytic properties. *J. Catal.* **2004**, *225* (1), 240–248.

(38) Bañares, M. A.; Martınez-Huerta, M. V.; Gao, X.; Fierro, J. L. G.; Wachs, I. E. Dynamic behavior of supported vanadia catalysts in the selective oxidation of ethane. *Catal. Today* **2000**, *61* (1–4), 295–301.

(39) Kropp, T.; Paier, J.; Sauer, J. Support effect in oxide catalysis: methanol oxidation on vanadia/ceria. *J. Am. Chem. Soc.* **2014**, *136* (41), 14616–14625.

(40) Wu, Z.; Rondinone, A. J.; Ivanov, I. N.; Overbury, S. H. Structure of Vanadium Oxide Supported on Ceria by Multiwavelength Raman Spectroscopy. *J. Phys. Chem. C* **2011**, *115* (51), 25368–25378.

(41) Filtschew, A.; Hofmann, K.; Hess, C. Ceria and Its Defect Structure: New Insights from a Combined Spectroscopic Approach. *J. Phys. Chem. C* **2016**, *120* (12), 6694–6703.

(42) Waleska, P. S.; Hess, C. Oligomerization of Supported Vanadia: Structural Insight Using Surface-Science Models with Chemical Complexity. *J. Phys. Chem. C* **2016**, *120* (33), 18510–18519.

(43) Ziemba, M.; Weyel, J.; Hess, C. Elucidating the mechanism of the reverse water-gas shift reaction over Au/CeO$_2$ catalysts using operando and transient spectroscopies. *Appl. Catal. B: Environmental* **2022**, *301*, 120825.

(44) Schilling, C.; Hofmann, A.; Hess, C.; Ganduglia-Pirovano, M. V. Raman Spectra of Polycrystalline CeO$_2$: A Density Functional Theory Study. *J. Phys. Chem. C* **2017**, *121* (38), 20834–20849.

(45) Schilling, C.; Ziemba, M.; Hess, C.; Ganduglia-Pirovano, M. V. Identification of single-atom active sites in CO oxidation over oxide-supported Au catalysts. *J. Catal.* **2020**, *383* (85), 264–272.

(46) Baurecht, D.; Fringeli, U. P. Quantitative modulated excitation Fourier transform infrared spectroscopy. *Rev. Sci. Instrum.* **2001**, *72* (10), 3782.

(47) Weyel, J. *Phase Sensitive Detection for Spectroscopy*. 2020. https://zenodo.org/record/3613876#.YtAxLBxCSUk.

(48) Yu, T.; Lim, B.; Xia, Y. Aqueous-Phase Synthesis of Single-Crystal Ceria Nanosheets. *Angew. Chem., Int. Ed.* **2010**, *122* (26), 4586−4589.

(49) Hess, C. New advances in using Raman spectroscopy for the characterization of catalysts and catalytic reactions. *Chem. Soc. Rev.* **2021**, *50* (5), 3519−3564.

(50) Baron, M.; Abbott, H.; Bondarchuk, O.; Stacchiola, D.; Uhl, A.; Shaikhutdinov, S.; Freund, H.-J.; Popa, C.; Ganduglia-Pirovano, M. V.; Sauer, J. Resolving the Atomic Structure of Vanadia Monolayer Catalysts: Monomers, Trimers, and Oligomers on Ceria. *Angew. Chem., Int. Ed.* **2009**, *121* (43), 8150−8153.

(51) Hu, Z.; Wang, Z.; Guo, Y.; Wang, L.; Guo, Y.; Zhang, J.; Zhan, W. Total Oxidation of Propane over a Ru/CeO$_2$ Catalyst at Low Temperature. *Environ. Sci. Technol.* **2018**, *52* (16), 9531−9541.

(52) Wang, H.; Zhou, H.; Li, S.; Ge, X.; Wang, L.; Jin, Z.; Wang, C.; Ma, J.; Chu, X.; Meng, X.; Zhang, W.; Xiao, F.-S. Strong Oxide-Support Interactions Accelerate Selective Dehydrogenation of Propane by Modulating the Surface Oxygen. *ACS Catal.* **2020**, *10* (18), 10559−10569.

(53) Davydov, A. Surface complexes of propylene and their role in catalytic oxidation. *J. Catal.* **1978**, *55* (3), 299−313.

(54) Wang, Y.; Li, D.; Li, K.; Farrauto, R. Enhanced propane and carbon monoxide oxidation activity by structural interactions of CeO$_2$ with MnO$_x$/Nb$_2$O$_{5-x}$ catalysts. *Appl. Catal. B: Environmental* **2020**, *267* (5), 118363.

(55) Wang, B.; Wu, X.; Ran, R.; Si, Z.; Weng, D. IR characterization of propane oxidation on Pt/CeO$_2$-ZrO$_2$: The reaction mechanism and the role of Pt. *J. Mol. Catal. A: Chemical* **2012**, *356*, 100−105.

(56) Huang, B.; Gillen, R.; Robertson, J. Study of CeO 2 and Its Native Defects by Density Functional Theory with Repulsive Potential. *J. Phys. Chem. C* **2014**, *118* (42), 24248−24256.

(57) Nitsche, D.; Hess, C. Structure of Isolated Vanadia and Titania: A Deep UV Raman, UV-Vis, and IR Spectroscopic Study. *J. Phys. Chem. C* **2016**, *120* (2), 1025−1037.

(58) Skorodumova, N. V.; Ahuja, R.; Simak, S. I.; Abrikosov, I. A.; Johansson, B.; Lundqvist, B. I. Electronic, bonding, and optical properties of CeO$_2$ and Ce$_2$O$_3$ from first principles. *Phys. Rev. B* **2001**, *64* (11), 115108.

(59) Liu, J.; Zhao, Z.; Xu, C.; Duan, A.; Jiang, G. CeO$_2$-supported vanadium oxide catalysts for soot oxidation: the roles of molecular structure and nanometer effect. *J. Rare Earths* **2010**, *28* (2), 198−204.

(60) Deeth, R. J. Electronic structures and d-d spectra of vanadium(IV) and VO^{2+} complexes: discrete variational Xα calculations. *J. Chem. Soc., Dalton Trans.* **1991**, No. 6, 1467−1477.

(61) Waleska, P.; Rupp, S.; Hess, C. Operando Multiwavelength and Time-Resolved Raman Spectroscopy: Structural Dynamics of a Supported Vanadia Catalyst at Work. *J. Phys. Chem. C* **2018**, *122* (6), 3386−3400.

(62) Rogg, S.; Hess, C. CO$_2$ as a soft oxidant for propane oxidative dehydrogenation: A mechanistic study using operando UV Raman spectroscopy. *J. CO2 Util.* **2021**, *50*, 101604.

(63) Schilling, C.; Hess, C. Real-Time Observation of the Defect Dynamics in Working Au/CeO$_2$ Catalysts by Combined Operando Raman/UV-Vis Spectroscopy. *J. Phys. Chem. C* **2018**, *122* (5), 2909−2917.

(64) Li, Y.; Wei, Z.; Gao, F.; Kovarik, L.; Baylon, R. A. L.; Peden, C. H. F.; Wang, Y. Effect of Oxygen Defects on the Catalytic Performance of VO$_x$/CeO$_2$ Catalysts for Oxidative Dehydrogenation of Methanol. *ACS Catal.* **2015**, *5* (5), 3006−3012.

(65) Hasan, M. A.; Zaki, M. I.; Pasupulety, L. IR Investigation of the Oxidation of Propane and Likely C$_3$ and C$_2$ Products over Group IVB Metal Oxide Catalysts. *J. Phys. Chem. B* **2002**, *106* (49), 12747−12756.

(66) Pokrovski, K.; Jung, K. T.; Bell, A. T. Investigation of CO and CO$_2$ Adsorption on Tetragonal and Monoclinic Zirconia. *Langmuir* **2001**, *17* (14), 4297−4303.

(67) Li, C.; Sakata, Y.; Arai, T.; Domen, K.; Maruya, K.-i.; Onishi, T. Carbon monoxide and carbon dioxide adsorption on cerium oxide studied by Fourier-transform infrared spectroscopy. Part 1.—Formation of carbonate species on dehydroxylated CeO$_2$, at room temperature. *J. Chem. Soc., Faraday Trans. 1* **1989**, *85* (4), 929.

(68) Burcham, L. J.; Deo, G.; Gao, X.; Wachs, I. E. In-Situ IR, Raman, and UV-Vis DRS Spectroscopy of Supported Vanadium Oxide Catalysts During Methanol Oxidation. *Top. Catal.* **2000**, *11*, 85−100.

(69) Sambeth, J. E.; Centeno, M. A.; Paúl, A.; Briand, L. E.; Thomas, H. J.; Odriozola, J. A. In situ DRIFTS study of the adsorption-oxidation of CH$_3$OH on V$_2$O$_5$. *J. Mol. Catal. A: Chemical* **2000**, *161* (1−2), 89−97.

(70) Badri, A.; Binet, C.; Lavalley, J.-C. An FTIR study of surface ceria hydroxy groups during a redox process with H$_2$. *Faraday Trans.* **1996**, *92* (23), 4669.

(71) Rozanska, X.; Fortrie, R.; Sauer, J. Oxidative Dehydrogenation of Propane by Monomeric Vanadium Oxide Sites on Silica Support. *J. Phys. Chem. C* **2007**, *111* (16), 6041−6050.

4.1.5 Investigation of the CO_2 Activation and Regeneration of Reduced VO_x/CeO_2 Catalysts Using Multiple In Situ Spectroscopies

The fifth publication is concerned with the understanding of the activation and regeneration processes over reduced VO_x/CeO_2 catalysts using CO_2 as the oxidizing agent. This was achieved by using multiple in situ and quasi in situ spectroscopies with differing depths of information to allow for the differentiated understanding of the surface/subsurface/bulk dynamics. The re-oxidation was investigated as the experimental basis for the understanding of the CO_2-assisted propane ODH reaction mechanism at 550 °C. The reduction and re-oxidation behavior was significantly influenced by the vanadia loading. The catalyst was reduced into the bulk under H_2 and bare CeO_2 was only partially re-oxidized in the bulk during the 16 h regeneration process. However, the subsurface and surface were quickly re-oxidized after the first 30 minutes. CO_2 was activated on the ceria lattice as carbonate, where it is able to regenerate vacancies. The desorption of CO is unlikely, however, leading to a deactivation of the ceria surface by irreversible carbonate formation, causing the surface to contain more oxygen species than under O_2 conditions. Vanadia changes this behavior significantly and slows down the regeneration. This is caused by the anchoring of vanadia to ceria surface oxygen, which is then unavailable to carbonate formation and subsequent lattice re-oxidation. However, over time, the lattice can be regenerated to a similar degree as for bare ceria. The ceria lattice can then regenerate the vanadia through oxygen spill over. This depends on the vanadia nuclearity since the full re-oxidation of monomeric vanadia by CO_2 is thermodynamically not favorable. Due to the increased thermodynamic stability of higher nuclearities, these can be fully regenerated. The regeneration behavior is therefore strongly dependent on the surface density of vanadia, i.e., its nuclearity distribution. This study enables a fundamental understanding of the re-oxidation processes during CO_2 exposure as an experimental basis for the mechanistic investigation of the CO_2-assisted propane ODH reaction.

5. Leon Schumacher, Marc Ziemba Christian Hess, Investigation of the CO_2 Activation and Regeneration of Reduced VO_x/CeO_2 Catalysts Using Multiple In-Situ Spectroscopies, Manuscript.

Investigation of the CO_2 Activation and Regeneration of Reduced VO_x/CeO_2 Catalysts Using Multiple In Situ Spectroscopies

Leon Schumacher, Marc Ziemba, Christian Hess*

Technical University of Darmstadt, Department of Chemistry, Eduard-Zintl-Institut für Anorganische und Physikalische Chemie, Peter-Grünberg-Str. 8, 64287 Darmstadt, Germany

*Corresponding Author (E-Mail: christian.hess@tu-darmstadt.de)

Abstract

Ceria-supported vanadium oxide (VO_x/CeO_2) is an important catalyst for various oxidation reactions. Recently, vanadia has emerged again as a much less toxic alternative to supported CrO_x-based catalysts for the CO_2-assisted ODH of alkanes. This is a promising process to produce basis chemicals, using undesirable greenhouse gases as the feed. However, VO_x/CeO_2 catalysts have not been studied mechanistically during such CO_2-assisted ODH reactions on a molecular level. To establish a basis of understanding, the catalyst regeneration during CO_2 exposure, which is often described as the rate-limiting step of these reactions, we investigated the regeneration of VO_x/CeO_2 catalysts with different vanadia loadings using multiple in situ spectroscopies, including multi-wavelength Raman, UV-Vis, DRIFT and X-ray photoelectron spectroscopy. Using CO_2, we find ceria is only partially regenerated in the bulk but fully regenerated in the subsurface. At the surface, stable carbonates form at vacancies, which are able to regenerate the lattice and deactivate ceria surface oxygen. The VO_x/CeO_2 samples show a loading-dependent behavior, with low-loaded samples regenerating vanadia only partially, due to the high amount of monomeric species, while at higher loadings, vanadia can be almost fully regenerated due to the higher nuclearities being thermodynamically more stable. Ceria is regenerated faster than vanadia, indicating that vanadia regenerates by oxygen spillover from the ceria lattice. Our results provide important new mechanistic insight into CO_2 activation over supported vanadia catalysts that will also be of great relevance for other reducible support materials relevant to CO_2 activation.

1. Introduction

CO_2 is an undesirable green-house gas, which is emitted in many industrial processes and significantly contributes to climate change.[1] One way to reduce emissions is to make carbon-capture more viable by finding uses for abundant CO_2 in industrial processes as a cheap feed gas to produce value-added products while reducing atmospheric CO_2 concentrations.[2,3] One such approach is to make CO_2 available as a feed gas for chemical industry,[4–6] enabling it to be used in different basis chemical processes like methanol synthesis[7] or CO_2-assisted selective alkane oxidations.[8] The usage of CO_2 instead of O_2 can even further improve processes, due to its high heat capacity, which leads to a more homogeneous temperature distribution through the reactor and decreases the flammability of some reactions, thus facilitating the scale-up.[9,10] However, the high thermodynamic stability of CO_2 requires high temperatures for its activation.[11,12] To avoid this, the activation needs to be suitably catalyzed to facilitate its adoption as an oxidizing agent.

An important class of catalysts for oxidation reactions is supported VO_x,[13,14] which is often used in oxidative dehydrogenations (ODH) of alcohols and short alkanes using O_2 as the oxidizing agent.[15,16] However, for alkanes, the CO_2-assisted reaction has been shown to be of interest for technical application, since alkane oxidation requires comparably high temperatures, while alcohols would be fully oxidized at the temperatures required.[17–21] In addition, the ODH of short alkanes shows great promise for adoption in industry to meet the high and further increasing demand for e.g. ethylene and propylene.[22] In CO_2-assisted propane ODH, CrO_x has been intensively investigated due to its very high activity.[9,23–26] However, chromium is highly toxic making its substitution with a different catalyst system highly desirable.[27] Supported vanadia has recently gained attention as a substitute since its activity and properties can be fine-tuned through the choice of the support material, influencing the vanadia structure.[28,29]

One of the most active support materials for vanadia in regard to the oxygen mobility is ceria,[30–32] which is also an established material for other reactions requiring CO_2 activation such as the reverse water-gas shift reaction (rWGSR),[33,34] the electro-reduction of CO_2[35] or methanol synthesis.[36,37] As oxygen mobility is a key factor for alkane ODH,[38–41] ceria is a promising vanadia support material for CO_2-assisted propane ODH, but has not been studied for its use in this reaction. The re-oxidation step becomes often rate-limiting in systems with less active supports (e.g. SiO_2 or

3

Al_2O_3), which may lead to insufficient re-oxidation can lead to the strong reduction of the catalyst, enabling unselective reaction pathways to occur, such as propane dry reforming (PDR) or cracking, thereby decreasing the propylene yield.[19,25,42–44] Coking can even lead to a full deactivation of the catalyst.[25,42–44] Therefore, understanding and improving the re-oxidation process is highly important in order to improve CO_2-assisted catalysis. The combination of vanadia and ceria might omit these problems, since CeO_2 is described as a good CO_2 activator,[45] while vanadia has previously been described to enhance CO_2 activation and re-oxidation while actively participating in the redox cycle during propane ODH on other supports (e.g. In_2O_3).[19,20] However, the open questions encompass re-oxidation pathways, the role of the ceria support, and the nuclearity dependence.

This study aims to elucidate the re-oxidation behavior of reduced VO_x/CeO_2 in detail, by combining multiple in situ and quasi in situ methods measured over 16 h during the regeneration of the catalyst. The methods applied include multi-wavelength Raman, UV-Vis, X-ray photoelectron and DRIFT spectroscopy, allowing for a detailed understanding of bulk, subsurface and surface processes. The use of multi-wavelength Raman spectroscopy allows for a dedicated investigation of the ceria support and the active vanadia phase by selective intensity enhancement caused by resonance effects. Our findings provide insight into the CO_2 activation pathway including the determination of the vanadia's influence, especially the nuclearity-dependent behavior of the catalysts, thus establishing an experimental basis to understand the re-oxidation process on a molecular level.

2. Experimental Section

2.1. Catalyst Preparation

The ceria support was prepared by two-fold calcination of cerium(III) nitrate hexahydrate (≥99.99%, Sigma Aldrich) staying at 600 °C for 12 h after heating using a rate of 1.5 °C/min, as previously described.[32] The ceria was loaded with vanadia by incipient wetness impregnation. Three different loadings were prepared by mixing 1 g of ceria with 0.5 mL of different-concentration precursor solutions (1.07 mol/L, 0.51 mol/L, and 0.21 mol/L) containing vanadium(V) oxytriisopropoxide (≥97%, Sigma Aldrich) and 2-propanol (99.5%, Sigma Aldrich). The samples were then heated to 600 °C at a heating rate of 1.5 °C/min and calcined for 12 h. The specific surface area of bare ceria was determined to be 61.4 m²/g by nitrogen physisorption experiments and the use of the Brunauer–Emmett–Teller (BET) method, yielding vanadium loadings of 2.83 V/nm² (2.32 wt% V_2O_5), 1.36 V/nm² (1.11 wt% V_2O_5), and 0.57 V/nm² (0.47 wt% V_2O_5), respectively. Higher vanadium loadings were not considered since vanadia crystallites were shown to be present at loadings >2.9 V/nm².[46] The resulting catalyst powders were subsequently pressed at a pressure of 2000 kg/m² for 20 s, ground and then sieved using a combination of sieves to obtain 200–300 µm particles.

2.2. Gas Treatment

The samples were first dehydrated in 12.5% O_2/He at 365 °C for 1h. For in situ experiments (UV-Raman, Vis-Raman, UV-Vis), the samples were then heated to 550 °C under the same gas feed (oxidative conditions) and after 30 minutes of equilibration a spectrum was recorded. Consecutive treatments consisted of 7.5% H_2/Ar (reductive conditions) and 12.5% CO_2/He (regenerative conditions) at 550 °C. A spectrum was recorded after 30 minutes of equilibration in H_2, while under CO_2, spectra were recorded after 30, 60, 90, 120, 150, and 960 minutes to follow the regeneration process. For the quasi in situ measurements (XPS, DRIFTS), the same procedure was applied but the samples were cooled down to room temperature in pure helium before spectra were recorded and the regeneration process was only followed for the first 30 minutes. The total flow rate during all measurements was 40 ml/min.

2.3. UV-Raman Spectroscopy

UV-Raman spectroscopy was performed at an excitation wavelength of 385 nm generated by a laser system based on a Ti:Sa solid state laser pumped by a frequency-doubled Nd:YAG laser (Coherent, Indigo). The fundamental wavelength was frequency doubled to 385 nm using a LiB_3O_5 crystal. The light was focused onto the sample, and the scattered light was collected by a confocal mirror setup and focused into a triple-stage spectrometer (Princeton Instruments, TriVista 555).[46] Finally, the Raman contribution was detected by a charge-coupled device (CCD, 2048 × 512 pixels) cooled to −120 °C. The spectral resolution of the spectrometer was 1 cm^{-1}. For Raman experiments, 70 mg of catalyst was placed in a CCR 1000 reactor (Linkam Scientific Instruments) equipped with a CaF_2 window (Korth Kristalle GmbH). A fluidized bed reactor was employed to avoid laser-induced damage, allowing the use of a laser power of 9 mW at the location of the sample. Data processing included cosmic ray removal and background subtraction. The spectra were further analyzed by a least-squares fitting analysis using four Lorentzian functions (see Figure S5).

2.4. Vis-Raman Spectroscopy

Visible (Vis) Raman spectroscopy was performed at 514 nm excitation, emitted from an argon ion gas laser (Melles Griot). The light was focused onto the sample, gathered by an optical fiber and dispersed by a transmission spectrometer (Kaiser Optical, HL5R). The dispersed Raman radiation was subsequently detected by an electronically cooled CCD detector (−40 °C, 1024 × 256 pixels). The spectral resolution was 5 cm^{-1} with a wavelength stability of better than 0.5 cm^{-1}. For Raman experiments, 70 mg of catalyst was filled into a CCR 1000 reactor (Linkam Scientific Instruments) equipped with a quartz window (Linkam Scientific Instruments). The laser power at the sample location was 4 mW. Data analysis of the Raman spectra included a cosmic ray removal and an auto new dark correction. The vanadyl areas were quantified by integration using OriginLab, while the nuclearity distribution was determined by performing a least-square fitting analysis using five Lorentzian functions at distinct spectral positions. The F_{2g} mode was fitted without any positional restrictions due to the possible occurrence of red-shifts.

2.5. Diffuse Reflectance UV-Vis Spectroscopy

Diffuse reflectance (DR) UV-Vis spectra were recorded on a Jasco V-770 UV-Vis spectrometer. Dehydrated $BaSO_4$ was used as the white standard. For each experiment, 90 mg of catalyst was put in the commercially available reaction cell (Praying Mantis High Temperature Reaction Chamber, Harrick Scientific) equipped with transparent quartz glass windows. The band gap energies were determined using Tauc plots, while the reduction peak area was quantified by a least square fitting analysis of the spectra using Gaussian-Lorentzian (70/30) product functions. Product functions were used to account for the large contribution of natural line broadening to the overall line-shape, caused by the short life-time of the electronically excited states (Lorentzian), while also accounting for the generally better convergence of the fit (Gaussian).[47]

2.6. X-Ray Photoelectron Spectroscopy

XP spectra were recorded on a modified LHS/SPECS EA200 MCD system described previously.[48–50] The XPS system was equipped with a Mg Kα source (1253.6 eV, 168 W); the calibration of the binding energy scale was performed with Au $4f_{7/2} = 84.0$ eV and Cu $2p_{3/2} = 932.67$ eV signals from foil samples. To account for sample charging, the C 1s peak of ubiquitous carbon at 284.4 eV was used to correct the binding-energy shifts in the spectra. Detailed spectra were recorded at a resolution of 0.1 eV. The X-ray satellite peaks due to the use of a non-monochromatic source were subtracted from the spectra. The deconvolutions of the spectra were performed analogously for all measurements using Gauss–Lorentzian product functions (30/70). The background was subtracted by the Shirley method.

For determination of surface compositions, peak areas were corrected with the corresponding relative sensitivity factors, i.e., 10 for the Ce 3d, 0.66 for the O 1s and 1.3 for the V $2p_{3/2}$ signal.[51]

2.7. Diffuse Reflectance Infrared Fourier Transform Spectroscopy

DRIFT spectra were recorded on a Vertex 70 spectrometer (Bruker), equipped with a liquid nitrogen–cooled mercury cadmium telluride (MCT) detector, operating at a

resolution of 1 cm^{-1}. Dehydrated potassium bromide was used as an infrared transparent sample for the background spectrum. For each experiment, 90 mg of the catalyst was placed in the reaction cell (Praying Mantis High Temperature Reaction Chamber, Harrick Scientific) equipped with transparent KBr windows.

Data processing consisted of background removal by subtraction of a baseline formed by 12 anchor points.

3. Results and Discussion

Extensive structural characterization of the samples used for this study was already performed in previous studies and is not given at this point apart from brief assignments of the respective peaks.[41,52,53]

Figure 1 shows the in situ UV-Vis spectra of bare ceria and the 1.36 V/nm² sample at 550 °C under oxidative, reductive, and after different times of CO_2 exposure. The band gap energy shifts as well as the reduction peak area (between 500 and 800 nm) were quantified (see experimental section) for all four samples and are given in Figures 1c and d, respectively. The in situ UV-Vis spectra for the 0.57 and 2.83 V/nm² sample are given in the SI (see Figure S1). For clarity, the spectra recorded in 12.5% CO_2/He after 90 and 150 minutes are not shown.
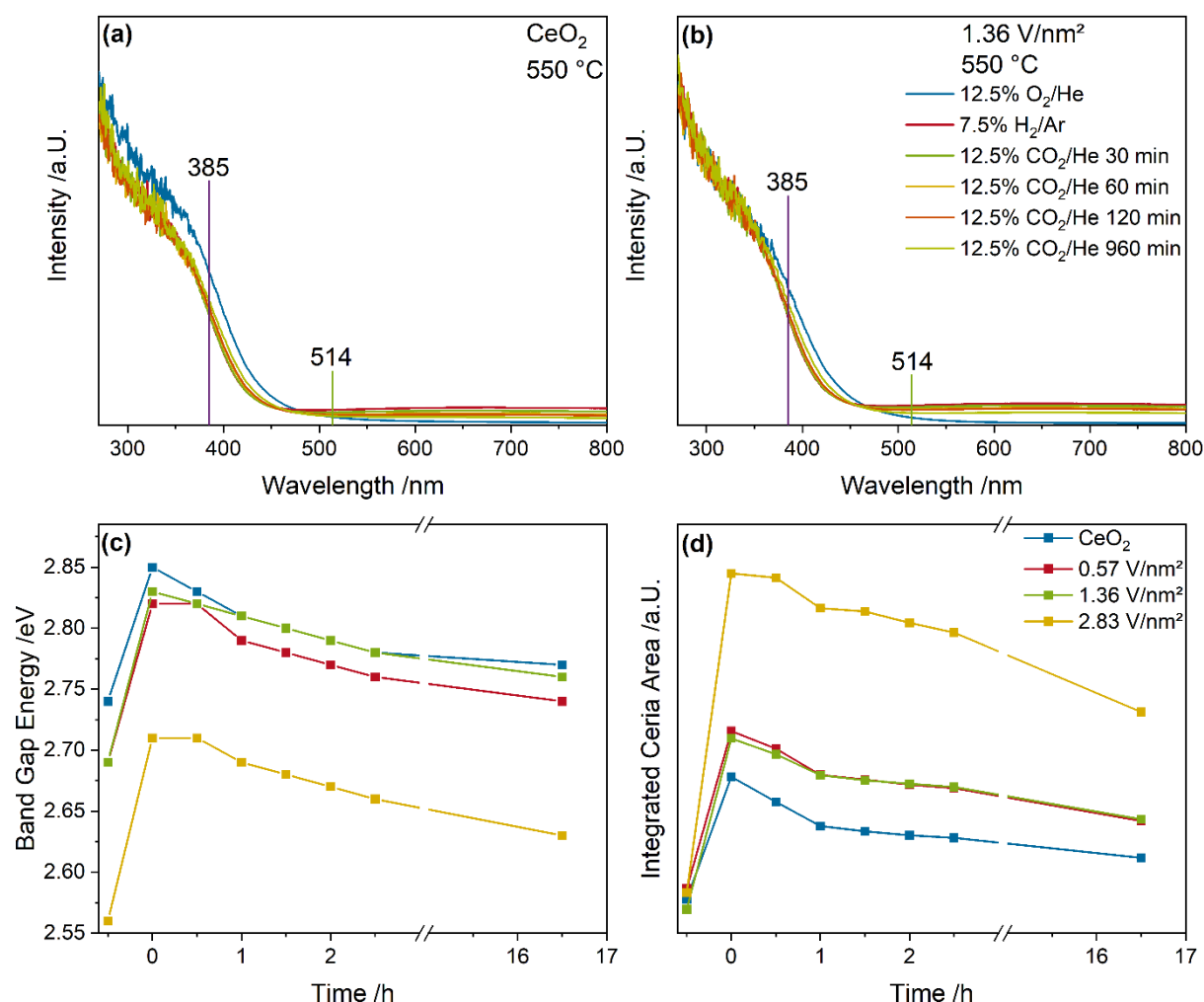
Figure 1: In situ UV-Vis spectra of **(a)** bare CeO_2 and **(b)** the 1.36 V/nm² sample recorded under different gas feeds at 550 °C. The used Raman excitations are indicated. The **(c)** band gap energy shifts and **(d)** the reduction peak area were determined using Tauc plots and a least-square fit analysis (see experimental section), respectively.

Figure 1a shows the UV-Vis spectra of bare ceria. The UV-region is dominated by features at 260 and 330 nm caused by band gap absorption from ceria (O 2p to Ce 4f transitions).[54,55] The two wavelengths at which Raman spectroscopy was performed are indicated, allowing for selective resonance enhancement of ceria (385 nm) and vanadia (514 nm).[41,56] Upon switching from oxidative to reductive conditions, an additional broad band is observed around 633 nm, which originates from a charge transfer from Ce^{3+} to Ce^{4+} indicative of ceria reduction.[57,58] Additionally, during this switch, the band gap energy shows a significant blue-shift. This is notable since a reduction typically induces a red-shift caused by the presence of additional reduced states being created in the band gap.[59] However, in addition to the shift, the band around 633 nm, which is indicative of reduced states, increases significantly. Such a behavior was previously observed to blue-shift the apparent band gap determined from Tauc plots due to the additional absorption,[41] and is confirmed under regenerative conditions, where the 633 nm declines and the band gap gradually red-shifts over time (both indicating re-oxidation).

The UV-Vis spectra of the 1.36 V/nm^2 sample show similar transitions as those of bare ceria (see Figure 1b), indicating that the spectrum is dominated by bulk ceria contributions. These overlap with ligand-to-metal-charge transfer (LMCT) transitions of short-chain vanadia species.[60] Under reductive conditions a very broad additional band around 775 nm, caused by d-d transitions of reduced vanadia states, can overlap with the broad reduction band around 633 nm.[61] This leads to an increase in the absorption within 500-800 nm. To better understand the changes in the band gap energy and reduction peak intensity, both changes were quantified using Tauc plots[32] and a least-square fitting procedure (compare experimental section), respectively (see Figures 1c and d).

The time axis is shifted so that the regeneration starts at 0 minutes. The band gap energies for all samples show a similar trend, where first, a significant blue-shift significantly under reductive conditions and then a gradual red-shift during CO_2 exposure is observed. A comparison of band gap energies reveals that bare ceria is characterized by the highest band gap but the lowest shift upon switching from oxidative to reductive conditions, whereas the observed shift increases with increasing vanadium loading. The regeneration of the sample only occurs partially, as the band gap is still shifted after 16 hours of regeneration in CO_2 compared to oxidative

conditions. Bare ceria is closest to a fully regenerated state, while the vanadia-loaded samples are more reduced.

Figure 1d shows the reduction peak intensity for bare ceria and vanadia-loaded samples. The behavior of the reduction peak intensity is inverted to that of the band gap, further indicating that the band gap energy behavior is caused by the significant intensity of the reduction peak, in agreement with our previous results.[41] The reduction peak shows a strong increase under reductive conditions for all samples. Ceria has the smallest increase, while vanadia-loaded samples show a more significant intensity increase. This is caused by the fact that ceria shows only $Ce^{3+} \rightarrow Ce^{4+}$ transitions, while vanadia is also subject to d-d transitions. Under regenerative conditions, the reduction peak intensity of bare ceria significantly decreases significantly throughout the first hour and then slows down, leaving the ceria partially reduced after 16 h. This indicates that Ce^{3+} states are still present in the ceria bulk. The 0.57 V/nm² sample shows a similar behavior as bare ceria, the 1.36 V/nm² sample exhibits a more constant regeneration rate with a slower initial regeneration. The 2.83 V/nm² sample shows the most significant deviation from this behavior. For the first 30 minutes, a plateau in the reduction peak intensity is observed, which then decreases faster than for the other samples. After 16 h, bare ceria shows the lowest reduction peak intensity (see Figure 1), while the other samples show increasing intensity with increasing vanadia loading. However, the difference between the 0.57 and 1.36 V/nm² samples after 16 h is very small. This indicates that vanadia is still significantly reduced or that ceria is more reduced due to a slowed bulk regeneration caused by the presence of vanadia.

To further understand the subsurface/bulk re-oxidation of the samples and to better separate between ceria and vanadia contributions, Vis-Raman spectroscopy (514 nm excitation) was performed under the same conditions. Figure 2 shows the in situ Vis-Raman spectra of bare ceria and ceria loaded with vanadia at a loading density of 1.36 V/nm² under oxidative, reductive, and regenerative conditions at 550 °C. The changes observed in the F_{2g} position and the vanadyl area were quantified for all four samples and are given in Figures 2c and d, respectively. The in situ Vis-Raman spectra for the 0.57 and 2.83 V/nm² sample are given in the SI (see Figure S2). For clarity, the spectra recorded in 12.5% CO_2/He after 150 minutes are not shown.
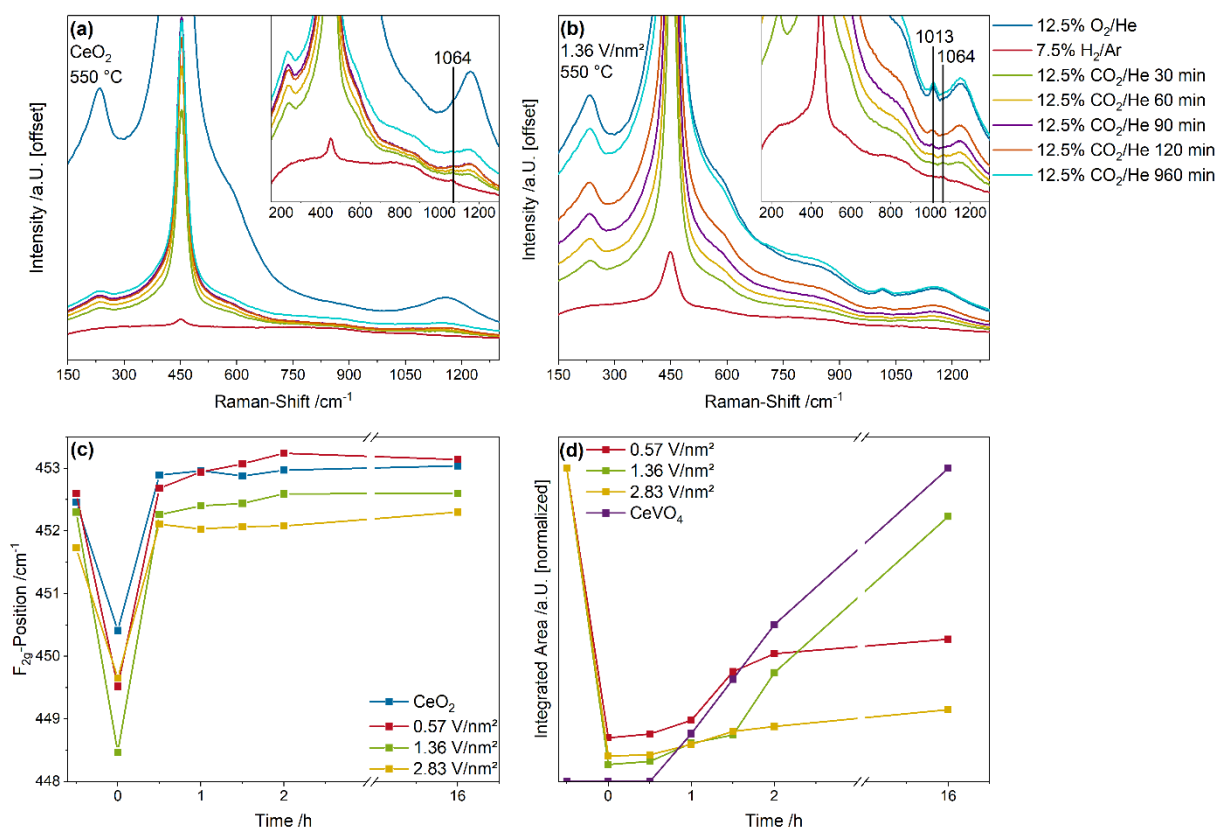
Figure 2: In situ Vis-Raman (514 nm excitation) spectra of **(a)** bare ceria and **(b)** the 1.36 V/nm² sample recorded under different gas feeds at 550 °C. The insets show an enlarged view of the region between 200 and 1300 cm^{-1}. **(c)** The F_{2g} shift and **(d)** the regeneration of the vanadyl peak over time were quantified. CeVO$_4$ was only detected for the 2.83 V/nm² sample (see Figure S2).

As can be seen in Figure 2a the intensity of the spectra decreases significantly under reductive conditions. The spectrum under oxidative conditions shows peaks at 245, 405, 455, 590, and 1170 cm^{-1}, which originate from the 2TA phonon, the transversal Ce-O surface phonon, the F_{2g} mode, the defect region (contributions from Ce^{3+} and oxygen vacancies), and the 2LO phonon, respectively.[32,62,63] Relevant spectral changes under reductive conditions (besides the general decrease in intensity) include the shift of the F_{2g} peak as an indicator for ceria reduction as well as the occurrence of a peak at 1064 cm^{-1}, which would be consistent with Ce-H bonds of bulk hydrides, indicating significant bulk reduction.[64] This reduction is still prominent after 16 h of regeneration with CO$_2$. The peak would also be consistent with carbonate signals but it already appears in the 7.5% H$_2$/Ar gas phase, where no CO$_2$ is present, which makes this very unlikely.

Figure 2b shows the Vis-Raman spectra of the 1.36 V/nm² sample at 550 °C. The spectra are dominated by ceria contributions but additional peaks due to the

presence of vanadia are located at 860, 920, and within the vanadyl region, the position of which varies depending on the loading (1008-1020 cm^{-1}). These signals are assigned to anchoring V-O-Ce, bridging V-O-V and terminal V=O bonds.[65] In addition, two peaks at 780 and 851 cm^{-1} are detected for the 2.83 V/nm² sample (see Figure S2b), which are indicative of the formation of $CeVO_4$.[65,66] Due to the resonance enhancement of vanadia at 514 nm excitation (see Figure 1), a fine structure of the vanadyl peak can be observed, which will be discussed separately below (see Figure 3).[67] The F_{2g} and Ce-H peaks show a similar behaviour on the vanadia-loaded sample as on bare ceria. The vanadyl peak fully disappears under reducing conditions and gradually increases in intensity under regenerative conditions.

Both the F_{2g} red-shift and the vanadyl intensity were quantified and the results are shown in Figures 2c and d, respectively. The red-shift of the F_{2g} peak is caused by the introduction of Ce^{3+} ions into the lattice upon reduction. These distort the lattice due to their larger diameter compared to Ce^{4+} ions.[54] Therefore, under reductive conditions, the F_{2g} mode of all four samples shows a significant red-shift. Ceria exhibits the smallest shift of ~2 cm^{-1}, while the red-shift increases with increasing vanadia loading up to 4 cm^{-1} for the 1.36 V/nm² sample, but then decreases again for the 2.83 V/nm² sample (2 cm^{-1}). The F_{2g} peak blue-shifts strongly for all samples during the first 30 minutes of regeneration, and subsequently stays almost constant for the following 16 h. Overall, ceria seems to be fully re-oxidized in the subsurface when regenerated with CO_2, while appearing even more oxidized than under O_2 atmosphere. A similar behavior is observed for the 2.83 V/nm² sample. In comparison, the F_{2g} positions of the 0.57 and 1.36 V/nm² samples also recover significantly during the initial 30 minutes but then show a further continuous shift for 2 h, until reaching a constant value that is blue-shifted compared to the initial position. These differences in behaviour between the vanadia samples might be caused by different vanadia nuclearities on the surface, which have previously been shown to have very different functionalities.[41,53,65,67–69] A comparison of Figures 1 and 2 reveals that there are differences between the UV-Vis and Vis-Raman results regarding the reduction peak area while the fact that the F_{2g} peak is back at its initial position after 16 h is likely caused by the increased absorption at 514 nm of a partially reduced catalyst (see Figure 1), which decreases the depth of information obtained by Vis-Raman spectroscopy as compared to UV-Vis spectroscopy.

Figure 2d shows the determined areas of the vanadyl peak and $CeVO_4$, which was only observed for the 2.83 V/nm² loading. Since the formation of $CeVO_4$ is favoured at high loadings, high temperatures, and under reducing conditions, this is expected.[52,65,66] The vanadyl peak almost fully disappears for all vanadia-loaded samples under reducing conditions. The V=O peaks of the 0.57 and 1.36 V/nm² samples barely regenerate for the first two hours, while at the same time, ceria is strongly re-oxidized, indicating that the regeneration of the ceria bulk is favourable. Afterwards, the V=O peaks regenerate gradually, but even after 16 h, after which vanadia is still partially reduced. This is more pronounced for the 0.57 V/nm² sample, while the vanadyl intensity almost regenerates back to its initial intensity for the 1.36 V/nm² sample. This difference might be caused by the different surface compositions of the catalysts and is explored in more detail below (see Figures 3-5). For the 2.83 V/nm² sample, the vanadyl peak regenerates slowly. After 16 h, only 22 % of the initial vanadyl area is regenerated. Additionally, a prominent $CeVO_4$ peak is observed, indicating the predominant formation of $CeVO_4$ during the regeneration process. The results for the vanadia-loaded samples are in good agreement with the UV-Vis results, as the reduction peak (see Figure 1d) was observed to be more intense for vanadia-loaded samples than for bare ceria after 16 h. Vis-Raman spectroscopy indicates that this difference originates to a significant degree from the presence of partially reduced vanadia. The slow regeneration with the significant decrease in reduction peak intensity observed during UV-Vis spectroscopy of the 2.83 V/nm² sample is likely caused by the delayed formation of $CeVO_4$, re-oxidizing the vanadia.

The vanadyl fine structure is used to quantify the nuclearity distribution of the vanadia species on the ceria surface. Figure 3a depicts the vanadyl region from Vis-Raman spectra at 514 nm excitation between 990 and 1050 cm^{-1} at 550 °C under 12.5% O_2/He conditions compared to bare ceria whereas Figure 3b shows the nuclearity distribution as a function of vanadium loading as a result of a peak-fitting analysis (see experimental section).
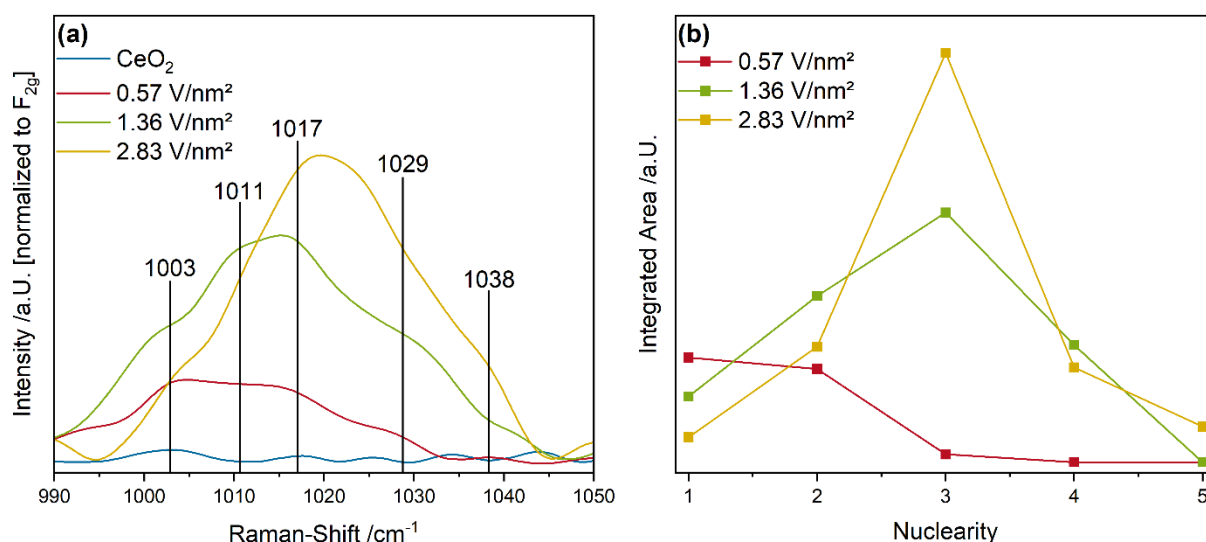
Figure 3: (a) Vanadyl fine structure between 990 and 1050 cm^{-1} of vanadia-loaded samples recorded under 12.5% O_2/He at 550 °C using 514 nm excitation. The positions of the individual nuclearities are marked. **(b)** Nuclearity distribution of the vanadia-loaded samples based on a peak-fit analysis.

The marked positions in Figure 3a represent different nuclearities, whereby the exact positions may vary by ~1 cm^{-1} as they depend on the exact structural environment. The fine structure is caused by dipole-dipole interactions between V=O groups, blue-shifting the V=O vibration for larger vanadia structures, allowing for the assignment of different chain lengths.[41,53,67] In the vanadyl fine structures displayed in Figure 3, peaks are observed at 1003, 1011, 1017, 1029, and 1038 cm^{-1}, which originate from the V=O stretching vibration of monomeric, dimeric, trimeric, tetrameric and oligomeric vanadia, respectively. For this work, it is assumed that the nuclearity distribution may only be varied by sintering, for which there is no evidence.[70] So far, there have been no indications that the nuclearity distribution changes as a function of the gas phase. The vanadyl signal of the 0.57 V/nm² sample is dominated by signals below 1035 cm^{-1}, indicating the presence of monomers/dimers (see below). With increasing loading the vanadyl signal shows a blue-shift, indicating a higher degree of oligomerization.

Figure 3b quantifies the intensity of the signals corresponding to the different nuclearities based on a peak-fitting analysis. For the 0.57 V/nm² sample, the fine structure is dominated by monomeric and dimeric contributions, while the 1.36 and especially the 2.83 V/nm² samples display a sharp focus around trimeric species, which are (except for hexameric rings) the most stable nuclearity.[68,69] The amount of

monomeric vanadia species decreases with increasing vanadia loading while oligomeric species (nuclearities ≥ 4) are most abundant on the 2.83 V/nm² sample. These differences in the nuclearity have been shown to result in a different reactivity behavior. For example, dimers and oligomers facilitate the hydrogen transfer and therefore catalyst reduction, while monomers can interact with surface oxygen vacancies.[53] Furthermore, ceria surface lattice oxygen in proximity to vanadia structures is more easily reduced than surface lattice oxygen of bare ceria. However, this effect depends on the nuclearity and is most pronounced for dimers and least for trimers due to their high stability.[68,69] This explains the increased reduction of the 0.57 and 1.36 V/nm² samples (see Figure 2c) and the decreased reduction of the 2.83 V/nm² sample due to the abundant amount of stable trimers. Furthermore, the re-oxidation of reduced vanadia species may also depend on the nuclearity. Monomeric species were previously shown to interact with surface oxygen vacancies in their proximity.[41,65,68] However, at elevated temperatures, they may be able to restructure out of the vacancies, although the regeneration may still be impeded. A fully/partially reduced monomeric vanadia species was shown not to be fully regenerated by ceria lattice oxygen or gas-phase CO_2 as its regeneration is thermodynamically unfavourable.[71] However, since a fully oxidized dimer or trimer is thermodynamically significantly more stable than a monomer, a full re-oxidation of these species might occur. This is evidenced by the regeneration of the vanadyl intensity (see Figure 2d), where the 0.57 V/nm² sample becomes only partially re-oxidized after 16 h and the 1.36 V/nm² sample is almost fully regenerated due to the presence of higher nuclearities. The 2.83 V/nm² sample cannot be directly compared to these samples due to the additional transformation of VO_x to $CeVO_4$.

To further investigate the nuclearity-dependent regeneration behavior, quasi in situ XP spectroscopy was applied to determine the vanadium oxidation state in the 0.57 and 1.36 V/nm² samples. Figure 4 shows the detailed spectra of the V $2p_{3/2}$ and O 1s regions of the 0.57 and 1.36 V/nm² samples after exposure to 30 min of oxidative and regenerative conditions and subsequent transfer to the analysis chamber. The detailed spectra of the V $2p_{3/2}$ photoemission were fitted using three components (see experimental section), and the resulting distribution of vanadium oxidation states as well as the average oxidation state is summarized in Table 3.
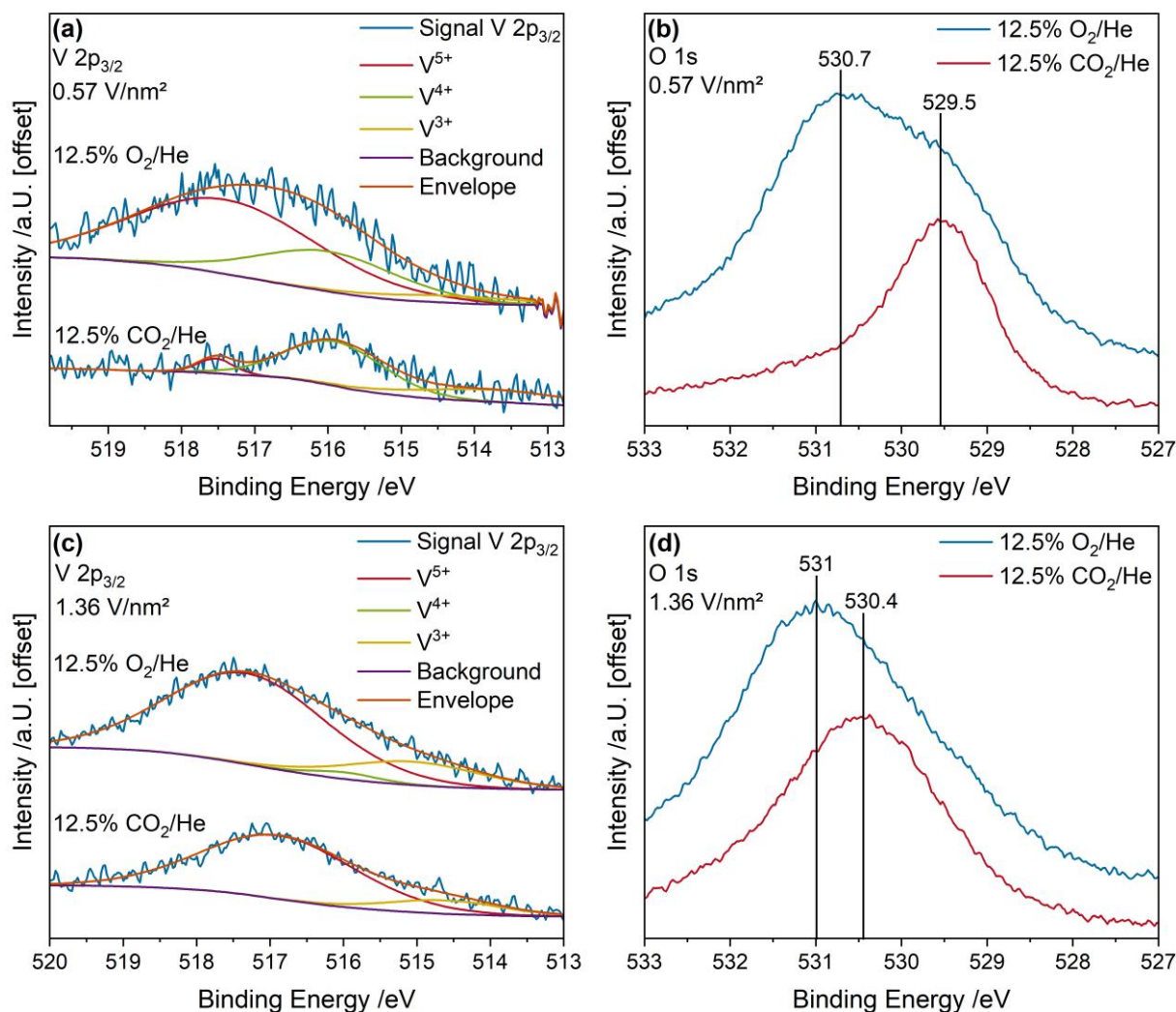
Figure 4: Quasi in situ XP spectra of the V $2p_{3/2}$ photoemission regions of the **(a)** 0.57 V/nm² and **(c)** 1.36 V/nm² samples after the pre-treatment in oxidative (12.5% O_2/He), reductive (7.5% H_2/Ar), and regenerative (12.5% CO_2/He) conditions at 550 °C, subsequent cooling to room temperature in He, and inert transfer into the XPS analysis chamber. The spectra shown were recorded after oxidizing and regenerative conditions. The results of the fitting analysis of the vanadium signal using three components were added in **(a)** and **(c)**. The O1s regions of the **(b)** 0.57 V/nm² and **(d)** 1.36 V/nm² samples after the same pre-treatment are shown and the respective maxima of the peaks are marked.

Table 1: Distribution of oxidation states of the 0.57 and 1.36 V/nm² samples after exposure to oxidative (12.5% O_2/He) and regenerative (after reduction in 7.5% H_2/Ar; 12.5% CO_2/He) conditions based on a fitting analysis of the V $2p_{3/2}$ region (see Figure 4).

Sample	V^{5+}	V^{4+}	V^{3+}	Average
0.57 V/nm² O_2	0.68	0.27	0.05	4.63
0.57 V/nm² CO_2	0.08	0.64	0.28	3.80
1.36 V/nm² O_2	0.72	0.18	0.10	4.62
1.36 V/nm² CO_2	0.86	0.00	0.14	4.72

Under oxidative conditions, the two samples show a very similar behavior and a higher oxidation state than under the same gas feed at 275 °C, as shown previously.[52] This is likely caused by the significantly higher temperature, allowing for a higher degree of oxidation of the surface vanadia. After reduction and subsequent re-oxidation of the samples, the V $2p_{3/2}$ photoemission regions of the two samples show significant differences. This is in agreement with the previous proposition of a nuclearity-dependent re-oxidation behavior. For the following discussion, the amount of V^{5+} species during reductive conditions is assumed to be 0 since V^{5+} species could not be observed in Vis-Raman spectra. For the 0.57 V/nm² sample, only a small amount of V^{5+} species is regenerated, while most species are present in the partially oxidized V^{4+} state, but V^{3+} species are also observed. This behavior is in very good agreement with previous DFT results on the regeneration of monomeric VO_x on CeO_2 using CO_2 where a re-oxidation from fully reduced to partially reduced is favoured over full re-oxidation,[71] which is emphasized by the fact that the average oxidation state after the regeneration is significantly reduced to 3.8, which is consistent with the preferential re-oxidation of higher nuclearities. To this end, the 1.36 V/nm² sample shows full regeneration after 16 h of re-oxidation, showing an average oxidation state that is constant after oxidative and regenerative gas treatments. Previously observed V^{4+} has possibly experienced disproportionation towards V^{3+} and V^{5+}, explaining the shifts in the relative contributions of each oxidation state (see Table 1). This further supports the presence of different re-oxidation pathways based on vanadia nuclearity.[68,71]

Figures 4b and d show the corresponding O 1s photoemission regions of the 0.57 and 1.36 V/nm² samples. The initial position of the maximum of the O 1s region

at ~531 eV is in agreement with ceria bulk oxygen, whereas contributions from VO_x might be overlapping this peak slightly.[72,73] After reduction and re-oxidation, the O 1s peak of the 0.57 V/nm² sample shows a significant red-shift by 1.2 eV to 529.5 eV, which was previously associated with the formation of defects interacting with lattice oxygen.[72–75] However, recent DFT calculations have shown the red-shift to originate from the formation of adsorbates, mainly Ce-OH and carbonates, rather than the introduction of Ce^{3+}.[76] This effect is also observable for the 1.36 V/nm² sample but to a lesser extent, indicating that adsorbates might form during the regeneration process.

To gain further insight into the nature of the adsorbates, the O/Ce ratio was determined based on a least-square fitting analysis of the Ce 3d and the O 1s photoemissions. From Table 2, it can be seen that the amount of carbon on the surface increases significantly for both samples between the initial oxidizing and the regenerative conditions, as does the O/Ce ratio. Both findings are indicative of carbonate formation.

Table 2: Elemental composition of the 0.57 and 1.36 V/nm² samples after exposure to oxidative (12.5% O_2/He) and regenerative (after reduction in 7.5% H_2/Ar; 12.5% CO_2/He) conditions based on XPS analysis.

Sample	Ce 3d	O 1s	V 2p$_{3/2}$	C 1s	O/Ce
0.57 V/nm² O_2	0.30	0.58	0.04	0.08	1.91
0.57 V/nm² CO_2	0.11	0.36	0.01	0.52	3.48
1.36 V/nm² O_2	0.25	0.61	0.04	0.10	2.54
1.36 V/nm² CO_2	0.16	0.49	0.04	0.31	3.11

To identify the kind and quantity of adsorbates present on the catalyst surface during regeneration DRIFT spectra were recorded. Figure 5 shows the quasi in situ DRIFT spectra of bare ceria and ceria loaded with 1.36 V/nm² after exposure to 30 min of oxidative, reductive, and regenerative conditions at 550 °C. The changes observed in the carbonate region between 1200 and 1800 cm^{-1} were quantified for all four samples and are given in Figure 5c. The quasi in situ DRIFT spectra for the 0.57 and 2.83 V/nm² samples are given in the SI (see Figure S3).
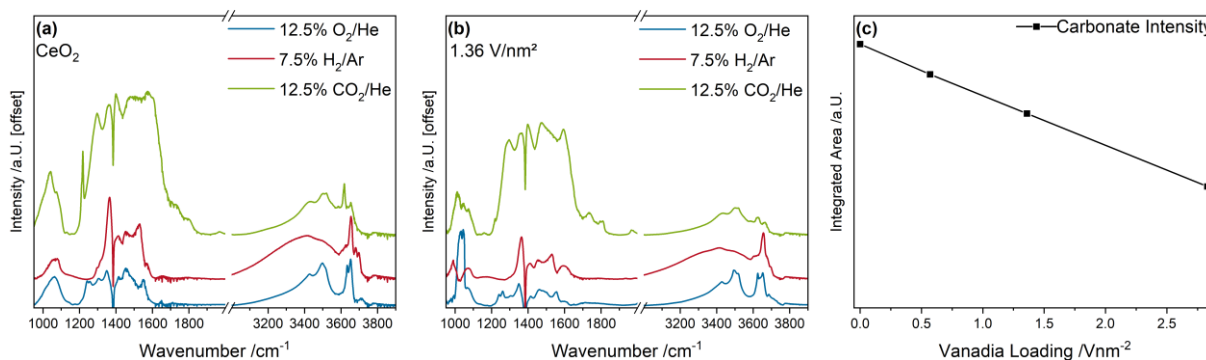
Figure 5: Quasi in situ DRIFT spectra of **(a)** bare ceria and **(b)** the 1.36 V/nm² sample recorded after exposure to the indicated gas feeds at 550 °C and subsequent cooling to room temperature in He. **(c)** The carbonate area between 1200 and 1800 cm^{-1} was quantified, based on the data recorded after oxidative conditions (12.5% CO_2/He).

Figure 5a shows the quasi in situ DRIFT spectra of bare ceria. Between oxidative and regenerative conditions, a significant increase of the intensity in the region between 1200 and 1800 cm^{-1} can be observed, where signals of carbon-based adsorbates such as carbonates and formates occur.[77–80] In addition, formates are observed, which is confirmed by the appearance of a pronounced peak at ~2880 cm^{-1} under CO_2 exposure. This increase is accompanied by a decrease of the Ce-OH signals between 3600 and 3700 cm^{-1}, which are likely consumed as water during the reduction and re-oxidized as carbonates.[32] An increase in carbonates/formates is consistent with the XPS results discussed above and likely causes a partial deactivation of the ceria surface due to the high desorption barrier of CO after the lattice is regenerated.[71] For the 1.36 V/nm² sample (see Figure 5b), similar changes can be observed between the oxidative and regenerative gas phase. However, the intensity increase in the carbonate region is not as pronounced, which likely originates from vanadia anchored to some of the surface lattice oxygen.[41,65] The carbonates are more likely to regenerate the ceria lattice first, before vanadia is regenerated by ceria due to oxygen spill-over.[71] This is in agreement with previous DFT studies, where ceria is the oxygen buffer that keeps vanadia oxidized to V^{5+}.[41,65,66,68] Direct oxidation of VO_x by CO_2 may proceed to a partially oxidized state for monomers and a fully oxidized state for higher nuclearities, as discussed above.[68,69,71] However, based on the time delay between ceria and vanadia regeneration, oxygen spill over seems to be the dominant path of regeneration, consistent with ceria keeping vanadia in oxidation state +V.

Figure 5c shows the amount of carbonates present on the surface for bare ceria and vanadia-loaded samples. A linear decrease in the carbonate area with increasing vanadia loading is observed, indicating that the anchoring of vanadia blocks surface lattice oxygen. Since ceria lattice oxygen is regenerated by CO_2 via carbonates[22,45,71] and the lattice subsequently re-oxidizes the VO_x, the time delay between ceria and vanadia re-oxidation can be readily explained (see Figures 1 and 2). The lower amount of possible carbonate formation sites with higher vanadia loading also explains the differences in the F_{2g} blue-shift between bare ceria and the 0.57 and 1.36 V/nm² samples. There, ceria fully regenerates in the first 30 minutes, while the other two samples regenerate only partially over the first 30 minutes and then continue to do so for 2h in total (see Figure 2c). The 2.83 V/nm² sample is not fully comparable due to the formation of $CeVO_4$, which likely follows a different regeneration mechanism. However, the F_{2g} peak is still blue-shifted after regeneration compared to the initial oxidative conditions, indicating that the samples are more oxidized after reduction in H_2 and regeneration in CO_2 than under O_2/He. In addition, the samples exhibit a partially reduced bulk after 16 h of regeneration (see Figure 1d).

To investigate this phenomenon in more detail, UV-Raman spectra were recorded. Due to the high absorption of ceria at 385 nm, UV-Raman spectroscopy is selective to the ceria support, due to resonance effects at this wavelength, enabling the detailed investigation of the surface/subsurface region. Figure 6 shows the in situ UV-Raman spectra of bare ceria and ceria loaded with 1.36 V/nm² under oxidative, reductive, and regenerative conditions after different exposure times at 550 °C. The changes observed in the spectra were quantified for all four samples and are given in Figures 4c and d, respectively. The in situ UV-Raman spectra for the 0.57 and 2.83 V/nm² samples are given in the SI (see Figure S4). For clarity, the spectra recorded in 12.5% CO_2/He after 150 minutes are not shown.
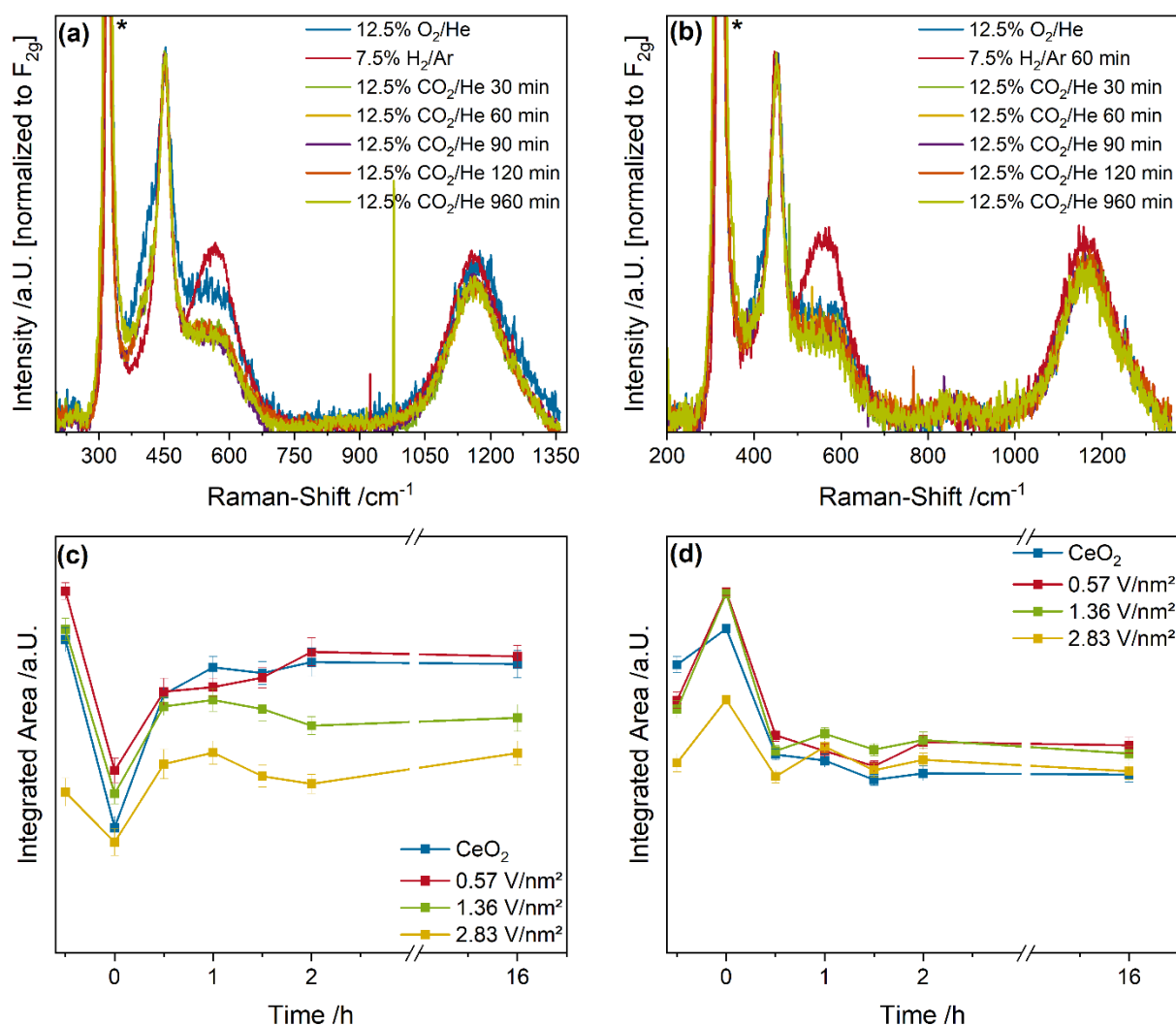
Figure 6: In situ UV-Raman (385 nm excitation) spectra of **(a)** bare ceria and **(b)** the 1.36 V/nm² sample recorded under different gas feeds at 550 °C. The areas of **(c)** the transversal Ce-O surface phonon **(d)** the defect area were quantified using a fitting procedure (see experimental section and Figure S4 for details). For the quantification, the sum of both defect peaks was used.

Figure 6a shows the in situ UV-Raman spectra of bare ceria. The observed peaks are the same as those observed in the Vis-Raman spectra (see Figure 2). However, due to the increased surface sensitivity and the resonance enhancement, the transversal Ce-O surface phonon and the defect region of the ceria are detected with significantly higher sensitivity,[41,62] allowing the surface oxygen dynamics to be discussed in more detail. The Ce-O surface phonon almost fully disappears upon switching from oxidative to reductive conditions and then gradually reappears during regeneration. In comparison, the intensity of the defect region first increases significantly during reductive conditions, as expected, and then decreases below its

initial intensity during regenerative conditions. This is likely caused by CO_2-induced carbonate formation oxidizing previously existing as well as newly formed defects, thereby regenerating the surface to a higher degree than would be possible under O_2. The changes discussed for bare ceria are also observable for the vanadia-loaded samples (see Figures 6b and S4).

To quantify the changes observed in the UV-Raman spectra, a fitting analysis was performed (see experimental section). An exemplary fit for the 0.57 V/nm^2 sample under oxidizing, reductive, and regenerative conditions is shown in the SI (see Figure S5). The quantification results are summarized in Figures 6c and d for the topmost ceria surface lattice oxygen layer and the defect region, respectively. The Ce-O surface phonon intensity first decreases for all samples under reductive conditions and then regenerates partially during the regenerative conditions, indicating that less Ce-O surface oxygen is present in the topmost ceria layer after regeneration. The initial reduction and regeneration is most significant for bare ceria and the 0.57 V/nm^2 sample and to a lower extent for the 1.36 and 2.83 V/nm^2 samples, as a number of surface Ce-O-Ce sites are consumed when anchoring the vanadia to the support during impregnation, thereby decreasing the maximum number of reducible Ce-O sites.

The quantification of the defect region shows an intensity increase for all samples under reductive conditions (see Figure 6d), which is most pronounced for the 0.57 and 1.36 V/nm^2 samples. Most significantly, after 16 h the defect intensity decreases below the intensity under oxidizing conditions for all samples, indicating that the samples are more oxidized after regeneration. Since the Ce-O surface phonon intensity decreases, however, this behavior can only be explained by the reaction of CO_2 to carbonate, consuming an oxygen vacancy. This has no influence on the regeneration of Ce-O surface lattice oxygen (explaining the decrease) but consumes defect sites, thus oxidizing Ce^{3+} to Ce^{4+}, which results in a blue-shift of the F_{2g} mode (see Figure 2c). Since CO_2 can consume more vacancies than O_2, less Ce^{3+} states are present, leading to a blue-shift of the F_{2g} mode when compared to the oxidizing conditions, which makes the proposed re-oxidation process fully consistent with all spectroscopies performed in this study. The results are summarized in a mechanistic scheme shown in Figure 7.
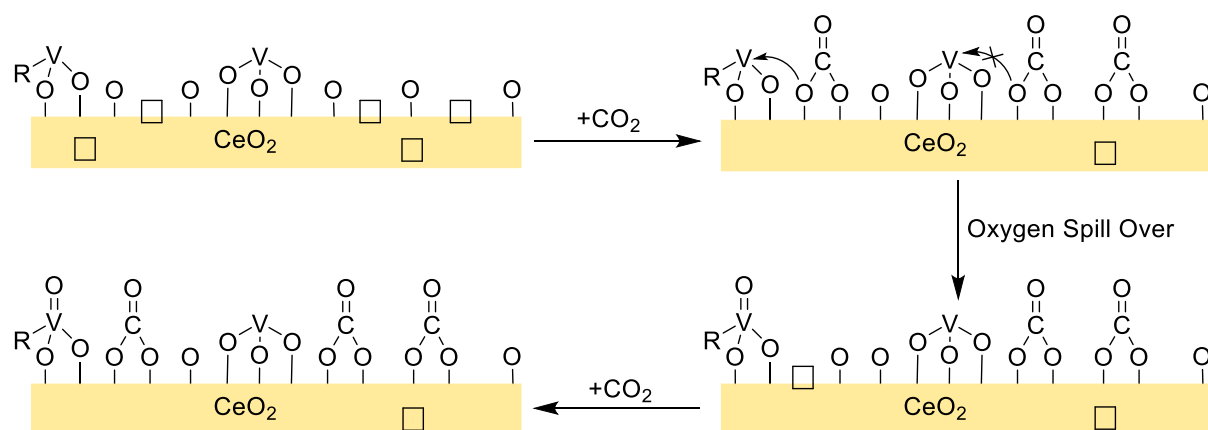
Figure 7: Re-oxidation processes occuring over a reduced VO_x/CeO_2 catalyst during regeneration with CO_2.

4. Conclusion

In this study, we investigated the CO_2 activation and re-oxidation process of differently loaded VO_x/CeO_2 catalysts from a mechanistic point of view, but also to establish a basis for catalytic applications like CO_2-assisted ODH reactions. Multiple in situ methods including UV-Vis and multi-wavelength Raman spectroscopy, supported by quasi in situ DRIFTS and XPS, were used to elucidate both bulk and surface processes. Throughout the re-oxidation under CO_2 for 16 h, spectroscopy was continuously performed to gain insight into the time-dependent regeneration behavior.

After reduction and 16 h of regeneration using CO_2, the ceria bulk showed only partial re-oxidation. However, closer to the surface, the regeneration seemed to be fully achieved for ceria, as the F_{2g} position even indicated a higher degree of oxidation after the regeneration than under the initial O_2 conditions. Furthermore, vanadia was regenerated on a slower time scale than ceria and could only be partially re-oxidized within the investigated timeframe.

The regeneration of ceria was determined to occur via carbonate formation on the reduced ceria surface, by adsorption of a CO_2 molecule into an oxygen vacancy. For bare ceria, this regeneration process could be observed via UV-Raman spectroscopy to occur on the topmost oxygen layer, where CO_2 can bind to defects. The resulting carbonates consume these defects but are stable enough to ensure that CO does not desorb after regeneration.[71] This process consumes clean surface lattice oxygen of ceria as well as defect sites. The formation of surface carbonates was observed using DRIFTS, leading to seemingly more oxidized ceria than under O_2 conditions. This formation of surface carbonates was also observed for the vanadia-loaded samples but to a lesser extent, as vanadia is anchored to some of the surface lattice oxygen, thereby blocking sites of ceria. This leads to a slower regeneration of the ceria subsurface/bulk with increasing vanadia loading. Only the sample with the highest loading deviated from that trend, as vanadia was transformed mostly to $CeVO_4$ during regeneration.

The samples showed a loading-dependent behavior. The regeneration of the VO_x/CeO_2 samples with the lowest vanadia loading was able to regenerate only partially and surface vanadium stayed in oxidation state V^{4+}, while the sample with a medium loading showed an almost full regeneration of V^{5+} states. This can be attributed to differences in the nuclearity distribution, which changes significantly with an increasing vanadium surface density. The different nuclearities also influence the

regeneration, as only a partial regeneration of monomeric vanadia species was predicted to be thermodynamically favorable.[71] However, higher nuclearities are thermodynamically more stable on ceria in their highest oxidized state, allowing for the full regeneration at higher vanadia loadings. Since the sample with the lowest vanadia loading is dominated by monomers, while higher loadings are dominated by the most stable trimers, the difference in the re-oxidation behavior can be readily explained.

The regeneration of the catalyst occurs mainly via the ceria lattice. The regeneration of vanadia can occur either by gas-phase CO_2 or by an oxygen spill-over from the ceria lattice. Due to the time delay between the ceria and vanadia regeneration, the oxygen spill-over pathway seems more likely and is in agreement with previous results according to which ceria keeps vanadium in oxidation state +V.

In summary, we present a comprehensive study in which the CO_2-based regeneration of differently-loaded and reduced VO_x/CeO_2 catalysts is investigated with multiple in situ methods. This enabled us to obtain a detailed understanding of the regeneration process on a molecular level using an oxidizing agent that will become a more relevant feed gas in chemical industry. Our results can further serve as an experimental basis for understanding CO_2-assisted ODH reactions (ethylene, propane, cyclohexane etc.), as green alternatives to fossil fuel-based processes. However, the regeneration can become the rate-determining step when the catalysts are not sufficiently oxidized, leading to deactivation. Our approach can readily transferred to other important catalysts for CO_2-assisted ODH (e.g. supported CrO_x) or other processes that involve ceria-mediated CO_2 activation.

Declaration of Competing Interest

The authors declare that they have no known competing financial interests or personal relationships that could have appeared to influence the work reported in this paper.

Acknowledgements

Supporting Information

The supporting information to this article contains additional in situ UV-Vis, Vis-Raman, UV-Raman, and DRIFTS data, as well as further information on the UV-Raman spectral analysis.

References

(1) Crowley, T. J.; Berner, R. A. Paleoclimate. CO_2 and climate change. *Science* **2001**, *292* (5518), 870–872. DOI: 10.1126/science.1061664.

(2) Baena-Moreno, F. M.; Rodríguez-Galán, M.; Vega, F.; Alonso-Fariñas, B.; Vilches Arenas, L. F.; Navarrete, B. Carbon capture and utilization technologies: a literature review and recent advances. *Energ. Sources A: Rec. Util. Environ. Effects* **2019**, *41* (12), 1403–1433. DOI: 10.1080/15567036.2018.1548518.

(3) Al-Mamoori, A.; Krishnamurthy, A.; Rownaghi, A. A.; Rezaei, F. Carbon Capture and Utilization Update. *Energy Technol.* **2017**, *5* (6), 834–849. DOI: 10.1002/ente.201600747.

(4) Chauvy, R.; Weireld, G. de. CO_2 Utilization Technologies in Europe: A Short Review. *Energy Technol.* **2020**, *8* (12), 1. DOI: 10.1002/ente.202000627.

(5) Aresta, M.; Dibenedetto, A.; Angelini, A. The changing paradigm in CO_2 utilization. *J. CO2 Util.* **2013**, *3-4* (14–15), 65–73. DOI: 10.1016/j.jcou.2013.08.001.

(6) Alper, E.; Yuksel Orhan, O. CO_2 utilization: Developments in conversion processes. *Petroleum* **2017**, *3* (1), 109–126. DOI: 10.1016/j.petlm.2016.11.003.

(7) Marlin, D. S.; Sarron, E.; Sigurbjörnsson, Ó. Process Advantages of Direct CO_2 to Methanol Synthesis. *Front. Chem.* **2018**, *6*, 446. DOI: 10.3389/fchem.2018.00446.

(8) Gambo, Y.; Adamu, S.; Tanimu, G.; Abdullahi, I. M.; Lucky, R. A.; Ba-Shammakh, M. S.; Hossain, M. M. CO_2-mediated oxidative dehydrogenation of light alkanes to olefins: Advances and perspectives in catalyst design and process improvement. *Appl. Catal. A: Gen.* **2021**, *623*, 118273. DOI: 10.1016/j.apcata.2021.118273.

(9) Baek, J.; Yun, H. J.; Yun, D.; Choi, Y.; Yi, J. Preparation of Highly Dispersed Chromium Oxide Catalysts Supported on Mesoporous Silica for the Oxidative Dehydrogenation of Propane Using CO_2: Insight into the Nature of Catalytically Active Chromium Sites. *ACS Catal.* **2012**, *2* (9), 1893–1903. DOI: 10.1021/cs300198u.

(10) Carter, J. H.; Bere, T.; Pitchers, J. R.; Hewes, D. G.; Vandegehuchte, B. D.; Kiely, C. J.; Taylor, S. H.; Hutchings, G. J. Direct and oxidative dehydrogenation of propane: from catalyst design to industrial application. *Green Chem.* **2021**, *23* (24), 9747–9799. DOI: 10.1039/D1GC03700E.

(11) Álvarez, A.; Borges, M.; Corral-Pérez, J. J.; Olcina, J. G.; Hu, L.; Cornu, D.; Huang, R.; Stoian, D.; Urakawa, A. CO_2 Activation over Catalytic Surfaces. *ChemPhysChem* **2017**, *18* (22), 3135–3141. DOI: 10.1002/cphc.201700782.

(12) Jacquemin, M.; Beuls, A.; Ruiz, P. Catalytic production of methane from CO_2 and H_2 at low temperature: Insight on the reaction mechanism. *Catal. Today* **2010**, *157* (1-4), 462–466. DOI: 10.1016/j.cattod.2010.06.016.

(13) Hess, C. Nanostructured vanadium oxide model catalysts for selective oxidation reactions. *ChemPhysChem* **2009**, *10* (2), 319–326. DOI: 10.1002/cphc.200800585.

(14) Wachs, I. E. Catalysis science of supported vanadium oxide catalysts. *Dalton Trans.* **2013**, *42* (33), 11762–11769. DOI: 10.1039/C3DT50692D.

(15) Argyle, M. D.; Chen, K.; Bell, A. T.; Iglesia, E. Effect of Catalyst Structure on Oxidative Dehydrogenation of Ethane and Propane on Alumina-Supported Vanadia. *J. Catal.* **2002**, *208* (1), 139–149. DOI: 10.1006/jcat.2002.3570.

(16) Beck, B.; Harth, M.; Hamilton, N. G.; Carrero, C.; Uhlrich, J. J.; Trunschke, A.; Shaikhutdinov, S.; Schubert, H.; Freund, H.-J.; Schlögl, R.; Sauer, J.; Schomäcker, R. Partial oxidation of ethanol on vanadia catalysts on supporting oxides with different redox properties compared to propane. *J. Catal.* **2012**, *296,* 120–131. DOI: 10.1016/j.jcat.2012.09.008.

(17) Balogun, M. L.; Adamu, S.; Ba-Shammakh, M. S.; Hossain, M. M. Promotional effects of CO_2 on the oxidative dehydrogenation of propane over mesoporous VO_x/γ-Al_2O_3 catalysts. *J. Industr. Eng. Chem.* **2021**, *96* (20), 82–97. DOI: 10.1016/j.jiec.2020.12.022.

(18) Ascoop, I.; Galvita, V. V.; Alexopoulos, K.; Reyniers, M.-F.; van der Voort, P.; Bliznuk, V.; Marin, G. B. The role of CO_2 in the dehydrogenation of propane over WO_x–VO_x/SiO_2. *J. Catal.* **2016**, *335*, 1–10. DOI: 10.1016/j.jcat.2015.12.015.

(19) Jiang, X.; Lis, B. M.; Purdy, S. C.; Paladugu, S.; Fung, V.; Quan, W.; Bao, Z.; Yang, W.; He, Y.; Sumpter, B. G.; Page, K.; Wachs, I. E.; Wu, Z. CO_2-Assisted Oxidative Dehydrogenation of Propane over VO_x/In_2O_3 Catalysts: Interplay between Redox Property and Acid–Base Interactions. *ACS Catal.* **2022**, *12* (18), 11239–11252. DOI: 10.1021/acscatal.2c02099.

(20) Jiang, X.; Lis, B. M.; Wu, Y.; Wachs, I. E.; Wu, Z. Effect of the Molecular Structure of Surface Vanadia on Activity and Regenerability of VO_x/In_2O_3 Catalysts for CO_2-Assisted Oxidative Dehydrogenation of Propane. *J. Phys. Chem. C* **2023**, *127* (13), 6311–6320. DOI: 10.1021/acs.jpcc.3c00183.

(21) Rogg, S.; Hess, C. CO_2 as a soft oxidant for propane oxidative dehydrogenation: A mechanistic study using operando UV Raman spectroscopy. *J. CO2 Util.* **2021**, *50* (9), 101604. DOI: 10.1016/j.jcou.2021.101604.

(22) Akah, A.; Al-Ghrami, M. Maximizing propylene production via FCC technology. *Appl. Petrochem. Res.* **2015**, *5* (4), 377–392. DOI: 10.1007/s13203-015-0104-3.

(23) Botavina, M. A.; Martra, G.; Agafonov, Y.A.; Gaidai, N. A.; Nekrasov, N. V.; Trushin, D. V.; Coluccia, S.; Lapidus, A. L. Oxidative dehydrogenation of C_3–C_4 paraffins in the presence of CO_2 over CrO_x/SiO_2 catalysts. *Appl. Catal. A: Gen.* **2008**, *347* (2), 126–132. DOI: 10.1016/j.apcata.2008.05.037.

(24) Gashoul Daresibi, F.; Khodadadi, A. A.; Mortazavi, Y.; Huotari, S.; Ritala, M. Highly dispersed atomic layer deposited CrO_x on SiO_2 catalyst with enhanced yield of propylene for CO_2–mediated oxidative dehydrogenation of propane. *Mol. Catal.* **2022**, *526* (80–), 112396. DOI: 10.1016/j.mcat.2022.112396.

(25) Michorczyk, P.; Pietrzyk, P.; Ogonowski, J. Preparation and characterization of SBA-1–supported chromium oxide catalysts for CO_2 assisted dehydrogenation of propane. *Microporous Mesoporous Mater.* **2012**, *161*, 56–66. DOI: 10.1016/j.micromeso.2012.05.011.

(26) Wang, H.; Nguyen, T. D.; Tsilomelekis, G. Propane oxidative dehydrogenation using CO_2 over CrO_x/Fe–CeO_2 catalysts. *Catal. Sci. Technol.* **2023**, *13* (8), 2360–2369. DOI: 10.1039/D2CY01563C.

(27) Wang, Z.-Y.; He, Z.-H.; Li, L.-Y.; Yang, S.-Y.; He, M.-X.; Sun, Y.-C.; Wang, K.; Chen, J.-G.; Liu, Z.-T. Research progress of CO_2 oxidative dehydrogenation of propane to propylene over Cr-free metal catalysts. *Rare metals* **2022**, *41* (7), 2129–2152. DOI: 10.1007/s12598-021-01959-y.

(28) Carrero, C. A.; Schloegl, R.; Wachs, I. E.; Schomaecker, R. Critical Literature Review of the Kinetics for the Oxidative Dehydrogenation of Propane over Well-

Defined Supported Vanadium Oxide Catalysts. *ACS Catal.* **2014**, *4* (10), 3357–3380. DOI: 10.1021/cs5003417.

(29) Dinse, A.; Frank, B.; Hess, C.; Habel, D.; Schomäcker, R. Oxidative dehydrogenation of propane over low-loaded vanadia catalysts: Impact of the support material on kinetics and selectivity. *J. Mol. Catal A: Chem.* **2008**, *289* (1-2), 28–37. DOI: 10.1016/j.molcata.2008.04.007.

(30) Cordatos, H.; Ford, D.; Gorte, R. J. Simulated Annealing Study of the Structure and Reducibility in Ceria Clusters. *J. Phys. Chem.* **1996**, *100* (46), 18128–18132. DOI: 10.1021/jp961110o.

(31) Duchoň, T.; Hackl, J.; Mueller, D. N.; Kullgren, J.; Du, D.; Senanayake, S. D.; Mouls, C.; Gottlob, D. M.; Khan, M. I.; Cramm, S.; Veltruská, K.; Matolín, V.; Nemšák, S.; Schneider, C. M. Establishing structure-sensitivity of ceria reducibility: real-time observations of surface-hydrogen interactions. *J. Mater. Chem. A* **2020**, *8* (11), 5501–5507. DOI: 10.1039/C9TA11784A.

(32) Filtschew, A.; Hofmann, K.; Hess, C. Ceria and Its Defect Structure: New Insights from a Combined Spectroscopic Approach. *J. Phys. Chem. C* **2016**, *120* (12), 6694–6703. DOI: 10.1021/acs.jpcc.6b00959.

(33) Ziemba, M.; Weyel, J.; Hess, C. Elucidating the mechanism of the reverse water–gas shift reaction over Au/CeO_2 catalysts using operando and transient spectroscopies. *Appl. Catal. B: Environ.* **2022**, *301*, 120825. DOI: 10.1016/j.apcatb.2021.120825.

(34) Liu, Y.; Li, Z.; Xu, H.; Han, Y. Reverse water–gas shift reaction over ceria nanocube synthesized by hydrothermal method. *Catal. Commun.* **2016**, *76*, 1–6. DOI: 10.1016/j.catcom.2015.12.011.

(35) Sala, E. M.; Mazzanti, N.; Mogensen, M. B.; Chatzichristodoulou, C. Current understanding of ceria surfaces for CO_2 reduction in SOECs and future prospects – A review. *Solid State Ion.* **2022**, *375* (2), 115833. DOI: 10.1016/j.ssi.2021.115833.

(36) Ouyang, B.; Tan, W.; Liu, B. Morphology effect of nanostructure ceria on the Cu/CeO_2 catalysts for synthesis of methanol from CO_2 hydrogenation. *Catal. Commun.* **2017**, *95* (3), 36–39. DOI: 10.1016/j.catcom.2017.03.005.

(37) Graciani, J.; Mudiyanselage, K.; Xu, F.; Baber, A. E.; Evans, J.; Senanayake, S. D.; Stacchiola, D. J.; Liu, P.; Hrbek, J.; Fernández Sanz, J.; Rodriguez, J. A. Catalysis. Highly active copper-ceria and copper-ceria-titania catalysts for methanol synthesis from CO_2. *Science* **2014**, *345* (6196), 546–550. DOI: 10.1126/science.1253057.

(38) Martínez-Huerta, M. V.; Deo, G.; Fierro, J. L. G.; Bañares, M. A. Changes in Ceria-Supported Vanadium Oxide Catalysts during the Oxidative Dehydrogenation of Ethane and Temperature-Programmed Treatments. *J. Phys. Chem. C* **2007**, *111* (50), 18708–18714. DOI: 10.1021/jp0772225.

(39) Iglesias-Juez, A.; Martínez-Huerta, M. V.; Rojas-García, E.; Jehng, J.-M.; Bañares, M. A. On the Nature of the Unusual Redox Cycle at the Vanadia Ceria Interface. *J. Phys. Chem. C* **2018**, *122* (2), 1197–1205. DOI: 10.1021/acs.jpcc.7b09832.

(40) Daniell, W.; Ponchel, A.; Kuba, S.; Anderle, F.; Weingand, T.; Gregory, D. H.; Knözinger, H. Characterization and Catalytic Behavior of VO_x-CeO_2 Catalysts for the Oxidative Dehydrogenation of Propane. *Topics Catal.* **2002**, *20* (1/4), 65–74. DOI: 10.1023/A:1016399315511.

(41) Schumacher, L.; Hess, C. The active role of the support in propane ODH over VO_x/CeO_2 catalysts studied using multiple operando spectroscopies. *J. Catal.* **2021**, *398* (13), 29–43. DOI: 10.1016/j.jcat.2021.04.006.

(42) Karakaya, C.; Kidder, M.; Wolden, C.; Kee, R. J.; Deutschmann, O. Mechanistic Interpretations and Insights for the Oxidative Dehydrogenation of Propane via CO_2 over Cr_2O_3/Al_2O_3 Catalysts. *Ind. Eng. Chem. Res.* **2022**, *61* (39), 14482–14493. DOI: 10.1021/acs.iecr.2c02298.

(43) Dou, J.; Funderburg, J.; Yang, K.; Liu, J.; Chacko, D.; Zhang, K.; Harvey, A. P.; Haribal, V. P.; Zhou, S. J.; Li, F. $Ce_xZr_{1-x}O_2$-Supported CrO_x Catalysts for CO_2-Assisted Oxidative Dehydrogenation of Propane—Probing the Active Sites and Strategies for Enhanced Stability. *ACS Catal.* **2023**, *13* (1), 213–223. DOI: 10.1021/acscatal.2c05286.

(44) Balogun, M. L.; Adamu, S.; Bakare, I. A.; Ba-Shammakh, M. S.; Hossain, M. M. CO_2 Assisted Oxidative Dehydrogenation of Propane to Propylene over Fluidizable

MoO$_3$/La$_2$O$_3$-γAl$_2$O$_3$ Catalysts. *J. CO2 Util.* **2020**, *42*, 101329. DOI: 10.1016/j.jcou.2020.101329.

(45) Staudt, T.; Lykhach, Y.; Tsud, N.; Skála, T.; Prince, K. C.; Matolín, V.; Libuda, J. Ceria reoxidation by CO$_2$: A model study. *J. Catal.* **2010**, *275* (1), 181–185. DOI: 10.1016/j.jcat.2010.07.032.

(46) Waleska, P. S.; Hess, C. Oligomerization of Supported Vanadia: Structural Insight Using Surface-Science Models with Chemical Complexity. *J. Phys. Chem. C* **2016**, *120* (33), 18510–18519. DOI: 10.1021/acs.jpcc.6b01672.

(47) Antonov, L.; Nedeltcheva, D. Resolution of overlapping UV–Vis absorption bands and quantitative analysis. *Chem. Soc. Rev.* **2000**, *29* (3), 217–227. DOI: 10.1039/A900007K.

(48) Hess, C. Direct correlation of the dispersion and structure in vanadium oxide supported on silica SBA-15. *J. Catal.* **2007**, *248* (1), 120–123. DOI: 10.1016/j.jcat.2007.02.024.

(49) Nottbohm, C. T.; Hess, C. Investigation of ceria by combined Raman, UV–vis and X-ray photoelectron spectroscopy. *Catal. Commun.* **2012**, *22*, 39–42. DOI: 10.1016/j.catcom.2012.02.009.

(50) Ziemba, M.; Schumacher, L.; Hess, C. Reduction Behavior of Cubic In$_2$O$_3$ Nanoparticles by Combined Multiple In Situ Spectroscopy and DFT. *J. Phys. Chem. Lett.* **2021**, *12* (15), 3749–3754. DOI: 10.1021/acs.jpclett.1c00892.

(51) Oelhafen, P. Practical surface analysis by auger and X-ray photoelectron spectroscopy. *J. Electr. Spectrosc. Rel. Phenom.* **1984**, *34* (2), 203. DOI: 10.1016/0368-2048(84)80044-4.

(52) Schumacher, L.; Ziemba, M.; Brunnengräber, K.; Totzauer, L.; Hofmann, K.; Etzold, B. J. M.; Albert, B.; Hess, C. Understanding the Reduction Behavior of VO$_x$/CeO$_2$ on a Molecular Level: Combining Temperature-Programmed Reduction with Multiple In-Situ Spectroscopies and X-ray Diffraction. *J. Phys. Chem. C* **2023**, *127* (12), 5810–5824. DOI: 10.1021/acs.jpcc.3c00622.

(53) Schumacher, L.; Weyel, J.; Hess, C. Unraveling the Active Vanadium Sites and Adsorbate Dynamics in VO$_x$/CeO$_2$ Oxidation Catalysts Using Transient IR

Spectroscopy. *J. Am. Chem. Soc.* **2022**, *144* (32), 14874–14887. DOI: 10.1021/jacs.2c06303.

(54) Schilling, C.; Hess, C. Real-Time Observation of the Defect Dynamics in Working Au/CeO$_2$ Catalysts by Combined Operando Raman/UV–Vis Spectroscopy. *J. Phys. Chem. C* **2018**, *122* (5), 2909–2917. DOI: 10.1021/acs.jpcc.8b00027.

(55) Huang, B.; Gillen, R.; Robertson, J. Study of CeO$_2$ and Its Native Defects by Density Functional Theory with Repulsive Potential. *J. Phys. Chem. C* **2014**, *118* (42), 24248–24256. DOI: 10.1021/jp506625h.

(56) Ober, P.; Rogg, S.; Hess, C. Direct Evidence for Active Support Participation in Oxide Catalysis: Multiple Operando Spectroscopy of VO$_x$/Ceria. *ACS Catal.* **2020**, *10* (5), 2999–3008. DOI: 10.1021/acscatal.9b05174.

(57) Binet, C.; Badri, A.; Lavalley, J.-C. A Spectroscopic Characterization of the Reduction of Ceria from Electronic Transitions of Intrinsic Point Defects. *J. Phys. Chem.* **1994**, *98* (25), 6392–6398. DOI: 10.1021/j100076a025.

(58) Castleton, C. W. M.; Kullgren, J.; Hermansson, K. Tuning LDA+U for electron localization and structure at oxygen vacancies in ceria. *J. Chem. Phys.* **2007**, *127* (24), 244704. DOI: 10.1063/1.2800015.

(59) Skorodumova, N. V.; Ahuja, R.; Simak, S. I.; Abrikosov, I. A.; Johansson, B.; Lundqvist, B. I. Electronic, bonding, and optical properties of CeO$_2$ and Ce$_2$O$_3$ from first principles. *Phys. Rev. B* **2001**, *64* (11), 548. DOI: 10.1103/PhysRevB.64.115108.

(60) Nitsche, D.; Hess, C. Structure of Isolated Vanadia and Titania: A Deep UV Raman, UV–Vis, and IR Spectroscopic Study. *J. Phys. Chem. C* **2016**, *120* (2), 1025–1037. DOI: 10.1021/acs.jpcc.5b10317.

(61) Lamoureux, B.; Singh, V. R.; Jovic, V.; Kuyyalil, J.; Su, T.-Y.; Smith, K. E. Structural and electronic properties of thermally evaporated V$_2$O$_5$ epitaxial thin films. *Thin Solid Films* **2016**, *615*, 409–414. DOI: 10.1016/j.tsf.2016.07.062.

(62) Schilling, C.; Hofmann, A.; Hess, C.; Ganduglia-Pirovano, M. V. Raman Spectra of Polycrystalline CeO$_2$: A Density Functional Theory Study. *J. Phys. Chem. C* **2017**, *121* (38), 20834–20849. DOI: 10.1021/acs.jpcc.7b06643.

(63) Weber, W. H.; Hass, K. C.; McBride, JR. Raman study of CeO_2: Second-order scattering, lattice dynamics, and particle-size effects. *Phys. Rev. B* **1993**, *48* (1), 178–185. DOI: 10.1103/PhysRevB.48.178.

(64) Li, Z.; Werner, K.; Chen, L.; Jia, A.; Qian, K.; Zhong, J.-Q.; You, R.; Wu, L.; Zhang, L.; Pan, H.; Wu, X.-P.; Gong, X.-Q.; Shaikhutdinov, S.; Huang, W.; Freund, H.-J. Interaction of Hydrogen with Ceria: Hydroxylation, Reduction, and Hydride Formation on the Surface and in the Bulk. *Chemistry* **2021**, *27* (16), 5268–5276. DOI: 10.1002/chem.202005374.

(65) Wu, Z.; Rondinone, A. J.; Ivanov, I. N.; Overbury, S. H. Structure of Vanadium Oxide Supported on Ceria by Multiwavelength Raman Spectroscopy. *J. Phys. Chem. C* **2011**, *115* (51), 25368–25378. DOI: 10.1021/jp2084605.

(66) Martínez-Huerta, M. Nature of the vanadia?ceria interface in V^{5+}/CeO_2 catalysts and its relevance for the solid-state reaction toward $CeVO_4$ and catalytic properties. *J. Catal.* **2004**, *225* (1), 240–248. DOI: 10.1016/j.jcat.2004.04.005.

(67) Baron, M.; Abbott, H.; Bondarchuk, O.; Stacchiola, D.; Uhl, A.; Shaikhutdinov, S.; Freund, H.-J.; Popa, C.; Ganduglia-Pirovano, M. V.; Sauer, J. Resolving the Atomic Structure of Vanadia Monolayer Catalysts: Monomers, Trimers, and Oligomers on Ceria. *Angew. Chem. Int. Ed.* **2009**, *121* (43), 8150–8153. DOI: 10.1002/ange.200903085.

(68) Penschke, C.; Paier, J.; Sauer, J. Oligomeric Vanadium Oxide Species Supported on the CeO_2(111) Surface: Structure and Reactivity Studied by Density Functional Theory. *J. Phys. Chem. C* **2013**, *117* (10), 5274–5285. DOI: 10.1021/jp400520j.

(69) Penschke, C.; Paier, J.; Sauer, J. Vanadium Oxide Oligomers and Ordered Monolayers Supported on CeO_2(111): Structure and Stability Studied by Density Functional Theory. *J. Phys. Chem. C* **2018**, *122* (16), 9101–9110. DOI: 10.1021/acs.jpcc.8b01998.

(70) Granger, P.; Siaka, H. W.; Umbarkar, S. B. What News in the Surface Chemistry of Bulk and Supported Vanadia Based SCR-Catalysts: Improvements in their Resistance to Poisoning and Thermal Sintering. *Chem. Rec.* **2019**, *19* (9), 1813–1828. DOI: 10.1002/tcr.201800092. Published Online: Oct. 18, 2018.

(71) Fan, H.-X.; Zhen, L.-F.; Rajendran, A.; Feng, J.; Li, W.-Y. Crucial role of H and O spillover in VO_x/CeO_2 catalysts reduction and re-oxidation during the ODH reaction. *Appl. Surf. Sci.* **2023**, *626*, 157250. DOI: 10.1016/j.apsusc.2023.157250.

(72) Flege, J. I.; Kaemena, B.; Gevers, S.; Bertram, F.; Wilkens, T.; Bruns, D.; Bätjer, J.; Schmidt, T.; Wollschläger, J.; Falta, J. Silicate-free growth of high-quality ultrathin cerium oxide films on Si(111). *Phys. Rev. B* **2011**, *84* (23). DOI: 10.1103/PhysRevB.84.235418.

(73) Allahgholi, A.; Flege, J. I.; Thieß, S.; Drube, W.; Falta, J. Oxidation-state analysis of ceria by X-ray photoelectron spectroscopy. *ChemPhysChem* **2015**, *16* (5), 1083–1091. DOI: 10.1002/cphc.201402729. Published Online: Feb. 20, 2015.

(74) Lykhach, Y.; Johánek, V.; Aleksandrov, H. A.; Kozlov, S. M.; Happel, M.; Skála, T.; St. Petkov, P.; Tsud, N.; Vayssilov, G. N.; Prince, K. C.; Neyman, K. M.; Matolín, V.; Libuda, J. Water Chemistry on Model Ceria and Pt/Ceria Catalysts. *J. Phys. Chem. C* **2012**, *116* (22), 12103–12113. DOI: 10.1021/jp302229x.

(75) Natile, M. M.; Glisenti, A. Nanostructured $CeO2$ Powders by XPS. *Surf. Sci. Spectra* **2006**, *13* (1), 17–30. DOI: 10.1116/11.20060401.

(76) Bosio, N.; Schaefer, A.; Grönbeck, H. Can oxygen vacancies in ceria surfaces be measured by O1s photoemission spectroscopy? *J. Phys. Condens. Matter* **2022**, *34* (17). DOI: 10.1088/1361-648X/ac4f7b. Published Online: Feb. 25, 2022.

(77) Hu, Z.; Wang, Z.; Guo, Y.; Wang, L. Total Oxidation of Propane over a Ru/CeO_2 Catalyst at Low Temperature. *Environ. Sci. Technol.* DOI: 10.1021/acs.est.8b03448.

(78) Meunier, F. C.; Tibiletti, D.; Goguet, A.; Reid, D.; Burch, R. On the reactivity of carbonate species on a Pt/CeO_2 catalyst under various reaction atmospheres: Application of the isotopic exchange technique. *Appl. Catal. A: Gen.* **2005**, *289* (1), 104–112. DOI: 10.1016/j.apcata.2005.04.018.

(79) Mokkelbost, T.; Kaus, I.; Grande, T.; Einarsrud, M.-A. Combustion Synthesis and Characterization of Nanocrystalline $CeO2$-Based Powders. *Chem. Mater.* **2004**, *16* (25), 5489–5494. DOI: 10.1021/cm048583p.

(80) Wang, B.; Wu, X.; Ran, R.; Si, Z.; Weng, D. IR characterization of propane oxidation on $Pt/CeO_2–ZrO_2$: The reaction mechanism and the role of Pt. *J. Mol. Catal A: Chem.* **2012**, *356*, 100–105. DOI: 10.1016/j.molcata.2011.12.030.

Supporting Information

Investigation of the CO_2 Activation and Regeneration of Reduced VO_x/CeO_2 Catalysts Using Multiple In Situ Spectroscopies

Leon Schumacher, Marc Ziemba, Christian Hess*

Technical University of Darmstadt, Department of Chemistry, Eduard-Zintl-Institut für Anorganische und Physikalische Chemie, Peter-Grünberg-Str. 8, 64287 Darmstadt, Germany

*Corresponding Author (E-Mail: christian.hess@tu-darmstadt.de)
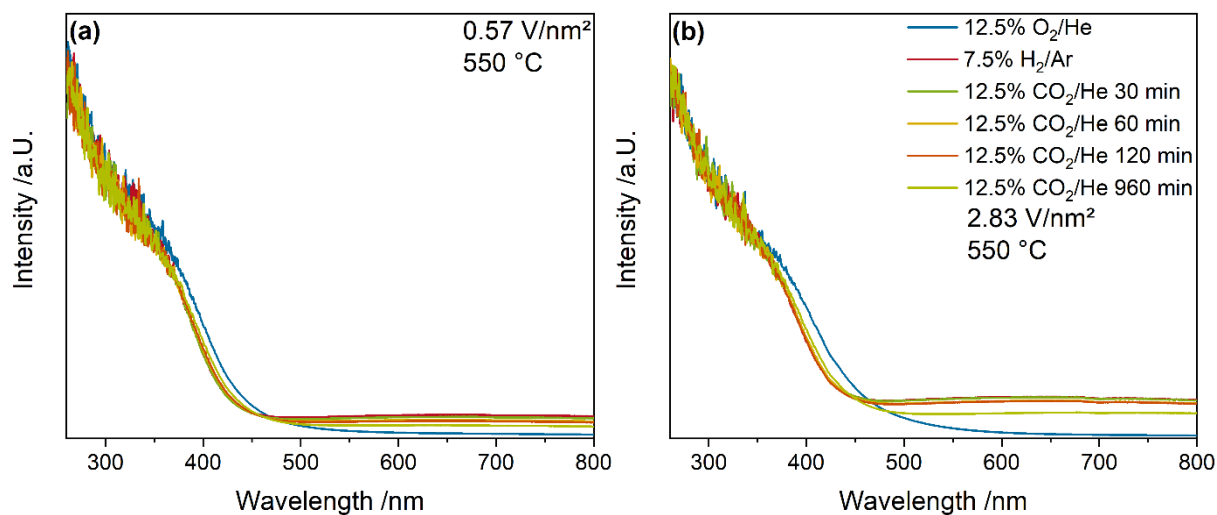
Figure S1: In situ UV-Vis spectra of **(a)** the 0.57 and **(b)** the 2.83 V/nm² sample recorded under different gas feeds at 550 °C.
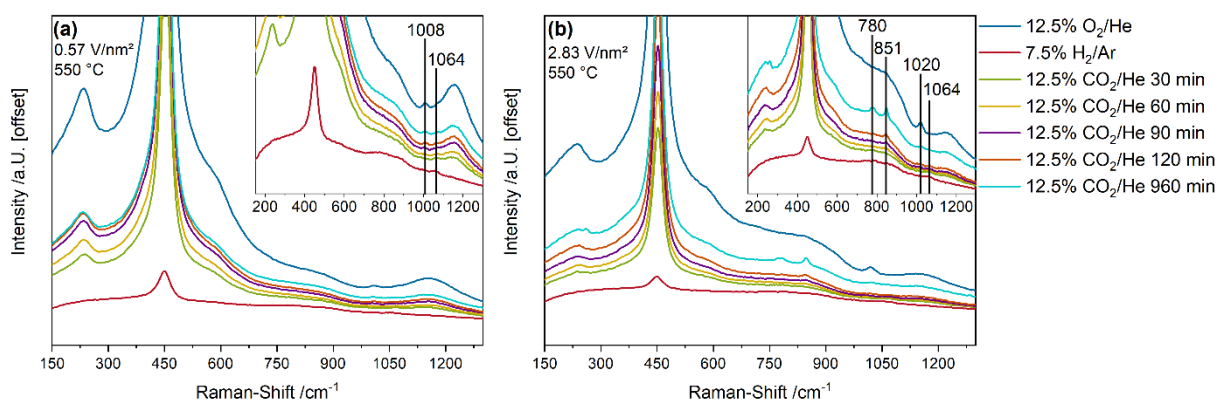
Figure S2: In situ Vis-Raman spectra (514 nm excitation) of **(a)** the 0.57 and **(b)** the 2.83 V/nm² sample recorded under different gas feeds at 550 °C. The insets show an enlarged view of the region between 150 and 1300 cm^{-1}.
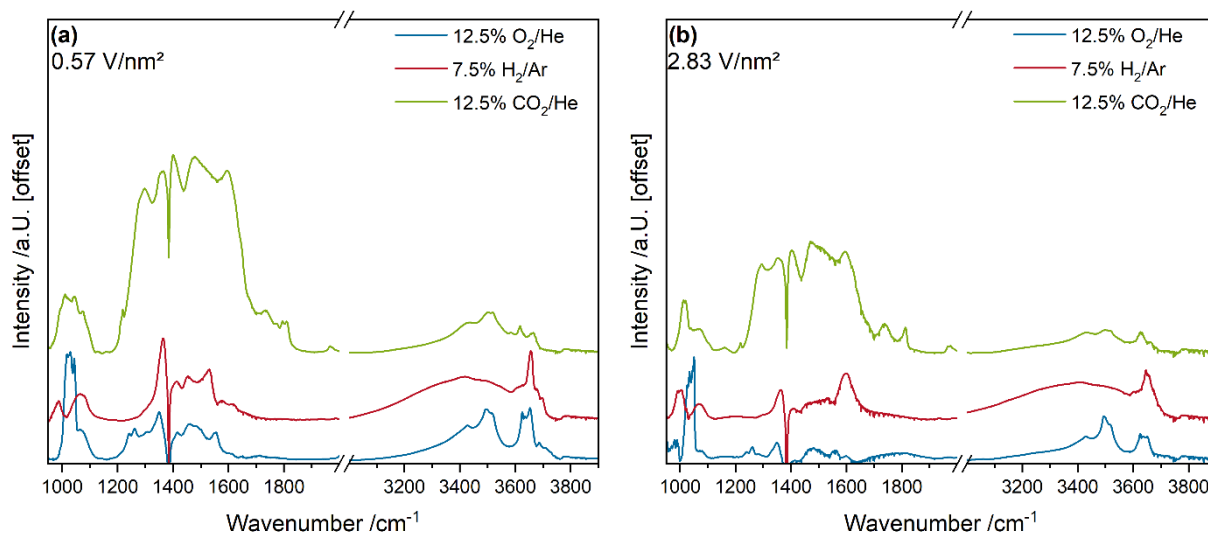
Figure S3: In situ DRIFT spectra of **(a)** the 0.57 and **(b)** the 2.83 V/nm² sample recorded under different gas feeds at 550 °C.
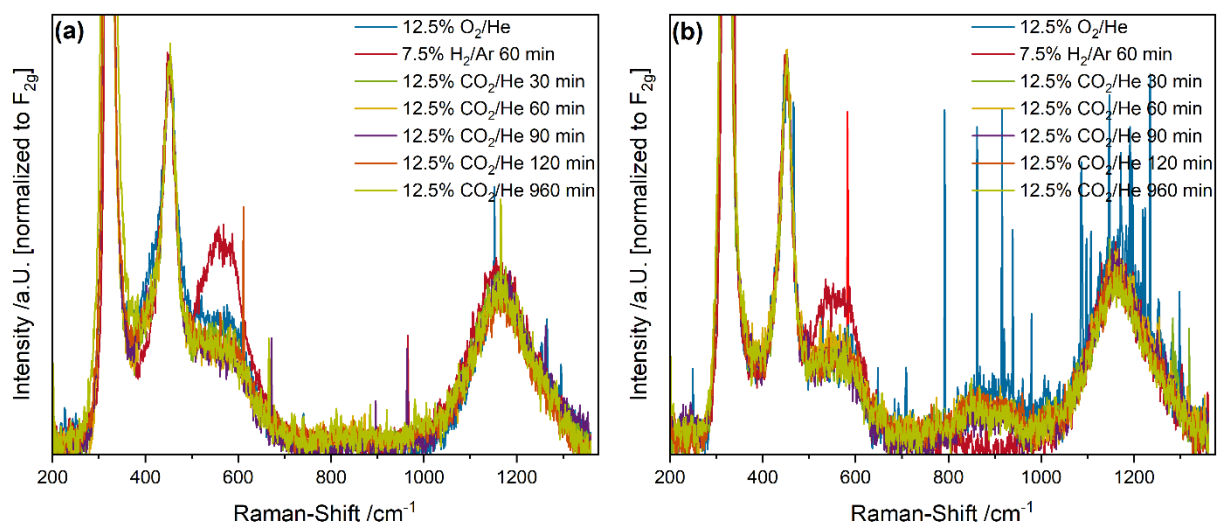
Figure S4: In situ UV-Raman spectra (385 nm excitation) of **(a)** the 0.57 and **(b)** the 2.83 V/nm² sample recorded under different gas feeds at 550 °C.
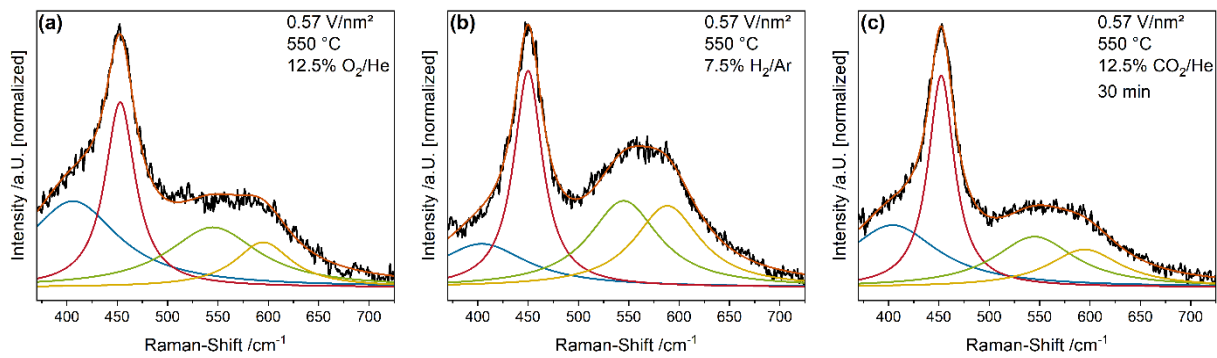
Figure S5: Exemplary fits of the UV-Raman spectra of the 0.57 V/nm² sample under **(a)** 12.5% O_2/He, **(b)** 7.5% H_2/Ar, and **(c)** 12.5% CO_2/He after 30 minutes of regeneration, using four Lorentzian functions.

4.1.6 Unraveling the Mechanism of the CO_2-Assisted Oxidative Dehydrogenation of Propane over VO_x/CeO_2: An Operando Spectroscopic Study

The sixth overall publication elucidates the reaction mechanism of CO_2-assisted propane ODH over VO_x/CeO_2 catalysts. To achieve this, ceria was loaded with different amounts of VO_x and was investigated, starting from a pre-reduced state that was investigated in detail in the fifth publication. A comparison between DDH and ODH conditions revealed that the conversion and selectivity during DDH are significantly higher than during ODH. However, the catalytic performance during DDH is not stable, as the conversion decreases sharply, indicating the depletion of lattice oxygen in the catalyst. Only ODH conditions lead to a stable catalytic performance, likely caused by the replenishment of lattice oxygen by CO_2. Analysis of the reaction network revealed that the selectivity goes through a maximum at a vanadia loading of 1.36 V/nm², while the CO_2 conversion is one order of magnitude larger than the propane conversion, which is indicative of the prevalence of side reactions, namely PDR, cracking and total oxidation of propane. Bare ceria exhibits the most significant amount of total oxidation, which decreases with increasing vanadia loading, while PDR becomes more dominant, especially for the 2.83 V/nm² sample. The reaction mechanism was investigated using multi-wavelength operando Raman, operando UV-Vis and quasi in situ DRIFT spectroscopy supported by in situ XRD. Results showed, that hydrogen is transferred from propane to lattice oxygen of bare ceria, forming a highly reactive bidentate Ce-OH group, which is likely to react with furhter hydrogen, leading to toal oxidation. Lattice oxygen is used as the active oxygen site, leading to the formation of oxygen vacancies, which are irreversibly blocked by the formation of carbonate adsorbates from gas phase CO_2. The presence of vanadia introduces additional hydrogen transfer paths, including the formation of bulk Ce-H, which reduces the amount of total oxidation. In addition, vanadia can facilitate the RWGSr with monodentate carbonates in proximity, which removes carbonates and regenerates active ceria surface oxygen sites. Upon the introduction of oligomeric vanadia, the active oxygen site shifts from ceria lattice oxygen to the more reactive oxygen of oligomeric vanadia, which leads to a sharp increase in PDR. These results demonstrate the relevance of combining multiple methods to obtain a full mechanistic picutre of reaction mechanisms at high temperatures.

6. Leon Schumacher, Marius Funke, Christian Hess, Unraveling the Mechanism of the CO_2-Assisted Oxidative Dehydrogenation of Propane over VO_x/CeO_2 Catalysts: An Operando Spectroscopic Study, Manuscript.

Unraveling the Mechanism of the CO_2-Assisted Oxidative Dehydrogenation of Propane over VO_x/CeO_2: An Operando Spectroscopic Study

Leon Schumacher, Marius Funke, Christian Hess*

Technical University of Darmstadt, Department of Chemistry, Eduard-Zintl-Institut für Anorganische und Physikalische Chemie, Peter-Grünberg-Str. 8, 64287 Darmstadt, Germany

*Corresponding Author (E-Mail: christian.hess@tu-darmstadt.de)

Abstract

The CO_2-assistend oxidative dehydrogenation (ODH) of propane is of great interest for the usage of CO_2 in chemical industry. Vanadia-based catalysts are a promising material class, which can replace highly toxic CrO_x, the current state-of-the-art catalyst. Ceria is a commonly used support material in CO_2 activation, but has not yet been used as a vanadia support for CO_2-assisted propane ODH. In this study, we address the interplay between vanadia and ceria as well as the nuclearity-dependent reaction behavior of VO_x/CeO_2 catalysts using XRD, multi-wavelength Raman, UV-Vis, and diffuse reflectance infrared Fourier transform spectroscopy (DRIFTS). While the vanadia loading increases the selectivity, the catalysts exhibit a significant amount of side reactions, including most prominently the total oxidation over bare ceria on surface oxygen sites due to their high reducibility and propane dry reforming (PDR) over catalysts with high vanadia loading. Mechanistic analysis reveals that dimers can transfer hydrogen from propane to the ceria lattice, forming Ce-H or to a monodentate carbonate, facilitating the reverse water-gas shift reaction (RWGSr), whereas a transfer to bridged Ce-OH surface species leads to total oxidation due to the high reactivity of the formed surface species. Oligomers facilitate PDR due to their high reducibility and the active oxygen site shifts from ceria to vanadia. The catalyst can be regenerated via carbonates, which are highly stable and can subsequently deactivate the catalyst surface. Our results highlight the benefit of applying multiple operando spectroscopies to enhance the mechanistic understanding of materials relevant for CO_2 activation and furthering the knowledge-based optimization of catalytic performance.

1. Introduction

Propylene is an important basis chemical that is used e.g. in the fabrication of polypropylene.[1,2] Different propylene production methods such as steam cracking, fluid catalytic cracking etc. are employed, which are however not sufficient to satisfy the high industry demand, resulting in the 'propylene gap'.[3,4] Therefore, additional methods to produce propylene are required, of which propane ODH is of great interest, as the introduction of oxygen into the gas feed leads to lower reaction temperatures and less catalyst leaching and the exothermicity of the reaction allows for heat integration of the process. However, stopping the reaction at the selective oxidation product instead of CO_x is challenging.[1,2,5] One approach to solve this issue is to use CO_2 as a soft oxidant instead of O_2, which increases selectivity. Additional benefits include a more homogeneous thermal distribution in the reactor due to the high heat capacity of CO_2, a lower flammability, less catalyst deactivation by carbon formation due to coal gasification, and the valorization of CO_2 as an unwanted green-house gas.[6,7] The latter is especially important in the industrial context to mitigate the influence of CO_2 on global climate change.[8–10] However, due to the high thermodynamics stability of CO_2, a suitable catalyst is required to make the reaction viable.[11–13]

The current state of the art catalyst used for the CO_2-assised ODH of propane is supported CrO_x due to its high activity.[7,14–17] In this catalyst, chromium was described to change its oxidation state under reactions conditions, that is, Cr^{6+} species are reduced to $Cr^{2+/3+}$, which are then involved in non-oxidative pathways towards propylene, namely direct dehydrogenation (DDH) followed by subsequent RWGSr. Alternatively, the direct ODH pathway can occur.[16] However, due to the high toxicity and potential damage to the environment when using chromium, its replacement with other active catalytic phases is highly desirable.[18] To that end, vanadia has been of interest due to its established commercial uses in oxidation reactions and high catalytic activity in propane ODH using O_2 as the oxidizing agent.[19–24] However, the activity of the vanadia strongly depends on its support, which can be categorized into inactive and active supports.[5,25,26] Inactive supports are not actively participating in the reaction and include SiO_2[20,23] or Al_2O_3,[19] while active supports can actively participate in the reaction by e.g. supplying lattice oxygen and include CeO_2, TiO_2[24] or In_2O_3.[21,22] Recently, the use of TiO_2 as vanadia support during CO_2-assisted propane ODH was studied and showed promising activities that were even comparable to those of CrO_x.[24] However, the use of ceria as a support, which is commonly used in reactions that

3

require the activation of CO_2, has not yet been reported to the literature despite its high potential.

Ceria is an established material for the conversion of C_1 materials, including CO oxidation,[27] CO_2 hydrogenation to methanol[28] and RWGSr.[29] So far, its potential for CO_2-assisted propane ODH is undisputed. Ceria in combination with vanadia has been used for ODH reactions using O_2 as the oxidizing agent, including alcohol ODH (methanol and ethanol),[30,31] and short alkane ODH (ethane, propane, butane).[32–34] In the context of propane ODH, it was shown that the complex interplay between vanadia and ceria is highly relevant to understand the reactivity behavior of the catalyst. On the ceria surface, vanadia is present in different nuclearities,[35] which perform different functions.[36] While monomeric vanadia is able to modulate the ceria oxygen mobility by interacting with surface vacancies,[33] dimeric and oligomeric nuclearities catalyze the initial C-H bond breakage and can quickly transfer hydrogen from propane to ceria lattice oxygen, while the trimeric nuclearity is very stable and does not participate.[36] In addition, ceria was shown to keep vanadia in oxidation state V^{5+}, while being reduced itself.[33,34,36–40] However, when using CO_2, it was shown that especially monomeric vanadia cannot be fully reoxidized after being reduced.[41] Understanding how these properties translate to the CO_2-assisted propane ODH will be an important step in understanding the reaction mechanism over VO_x/CeO_2.

In addition to elucidating the catalyst's behavior, understanding the reaction network is of high importance to obtain a full mechanistic picture and assign the identified active sites to the individual reactions. Besides the ODH reaction, multiple side reactions can occur, which include PDR, coking, cracking, and coal gasification of the formed carbon.[13] In addition, the dehydrogenation pathway was shown by experimental and theoretical work of Ascoop et al.[20] to occur via two routes, that is, a direct ODH pathway and an indirect two-step pathway. The latter is based on direct dehydrogenation, resulting in hydrogen and propylene, and subsequent reaction of hydrogen with CO_2 yielding CO and water via RWGSr. The presence of these two pathways was further confirmed experimentally by Rogg et al.[23] for VO_x/SiO_2 using operando spectroscopy, highlighting the importance of understanding this highly complex reaction network and the mode of operation of the vanadia catalyst under reaction conditions.

In this study, we investigate the CO_2-assisted propane ODH over VO_x/CeO_2 with the goal of elucidating the detailed reaction mechanism using multiple operando

and in situ spectroscopies. These include in situ XRD operando multi-wavelength Raman, operando UV-Vis, and quasi in situ DRIFT spectroscopy. In addition, the reaction network will be analyzed in detail to understand the reactivity behavior. Using the above methods the question of the interaction between ceria and vanadia, the identification of the active site, and the nuclearity-dependent reactivity behavior will be addressed to obtain a full mechanistic picture. Furthermore, we will address the active sites involved in potential side reactions and the common problem of catalyst deactivation during CO_2-assisted propane ODH. Our results demonstrate the potential of combining multiple methods to obtain detailed mechanistic insights into a catalytic reaction with potential industrial applicability. The approach can be readily transferred to other reactions and materials relevant to CO_2 activation and valorization.

2. Experimental Section

2.1. Catalyst Preparation

The ceria support was prepared by two-fold calcination of cerium(III) nitrate hexahydrate (≥99.99%, Sigma Aldrich) staying at 600 °C for 12 h after heating using a rate of 1.5 °C/min, as previously described.[42] Ceria was loaded with vanadia by incipient wetness impregnation. Three different loadings were prepared by mixing 1 g of ceria with 0.5 mL of different-concentration precursor solutions (1.07 mol/L, 0.51 mol/L, and 0.21 mol/L) containing vanadium(V) oxytriisopropoxide (≥97%, Sigma Aldrich) and 2-propanol (99.5%, Sigma Aldrich). The samples were then heated to 600 °C at a heating rate of 1.5 °C/min and calcined for 12 h. The specific surface area of bare ceria was determined to be 61.4 m²/g by nitrogen physisorption experiments and the use of the Brunauer–Emmett–Teller (BET) method, yielding vanadium loadings of 2.83 V/nm² (2.32 wt% V_2O_5), 1.36 V/nm² (1.11 wt% V_2O_5), and 0.57 V/nm² (0.47 wt% V_2O_5), respectively. Higher vanadium loadings were not considered since vanadia crystallites were shown to be present at loadings >2.9 V/nm².[43] The resulting catalyst powders were subsequently pressed at a pressure of 2000 kg/m² for 20 s, ground and then sieved using a combination of sieves to obtain 200–300 µm particles.

2.2. Catalytic Testing

Catalytic testing was performed in a CCR 1000 reaction cell (Linkam Scientific) equipped with a membrane pump to allow for operation in a fluidized-bed mode, using 70 mg of catalyst. The samples were first dehydrated in 12.5% O_2/He for 1 h at 550 °C, subsequently cooled to 50 °C, exposed to 12.5% CO_2/12.5% C_3H_8/He with a total flow rate of 40 ml$_n$/min, and then heated in 45 °C steps up to 550 °C, staying at each temperature for 1 h. The direct dehydrogenation of propane (DDH) was tested in the same way but no CO_2 was added to the gas feed. The gas-phase composition was analyzed continuously using a gas chromatograph (GC, Agilent Technologies 7890B) equipped with a PoraPlotQ and a Molsieve column. The separated gases were analyzed by a thermal conductivity detector (TCD) and a flame ionization detector (FID) in series. The set-up is connected through a twelve-way valve. One chromatogram is measured every 29 min, resulting in two chromatograms for each temperature, which were averaged. The pressure before and after the GC was monitored to correct the

6

detected areas for pressure fluctuations. To analyze the reaction network, the temporal evolution of the reactivity behavior was analyzed at 550 °C. The samples were first dehydrated in 12.5% O_2/He for 1 h, then treated consecutively in 7.5% H_2/Ar, 12.5% CO_2/He, 12.5% CO_2/12.5% C_3H_8/He, and finally regenerated in 12.5% CO_2/He (for 2 h for each gas phase), respectively. The reaction products were analyzed and time-dependent ratios between different products were calculated to determine the relative contributions of the different reaction pathways to the overall product distribution.

2.3. X-Ray Diffraction

X-ray diffraction patterns were recorded on an Empyrean system (Malvern Panalytical) in Bragg–Brentano geometry using CuK_α radiation and a PIXcel[1D] detector. For in situ analysis, 90 mg of catalyst was placed in an XRK 900 reaction chamber (Anton Paar) equipped with a NiCr-NiAl thermocouple to measure the temperature directly next to the sample surface. The samples were first dehydrated in 12.5% O_2/N_2, cooled to room temperature, and subsequently treated in 12.5% CO_2/12.5% C_3H_8/He. The samples were then heated in 100 °C steps up to 750 °C, with an equilibration time of 30 minutes at each temperature, and measured for 10 minutes in a *2θ* range from 20-70° with a step-width of 0.025° for each step. A Rietveld analysis was performed for the diffraction pattern recorded at 750 C° using the TOPAS software together with reference structures from the ICSD database. The background was corrected by using a Chebychev function with ten polynomials.

2.4. UV-Raman Spectroscopy

UV-Raman spectroscopy was performed at an excitation wavelength of 385 nm generated by a laser system based on a Ti:Sa solid-state laser pumped by a frequency-doubled Nd:YAG laser (Coherent, Indigo). The fundamental wavelength was frequency doubled to 385 nm using a LiB_3O_5 crystal. The light was focused onto the sample, and the scattered light was collected by a confocal mirror setup and focused into a triple-stage spectrometer (Princeton Instruments, TriVista 555).[43] Finally, the Raman contribution was detected by a charge-coupled device (CCD, 2048 × 512 pixels) cooled to –120 °C. The spectral resolution of the spectrometer was 1 cm^{-1}. For Raman experiments, 70 mg of catalyst was placed in a CCR 1000 reactor (Linkam Scientific

Instruments) equipped with a CaF_2 window (Korth Kristalle GmbH). A fluidized bed reactor was employed to avoid laser-induced damage, allowing the use of a laser power of 9 mW at the location of the sample. Data processing included cosmic ray removal and background subtraction. The spectra were further analyzed by a least-squares fitting analysis using four Lorentzian functions (see Figure S5). Operando spectra were measured after dehydration for 1 h in 12.5% O_2/He and further pre-treatment in 7.5% H_2/Ar and 12.5% CO_2/He at 550 °C to start from a partially oxidized state. Afterwards, the catalyst was exposed to reactive conditions (12.5% CO_2/12.5% C_3H_8/He) and regenerated under oxidizing conditions (12.5% CO_2/He) with a total flow rate of 40 ml_n/min for each gas phase. The spectra were further analyzed by a least-squares fitting analysis using Lorentzian functions after normalization to the F_{2g} peak of ceria.

2.5. Vis-Raman Spectroscopy

Visible (Vis) Raman spectroscopy was performed at 514 nm excitation, emitted from an argon ion gas laser (Melles Griot). The light was focused onto the sample, gathered by an optical fiber and dispersed by a transmission spectrometer (Kaiser Optical, HL5R). The dispersed Raman radiation was subsequently detected by an electronically cooled CCD detector (–40 °C, 1024 × 256 pixels). The spectral resolution was 5 cm^{-1} with a wavelength stability of better than 0.5 cm^{-1}. For Raman experiments, 70 mg of catalyst was filled into a CCR 1000 reactor (Linkam Scientific Instruments) equipped with a quartz window (Linkam Scientific Instruments). The laser power at the sample location was 4 mW. Data analysis of the Raman spectra included cosmic ray removal and an auto new dark correction. Operando spectra were measured after dehydration for 1 h in 12.5% O_2/He and further pre-treatment in 7.5% H_2/Ar and 12.5% CO_2/He at 550 °C to start from a partially oxidized state. Afterwards, the catalyst was exposed to reactive conditions (12.5% CO_2/12.5% C_3H_8/He) and regenerated under oxidizing conditions (12.5% CO_2/He) with a total flow rate of 40 ml_n/min for each gas phase. The spectra were normalized to the F_{2g} peak of ceria. The F_{2g} position was determined by a least-square fitting analysis. The nuclearity distribution was determined from the vanadyl peaks by performing a least-square fitting analysis using five Lorentzian functions at distinct spectral positions.[36]

2.6. Diffuse Reflectance UV-Vis Spectroscopy

Diffuse reflectance (DR) UV-Vis spectra were recorded on a Jasco V-770 UV-Vis spectrometer. Dehydrated $BaSO_4$ was used as the white standard. For each experiment, 90 mg of catalyst was placed in the commercially available reaction cell (Praying Mantis High Temperature Reaction Chamber, Harrick Scientific) equipped with transparent quartz glass windows. Operando spectra were measured after dehydration for 1 h in 12.5% O_2/He and further pre-treatment in 7.5% H_2/Ar and 12.5% CO_2/He at 550 °C to start from a partially oxidized state. Afterwards, the catalyst was exposed to reactive conditions (12.5% CO_2/12.5% C_3H_8/He) and regenerated under oxidizing conditions (12.5% CO_2/He) with a total flow rate of 40 ml_n/min for each gas phase. The band gap energies were determined using Tauc plots, while the reduction peak area was quantified by a least-squares fitting analysis of the spectra using Gaussian-Lorentzian (70/30) product functions. Product functions were used to account for the large contribution of natural line broadening to the overall line-shape (Lorentzian), caused by the short life-time of the electronically excited states.[44]

2.7. Diffuse Reflectance Infrared Fourier Transform Spectroscopy

Diffuse reflectance infrared Fourier transform spectroscopy (DRIFTS) was performed using a Vertex 70 spectrometer (Bruker). A liquid nitrogen-cooled mercury cadmium telluride (MCT) detector was used, operating at a resolution of 1 cm^{-1}. Dehydrated potassium bromide was employed as an infrared transparent sample for the background spectrum. For each experiment, 90 mg of catalyst was placed in the commercially available reaction cell (Praying Mantis High Temperature Reaction Chamber, Harrick Scientific) equipped with transparent KBr windows.

For quasi in-situ measurements the samples were treated in 12.5% O_2/He, 7.5% H_2/Ar, 12.5% CO_2/He, 12.5% CO_2/12.5% C_3H_8/He, and finally regenerated in 12.5% CO_2/He for 1 h at 550 °C, respectively. For each gas phase the sample was cooled rapidly to room temperature (200 °C/min) in pure helium in the Linkam reactor for the measurement before heating it back to 550 °C for the next gas treatment.

Data processing consisted of background removal by subtracting a baseline formed by 12 anchor points. To quantify the adsorbate peaks in the Ce-OH region, the spectra were fitted using Lorentzian functions employing the Levenberg-Marquardt

algorithm implemented in OriginLab 2022b. Finally, to quantify the total amount of carbonates on the surface, the region between 1200 and 1800 cm^{-1} was integrated.

3. Results and Discussion

First, the catalytic activity of the sample will be discussed. Due to the plethora of possible reactions over the catalyst, an analysis of the reaction network will be performed, followed by an operando and quasi in situ spectroscopic investigation. Since the samples used for this study are identical to those in our previous studies on the VO_x/CeO_2 system, structural characterization will not be performed in this study. For the detailed characterization results, please refer to our previous work.[33,36,45]

3.1. Activity Data and Reaction Network Analysis

Figure 1 shows the temperature-dependent propane conversions and propylene selectivities of bare ceria and vanadia-loaded samples during ODH (12.5% CO_2/12.5% C_3H_8/He) and DDH conditions (12.5% C_3H_8/He) between 225 and 550 °C. Exemplary product amounts of CO and ethylene produced during the ODH and DDH in the same temperature range are given in the SI (see Figure S1).
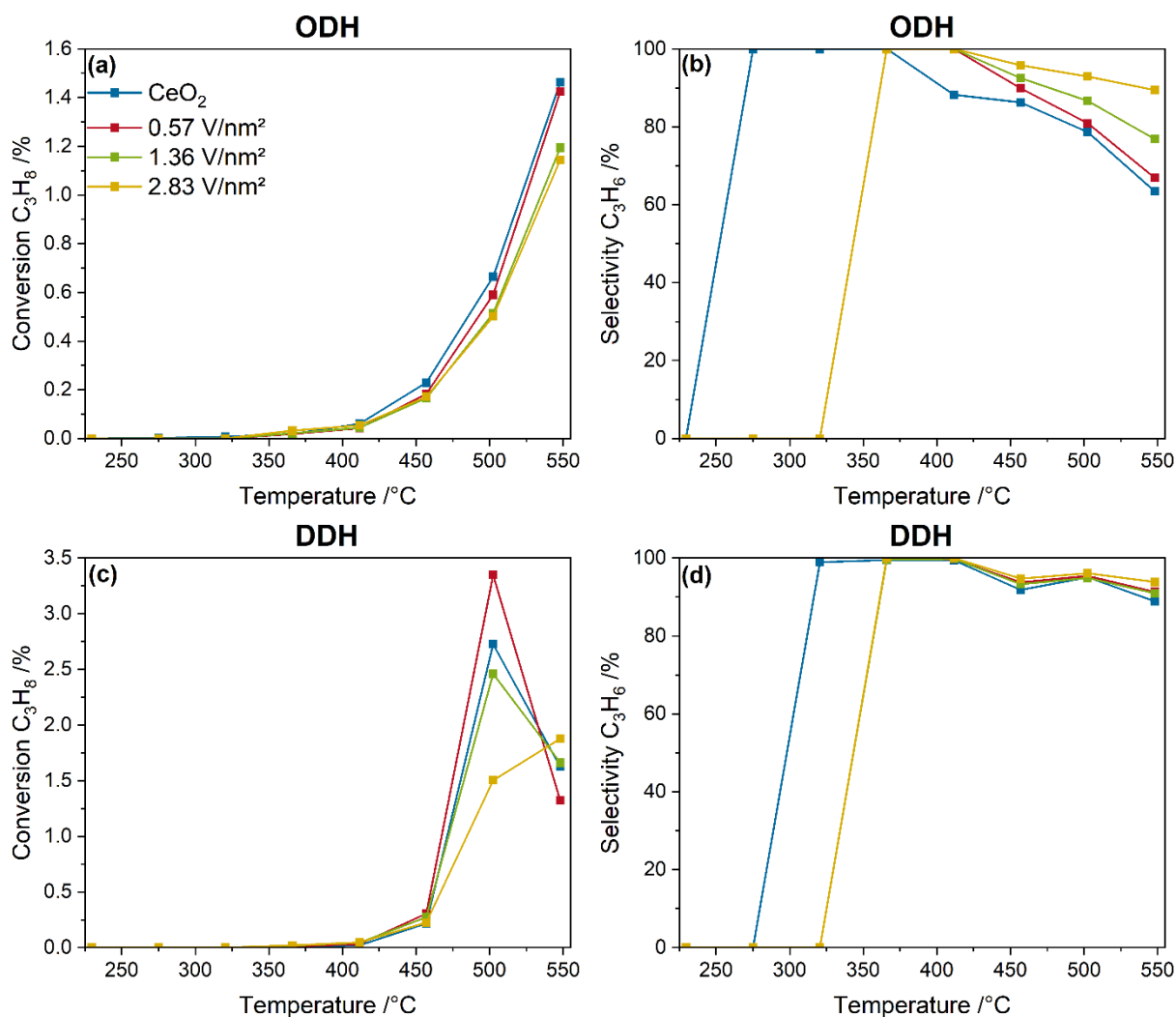
Figure 1: Comparison between the temperature-dependent conversions **(a, c)** and selectivities **(b, d)** of bare ceria and vanadia-loaded samples between 225 and 550 °C under ODH (12.5% CO_2/12.5% C_3H_8/He) and DDH (12.5% C_3H_8/He) conditions.

As shown in Figure 1a, the temperature-dependent propane conversion of bare ceria and vanadia-loaded samples is characterized by an exponential increase. The background conversion caused by the Linkam reactor is already removed from the data presented. Ceria shows the highest conversion at all temperatures, while the conversion for the vanadia-loaded samples decreases with increasing amount of vanadia. However, the conversion stays below 1.5 % for all samples at all temperatures. The propylene selectivities, shown in Figure 1b, start at 100 % for low temperatures where the conversions are < 0.1 %, and start to decrease at 365 °C for ceria, gradually decreasing to 60 %. The propylene selectivities of the vanadia-loaded samples stay above those of bare ceria and increases with the vanadia loading for all temperatures. Most of these differences in the propylene selectivities are likely caused

by the different conversion, which show an inverse trend. Since the selectivities are values between 65 and 90 % at 550 °C, this temperature was chosen for the spectroscopic investigation of the system to maximize the conversions, thus enhancing the visibility of spectroscopic changes. The catalytic performance of the VO_x/CeO_2 system compares rather poorly to other supported vanadia catalysts during the CO_2-assisted propane ODH. The activity is similar to VO_x/SiO_2 catalysts for bare ceria and lower vanadia loadings, but better for the highest loading, while the selectivity is slightly lower.[23] In comparison to VO_x/In_2O_3 it reaches only ~50 % of the conversion[21,22] and compared to VO_x/TiO_2 about 30 %.[24] However, the VO_x/CeO_2 system is still of great interest to obtain a better understanding of supported VO_x catalysts in the CO_2-assisted propane ODH in general. It might also be of use for the development of multi-oxide catalysts, as was done for the VO_x/SiO_2 system by adding WO_x, significantly improving the catalytic activity.[20]

In comparison, Figure 1c shows the propane conversion of bare ceria and the vanadia-loaded samples under DDH conditions. The conversion starts to be detected at significantly higher temperatures than under ODH conditions, then shows a stronger increase for all samples at 500 °C to 1.5-3.5 %, and finally decreases sharply. This effect is attributed to the depletion of ceria lattice oxygen, giving a first important hint towards involvement of ceria lattice oxygen in the reaction mechanism, while CO_2 is required to stabilize the catalytic performance. The propylene selectivities under DDH conditions, shown in Figure 1d, also show significantly higher values, staying above 85 % for all temperatures. This emphasizes that the DDH reaction exhibits significantly higher conversions and selectivities but has no stable performance. This is further emphasized by the molar product amounts of CO and ethylene for both reaction conditions (see Figure S1). First, the amount of CO produced during ODH conditions is increased by 1.5 orders of magnitude. The formation of CO during DDH conditions indicates that some total oxidation or propane dry reforming occurs during the DDH. However, the significantly higher amount during ODH conditions indicates the consumption of CO_2 towards CO, possibly regenerating the ceria lattice, thereby stabilizing the catalytic activity. A similar behavior can be observed for ethylene that is one order of magnitude higher under ODH conditions. This indicates that much more cracking occurs under ODH conditions, which is likely to be one reason for the lower propylene selectivities. Comparison between the ODH and DDH data reveals that introduction of CO_2 into the gas feed diminishes the reaction performance significantly

but is required for a stable performance of VO_x/CeO_2 catalysts. Therefore, only ODH conditions will be considered in the following.

Figure 2 shows the influence of the pre-treatment conditions on the catalytic performance of the VO_x/CeO_2 system under ODH conditions. Two different pre-treatment conditions were tested. First, switching to ODH conditions directly from a fully oxidized catalyst (12.5% O_2/He), and second, ODH conditions after catalyst treatment in 12.5% O_2/He, 7.5% H_2/Ar and 12.5% CO_2/He, which ensures a catalyst in a pre-reduced state that is more representative of reaction conditions.
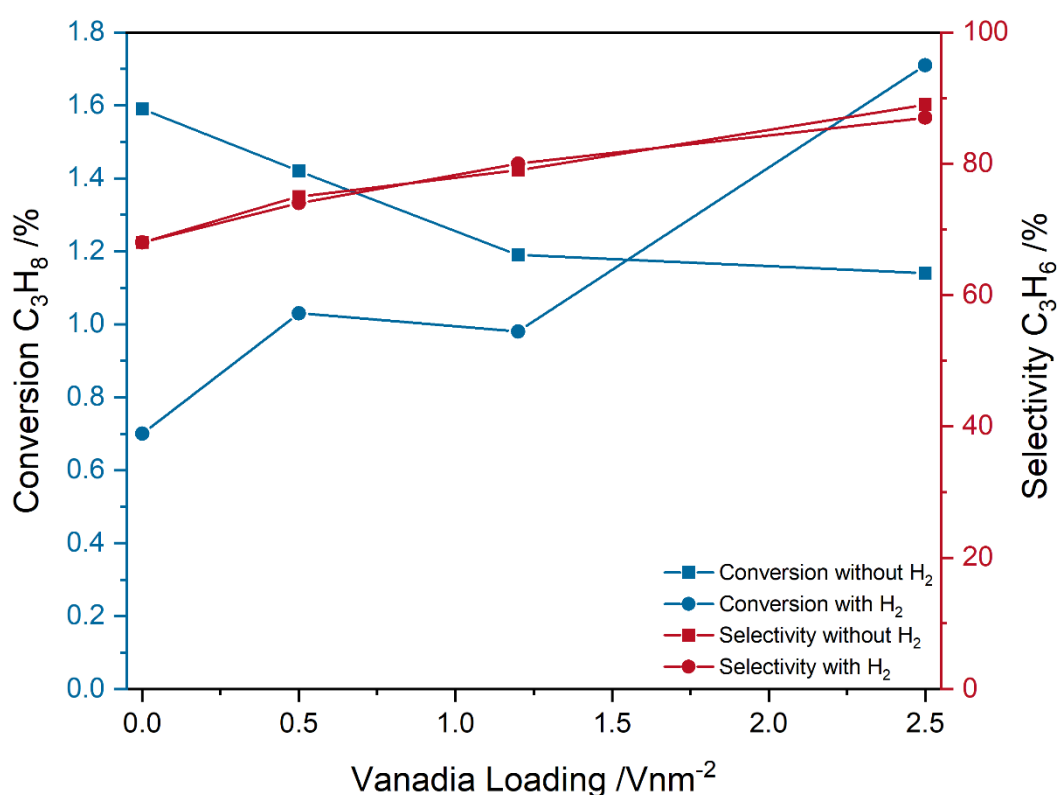
Figure 2: Comparison between the conversions and selectivities of bare ceria and vanadia-loaded samples after different pre-treatments (fully oxidized with O_2 and partially reduced with H_2 and subsequently regenerated with CO_2) under ODH conditions (12.5% CO_2/12.5% C_3H_8/He) at 550 °C.

As can be seen in Figure 2, the pre-treatment conditions have no significant influence on the measured propylene selectivities. However, the loading-dependent propane conversions are significantly influenced. The conversions decrease from bare ceria to the 2.83 V/nm² sample for only oxidative pre-treatment conditions, but increase when the reaction is started from a partially reduced state. The propane conversion of bare ceria decreases from 1.6 to 0.7 %, while the conversion of the 2.83 V/nm² sample

increases from 1.1 to 1.7 %, which is the highest conversion overall. The conversion of the 0.57 and 1.36 V/nm² samples is similar but is slightly lower for the 1.36 V/nm² sample. When starting from a partially reduced state, both the conversion and selectivity increase with increasing vanadia loading, which indicates that the vanadia loading influences the selectivity not by only changing the conversion but by an actual change in the reaction pathway. The influence of the pre-treatment conditions on the mechanism is therefore of relevance to understand the changes in the conversion trends.

To understand the reaction network in more detail, Figure 3 depicts the analysis of the reaction products based on the obtained product distributions shown in the SI (see Figure S2), including the propane and CO_2 conversions, the propylene selectivity, and the C_3H_6/CO, C_2H_4/H_2, and CO/X_{CO2} ratio, as indicators for the ODH, cracking and propane dry reforming (PDR) reactions, respectively. In addition, the SI shows the CO/H_2 ratio, as an indicator for the contribution from the reverse water-gas shift reaction (RWGSr, see Figure S3).
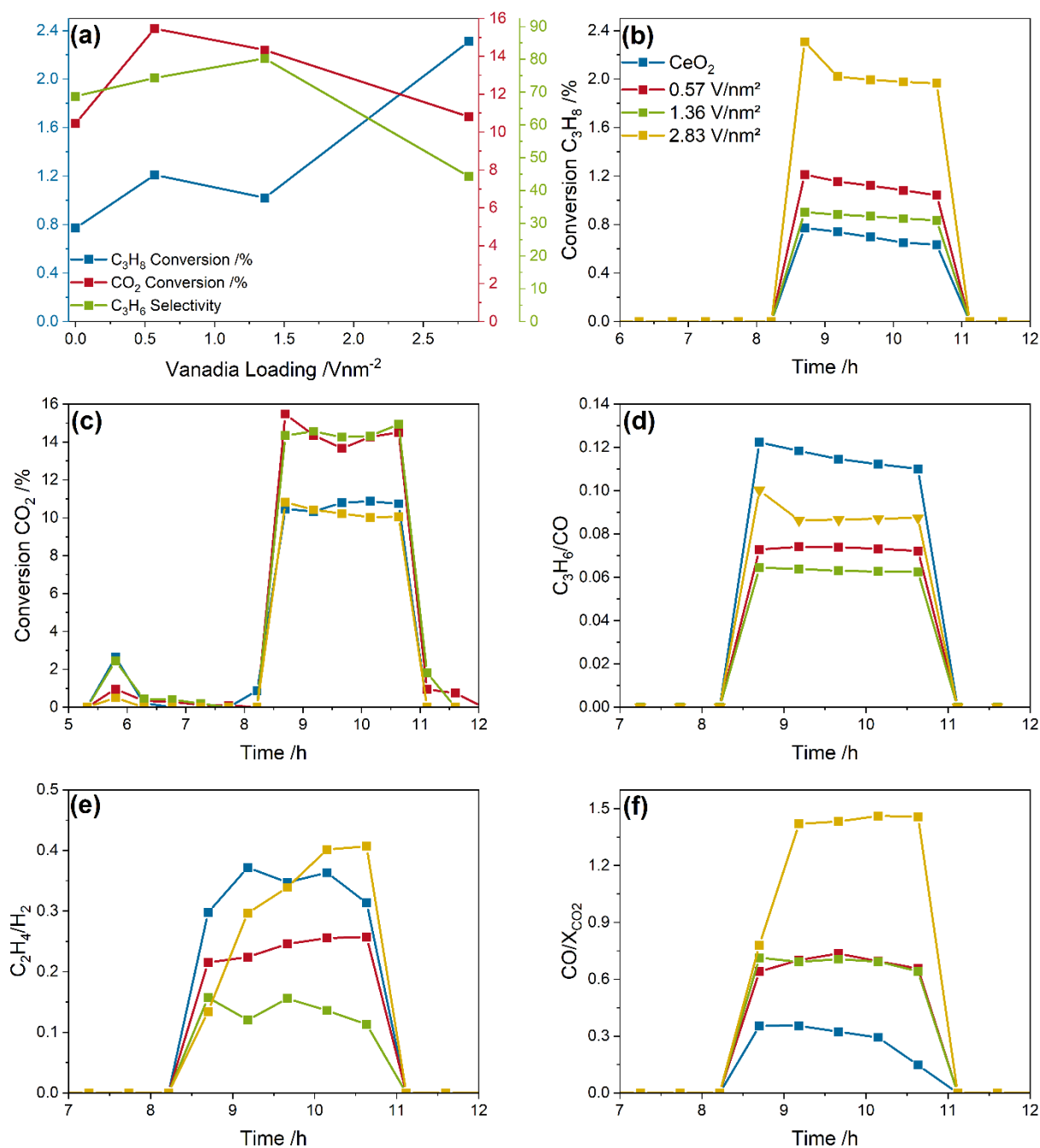
Figure 3: Analysis of the CO_2-assisted propane ODH reaction network over bare ceria and vanadia-loaded samples: **(a)** Loading-dependent propane and CO_2 conversions and propylene selectivities, **(b)** time-dependent propane and **(c)** CO_2 conversions, and time-dependent **(d)** propylene/CO, **(e)** ethylene/H_2 and **(f)** CO/converted CO_2 ratio.

Figure 3a gives an overview of the initial (first 30 minutes of the reaction phase) propane and CO_2 conversions and the propylene selectivity. The propane conversion slightly increases from 0.8 % for bare ceria to 1.2 and 1 % for the 0.57 and 1.36 V/nm² samples but significantly increases to 2.3 % for the 2.83 V/nm² sample. The selectivity shows a linear increase from 65 to 80 % with increasing vanadia loading up to 1.36

16

V/nm². For the 2.83 V/nm² sample, the propylene selectivity drops significantly to 42 % concurrently to the sharp increase in propane conversion observed. The selectivity values include the cracking and PDR reaction determined in the discussion below. Importantly, the total amount of propylene produced stays constant for all four samples (see Figure S2). The selectivity decrease caused by propane total oxidation is not included, since the exact amount cannot be determined due to the different reaction routes in which CO and CO_2 are involved. In comparison, the CO_2 conversion (10-16 %) is significantly higher than the propane by about one order of magnitude, indicating the occurrence of side reactions or processes unrelated to the ODH reaction. Since the stoichiometry of propane and CO_2 during CO_2-assisted propane ODH is 1:1, the difference between the propane and CO_2 conversion can be understood as the total amount of side reactions occurring. However, since different reaction pathways can be responsible for CO_2 consumption and CO formation, this is only a qualitative trend. The time-dependent propane conversions (see Figure 3b) change only slightly over time, indicating a stable reaction performance within the investigated time frame. Only the 2.83 V/nm² sample shows a slightly higher conversion with in the first 30 minutes (2.3 %) compared to the stable conversion of 2 % afterwards, which might be indicative of surface species that are highly reactive towards propane but cannot be regenerated during reaction, leading to a stable but lowered conversion. This is different from the reaction behavior of VO_x/TiO_2 catalysts under the same reaction conditions, which exhibited a significant deactivation behavior unless more CO_2 was present.[24]

Figure 3c depicts the time-dependent CO_2 conversion of the catalysts, showing only small variations. The small consumption of CO_2 at ~6 h is caused by the regeneration of the material after the reduction in 7.5% H_2/Ar and is indicative of a partial regeneration of VO_x/CeO_2. It is particularly notable that the trend in the CO_2 conversions does not follow that of the propane conversions, as bare ceria and the 2.83 V/nm² sample exhibit the lowest CO_2 conversions. Therefore, the CO_2 conversion goes through a maximum with increasing vanadia loading, indicating that CO_2 is used in other processes than the ODH reaction that are, in part, not related to propane conversion due to the different loading-dependent reactivity behavior towards propane and CO_2.

To disentangle the observed reactivity behavior, the C_3H_6/CO, C_2H_4/H_2, and CO/X_{CO2} ratio is formed from the molar product distributions shown in the SI (see Figure S2), serving as an indicator for the ODH, cracking and propane dry reforming

(PDR) reactions, respectively (see Figures 3d-f). The RWGSr is probed by the CO/H_2 ratio shown in Figure S3. The C_3H_6/CO ratio decreases from a value of 0.12 for bare ceria to a value of 0.06 for the 1.36 V/nm^2 sample before increasing again for the 2.83 V/nm^2 sample. If the ODH reaction was the only relevant reaction, CO and propylene would be produced in a 1:1 ratio. The observed ratios, however, clearly show, that much more CO is produced than would be expected for the ODH reaction, pointing to additional reaction pathways occur like PDR and total oxidation. It is also apparent, that the relative amount of produced propylene goes through a minimum for the 1.36 V/nm^2 sample, which might be caused by the changes in nuclearities of surface vanadia species.[36]

Figure 3e shows the time-dependent C_2H_4/H_2 ratio, which is an indicator for the prevalence of cracking. The values range between 0.13 for the 1.36 V/nm^2 sample at the low and values of 0.4 for the bare ceria and 2.83 V/nm^2 sample at the high end, indicating that much more H_2 is produced than ethylene. During the cracking reaction, propane is consumed and ethylene, methane and H_2 are produced in a stoichiometric ratio.[46,47] Therefore, the higher amount of detected hydrogen is indicative of further side reactions, e.g. PDR, which can produce hydrogen and also CO, which would additionally explain the observed C_3H_6/CO ratios. The loading-dependent trend in the ratios is similar to that observed in Figure 3d, that is, much more CO and H_2 is detected than ethylene and propylene. This behavior points to a significant proportion of PDR occurring, while the amount of cracking seems to be negligible. Notably, the C_2H_4/H_2 ratio increases sharply for the 2.83 V/nm^2, which may indicate structural changes favouring cracking over PDR.

To obtain further insight into the reactivity behavior of the VO_x/CeO_2 samples, Figure 3f shows the CO/X_{CO2} ratio, which is indicative of the amount of PDR. Here, only the 2.83 V/nm^2 sample shows a value larger than one, which is indicative of PDR, since additional CO must be produced from propane. This is fully consistent with the observed propane conversions and propylene selectivities (see Figure 3a). The overall propylene yield therefore does not benefit from the increased propane conversion.[48] For the remaining samples, the ratio is below one, which indicates that more CO_2 is converted than CO is produced. The additional converted CO_2 will be used in other reactions like surface adsorbate formation or will be produced by total oxidation of propane. The other two samples are in between the behavior of bare ceria and the 2.83 V/nm^2 sample, with a value of almost one. This would typically indicate that mostly

the dehydrogenation reaction occurs. However, the much higher CO_2 conversion compared to propane and the very low C_3H_6/CO ratios indicate that significant amounts of CO_2 and CO need to be additionally produced to explain this behavior, which would be consistent with a mix of PDR, cracking and total oxidation. The total oxidation is especially well suited to produce these gases, since propane is converted to CO_x, consuming more lattice oxygen than selective oxidation. These need to be regenerated by additional CO_2 creating additional CO. Since the total oxidation can produce both CO and CO_2 but the regeneration of lattice oxygen can only lead to CO, this affects the CO/X_{CO2} ratio.

At last, Figure S3 shows the CO/H_2 ratio, which has been considered as an indicator of the ratio between ODH and DDH+RWGSr. However, due to many other pathways towards H_2 and especially CO, this becomes overlapped by other effects. This is reflected in the detected values, which vary between 5 and 30. Therefore, the two dehydrogenation pathways cannot be differentiated. Table S1 summarizes the carbon balances. The values range from 6.2 to 7.2 %, which is comparably low to reactions that create significant amounts of carbon, indicating that carbon formation on the catalyst surface is negligible.

In summary, the catalyst samples exhibit a detectable activity under 12.5% CO_2/12.5% C_3H_8/He conditions at 550 °C. While under DDH conditions higher activities and selectivities are observed, only the ODH conditions lead to a stable reaction behavior. Additionally, the pre-treatment conditions are of importance, and a consecutive pre-treatment in hydrogen and CO_2 facilitates the ODH reaction. Regarding the side reactions determined from the analysis of the reaction network, a nuclearity-dependent behavior is observed. Bare ceria shows the smallest contribution from PDR but has the highest prevalence of total oxidation. With increasing vanadia loading, the relative contribution from total oxidation of propane decreases while that of PDR increases. The 2.83 V/nm^2 sample shows the lowest conversion of CO_2 despite its higher propane conversion. This indicates the least prevalence of side reactions overall, despite its lower selectivity compared to the other samples, stemming from the high PDR rate. The total amount of consumed CO_2 can be used as an indicator for the total amount of side reactions, since cracking was determined to be negligible and the amount of dehydrogenation seems to stay constant.

3.2. Operando and In Situ Spectroscopic Analysis

To understand the reactivity behavior in more detail, the catalysts are investigated by employing different operando and in situ spectroscopies as well as diffraction. The overall structural characterization of the catalysts was performed in great detail previously and will not be discussed again here.[33,36] However, the relevant peaks of each spectrum will be briefly assigned for better readability and crucial information about the system will be given at the relevant points. For VO_x/CeO_2, selective resonance enhancement by multi-wavelength excitation can be achieved, by using 385 and 514 nm excitation, as described previously.[33] 385 nm UV excitation was used at the position of the band gap absorption of ceria, leading to a significant and selective intensity increase of ceria-related features, allowing for their dedicated analysis. 514 nm Vis excitation is used to enhance the vanadia-based features enabling the detection of the vibrational vanadyl fine structure related to the vanadia nuclearities.

To exclude the formation of crystalline $CeVO_4$ due to the elevated temperatures and reducing conditions, in situ XRD was performed under 12.5% CO_2/12.5% C_3H_8/He for the 2.83 V/nm^2 sample between room temperature and 700 °C. Samples with lower loadings were not investigated since $CeVO_4$ formation is favored at high vanadium contents.[34,39,40] Figure S4 shows that signals from $CeVO_4$ are only observable starting at 700 °C. Therefore, the formation of crystalline $CeVO_4$ has no relevance for the following study. However, the possibility of formation of nanodispersive $CeVO_4$ remains, which can be observed via Raman spectroscopy.[37,39]

Figure 4 depicts UV-Raman spectra (385 nm excitation) of bare ceria and the 1.36 V/nm^2 sample recorded under different gas conditions at 550 °C. The spectra were normalized to the F_{2g} peak. Here, a selective intensity enhancement of the ceria peaks is expected due to resonance effects caused by the absorption of ceria. The observed intensity changes between the spectra recorded during initial CO_2 and ODH conditions were quantified by a peak-fitting analysis and the results are summarized in Figures 4c and d. The UV-Raman spectra for the 0.57 and 2.83 V/nm^2 sample are given in the SI (see Figure S5). An exemplary fit of the UV-Raman spectrum of the 1.36 V/nm^2 sample under 12.5% O_2/He is shown in the SI (see Figure S6).
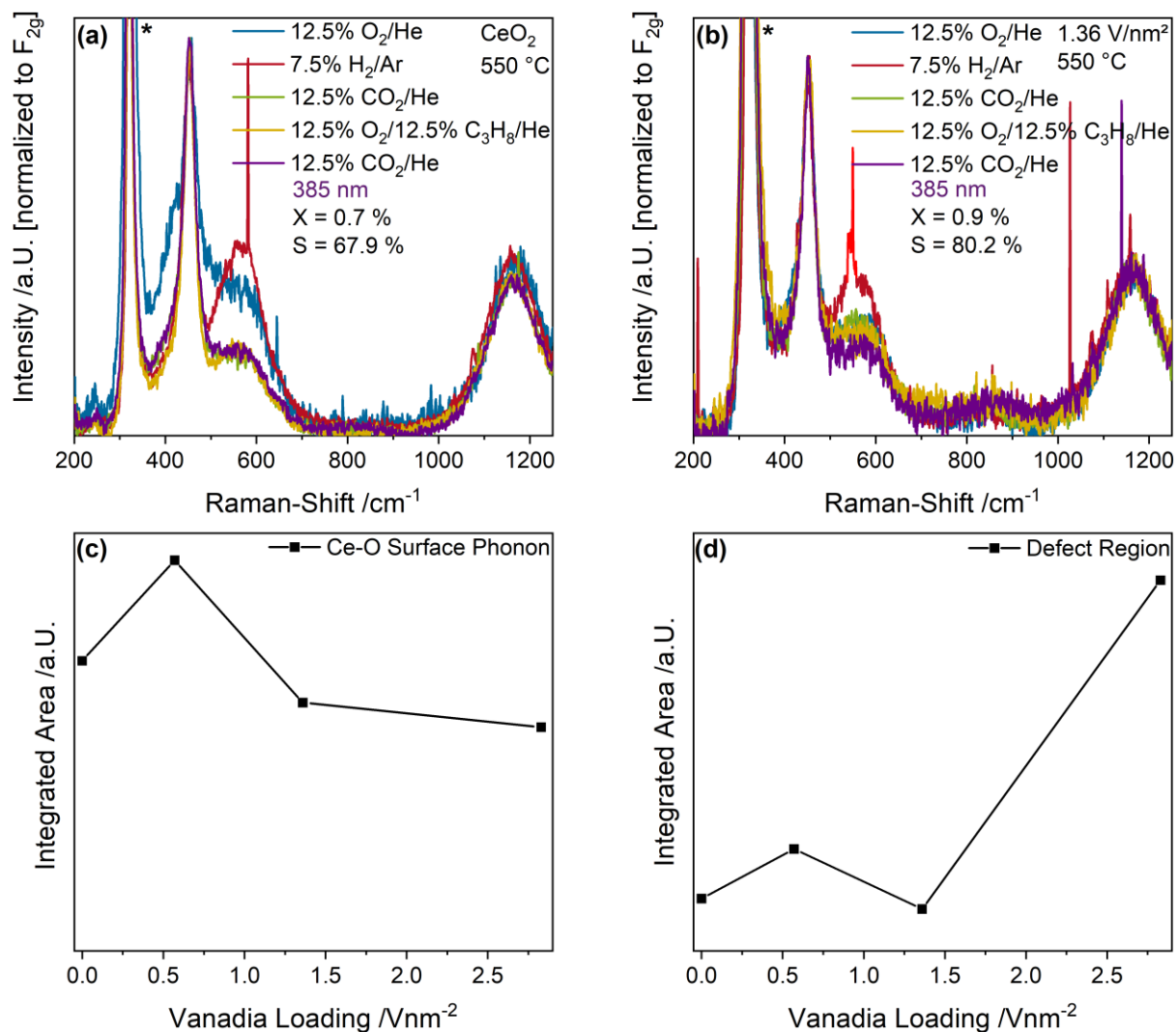
Figure 4: UV-Raman spectra (385 nm excitation) of **(a)** CeO_2 and **(b)** the 1.36 V/nm² sample recorded under the indicated gas feeds at 550 °C. Spectra were normalized to the F_{2g} peak and the CaF_2 signal is marked with an asterisk. Quantification of the **(c)** Ce-O surface phonon and **(d)** defect region changes between spectra recorded under 12.5% CO_2/He and 12.5% CO_2/12.5% C_3H_8/He.

The UV-Raman spectra of bare ceria under different gas conditions are characterized by peaks at 250, 405, 455, 590 and 1170 cm^{-1}, which are caused by the longitudinal and transversal Ce-O surface phonon, the F_{2g} mode, the defect region and the 2LO peak, respectively (see Figure 4a).[42,49] At the 250 cm^{-1} position, the longitudinal surface phonon is overlapped by the 2TA signal of ceria. The reduction and re-oxidation behavior of the sample was discussed in detail before.[45] Briefly, under reducing conditions, the defect region increases in intensity, while the surface Ce-O oxygen signals show a decrease, consistent with the consumption of lattice oxygen and formation of vacancies. When CO_2 is introduced for re-oxidation after H_2/Ar

treatment, the surface phonon regenerates very slightly, while the defect region decreases in intensity significantly below the initial intensity under O_2 conditions. This was previously explained by the formation of carbonates which block surface oxygen sites, while regenerating vacancies. Upon switching to ODH conditions, similar changes as upon the switch from O_2 to H_2 can be observed but to a significantly smaller extent, which are regenerated in the second CO_2 containing feed. This indicates that under reaction conditions some additional surface oxygen can be used despite carbonate formation, or alternatively that surface carbonates can act as an oxygen source for the reaction.

As shown in Figure 4b, UV-Raman spectra of the 1.36 V/nm² sample at 550 °C under different gas feeds do not exhibit additional peaks compared to the spectra of bare ceria. A similar behavior was previously observed for the VO_x/TiO_2 system under the same gas feeds and at the same temperature.[24] It is caused by the high temperature decreasing the overall intensity together with the increased absorption of the support material which leads to resonance enhancement of the support and can diminish the vanadia signal. Comparison of all samples reveals the same structural dynamics when switching to reaction conditions, the extent of which decreases with increasing amounts of vanadia. This might be caused by vanadia blocking surface oxygen sites since vanadia is anchored to these sites, and as a consequence, less carbonates can be formed, which seems likely since all changes in the spectra are caused by ceria lattice oxygen. Notably, neither for bare ceria nor for the 1.36 V/nm² sample a signal of the D- and G-bands originating from amorphous carbon is observed, consistent with the low carbon balances detected by GC (see Table S1).

To fully understand the observed behavior, the changes in the UV-Raman spectra between the initial CO_2 exposure and ODH conditions were quantified by a fitting analysis. An exemplary fit is shown in the SI (see Figure S6). The results for the transversal surface phonon at 405 cm^{-1} and the defect region at 590 cm^{-1} are shown in Figure 4c and d, respectively. The intensity difference of the Ce-O surface phonon increases from bare ceria to the 0.57 V/nm² sample and then decreases again for higher vanadia loadings. The observed maximum for the 0.57 V/nm² sample is in agreement with the increased propane and CO_2 conversion at this loading, the latter representing the highest overall amount of CO_2 being converted. The decrease at a loading of 1.36 V/nm² can be explained by the lower conversion of propane as well as the decreased prevalence of the total oxidation reaction. It stays almost constant

afterwards, since the total oxidation rate decreases again, while the PDR rate increases sharply. Overall, the behavior of the Ce-O surface phonon indicates that the surface may be mostly deactivated by CO_2 due to carbonate formation caused by the pretreatment, but that the remaining surface oxygen atoms can still participate in the reaction and seem to provide the oxygen for all occurring reactions, correlating with the overall conversion of all reactants.

Figure 4d shows the corresponding intensity changes of the defect region, which correlate well with the propane conversion, indicating that the conversion of propane leads to the formation of new defects in the material, which occurs concurrently with the consumption of Ce-O surface oxygen. However, the determined trends are very different: while the Ce-O surface phonon intensity changes correlate with the conversion of all molecules, the defect region only correlates with the propane conversion. Therefore, some reactions might lead to the consumption of clean surface Ce-O oxygen without vacancy formation, i.e. carbonate/formate formation, further emphasizing its importance. It is apparent that newly created vacancies are relevant in the conversion of propane but might be regenerated by CO_2, making them unavailable for further propane conversion due to possible adsorbate formation. This will be discussed in more detail in the DIRFTS section of this manuscript (see Figure 8 and discussion). In addition, the defect region may be influenced by the presence of monomeric vanadia species due to their known interaction with ceria surface vacancies.[33,38,50] These would exhibit the most significant effect at low loadings due to their prominence, which is discussed in more detail below (see Figure 6 and discussion) .

To investigate the changes in ceria and vanadia structure in more detail Figure 5 shows Vis-Raman spectra (514 nm excitation) of bare ceria and the 1.36 V/nm² sample recorded under different gas conditions at 550 °C. At this wavelength a selective intensity enhancement of the vanadia-related signals is expected due to resonance conditions. The F_{2g} shift and the change in hydride area between the initial CO_2 and ODH conditions were quantified by a peak-fitting analysis and integration, respectively, (for details see experimental section), as shown in Figures 5c and d. The Vis-Raman spectra of the 0.57 and 2.83 V/nm² samples are given in the SI (see Figure S7).
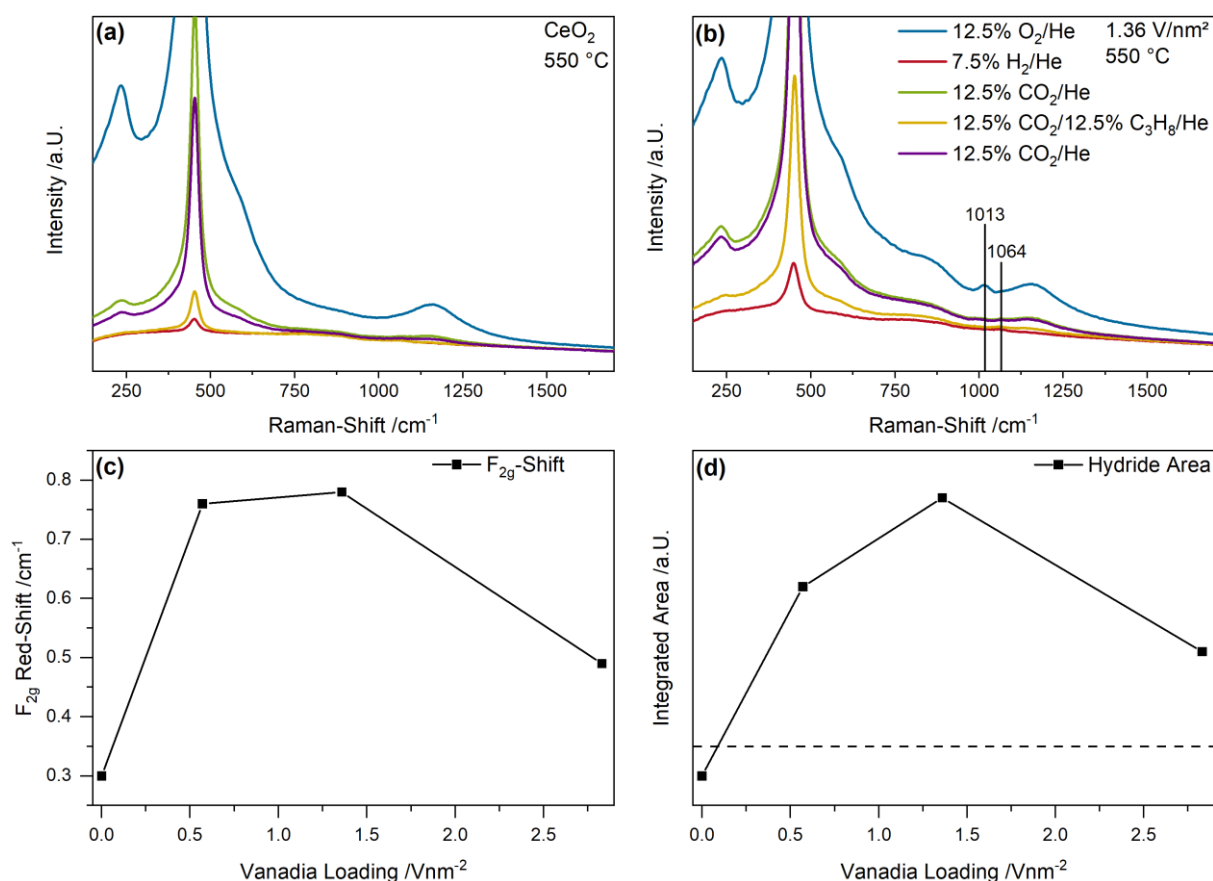
Figure 5: Vis-Raman spectra (514 nm excitation) of **(a)** bare ceria and **(b)** the 1.36 V/nm² samples under different gas feeds recorded at 550 °C. **(c)** The F_{2g} shift and **(d)** the hydride areas were determined by fitting and integration. The dashed line in panel d indicates no intensity change. For details see text.

Figure 5a shows the Vis-Raman spectra of bare ceria under different gas feeds at 550 °C. The spectrum under oxidizing conditions generally exhibits the same peaks observed in the UV-Raman spectra but with different relative intensities. Here, as a result of the different reductive properties of the gas feeds and the high temperatures, the overall intensity of the spectra and the background varies significantly, hindering intensity trends to be clearly determined. However, the F_{2g} red-shift is a good indicator for subsurface/bulk reduction of ceria, caused by the formation of Ce^{3+} ions, which, due to their larger radius than Ce^{4+} ions distort the lattice, thus leading to a mode softening.[51] In addition, after the exposure to H_2, a peak at 1064 cm^{-1} can be observed that has previously been assigned to Ce-H bulk hydrides and may be of importance regarding hydrogen transfer during the reaction.[45,52]

In comparison, the Vis-Raman spectra of the 1.36 V/nm² sample show similar changes with respect to the F_{2g} position and the Ce-H peak at 1064 cm^{-1} (see Figure 5b). In

addition, the fine structure of the V=O stretching vibration is detected between 1000-1050 cm^{-1}, showing a blue-shift of the maximum with increasing vanadia loading (see Figure 6a), allowing for the discrimination between different nuclearities (see Figure 6b).[33,35,37,53] The vanadyl peak decreases to zero under both reductive gas feeds but is regenerated in the first and second CO_2 containing atmosphere, indicating its participation in the reaction. However, as previously shown, depending on the nuclearity, only some vanadia species fully regenerate to V^{5+} species, which are often described as the catalytically most active species.[41] Since V^{4+} and V^{3+} species cannot be observed in Raman spectroscopy due to their small scattering cross sections,[54–56] these species will be discussed in the UV-Vis section (see Figure 7 and discussion). The vanadyl fine structure will also be discussed in more detail below (see Figure 6 and discussion).

The F_{2g} shift between the initial CO_2 exposure and the subsequent ODH conditions serves as an indicator for the ceria reduction upon reaction (see Figure 5c). The F_{2g} shifts range between a minimum of 0.3 cm^{-1} for bare ceria, and a maximum of 0.75 and 0.8 cm^{-1} for the 0.57 and 1.36 V/nm² samples, while the 2.83 V/nm² sample is characterized by a shift of 0.5 cm^{-1}. These values are comparably small,[45] which might be caused by the overall high oxygen mobility at this temperature, leading to an additional regeneration route via diffusion of bulk oxygen.[57] The observed behavior indicates that the participation of ceria lattice oxygen varies significantly with the vanadia loading. It correlates well with the conversion of all reactants with a significant increase between bare ceria and the 0.57 and 1.36 V/nm² samples, as observed for the propane and CO_2 conversions, indicating that ceria lattice oxygen is an important driver for the occurring reactions. In comparison, the 2.83 V/nm² sample shows a significantly different behavior. Despite it showing similar conversions of both propane and CO_2 as the other samples the F_{2g} red-shift decreases, which suggests that ceria lattice oxygen is replaced as the active oxygen site by vanadia oxygen, located in oligomeric vanadia species present primarily at higher loadings. Such a change in active site would also explain the sudden shift in reactivity behavior when the loading is increased from 1.36 to 2.83 V/nm².

Finally, the intensity change in the region between 1050 and 1100 cm^{-1}, referred to as hydride area, was quantified by integration (see Figure 5d). The dashed line corresponds to no intensity change. Hence, for bare ceria, the amount of subsurface/bulk hydrides decreases from the initial CO_2 to the ODH conditions, while

a strong increase is observed for the 0.57 and 1.36 V/nm² samples that decreases again for the 2.83 V/nm² sample. These changes might be caused by the ability of vanadia to transfer hydrogen from propane to the ceria surface. Due to the high temperature at which the CO_2-assisted ODH is performed, a strong diffusion of hydrogen into the bulk, which was already observed at temperatures ~300 °C, is likely.[45] Overall, the observed intensity trend for the bulk hydrides is similar to the determined propylene selectivity, which might be one way by which vanadia increases the propylene selectivity since the hydrogen transfer from propane to ceria is increased, leading to the formation of bulk hydrides. This effect is not observed for bare ceria, indicating that it is caused by the presence of surface vanadia. However, bare ceria still exhibits a propylene selectivity of 65 %, also other routes towards selective oxidation must be operating. The amount of hydrides formed by the 2.83 V/nm² sample decreases significantly in line with the propylene selectivity, which indicates that in this case hydride formation plays only a minor role, further highlighting a nuclearity-dependent catalytic behavior. Therefore, the quantification of the nuclearity distribution is crucial to understand the reactivity behavior in more detail.

Figure 6a shows the vanadyl stretching region of the vanadia-loaded samples, compared to bare ceria as a reference, recorded during 12.5% O_2/He exposure using Vis-Raman spectroscopy (514 nm excitation), together with the results of peak-fitting analysis.
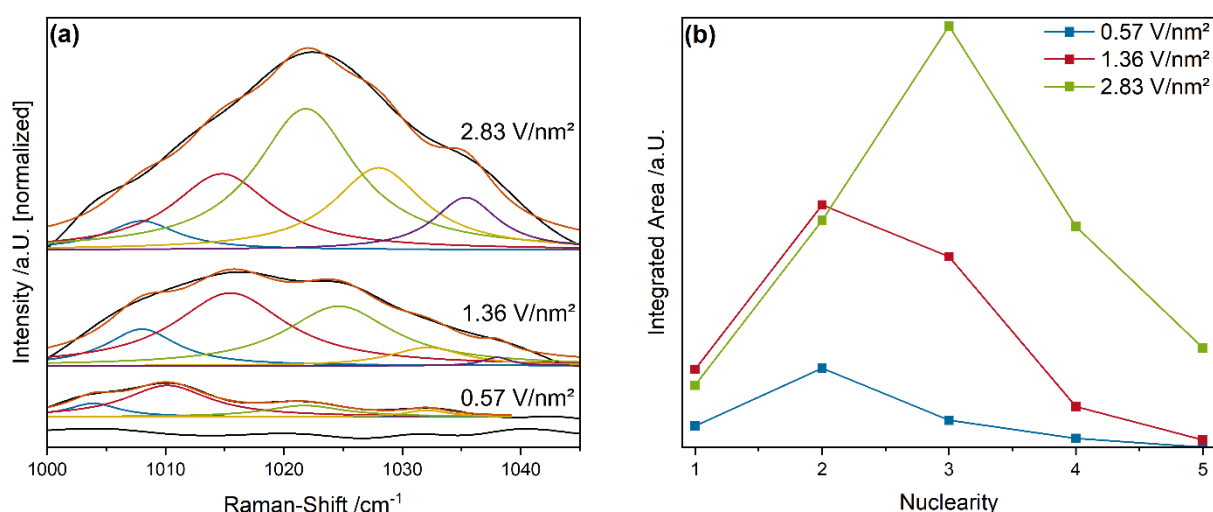
Figure 6: (a) Vanadyl region from the Vis-Raman spectra (514 nm excitation) between 1000 and 1045 cm^{-1} for bare ceria and vanadia-loaded samples during 12.5% O_2/He exposure at 550 °C together with

the results of a peak fit analysis. **(b)** Loading-dependent nuclearity distribution based on the analysis shown in **(a)**. For details see text.

In the following, it is assumed that the chain length does not change significantly with the gas phase, but only with the temperature through sintering.[58] As expected, bare ceria does not show any relevant signals in this region. For the VO$_x$/CeO$_2$ samples, the overall intensity increases with increasing vanadia loading, and while the maximum gradually shifts towards higher Raman-shifts. This behavior is caused by the increased prevalence of higher vanadia nuclearities, which facilitate dipole-dipole coupling between V=O groups of the same chain, leading to a blue-shift.[33,35,36] As a result, a fine structure can be observed with five separable peaks that are shifted with respect to each other in a small range, due to different local chemical environments.

Fitting this fine structure with five Lorentz functions at restricted positions allows to extract a nuclearity distribution for each loading (see Figure 6b). Note that this distribution differs from that obtained in our previous study at 275 °C using O$_2$ as the oxidizing agent,[33,36] due to the significantly different temperature. Since the clusters are more mobile on the ceria surface at 550 °C a higher relative contribution from stable nuclearities (i.e. trimers) is expected.[38,59] The 0.57 V/nm² sample exhibits the strongest contributions from dimers, with significant contributions from monomers and trimers and a small tetrameric contribution. No oligomeric nuclearities are present. In comparison, the 1.36 V/nm² sample shows significantly higher contributions from all nuclearities as expected for the higher loading. The relative contribution shifts in part from monomers to trimers, with dimers still being the largest fraction. However, the relative amount of each nuclearity is similar for both the 0.57 and 1.36 V/nm² samples, which is in good agreement with their similar reactivity behavior. Functions of the individual nuclearities during propane ODH were previously assigned based on ME-DRIFTS results.[36] Monomeric species can inhibit the oxygen mobility in the ceria lattice by interaction with oxygen vacancies due to their structural relaxation into them.[33] However, due to the elevated temperatures the mobility of the monomeric species is expected to increase the ability to move out of the vacancy.[38] Such facilitated mobility is consistent with the fact that the 0.57 V/nm² sample with the highest relative amount of monomers shows the strongest F$_{2g}$ shift as well as the overall highest amount of CO$_2$ conversion with significant total oxidation contributions. Trimeric species, due to their highly stable ring configuration, were determined to be observer species with no

27

catalytic function in the reaction.[36,38] Dimeric species were proposed to transfer hydrogen atoms from propane to the ceria surface, facilitating the propane ODH reaction by catalyzing the rate-determining step.[36] The amount of dimeric species present on the surface is similar to the amount of bulk hydrides and appears to be related, indicating that dimers might transfer hydrogen, resulting in bulk hydride formation, which seems to be crucial for the selective conversion of propane to propylene (see Figure 5d). The formation of additional Ce-OH groups from the transferred hydrogen might also be viable and will be discussed in more detail in the DRIFTS section (see Figure 8 and discussion).

The 2.83 V/nm² samples contains the highest amount of trimers and a lower relative contribution from the other nuclearities. In addition, it is the only sample that exhibits a significant fraction of oligomeric vanadia species. Besides dimers, oligomeric vanadia species were previously shown to transfer hydrogen from propane to the ceria surface during propane ODH.[36] Since the reactivity and spectroscopic behavior of this sample differs in many ways, including its higher PDR activity, less hydride formation and a shift from ceria to vanadia oxygen as the active oxygen site, oligomeric species seem to play an important role in this regard. Infact, oligomeric vanadia species in VO_x/CeO_2 during CO_2-assisted propane ODH behave similar to oligomeric species in VO_x/TiO_2 systems during regular propane ODH, where they deliver oxygen to facilitate the reactions but exhibit a lower propylene selectivity, indicating their high reducibility.[24] The V=O group of the oligomeric species might still be able to transfer the hydrogen, however, the target oxygen is not on the ceria surface. To investigate the reduced vanadia species and the bulk reduction of ceria in more detail, operando UV-Vis spectroscopy was performed.

Figure 7 shows UV-Vis spectra of bare ceria and the 1.36 V/nm² sample recorded under different gas conditions at 550 °C. Based on these spectra, the band gap energy shift and the change in reduction peak area between the initial CO_2 and the ODH conditions were determined (for details see experimental section), as shown in Figures 7c and d. UV-Vis spectra of the 0.57 and 2.83 V/nm² samples are given in the SI (see Figure S8), as well as an exemplary fit of a UV-Vis spectrum (see Figure S9). The exact fitting procedure was described in one of our previous studies in detail.[45]
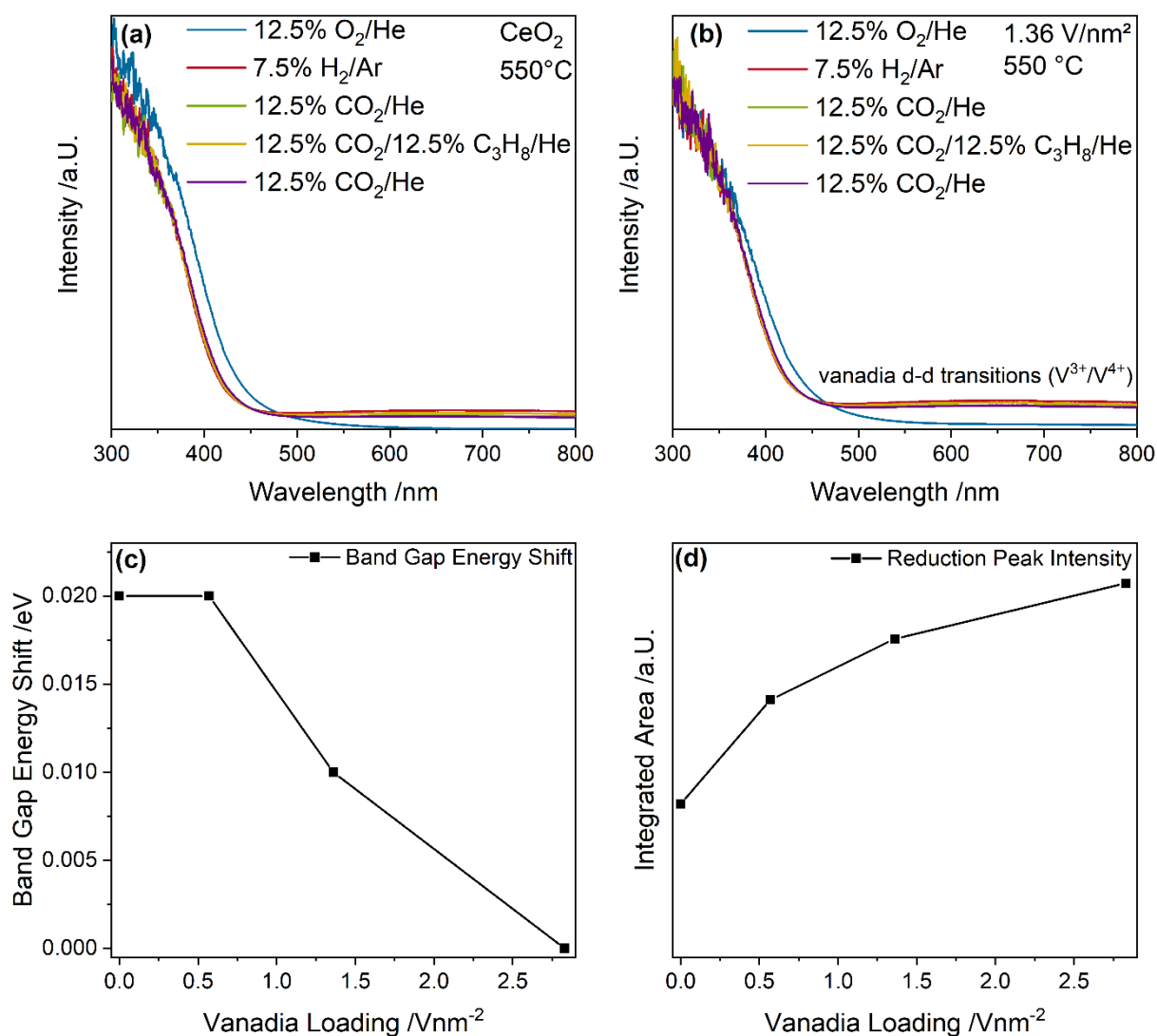
Figure 7: UV-Vis spectra of **(a)** bare ceria and **(b)** the 1.36 V/nm² sample under different gas feeds, recorded at 550 °C. **(c)** Band gap energies as determined using Tauc plots and **(d)** the reduction peak area based on the results of a fitting analysis.

As shown in Figure 7a, the UV-Vis spectra of bare ceria are dominated by strong band gap absorption caused by O2p → Ce4f transitions.[60,61] Upon switching from oxidizing to reductive conditions, two changes in the spectra become apparent. First, the band gap shifts, which is caused by the introduction of additional states in the band gap when the sample is reduced, lowering the energy required for a transition, which red-shifts the band gap.[42,61] However, in this case, the band gap blue-shifts significantly during this initial switch, which is typically associated with an oxidation of ceria.[42,61] This was previously observed under strongly reducing conditions due to the newly appearing absorption at 633, changing the spectra shape significantly, which influences the graphical analysis via Tauc plots.[45] However, for small changes in the absorption region above 500 nm (as observed for the other gas phase changes), the

results of the Tauc analysis are not significantly affected and the differences between the initial CO_2 exposure and ODH conditions can be analyzed. Second, a peak at 633 nm is observed, which is caused by a $Ce^{3+} \rightarrow Ce^{4+}$ charge transition, which is also caused by the reduction of ceria introducing Ce^{3+} states into the lattice.[62,63] Both are suitable descriptors for the bulk reduction of ceria. As can be seen in Figure 7b, UV-Vis spectra of the 1.36 V/nm² sample under different gas feeds at 550 °C are also dominated by the ceria absorption but also show overlapping d-d transitions from reduced (V^{3+}, V^{4+}) vanadia, which depends on the vanadia species.[64,65] Shorter vanadia nuclearities absorb at lower wavelengths while higher nuclearities absorb at higher wavelengths.[66] In the following, the intensity of the region above 500 nm will be referred to as the reduction peak, describing the combined contributions from reduced ceria and vanadia. Therefore, both the bulk reduction of the ceria as well as the prevalence of reduced vanadia states can be probed.

Figure 7c summarizes the band gap red-shifts between the initial CO_2 and the ODH conditions for bare ceria and the vanadia-loaded samples. The band gap is most red-shifted for bare ceria and ceria loaded with 0.57 V/nm², indicating that these samples exhibit the highest degree of bulk reduction, which differs from the trend deduced from the F_{2g} mode. This indicates that the degree of reduction in the ceria differs between the surface, subsurface and the bulk. The surface is influenced by the anchored vanadia and possibly by the presence of adsorbates. The subsurface exhibits a trend that follows the involvement of ceria lattice oxygen and is influenced by the overall reactivity. It can be regenerated by both gas phase CO_2 and subsequent oxygen diffusion into the subsurface or through oxygen diffusion from the bulk. The F_{2g} red-shift decreases for the highest vanadia loading (see Figure 5c), which is in agreement with vanadia oxygen instead of ceria oxygen becoming the active site. This is likely caused by oligomers, only significantly present for the 2.83 V/nm² sample. This sample also shows no shift of the band gap anymore, indicating that the reduction of ceria in this sample is limited to the surface shifting away from significant ceria participation. Notably, the differences between the samples are comparably small, and since the error of the Tauc method is estimated to be ±0.01 eV, this trend needs to be supported by additional data. The small shift might originate from a small bulk contribution to the reaction, which mostly occurs in the surface/subsurface regions.

Figure 7d quantifies the reduction peak area for bare ceria and vanadia-loaded samples including contributions from ceria and vanadia reduction. The reduction peak

area shows an increase with increasing vanadia loading, while the slope shows a stepwise decrease. Since the vanadia-loaded samples are characterized by a significantly higher absorption than bare ceria this behavior indicates, that the peak includes reduced vanadia species, showing their participation in the reaction. However, this trend does not correlate with any specific reaction pathway, which may be caused by the fact that both ceria and vanadia are involved in a plethora of reactions, which all show a nuclearity-dependent behavior. Nevertheless, it still supports the previous interpretations that both vanadia and ceria reduction are crucial for the reaction mechanism.

Figure 8 shows the quasi in situ DRIFT spectra of bare ceria and the 1.36 V/nm² sample recorded after pre-treatment under different gas conditions and cooling to room temperature in pure helium. The carbonate area was quantified by integration and the Ce-OH region by a peak-fitting analysis (for details see experimental section), as shown in Figures 8c and d. The quasi in situ DRIFT spectra of the 0.57 and 2.83 V/nm² sample are given in the SI (see Figure S10), while an exemplary fit of the Ce-OH region is shown in Figure S11.
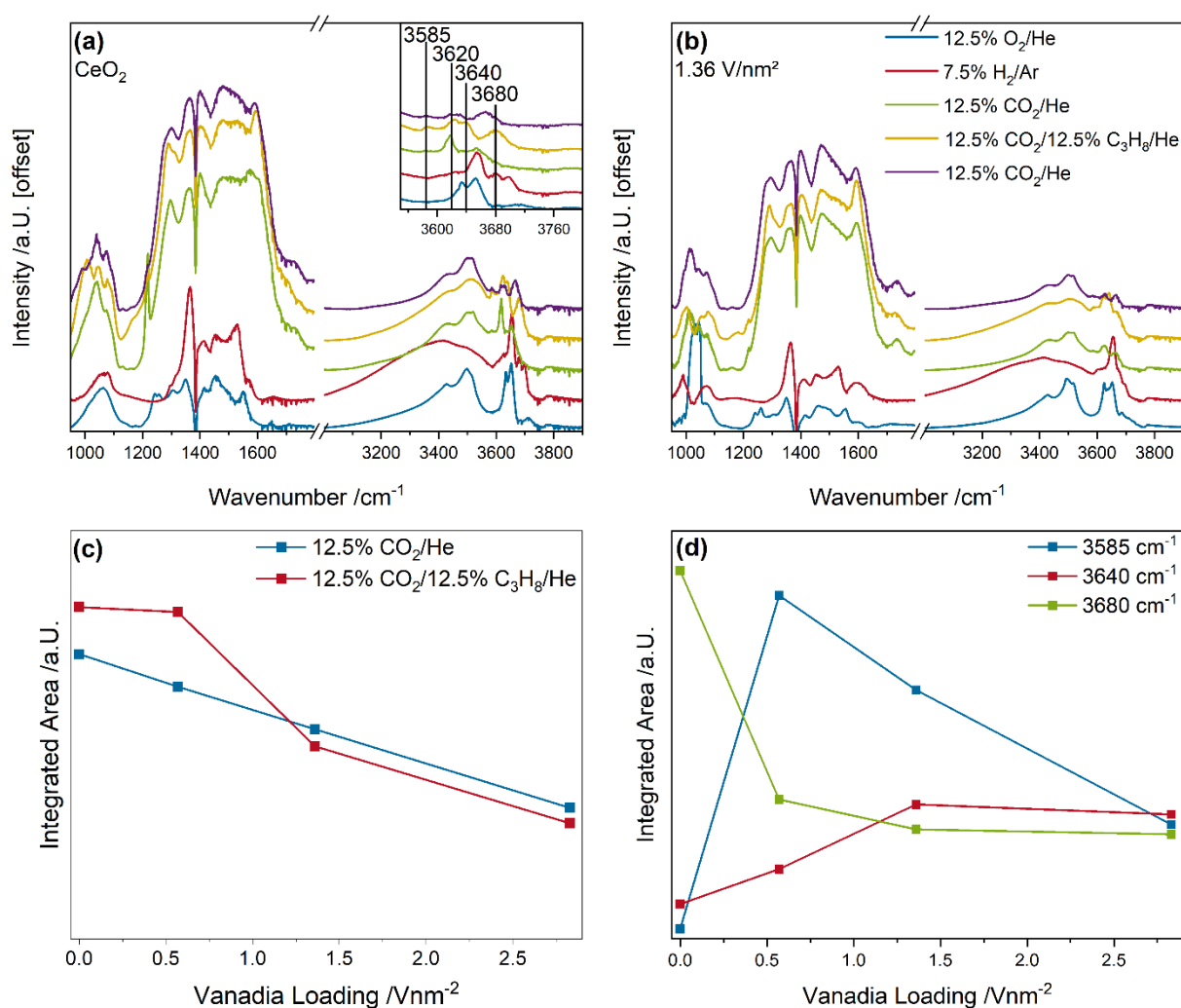
Figure 8: Quasi in situ DRIFT spectra of **(a)** CeO_2 and **(b)** the 1.36 V/nm² sample recorded after treatment under the indicated gas feeds at 550 °C and subsequent cooling to room temperature in helium. The inset shows an enlarged view of the Ce-OH region. **(c)** Carbonate areas during the first CO_2/He and the reactive gas phase and **(d)** relevant Ce-OH peaks, which show a significant change in intensity upon switching from 12.5% CO_2/He to 12.5% CO_2/12.5% C_3H_8/He.

The quasi in situ DRIFT spectra of bare ceria and the 1.36 V/nm² sample show significant changes in the carbonate and Ce-OH regions between the different gas phases but to a different extent (see Figure 8a and b). Especially the carbonate region shows a sharp increase in the overall intensity after the initial CO_2 exposure, which is indicative of the formation of ubiquitous amounts of carbonate adsorbates (which can deactivate surface sites),[67] while no significant contribution of formates was observed. This behavior might explain the significant differences in the activity of the samples after differing pre-treatment conditions and between ODH and DDH conditions.

To analyze these changes in more detail, the carbonate region and the Ce-OH region of the bare ceria and vanadia-loaded samples were quantified. In the carbonate

region, the intensity decreases linearly with increasing vanadia loading from bare ceria to the 2.83 V/nm² during the initial CO_2 exposure. This is explained by the anchoring of vanadia to surface oxygen atoms, which cannot be reduced under H_2 conditions. Therefore, less surface sites are available for reduction and subsequent adsorbate formation. When the conditions are switched from CO_2 to ODH conditions, a nuclearity-dependent behavior is observed. For bare ceria and the 0.57 V/nm² sample an increase in the carbonate intensity is observed, while for the 1.36 and 2.83 V/nm² samples, an intensity decrease is observed, indicating a fundamental difference in the reaction behavior. The increase in the carbonate region is explained by the further reduction of surface oxygen sites due to the transfer of hydrogen from propane to ceria, leading to oxygen vacancy creation, which can be regenerated by gas phase CO_2. This is supported by the fact that the intensity of the entire carbonate region increases for these samples. In comparison, the intensity for the 1.36 and 2.83 V/nm² samples decreases at ~1750 and ~1210 cm^{-1}, which is indicative of monodentate carbonates.[67] This might indicate that hydrogen can be transferred to an oxygen atom of monodentate carbonate species in proximity of vanadia species. These can react to CO and H_2O via RWGSr, leaving a clean surface site, which can then react with propane and create new adsorbates or vacancies. This also explains the more significant intensity increase in the defect region in the UV-Raman spectra (see Figure 4) under ODH conditions due to the possible depletion of surface adsorbates. This effect seems to occur to a similar extent for both samples, which indicates that it is facilitated by monomers or dimers, which are present in similar amounts for both samples. However, since monomers cannot be fully regenerated by CO_2, dimers seem to be the most likely nuclearity. Since the total amount of monomers and dimers is much higher in the 1.36 and 2.83 V/nm² samples compared to the 0.57 V/nm² sample, this seems to be likely. This effect seems to occur only for monodentate carbonate species, while bidentate carbonate species may be to stable to participate in this reaction.

At last, the changes in the intensity of the Ce-OH region between the initial CO_2 and ODH conditions were quantified (see Figure 8d). Three peaks are observed at 3585, 3640, and 3680 cm^{-1}, which are assigned to vibrations of V-OH, Ce-OH II-B, and Ce-OH II-A, respectively.[68,69] The V-OH bond exhibits an intensity of zero for bare ceria, increases significantly for the 0.57 V/nm² sample, and then decreases gradually towards the 2.83 V/nm² sample. This indicates, that the V-OH species is less prevalent

at higher loadings, whereas the shift towards the direct participation of vanadia oxygen occurs. It indicates the very fast transfer to other oxygen sites at higher loadings. In comparison, the peak located at 3640 cm^{-1} originates from a doubly bridged Ce-OH species in proximity to oxygen vacancies. Since the amount of created oxygen vacancies during ODH conditions increases with increasing vanadia loading, these species also increase in concentration. Their intensity does not correlate with the prevalence of PDR, by comparison with Figure 3f. Therefore, it seems likely that this Ce-OH species is involved in different selective oxidation routes in addition to Ce-H formation and the reaction with monodentate carbonates. At last, the peak at 3680 cm^{-1} originates from a doubly bridged Ce-OH species on the clean ceria surface with no vacancies in proximity. This species is especially reactive towards further hydrogen,[68] which makes it a target for the quick hydrogen transfer of hydrogen from the total oxidation reaction. It can then be quickly reduced to a vacancy. This is in agreement with its intensity, which decreases with increasing vanadia loading, in good agreement with the decrease in total oxidation rate.

In summary, the spectroscopic results show that different reactions occur on the VO$_x$/CeO$_2$ surface, exhibiting different reaction paths depending on the vanadia nuclearities. First, after the pre-treatment, the catalyst surface is saturated with mostly carbonate adsorbates and little surface oxygen remains exposed. The main hydrogen transfer route towards propylene is the hydrogen transfer to monodentate carbonates or doubly bridged Ce-OH species in proximity of an oxygen vacancy and a bulk Ce-H. The transfer is facilitated by the V=O group of dimeric vanadia and ceria lattice oxygen is used as the active oxygen site for the reaction. The extent to which side reactions occur is nuclearity-dependent and different reaction routes are involved. Due to the reduction and exposure to CO$_2$, most of the catalyst surface is deactivated by stable carbonate species blocking surface oxygen and creating vacancies. Figure 9 summarizes the findings in a mechanistic scheme of the propane ODH reaction over the 1.36 V/nm² sample.
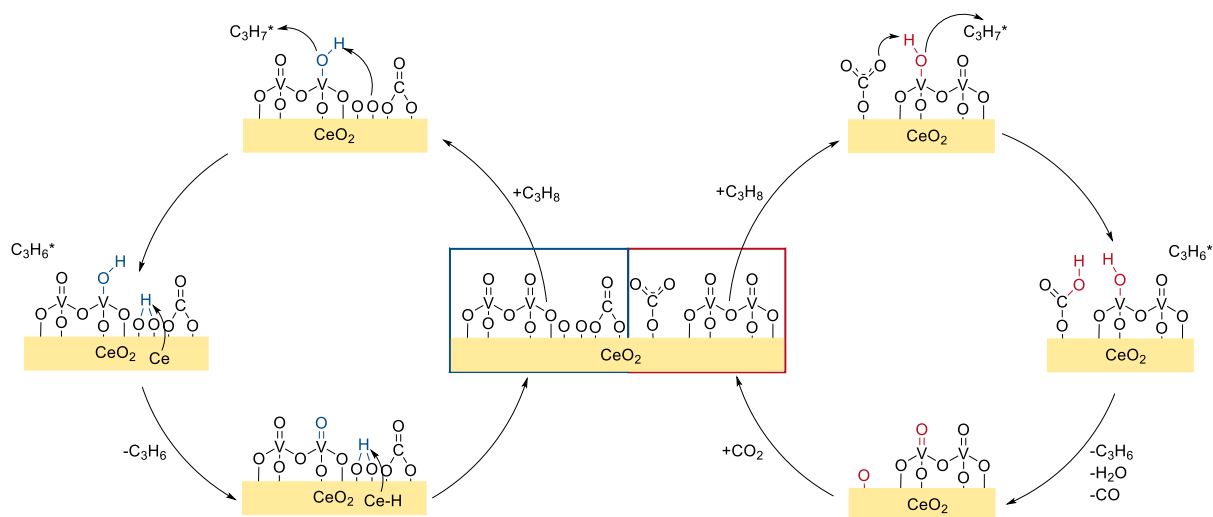
Figure 9: Mechanistic scheme of the CO_2-assisted propane ODH over VO_x/CeO_2. Details regarding the role of the bare support and side reactions are given in the text.

4. Conclusion

In this study, we addressed the CO_2-assisted ODH of propane over VO_x/CeO_2 catalysts, by analyzing the complex reaction network, identifying important structural features for the different reactions occurring and elucidating a mechanistic scheme by combining multiple operando and in situ methods. To determine the influence of vanadia nuclearities on the catalytic performance, differently loaded vanadia catalysts were employed (0-2.5 V/nm²).

The catalytic activity of the samples under DDH conditions is significantly higher and more selective than under ODH conditions but is not stable, leading to catalyst deactivation. Under ODH conditions, a stable performance is obtained, which depends strongly on the pre-treatment conditions. A pre-treatment in H_2 and CO_2 results in a partially reduced state of the catalyst, which leads to the highest conversions for vanadia-loaded catalysts. The reaction network is significantly influenced by the vanadia surface density of the catalyst, while the CO_2 conversions are significantly higher for all samples than the propane conversions, caused by a significant amount of side reactions. On bare ceria, the total oxidation of propane dominates, while small amounts of cracking can be observed. With increasing vanadia loading, less total oxidation but more cracking and PDR occurs. An especially sharp increase is observed for the 2.83 V/nm² sample, which exhibits the highest PDR rates but the lowest total contribution of side reactions.

As a result of the mechanistic analysis, different pathways towards propylene and different active sites towards side reactions were identified. For bare ceria, the total oxidation was identified to occur via surface lattice oxygen, while the conversion of propane is initiated by its adsorption onto the catalyst, creating defect sites. Hydrogen is transferred directly to the surface, and the subsequent transfer path of hydrogen determines the reaction pathway. Bridged Ce-OH species are highly reactive towards further hydrogen, leading to total oxidation, while the transfer to monodentate carbonates can lead to the selective conversion towards propylene. Bidentate carbonates are not affected by the hydrogen transfer. In comparison, vanadia-loaded catalysts exhibit additional pathways compared to bare ceria that lead to propylene formation, increasing the selectivity. First, vanadia is able to transfer hydrogen from propane to ceria, forming relatively stable bulk hydrides, which removes hydrogen from the surface and decreases the prevalence of the total oxidation reaction. In addition, vanadia is anchored to ceria surface oxygen, poisoning some of the oxygen sites

responsible for total oxidation. At the 2.83 V/nm² loading, a sharp increase in the PDR rate can be observed, indicating a clear loading dependence of the catalytic behavior. In addition, a shift from ceria oxygen to vanadia oxygen atoms as the active site in propane conversion was observed via the F_{2g} red-shift. At last, the reduced catalyst can be regenerated by CO_2, which is crucial for the stability of the catalytic performance. This regeneration occurs via carbonate formation from CO_2 and an oxygen vacancy on the surface, leading to lattice oxygen regeneration. However, due to the high stability of the carbonates and the high desorption barrier of CO, surface sites are blocked, explaining the reactivity difference between ODH and DDH conditions.

To disentangle the nuclearity distribution and assign the individual nuclearities to catalytic functions, the vibrational vanadyl fine structure was analyzed. Monomeric vanadia, which was previously described to interact with ceria oxygen vacancies,[33] is able to move out of the vacancies at the elevated temperatures required for CO_2-assisted propane ODH, leading to a less significant decrease in oxygen mobility compared to lower temperatures, increasing the prevalence of total oxidation. Furthermore, at 550 °C, an increased amount of trimers are expected to be present on the surface due to their high energetic stability.[38] Based on this stability, they were previously described to be observer species, which do not participate in the reaction, which was confirmed for the CO_2-assisted propane ODH.[36] Dimers instead of oligomers are the main hydrogen transfer site during selective conversion and are able to transfer hydrogen into the bulk, forming hydrides, and to transfer hydrogen to monodentate carbonates, leading to RWGSr and propylene formation. The presence of oligomers was shown to lead to a significant contribution of PDR and a shift towards vanadia oxygen as the active oxygen site. This is likely caused by the increased reducibility of these samples.[59]

Our results highlight the potential of combining multiple operando and in situ methods to obtain detailed understanding of the reaction mechanism of the CO_2-assisted propane ODH, which is an important reaction regarding CO_2 activation and usage in chemical industry. While the VO_x/CeO_2 catalyst does not show the highest catalytic performance, its reaction mechanism as well as the complex interplay between different vanadia nuclearities, the ceria surface and the bulk, as well as their relevance for the occurrence of selective oxidation or side reactions were understood in detail for the first time. This is of great importance for future developments, since

ceria is a promising material for the activation of CO_2 while vanadia can be highly active for propane activation. This catalyst is envisioned to be part of a multi-oxide system that reduces catalyst deactivation through carbonate formation, thereby leading to significantly higher activities. Our approach is readily transferable to other systems of interest in the context of CO_2 activation and contributes to a knowledge-based design of vanadia materials to replace highly toxic CrO_x for CO_2-assisted ODH reactions.

Declaration of Competing Interest

The authors declare that they have no known competing financial interests or personal relationships that could have appeared to influence the work reported in this paper.

Supporting Information

The supporting information contains additional information about the reactivity behavior and operando spectroscopic results.

References

(1) Amghizar, I.; Vandewalle, L. A.; van Geem, K. M.; Marin, G. B. New Trends in Olefin Production. *Eng.* **2017**, *3* (2), 171–178. DOI: 10.1016/j.eng.2017.02.006.

(2) Cavani, F.; Ballarini, N.; Cericola, A. Oxidative dehydrogenation of ethane and propane: How far from commercial implementation? *Catal. Today* **2007**, *127* (1-4), 113–131. DOI: 10.1016/j.cattod.2007.05.009.

(3) Lavrenov, A. V.; Saifulina, L. F.; Buluchevskii, E. A.; Bogdanets, E. N. Propylene production technology: Today and tomorrow. *Catal. Ind.* **2015**, *7* (3), 175–187. DOI: 10.1134/S2070050415030083.

(4) Phung, T. K.; Le Pham, T. M.; Vu, K. B.; Busca, G. (Bio)Propylene production processes: A critical review. *J. Environ. Chem. Eng.* **2021**, *9* (4), 105673. DOI: 10.1016/j.jece.2021.105673.

(5) Carrero, C. A.; Schloegl, R.; Wachs, I. E.; Schomaecker, R. Critical Literature Review of the Kinetics for the Oxidative Dehydrogenation of Propane over Well-Defined Supported Vanadium Oxide Catalysts. *ACS Catal.* **2014**, *4* (10), 3357–3380. DOI: 10.1021/cs5003417.

(6) Carter, J. H.; Bere, T.; Pitchers, J. R.; Hewes, D. G.; Vandegehuchte, B. D.; Kiely, C. J.; Taylor, S. H.; Hutchings, G. J. Direct and oxidative dehydrogenation of propane: from catalyst design to industrial application. *Green Chem.* **2021**, *23* (24), 9747–9799. DOI: 10.1039/D1GC03700E.

(7) Baek, J.; Yun, H. J.; Yun, D.; Choi, Y.; Yi, J. Preparation of Highly Dispersed Chromium Oxide Catalysts Supported on Mesoporous Silica for the Oxidative Dehydrogenation of Propane Using CO_2: Insight into the Nature of Catalytically Active Chromium Sites. *ACS Catal.* **2012**, *2* (9), 1893–1903. DOI: 10.1021/cs300198u.

(8) Baena-Moreno, F. M.; Rodríguez-Galán, M.; Vega, F.; Alonso-Fariñas, B.; Vilches Arenas, L. F.; Navarrete, B. Carbon capture and utilization technologies: a literature review and recent advances. *Energ. Sources A Rec. Util. Environ. Effects* **2019**, *41* (12), 1403–1433. DOI: 10.1080/15567036.2018.1548518.

(9) Al-Mamoori, A.; Krishnamurthy, A.; Rownaghi, A. A.; Rezaei, F. Carbon Capture and Utilization Update. *Energy Tech.* **2017**, *5* (6), 834–849. DOI: 10.1002/ente.201600747.

(10) Kätelhön, A.; Meys, R.; Deutz, S.; Suh, S.; Bardow, A. Climate change mitigation potential of carbon capture and utilization in the chemical industry. *Proc. Natl. Acad. Sci. USA* **2019**, *116* (23), 11187–11194. DOI: 10.1073/pnas.1821029116.

(11) Álvarez, A.; Borges, M.; Corral-Pérez, J. J.; Olcina, J. G.; Hu, L.; Cornu, D.; Huang, R.; Stoian, D.; Urakawa, A. CO_2 Activation over Catalytic Surfaces. *ChemPhysChem* **2017**, *18* (22), 3135–3141. DOI: 10.1002/cphc.201700782.

(12) Jacquemin, M.; Beuls, A.; Ruiz, P. Catalytic production of methane from CO_2 and H_2 at low temperature: Insight on the reaction mechanism. *Catal. Today* **2010**, *157* (1-4), 462–466. DOI: 10.1016/j.cattod.2010.06.016.

(13) Lei, T.-q.; Cheng, Y.-h.; Miao, C.-x.; Hua, W.-m.; Yue, Y.-h.; Gao, Z. Silica-doped TiO_2 as support of gallium oxide for dehydrogenation of ethane with CO_2. *Fuel Process. Technol.* **2018**, *177*, 246–254. DOI: 10.1016/j.fuproc.2018.04.037.

(14) Botavina, M. A.; Martra, G.; Agafonov, Y.A.; Gaidai, N. A.; Nekrasov, N. V.; Trushin, D. V.; Coluccia, S.; Lapidus, A. L. Oxidative dehydrogenation of C_3–C_4 paraffins in the presence of CO_2 over CrO_x/SiO_2 catalysts. *Appl. Catal. A Gen.* **2008**, *347* (2), 126–132. DOI: 10.1016/j.apcata.2008.05.037.

(15) Gashoul Daresibi, F.; Khodadadi, A. A.; Mortazavi, Y.; Huotari, S.; Ritala, M. Highly dispersed atomic layer deposited CrO_x on SiO_2 catalyst with enhanced yield of propylene for CO_2–mediated oxidative dehydrogenation of propane. *Mol. Catal.* **2022**, *526* (80–), 112396. DOI: 10.1016/j.mcat.2022.112396.

(16) Michorczyk, P.; Pietrzyk, P.; Ogonowski, J. Preparation and characterization of SBA-1–supported chromium oxide catalysts for CO_2 assisted dehydrogenation of propane. *Microporous Mesoporous Mater.* **2012**, *161*, 56–66. DOI: 10.1016/j.micromeso.2012.05.011.

(17) Wang, H.; Nguyen, T. D.; Tsilomelekis, G. Propane oxidative dehydrogenation using CO_2 over CrO_x/Fe–CeO_2 catalysts. *Catal. Sci. Technol.* **2023**, *13* (8), 2360–2369. DOI: 10.1039/D2CY01563C.

(18) Wang, Z.-Y.; He, Z.-H.; Li, L.-Y.; Yang, S.-Y.; He, M.-X.; Sun, Y.-C.; Wang, K.; Chen, J.-G.; Liu, Z.-T. Research progress of CO_2 oxidative dehydrogenation of propane to propylene over Cr-free metal catalysts. *Rare Met.* **2022**, *41* (7), 2129–2152. DOI: 10.1007/s12598-021-01959-y.

(19) Balogun, M. L.; Adamu, S.; Ba-Shammakh, M. S.; Hossain, M. M. Promotional effects of CO_2 on the oxidative dehydrogenation of propane over mesoporous VOX/γAl2O3 catalysts. *J. Industr. Eng. Chem.* **2021**, *96* (20), 82–97. DOI: 10.1016/j.jiec.2020.12.022.

(20) Ascoop, I.; Galvita, V. V.; Alexopoulos, K.; Reyniers, M.-F.; van der Voort, P.; Bliznuk, V.; Marin, G. B. The role of CO_2 in the dehydrogenation of propane over WO_x–VO_x/SiO_2. *J. Catal.* **2016**, *335*, 1–10. DOI: 10.1016/j.jcat.2015.12.015.

(21) Jiang, X.; Lis, B. M.; Purdy, S. C.; Paladugu, S.; Fung, V.; Quan, W.; Bao, Z.; Yang, W.; He, Y.; Sumpter, B. G.; Page, K.; Wachs, I. E.; Wu, Z. CO_2-Assisted Oxidative Dehydrogenation of Propane over VO_x/In_2O_3 Catalysts: Interplay between Redox Property and Acid–Base Interactions. *ACS Catal.* **2022**, *12* (18), 11239–11252. DOI: 10.1021/acscatal.2c02099.

(22) Jiang, X.; Lis, B. M.; Wu, Y.; Wachs, I. E.; Wu, Z. Effect of the Molecular Structure of Surface Vanadia on Activity and Regenerability of VO_x/In_2O_3 Catalysts for CO_2-Assisted Oxidative Dehydrogenation of Propane. *J. Phys. Chem. C* **2023**, *127* (13), 6311–6320. DOI: 10.1021/acs.jpcc.3c00183.

(23) Rogg, S.; Hess, C. CO_2 as a soft oxidant for propane oxidative dehydrogenation: A mechanistic study using operando UV Raman spectroscopy. *J. CO2 Util.* **2021**, *50* (9), 101604. DOI: 10.1016/j.jcou.2021.101604.

(24) Schumacher, L.; Hofmann, K.; Hess, C. *Insight into the Reaction Mechanism and Deactivation during CO_2-Assisted Propane ODH over VO_x/TiO_2 Catalysts: An Operando Spectroscopic Study*, 2023. DOI: 10.26434/chemrxiv-2023-rnfrd.

(25) Dinse, A.; Frank, B.; Hess, C.; Habel, D.; Schomäcker, R. Oxidative dehydrogenation of propane over low-loaded vanadia catalysts: Impact of the support material on kinetics and selectivity. *J. Mol. Catal. A Chem.* **2008**, *289* (1-2), 28–37. DOI: 10.1016/j.molcata.2008.04.007.

(26) Beck, B.; Harth, M.; Hamilton, N. G.; Carrero, C.; Uhlrich, J. J.; Trunschke, A.; Shaikhutdinov, S.; Schubert, H.; Freund, H.-J.; Schlögl, R.; Sauer, J.; Schomäcker, R. Partial oxidation of ethanol on vanadia catalysts on supporting oxides with different redox properties compared to propane. *J. Catal.* **2012**, *296*, 120–131. DOI: 10.1016/j.jcat.2012.09.008.

(27) Ziemba, M.; Hess, C. Influence of gold on the reactivity behaviour of ceria nanorods in CO oxidation: combining operando spectroscopies and DFT calculations. *Catal. Sci. Technol.* **2020**, *10* (11), 3720–3730. DOI: 10.1039/D0CY00392A.

(28) Lin, L.; Yao, S.; Liu, Z.; Zhang, F.; Li, N.; Vovchok, D.; Martínez-Arias, A.; Castañeda, R.; Lin, J.; Senanayake, S. D.; Su, D.; Ma, D.; Rodriguez, J. A. In Situ Characterization of Cu/CeO_2 Nanocatalysts for CO_2 Hydrogenation: Morphological Effects of Nanostructured Ceria on the Catalytic Activity. *J. Phys. Chem. C* **2018**, *122* (24), 12934–12943. DOI: 10.1021/acs.jpcc.8b03596.

(29) Ziemba, M.; Weyel, J.; Hess, C. Elucidating the mechanism of the reverse water–gas shift reaction over Au/CeO_2 catalysts using operando and transient spectroscopies. *Appl. Catal. B Environ.* **2022**, *301*, 120825. DOI: 10.1016/j.apcatb.2021.120825.

(30) Ober, P.; Rogg, S.; Hess, C. Direct Evidence for Active Support Participation in Oxide Catalysis: Multiple Operando Spectroscopy of VO_x/Ceria. *ACS Catal.* **2020**, *10* (5), 2999–3008. DOI: 10.1021/acscatal.9b05174.

(31) Li, Y.; Wei, Z.; Gao, F.; Kovarik, L.; Peden, C. H.F.; Wang, Y. Effects of CeO_2 support facets on VO_x/CeO_2 catalysts in oxidative dehydrogenation of methanol. *J. Catal.* **2014**, *315*, 15–24. DOI: 10.1016/j.jcat.2014.04.013.

(32) Sánchez-García, J.-L.; Handy, B. E.; Rodríguez, Á. G.; González-Chávez, M. M.; García de León, R.; Cardenas-Galindo, M.-G. Relating the Synthesis Method of $VO_x/CeO_2/SiO_2$ Catalysts to Red-Ox Properties, Acid Sites, and Catalytic Activity for the Oxidative Dehydrogenation of Propane and n-Butane. *Top. Catal.* **2022**, *65* (13-16), 1408–1418. DOI: 10.1007/s11244-022-01661-y.

(33) Schumacher, L.; Hess, C. The active role of the support in propane ODH over VO_x/CeO_2 catalysts studied using multiple operando spectroscopies. *J. Catal.* **2021**, *398* (13), 29–43. DOI: 10.1016/j.jcat.2021.04.006.

(34) Martínez-Huerta, M. V.; Deo, G.; Fierro, J. L. G.; Bañares, M. A. Changes in Ceria-Supported Vanadium Oxide Catalysts during the Oxidative Dehydrogenation of Ethane and Temperature-Programmed Treatments. *J. Phys. Chem. C* **2007**, *111* (50), 18708–18714. DOI: 10.1021/jp0772225.

(35) Baron, M.; Abbott, H.; Bondarchuk, O.; Stacchiola, D.; Uhl, A.; Shaikhutdinov, S.; Freund, H.-J.; Popa, C.; Ganduglia-Pirovano, M. V.; Sauer, J. Resolving the Atomic Structure of Vanadia Monolayer Catalysts: Monomers, Trimers, and Oligomers on Ceria. *Angew. Chem. Int. Ed.* **2009**, *121* (43), 8150–8153. DOI: 10.1002/ange.200903085.

(36) Schumacher, L.; Weyel, J.; Hess, C. Unraveling the Active Vanadium Sites and Adsorbate Dynamics in VO_x/CeO_2 Oxidation Catalysts Using Transient IR Spectroscopy. *J. Am. Chem. Soc.* **2022**, *144* (32), 14874–14887. DOI: 10.1021/jacs.2c06303. Published Online: Aug. 2, 2022.

(37) Wu, Z.; Rondinone, A. J.; Ivanov, I. N.; Overbury, S. H. Structure of Vanadium Oxide Supported on Ceria by Multiwavelength Raman Spectroscopy. *J. Phys. Chem. C* **2011**, *115* (51), 25368–25378. DOI: 10.1021/jp2084605.

(38) Penschke, C.; Paier, J.; Sauer, J. Oligomeric Vanadium Oxide Species Supported on the CeO_2 (111) Surface: Structure and Reactivity Studied by Density Functional Theory. *J. Phys. Chem. C* **2013**, *117* (10), 5274–5285. DOI: 10.1021/jp400520j.

(39) Martínez-Huerta, M. V.; Deo, G.; Fierro, J. L. G.; Bañares, M. A. Operando Raman-GC Study on the Structure−Activity Relationships in V^{5+}/CeO_2 Catalyst for Ethane Oxidative Dehydrogenation: The Formation of $CeVO_4$. *J. Phys. Chem. C* **2008**, *112* (30), 11441–11447. DOI: 10.1021/jp802827t.

(40) Martínez-Huerta, M.; Coronado, J. M.; Fernández-García, M.; Iglesiaz-Juez, A.; Deo, G.; Fierro, J. L. G.; Banares, M. A. Nature of the vanadia-ceria interface in V^{5+}/CeO_2 catalysts and its relevance for the solid-state reaction toward $CeVO_4$ and catalytic properties. *J. Catal.* **2004**, *225* (1), 240–248. DOI: 10.1016/j.jcat.2004.04.005.

(41) Fan, H.-X.; Zhen, L.-F.; Rajendran, A.; Feng, J.; Li, W.-Y. Crucial role of H and O spillover in VO_x/CeO_2 catalysts reduction and re-oxidation during the ODH reaction. *Appl. Surf. Sci.* **2023**, *626*, 157250. DOI: 10.1016/j.apsusc.2023.157250.

(42) Filtschew, A.; Hofmann, K.; Hess, C. Ceria and Its Defect Structure: New Insights from a Combined Spectroscopic Approach. *J. Phys. Chem. C* **2016**, *120* (12), 6694–6703. DOI: 10.1021/acs.jpcc.6b00959.

(43) Waleska, P. S.; Hess, C. Oligomerization of Supported Vanadia: Structural Insight Using Surface-Science Models with Chemical Complexity. *J. Phys. Chem. C* **2016**, *120* (33), 18510–18519. DOI: 10.1021/acs.jpcc.6b01672.

(44) Antonov, L.; Nedeltcheva, D. Resolution of overlapping UV–Vis absorption bands and quantitative analysis. *Chem. Soc. Rev.* **2000**, *29* (3), 217–227. DOI: 10.1039/A900007K.

(45) Schumacher, L.; Ziemba, M.; Brunnengräber, K.; Totzauer, L.; Hofmann, K.; Etzold, B. J. M.; Albert, B.; Hess, C. Understanding the Reduction Behavior of VO_x/CeO_2 on a Molecular Level: Combining Temperature-Programmed Reduction with Multiple In-Situ Spectroscopies and X-Ray Diffraction. *J. Phys. Chem. C* **2023**, *127* (12), 5810–5824. DOI: 10.1021/acs.jpcc.3c00622.

(46) Buekens, A. G.; Froment, G. F. Thermal Cracking of Propane. Kinetics and Product Distributions. *Ind. Eng. Chem. Proc. Des. Dev.* **1968**, *7* (3), 435–447. DOI: 10.1021/i260027a022.

(47) Gomez, E.; Kattel, S.; Yan, B.; Yao, S.; Liu, P.; Chen, J. G. Combining CO_2 reduction with propane oxidative dehydrogenation over bimetallic catalysts. *Nat. Commun.* **2018**, *9* (1), 1398. DOI: 10.1038/s41467-018-03793-w.

(48) Siahvashi, A.; Adesina, A. A. Hydrogen production via propane dry reforming: Carbon deposition and reaction-deactivation study. *Int. J. Hydrog. Energ.* **2018**, *43* (36), 17195–17204. DOI: 10.1016/j.ijhydene.2018.07.118.

(49) Schilling, C.; Hofmann, A.; Hess, C.; Ganduglia-Pirovano, M. V. Raman Spectra of Polycrystalline CeO_2 : A Density Functional Theory Study. *J. Phys. Chem. C* **2017**, *121* (38), 20834–20849. DOI: 10.1021/acs.jpcc.7b06643.

(50) Iglesias-Juez, A.; Martínez-Huerta, M. V.; Rojas-García, E.; Jehng, J.-M.; Bañares, M. A. On the Nature of the Unusual Redox Cycle at the Vanadia Ceria Interface. *J. Phys. Chem. C* **2018**, *122* (2), 1197–1205. DOI: 10.1021/acs.jpcc.7b09832.

(51) Schilling, C.; Hess, C. Real-Time Observation of the Defect Dynamics in Working Au/CeO_2 Catalysts by Combined Operando Raman/UV–Vis Spectroscopy. *J. Phys. Chem. C* **2018**, *122* (5), 2909–2917. DOI: 10.1021/acs.jpcc.8b00027.

(52) Li, Z.; Werner, K.; Chen, L.; Jia, A.; Qian, K.; Zhong, J.-Q.; You, R.; Wu, L.; Zhang, L.; Pan, H.; Wu, X.-P.; Gong, X.-Q.; Shaikhutdinov, S.; Huang, W.; Freund, H.-J. Interaction of Hydrogen with Ceria: Hydroxylation, Reduction, and Hydride Formation on the Surface and in the Bulk. *Chemistry* **2021**, *27* (16), 5268–5276. DOI: 10.1002/chem.202005374.

(53) Waleska, P.; Rupp, S.; Hess, C. Operando Multiwavelength and Time-Resolved Raman Spectroscopy: Structural Dynamics of a Supported Vanadia Catalyst at Work. *J. Phys. Chem. C* **2018**, *122* (6), 3386–3400. DOI: 10.1021/acs.jpcc.7b10518.

(54) Burcham, L. J.; Deo, G.; Gao, X.; Wachs, I. E. In situ IR, Raman, and UV-Vis DRS spectroscopy of supported vanadium oxide catalysts during methanol oxidation. *Top. Catal.* **2000**, *11/12* (1/4), 85–100. DOI: 10.1023/A:1027275225668.

(55) Shvets, P.; Dikaya, O.; Maksimova, K.; Goikhman, A. A review of Raman spectroscopy of vanadium oxides. *J. Raman Spectr.* **2019**, *50* (8), 1226–1244. DOI: 10.1002/jrs.5616.

(56) Wu, Z.; Kim, H.-S.; Stair, P. C.; Rugmini, S.; Jackson, S. D. On the structure of vanadium oxide supported on aluminas: UV and visible raman spectroscopy, UV-visible diffuse reflectance spectroscopy, and temperature-programmed reduction studies. *J. Phys. Chem. B* **2005**, *109* (7), 2793–2800. DOI: 10.1021/jp046011m.

(57) López, J. M.; Gilbank, A. L.; García, T.; Solsona, B.; Agouram, S.; Torrente-Murciano, L. The prevalence of surface oxygen vacancies over the mobility of bulk oxygen in nanostructured ceria for the total toluene oxidation. *Appl. Catal. B Environ.* **2015**, *174-175*, 403–412. DOI: 10.1016/j.apcatb.2015.03.017.

(58) Granger, P.; Siaka, H. W.; Umbarkar, S. B. What News in the Surface Chemistry of Bulk and Supported Vanadia Based SCR-Catalysts: Improvements in their Resistance to Poisoning and Thermal Sintering. *Chem. Rec.* **2019**, *19* (9), 1813–1828. DOI: 10.1002/tcr.201800092.

(59) Penschke, C.; Paier, J.; Sauer, J. Vanadium Oxide Oligomers and Ordered Monolayers Supported on CeO_2 (111): Structure and Stability Studied by Density Functional Theory. *J. Phys. Chem. C* **2018**, *122* (16), 9101–9110. DOI: 10.1021/acs.jpcc.8b01998.

(60) Huang, B.; Gillen, R.; Robertson, J. Study of CeO_2 and Its Native Defects by Density Functional Theory with Repulsive Potential. *J. Phys. Chem. C* **2014**, *118* (42), 24248–24256. DOI: 10.1021/jp506625h.

(61) Skorodumova, N. V.; Ahuja, R.; Simak, S. I.; Abrikosov, I. A.; Johansson, B.; Lundqvist, B. I. Electronic, bonding, and optical properties of CeO_2 and Ce_2O_3 from first principles. *Phys. Rev. B* **2001**, *64* (11), 548. DOI: 10.1103/PhysRevB.64.115108.

(62) Binet, C.; Badri, A.; Lavalley, J.-C. A Spectroscopic Characterization of the Reduction of Ceria from Electronic Transitions of Intrinsic Point Defects. *J. Phys. Chem.* **1994**, *98* (25), 6392–6398. DOI: 10.1021/j100076a025.

(63) Castleton, C. W. M.; Kullgren, J.; Hermansson, K. Tuning LDA+U for electron localization and structure at oxygen vacancies in ceria. *J. Chem. Phys.* **2007**, *127* (24), 244704. DOI: 10.1063/1.2800015.

(64) Liu, J.; Zhao, Z.; Xu, C.; Duan, A.; Jiang, G. CeO_2-supported vanadium oxide catalysts for soot oxidation: the roles of molecular structure and nanometer effect. *J. Rare Earths* **2010**, *28* (2), 198–204. DOI: 10.1016/S1002-0721(09)60080-6.

(65) Deeth, R. J. Electronic structures and d-d spectra of vanadium(IV) and VO^{2+} complexes: discrete variational Xα calculations. *J. Chem. Soc., Dalton Trans.* **1991**, *65* (6), 1467–1477. DOI: 10.1039/DT9910001467.

(66) Nitsche, D.; Hess, C. Structure of Isolated Vanadia and Titania: A Deep UV Raman, UV–Vis, and IR Spectroscopic Study. *J. Phys. Chem. C* **2016**, *120* (2), 1025–1037. DOI: 10.1021/acs.jpcc.5b10317.

(67) Vayssilov, G. N.; Mihaylov, M.; St. Petkov, P.; Hadjiivanov, K. I.; Neyman, K. M. Reassignment of the Vibrational Spectra of Carbonates, Formates, and Related Surface Species on Ceria: A Combined Density Functional and Infrared Spectroscopy Investigation. *J. Phys. Chem. C* **2011**, *115* (47), 23435–23454. DOI: 10.1021/jp208050a.

(68) Badri, A.; Binet, C.; Lavalley, J.-C. An FTIR study of surface ceria hydroxy groups during a redox process with H_2. *Faraday Trans.* **1996**, *92* (23), 4669. DOI: 10.1039/FT9969204669.

(69) Sambeth, J. E.; Centeno, M. A.; Paúl, A.; Briand, L. E.; Thomas, H. J.; Odriozola, J. A. In situ DRIFTS study of the adsorption–oxidation of CH_3OH on V_2O_5. *J. Mol. Catal. A Chem.* **2000**, *161* (1-2), 89–97. DOI: 10.1016/S1381-1169(00)00152-7.

Supporting Information

Unraveling the Mechanism of the CO_2-Assisted Oxidative Dehydrogenation of Propane over VO_x/CeO_2: An Operando Spectroscopic Study

Leon Schumacher, Marius Funke, Christian Hess*

Technical University of Darmstadt, Department of Chemistry, Eduard-Zintl-Institut für Anorganische und Physikalische Chemie, Peter-Grünberg-Str. 8, 64287 Darmstadt, Germany

*Corresponding Author (E-Mail: christian.hess@tu-darmstadt.de)
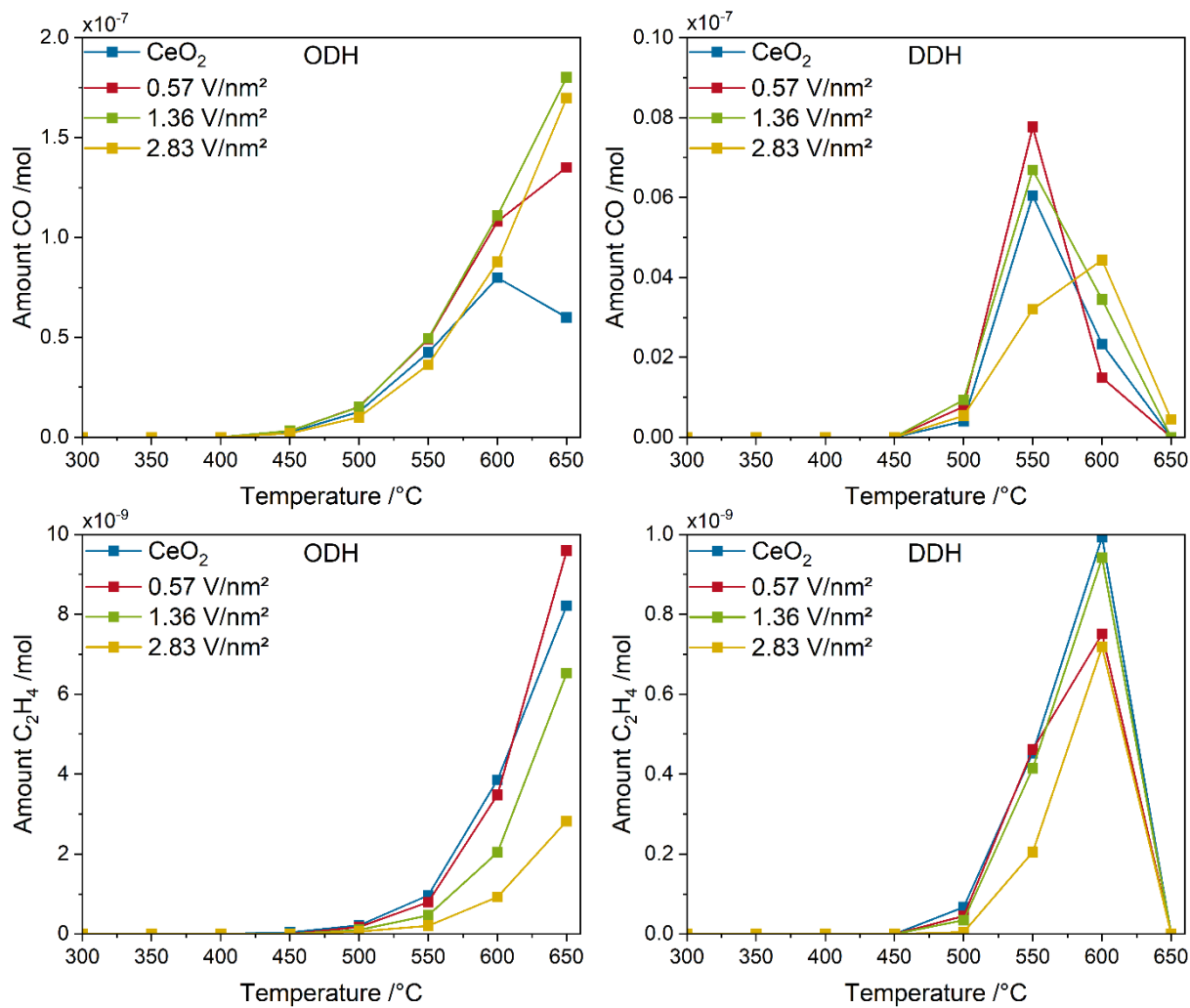
Figure S1: Comparison between the amounts of CO and C_2H_4 created under ODH (12.5% CO_2/12.5% C_3H_8/He) and DDH (12.5% C_3H_8/He) conditions for ceria and vanadia-loaded samples.
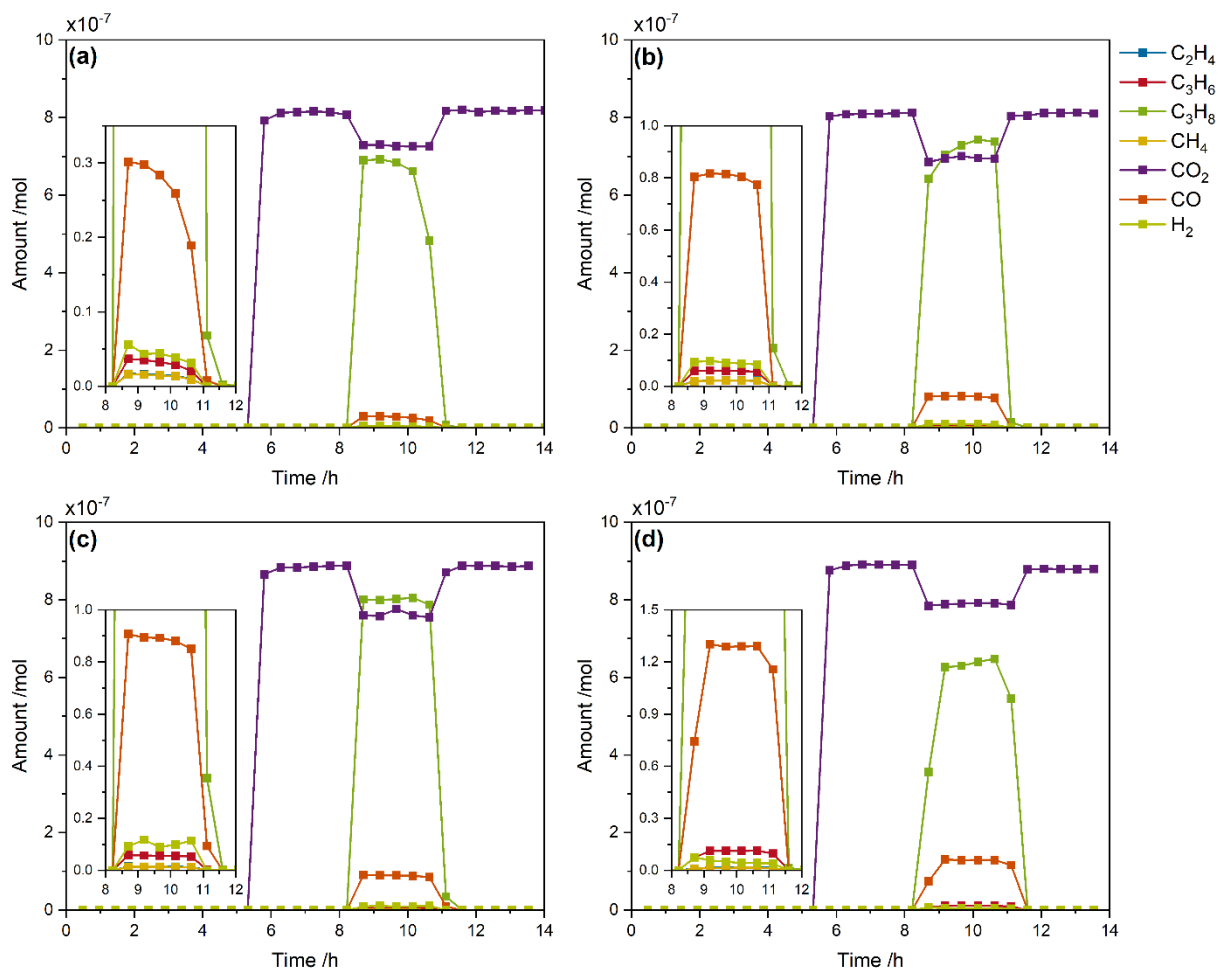
Figure S2: Molar product distributions of all detected reaction products formed by **(a)** CeO$_2$, **(b)** 0.57, **(c)** 1.36, and **(d)** 2.83 V/nm² under different gas feeds (see experimental section) at 550 °C. The insets show the product distribution during ODH conditions (12.5% CO$_2$/12.5% C$_3$H$_8$/He) in an enlarged view for each sample.
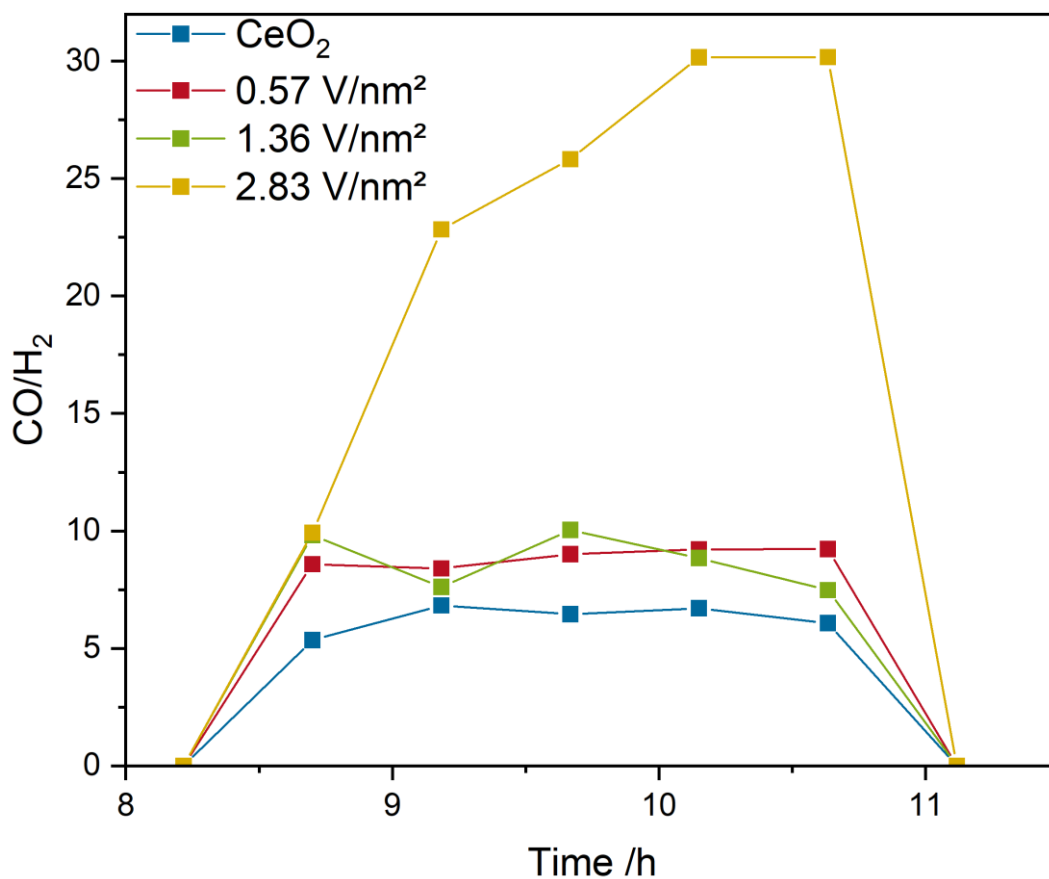
Figure S3: CO/H_2 ratio under ODH conditions (12.5% CO_2/12.5% C_3H_8/He) for ceria and vanadia-loaded samples as an indicator for the ODH/DDH+RWGS ratio.

Table S1: Calculated carbon balances from chromatograms measured during 12.5% CO_2/12.5% C_3H_8/He exposure at 550 °C.

Sample	CeO₂	0.57 V/nm²	1.36 V/nm²	2.83 V/nm²
Carbon Balance /%	6.6	6.2	6.3	7.2
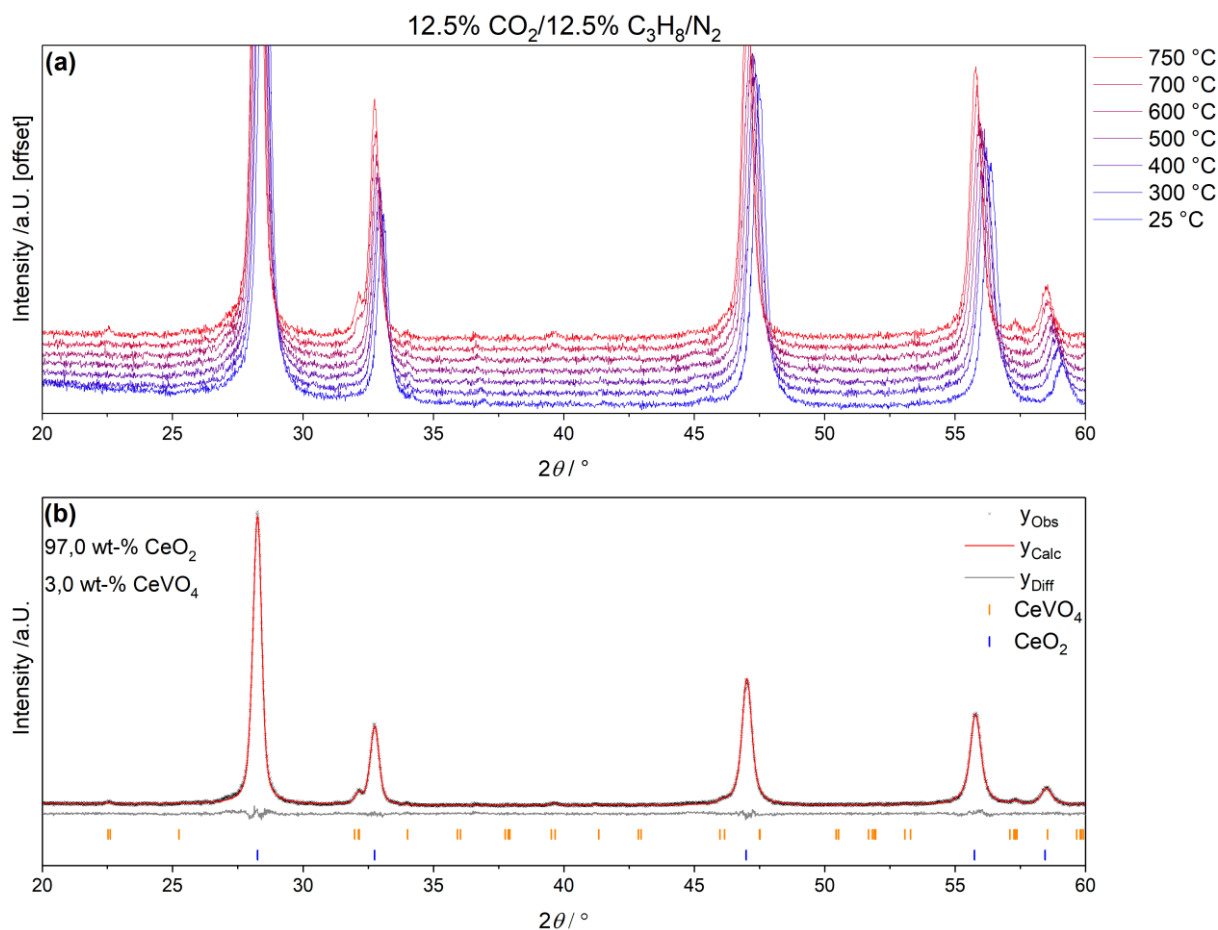
Figure S4: (a) In situ XRD patterns of the 2.83 V/nm² sample under ODH conditions (12.5% CO_2/12.5% C_3H_8/N_2) between 25 and 750 °C and **(b)** Rietveld analysis of the diffraction pattern recorded at 750 °C to quantify $CeVO_4$.
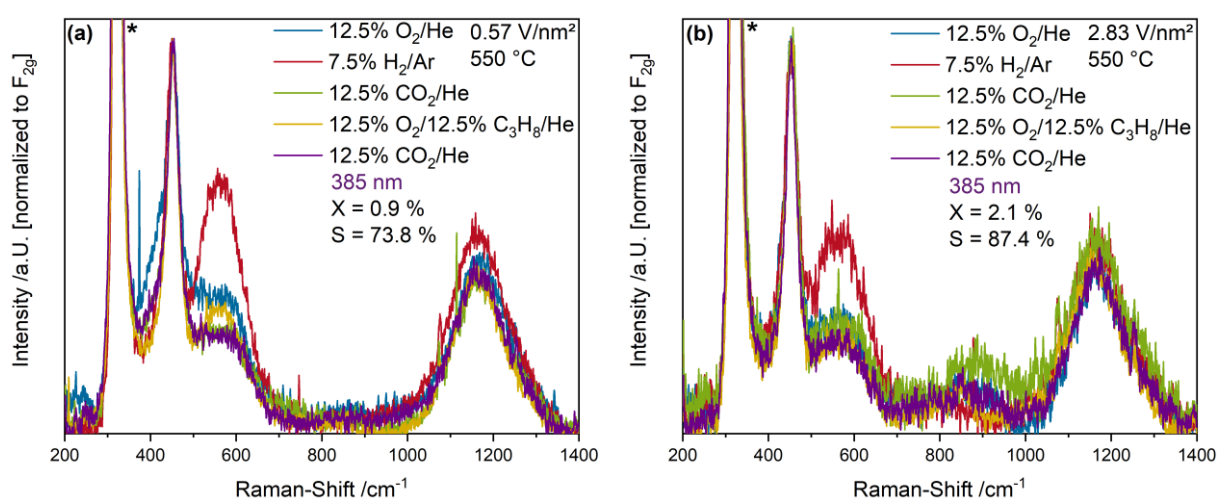
Figure S5: Operando UV-Raman spectra (385 nm excitation) of **(a)** the 0.57 and **(b)** the 2.83 V/nm² sample recorded under different gas feeds at 550 °C. The spectra are normalized to the F_{2g} mode and the peak caused by the CaF_2 window is marked with an asterisk. The conversions and selectivities are given.
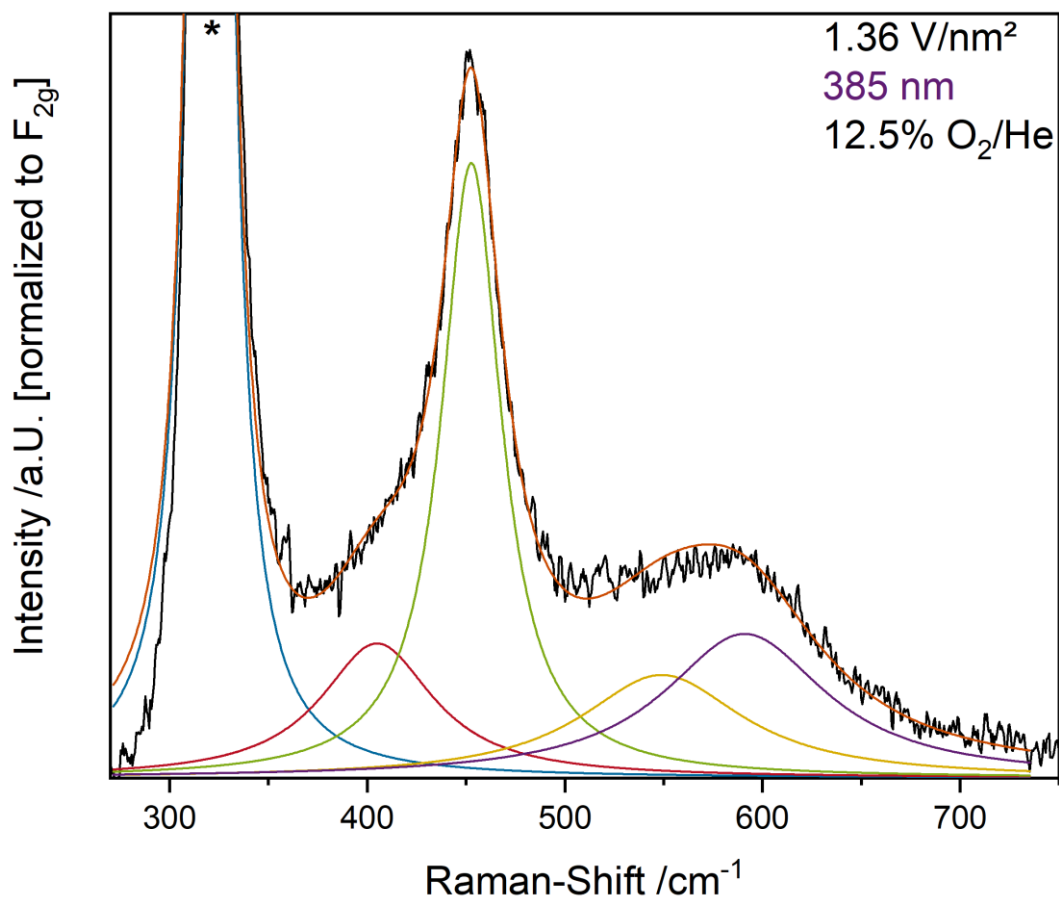
Figure S6: Exemplary fit of the 1.36 V/nm² sample under 12.5% O_2/He at 550 °C. The spectrum was normalized to the F_{2g} peak and the peak caused by the CaF_2 peak is marked with an asterisk. Two components were used to fit the defect region in agreement with previous literature. The CaF_2 peak was also fitted as it overlapped notably with the other signals.
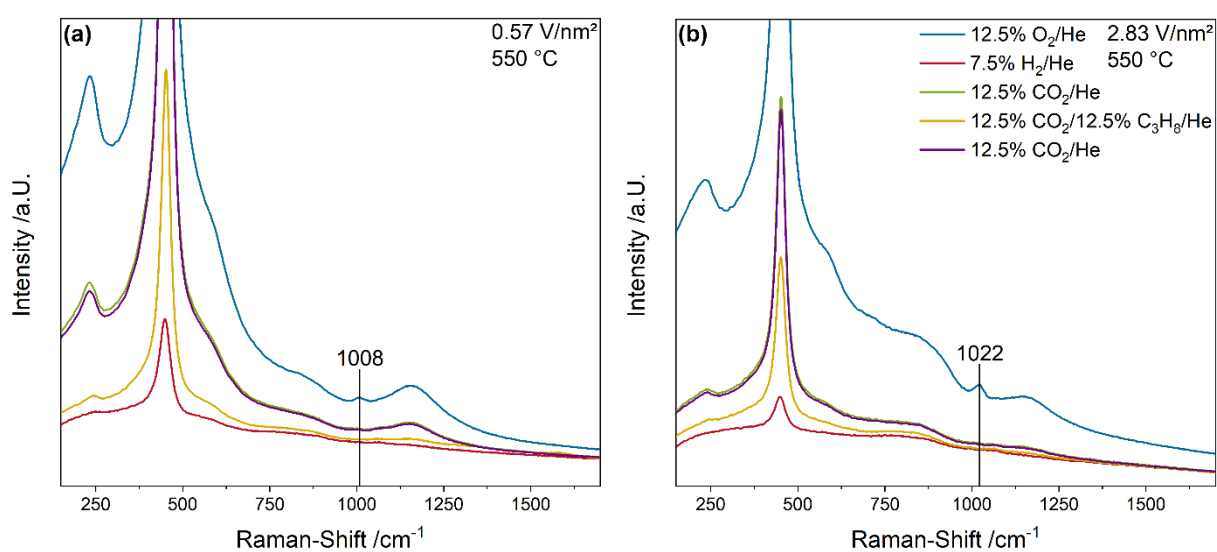
Figure S7: Operando Vis-Raman spectra (514 nm excitation) of **(a)** the 0.57 and **(b)** the 2.83 V/nm² samples under different gas feeds recorded at 550 °C. The vanadyl peak is highlighted.
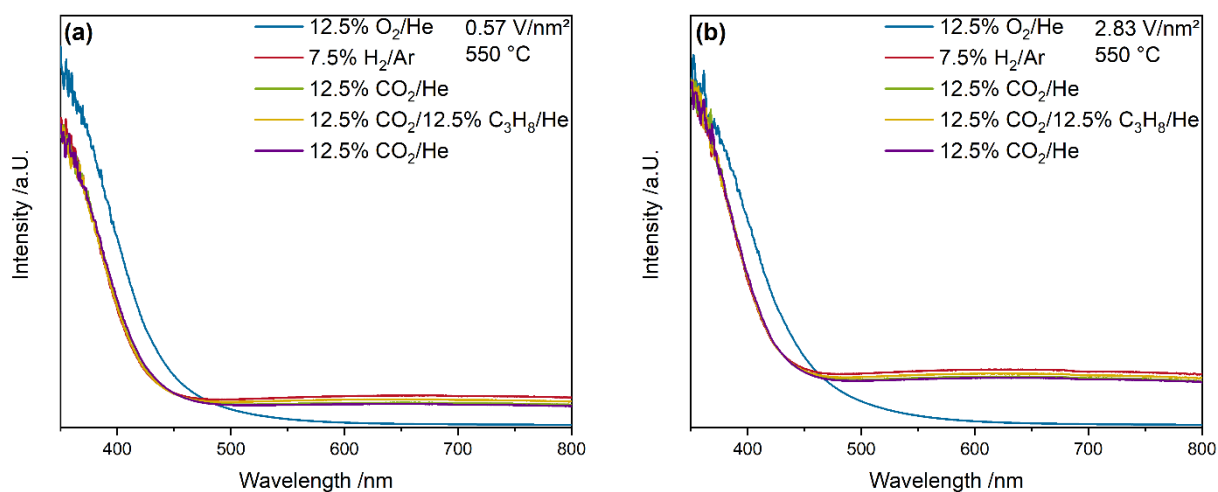
Figure S8: Operando UV-Vis spectra (385 nm excitation) of **(a)** the 0.57 and **(b)** the 2.83 V/nm² sample recorded under different gas feeds at 550 °C.
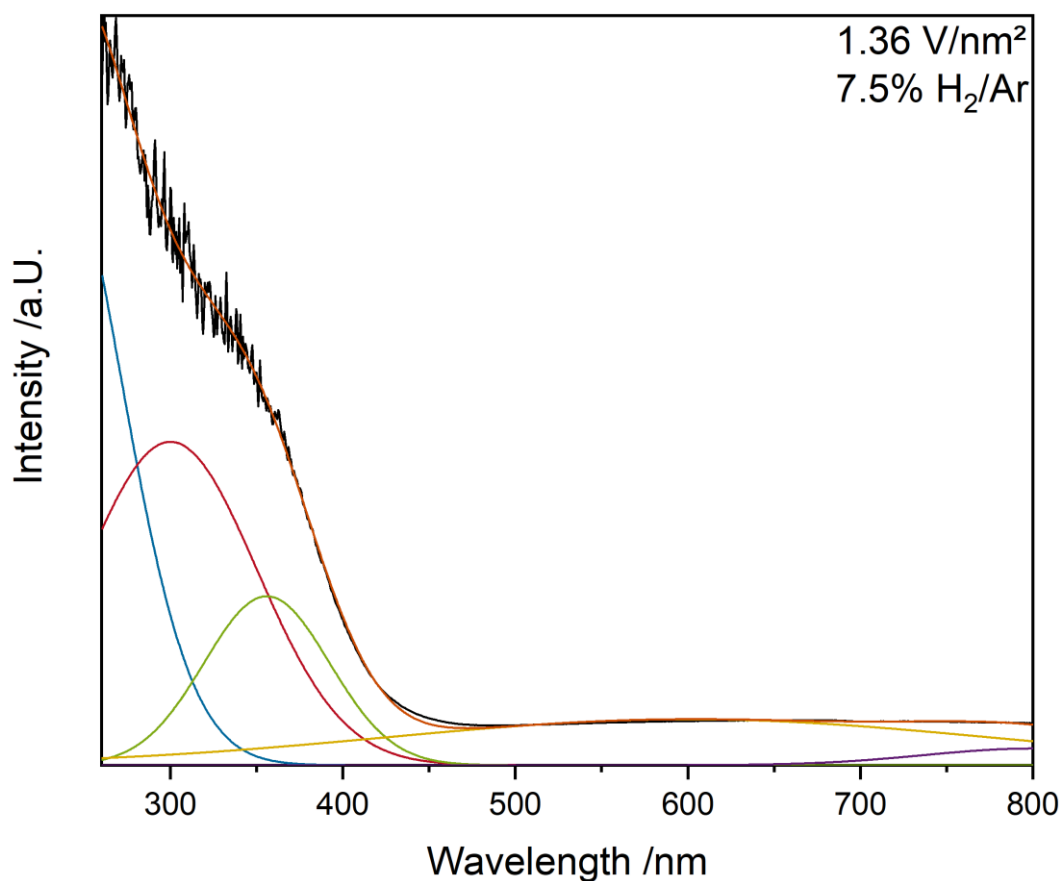
Figure S9: Exemplary fit of the UV-Vis spectrum of the 1.36 V/nm² sample under reductive conditions at 550 °C using five Gaussian-Lorentzian product functions (see experimental section).
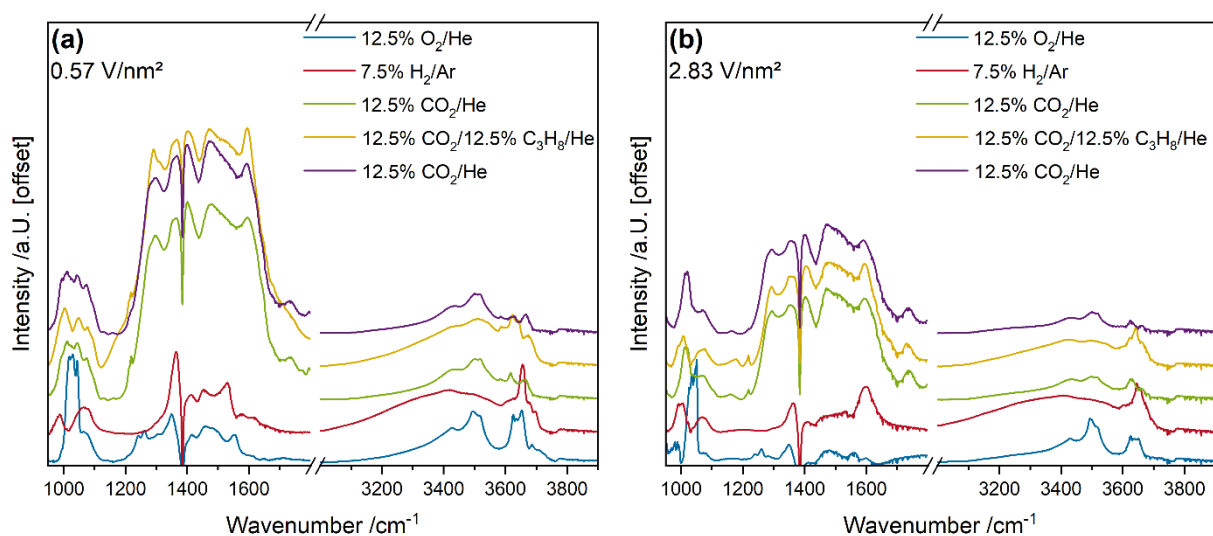
Figure S10: Quasi in situ DRIFT spectra of (a) the 0.57 and (b) the 2.83 V/nm² sample recorded after pre-treatment under the indicated gas feeds at 550 °C and subsequent rapid cooling (200 °C/min) to room temperature under helium.
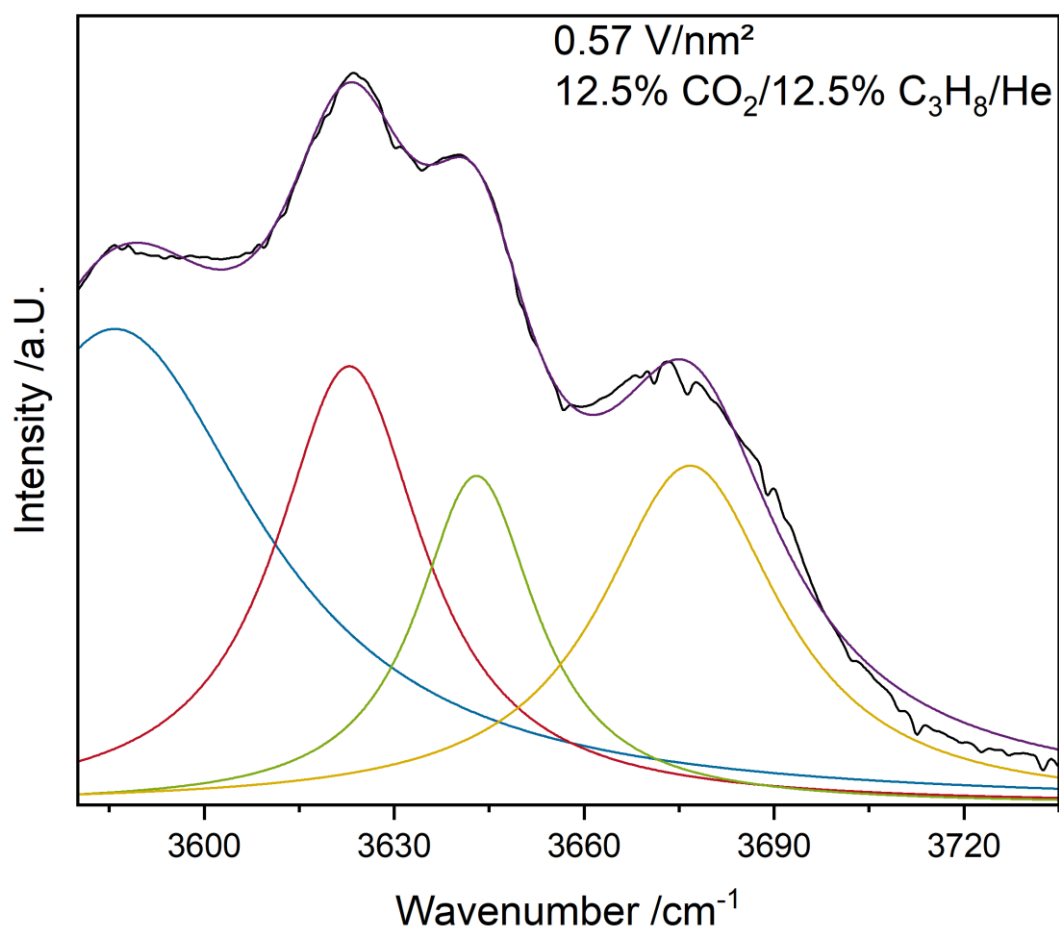
Figure S11: Exemplary fit of the Ce-OH region of the 0.57 V/nm² sample under ODH conditions using four Lorentzian functions.

4.2 Propane ODH over VO_x/TiO_2 Catalysts Using O_2 and CO_2 as the Oxidizing Agents

The second part of this work deals with the elucidation of the reaction mechanism of the propane ODH reaction over VO_x/TiO_2 catalysts using O_2 and CO_2 as the oxidizing agent. This allows to obtain detailed insight into the role of the support on the reaction mechanism compared to VO_x/CeO_2.

4.2.1 Collaborative Mechanistic Effects between Vanadia and Titania during the Oxidative Dehydrogenation of Propane Investigated by Operando and Transient Spectroscopies

The seventh overall publication elucidates the reaction mechanism of the propane ODH reaction over VO_x/TiO_2 catalysts. To achieve this, differently loaded VO_x samples supported on P25 were investigated by a combination of operando multi-wavelength Raman, UV-Vis, ME-DRIFT, quasi in situ XP, and ^{51}V ssNMR spectroscopy, as well as XRD. As a comparison, $VO_x/TiO_2/SiO_2$ samples were prepared by ALD to investigate the transferability of the obtained results to different titania systems. First, the active site, which facilitated the oxidation reaction, was identified to be oxygen from vanadia, where dimeric species are preferred over monomeric species. Second, a loading dependence during propane ODH could be established for the first time due to the combination of UV-Raman with ^{51}V ssNMR spectroscopy. V=O oxygen was identified to be most active at low loadings, which shifts to more reducible V-O-V species of oligomeric species at high loadings, becoming linear compared to the doubly bridged V-O-V of dimers. Third, the anatase/rutile content can vary under reaction conditions and the increased rutile concentration facilitates vanadia's mobility on the titania surface. This facilitates oligomerization, which influences reactivity. Furthermore, using ME-DRIFTS, the direct hydrogen transfer from propane to vanadia oxygen atoms, which occurs via titania surface lattice oxygen, was observed for the first time. At last, CO_x formation was determined to be site-dependent and to occur in parallel to propylene formation. The combination of these results allowed for the proposal of a detailed mechanistic picture, highlighting the importance of combining multiple operando and transient methods to enhance the level of understanding of oxidation catalysts.

7. Reprinted with permission from Leon Schumacher, Johannes Pfeiffer, Jun Shen, Torsten Gutmann, Hergen Breitzke, Gerd Buntkowsky, Kathrin Hofmann, Christian Hess, Collaborative Effects

between Vanadia and Titania during the Oxidative Dehydrogenation of Propane Investigated by Operando and Transient Spectroscopies, ACS Catal., 13, 8139–8160 (2023). Copyright 2023 American Chemical Society.

Collaborative Mechanistic Effects between Vanadia and Titania during the Oxidative Dehydrogenation of Propane Investigated by Operando and Transient Spectroscopies

Leon Schumacher, Johannes Pfeiffer, Jun Shen, Torsten Gutmann, Hergen Breitzke, Gerd Buntkowsky, Kathrin Hofmann, and Christian Hess*

Read Online

ACCESS | Metrics & More | Article Recommendations | Supporting Information

ABSTRACT: The oxidative dehydrogenation (ODH) of propane is of great technical importance, and supported VO_x catalysts have shown promising properties for the reaction. One of the most prominent and active supports is titania, which exhibits a high activity but many questions regarding the catalyst system are still in debate. In this study, we elucidate the mechanism of the propane ODH reaction over VO_x/TiO_2, using P25 and ALD (atomic layer deposition) synthesized TiO_2/SBA-15 as a support, with X-ray photoelectron spectroscopy (XPS), X-ray diffraction (XRD), ^{51}V solid-state (ss)NMR, operando multiwavelength Raman, operando UV−vis, and transient IR spectroscopies. Bare titania shows a small conversion, leading to carbon formation, and the reaction occurs at the interface between anatase and rutile. In comparison, in VO_x/TiO_2 catalysts, the activity shifts from titania to vanadia sites. UV-Raman spectroscopy and structural characterization data revealed the reaction to involve preferentially the V═O bonds of dimeric species rather than doubly bridged V−O−V bonds, which leads to higher propene selectivities. The active vanadium site shows a nuclearity-dependent behavior; that is, at higher loadings, when oligomeric vanadia is present, it shifts from V═O bonds to linear V−O−V bonds in oligomers, leading to less selective oxidation due to the better reducibility. Our operando/transient spectroscopic results demonstrate the direct participation of the titania support in the reaction by influencing the degree of vanadia oligomerization and enabling rapid hydrogen transfer from propane to vanadia via Ti−OH groups on anatase, accelerating the rate-determining step of the initial C−H bond breakage. The broader applicability of the results is confirmed by the behavior of the ALD-synthesized sample, which resembles that of P25. Our results highlight the detailed level of mechanistic understanding accessible from multiple spectroscopic approaches, which can be readily transferred to other materials and/or reactions.

KEYWORDS: propane ODH, vanadia, titania, transient IR spectroscopy, operando spectroscopy, nuclearity dependence, support interaction
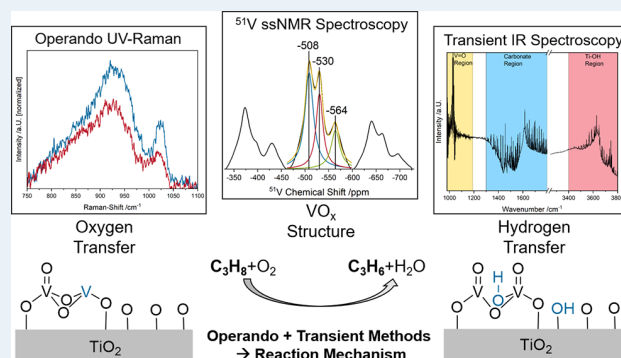
1. INTRODUCTION

Propylene is an important basic chemical that is used to produce a variety of different industrial and consumer products, such as polypropylene, propylene glycol, etc. The large demand for propylene by the chemical industry cannot be met by traditional production methods such as steam cracking. Therefore, the use of alternative methods of propylene production would be of great utility to close the gap between demand and supply.[1−3] One promising alternative way to produce propylene is the oxidative dehydrogenation (ODH) of propane, where, in contrast to traditional processes, oxygen is added to the feed. This has multiple advantages, including that the reaction becomes exothermic, allowing energy to be saved by heat integration of the additionally released energy. Furthermore, the reaction can occur at lower temperatures,

further increasing the energy savings. Finally, the amount of coke that is traditionally formed on the catalysts during conventional processes by their oxidation to CO_x is reduced, hence increasing the catalyst lifetime and reducing waste.[1−3] The main issue in making propane ODH viable is the low selectivity of the reaction due to the over-oxidation of propane to CO_x. Therefore, the reaction needs to be suitably catalyzed.

A promising class of catalysts for the reaction is supported vanadia (VO_x), which has previously been shown to be active on multiple supports (SiO_2, Al_2O_3, TiO_2, CeO_2, ZrO_2) with good selectivities.[4−8] One of the most active systems for the reaction is vanadia supported on titania (VO_x/TiO_2), which shows one of the lowest activation energies for the reaction.[4,5] The high activity has been proposed to be caused by the active participation of the support in the reaction,[3,5,6] but the elucidation of the detailed interactions within the VO_x/TiO_2 system is still a challenge. This is partly due to the strong absorption of titania in the UV range, which can lead to the self-absorption of the spectroscopic signal if it is located in a similar range (e.g., UV-Raman).[9]

In previous studies, VO_x/TiO_2 catalysts were investigated for a large variety of reactions, including NH_3 selective catalytic reduction (SCR),[10−13] the combustion of volatile organic compounds (VOCs),[14,15] hydrodeoxygenation,[16] selective alcohol oxidation (methanol,[17] ethanol[18]), photocatalytic reactions[19,20] (due to the semiconducting properties of TiO_2), and also ethane[21,22] and propane ODH.[4−6,23−29] In the context of ODH reactions, a major point of discussion has been the interaction between titania and vanadia and, in particular, the exact role of titania support. On the one hand, this has been proposed to actively participate in the reaction via defect formation (i.e., Ti−OH or oxygen vacancy formation) and, on the other, to coordinate the vanadium in a way that renders it more active than on other support materials.[6,30] Furthermore, the exact vanadia structure and the influence of the vanadia nuclearity on the reactivity are not clear.[13,31] The vanadyl peak for VO_x/CeO_2 shows a detailed fine structure in Raman spectra, which allows for the assignment and quantification of the distribution of vanadia nuclearities, thus determining their detailed influence on the catalytic activity.[8,32] For VO_x/TiO_2 systems, however, the situation appears to be more complex, as there are only two contributions in the vanadyl region of the Raman spectrum, which have previously been assigned to short- and long-chain vanadia species.[13,31,33] For ODH reactions over VO_x/TiO_2, previous studies have provided valuable insight into some of the aspects outlined above. For example, by use of operando X-ray absorption spectroscopy (XAS) during ethanol ODH, Zabilska et al.[18] showed that the redox cycle of the reaction takes place over vanadia rather than titania, which does not change its oxidation state. For propane ODH, despite the large number of studies on supported vanadia, including VO_x/TiO_2, there are only a few operando[34] and no transient spectroscopic studies available in the literature that provide direct spectroscopic evidence of the reaction mechanism and the catalyst's mode of operation.[4−6,23−29]

In this study, we aim to provide an answer to the following key questions debated in the literature in the context of the mechanism of propane ODH over VO_x/TiO_2 catalysts: What is the active site of the catalyst, and what is its nuclearity dependence? How does the titania support influence the reaction, and, more specifically, does it directly participate in the reaction? How can the selectivity behavior be explained? For that, we combine multiple experimental approaches, which have rarely been used in the context of alkane ODH before, to obtain a fresh perspective on structural dynamics. First, we use multiwavelength Raman spectroscopy, which has shown great potential for VO_x/CeO_2 systems, to investigate bulk titania by tuning the excitation wavelength to 385 nm. There we avoid most of the strong UV absorption of titania but can still selectively enhance the support's signal intensity due to resonance effects, allowing for the dedicated investigation of titania (385 nm) and vanadia (514 nm).[7,8] By combining this with further methods, including ^{51}V ssNMR, X-ray photoelectron spectroscopy (XPS), X-ray diffraction (XRD), and operando UV−vis as well as modulation-excitation (ME) DRIFTS (diffuse reflectance infrared Fourier transform spectroscopy), we aim to elucidate structure−activity relationships, leading to a detailed mechanistic picture. The combination of multiple operando spectroscopies and ME-DRIFTS has previously been shown to enable an enhanced level of understanding of other oxidation catalysts.[8,35] Finally, as a reference system and to demonstrate the broader applicability of the results, we investigate the behavior of ALD-synthesized samples, which reduce the amount of bulk titania, thus minimizing the influence of UV absorption in comparison to the P25 samples with different vanadium loadings.[12,36]

2. EXPERIMENTAL SECTION

2.1. Sample Preparation. As a support, two different materials were used. Titania P25 (Aeroxide, Sigma-Aldrich, ≥99.5%) was purchased, whereas silica SBA-15 was synthesized as described previously.[37] The P25 samples were characterized by nitrogen physisorption and subsequent analysis by the Brunauer−Emmet−Teller (BET) method, yielding a surface area of 73 m^2/g. They were loaded by wet-impregnation using an aqueous solution containing a 1:2 ratio of ammonium metavanadate (AMV) and oxalic acid with four different concentrations (1.219, 0.585, 0.244, and 0.049 mol/L), resulting in samples loaded with vanadium surface densities of 2.5, 1.2, 0.5, and 0.1 V/nm^2, respectively, which is below monolayer loading, thus ensuring that only amorphous vanadia was present.[27] The loaded samples were dried at 120 °C for 12 h and then calcined for 4 h at 480 °C.

SBA-15 was coated with TiO_2 by ALD in a custom-build setup.[38] After 200 mg of SBA-15 had been placed in the ALD reactor, the reactor temperature was set to 60 °C (pressure: 1.3 Torr). The SBA-15 was then coated with 72 ALD cycles, where one cycle consisted of three half cycles of $TiCl_4$ and three half cycles of H_2O.[12] During each half cycle, the sample was exposed to $TiCl_4$/H_2O for 60 s and then flushed for 60 s with nitrogen.[39] The theoretical thickness of the resulting TiO_2 thin film corresponds to 10 nm on a silicon wafer as determined by ellipsometry.[40] The coated samples were calcined in air at 600 °C for 12 h to crystallize the deposited TiO_2 and will be referred to as SBA15-T (SBA-15 coated with titania). The specific surface area was determined to be 78 m^2/g by using nitrogen physisorption and subsequent BET analysis. The sample was then loaded with vanadia in the same way as the P25 samples, and the precursor concentration was adjusted for the different surface area, resulting in an aqueous solution with a 1:2 ratio of AMV and oxalic acid with a concentration of 0.621 mol/L, resulting in a vanadium surface density of 1.2 V/nm^2. A summary of the prepared samples is given in Table 1.

2.2. Catalytic Testing. Catalytic testing was performed in a CCR 1000 reaction cell (Linkam Scientific) in a fluidized bed operating mode, using 60 mg of catalyst for the P25 samples and, due to its much lower density, 25 mg of the ALD-synthesized samples. The samples were first dehydrated in 12.5% O_2/He for 1 h at 365 °C, subsequently cooled to 50 °C, exposed to 12.5% O_2/12.5% C_3H_8/He with a total flow rate of

Table 1. Overview of the P25- and ALD-Synthesized Samples Used in This Study

sample name	surface area (m^2/g)	vanadia density (V/nm^2)	ALD substrate	number of cycles
P25	73			
P25+0.1 V/nm^2	73	0.1		
P25+0.5 V/nm^2	73	0.5		
P25+1.2 V/nm^2	73	1.2		
P25+2.5 V/nm^2	73	2.5		
SBA15-T	78		SBA-15	72
SBA15-T+1.2 V/nm^2	78	1.2	SBA-15	72

40 mL_n/min, and then heated in 45 °C steps up to 550 °C, staying at each temperature for 1 h. The gas-phase composition was analyzed continuously using a gas chromatograph (GC, Agilent Technologies 7890B) equipped with a PoraPlot Q and a Molsieve column as well as a thermal conductivity detector (TCD) and a flame ionization detector (FID) in series. The set-up is connected through a twelve-way valve. One chromatogram is measured every 29 min, resulting in two chromatograms for each temperature, which were averaged. The pressure before and after the GC was monitored to correct the detected areas for pressure fluctuations. The obtained conversions were normalized to the surface area of the catalyst due to the significantly different sample masses used for P25 and ALD-synthesized catalysts.

2.3. X-Ray Diffraction. Powder X-ray diffraction (XRD) patterns were recorded on a Stadi-P (Stoe & Cie) diffractometer with a Ge(111)-monochromator, Cu Kα_1 radiation (λ = 1.54060 Å), and a MYTHEN-1K (Dectris) detector, using a flat sample holder in transmission geometry. The powder XRD patterns were recorded ex situ.

2.4. Diffuse Reflectance UV−Vis Spectroscopy. Diffuse reflectance (DR) UV−vis spectra were recorded on a Jasco V-770 UV−Vis spectrometer. Dehydrated $BaSO_4$ was used as the white standard. For each experiment, 90 mg of catalyst was placed in the commercially available reaction cell (Praying Mantis High-Temperature Reaction Chamber, Harrick Scientific) equipped with transparent quartz glass windows. For structural characterization, spectra were measured at room temperature after dehydration in 12.5% O_2/He for 1 h at 365 °C. Operando spectra were measured at 320 °C during reactive conditions (12.5% C_3H_8/12.5% O_2/He) and for comparison under oxidizing conditions (12.5% O_2/He), both after dehydration in 12.5% O_2/He for 1 h at 365 °C with a total flow rate of 40 mL_n/min. The spectra were further analyzed by a least-squares fitting analysis using Gaussian−Lorentzian (70/30) product functions. Product functions instead of purely Lorentzian functions were used to account for the large contribution of natural line broadening to the overall line shape caused by the short lifetime of the electronically excited states.

2.5. UV-Raman Spectroscopy. UV-Raman spectroscopy was performed at an excitation wavelength of 385 nm generated by a laser system based on a Ti:Sa solid-state laser pumped by a frequency-doubled Nd:YAG laser (Coherent, Indigo). The fundamental wavelength is frequency doubled to 385 nm using a LiB_3O_5 crystal. The light is focused onto the sample, and the scattered light is collected by a confocal mirror set-up and focused into a triple-stage spectrometer (Princeton Instruments, TriVista 555).[41] Finally, the Raman contribution is detected by a charge-coupled device (CCD, 2048 × 512

pixels) cooled to −120 °C. The spectral resolution of the spectrometer is 1 cm^{-1}. For Raman experiments, 70 mg of catalyst was placed in a CCR 1000 reactor (Linkam Scientific Instruments) equipped with a CaF_2 window (Korth Kristalle GmbH). A fluidized bed reactor was employed to avoid laser-induced changes in the sample by moving the particles in and out of the laser beam, allowing the use of a laser power of 7.5 mW at the location of the sample. Furthermore, the fluidized bed helps to homogenize the temperature profile across the sample. Data processing included cosmic ray removal and background subtraction. For structural characterization, spectra were measured at room temperature after dehydration at 365 °C for 1 h in 12.5% O_2/He. Operando spectra were measured at 320 °C during exposure to reactive conditions (12.5% C_3H_8/12.5% O_2/He) and for comparison under oxidizing conditions (12.5% O_2/He) after 1 h of dehydration in 12.5% O_2/He at 365 °C with a total flow rate of 40 mL_n/min. The spectra were normalized by setting the value of the anatase E_g peak to one and adjusting the remaining intensity values accordingly. The spectra were further analyzed by a least-squares fitting analysis using Lorentzian functions.

2.6. Vis-Raman Spectroscopy. Visible (Vis) Raman spectroscopy was performed at 514 nm excitation, emitted from an argon ion gas laser (Melles Griot). The light was focused onto the sample, gathered by an optical fiber, and dispersed by a transmission spectrometer (Kaiser Optical, HL5R). The dispersed Raman radiation was subsequently detected by an electronically cooled CCD detector (−40 °C, 1024 × 256 pixels). The spectral resolution was 5 cm^{-1} with wavelength stability of better than 0.5 cm^{-1}. For Raman experiments, 70 mg of catalyst was filled into a CCR 1000 reactor (Linkam Scientific Instruments) equipped with a quartz window (Linkam Scientific Instruments). A fluidized bed reactor was employed to avoid laser-induced damage, allowing the use of a laser power of 5 mW at the location of the sample. Data analysis of the Raman spectra included cosmic ray removal and an auto new dark correction as well as normalization to the anatase E_g peak. For structural characterization, spectra were measured at room temperature after dehydration in 12.5% O_2/He for 1 h at 365 °C. Operando spectra were measured at 320 °C during exposure to 12.5% C_3H_8/12.5% O_2/He, and for comparison under oxidizing conditions (12.5% O_2/He), both measured after 1 h of dehydration in 12.5% O_2/He at 365 °C with a total flow rate of 40 mL_n/min. The spectra were further analyzed by a least-squares fitting analysis using Lorentzian functions.

2.7. X-ray Photoemission Spectroscopy. X-ray photoelectron spectroscopy (XPS) was carried out on an SSX 100 ESCA spectrometer (Surface Science Laboratories Inc.) employing a monochromatic Al Kα X-ray source (1486.6 eV) operated at 9 kV and 10 mA; the spot size was approximately 1 mm × 0.25 mm. The base pressure of the analysis chamber was <10^{-8} Torr. Survey spectra (eight measurements) were recorded between 0 and 1100 eV with 0.5 eV resolution, whereas detailed spectra (30 measurements) were recorded with 0.05 eV resolution. To account for sample charging, the C 1s peak of ubiquitous carbon at 284.4 eV was used to correct the binding-energy shifts in the spectra. Data analysis included a Shirley background subtraction and a peak-fit analysis using Gaussian−Lorentzian (70/30) production functions. Atomic concentrations were calculated using the relative sensitivity factors (RSFs) given in Table 2.

Table 2. Relative Sensitivity Factors (RSFs) Used for the XPS Analysis

	C 1s	O 1s	Si 2p	Ti 2p	V 2p
RSF	0.537	2.930	0.817	7.810	9.660

2.8. Physical Characterization. The specific surface area and the pore diameter were determined by analysis of the nitrogen adsorption and desorption isotherms recorded on a Surfer BET analyzer (Thermo Fisher) after drying the samples in a vacuum for 24 h. The isotherms were then analyzed by multipoint BET analysis.

2.9. ^{51}V ssNMR Spectroscopy. ^{51}V ss (solid-state) NMR spectra at 14.1 T were recorded on a Bruker Avance III HD 600 MHz spectrometer operating at a frequency of 157.75 MHz for ^{51}V as reported previously.[42] Experiments were performed with a 3.2 mm ^{1}H/X/Y triple resonance probe under magic angle spinning (MAS) at spinning rates of 18 and 21 kHz. Spectra were acquired using single-pulse excitation with a pulse length of 0.8 μs. This corresponds to flip-angles of ca. 30° at this probe. The relaxation delay was set to 1 s, and 2.65×10^4 to 3.6×10^5 scans were accumulated for each spectrum. The ^{51}V chemical shifts were referenced to VOCl$_3$, employing V$_2$O$_5$ ($\delta = -614$ ppm) as an external standard.[43]

^{51}V ssNMR spectra at 9.4 T were recorded on a Bruker Avance II+ 400 MHz spectrometer operating at a frequency of 105.25 MHz for ^{51}V. Experiments were performed with a 3.2 mm ^{1}H/X/Y triple resonance probe under MAS at a spinning rate of 21 kHz. Spectra were acquired using single-pulse excitation with a pulse length of 0.66 μs. This corresponds to a flip-angle of ca. 30° with respect to a 90° pulse on ^{13}C. The relaxation delay was set to 1 s, and 1.8×10^5 scans were accumulated for each spectrum. The ^{51}V chemical shifts were referenced to VOCl$_3$, employing V$_2$O$_5$ ($\delta = -614$ ppm) as an external standard.[43]

To avoid a structural change of the vanadia-loaded samples by water adsorption, samples were first dehydrated in 12.5% O$_2$/He for 1 h at 365 °C in the Linkam reactor, cooled down to 25 °C in pure helium, and then transferred via an argon flushed glovebox into a watertight NMR rotor. The spectra were analyzed by a least-squares fitting analysis using Lorentzian/Gaussian product functions.

2.10. Modulation-Excitation DRIFTS. ME-DRIFT spectroscopy was performed on a Vertex-70 IR spectrometer (Bruker); the modifications made for recording ME-DRIFT spectra have been described elsewhere.[8,35,44] For each experiment, 90 mg of catalyst was used.

We used the rapid scan mode extension of Bruker's spectrometer software OPUS 7.2. Spectra were measured from 850 to 3800 cm^{-1} with a resolution of 0.5 cm^{-1}, an aperture of 8 mm, and a mirror speed of 40 kHz. A Valco Instruments 4/2 valve (Model E2CA, version ED), communicating with the Vertex-70, was used to rapidly switch between different gas feeds, which were controlled via digital mass flow controllers (Bronkhorst).

As gases, we used C$_3$H$_8$ (Westfalen, 3.5), C$_3$D$_8$ (Eurisotop, 98% isotopic labeling), O$_2$ (Westfalen, 5.0), and helium (Westfalen, 5.0). One measurement series consisted of 20 periods, each of which had a duration of 360 s and consisted of 240 spectra. During each period, the gas phase was switched after 120 spectra and back to the initial gas phase with the start of the new period. For one spectrum, five consecutive interferograms were averaged so that a new spectrum was acquired every 1.54 s.

As background, the catalyst spectrum itself was used after 60 min of dehydration in a 12.5% O$_2$/helium atmosphere at 365 °C and a 10 min treatment at 320 °C in one of the reaction gases for conventional ME-DRIFTS (12.5% O$_2$ or 12.5% C$_3$H$_8$ in helium) or in reaction gas atmosphere (12.5% C$_3$H$_8$/12.5% O$_2$/75% He) for isotope ME-DRIFTS. The flow was kept constant at 100 mL$_n$/min during the pretreatment and experiment.

During conventional ME-DRIFTS, a flow of either 12.5% C$_3$H$_8$ or 12.5% O$_2$ in helium was kept constant over the sample while the other feed gas was pulsed over the sample. In our isotope ME-DRIFTS experiments, the propane-h8-containing reaction atmosphere was switched to a propane-d8-containing reaction atmosphere, while the flow of oxygen through the reaction chamber was constant.

During all ME experiments, the temperature was kept at 320 °C. To remove the gas-phase contribution, we subtracted gas-phase phase-sensitive detection (PSD) spectra over KBr (see Figure S1) from each recorded DRIFT spectrum. To exclude the possibility of intensity fluctuations over multiple periods, we checked the intensity profile at three distinct wavenumbers, representative of the background, an adsorbate peak, and a gas-phase peak, but detected no absolute intensity changes over multiple periods that could influence the Fourier transform (see Figure S2). Peak-fitting analysis of ME-DRIFT spectra was performed using Lorentzian functions employing the Levenberg−Marquardt algorithm implemented in OriginLab 2018.

To obtain phase-sensitive spectra, the time-resolved three-dimensional (3D) spectral data was converted from the time to the phase domain. For an overview, the resolution of phase spectra was chosen to be 30°, whereas mechanistic insights were obtained using a resolution of 1°. The main operation of PSD is a Fourier transform according to[45]

$$I_{\tilde{\nu}}(\varphi) = \frac{2}{T} \int_0^T I_{\tilde{\nu}}(t) \cdot \sin(2\pi f t + \varphi) \mathrm{d}t$$

where $I(t)$ is the time-dependent intensity at one specified wavenumber ($\tilde{\nu}$) that is convoluted with the sine function representing the modulation of the external parameter (e.g., the gas-phase concentration), thus forming $I(\varphi)$, the phase-resolved intensity. The frequency of the external modulation is f, whereas 0 and T represent the times at which the considered dataset begins and ends, respectively. To obtain a complete phase-resolved spectrum, this procedure is repeated for every wavenumber. By varying φ from 0 to 360° with a chosen resolution and repeating the steps above, the complete phase-resolved dataset is created.

To obtain time constants for a particular wavenumber, first, the phase angle in the PSD function is determined where $I(t)$ shows the best overlap with the external modulation function. This is done for a set of chosen peak positions. To this end, the phase angle corresponding to the phase spectrum with the largest signal at the particular wavenumber is extracted by automatically comparing the intensities for spectra of all of the different phase angles. The following equation is used to translate this phase angle back into a time value within the interval of one period in order to make it more interpretable.

$$t_{\mathrm{per}} = (360 - \varphi_{\mathrm{max}}) 360 \cdot t_{\mathrm{per}}$$
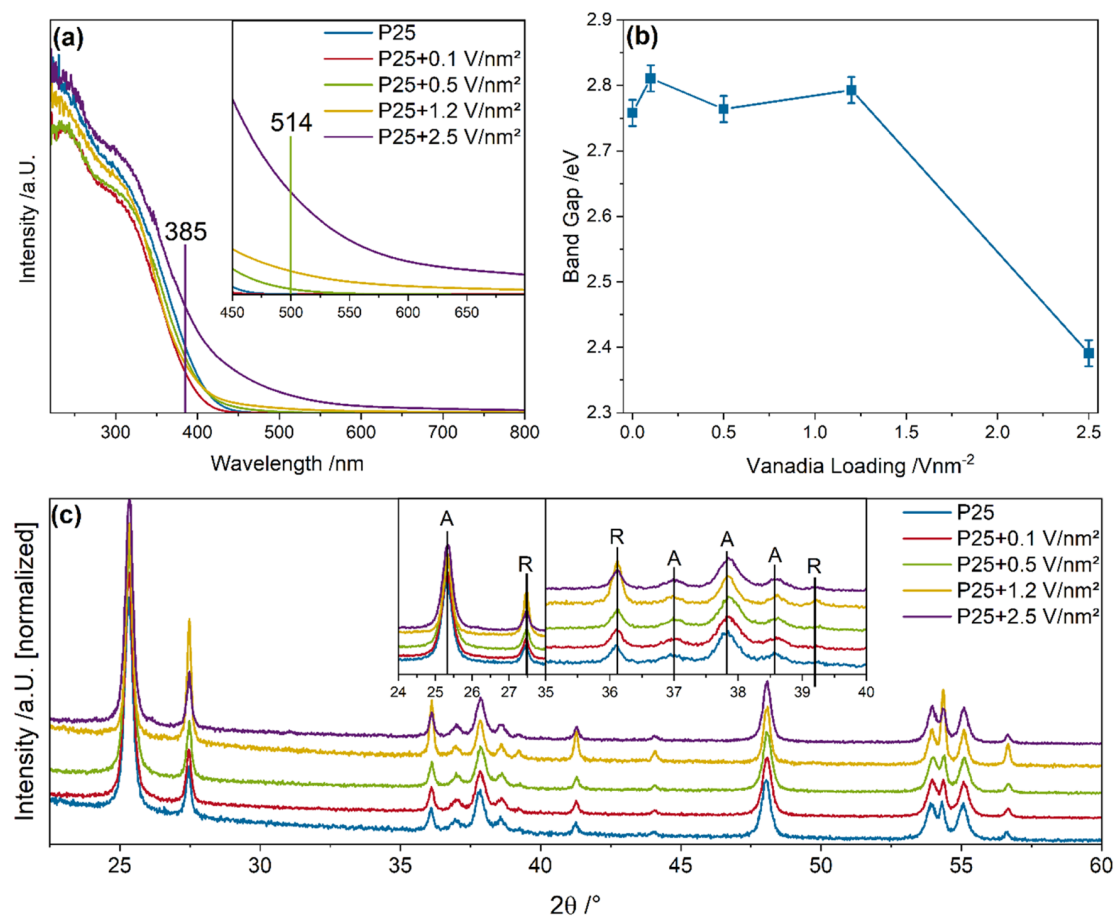
Figure 1. Structural characterization of VO_x/TiO_2: (a) UV−vis spectra of bare P25 and vanadia-loaded samples. The inset provides an enlarged view of the visible region. The used Raman excitation wavelengths are marked. (b) Band gaps of bare P25 and vanadia-loaded samples as determined from Tauc plots. (c) XRD patterns of bare P25 and vanadia-loaded samples. In the insets, the reflexes assigned to rutile and anatase within 24−28 and 35−40° are marked. The spectra and diffractograms were recorded under pristine conditions after dehydration in 12.5% O_2/He for 1 h at 365 °C and subsequent cooling to room temperature.

The experimental error is 1.54 s, which represents the measurement time of one spectrum. For the temporal analysis of the vanadyl peak, the time constants of the overtones were considered due to their much higher accuracy in comparison to the fundamental vibration (see Figure S3), as discussed previously.[8] Further details of the used software and the full code, which is available free of charge at GitHub, can be found elsewhere.[46]

3. RESULTS AND DISCUSSION

In the following, the results for the P25-based samples (VO_x/TiO_2) will be discussed. The results for the SBA-15-based $VO_x/TiO_2/SiO_2$ samples are presented in the Supporting Information (SI) and will be discussed there, establishing a detailed structural model describing the layered ALD system. They will be referenced throughout the manuscript as an addition to the points made in the following.

3.1. Characterization. The P25 samples were first characterized regarding their electronic and geometric structure. Figure 1 shows their UV−vis spectra, determined band gap energies, and XRD patterns. The UV−vis spectra and XRD patterns of the $VO_x/TiO_2/SiO_2$ samples are given in the SI (see Figure S4) and will be discussed there. Tauc plots were used to determine the band gap energies (see Figures S5 and S6). The wavelengths at which Raman spectroscopy was

performed are marked in the UV−vis spectra because they are highly important for the selective enhancement of Raman intensities, as will be discussed below.

Figure 1a depicts the UV−vis spectra of bare and vanadia-loaded P25 samples. The optical properties of titania and its different phases have been studied extensively,[47] and the absorption below 400 nm is dominated by the TiO_2 absorption of P25, which contains anatase and rutile and exhibits transitions at 203, 232, and 310 nm, as well as at 168 and 154 nm.[48,49] A contribution from TiO_2 in the rutile phase is located at absorption energies lower than those of anatase, red-shifting the observed absorptions.[50] Within the same region, the absorptions from monomeric and dimeric vanadia are expected,[31,51] but due to the high titania absorption, their exact contribution is hard to determine. Despite the additional absorption of vanadia below 400 nm, the overall absorption is lower for vanadia-loaded P25 samples, except for the P25+2.5 V/nm^2 sample, which may be caused by a perturbation of the TiO_2 conduction band by the V 3d orbitals.[52] This effect might be compensated by the high amount of vanadia loaded onto the P25+2.5 V/nm^2 sample, leading to a stronger increase in absorption than the decrease caused by the perturbation. Such behavior is confirmed by the increased absorption of the higher-loaded samples compared to P25+0.1 V/nm^2. Above 400 nm, the dominance of the titania absorption decreases,
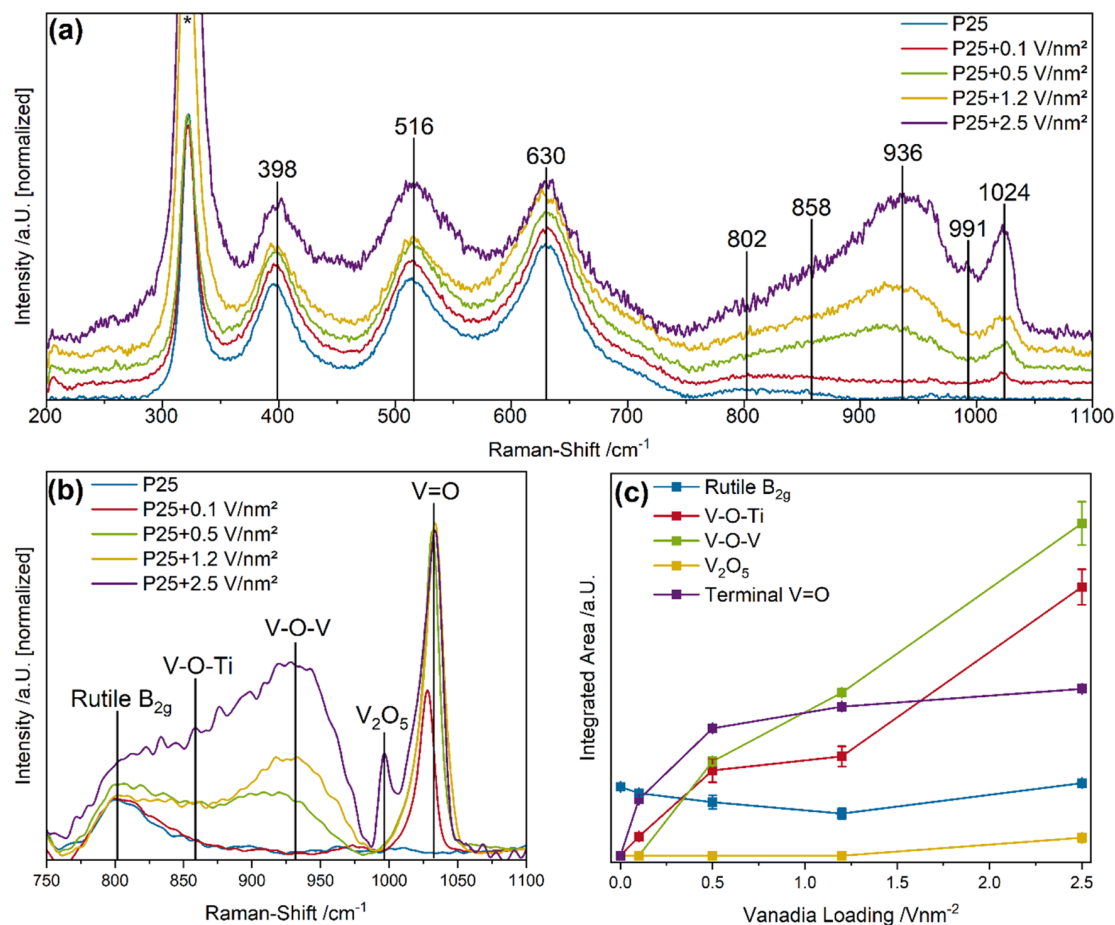
Figure 2. Raman characterization of VO_x/TiO_2: (a) Normalized UV-Raman spectra (385 nm) of bare P25 and vanadia-loaded samples. The signal from the used CaF_2 window is marked with an asterisk. (b) Normalized Vis-Raman spectra (514 nm) of bare P25 and vanadia-loaded samples used for the quantification of vanadia features via deconvolution based on Lorentzian functions (c). All spectra were recorded after dehydration in 12.5% O_2/He for 1 h at 365 °C and subsequent cooling to room temperature.

and higher vanadia nuclearities (oligomers) start to contribute, dominating the absorption at ~450 nm.[31] Here, the P25 sample with 0.1 V/nm^2 shows no significant absorption, indicating that no oligomerized species are present. The absorption then increases nearly linearly for the P25 samples loaded with 0.5 and 1.2 V/nm^2, pointing to a small amount of oligomerized species, but the overall absorption is still comparably small. For the 2.5 V/nm^2 sample, the absorption increases much more significantly, indicating that a significant amount of oligomerization of vanadia occurs between 1.2 and 2.5 V/nm^2, changing the surface chemistry of the sample. The absorption for this sample increases between 275 and 600 nm. As different vanadia nuclearities absorb at different wavelengths[31] and the increase in absorption observed in the UV−vis spectrum is not the same at all wavelengths, this can lead to differences in nuclearity-dependent resonance enhancements between the two excitation wavelengths used for Raman spectroscopy.

The band gap energies determined from Tauc plots are shown in Figure 1b. The typical band gap energies for titania have values between 2.7 and 3.3 eV, depending on their composition, where anatase is closer to 3.2 eV and rutile closer to 3.0 eV, but the presence of oxygen vacancies further decreases the band gap to below 3.0 eV.[53,54] In addition, highly oligomerized vanadia can also red-shift the band gap energy

due to the absorption between 400 and 450 nm.[31] The band gaps of bare P25 and P25 loaded with vanadia up to 1.2 V/nm^2 reveal, within the margin of error, very similar band gap energies that are only slightly lower than those of bare P25 due to the presence of surface vanadia species and are all in the range between 2.7 and 2.9 eV.[52] This is in good agreement with the literature values of defective titania samples.[53,55] When the loading is further increased to 2.5 V/nm^2, the band gap decreases significantly in concurrence with the sharp increase in absorption above 400 nm. The decrease in the band gap energy can be attributed to the tailing of the absorption caused by the presence of oligomerized vanadia as well as the charge-transfer transition from d-orbitals of V^{4+} to the conduction band of TiO_2.[56,57]

Figure 1c shows the XRD patterns of the P25-based samples. As P25 is composed of 77% anatase, 16% rutile, and 7% amorphous titania,[58] there are reflexes from the anatase and the rutile phase. The half-width of the reflexes indicates the presence of crystallites with a significant size of >15 nm (determined using the Scherrer equation). The overall shape and line width do not vary with the vanadia surface density, and no additional peaks are present at the highest loadings, indicating only amorphous vanadia or crystallites with a size below the XRD detection limit. The P25+1.2 V/nm^2 sample shows a slightly higher intensity in the rutile-related reflexes,

which might be caused by a not fully inert sample transfer. As the support is a commercial one and the same for all samples, we conclude that this is likely caused by a slightly different pretreatment of the sample. However, this has no effect on the operando/transient spectra shown below, as each of the measurements was performed with a fresh sample.

Figure 2 shows the results of the multiwavelength Raman spectroscopic characterization of VO_x/TiO_2 with UV (385 nm) and visible (514 nm) laser excitation. The corresponding Raman spectra of $VO_x/TiO_2/SiO_2$ are provided in the SI (see Figure S7) and are discussed there in detail. An exemplary fit of the P25+1.2 V/nm^2 sample, used to quantify the vanadia-related features from the Vis-Raman spectra, is shown in Figure S8.

Figure 2a shows the UV-Raman spectra of bare and vanadia-loaded P25 within the phonon region after 1 h of dehydration in 12.5% O_2/He at 365 °C and subsequent cooling to room temperature. As the excitation wavelength is located within the region of titania absorption (see Figure 1a), an intensity increase due to resonance enhancement would be expected for titania. Titania features are located at 398, 516, 630, and 802 cm^{-1} and can be assigned to different anatase and rutile phonons. The vanadia-related features at 858, 936, 991, and 1024 cm^{-1} are attributed to interface V−O−Ti, bridging V−O−V, the terminal vanadyl bond of V_2O_5, and the terminal vanadyl bond of amorphous vanadia, respectively. A feature at 936 cm^{-1} was previously reported to be indicative of V^{4+} species or V−O−Ti bonds. However, the presence of V^{4+} species can be ruled out due to the significantly smaller Raman scattering cross-section compared to V^{5+} species.[59] Furthermore, V−O−Ti bonds were ruled out since the lowest-loaded sample (P25+0.1 V/nm^2) shows no intensity at 936 cm^{-1} despite the presence of V−O−Ti bonds, as evidenced by the intensity recorded at 858 cm^{-1}, while all higher loadings show significant intensity at 936 cm^{-1}, consistent with the above assignment of this Raman feature to V−O−V bonds exclusively. Table 3 summarizes the Raman assignments for all samples.

Table 3. UV- and Vis-Raman Assignments of Bare Titania and Vanadia-Loaded Samples

position (cm^{-1})	assignment	reference
398	B_{1g} anatase	60
516	A_{1g} and B_{1g} anatase	60
630	E_g anatase	60
802	B_{2g} rutile	60
858	V−O−Ti	61
936	V−O−V	59
991	V=O of V_2O_5	27
1020−1030	V=O of VO_x	31

Figure 2b depicts the phonon region of the Vis-Raman spectra assigned to vanadia-related features. The excitation wavelength was located within the absorption of oligomerized vanadia to facilitate the quantification of vanadia-related features, avoiding the influence of TiO_2 absorption. The same peaks are observed with 385 nm excitation but with higher intensity. The peaks were then quantified by using a fit analysis with Lorentzian functions (see Figure S8), yielding the results shown in Figure 2c. The rutile B_{2g} mode overlaps with the vanadia-related features but does not change significantly with the vanadium loading. We therefore conclude that the

phase composition of P25 is not affected by the amount of surface vanadia, which is in good agreement with the XRD results.

The 0.1 V/nm^2 sample is characterized by features from terminal V=O bonds of amorphous VO_x, and V−O−Ti bonds appear, while no V−O−V related features are detected, indicating that at the lowest loading, vanadia is present in its monomeric form, which is consistent with the absorption at ~450 nm being absent for the sample (see Figure 1a). When the surface density is increased, the amount of terminal V=O and V−O−Ti bonds increases accordingly, while at a loading of 0.5 V/nm^2 V−O−V, bonds can be detected for the first time, indicating that vanadia starts to form surface species with higher nuclearity. When the VO_x surface density is increased to 1.2 V/nm^2, the V=O and V−O−Ti peaks show a further increase, but the V−O−V intensity increases more significantly, which suggests that cross-linking of vanadia species is an important process at these loadings, whereas the formation of new V−O−Ti bonds is less likely. For the sample with the highest loading, small amounts of V_2O_5 are formed in addition to an increase in all vanadia-related signals, except for the terminal V=O bond of amorphous vanadia, which only increases slightly. The V=O signal of V_2O_5 is not included in the amount of the quantified V=O shown in Figure 2c. For this loading, the V−O−Ti peak again shows a significant increase since the amorphous 3D particles might add additional linkage to the titania support while new chains are also formed, in line with the significant V−O−V intensity increase due to 3D cross-linking.

Note that the Raman cross-section of vanadyl in V_2O_5 has been estimated to be at least five times larger than that of dispersed vanadia, confirming that only small amounts of V_2O_5 are formed.[62,63] Thus, the very small amount of V_2O_5 present on the surface is not expected to have a significant influence on the catalyst's behavior. As the monolayer coverage of oligomeric VO_x on titania is normally described to be much higher than 2.5 V/nm^2 (7.5−7.9 V/nm^2),[64−66] the formation of V_2O_5, that is, the oligomerization of vanadia is likely to be caused by the large number of defects in P25, as determined from the measured band gap energies (see Figure 1b). Even though the SBA15-T+1.2 V/nm^2 sample shows a much lower VO_x defect density, it still contains V_2O_5 on the surface. This is not necessarily a contradiction since the titania phase of the ALD-synthesized sample is almost fully amorphous, and the SBA-15 support possesses pores coated by titania, in which vanadia might be crowded, inducing the formation of V_2O_5, even at lower loadings, and despite the lower defect density. The presence of small amounts of V_2O_5 would also explain the increased absorption intensity above 400 nm in the UV−vis spectra (see Figure 1a). Due to the presence of V_2O_5, amorphous 3D particles are also likely to be present on the surface, which contain vanadium atoms linked by V−O−V, contributing to the steep increase of V−O−V in comparison to V−O−Ti and V=O.

Additionally, the resonance enhancement of oligomers leads to a stronger increase in V−O−V intensity as well, unlike V=O, which is also present in monomers, which are only resonantly enhanced in the UV range. The discrepancy in the loading-dependent V=O intensities between the UV- and Vis-Raman spectra is well explained by the different resonance enhancements of the different nuclearities and the different absorption increases in the UV−vis spectra of P25+2.5 V/nm^2, as discussed above (see Figure 1a). This leads to a much larger
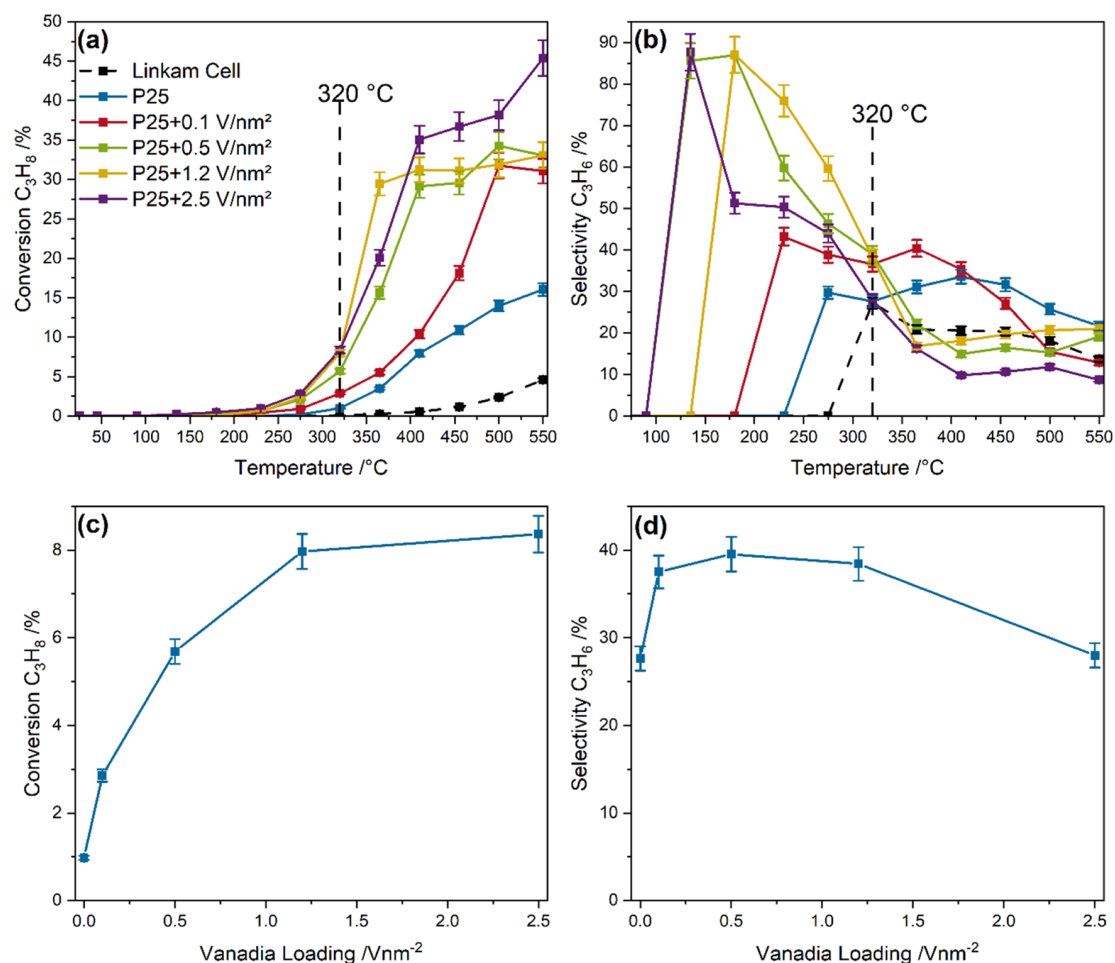
Figure 3. Reactivity behavior of VO_x/TiO_2 in propane ODH: Temperature-dependent (a) conversions and (b) selectivities of bare P25 and vanadia-loaded samples and the empty reaction chamber. The temperature at which operando spectroscopy was performed is marked. Loading-dependent (c) conversions and (d) selectivities of bare P25 and vanadia-loaded samples at 320 °C.

increase in the V≡O signal for this sample at the 385 nm excitation wavelength than for the 514 nm excitation wavelength, which is further underlined when the loading-dependent V≡O intensity is compared for both excitation wavelengths (see Figure S9). The presence of resonance enhancements is supported by the small intensities of the V≡O and V−O−V overtones observable for the P25+2.5 V/nm^2 sample in the UV−Raman spectra, while they are barely visible for lower loadings due to the overlap with the overtone of the rutile E_{2g} mode (not separately shown) and their low intensities. Furthermore, the amount of rutile is very important for the degree of oligomerization of vanadia on titania, as the presence of some rutile in the anatase phase increases the mobility of the vanadia species.[67] All in all, vanadia starts to form 3D particles much more readily on P25 than would be expected from the typical value of the monolayer coverage. Translating this behavior to the P25 samples with lower vanadia loadings may result in a higher degree of V−O−V bonds than would be typically expected.

For the SBA-15-based $VO_x/TiO_2/SiO_2$ sample, XPS measurements (see Tables S1 and S2 and Figures S10 and S11) and nitrogen physisorption analyzed by the BET method are shown in the SI and combined with the UV−vis, XRD, and multiwavelength Raman data to establish a structural model of

the layered ALD system, which will be used as a reference in the context of the mechanistic interpretation.

3.2. Catalytic Activity and Operando Spectroscopy.
Before the operando spectroscopic measurements were made, the catalytic activity of the catalyst was measured. Figure 3a,b presents temperature-dependent conversions and selectivities for bare and vanadia-loaded P25 samples, while Figure 3c,d presents the loading dependence of the conversions and selectivities at 320 °C. Temperature-dependent conversions and selectivities of the $VO_x/TiO_2/SiO_2$ sample are given in the SI (see Figure S13).

Figure 3a shows the temperature-dependent propane conversion over bare and vanadia-loaded P25 samples, which is the smallest for bare P25 but increases with the vanadium loading, in particular from 0.1 to 0.5 V/nm^2. For comparison, the behavior of the empty Linkam reactor is shown, which shows conversions that are significantly smaller than those of the catalyst samples. At a temperature of 320 °C, conversions of <0.05% are measured, which are within the margin of error. Therefore, we exclude any contributions of homogeneous gas-phase reactions or the reactor at the temperature chosen for the operando spectroscopy. Figure 3b depicts the corresponding selectivities toward propylene. For bare P25, the selectivity stays almost constant at around 30% for all temperatures, indicating that the oxygen mobility in titania has no significant
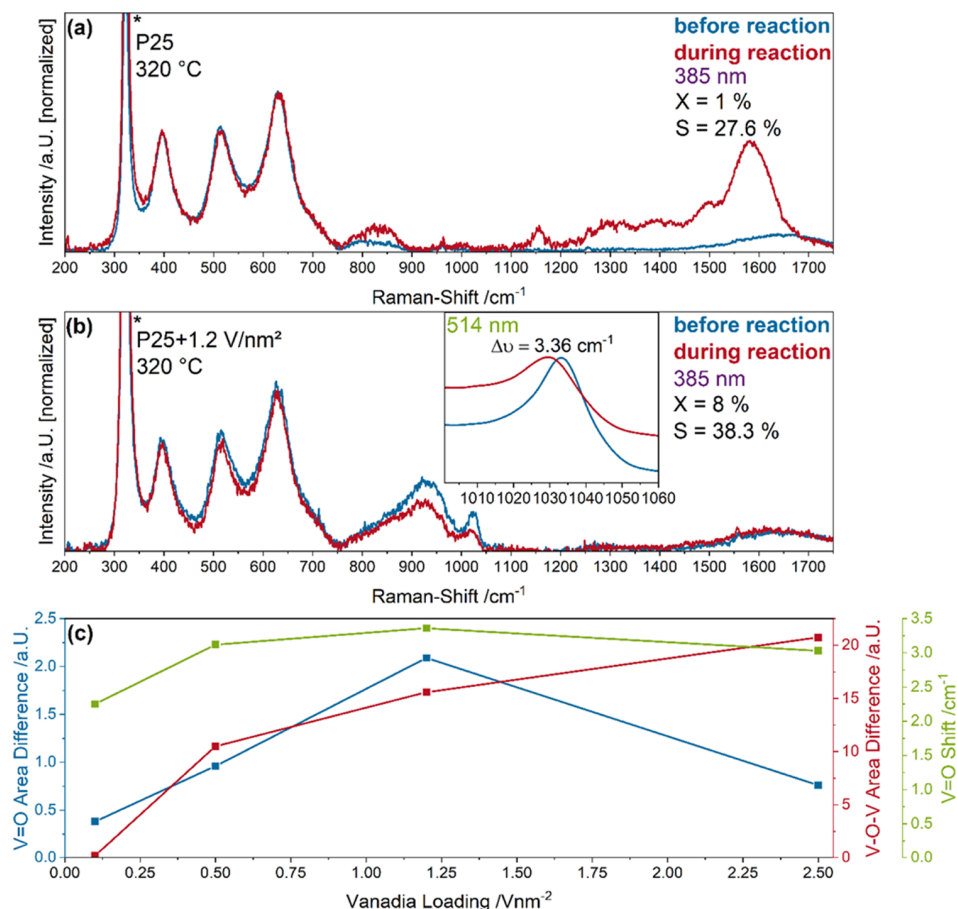
Figure 4. Normalized UV-Raman (385 nm excitation) spectra of (a) bare P25 and (b) P25+1.2 V/nm^2 recorded at 320 °C under oxidizing (blue; 12.5% O_2/He) and reactive (red; 12.5% O_2/12.5% C_3H_8/He) conditions, characterized by the given conversions and selectivities. The peak originating from the used CaF$_2$ window is marked with an asterisk. The inset shows the Vis-Raman spectrum (514 nm) of the vanadyl peak. (c) Observed intensity changes of the vanadia-loaded samples. The operando UV-Raman spectra for the other samples as well as an exemplary fit are given in the SI (see Figures S14−S16).

influence on the observed selectivities. The vanadia-loaded samples have a very high selectivity of 80−90% at low temperatures, where the conversions are <0.1%, but show a decline to 40−50% as the conversions start to increase to a significant level at ≥275 °C. Up to 400 °C, the selectivities of the vanadia-loaded P25 samples are higher than for bare P25 despite the higher conversions, indicating that the vanadia loading significantly changes the surface chemistry of the catalyst, which leads to a different reaction mechanism. A temperature of 320 °C was chosen for the spectroscopic investigation, as the vanadia-loaded samples and even the bare support show significant conversions and selectivities that can be detected reproducibly. The loading-dependent conversions and selectivities for bare and vanadia-loaded P25 samples at 320 °C are summarized in Figure 3c,d. The conversions first increase significantly with increasing vanadium loading but then level off, especially for the increase from 1.2 to 2.5 V/nm^2, which is consistent with previous studies reporting no dependence of the conversion on the surface density above 2.5 V/nm^2.[3] As shown in Figure 3d, the selectivity for bare P25 is about 30%, increases to 38% for a loading of 0.1 V/nm^2, then stays constant within the margin of error and finally starts to decrease back to 30% at a loading of 2.5 V/nm^2. Besides propylene, the only products detected were CO and CO$_2$, and carbon on the catalyst surface. The selectivity behavior is

mostly explained by the different conversions (see also discussion below), but for the highest loading, the higher degree of oligomerization (i.e., the large number of V−O−V bonds) and the presence of V$_2$O$_5$ might explain the decline in selectivity while the conversion stays constant.

There are a number of kinetic studies on propane ODH over VO$_x$/TiO$_2$ catalysts available in the literature,[5,6,23−29,68] covering a variety of titania supports, temperatures, and vanadia loadings. Our activity data is similar to results reported for a fixed bed reactor operated closest to our conditions, indicating the comparability of the Linkam reactor to a fixed bed reactor,[5,23] as discussed previously.[7] Especially the loading-dependent conversions reported in this study show a very similar course when compared to literature data acquired at the same temperature and for the same range of vanadium surface densities,[23] while the corresponding selectivities are in line with reported fixed bed reactor results.[5]

Figure 4a,b shows the UV-Raman spectra of bare P25 and P25+1.2 V/nm^2 samples during oxidizing and reactive conditions, as well as Vis-Raman data of the vanadyl region in the inset. The UV- and Vis-Raman spectra for the other P25 and ALD-synthesized samples are given in the SI (see Figures S14 and S15). The observed intensity changes were quantified by a peak-fit analysis using Lorentzian functions (see Figure 4c). An exemplary fit of the vanadyl region in the UV-Raman
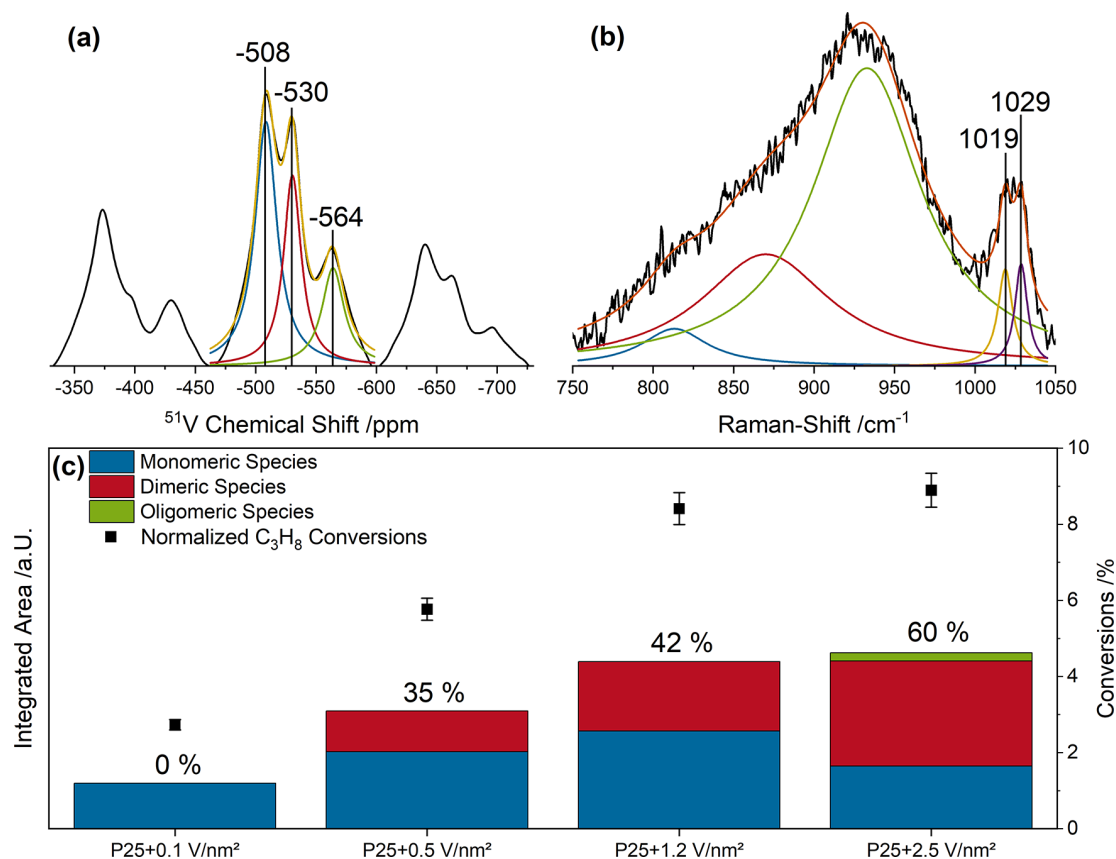
Figure 5. (a) ^{51}V ssNMR spectrum of P25+1.2 V/nm^2 measured at 14.1 T and 21 kHz rotational frequency referenced to VOCl$_3$ with V$_2$O$_5$ as the external standard. The isotropic signal (determined by measurements at two MAS rates, see Figure S19) was fitted using three Lorentzian/Gaussian product functions. (b) UV-Raman (385 nm excitation) spectrum of the vanadia region of P25+1.2 V/nm^2 together with an exemplary fit, using five Lorentzian functions. (c) Quantified areas of the monomeric, dimeric, and oligomeric components of the vanadyl peak in the UV-Raman spectra. The relative amount of dimeric species in relation to the overall amount of vanadia species is given and compared to the propane conversions.

spectrum of the P25+1.2 V/nm^2 sample is given in the SI (see Figure S16).

In Figure 4a, UV-Raman spectra of bare P25 are shown. Exposure to reaction conditions leads to an increase in the intensity of the rutile B$_{2g}$ peak at 820 cm^{-1}. In the literature, this peak is normally described as a low-intensity Raman feature, which highlights the selective enhancement of TiO$_2$.[60] The absorption maximum of rutile is also closer to the excitation wavelength than that of anatase, leading to more absorption in the near visible UV region for rutile than for anatase, which is in good agreement with the observed enhancements in the Raman spectra. Additionally, multiple peaks in the region between 1100 and 1750 cm^{-1} appear, which can be assigned to different amorphous carbon species on the surface.[69,70] The sharp peak at 1150 cm^{-1} is not compatible with this assignment and has been attributed to carbon in the hexagonal diamond configuration.[71] This indicates that over bare P25, a significant part of the converted propane is deposited as carbon on the surface, which, however, cannot be caused by oxygen depletion, as the samples with the largest carbon deposits (P25 and P25+0.1 V/nm^2) use the least oxygen, showing oxygen consumptions of 4 and 11%, respectively (see Figure S17). As can be seen by the change of the rutile band at 820 cm^{-1} upon exposure to reaction conditions, a TiO$_2$ phase transition occurs, partially transforming anatase to rutile as nanocrystals, as the change is not detectable by XRD (see operando XRD results in Figure S18).

This phase transition might be linked to oxygen vacancy formation, as oxygen vacancies are more easily formed at the boundary between the anatase and rutile phases and can facilitate a phase transition.[53] The amount of transformed titania is probably small due to the low conversion of bare titania and is expected to lead to only a small amount of oxygen vacancies because titania shows lower oxygen mobility than other supports such as CeO$_2$.[72,73]

When vanadia is introduced, the observed changes in the catalysts' behavior differ significantly, as no more changes of the carbon and rutile features are detected in the Raman spectra (see Figure 4b). Instead, there are apparent intensity changes of the vanadia features related to V−O−V and V=O. Additionally, a significant red shift of the vanadyl position can be observed in the Vis-Raman spectra (see inset). This behavior is consistent with a decrease in V−O−V intensity, as the breaking of V−O−V bonds reduces the average nuclearity of vanadia and hence the degree of dipole−dipole coupling between the vanadyl groups, resulting in a red-shift of the vanadyl position.[32] This red shift occurs concurrently with a significant intensity decrease of the V=O peak intensity in both UV- and Vis-Raman spectra, as well as a significant decrease in V−O−V intensity in the UV-Raman spectra. The same intensity changes are observed for the 0.5 V/nm^2 and the 2.5 V/nm^2 samples (see Figure S14), whereas the 0.1 V/nm^2 sample is characterized by a mixture of the bare titania and vanadia-related dynamics. That is, the rutile band increases,

and the carbon features appear, but to a lesser degree than for bare P25, and the vanadyl feature shows a red shift and an intensity decrease. For this sample, no V−O−V dynamics are observed, consistent with the presence of monomeric vanadia species, as discussed above.

The intensity changes of all vanadia-loaded P25 samples (V=O shift, V=O, and V−O−V area differences) upon exposure to reaction conditions are summarized in Figure 4c. Starting with the V−O−V dynamics, the observed trend correlates well with the determined conversions (see Figure 3c), whereas the vanadyl area change and position follow the trend only up to a surface density of 1.2 V/nm^2. For the P25+2.5 V/nm^2 sample, the V=O area change and V=O position decrease in comparison to the P25+1.2 V/nm^2 sample, and only the V−O−V area change increases significantly, while the conversion stays almost unchanged between 1.2 and 2.5 V/nm^2. This behavior suggests that both V=O and V−O−V oxygen atoms can support propane ODH, but at higher loadings, the high amount of V−O−V oxygen becomes the dominant oxygen site where, based on UV−vis characterization (see Figure 1), more oligomeric species are present. As the conversion stays constant, but the selectivity decreases between these samples, V−O−V bonds of oligomeric vanadia appear to be less selective than vanadyl oxygen. This trend becomes even more apparent when the SBA-15-based sample is considered, which is dominated by V=O dynamics (with very little V−O−V dynamics) and has a higher selectivity (see Figure S15 and discussion). This indicates that the reactivity behavior depends on the detailed vanadia site, specified by the type of oxygen atom as well as its nuclearity.

For VO$_x$/CeO$_2$, it was possible to determine the distribution of different nuclearities on the surface from the vanadyl signal from either Raman or IR spectroscopy,[7,32] but for other catalyst systems, such a detailed vanadyl fine structure has not been detected. To identify the significant vanadia sites on the P25-based catalysts, we applied a combination of Raman spectroscopy and ^{51}V ssNMR spectroscopy. As V^{4+} and V^{3+} species have very short relaxation times due to their paramagnetic character, the ssNMR spectra show only signals attributed to V^{5+} species, enabling a direct comparison with Raman results.[42,59] Note that V^{5+} species located close to paramagnetic species, such as reduced vanadia or titania, may not be observed in the spectra due to paramagnetic bleaching. Since ssNMR spectra of the P25+1.2 V/nm^2 sample obtained at different field strengths reveal a significant contribution from second-order quadrupolar interactions (see Figure S19), the identification of various vanadia species via ssNMR line-shape analysis of the sideband pattern to extract the quadrupolar and the chemical shift anisotropy parameters is not feasible. The same is valid for the quantification of the vanadia species. Thus, a qualitative analysis of the isotropic signals obtained in the spectrum of the P25+1.2 V/nm^2 sample measured at 14.1 T and 21 kHz spinning was performed by using a peak-fit analysis with three Lorentzian/Gaussian product functions (see Figure 5a). The results can be compared to those obtained for the vanadyl region from UV-Raman spectra (see Figure 5b). The NMR spectra of P25+1.2 V/nm^2 are characterized by three signals located at ∼−508, ∼−530, and ∼−564 ppm, which have previously been attributed to two monomeric sites (ordered and distorted) and dimeric sites that are doubly bridged by V−O−V, respectively.[67,74,75] Interestingly, the isotropic signal shows no contributions from higher

oligomerized species that would all be present above −600 ppm. This might be due to the unique interaction of P25 with vanadia or the complete absence of water, which would facilitate the oligomerization of vanadia if present.[76−78]

Since for the P25+1.2 V/nm^2 sample, only signals from monomeric and dimeric species are detected, it stands to reason that samples with lower loadings also contain only monomeric and dimeric species. For the P25+2.5 V/nm^2 sample, the significantly increased absorption at ∼450 nm (see Figure 1) points to the presence of vanadia species with a higher degree of oligomerization, as discussed above. Thus, the vanadyl peaks in the Raman spectra of the P25-based samples were fitted by using one component for the P25+0.1 V/nm^2 sample (only monomers; see Figure S14), two components for the P25+0.5 and P25+1.2 V/nm^2 samples (monomers and dimers), and three components for the P25+2.5 V/nm^2 sample (monomers, dimers, and oligomers), i.e., by including species with a higher degree of oligomerization. The fact that the vanadyl fine structure in the Raman spectra comprises only two contributions is fully consistent with the exclusive presence of monomeric and dimeric species at loadings up to 1.2 V/nm^2. This approach is also in very good agreement with the shapes of the vanadyl peaks. To obtain accurate peak areas, the position of the monomeric species was determined from the spectrum of the 0.1 V/nm^2 sample and fixed when fitting the spectra of the other samples. The results of the quantification of monomeric and dimeric species are shown in Figure 5c, together with the conversions of each sample and the percentage of dimeric species to the overall amount of vanadia loaded onto the sample.

For validation, the same approach for quantification of vanadia nuclearities by combining NMR and Raman spectroscopies was applied to a reference VO$_x$/CeO$_2$ system, as in this case, the vanadia nuclearity distribution is well known due to the pronounced vanadyl fine structure in the Raman spectra of VO$_x$/CeO$_2$ systems, extending from monomeric to oligomeric species.[8,32] This analysis confirms the above assignments and underlines that our NMR method is able to detect oligomeric vanadia structures and rule out any external effects that would cover the oligomeric species in the NMR spectrum of P25+1.2 V/nm^2. The results, together with their assignments, are given in the SI (see Figures S20 and S21 and Table S4).

The quantification of the vanadia species from the Raman spectra, as outlined above, reveals that for the 0.1 V/nm^2 sample, there are only monomers and that the relative amount of dimeric species increases with every loading step. The increase is especially relevant from 0.1 to 0.5 V/nm^2, where the increase in the conversion is also most significant, as well as from 1.2 to 2.5 V/nm^2, where there is only a small change in conversion. As discussed in the context of the operando UV-Raman spectra (see Figure 4c), the latter behavior is a result of the shift in the composition of surface vanadia species toward dimers, leading to an increased activity due to V−O−V bonds and a decreased activity of the vanadyl oxygen, while simultaneously the selectivity decreases. This significant increase in dimeric species from P25+1.2 to P25+2.5 V/nm^2, as well as the small amount of species with a higher degree of oligomerization (based on the vanadyl deconvolution), is in good agreement with the results from UV−vis spectra (see Figure 1). The above findings lead to the conclusion that the V=O oxygen is an important site for the selective oxidation of propane. As the introduction of vanadia monomers already triples the catalyst activity compared to bare titania, and the
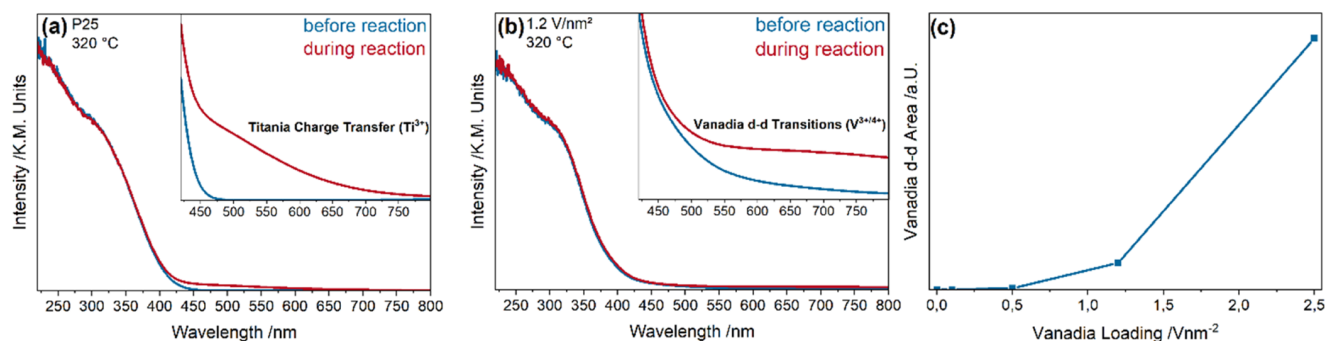
Figure 6. UV–vis spectra of (a) P25 and (b) P25+1.2 V/nm^2 measured under oxidizing (12.5% O$_2$/He) and reactive (12.5% O$_2$/12.5% C$_3$H$_8$/He) conditions at 320 °C. The insets show enlarged views of the visible region. (c) Quantification of the loading-dependent spectral changes.

increase between bare titania is larger than that from 0.1 to 0.5 V/nm^2 despite the fact that only 1/5 of vanadium is present, it stands to reason that monomeric species are highly active. In comparison, doubly bridged V–O–V bonds appear to be less preferential to supply the oxygen atoms facilitating propane oxidation up to a loading of 1.2 V/nm^2. However, the activity shifts at least in part from monomers to dimers, as the participation of V–O–V is clearly evidenced. Thus, the V–O–V site plays an important role in the further increase in reactivity, together with the monomers, which contribute to the V=O dynamics. When the loading is further increased to 2.5 V/nm^2, a significant amount of oligomerized species will be present on the surface (see Figure 1), which are linearly bridged with V–O–V,[75] which becomes the preferential site that is more active but less selective than the previously preferential V=O bond of monomers and dimers due to its better reducibility. As shown in Figure 5c, the conversion scales with the overall amount of vanadia present due to oxidation at both V=O and V–O–V sites. It does, however, not increase linearly with the vanadium loading, as, at the highest loading, more linear V–O–V sites are formed that replace V=O bonds as the active site. This is further emphasized by the significant decrease of V=O dynamics between 1.2 and 2.5 V/nm^2 in UV-Raman spectra (see Figure 4c) but still increased V–O–V dynamics concurrently with the appearance of oligomerized vanadia. These also show a lower selectivity, which is in very good agreement with the quantification of the vanadyl peak in Figure 5c. Summarizing, the combination of ^{51}V ssNMR and UV-Raman spectroscopies can lead to an advanced identification and even quantification of the nuclearity- and loading-dependent active vanadia sites in VO$_x$/TiO$_2$ catalysts.

To further understand the catalysts' mode of operation and, in particular, the role of reduced vanadia, which cannot be probed by NMR or Raman spectroscopy, UV–vis spectroscopy was employed. Figure 6a,b shows UV–vis spectra of bare P25 and P25+1.2 V/nm^2 under oxidizing (12.5% O$_2$/He) and reactive (12.5% O$_2$/12.5% C$_3$H$_8$/He) conditions at 320 °C, while Figure 6c summarizes the structural dynamics of the vanadia-loaded samples. Quantification was performed by fitting the entire UV–vis spectrum, using Gaussian functions located at the positions of titania[48,49] and vanadia[79] transitions reported in the literature. The operando UV–vis spectra for the remaining P25 and ALD-synthesized samples are given in the SI (see Figures S22 and S23), and an exemplary fit used for the quantification of UV–vis spectra is shown in Figure S24.

Starting with the UV–vis spectra of bare P25, switching from oxidizing to reactive conditions leads to the appearance of

a new absorption band at 520 nm that gradually decreases in intensity until its disappearance at 750 nm (see Figure 6a). The detected band can be attributed to a charge-transfer transition due to titania reduced from Ti^{4+} to Ti^{3+} caused by oxygen vacancy formation.[80,81] The band gap shows a slight red shift, as determined by Tauc plots, which is also caused by defect creation; that is, Ti–OH and oxygen vacancies create new states in the band gap, close to the conduction band, resulting in a decrease of the band gap energy.[55] Both of these effects are rather small and, as the conversions of bare titania samples are small, appear to be caused by propane ODH. This leads to the following mechanistic picture of propane ODH over bare titania samples: propane first interacts with the catalyst, whereby lattice oxygen is then used to oxidize propane, leading to the formation of oxygen vacancies (see Figure 6a) on the interface between anatase and rutile where the defects are favorably formed besides additional rutile (see Figure 4a). In comparison to other oxide supports, titania is difficult to reduce; that is, high temperatures are needed to mobilize lattice oxygen.[72,73] Due to the high temperatures required, propane is often overoxidized or converted to carbon on the catalyst surface once the oxygen becomes mobile, as is apparent from the carbon deposits detected by UV-Raman spectroscopy (see Figure 4a).

For comparison, the UV–vis spectra of the vanadia-loaded samples do not show a band gap energy shift or a Ti^{3+} charge-transfer signal, except for the P25+0.1 V/nm^2 sample, but a significant intensity caused by vanadium d–d transitions, due to the reduction of vanadium from 5+ to 3+/4+ (see Figure 6b).[78] The spectra of the P25+0.1 V/nm^2 sample resemble those of bare titania but to a lesser degree, as they already contain features of the vanadia-loaded samples. Figure 6c summarizes the extent of reduction of the P25-based samples, as measured via the d–d transitions, which shows a strong increase with increasing loading. For the P25+0.1 V/nm^2 sample, the integrated intensity of the d–d transitions is small, which at first sight disagrees with the more pronounced changes seen in the UV-Raman spectra (see Figure 4c), but may be explained by resonance enhancement of the V=O peak caused by the use of UV excitation. In fact, at such low loadings, the sample is characterized by the presence of monomeric vanadia species, which experience a resonance enhancement at 350–400 nm,[31] resulting in an increase of the Raman signal not present in the UV–vis spectra. Likewise, the P25+1.2 V/nm^2 sample is subject to an enhancement in the UV-Raman spectra due to similar surface vanadia species (see Figure 5), which are now present in larger amounts, and with the addition of dimers, which are more easily reduced, this
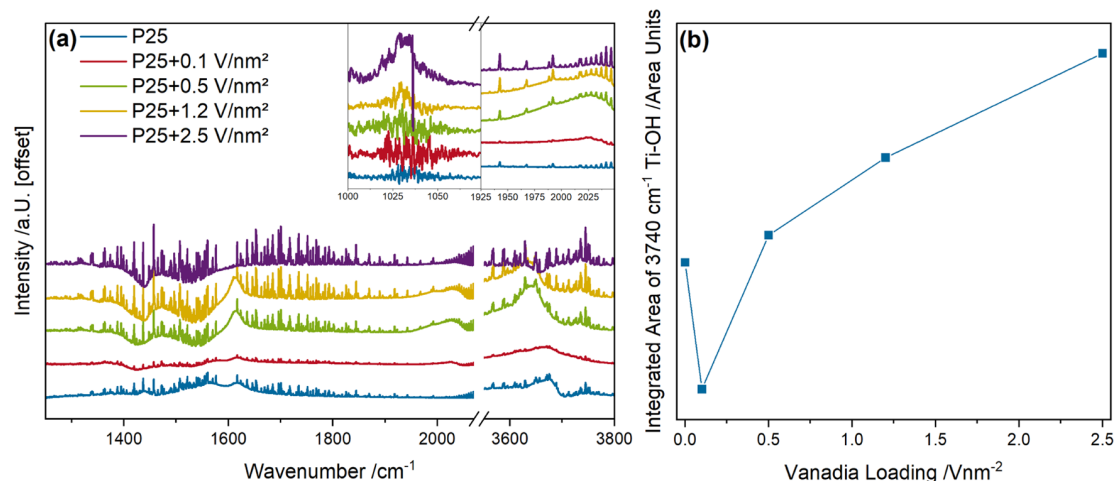
Figure 7. (a) PSD spectra of bare P25 and vanadia-loaded samples in a pulsed oxygen and constant propane flow at 320 °C at a phase angle of 360°. The insets give an enlarged view of the fundamental and overtone of the vanadyl vibration. The transient Ti−OH species at 3740 cm^{-1} was first corrected for water rotational bands and then quantified (b).

leads to an increased signal of d−d transitions in UV−vis spectroscopy. Overall, the results from UV−vis spectroscopy are in good agreement with the Raman and NMR results, supporting the proposed behavior of the VO$_x$/TiO$_2$ catalysts.

Using static operando experiments, a provisional reaction mechanism can be deduced, which provides answers to three of the four key questions outlined in the introduction, i.e., the definition of the vanadia active site, its nuclearity dependence, and the role of titania in controlling the vanadia structure, including the degree of oligomerization, via its phase composition.[67] The oxygen transfer paths have been followed and can explain most of the activity behavior of the VO$_x$/TiO$_2$ systems, but so far, there has been no information on the role of the hydrogen dynamics that were previously established to be of significance for propane ODH.[8] Additionally, the structural dynamics on VO$_x$/TiO$_2$ samples shown here resemble that of VO$_x$ on an inactive support like SiO$_2$, as titania does not seem to participate in the reaction itself. To further understand the role of titania in hydrogen transfers, transient IR spectroscopy was applied due to its potential to provide crucial mechanistic information for alkane ODH reactions.[8]

3.3. Modulation-Excitation DRIFTS. Figure 7a depicts the PSD spectra of P25-based samples at a phase angle of 360° during pulsed oxygen and constant propane flow at 320 °C. This specific flow scheme has previously been shown to provide more mechanistic information than a constant oxygen and pulsed propane flow mode.[8] Figure 7b summarizes the loading-dependent quantification of the transient Ti−OH species detected during ME-DRIFTS. Static DRIFTS results (as a reference for the transient results), P25 and P25+1.2 V/nm^2 PSD spectra with a 30° phase resolution, as well as PSD spectra of all samples at 360° in constant oxygen and pulsed propane flow as well as pulsed oxygen and constant propane flow, are shown in the SI (see Figures S25−S29). For the quantification of the Ti−OH peaks, water rotational bands were removed from the spectrum, and exemplary data processing spectra are shown in Figure S30.

The PSD spectra of P25-based samples in Figure 7a reveal multiple peaks that are not visible in static operando DRIFTS. In the carbonate region, three peaks are most prominent, located at 1438, 1562, and 1618 cm^{-1} and at ~1370, 1480, and

1610 cm^{-1} for bare P25 and vanadia-loaded samples, respectively. These peaks can be assigned to various species of formates and carbonates, as well as the propylene C=C double bond.[82,83] For the vanadia-loaded samples, additional peaks appear within 1010−1040 and 1990−2040 cm^{-1}, which can be assigned to the vanadyl fundamental and overtone vibrations.[84] In the Ti−OH region, multiple OH groups can be detected at ~3610, 3640, and 3740 cm^{-1}. These can be attributed to V−OH, isolated Ti−OH on rutile, and isolated Ti−OH on anatase, respectively.[84−87] The peaks in the carbonate region, the vanadyl peaks, and the Ti−OH groups at 3610 and 3640 cm^{-1} already show dynamics in the static operando DRIFT spectra. All of these regions improve significantly in their spectral quality due to the removal of the background, noise, and spectator species. Only the Ti−OH peak at 3740 cm^{-1} is not present in static operando DRIFT spectra but in the PSD spectra of all samples, with varying intensity. It is assigned to a singly bound Ti−OH group on anatase, which is the dominant phase in P25. Figure 7b shows the integrated areas after the removal of the water rotational bands. P25 has a higher amount of transient Ti−OH species than P25+0.1 V/nm^2, but at higher loadings, starting at 0.5 V/nm^2, the amount of anatase Ti−OH species correlates very well with the observed conversions. This indicates that the titania support not only influences the degree of oligomerization of the vanadia species but also participates in the reaction by abstracting hydrogen from propane to the catalyst surface during a quick hydrogen transfer to a more stable species. Thus, the reaction is facilitated by surface oxygen, as has been observed previously for other vanadia-based catalysts.[8] The higher amount of Ti−OH in P25 might be caused by the absence of vanadia and the consequently sharp slow-down of the reaction rate if no readily reducible oxygen from vanadia is present. Therefore, the otherwise metastable Ti−OH species becomes more prominent due to a lack of transfer targets that would facilitate a further reaction. When the loading is increased to 0.1 V/nm^2, the amount of Ti−OH species decreases, as they can be transferred to vanadia. The overall amount for this sample is smaller than for the other samples, due to the lack of V−O−V and V=O species at such low loadings, which would drive the conversion. At higher loadings, the amount of Ti−OH species correlates very well with the
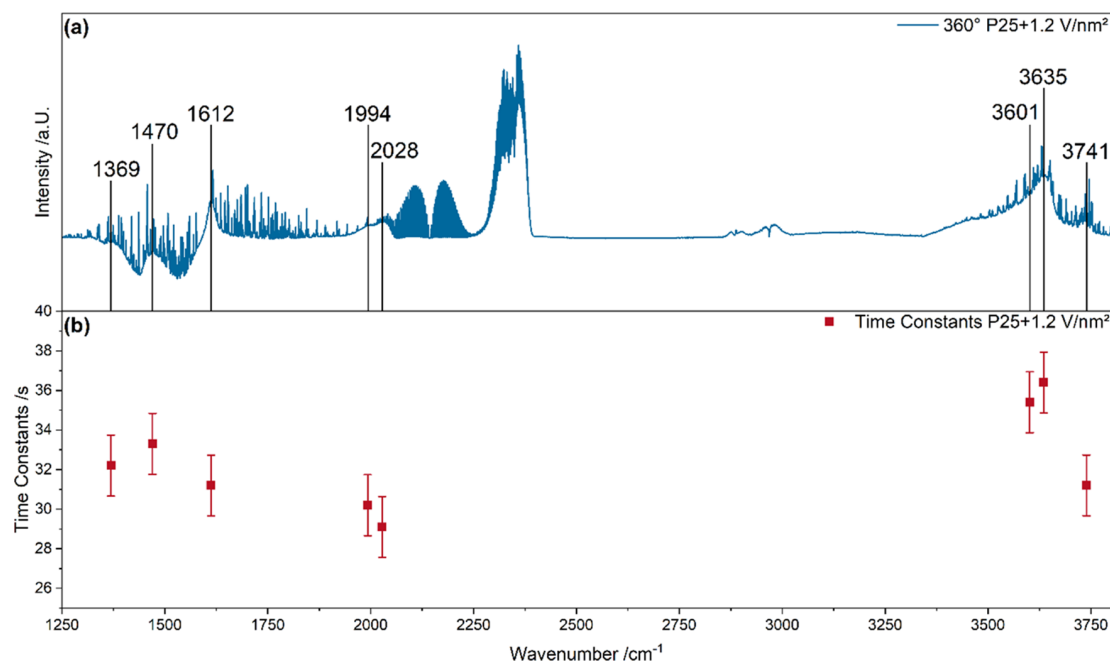
Figure 8. (a) PSD spectrum of the P25+1.2 V/nm² sample at a phase angle of 360 °C measured at 320 °C in a constant oxygen and pulsed propane flow. The features analyzed by in-phase angle analysis are marked, and the respective time constants are given in the lower plot (b), together with the experimental uncertainty.

conversion, indicating that the initial C−H bond breaking is the rate-determining step that can be catalyzed by the titania surface. As the Ti−OH species was determined to be transient, it is regenerated very fast by the transfer to vanadia. This provides an answer to the fourth question on the role of titania during propane ODH by demonstrating its direct participation in the rate-determining step, leading to a further increase in the reaction rate in comparison to, for example, SiO₂, in addition to the control of the degree of vanadia oligomerization via the phase composition. This behavior of titania is in agreement with recent studies, which proposed titania to be redox inactive during ethanol ODH.[18] An alternative explanation for the observed behavior may be the dissociation of produced water, which would also correlate with the conversion. However, this is not supported by the higher amount of anatase Ti−OH on bare P25 and P25+0.1 V/nm², where the conversion is lower. Therefore, the observed intensity trend of this peak is in agreement with the initial C−H abstraction but not with the dissociation of water after product formation, as a strict correlation of the Ti−OH intensity with the conversion for all samples would be expected.

To investigate the detected transient adsorbates in more detail, the time evolution of the adsorbates was determined by in-phase angle analysis to obtain the time constants for each sample. Exemplary results for the P25+1.2 V/nm² sample are shown in Figure 8, and the values of the time constants are summarized in Table 4. A detailed explanation of the in-phase angle analysis can be found in Section 2 and the literature.[8,35] The time constants for the remaining P25-based samples are given in the SI (see Table S5), while time constants were not determined for the SBA-15-based samples, as they only showed significant structural changes in the transient Ti−OH species at 3740 cm⁻¹ and no other signals (more details in the SI, Figure S29). As the measurement time of one IR spectrum was 1.54 s, this value was taken as the experimental error of all time constants, as multiple subsequent measurements of the same

Table 4. Time Constants of the P25+1.2 V/nm² Sample Determined from In-Phase Angle Analysis of PSD Data with a 1° Phase Angle Resolution[a]

wavenumber (cm⁻¹)	assignment	time (s)
2028	V=O overtone	29.1
1993	V=O overtone	30.2
1612	ν_{as} propylene C=C	31.2
3739	isolated anatase Ti−OH	31.2
1369	ν_s formate O−C−O	32.2
1470	ν_s carbonate O−C−O	33.3
3601	V−OH	35.4
3635	isolated rutile Ti−OH	36.4

[a]The time constants of the other samples are given in the SI (see Table S5). The experimental error of all peaks was determined to be ±1.54 s.

sample led to a smaller divergence. For the vanadyl peak, the overtone region was used to determine the time constants due to its better accuracy (compare Section 2 and Figure S3).

In-phase angle analysis shows that all time constants for P25+1.2 V/nm² are in a very similar range, especially when the experimental uncertainty is considered. The peaks at 2028, 1993, 1612, and 3739 cm⁻¹ appear quite simultaneously as one group. This behavior is similar to that of VOₓ/CeO₂, as the vanadyl peak and the Ti−OH species react first, indicating a fast transfer of hydrogen from propane to the titania surface and then to the vanadyl group. The Ti−OH species is a transient species mediating the hydrogen transfer, as determined from ME-DRIFTS (see Figure 7), while hydrogen binds more permanently to vanadia as these species can be observed in static operando experiments. The inverted reaction sequence, where the first hydrogen is rapidly transferred to rutile Ti−OH via vanadia with subsequent V−OH formation and concurrent olefin formation, thereby seems unlikely, as this would necessitate the presence of a transient V−OH group at
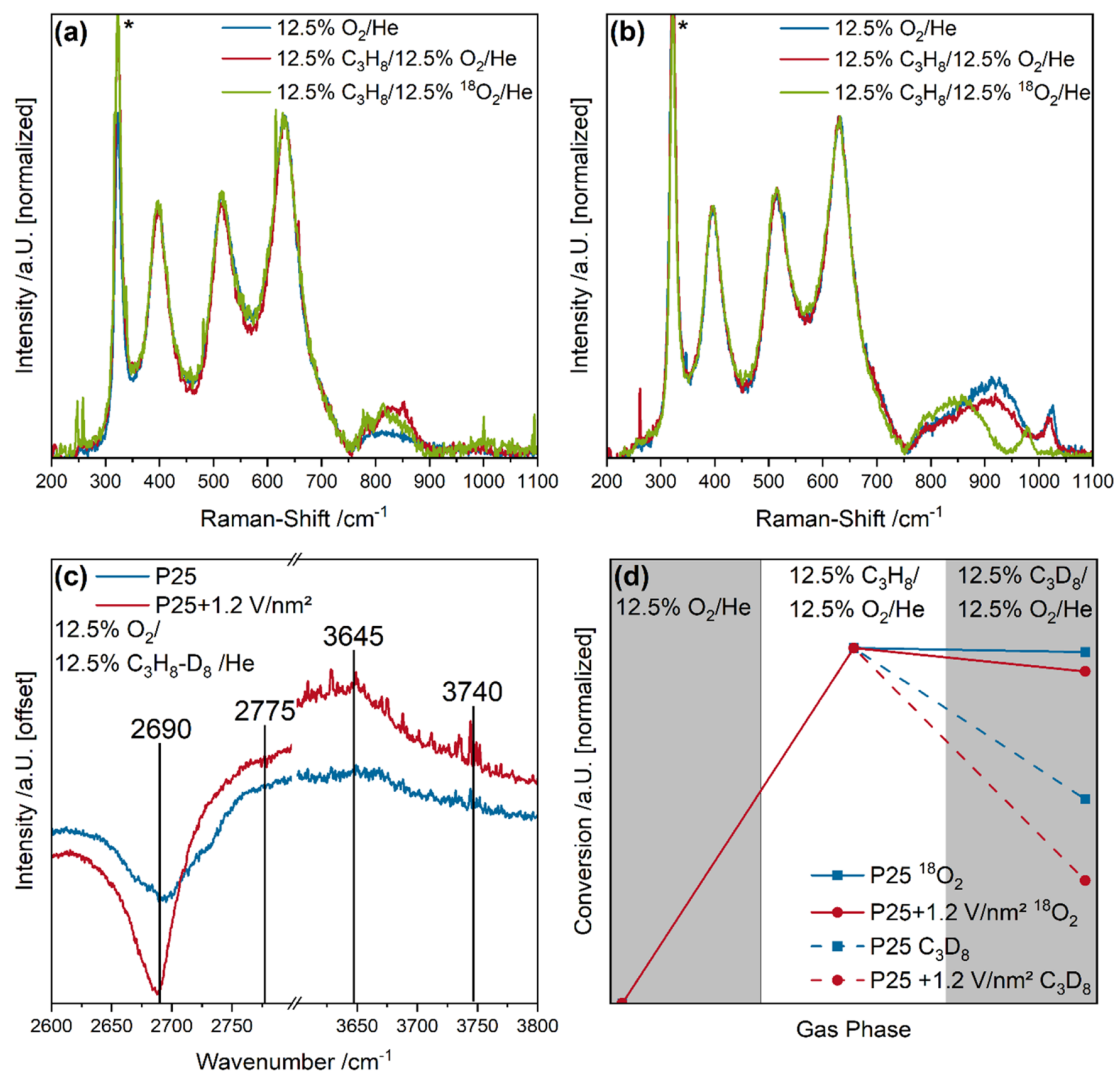
Figure 9. UV-Raman (385 nm excitation) spectra of (a) bare P25 and (b) P25+1.2 V/nm^2 measured under oxidizing (12.5% O_2/He), reactive (12.5% O_2/12.5% C_3H_8/He), and $^{18}O_2$ isotopically labeled reactive (12.5% $^{18}O_2$/12.5% C_3H_8/He) conditions. The spectra were normalized, and the peak originating from the used CaF$_2$ window is marked with an asterisk. For comparison, ME-DRIFTS was recorded during the isotopic exchange (constant oxygen and propane flow switched between h8-propane and d8-propane), and in (c), the resulting PSD spectra are shown, with the positions of the exchanged Ti−OH positions being highlighted. (d) Conversions were determined for operando experiments using $^{18}O_2$ and C_3D_8 to determine the kinetic isotopic effect. The full isotopically labeled PSD spectra of the samples are given in the SI (see Figure S31).

the beginning of the reaction sequence. As can be seen in Table 4, V−OH appears toward the end of the sequence, which supports the proposed reaction sequence where hydrogen is transferred from propane to vanadia via titania exclusively. Interestingly, the sequence of steps is inverted compared to VO$_x$/CeO$_2$ catalysts used for the same reaction, where the vanadyl peak mediated the hydrogen transfer from propane to the ceria surface.[7,8] This catalyst-dependent behavior can be explained by the different reducibilities, as the vanadia oxygen atoms are more reducible than titania, thereby delivering the oxygen necessary for the reaction, whereas, on a ceria catalyst, ceria lattice oxygen is much more reducible than vanadia.[72,73] Thus, the component that is more difficult to reduce is used as the transfer site, as the hydrogen is bound only loosely so that it can be readily transferred to the active oxygen component. This further shows that the oxygen atoms used for the hydrogen transfer are different from those used to facilitate oxidation by the formation of water. The additional peak at 1612 cm^{-1} is caused by the C=C vibration

of the newly formed propylene, which indicates that propylene formation occurs directly after the initial hydrogen abstraction, consistent with a mechanism in which the first C−H abstraction is the rate-determining step and the remaining reaction steps follow directly afterward.

After the initial hydrogen transfer and propylene formation, peaks at 1369 and 1470 cm^{-1} appear, which are attributed to formate and carbonate species, indicating that CO$_x$ is formed on a similar time scale as propylene. This suggests that both propylene and CO$_x$ are formed in parallel instead of CO$_x$ being formed from propylene as a result of over-oxidation, as the time difference between the C=C bond and the formate/carbonate is within the margin of error. However, a very fast over-oxidation of propylene to CO$_x$ within the experimental error cannot be excluded. Subsequently, additional OH groups are detected, which are assigned to bridged OH and terminal OH groups on rutile. These may constitute a more stable state, not facilitating further reaction, and may be created by the dissociation of water produced during the reaction.[85−87] An

additional peak is observed at ~1560 cm^{-1}, which can be assigned to different formate species, which are probably exclusive to the clean titania surface, as they show a significant presence on P25 but are only weakly present on the 0.1 V/nm^2 sample and absent on any of the samples with higher vanadia loading. For P25+0.5 V/nm^2, a similar temporal evolution is observed (see Figure S28 and Table S5), while P25, P25+0.1, and P25+2.5 V/nm^2 deviate from the described behavior. Propane ODH over bare P25 follows a different reaction mechanism, which changes the determined time constants, and P25+0.1 V/nm^2 shows a mixture of the reaction mechanisms over bare P25 and vanadia-loaded P25, explaining that the C═C double bond appears before the V═O signal, as some of the propane is converted earlier on the bare P25 surface. This is in line with all of the previous observations, where the P25+0.1 V/nm^2 sample seems to represent an intermediate state between bare titania and vanadia-loaded titania, showing characteristics of both systems. The time constant of the V═O bond on the P25+2.5 V/nm^2 sample is shifted to much larger time values compared to the other vanadia-loaded samples, which agrees with the proposed change in the reaction mechanism when oligomers occur at this loading, where linear V−O−V bonds are the main active site providing the oxygen that drives the oxidation reaction. This further supports the change in the reaction mechanism between the 1.2 and 2.5 V/nm^2 samples.

3.4. Isotopic Exchange Experiments. To confirm the previous assignments made for the structural dynamics during operando UV-Raman and transient IR spectroscopies, isotopic exchange experiments were performed (see Figure 9). Using $^{18}O_2$ allows the oxygen transfer paths to be followed during UV-Raman spectroscopy, while the use of C_3D_8 can map the hydrogen transfer paths during ME-DRIFTS. Additionally, the influence of the isotopic exchange on the conversions was measured to obtain additional confirmation about the rate-determining step, which may in principle be due to either C−H bond breaking or catalyst reoxidation (see Figure 9d). The full PSD spectra for P25 and P25+1.2 V/nm^2 are shown in the SI (see Figure S31). For the exchange experiments, the samples were measured at 320 °C in different gas atmospheres: first under oxidizing conditions (12.5% O_2/He), then under reactive conditions (12.5% O_2/12.5% C_3H_8/He), and finally under reactive conditions with the isotopically labeled gas (12.5% $^{18}O_2(O_2)$/12.5% $C_3D_8(C_3H_8)$/He) to determine which changes are caused by the isotopically labeled gas.

Bare P25 shows an increase in the rutile E_{2g} mode when switching from oxidative to reactive conditions, as discussed above (see Figure 4a). When switching to isotopically labeled $^{18}O_2$, a shift at the rutile E_{2g} mode at 820 cm^{-1} is detected, indicating that the phase transition between anatase and rutile is facilitated by an oxygen exchange with an affiliated reduction due to oxygen vacancy formation, confirming our proposal that the reaction occurs on a defective rutile/anatase interface. For the vanadia-loaded sample, we see a red-shift of the features at 920 and 1020 cm^{-1}, related to V−O−V and V═O bonds, respectively. Notably, the peaks at 820 and 860 cm^{-1} appear to be unchanged, indicating that neither the V−O−Ti interface nor the titania support itself is directly participating in the reaction, which confirms our previously proposed mechanism where only the vanadia-related oxygen atoms contribute to the overall propane conversion. In addition, the C_3H_8/C_3D_8 isotopic exchange experiment during ME-DRIFTS reveals that both Ti−OH groups at 3645 and 3740 cm^{-1} are present in

the PSD spectra, indicating that they actively participate in the reaction. The full isotopic exchange ME-DRIFT spectra (see Figure S31) reveal that also formate species are detected during the experiment, indicating that they are an active species in the formation of CO_x, confirming the assignments, as only hydrogen-containing adsorbate peaks should be observable during isotopic exchange MES of h/d-propane.

The determined conversions during the isotopic exchange experiments show that the extent of the kinetic isotopic effect (KIE) depends on the isotopically labeled gas used. For the C_3H_8/C_3D_8 measurements, the KIE is 1.83 for bare P25 and 3.12 for P25+1.2 V/nm^2, which is in agreement with previously determined KIEs of hydrogen/deuterium exchange if the hydrogen bond is broken during the rate-determining step.[88] For comparison, the KIE of the $^{18}O_2/^{16}O_2$ isotopic exchange is 1.01 and 1.07 for bare P25 and P25+1.2 V/nm^2, respectively. Despite the lower mass difference between $^{18}O_2$ and $^{16}O_2$ in comparison to D_2 and H_2, the expected KIE for a reaction that uses molecular oxygen for the reoxidation as the rate-determining step would be much higher, at approximately 1.15.[89] The very low oxygen KIE for bare P25 might be caused by the fact that P25 is barely reduced during the reaction and the main reaction occurs from propane to carbon; little reoxidation is needed. Therefore, from the determined KIEs, we can conclude that the C−H bond breaking in propane is the rate-determining step, in agreement with our time-constant results from MES. The TiO$_2$ support facilitates this bond breakage through Ti−OH formation, thus providing an explanation for the low activation energies and high reaction rates typically observed for VO$_x$/TiO$_2$ catalysts.[5]

3.5. Reaction Mechanism. In this section, we propose a reaction mechanism for propane ODH over VO$_x$/TiO$_2$ catalysts based on the results from multiple operando and transient spectroscopies. First, the first C−H bond in propane is broken over the titania surface lattice oxygen (Ti−O−Ti) (see Figure 9d), and one hydrogen is abstracted to the titania surface, forming a singly bound Ti−OH group on anatase (see Figure 7b). A bond breakage at the V−O−Ti interface appears unlikely since no changes of the V−O−Ti feature were observed in operando UV-Raman spectroscopy. The nature of the C−H bond breakage cannot be further specified. On the one hand, no paramagnetic electrons were detected during previous operando EPR experiments,[34] which may suggest a heterolytic bond breakage. On the other hand, as the initial state is expected to be short-lived, it is likely to occur below the detection limit of the method. The hydrogen is then quickly transferred to the V−O−V bond of a doubly bridged dimeric species as interim storage for the hydrogen before the reduction of vanadia (see Figures 1, 4, and 5). Here, the transfer step of the proton and the electron required for the V−OH formation and reduction from V^{5+} to V^{4+} can either proceed sequentially or coupled (PCET). However, a further specification is not possible as it would require knowledge of the activation energy of the respective steps,[90] which is not available from the presented data. Possible electron donors may include reduced Ti^{3+} sites, which are formed during the reaction (see Figure 6). The transfer to the doubly bridged V−O−V oxygen instead of V═O is probably favored for the first hydrogen transfer from titania to vanadia during the selective conversion, which due to its worse reducibility, decreases the likelihood of over-oxidation to CO_x.[10,11,13] Furthermore, the V−O−V structure is, due to the double bridge, not fully broken during this transfer, and therefore, the deflection from
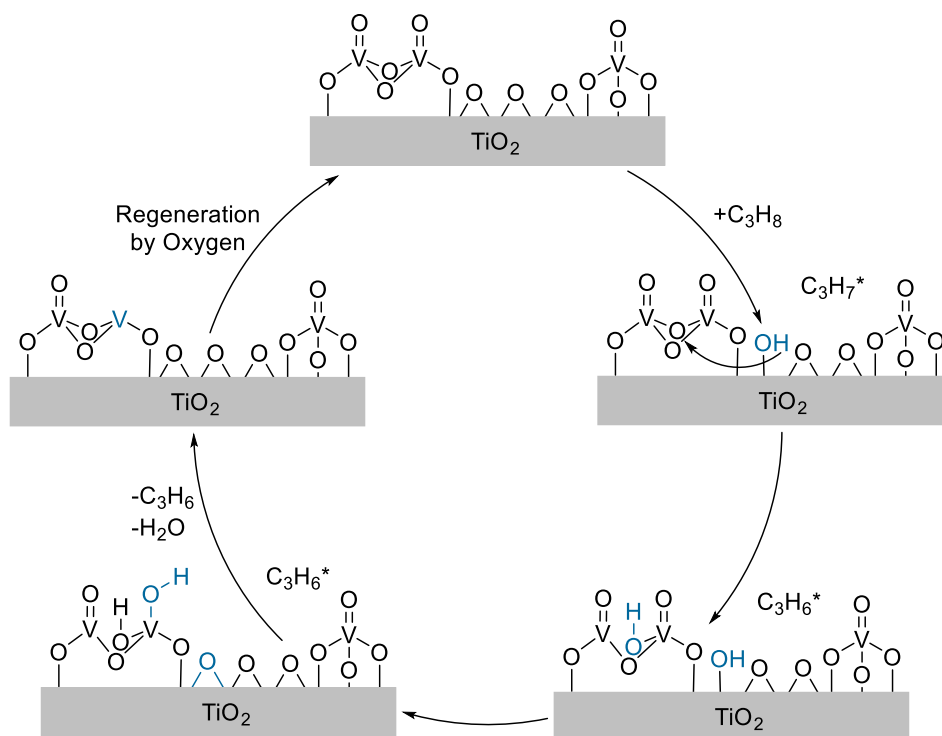
Figure 10. Proposed reaction mechanism for the ODH of propane over vanadia-loaded titania (P25) based on operando and transient spectroscopic analyses. Exemplarily, the reaction of one propane molecule over a dimer species is shown. Broken and newly formed bonds are marked in blue. For details, see the text.

the equilibrium structure is comparably small. The transfer step may thus be kinetically favored compared to the direct transfer. Along these lines, previous DFT calculations for VO_x/CeO_2 have shown that the direct and indirect transfer transition states had, within the margin of error, similar energies.[91] The proposed scenario is supported by our experimental findings (see Table 4 and Figure 7), as the spectroscopic data clearly presents a transient Ti−OH species that occurs first in the temporal evolution of adsorbates and is therefore linked to the initial C−H bond breakage. Hereby, the number of bridged V−O−V bonds in vanadia dimers seems to be important for the conversion of propane (see Figure 5c) as they are an important structure for the intermediate storage of hydrogen and show large structural changes (see Figure 4). Nevertheless, besides dimers, also monomeric vanadia species are highly active during the reaction, based on the large increase in activity for the P25+0.1 V/nm² sample, and are likely to significantly contribute in parallel to the conversion at higher loadings. Since the V−O−V bond clearly participates in the reaction if it is available on the surface, we expect a mixture of active sites to be formed. Following the first hydrogen abstraction, the second hydrogen abstraction, also mediated by the titania surface, is transferred to a V═O bond, which is then used to facilitate propane ODH by its reduction together with the hydrogen stored at the V−O−V bond. The mechanism of this hydrogen transfer appears to be similar to the first one, as no additional intermediates are observed in PSD spectra on the time scale of the C═C bond formation (compare Figure 8 and Table 4). From the analysis of the rutile content and the previous literature, it seems that the amount of rutile dispersed in the catalytically more active anatase phase is crucial in increasing the degree of oligomerization of vanadia due to its higher mobility on the

rutile surface. The higher degree of oligomerization leads to a higher concentration of dimeric species, that is, more V−O−V bonds, and therefore increases the reaction rate. The additional hydrogen atoms form a water molecule using a vanadyl oxygen atom, leaving the vanadium atom in a reduced state (see Figure 6c). At higher loadings (2.5 V/nm²), the first oligomeric species start to appear (see Figures 1, 2, and 5), which are likely to have more linear V−O−V bonds and the active oxygen that is reduced in the reaction shifts from the V═O to the linearly bound V−O−V bond (see Figures 4c and 5c), indicating that it is likely to be more reducible than the V═O bonds that were previously used. The conversion via this V−O−V bond appears to be less selective than via the V═O bonds, which would be in agreement with its higher reducibility, as the P25+2.5 V/nm² sample shows a lower selectivity than the P25+1.2 V/nm² sample at the same conversion (see Figure 3), while also showing less V═O dynamics and more V−O−V dynamics (see Figure 4). This might be caused by the higher reducibility of linear V−O−V bonds formed in the oligomers at higher loadings compared to doubly bridged V−O−V or V═O atoms and demonstrates the strong dependence of the vanadia active site on its nuclearity. The reduced vanadium atom can then be reoxidized by gas-phase oxygen, as the oxygen mobility in titania is too low to participate in the redox cycle.[18] The reoxidation of vanadia is not rate-determining (see Figure 9d). A reaction mechanism where hydrogen is both stored and reduces the V−O−V or the V═O bond at which it is stored cannot be excluded due to the simultaneous dynamics of the two bonds (see Figure 4c) but seems to be less likely due to the different reducibilities. During the entire selective oxidation process, propane does not seem to be directly adsorbed on the catalyst surface, as in neither static operando DRIFTS nor ME-DRIFTS could any

propane-related adsorbates be detected, indicating a pure redox mechanism. For the formation of CO_x, multiple carbonate and formate adsorbates could be detected, indicating a change of the reaction mechanism to an associative mechanism during total oxidation. As these processes occur on a very similar time scale (see Figure 8b and Table 4), whether the propane is adsorbed seems to play an important role in determining whether it is selectively or totally oxidized, indicating a site dependence in addition to the nuclearity dependence.

To close the catalytic cycle, the catalyst is regenerated by oxygen, which may happen in different ways. One possibility would be that starting from a dimeric V^{3+} site, which results from the oxidation of two propane molecules, adsorption of molecular oxygen first leads to the formation of a V−O−O−V bridge and then, after O−O bond breakage to the formation of two V=O sites. Another possibility, which is also compatible with monomeric sites, might be coupled to the total oxidation reaction. Here, a V^{3+} site might adsorb an O_2 molecule, which results in a very reactive oxygen molecule that might react with additional propane toward the detected formate/carbonate species while regenerating the catalyst. This pathway could explain the limited reaction selectivity, besides the presence of bare TiO_2 facilitating total oxidation, and would also be in favor of the argument that total oxidation occurs in parallel to selective oxidation. Therefore, depending on the vanadia nuclearity, a combination of both pathways seems likely.

In comparison, bare titania also shows the transient formation of Ti−OH groups (see Figure 7), but the abstracted hydrogen cannot be transferred to vanadia. As titania is much harder to reduce than vanadia, the conversions are lower due to reduced oxygen availability. When selective oxidation takes place, lattice oxygen from the anatase/rutile interface is used for the oxidation, resulting in an increased amount of rutile (see Figure 4a) and an oxygen vacancy (see Figure 6c). Besides the selective oxidation, the main side product formed by the bare titania samples is carbon, which deposits on the catalyst surface and is likely to be caused by the high temperatures needed to activate titania lattice oxygen. This may result, for example, from propane adsorption at a site where no anatase/rutile interface is present and therefore a higher defect formation energy is expected, which may lead to propane reaction to carbon.

The broad applicability of the results obtained in this study is demonstrated by the SBA-15-based $VO_x/TiO_2/SiO_2$ layered system, which was investigated in the same way as the P25 samples and is discussed in detail in the SI. Even though the titania structure (especially the phase composition between anatase, rutile, and amorphous titania) is very different from P25, the structural dynamics are very similar to those of the P25 samples and can explain the reactivity behavior of this sample.

Based on the previous results and discussion, a mechanistic scheme is proposed (see Figure 10) that summarizes the main processes during the selective oxidation of propane over VO_x/TiO_2, but additional processes can occur simultaneously to form CO_x at spots that are nuclearity- and site-dependent. The arrow from bridged V−O−V to Ti−OH in the first hydrogen transfer step of the mechanistic scheme indicates that the hydrogen bound to the titania surface is transferred to V−O−V, and new hydrogen is transferred from propane to the titania surface via an additional Ti−OH instead of a direct transfer from propane to V−O−V. The asterisk (C_3H_6, C_3H_7)

indicates that the exact geometry and interaction between the adsorbate molecule and the catalyst surface are not known, which is due to the fact that the adsorbate is short-lived (see Table 4). The catalytic cycle is closed by the regeneration of molecular oxygen, as discussed above.

4. CONCLUSIONS

In this work, we present a combination of extensive structural characterization, static operando, and transient spectroscopies, including multiwavelength Raman, UV−vis, ^{51}V ssNMR, XPS, XRD, and ME-DRIFT spectroscopies, to understand the structure and the reaction mechanism of propane ODH over VO_x/TiO_2 catalysts. To avoid typical problems of UV methods with self-absorption on highly UV-absorbing TiO_2, we used multiple Raman wavelengths tuned to avoid most of the TiO_2 absorption while still selectively enhancing the titania intensity through resonance effects. We also synthesized $VO_x/TiO_2/SiO_2$ samples in order to reduce the amount of bulk TiO_2 and to obtain more insights into its structure by decreasing its absorption even further. The ALD-synthesized samples can furthermore demonstrate the applicability of our results over a broader range of different types of titania. In combination with other spectroscopic methods, especially transient IR spectroscopy, we established an experimental basis to obtain a detailed mechanistic understanding of the propane ODH reaction.

By using the described set-up, we were able to answer the four key questions often debated in the literature for VO_x/TiO_2 systems for the propane ODH reaction, which are outlined in the introduction. First, the active sites could be identified by a combination of ^{51}V ssNMR and UV-Raman spectroscopies and were determined to be oxygen atoms of vanadia, where the oxygen atoms of dimeric species are preferred over oxygen atoms from monomeric sites. Second, the loading dependence of the active site was determined by a nuclearity-dependent analysis of the vanadia structure and its reactivity. This type of analysis has proved to be difficult in the past for VO_x/TiO_2 systems, as the Ti:V contrast is much too low for electron microscopy, and the vanadyl fine structure is not very defined using vibrational spectroscopy (unlike for VO_x/CeO_2). Combining ^{51}V ssNMR and UV-Raman spectroscopies, we were able to show that for P25 as a titania support, vanadia nuclearities could be determined and quantified using direct spectroscopic evidence. Hereby, the V=O oxygen was identified to be the most active as the propane ODH facilitating oxygen atom as long as only doubly bridged V−O−V bonds from dimeric vanadia species were present at low loadings. When the loading was increased to a point where oligomeric species with linearly bridged oxygen atoms started to form, they began to become more active due to their better reducibility, accompanied by a lower selectivity toward propylene.

Besides the structural changes in vanadia, the exact influence of titania on the catalysts' activity was of debate. Possible influences could be (1) active participation in the reaction of the titania by providing lattice oxygen to participate in the redox cycle, (2) the coordination of vanadia in comparison to other supports, lowering the activation barrier, or (3) both ways of titania participation happening simultaneously.[4−6] For propane ODH, we were able to identify two ways in which titania influences the reaction. First, the amount of rutile dispersed in the anatase phase in the titania support can lead to different degrees of oligomerization of vanadia, and as the oligomerization degree is highly important and changes the

active oxygen atom, it can thereby influence the activity significantly. The second way in which titania participates in the reaction was identified directly via spectroscopy for the first time using transient IR spectroscopy. Titania facilitates the first C−H bond breaking, which is the rate-determining step, via a very quick hydrogen transfer onto the titania surface, forming a Ti−OH group, only detectable using transient spectroscopy, followed by a hydrogen transfer onto the vanadia V═O or V−O−V bonds, depending on the nuclearity. Therefore, for propane ODH, titania enhances the activity by both directly participating in the reaction and coordinating the vanadia in a way that facilitates the reaction. Oxygen vacancies in the titania lattice could not be detected for vanadia-loaded samples, indicating that titania lattice oxygen is not actively participating during propane ODH.

Finally, the CO_x formation was determined to be a parallel reaction to propylene formation by transient IR spectroscopy, and the decision whether selective or total oxidation occurs depends on whether propane adsorbs onto the catalyst or not, as carbonate and formate were the only adsorbates detectable in IR spectroscopy, indicating a site dependence for both reaction pathways.

Based on our results, we were able to observe both the oxygen and hydrogen transfer paths on the catalyst and determine the influence of the titania support on both pathways, including the adsorbate dynamics on both the propylene and the CO_x pathways, as well as their influence on the selectivity. Combining all of the mechanistic information, we were able to propose a detailed mechanistic picture of the propane ODH reaction mechanism over VO_x/TiO_2 catalysts.

Our results demonstrate the potential of the combination of different operando spectroscopic methods with transient spectroscopy for elucidating the surface dynamics during ODH reactions over supported metal oxide systems. The approach can also be easily transferred to different materials and reactions, and due to the widespread use of IR spectroscopy, the transient IR approach can readily be adapted to many different systems, performing detailed mechanistic analysis.

■ ASSOCIATED CONTENT

Ⓢ Supporting Information

The Supporting Information is available free of charge at https://pubs.acs.org/doi/10.1021/acscatal.3c01404.

Additional technical information and results from structural characterization, operando spectroscopic analysis, and transient DRIFTS (PDF)

■ AUTHOR INFORMATION

Corresponding Author

Christian Hess − *Department of Chemistry, Eduard-Zintl-Institut für Anorganische und Physikalische Chemie, Technical University of Darmstadt, 64287 Darmstadt, Germany;* ⓞ orcid.org/0000-0002-4738-7674; Email: christian.hess@tu-darmstadt.de

Authors

Leon Schumacher − *Department of Chemistry, Eduard-Zintl-Institut für Anorganische und Physikalische Chemie, Technical University of Darmstadt, 64287 Darmstadt, Germany*

Johannes Pfeiffer − *Department of Chemistry, Eduard-Zintl-Institut für Anorganische und Physikalische Chemie, Technical University of Darmstadt, 64287 Darmstadt, Germany*

Jun Shen − *Department of Chemistry, Eduard-Zintl-Institut für Anorganische und Physikalische Chemie, Technical University of Darmstadt, 64287 Darmstadt, Germany*

Torsten Gutmann − *Department of Chemistry, Eduard-Zintl-Institut für Anorganische und Physikalische Chemie, Technical University of Darmstadt, 64287 Darmstadt, Germany;* ⓞ orcid.org/0000-0001-6214-2272

Hergen Breitzke − *Department of Chemistry, Eduard-Zintl-Institut für Anorganische und Physikalische Chemie, Technical University of Darmstadt, 64287 Darmstadt, Germany*

Gerd Buntkowsky − *Department of Chemistry, Eduard-Zintl-Institut für Anorganische und Physikalische Chemie, Technical University of Darmstadt, 64287 Darmstadt, Germany;* ⓞ orcid.org/0000-0003-1304-9762

Kathrin Hofmann − *Department of Chemistry, Eduard-Zintl-Institut für Anorganische und Physikalische Chemie, Technical University of Darmstadt, 64287 Darmstadt, Germany*

Complete contact information is available at: https://pubs.acs.org/10.1021/acscatal.3c01404

Notes

The authors declare no competing financial interest.
The authors declare that they have no known competing financial interests or personal relationships that could have appeared to influence the work reported in this paper.

■ ACKNOWLEDGMENTS

■ REFERENCES

(1) Amghizar, I.; Vandewalle, L. A.; van Geem, K. M.; Marin, G. B. New Trends in Olefin Production. *Engineering* **2017**, *3*, 171−178.

(2) Cavani, F.; Ballarini, N.; Cericola, A. Oxidative dehydrogenation of ethane and propane: How far from commercial implementation? *Catal. Today* **2007**, *127*, 113−131.

(3) Carrero, C. A.; Schloegl, R.; Wachs, I. E.; Schomaecker, R. Critical Literature Review of the Kinetics for the Oxidative Dehydrogenation of Propane over Well-Defined Supported Vanadium Oxide Catalysts. *ACS Catal.* **2014**, *4*, 3357−3380.

(4) Chen, K.; Bell, A. T.; Iglesia, E. Kinetics and Mechanism of Oxidative Dehydrogenation of Propane on Vanadium, Molybdenum, and Tungsten Oxides. *J. Phys. Chem. B* **2000**, *104*, 1292−1299.

(5) Dinse, A.; Frank, B.; Hess, C.; Habel, D.; Schomäcker, R. Oxidative dehydrogenation of propane over low-loaded vanadia catalysts: Impact of the support material on kinetics and selectivity. *J. Mol. Catal. A: Chem.* **2008**, *289*, 28−37.

(6) Beck, B.; Harth, M.; Hamilton, N. G.; Carrero, C.; Uhlrich, J. J.; Trunschke, A.; Shaikhutdinov, S.; Schubert, H.; Freund, H.-J.; Schlögl, R.; Sauer, J.; Schomäcker, R. Partial oxidation of ethanol on vanadia catalysts on supporting oxides with different redox properties compared to propane. *J. Catal.* **2012**, *296*, 120−131.

(7) Schumacher, L.; Hess, C. The active role of the support in propane ODH over VOₓ/CeO₂ catalysts studied using multiple operando spectroscopies. *J. Catal.* **2021**, *398*, 29–43.

(8) Schumacher, L.; Weyel, J.; Hess, C. Unraveling the Active Vanadium Sites and Adsorbate Dynamics in VOₓ/CeO₂ Oxidation Catalysts Using Transient IR Spectroscopy. *J. Am. Chem. Soc.* **2022**, *144*, 14874–14887.

(9) Zaleska, A. Doped-TiO₂: A Review. *Recent Pat. Eng.* **2008**, *2*, 157–164.

(10) Arnarson, L.; Falsig, H.; Rasmussen, S. B.; Lauritsen, J. V.; Moses, P. G. A complete reaction mechanism for standard and fast selective catalytic reduction of nitrogen oxides on low coverage VOₓ/TiO₂(001) catalysts. *J. Catal.* **2017**, *346*, 188–197.

(11) Kwon, D. W.; Park, K. H.; Hong, S. C. Influence of VOₓ surface density and vanadyl species on the selective catalytic reduction of NO by NH₃ over VOₓ/TiO₂ for superior catalytic activity. *Appl. Catal., A* **2015**, *499*, 1–12.

(12) Shen, J.; Hess, C. High Surface Area VOₓ/TiO₂/SBA-15 Model Catalysts for Ammonia SCR Prepared by Atomic Layer Deposition. *Catalysts* **2020**, *10*, 1386.

(13) Won, J. M.; Kim, M. S.; Hong, S. C. Effect of vanadium surface density and structure in VOₓ/TiO₂ on selective catalytic reduction by NH₃. *Korean J. Chem. Eng.* **2018**, *35*, 2365–2378.

(14) Bertinchamps, F.; Treinen, M.; Blangenois, N.; Mariage, E.; Gaigneaux, E. Positive effect of NO on the performances of VOₓ/TiO₂-based catalysts in the total oxidation abatement of chlorobenzene. *J. Catal.* **2005**, *230*, 493–498.

(15) Bertinchamps, F.; Treinen, M.; Eloy, P.; Dos Santos, A.-M.; Mestdagh, M. M.; Gaigneaux, E. M. Understanding the activation mechanism induced by NOₓ on the performances of VOₓ/TiO₂ based catalysts in the total oxidation of chlorinated VOCs. *Appl. Catal., B* **2007**, *70*, 360–369.

(16) Ghampson, I. T.; Pecchi, G.; Fierro, J.L.G.; Videla, A.; Escalona, N. Catalytic hydrodeoxygenation of anisole over Re-MoOₓ/TiO₂ and Re-VOₓ/TiO₂ catalysts. *Appl. Catal., B* **2017**, *208*, 60–74.

(17) Liu, J.; Sun, Q.; Fu, Y.; Shen, J. Preparation and characterization of mesoporous VOₓ-TiO₂ complex oxides for the selective oxidation of methanol to dimethoxymethane. *J. Colloid Interface Sci.* **2009**, *335*, 216–221.

(18) Zabilska, A.; Clark, A. H.; Moskowitz, B. M.; Wachs, I. E.; Kakiuchi, Y.; Copéret, C.; Nachtegaal, M.; Kröcher, O.; Safonova, O. V. Redox Dynamics of Active VOₓ Sites Promoted by TiOₓ during Oxidative Dehydrogenation of Ethanol Detected by Operando Quick XAS. *J. Am. Chem. Soc. Au* **2022**, *2*, 762–776.

(19) Sannino, D.; Vaiano, V.; Ciambelli, P. Innovative structured VOₓ/TiO₂ photocatalysts supported on phosphors for the selective photocatalytic oxidation of ethanol to acetaldehyde. *Catal. Today* **2013**, *205*, 159–167.

(20) Ohtani, B. Titania Photocatalysis beyond Recombination: A Critical Review. *Catalysts* **2013**, *3*, 942–953.

(21) Ciambelli, P.; Lisi, L.; Ruoppolo, G.; Russo, G.; Volta, J. C. In *Oxidative Dehydrogenation of Ethane over Vanadium and Niobium Oxides Supported Catalysts*, Proceedings of the 3rd World Congress on Oxidation Catalysis; Studies in Surface Science and Catalysis; Elsevier, 1997; pp 285–294.

(22) Martínez-Huerta, M.; Fierro, J.L.G.; Bañares, M. A. Monitoring the states of vanadium oxide during the transformation of TiO₂ anatase-to-rutile under reactive environments: H₂ reduction and oxidative dehydrogenation of ethane. *Catal. Commun.* **2009**, *11*, 15–19.

(23) Khodakov, A.; Olthof, B.; Bell, A. T.; Iglesia, E. Structure and Catalytic Properties of Supported Vanadium Oxides: Support Effects on Oxidative Dehydrogenation Reactions. *J. Catal.* **1999**, *181*, 205–216.

(24) Heracleous, E.; Machli, M.; Lemonidou, A. A.; Vasalos, I. A. Oxidative dehydrogenation of ethane and propane over vanadia and molybdena supported catalysts. *J. Mol. Catal. A: Chem.* **2005**, *232*, 29–39.

(25) Lemonidou, A. A.; Nalbandian, L.; Vasalos, I. A. Oxidative dehydrogenation of propane over vanadium oxide based catalysts. *Catal. Today* **2000**, *61*, 333–341.

(26) Martra, G.; Arena, F.; Coluccia, S.; Frusteri, F.; Parmaliana, A. Factors controlling the selectivity of V₂O₅ supported catalysts in the oxidative dehydrogenation of propane. *Catal. Today* **2000**, *63*, 197–207.

(27) Christodoulakis, A.; Machli, M.; Lemonidou, A. A.; Boghosian, S. Molecular structure and reactivity of vanadia-based catalysts for propane oxidative dehydrogenation studied by in situ Raman spectroscopy and catalytic activity measurements. *J. Catal.* **2004**, *222*, 293–306.

(28) Shee, D.; Rao, T.; Deo, G. Kinetic parameter estimation for supported vanadium oxide catalysts for propane ODH reaction: Effect of loading and support. *Catal. Today* **2006**, *118*, 288–297.

(29) Viparelli, P. Oxidative dehydrogenation of propane over vanadium and niobium oxides supported catalysts. *Appl. Catal., A* **1999**, *184*, 291–301.

(30) Grzybowska, B.; Słoczyński, J.; Grabowski, R.; Samson, K.; Gressel, I.; Wcisło, K.; Gengembre, L.; Barbaux, Y. Effect of doping of TiO₂ support with altervalent ions on physicochemical and catalytic properties in oxidative dehydrogenation of propane of vanadia–titania catalysts. *Appl. Catal., A* **2002**, *230*, 1–10.

(31) Nitsche, D.; Hess, C. Structure of Isolated Vanadia and Titania: A Deep UV Raman, UV–Vis, and IR Spectroscopic Study. *J. Phys. Chem. C* **2016**, *120*, 1025–1037.

(32) Baron, M.; Abbott, H.; Bondarchuk, O.; Stacchiola, D.; Uhl, A.; Shaikhutdinov, S.; Freund, H.-J.; Popa, C.; Ganduglia-Pirovano, M. V.; Sauer, J. Resolving the Atomic Structure of Vanadia Monolayer Catalysts: Monomers, Trimers, and Oligomers on Ceria. *Angew. Chem.* **2009**, *121*, 8150–8153.

(33) Avdeev, V. I.; Zhidomirov, G. M. Modeling the active centers of V₂O₅/SiO₂ and V₂O₅/TiO₂ supported catalysts. DFT theoretical analysis of optical properties. *J. Struct. Chem.* **2005**, *46*, 577–590.

(34) Brückner, A. Killing three birds with one stone–simultaneous operando EPR/UV–vis/Raman spectroscopy for monitoring catalytic reactions. *Chem. Commun.* **2005**, 1761–1763.

(35) Weyel, J.; Ziemba, M.; Hess, C. Elucidating Active CO–Au Species on Au/CeO₂(111): A Combined Modulation Excitation DRIFTS and Density Functional Theory Study. *Top. Catal.* **2022**, *65*, 779–787.

(36) Scheurell, K.; Hoppe, E.; Brzezinka, K.-W.; Kemnitz, E. Bulk and surface properties of highly dispersed VOₓ/ZrO₂, VOₓ/SiO₂ and VOₓ/TiO₂/SiO₂ systems and their relevance for propane oxidation. *J. Mater. Chem.* **2004**, *14*, 2560.

(37) Rogg, S.; Hess, C. CO₂ as a soft oxidant for propane oxidative dehydrogenation: A mechanistic study using operando UV Raman spectroscopy. *J. CO2 Util.* **2021**, *50*, No. 101604.

(38) Sobel, N.; Hess, C.; Lukas, M.; Spende, A.; Stühn, B.; Toimil-Molares, M. E.; Trautmann, C. Conformal SiO₂ coating of sub-100 nm diameter channels of polycarbonate etched ion-track channels by atomic layer deposition. *Beilstein J. Nanotechnol.* **2015**, *6*, 472–479.

(39) Ruff, P.; Schumacher, L.; Rogg, S.; Hess, C. Atomic Layer Deposition-Assisted Synthesis of Embedded Vanadia Catalysts. *ACS Catal.* **2019**, *9*, 6349–6361.

(40) Spende, A.; Sobel, N.; Lukas, M.; Zierold, R.; Riedl, J. C.; Gura, L.; Schubert, I.; Moreno, J. M. M.; Nielsch, K.; Stühn, B.; Hess, C.; Trautmann, C.; Toimil-Molares, M. E. TiO₂, SiO₂, and Al₂O₃ coated nanopores and nanotubes produced by ALD in etched ion-track membranes for transport measurements. *Nanotechnology* **2015**, *26*, No. 335301.

(41) Waleska, P. S.; Hess, C. Oligomerization of Supported Vanadia: Structural Insight Using Surface-Science Models with Chemical Complexity. *J. Phys. Chem. C* **2016**, *120*, 18510–18519.

(42) de Oliveira, M.; Seeburg, D.; Weiß, J.; Wohlrab, S.; Buntkowsky, G.; Bentrup, U.; Gutmann, T. Structural characterization of vanadium environments in MCM-41 molecular sieve catalysts by solid state ⁵¹V NMR. *Catal. Sci. Technol.* **2019**, *9*, 6180–6190.

(43) Fernandez, C.; Bodart, P.; Amoureux, J. P. Determination of ^{51}V quadrupole and chemical shift tensor orientations in V_2O_5 by analysis of magic-angle spinning nuclear magnetic resonance spectra. *Solid State Nucl. Magn. Reson.* **1994**, *3*, 79−91.

(44) Ziemba, M.; Weyel, J.; Hess, C. Elucidating the mechanism of the reverse water−gas shift reaction over Au/CeO$_2$ catalysts using operando and transient spectroscopies. *Appl. Catal., B* **2022**, *301*, No. 120825.

(45) Baurecht, D.; Fringeli, U. P. Quantitative modulated excitation Fourier transform infrared spectroscopy. *Rev. Sci. Instrum.* **2001**, *72*, 3782−3792.

(46) Weyel, J. *Phase Sensitive Detection for Spectroscopy*; Zenodo, 2020.

(47) Lettieri, S.; Pavone, M.; Fioravanti, A.; Santamaria Amato, L.; Maddalena, P. Charge Carrier Processes and Optical Properties in TiO$_2$ and TiO$_2$-Based Heterojunction Photocatalysts: A Review. *Materials* **2021**, *14*, No. 1645.

(48) Glassford, K. M.; Chelikowsky, J. R. Optical properties of titanium dioxide in the rutile structure. *Phys. Rev. B* **1992**, *45*, 3874−3877.

(49) Daude, N.; Gout, C.; Jouanin, C. Electronic band structure of titanium dioxide. *Phys. Rev. B* **1977**, *15*, 3229−3235.

(50) Tang, H.; Berger, H.; Schmid, P. E.; Lévy, F. Optical properties of anatase (TiO$_2$). *Solid State Commun.* **1994**, *92*, 267−271.

(51) Hess, C.; Hoefelmeyer, J. D.; Tilley, T. D. Spectroscopic Characterization of Highly Dispersed Vanadia Supported on SBA-15. *J. Phys. Chem. B* **2004**, *108*, 9703−9709.

(52) Larrubia, M. A.; Busca, G. An ultraviolet−visible−near infrared study of the electronic structure of oxide-supported vanadia−tungsta and vanadia−molybdena. *Mater. Chem. Phys.* **2001**, *72*, 337−346.

(53) Choudhury, B.; Choudhury, A. Oxygen defect dependent variation of band gap, Urbach energy and luminescence property of anatase, anatase−rutile mixed phase and of rutile phases of TiO$_2$ nanoparticles. *Phys. E* **2014**, *56*, 364−371.

(54) Landmann, M.; Rauls, E.; Schmidt, W. G. The electronic structure and optical response of rutile, anatase and brookite TiO$_2$. *J. Condens. Matter Phys.* **2012**, *24*, No. 195503.

(55) Amore Bonapasta, A.; Filippone, F.; Mattioli, G.; Alippi, P. Oxygen vacancies and OH species in rutile and anatase TiO$_2$ polymorphs. *Catal. Today* **2009**, *144*, 177−182.

(56) Bhattacharyya, K.; Varma, S.; Tripathi, A. K.; Bharadwaj, S. R.; Tyagi, A. K. Effect of Vanadia Doping and Its Oxidation State on the Photocatalytic Activity of TiO$_2$ for Gas-Phase Oxidation of Ethene. *J. Phys. Chem. C* **2008**, *112*, 19102−19112.

(57) Nagaveni, K.; Hegde, M. S.; Madras, G. Structure and Photocatalytic Activity of Ti$_{1-x}$M$_x$O$_{2\pm\delta}$ (M = W, V, Ce, Zr, Fe, and Cu) Synthesized by Solution Combustion Method. *J. Phys. Chem. B* **2004**, *108*, 20204−20212.

(58) Jiang, X.; Manawan, M.; Feng, T.; Qian, R.; Zhao, T.; Zhou, G.; Kong, F.; Wang, Q.; Dai, S.; Pan, J. H. Anatase and rutile in evonik aeroxide P25: Heterojunctioned or individual nanoparticles? *Catal. Today* **2018**, *300*, 12−17.

(59) Burcham, L. J. In situ IR, Raman, UV-Vis DRS spectroscopy of supported vanadium oxide catalysts during methanol oxidation. *Top. Catal.* **2000**, *11/12*, 85−100.

(60) Balachandran, U.; Eror, N. G. Raman spectra of titanium dioxide. *J. Solid State Chem.* **1982**, *42*, 276−282.

(61) Kryukova, G. N.; Zenkovets, G. A.; Mestl, G.; Schlögl, R. Structural study of titanium doped vanadia and vanadium doped titania catalysts. *React. Kinet. Catal. Lett.* **2003**, *80*, 161−169.

(62) Xie, S.; Iglesia, E.; Bell, A. T. Effects of Hydration and Dehydration on the Structure of Silica-Supported Vanadia Species. *Langmuir* **2000**, *16*, 7162−7167.

(63) Hess, C.; Tzolova-Müller, G.; Herbert, R. The Influence of Water on the Dispersion of Vanadia Supported on Silica SBA-15: A Combined XPS and Raman Study. *J. Phys. Chem. C* **2007**, *111*, 9471−9479.

(64) Centi, G. Nature of active layer in vanadium oxide supported on titanium oxide and control of its reactivity in the selective oxidation and ammoxidation of alkylaromatics. *Appl. Catal., A* **1996**, *147*, 267−298.

(65) Sanati, M.; Andersson, A. Ammoxtoation of toluene over TiO$_2$(B)-supported vanadium oxide catalysts. *J. Mol. Catal.* **1990**, *59*, 233−255.

(66) Wachs, I. E. Raman and IR studies of surface metal oxide species on oxide supports: Supported metal oxide catalysts. *Catal. Today* **1996**, *27*, 437−455.

(67) Lian, Z.; Deng, H.; Xin, S.; Shan, W.; Wang, Q.; Xu, J.; He, H. Significant promotion effect of the rutile phase on V$_2$O$_5$/TiO$_2$ catalysts for NH$_3$-SCR. *Chem. Commun.* **2021**, *57*, 355−358.

(68) Arena, F.; Frusteri, F.; Parmaliana, A. How oxide carriers affect the reactivity of V$_2$O$_5$ catalysts in the oxidative dehydrogenation of propane. *Catal. Lett.* **1999**, *60*, 59−63.

(69) Schwan, J.; Ulrich, S.; Batori, V.; Ehrhardt, H.; Silva, S. R. P. Raman spectroscopy on amorphous carbon films. *J. Appl. Phys.* **1996**, *80*, 440−447.

(70) Sadezky, A.; Muckenhuber, H.; Grothe, H.; Niessner, R.; Pöschl, U. Raman microspectroscopy of soot and related carbonaceous materials: Spectral analysis and structural information. *Carbon* **2005**, *43*, 1731−1742.

(71) Silva, S. R. P.; Amaratunga, G. A. J.; Salje, E. K. H.; Knowles, K. M. Evidence of hexagonal diamond in plasma-deposited carbon films. *J. Mater. Sci.* **1994**, *29*, 4962−4966.

(72) Dutta, G.; Waghmare, U. V.; Baidya, T.; Hegde, M. S.; Priolkar, K. R.; Sarode, P. R. Origin of Enhanced Reducibility/Oxygen Storage Capacity of Ce$_{1-x}$Ti$_x$O$_2$ Compared to CeO$_2$ or TiO$_2$. *Chem. Mater.* **2006**, *18*, 3249−3256.

(73) Watanabe, S.; Ma, X.; Song, C. Characterization of Structural and Surface Properties of Nanocrystalline TiO$_2$-CeO$_2$ Mixed Oxides by XRD, XPS, TPR, and TPD. *J. Phys. Chem. C* **2009**, *113*, 14249−14257.

(74) Jaegers, N. R.; Lai, J.-K.; He, Y.; Walter, E.; Dixon, D. A.; Vasiliu, M.; Chen, Y.; Wang, C.; Hu, M. Y.; Mueller, K. T.; Wachs, I. E.; Wang, Y.; Hu, J. Z. Mechanism by which Tungsten Oxide Promotes the Activity of Supported V$_2$O$_5$/TiO$_2$ Catalysts for NO$_x$ Abatement: Structural Effects Revealed by ^{51}V MAS NMR Spectroscopy. *Angew. Chem., Int. Ed.* **2019**, *58*, 12609−12616.

(75) Hu, J. Z.; Xu, S.; Li, W.-Z.; Hu, M. Y.; Deng, X.; Dixon, D. A.; Vasiliu, M.; Craciun, R.; Wang, Y.; Bao, X.; Peden, C. H. F. Investigation of the Structure and Active Sites of TiO$_2$ Nanorod Supported VO$_x$ Catalysts by High-Field and Fast-Spinning ^{51}V MAS NMR. *ACS Catal.* **2015**, *5*, 3945−3952.

(76) Jehng, J.-M.; Deo, G.; Weckhuysen, B. M.; Wachs, I. E. Effect of water vapor on the molecular structures of supported vanadium oxide catalysts at elevated temperatures. *J. Mol. Catal. A: Chem.* **1996**, *110*, 41−54.

(77) Walter, A.; Herbert, R.; Hess, C.; Ressler, T. Structural characterization of vanadium oxide catalysts supported on nanostructured silica SBA-15 using X-ray absorption spectroscopy. *Chem. Cent. J.* **2010**, *4*, No. 3.

(78) van der Voort, P.; White, M. G.; Mitchell, M. B.; Verberckmoes, A. A.; Vansant, E. F. The effect of water on the structure of supported vanadium oxide structures. An FT-Raman, in situ DRIFT and in situ UV−VIS diffuse reflectance study. *Spectrochim. Acta, Part A* **1997**, *53*, 2181−2187.

(79) Lamoureux, B.; Singh, V. R.; Jovic, V.; Kuyyalil, J.; Su, T.-Y.; Smith, K. E. Structural and electronic properties of thermally evaporated V$_2$O$_5$ epitaxial thin films. *Thin Solid Films* **2016**, *615*, 409−414.

(80) Kuriechen, S. K.; Murugesan, S.; Paul Raj, S. Mineralization of Azo Dye Using Combined Photo-Fenton and Photocatalytic Processes under Visible Light. *J. Catal.* **2013**, *2013*, 1−6.

(81) Yang, J.; Bai, H.; Tan, X.; Lian, J. IR and XPS investigation of visible-light photocatalysis—Nitrogen−carbon-doped TiO$_2$ film. *Appl. Surf. Sci.* **2006**, *253*, 1988−1994.

(82) Cano-Casanova, L.; Mei, B.; Mul, G.; Lillo-Ródenas, M. Á.; Román-Martínez, M. D. C. Photocatalytic Oxidation of Propane Using Hydrothermally Prepared Anatase-Brookite-Rutile TiO$_2$

Samples. An In Situ DRIFTS Study. *Nanomaterials* **2020**, *10*, No. 1314.

(83) Hu, Z.; Wang, Z.; Guo, Y.; Wang, L.; Guo, L.; Zhang, J.; Zhan, W. Total Oxidation of Propane over a Ru/CeO$_2$ Catalyst at Low Temperature. *Environ. Sci. Technol.* **2018**, *52*, 9531−9541.

(84) Hadjiivanov, K. I.; Klissurski, D. G. Surface chemistry of titania (anatase) and titania-supported catalysts. *Chem. Soc. Rev.* **1996**, *25*, 61.

(85) Mathieu, M. V.; Primet, M.; Pichat, P. Infrared study of the surface of titanium dioxides. II. Acidic and basic properties. *J. Phys. Chem. A* **1971**, *75*, 1221−1226.

(86) Primet, M.; Pichat, P.; Mathieu, M. V. Infrared study of the surface of titanium dioxides. I. Hydroxyl groups. *J. Phys. Chem. A* **1971**, *75*, 1216−1220.

(87) Tanaka, K.; White, J. M. Characterization of species adsorbed on oxidized and reduced anatase. *J. Phys. Chem. A* **1982**, *86*, 4708−4714.

(88) Sharp, T. E.; Johnston, H. S. Hydrogen—Deuterium Kinetic Isotope Effect, an Experimental and Theoretical Study over a Wide Range of Temperature. *J. Chem. Phys.* **1962**, *37*, 1541−1553.

(89) Monnier, J. R.; Medlin, J. W.; Barteau, M. A. Use of Oxygen-18 to Determine Kinetics of Butadiene Epoxidation over Cs-Promoted, Ag Catalysts. *J. Catal.* **2001**, *203*, 362−368.

(90) Weinberg, D. R.; Gagliardi, C. J.; Hull, J. F.; Murphy, C. F.; Kent, C. A.; Westlake, B. C.; Paul, A.; Ess, D. H.; McCafferty, D. G.; Meyer, T. J. Proton-coupled electron transfer. *Chem. Rev.* **2012**, *112*, 4016−4093.

(91) Huang, C.; Wang, Z.-Q.; Gong, X.-Q. Activity and selectivity of propane oxidative dehydrogenation over VO$_3$/CeO$_2$(111) catalysts: A density functional theory study. *Chin. J. Catal.* **2018**, *39*, 1520−1526.

4.2.2 Insight into the Reaction Mechanism and Deactivation during CO_2-Assisted Propane ODH over VO_x/TiO_2 Catalysts: An Operando Spectroscopic Study

The eighth overall publication provides insight into the reaction mechanism and deactivation mechanisms of the CO_2-assisted propane ODH over differently loaded VO_x/TiO_2 catalysts, compared to ALD synthesized $VO_x/TiO_2/SiO_2$ samples. Analysis of the reaction network revealed that the catalysts are highly active and selective. The propane conversion depends on the vanadium content and decreases over time, while the CO_2 conversion stays constant, indicating that re-oxidation is rate-limiting and important for catalyst deactivation. The selectivity goes through a maximum within loadings of 0.5-1.2 V/nm^2. The selectivity is most influenced by PDR, while the only other side reaction is a negligable amount of cracking. The reaction mechanism was investigated by operando multi-wavelength Raman (385 and 514 nm excitation), UV-Vis, quasi in situ DRIFT spectroscopy and XRD. The results showed that bare titania was strongly reduced from the surface to the bulk. This deactivates the catalyst and shifts the main reaction from dehydrogenation to PDR, decreasing its selectivity. The introduction of vanadia increased the rate of re-oxidation by preventing subsurface/bulk reduction. Shorter vanadia chains reduce the PDR rate by decrasing titania reduction and actively participating in the reaction, while longer vanadia chains exhibit highly reducible oxygen atoms that increase the PDR rate and conversion, explaining the maximum in selectivity. Using reaction tests at different CO_2 partial pressures, the full reduction of the catalyst was identified as the main deactivation route, while vanadia consumption is also important. These results show that mechanistic insight into complex high-temperature reactions is accessible by combining multiple spectroscopic methods.

8. Leon Schumacher, Kathrin Hofmann, Christian Hess, Insight into the Reaction Mechanism and Deactivation during CO_2-Assisted Propane ODH over VO_x/TiO_2 Catalysts: An Operando Spectroscopic Study, ChemRxiv (DOI: 10.26434/chemrxiv-2023-rnfrd) (2023).

Insight into the Reaction Mechanism and Deactivation during CO$_2$-Assisted Propane ODH over VO$_x$/TiO$_2$ Catalysts: An Operando Spectroscopic Study

Leon Schumacher, Kathrin Hofmann, Christian Hess*

Technical University of Darmstadt, Department of Chemistry, Eduard-Zintl-Institut für Anorganische und Physikalische Chemie, Peter-Grünberg-Str. 8, 64287 Darmstadt, Germany.

*Corresponding Author (E-Mail: christian.hess@tu-darmstadt.de)

Abstract

The CO_2-assisted oxidative dehydrogenation (ODH) of propane is of great interest for technical applications, enabling the use of the greenhouse gas CO_2 in a value-adding process. Supported vanadium oxide (VO_x) catalysts are a promising alternative to more active but toxic chromium oxide catalysts. Despite its common use, TiO_2 has not been investigated as support material for VO_x in the CO_2-assisted ODH of propane. In this study, we address the interaction between titania (P25) and vanadia within the reaction mechanism using XRD, multi-wavelength Raman, UV-Vis and DRIFT spectroscopy. Besides direct and indirect ODH reaction pathways, propane dry-reforming (PDR) is identified as a side reaction, which is more prominent on bare titania. The presence of VO_x enhances the stability and selectivity by participating in the redox cycle, activating CO_2 and leading to a higher rate of regeneration. As main deactivation mechanisms of the catalyst system we propose the reduction of the titania lattice and the consumption of vanadium, while carbon formation appears to be less relevant. Our results highlight the importance of analysing the CO_2-ODH reaction network and applying combined steady-state spectroscopies as a first step towards a detailed mechanistic understanding of CO_2-assisted propane ODH over supported VO_x catalysts.

1. Introduction

The oxidative dehydrogenation (ODH) of propane is a promising additional process towards propylene production to meet the ever growing demand for this base chemical.[1,2] This demand cannot be satisfied by traditional production methods like steam cracking or fluid catalytic cracking, resulting in the 'propylene gap'.[3,4] The ODH of propane adds oxygen to the gas-feed, resulting in several advantages like lower reaction temperatures and therefore energy consumption and less catalyst leaching. However, it is still a challenge to control the oxidation process towards the selective oxidation product and significant amounts of CO_x are formed as a side product.[1,2,5] To avoid the over-oxidation of propane, CO_2 can be used as a soft-oxidant to increase the selectivity towards propylene. In addition, the heat capacity of CO_2 leads to a more homogenous temperature distribution throughout the reactor and a lower risk of flammability compared to O_2, facilitating a scale-up of the process.[6,7] From the environmental perspective, the use of the greenhouse gas CO_2 as a soft-oxidant in technical applications would directly assist in the efforts to mitigate the climate change, while creating value-added products in the form of propylene and CO.[8–10] However, due to the high temperature required for CO_2 activation,[11,12] a suitable catalyst needs to be employed to obtain sufficient conversions at moderate temperatures without catalyst deactivation (e.g. coking)[13].

A promising class of catalysts for the CO_2-assisted ODH of propane are supported transition metal oxide catalysts.[14–17] In the past, a research focus was put on chromium oxide (CrO_x) due to its high activity.[7,18–21] In this context, Mychorczyk et al.[20] described the oxidation state of chromium, as measured via operando UV-Vis spectroscopy, to be of great importance to differentiate between the oxidative and non-oxidative reaction paths, where Cr^{6+} species are reduced rapidly to $Cr^{2+/3+}$ species under reaction conditions, which participate in the non-oxidative pathway. However, as chromium oxides are toxic and harmful to the environment, other materials have attracted renewed interest.[22] Vanadium oxide (VO_x) is a promising catalyst for CO_2-assisted ODH reactions,[23–27] since it is commonly used for oxidation reactions in industrial applications and shows high activity for the ODH of propane using O_2.[5,28] Besides VO_x, molybdenum oxide (MoO_x) was recently used as the active phase.[29,30] For the vanadia-based catalysts, a variety of supports such as SiO_2,[23,27] Al_2O_3,[24] and In_2O_3[25,26] were already studied theoretically and experimentally in the literature. However, the use of CeO_2- and TiO_2-supported vanadia catalysts, which are the most

3

active support materials in propane ODH using O_2,[31,32] has not been reported in the context of CO_2-assisted ODH reactions.

An important aspect towards mechanistic understanding is the characterization of the reaction network using CO_2-assisted propane ODH, as multiple side reactions, like propane dry reforming (PDR),[25] carbon formation, cracking, and coke gasing may occur simultaenously.[13] Furthermore, based on experimental and theoretical work on a WO_x-VO_x/SiO_2 catalyst, Ascoop et al.[23] proposed the occurrence of two pathways for propylene formation, that is a direct pathway via the ODH reaction and an indirect two-step pathway, including direct propane dehydrogenation, resulting in propylene and hydrogen, followed by a reaction of H_2 with CO_2 to CO and water via the reverse water-gas shift (RWGS) reaction. The presence of two simultaneous reaction pathways towards propylene was confirmed experimentally by Rogg et al.[27] for VO_x/SiO_2 catalysts, using operando spectroscopy, highlighting the importance of the pre-treatment conditions as partly reduced vanadia chains seem to limit the deep oxidation potential, increasing the propylene selectivity. Regarding the use of active support materials, Jiang et al.[25,26] have recently described the potential of VO_x/In_2O_3 catalysts, where vanadia was identified to reduce dry-reforming and participate in the redox cycle, resulting in good ODH selectivities. Monomeric VO_x species were proposed as the most active site, due to their strong interaction with indium.[26] However, despite these studies, there is a number of open questions related to the mode of operation of VO_x catalysts in CO_2-assisted propane ODH: What is the role of CO_2 within the reaction network? Is the support actively participating in the reaction? How can the selectivity behavior be explained and possibly controlled? How does the catalyst deactivate?

To answer these questions, we address the mode of operation of different VO_x/TiO_2 catalysts during CO_2-assisted propane ODH, by combining multiple quasi in-situ and operando methods in this study. These include multi-wavelength Raman, UV-Vis, and DRIFT spectroscopy, as well as XRD to gain insight into the reaction mechanism and to identify the exact role of CO_2 and the support, and to elucidate vanadia nuclearity-dependence of the observed reactivity behavior. The combination of these methods allows for a dedicated investigation of the active and support phases based on differing selective intensity enhancements and a differentiation between surface, subsurface, and bulk processes due to the different information depth of the applied methods. Furthermore, we address the common problem of catalyst

deactivation during the reaction by identifying key catalyst deactivation mechanisms relevant to VO_x/TiO_2 catalysts. Our results demonstrate the great potential of combining multiple operando methods to provide a mechanistic understanding of catalytic reactions with potential industrial applicability. Our approach can readily be transferred to other catalyst materials based on ceria, molybdena or tungstia.

2. Experimental Section

2.1. Catalyst Preparation

Bulk titania and thin-film titania prepared by atomic layer deposition (ALD) was used as support material. Titania P25 (Aeroxide, Sigma-Aldrich, ≥99.5%), consisting of 77% anatase, 16% rutile, and 7% amorphous titania, was purchased.[33] The P25 samples were first characterized by nitrogen physisorption and subsequent analysis by the Brunauer-Emmet-Teller (BET) method, yielding a surface area of 73 m²/g and then loaded by wet-impregnation using an aqueous solution containing a 1:2 ratio of ammonium meta vanadate (AMV) and oxalic acid with four different concentrations (1.2, 0.59, 0.25, and 0.05 mol/l), resulting in vanadium surface densities of 2.5, 1.2, 0.5, and 0.1 V/nm², respectively. All samples were loaded below monolayer loading (as confirmed by Raman analysis), thus guaranteeing that only amorphous vanadia was present.[34] The loaded samples were dried at 120 °C for 12 h and then calcined at 480 °C for 4 h.

Mesoporous silica SBA-15 was synthesized as described previously,[27] and coated with titania using a custom-built ALD set-up, as described previously.[28] The theoretical thickness of the thin-film titania corresponds to 10 nm, as determined by ellipsometry for a silicon wafer.[35] The sample was calcined in air at 600 °C for 12 h to crystallize the titania. The specific surface area was determined to be 81 m²/g by nitrogen physisorption with subsequent BET analysis. The samples were also loaded by wet-impregnation, employing an aqueous solution with a 1:2 ratio of AMV and oxalic acid with a concentration of 0.67 mol/l, resulting in a vanadium surface density of 1.2 V/nm². The samples were dried and calcined as described above. All samples were prepared in the same exact way as in our previous VO_x/TiO_2 study on propane ODH using O_2, to guarantee comparability.**[28]**

2.2. Catalytic Testing

Catalytic testing was performed in a CCR 1000 reaction cell (Linkam Scientific) equipped with a membrane pump to allow for operation in a fluidized-bed mode, using 60 mg of catalyst for the P25 samples and, due to its much lower density, 25 mg of the ALD-synthesized samples. The samples were first dehydrated in 12.5% O_2/He for 1 h at 550 °C, subsequently cooled to 50 °C, exposed to 12.5% CO_2/12.5% C_3H_8/He with a total flow rate of 40 ml_n/min, and then heated in 45 °C steps up to 550 °C, staying at

each temperature for 1 h. The gas-phase composition was analyzed continuously using a gas chromatograph (GC, Agilent Technologies 7890B) equipped with a PoraPlotQ and a Molsieve column as well as a thermal conductivity detector (TCD) and a flame ionization detector (FID) in series. The set-up is connected through a twelve-way valve. One chromatogram is measured every 29 min, resulting in two chromatograms for each temperature, which were averaged. The pressure before and after the GC was monitored to correct the detected areas for pressure fluctuations. The obtained conversions were normalized to the surface area of the catalyst, due to the significantly different sample masses used for P25 and ALD-synthesized catalysts. To analyze the reaction network, the temporal evolution of the reactivity behavior was analyzed at 550 °C. The samples were first dehydrated in 12.5% O_2/He for 1 h, then treated consecutively in 7.5% H_2/Ar, 12.5% CO_2/He, 12.5% CO_2/12.5% C_3H_8/He, and finally regenerated in 12.5% CO_2/He (for 2 h for each gas phase), respectively. The reaction products were analyzed and time-dependent ratios between different products were calculated to determine the relative contributions of the different reaction pathways to the overall product distribution.

2.3. UV-Raman Spectroscopy

UV-Raman spectroscopy was performed at an excitation wavelength of 385 nm generated by a laser system based on a Ti:Sa solid-state laser pumped by a frequency-doubled Nd:YAG laser (Coherent, Indigo). The fundamental wavelength is frequency doubled to 385 nm using a LiB_3O_5 crystal. The light is focused onto the sample, and the scattered light is collected by a confocal mirror setup and focused into a triple-stage spectrometer (Princeton Instruments, TriVista 555).[36] Finally, the Raman contribution is detected by a charge-coupled device (CCD, 2048 × 512 pixels) cooled to –120 °C. The spectral resolution of the spectrometer is 1 cm^{-1}. For Raman experiments, 60 mg of catalyst was placed in a CCR 1000 reactor (Linkam Scientific Instruments) equipped with a CaF_2 window (Korth Kristalle GmbH). A fluidized-bed reactor was employed to avoid laser-induced damage, allowing the use of a laser power of 8 mW at the location of the sample. Data processing included cosmic ray removal and background subtraction. Operando spectra were measured after dehydration for 1 h in 12.5% O_2/He and further pre-treatment in 7.5% H_2/Ar and 12.5% CO_2/He at 550 °C to start from a partially oxidized state. Afterwards, the catalyst was exposed to reactive

conditions (12.5% CO_2/12.5% C_3H_8/He) and regenerated under oxidizing conditions (12.5% CO_2/He) with a total flow rate of 40 ml_n/min for each gas phase. The spectra were further analyzed by a least-squares fitting analysis using Lorentzian functions after normalization to the anatase E_g peak at 630 cm^{-1}. The intensity of the carbon signal was determined by integration over all carbon peaks.

2.4. Vis-Raman Spectroscopy

Visible (Vis) Raman spectroscopy was performed at 514 nm excitation, emitted from an argon ion gas laser (Melles Griot). The light was focused onto the sample, gathered by an optical fiber, and dispersed by a transmission spectrometer (Kaiser Optical, HL5R). The dispersed Raman radiation was subsequently detected by an electronically cooled CCD detector (–40 °C, 1024 × 256 pixels). The spectral resolution was 5 cm^{-1} with a wavelength stability of better than 0.5 cm^{-1}. For Raman experiments, 60 mg of catalyst was filled into a CCR 1000 reactor (Linkam Scientific Instruments) equipped with a quartz window (Linkam Scientific Instruments). A fluidized-bed reactor was employed to avoid laser-induced damage, allowing the use of a laser power of 5 mW at the location of the sample. Data analysis of the Raman spectra included cosmic ray removal and an auto new dark correction. Operando spectra were measured after dehydration in 12.5% O_2/He and further pre-treatment in 7.5% H_2/Ar and 12.5% CO_2/He at 550 °C for 1 h, respectively, to start from a partially oxidized state. Afterwards, the catalyst was exposed to reactive conditions (12.5% CO_2/12.5% C_3H_8/He) for 2 h for time-dependent measurements and regenerated under oxidizing conditions (12.5% CO_2/He) for 1 h with a total flow rate of 40 ml_n/min for each gas phase. The spectra were further analyzed by a least-squares fitting analysis using Lorentzian functions after normalization to the anatase E_g peak at 630 cm^{-1}.

2.5. X-Ray Diffraction

Powder X-ray diffraction (XRD) patterns were recorded on a Stadi-P (Stoe & Cie) diffractometer with a Ge(111)-monochromator, Cu $K\alpha_1$ radiation (λ = 1.54060 Å), and a MYTHEN-1K (Dectris) detector, using a flat sample holder in transmission geometry. For quasi in-situ XRD measurements the samples were measured in pristine condition after dehydration in 12.5% O_2/He for 1 h at 550 °C, followed by rapid cooling to room

temperature in pure helium in the Linkam reactor and an inert transfer to the diffractometer. For the second set of experiments, the samples were pre-treated consecutively in 12.5% O_2/He, 7.5% H_2/Ar, 12.5% CO_2/He, and 12.5% CO_2/12.5% C_3H_8/He for 1 h at 550 °C, respectively, followed by rapid cooling to room temperature (200 °C/min) in pure helium in the Linkam reactor and an inert transfer to the diffractometer.

2.6. Diffuse Reflection UV-Vis Spectroscopy

Diffuse reflectance (DR) UV-Vis spectra were recorded on a Jasco V-770 UV-Vis spectrometer. Dehydrated $BaSO_4$ was used as the white standard and 75 mg of catalyst were placed in the commercially available reaction cell (Praying Mantis High Temperature Reaction Chamber, Harrick Scientific) equipped with transparent quartz glass windows for each experiment. Operando spectra were measured after dehydration in 12.5% O_2/He and further pre-treatment in 7.5% H_2/Ar and 12.5% CO_2/He at 550 °C for 1 h, respectively, to start from a partially oxidized state. Afterwards, the catalyst was exposed to reactive conditions (12.5% CO_2/12.5% C_3H_8/He) for 1.5 h for time-dependent measurements and regenerated under oxidizing conditions (12.5% CO_2/He) at 550 °C for 1 h with a total flow rate of 40 ml_n/min for each gas phase. The spectra were further analyzed by a least-squares fitting analysis using Gaussian-Lorentzian (70/30) product functions. Product functions were used to account for the large contribution of natural line broadening to the overall line-shape, caused by the short life-time of the electronically excited states (Lorentzian), while also accounting for the generally better convergence of the fit (Gaussian).[37] The band gap energies were determined using Tauc plots.[38,39]

2.7. Diffuse Reflection Infrared Fourier Transform Spectroscopy

Diffuse reflectance infrared Fourier transform spectroscopy (DRIFTS) was performed using a Vertex 70 spectrometer (Bruker). A liquid nitrogen-cooled mercury cadmium telluride (MCT) detector was used, operating at a resolution of 1 cm^{-1}. Dehydrated potassium bromide was employed as an infrared transparent sample for the background spectrum. For each experiment, 75 mg of catalyst was placed in the

commercially available reaction cell (Praying Mantis High Temperature Reaction Chamber, Harrick Scientific) equipped with transparent KBr windows.

For quasi in-situ measurements the samples were treated in 12.5% O_2/He, 7.5% H_2/Ar, 12.5% CO_2/He, 12.5% CO_2/12.5% C_3H_8/He, and finally regenerated in 12.5% CO_2/He for 1 h at 550 °C, respectively. For each gas phase the sample was cooled rapidly to room temperature (200 °C/min) in pure helium in the Linkam reactor for the measurement before heating it back to 550 °C for the next measurement.

Data processing consisted of background removal by subtracting a baseline formed by 12 anchor points and removal of the spectrum recorded in 12.5% O_2/He to subtract the contributions from the pristine catalyst, targeting the surface species formed by the additional gas treatments only. Finally, to quantify the adsorbate peaks in the vanadyl and Ti-OH regions, the spectra were fitted using Lorentzian functions employing the Levenberg-Marquardt algorithm implemented in OriginLab 2022b.

3. Results and Discussion

Reactivity Behavior and Analysis of the Reaction Network

To choose a temperature that is most ideal for the operando spectroscopic investigation of the CO_2-assisted ODH of propane over VO_x/TiO_2, a temperature-dependent analysis of the catalytic activity was performed. Figure 1 summarizes the catalytic performance between 45 and 550 °C, showing the propane conversions (left panel) and selectivities to propylene (right panel).
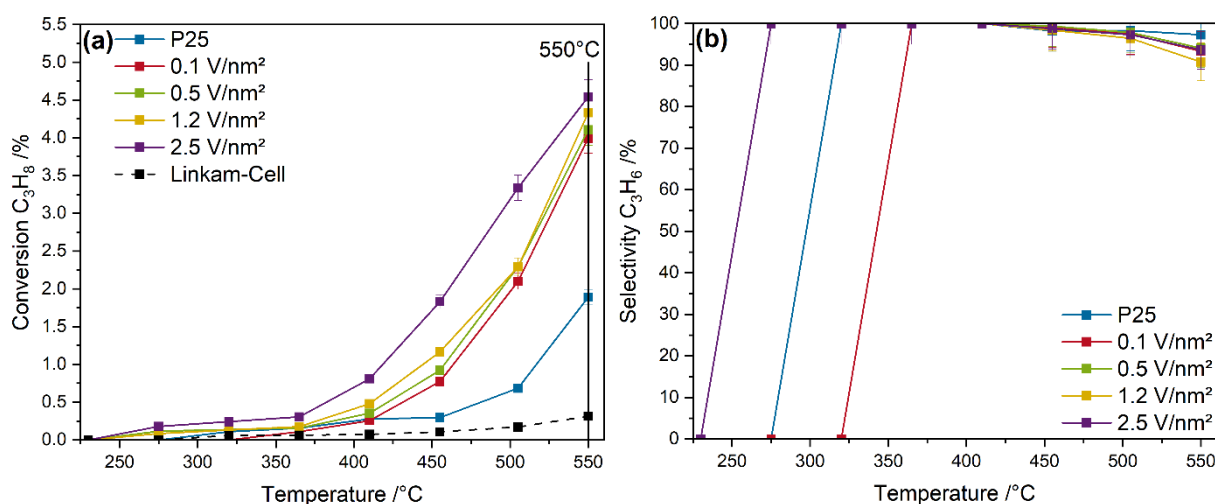
Figure 1: Reactivity behaviour of VO_x/TiO_2 catalysts in CO_2-assisted propane ODH. Temperature-dependent **(a)** conversion of propane and **(b)** selectivity towards propylene of the bare TiO_2 P25 support, the vanadia-loaded samples, and the empty Linkam reactor recorded in a feed of 12.5% CO_2/12.5% C_3H_8/He (total flow rate: 40 ml/min). The black line (left panel) highlights the temperature chosen for the mechanistic analysis.

Figure 1a depicts the temperature-dependent conversion of propane, starting at 275 °C for the three samples with the highest vanadium loading and at 320 °C for the P25 and P25+0.1 V/nm² samples. The conversion then increases exponentially with the increasing temperature up to 550 °C, where the catalysts reach propane conversions between 2.35 % (bare P25) and 4.54 % (P25+2.5 V/nm²), showing an increase with increasing vanadium loading. Importantly, the onset of propane conversion jumps from P25 to P25+0.1 V/nm², indicating that the presence of vanadium greatly increases the catalytic activity. The propane conversion of the empty Linkam reactor (0.31 %) is small compared to that of the VO_x/TiO_2 catalysts. The homogeneous gas-phase reaction occurring in the reactor does not lead to the formation of propane, but rather mostly

C_2H_4, CH_4, and CO, indicative of mostly cracking or total oxidation reactions. Therefore, the ODH reaction is determined to be exclusively caused by the catalysts. In general, the P25+2.5 V/nm² sample is the most active, showing the earliest onset of the reaction, and a significantly higher propane conversion than the other samples, while the other three VO_x/TiO_2 samples, show a somewhat similar conversion behaviour. The conversions are in the same order of magnitude compared those obtained under similar conditions (vanadia loading, catalyst mass, temperature) in a fixed bed reactor.[25] However, due to a lack of literature data, a direct comparison to other titania catalysts is not possible. The selectivities remain at 100 % for temperatures up to 410 °C, while at higher temperatures, the selectivity drops to an absolute minimum of 91% for the P25+1.2 V/nm² sample at 550 °C, which compares very favourably with other vanadia-based catalysts.[23–25,27] Therefore, a reaction temperature of 550 °C was chosen for the mechanistic analysis.

To analyse the reaction network in more detail, the catalytic activity of the samples was determined at 550 °C in 12.5% CO_2/12.5% C_3H_8/He, after dehydration at 550 °C in 12.5% O_2/He for 1 h and pre-treatment in 7.5% H_2/Ar and 12.5% CO_2/He, to establish a partially reduced initial state, that is more representative of the state at which the catalyst will be operating during the reaction. Afterwards, the samples are regenerated in 12.5% CO_2/He. The molar product distributions for all gas phases of the P25-based samples are given in the SI (see Figure S1). The most important kinetic results used to differentiate the different reactions occurring on the catalyst are given in Figure 2.
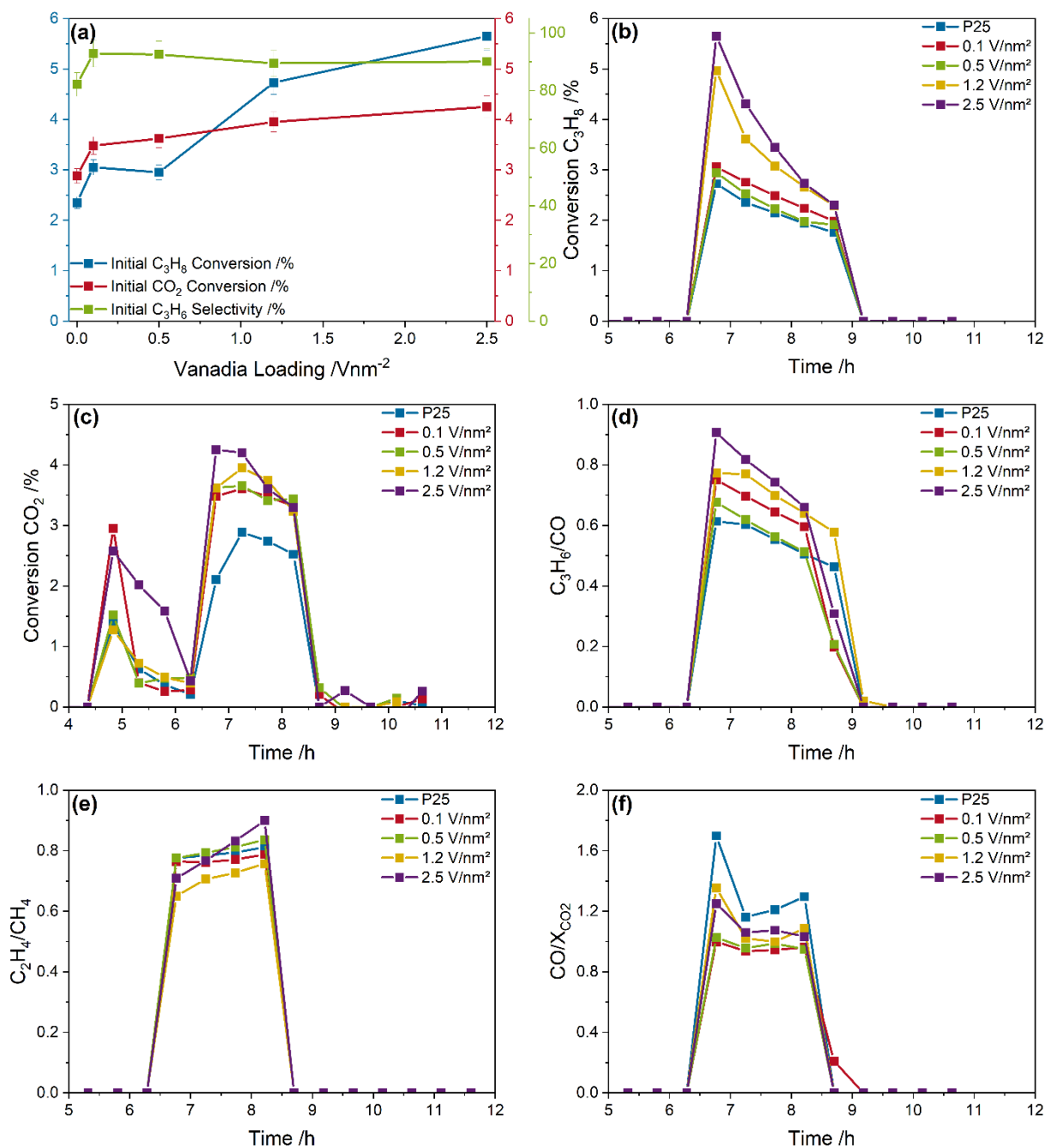
Figure 2: Analysis of the reaction network for bare P25 and vanadia-loaded samples during CO_2-assisted propane ODH: **(a)** Loading-dependent initial conversions of C_3H_8 and CO_2, and C_3H_6 selectivity, **(b)+(c)** time-dependent conversions of C_3H_8 and CO_2, **(d)** time-dependent C_3H_6/CO ratio, **(e)** time-dependent C_2H_4/H_2 ratio, and **(f)** time-dependent CO/X_{CO2} ratio. Between 0 and 2 h 12.5% O_2/He, between 2 and 4 h 7.5% H_2/Ar, between 4 and 6 h 12.5% CO_2/He, between 6 and 9 h 12.5% $CO_2/12.5\%$ C_3H_8/He, and between 9 and 11 h 12.5% CO_2/He were used as the gas feed.

Figure 2a depicts the loading-dependent initial conversions of C_3H_8 and CO_2, as well as the initial C_3H_6 selectivity for the bare P25 support and the VO_x/TiO_2 samples,

obtained at 550 °C after pre-treatment in O_2, H_2, and CO_2 for 1 h each (see experimental section for details). Starting at 2.35% for P25, the C_3H_8 conversion increases with the vanadium loading up to 5.65% for P25+2.5 V/nm², after showing a distinct jump from P25 to P25+0.1 V/nm² and from 0.5 to 1.2 V/nm². In contrast, the CO_2 conversion starts at 2.88% for P25 and then increases to a maximum of 4.25% for P25+2.5 V/nm², staying slightly above the C_3H_8 conversions at all vanadium loadings, except for the P25+2.5 V/nm² sample, indicative of side reactions, such as PDR or cracking, as the dehydrogenation pathways would consume propane and CO_2 at the same rate. In comparison to the propane conversion, the CO_2 conversion increases almost linear with the vanadium loading and exhibits no plateau between 0.1 and 0.5 V/nm². Similar to the conversions, the initial selectivities towards propylene jump from bare P25 to the P25+0.1 V/nm² sample increasing from 82.2% for P25 to 92.9%. It then decreases again to 90% for the P25+2.5 V/nm² sample. These selectivities already include the PDR side reaction, which is discussed below. However, the selectivities are high at >80% and do not fluctuate significantly. Therefore, the presence of vanadium seems to mostly increase the rate of propylene formation. Overall, the initial values of propane and CO_2 conversions in combination with the propylene selectivities are at a higher level than those of other VO_x-based catalyst systems,[23–25,27] and even reach those of some of the supported CrO_x systems.[18,21,40]

Figures 2b and c depict the time-dependent conversions of C_3H_8 and CO_2 for the P25-based samples. As shown in Figure 2b, the propane conversion is significantly higher at the beginning of the reaction, which is most pronounced for the samples loaded with 1.2 and 2.5 V/nm². The C_3H_8 conversion decreases to a similar value of around 2% for all samples after ~3h (P25: 1.75%, P25+2.5 V/nm²: 2.4%), but still follows the same trend of a conversion, which increases with the vanadium loading. Thus, the decrease in propane conversion is most significant for the samples with the highest loadings. In comparison, the CO_2 conversion stays more constant during the reaction, except for the P25+2.5 V/nm² sample. This is a first indicator that catalyst reoxidation with CO_2 is rate-limiting, that is, the catalyst decreases its overall activity due to an overall catalyst reduction. After the initial 30 minutes, the CO_2 conversion is similar to that of propane for all samples, except for the P25 sample, indicating the occurrence of more side reactions on the bare support. However, since the propane conversion gradually decreases further and the CO_2 conversion stays more constant,

the CO_2 conversion is, at the end of the reaction phase, higher than that of propane. This indicates a deactivation of the catalyst for the ODH reaction, with reoxidation being the rate-limiting step.

For further analysis of the reaction network, the relative amount of different reactions occurring on the catalyst surface and the importance of the ODH route was studied. To this end, Figures 2d-f show the C_3H_6/CO ratio, as an indicator for the extent of dehydrogenation, the C_2H_4/CH_4 ratio, as an indicator for the amount of cracking, and the CO/X_{CO2} ratio, as an indicator for PDR, respectively. The time-dependent molar product distributions are given in Figure S1. Starting with the C_3H_6/CO ratio, the values decrease over time due to the decreasing propane conversion. The initial values are lowest for bare P25 (0.61) and highest for P25+2.5 V/nm² (0.91), following an increase with increasing vanadium loading. At the end of the reaction phase, values drop to 0.46 for P25 and 0.66 for P25+2.5 V/nm². Generally, more CO than propylene is produced. Since the C_3H_6 to CO ratio should be 1 for the direct (ODH) and indirect (DDH+RWGS) reaction routes, additional reactions are expected to occur. This is supported by the observed CO_2 conversions, which are consistently higher than those of propane. However, the ratio is, especially for the P25+2.5 V/nm² sample, close to a value of one, indicating a full dehydrogenation route over the catalyst, in good agreement with other actively supported VO_x systems,[24–26] which show side reactions in a similar range, but the TiO_2 system seems to be slightly more selective towards propylene.

To gain insight into the side reactions, Figure 2e depicts the C_2H_4 to CH_4 ratio, which is indicative of propane cracking, leading to ethylene and methane. The ratio is close to one with slightly more methane being produced, which is in agreement with the expected product distribution of thermal propane cracking at this temperature.[41] It is important to note that the overall amount of ethylene and methane is comparably small, especially when considering the fact that one methane and one ethylene molecule are produced from one propane molecule. In fact, the amount of cracking is determined to be <5% of the overall conversion for all samples, based on the molar product distributions (see Figure S1). Furthermore, around ~50% of the detected methane and ethylene (depending on the sample) is produced by the empty reactor, further decreasing the relevance of propane cracking on the catalyst. While the C_2H_4 to CH_4 ratio increases with propane conversion, the overall extent of cracking slightly decreases, which is in good agreement with the ~2% cracking occurring on the catalyst itself, while half of these products are formed by the reactor, which should have a

constant product distribution. The slight increase in the C_2H_4 to CH_4 ratio towards the end of the reaction phase is in good agreement with the less conversion via the ODH reaction, which is exothermic in nature.[42] As a result, the amount of reaction heat is decreased and the temperature of the system is also slightly decreased (a few degrees), which shifts the cracking products towards ethylene.[41] Overall, due to its weak contribution, propane cracking is considered as less important for the overall reaction network and the behavior of the catalyst.

Last, Figure 2f shows the ratio between the produced CO and the converted CO_2 (CO_2 based CO selectivity), as an indicator for PDR. For bare P25, within the first 30 minutes, 70% more CO is produced than CO_2 is converted, indicating a high degree of PDR, which then decreases to a stable level of around ~25% more CO. While the ODH/DDH+RWGS should create one CO molecule each, this always converts a CO_2 molecule. Therefore, the excess CO must be produced from propane by PDR. This behaviour might be indicative of highly reducible active sites for the PDR reaction that are quickly consumed, leading to a stable level of CO production. In comparison, the vanadia-loaded samples depict a CO_2 based CO selectivity that is only slightly above one (1.02-110), indicating a small contribution of PDR but to a much smaller degree as for bare P25. A similar behaviour was previously observed for supported vanadia systems and explained by the acid-base properties of the system, as the introduction of vanadia as an acidic oxide increases the rate of C-H bond activation in comparison to the more basic support, in this case TiO_2, which activates the C=O bond.[25] In principle, such a scenario is consistent with the results observed here for the VO_x/TiO_2 system. Considering the loading dependence the reactivity behaviour of the 0.1 and 0.5 V/nm² samples is characterized mainly by the ODH of propane, whereas the 1.2 and 2.5 V/nm² samples show slightly higher ratios (~1.1) and also exhibit a much higher ratio in the first 30 minutes, indicating structural and/or chemical changes on the surface, which influences the PDR rate. The loading-dependent behaviour may be caused by the different vanadia nuclearity distributions, which has been shown to vary significantly for VO_x/TiO_2 catalysts.[28] For example, oligomers, present on the P25+2.5 V/nm² sample, are more reducible and prone to less selective oxidation as compared to monomers and dimers.[28]

During the reaction, a significant amount of hydrogen is formed (see Figure S1), which increases with the vanadium loading. To explain this behaviour, the following two scenarios are conceivable: First, hydrogen formed by the direct dehydrogenation

of propane, might not be fully converted to H_2O in the RWGS, as titania is typically a good RWGS reaction catalyst only in combination with a metal.[43,44] The second scenario is based on the formation of carbon during the dry reforming process, resulting in a conversion of propane to CO, methane, hydrogen, and carbon coking on the catalyst surface.[45] The plethora of different PDR reaction products can explain the presence of free hydrogen and might also explain the higher amount of methane than ethylene produced during cracking. In addition, the main product, CO, explains the higher amount of detected CO than converted CO_2 (see Figure 2f). The presence of carbon on the catalyst during the reaction will be discussed in more detail in the operando spectroscopy section. Due to the different possibilities for the hydrogens origin, the H_2/CO ratio to determine the amount of DDH vs ODH is not feasible in this context.

Additionally, to compare the results of a bulk TiO_2 to a different TiO_2-based support material, we exposed vanadia-loaded TiO_2/SBA-15 (SBA15-T) samples prepared by ALD to the same gas-treatments to investigate their catalytic behaviour. The results are given in the SI (see Figures S2 and S3). While the samples show less conversion than the corresponding P25-based samples discussed above, the difference between the vanadia-loaded sample and the bare support regarding C_3H_8 conversion is much less pronounced than for the P25-based samples. An important feature of the ALD-based TiO_2 material is that its propane conversion stays much more stable than that of bulk TiO_2, which shows a rapid decrease with time on stream. The propane and CO_2 conversions are very similar for both materials, while significantly more CO than propylene is produced, which is supported by the CO_2-based CO selectivity, which reaches a maximum of 285% for the SBA15-T+1.2 V/nm² sample, indicating a strong contribution of PDR. Bare SBA15-T, on the other hand, rather follows selective dehydrogenation pathways and is more directly comparable to the bulk TiO_2, while maintaining a stable C_3H_8 and CO_2 conversion.

In summary, the VO_x/TiO_2 systems show a good catalytic activity, with overall selectivities above 90% for the vanadia-loaded samples. Typical side reactions like PDR are of relevance on the bare support where significantly more CO is produced than CO_2 is converted, indicating that some propane is consumed to form CO. When vanadia is introduced, the PDR rates are reduced significantly, allowing for an almost exclusive dehydrogenation of propane via either ODH or DDH+RWGS reaction pathways. The presence of free H_2 indicates the occurrence of some PDR that also

produces CH_4 and carbon on the catalyst surface, which will be subject to operando spectroscopic analysis (see below).

Operando Spectroscopy

To gain insight into the reaction mechanism, multiple operando spectroscopies were employed during the different gas feeds (compare experimental section). However, since the propane conversion, especially on the vanadia-loaded samples, does not stay constant and the measurements of different operando/quasi in situ methods occur on different time scales, each method may probe a different state of the catalyst. Therefore, multiple spectra of methods with short acquisition times (Vis-Raman: 30 min, UV-Vis: 5 min) were recorded, to obtain time-dependent insight into the catalyst behaviour, while methods requiring longer acquisition times (UV-Raman: 120 min) were applied in a more integral manner. To further clarify this point Figure S4 gives an temporal overview of the time of measurement of operando UV-Raman, Vis-Raman, and UV-Vis spectra in comparison to the molar product distributions for P25 and P25+1.2 V/nm².

Starting with UV-Raman spectroscopy, Figure 3 shows spectra of bare P25 and P25+1.2 V/nm² recorded at 385 nm excitation, as well as the results of a quantitative analysis of the observed spectral changes. The UV-Raman spectra for the other vanadia-loaded P25 samples and the ALD-based samples are given in the SI (see Figures S5 and S6).
.
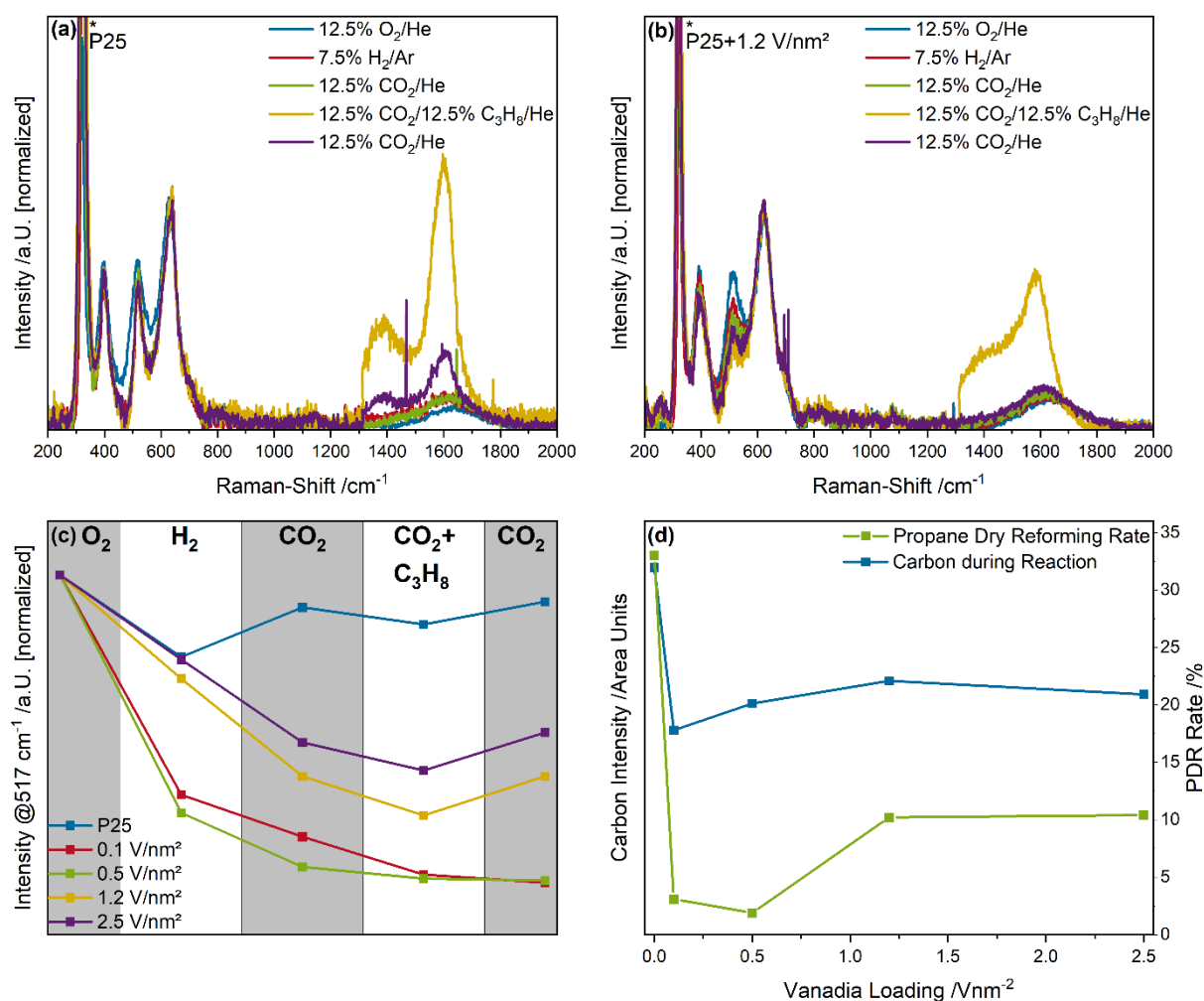
Figure 3: Operando UV-Raman spectra at 385 nm excitation of **(a)** P25 and **(b)** 1.2 V/nm² recorded at 550 °C in different gas feeds (see experimental section). Spectra were normalized to the E_g phonon of anatase at 630 cm^{-1}. The signal marked with an asterisk is caused by the CaF_2 spectroscopic window. The anatase phonon intensity **(c)** and the amount of amorphous carbon detected during reaction conditions **(d)** were quantified and compared to the PDR rate.

Figure 3a shows the UV-Raman spectra of bare P25 at 550 °C for different gas feeds. During the three pre-treatment gas feeds, that is O_2/He, H_2/Ar, and CO_2/He, the most significant spectral changes are detected for the B_{1g} and A_{1g} phonons of anatase at 398 and 517 cm^{-1}, respectively,[46] which decrease in intensity in the hydrogen phase and stay constant afterwards. When propane is introduced, a significant amount of carbon appears on the catalyst surface, which cannot be fully removed in the 2 h regenerative CO_2 treatment after the reaction, indicating a slow oxidation of carbon by CO_2. The P25+1.2 V/nm² sample shows a more pronounced decrease in its anatase phonon intensity, especially the A_{1g} phonon. Additionally, the formation of carbon is observed during reaction conditions, which however is fully regenerated by the CO_2

19

phase after reaction. The overall amount of deposited carbon during the reaction is smaller than for bare titania, indicating a higher rate of oxidation, which correlates with the increased conversion. The P25 samples loaded with 0.1, 0.5, and 2.5 V/nm² (see Figure S5) show similar structural dynamics to different extents, which is quantified in Figures 3c and d. Notably, no vanadia signals are observed in the UV-Raman spectra, indicating that the high temperature and absorbance of titania inhibits their detection.

The phonon band at 517 cm^{-1} was used as an indicator for the surface reduction of the samples. Its selective decrease at 517 cm^{-1} was observed previously observed and is caused by two factors.[47,48] The first factor is the integration of vanadia into the titania lattice as detected during the phase transition from anatase to rutile introducing a doped metal atome that distorts the lattice of titania.[49] The second is, the unilateral disturbance in the local order of the lattice, resulting from a reduction of the lattice with an oxygen gradient towards the surface.[48] However, no phonons of rutile were observed since their intensity is smaller than those of anatase and the temperature at which the experiments were performed leads to a lower signal to noise ratio.[46] Furthermore, due to the different absorption behavior, anatase absorbs stronger in the UV region, which leads to different resonance enhancements for anatase and rutile. Due to the strong absorption of titania at 385 nm, a quantification of the anatase phase is only possible at the catalyst surface, while the subsurface and bulk will be discussed later.[50–52] The phonon intensity of all samples decreases significantly upon reduction of the material via reaction of lattice oxygen with hydrogen to water, which is released from the catalyst surface into the gas phase. The surface of bare P25 is least reduced, while the samples with loading densities of 0.1 and 0.5 V/nm² become much more reduced, leading to an almost complete disappearance of the anatase phonon at 517 cm^{-1}. With increasing vanadium loading, the degree of reduction decreases again. This indicates that vanadia increases the surface reduction at low loadings while increasing the conversion, whereas at higher loadings the reduction might shift from the titania to the vanadia species present at that loading, thus reducing the titania surface to a smaller extent.

Figure 3d shows the integrated carbon signal during reaction as a function of vanadium loading and its comparison with the observed PDR rate (percentage of CO formed from C_3H_8), indicating that the carbon formation is not necessarily a function of the oxygen mobility in the sample but rather of the PDR activity, which is high in P25, decreases at low vanadia loadings, and increases again at higher loadings. However,

a combination of both mechanisms seems most likely, as the samples loaded with 0.1 and 0.5 V/nm² show no PDR and still form a significant amount of carbon on the surface. Therefore, the reduction of the catalyst might lead to an increased amount of carbon in addition to a high level of PDR. The vanadia-loaded samples show less carbon deposition, which can only be explained by a higher rate of surface reduction, while the subsurface/bulk might be less reduced due to increased surface regeneratio using CO_2, facilitated by vanadia.

Notably, for the P25+2.5 V/nm² sample (see Figure S5), the V-O-V and V=O peaks are visible during the initial oxidative phase, but disappear for the other gas feeds, only regenerating slightly at 920 cm^{-1} for the regenerative CO_2 phase, indicating V-O-V participation.[53] The peak at 860 cm^{-1}, representing the V-O-Ti signal is also present (as for the P25+1.2 V/nm² sample), but does not change upon switching between the different gas feeds.[54] Therefore, the results indicate that similar vanadia species as during the propane ODH using O_2 are participating in the reaction.[28] A detailed analysis of the vanadyl region will be performed on the basis of DRIFTS data (see below).

The UV-Raman spectra of the ALD-based samples (see Figure S6) also shows carbon formation on the surface but no structural changes of the titania phonons. The vanadyl peak is clearly visible for the SBA15-T+1.2 V/nm² sample during initial oxidative conditions, as well as under CO_2 exposure, indicating vanadyl reduction and reoxidation.

To further understand the reduction of titania, the anatase E_g shift was determined from Vis-Raman spectra (see Figures S7 and S8) as an indicator of titania subsurface reduction.[55,56] The results are shown in Figure 4. The Vis-Raman spectra of the ALD-based samples are given in Figure S9.
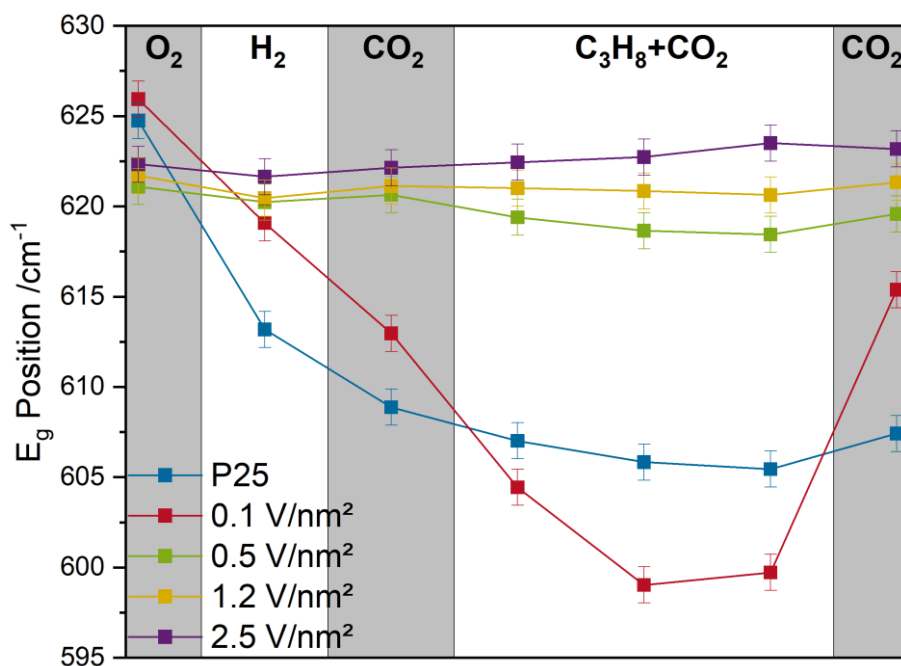
Figure 4: Position of the anatase E_g phonon determined from operando Vis-Raman spectra (at 514 nm excitation) recorded during exposure to 12.5% O_2/He, 7.5% H_2/Ar, 12.5% CO_2/He, 12.5% CO_2/12.5% C_3H_8, and 12.5% CO_2/He. The spectra are given in the SI (see Figures S7 and S8).

The E_g position of bare P25 strongly red-shifts when switching from the 12.5% O_2/He to the 7.5% H_2/Ar feeds, only red-shifting slightly further in the following CO_2-containing feeds, while it blue-shifts again in the last regenerative 12.5% CO_2/He phase. In comparison, the P25+0.1 V/nm² sample red-shifts less in its intensity in the first three pre-treatment phases, but red-shifts even stronger under reaction conditions, indicating strong sub-surface reduction of titania. It is then regenerated more significantly than for bare P25 in the last CO_2/He phase, indicating a stronger activation of CO_2 on the vanadia-loaded catalyst, which is likely caused by the short vanadia species present on the sample.[28] At vanadia loadings higher than 0.1 V/nm², no shift of the E_g position is observed. In agreement with the UV-Raman results, the P25 and 0.1 V/nm² sample show a similar behavior, pointing to a reduction of the surface and subsurface, while the P25+0.5 V/nm² sample shows the strongest surface reduction, but exhibits no subsurface reduction. For the 1.2 and 2.5 V/nm² samples no subsurface reduction is detected, while the surface reduction is less pronounced than that for the 0.5 V/nm² sample. This indicates that part of the redox cycle shifts from titania to surface-located vanadia and/or that CO_2 is much more easily activated over the

VOₓ/TiO₂ samples, which increases the rate of regeneration of titania by gas phase CO_2, necessitating less oxygen diffusion within the support.

To obtain a more integral picture of the titania reduction, as well as potential phase-transformation of titania to the rutile phase, which is difficult to observe in the Raman spectra, quasi in situ XRD of P25 and the 1.2 V/nm² sample were recorded (see Figure 5).
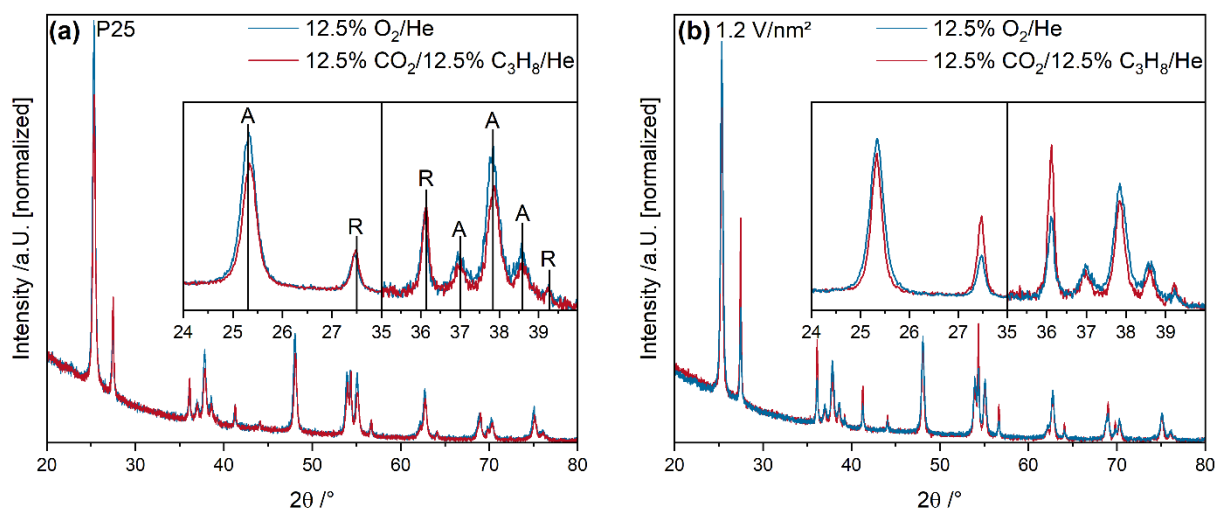
Figure 5: Quasi in-situ XRD patterns for **(a)** P25 and vanadia-loaded P25 with a loading density of **(b)** 1.2 V/nm² between 20 and 80° 2θ recorded after treatment in 12.5% O_2/He and the gas sequence up to 12.5% CO_2/12.5% C_3H_8/He at 550 °C, followed by rapid cooling to room temperature in He. The diffraction patterns were normalized and the inset shows selected regions in an enlarged view to highlight the relative intensity changes, where the detected reflexes are assigned to the anatase and rutile phases of TiO_2.

Figure 5a shows the quasi in situ XRD patterns of bare P25 recorded after pre-treatments in 12.5% O_2/He, and the gas sequence up to 12.5% CO_2/12.5% C_3H_8/He at 550 °C, followed by rapid cooling and inert transfer into the XRD sample holder. It can be seen that the amount of rutile in bare P25 stays unchanged, while the amount of anatase significantly decreases, which is in agreement with the Raman spectra and which indicates that bare titania reduces down to the bulk to regenerate the surface for the reaction.[57] This continuously reduces the titania to a point where the reaction slows down due to a depletion of available surface oxygen sites, which is reflected in the decreasing propane conversion (see Figure 2).

In comparison, Figure 5b shows the quasi in situ XRD patterns of the 1.2 V/nm² sample after the same pre-treatments as for bare P25. It shows a small decrease in the anatase intensity, while the rutile intensity simultaneously increases. This indicates that anatase is not reduced as in case of bare titania, but instead a phase transition towards a higher rutile content occurs. This was not observed during Raman spectroscopy, due to the small rutile intensity. This phase transition to rutile likely occurs since rutile activates CO_2 more easily than the anatase phase, as shown previously, to omit the bulk reduction and facilitate catalyst reoxidation.[58,59] This is catalyzed by the presence of vanadia, which can also be encapsulated in the titania during that transformation when it is present as V^{4+}, which is likely during the strongly reducing reaction conditions at 550 °C.[49] The fact that P25 does not show an increase in rutile during reaction might be caused by the lack of surface vanadia species catalysing this transformation. The transformation in the presence of V^{4+} species also correlates well with the increased conversions and the less pronounced reduction of titania, as rutile might regenerate the catalyst more quickly due to its easier CO_2 activation in addition to the surface vanadia species which might be able to participate in the redox cycle, increasing the overall amount of surface oxygen sites present for the reaction. On the other hand, the increased presence of rutile might also be responsible for the higher contribution of PDR occurring at higher loadings, which will be discussed in more detail in the DRIFTS section.

To obtain an integral picture of the reduction of all samples, including the reduction of vanadia, operando UV-Vis spectra were recorded and the structural changes observed were quantified. To gain insight into the temporal evolution of the catalysts, three spectra were recorded during the reaction and during the last regenerative phase. The results for P25 and the 1.2 V/nm² sample are depicted in Figure 6, whereas the UV-Vis spectra of the remaining samples are given in Figure S10 and those of the ALD-based samples are given in Figure S11.
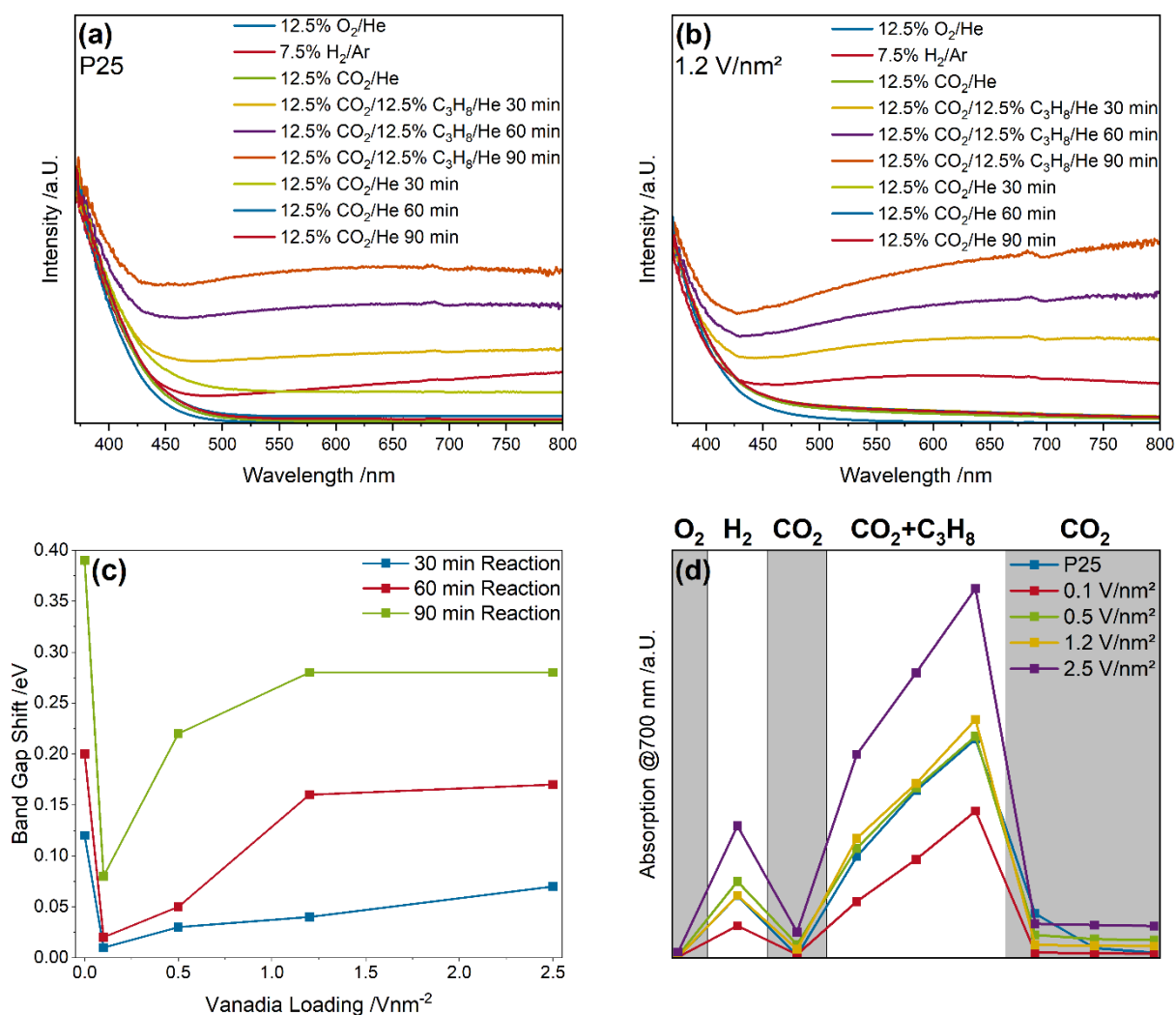
Figure 6: Operando UV-Vis spectra between 375 and 800 nm for **(a)** P25 and vanadia-loaded P25 with a loading density of **(b)** 1.2 V/nm² recorded at 550 °C in different gas feeds (see experimental section). Based on the UV-Vis spectra, the band gap energy shift **(c)** and the absorption at 700 nm (indicative of the degree of reduction) **(d)** were quantified. The spectra of the other P25-based samples are given in the SI (see Figure S10).

Figure 6a shows the operando UV-Vis spectra of bare P25. Two spectral changes can be observed, a shift in the band gap energy and an increase in the absorption between 500 and 800 nm. The red-shift in the band gap energy is associated with the reduction of titania and the subsequent creation of states within the band gap, lowering its energy,[60] while the increase in absorption between 500 and 800 nm originates from charge transfer between reduced and oxidized states of titania (Ti^{3+} to Ti^{4+}).[61,62] The observed red-shift in the band gap and the absorption increase between 500-800 nm correlate well with the reducibility of the corresponding gas phase. In comparison, the 1.2 V/nm² sample, shows the same kind of spectral changes, but with the vanadia

causing an additional contribution in the region between 500 and 800 nm, due to the possibility of vanadia d-d transitions.[63]

Figures 6c and 6d summarize the results of the quantifications of the band gap shifts and the absorption increase between 500 and 800 nm for all samples. Starting with the band gap energies for the P25 sample a continuous red-shift of the band gap energy between 30 and 90 minutes is observed, with a shift of 0.4 eV in total, indicating a strong reduction of titania that cannot be explained by a phase transition that increases the amount of rutile, as bare P25 only reduces the anatase phase (see Figure 5). In comparison, the samples loaded with 0.1 and 0.5 V/nm² show almost no red-shift during the first 60 minutes, which however significantly increases after 90 minutes, indicating the much slower reduction of titania, in good agreement with the results from UV- and Vis-Raman spectroscopy. The phase transition from anatase to rutile, catalyzed by V^{4+}, might red-shift the band gap energy, as rutile has a lower band gap energy than anatase.[64,65] This seems to be especially true for the 0.5, 1.2, and 2.5 V/nm² samples, showing a significant shift in their band gap energy, despite their lack of subsurface reduction, which is likely caused by the larger transformation of anatase to rutile, as more vanadia is present on the catalyst to catqalyze the transformation.

The above findings are confirmed by the quantification of the absorption between 500 and 800 nm (see Figure 6d). During reaction conditions, P25 shows a continuously increasing absorption indicative of titania reduction due to $Ti^{3+} \rightarrow Ti^{4+}$ transitions, in agreement with the band gap energy shift and previous results. The introduction of small amounts of vanadium (0.1 V/nm²) leads to a smaller increase in absorption, that indicates significantly less titania reduction, particularly when considering the contribution of vanadia d-d transitions. This behavior is in agreement with the band gap energy shift and shows that this sample is not as strongly reduced as bare titania, as a result of increased regeneration via CO_2. At higher loadings (0.5 and 1.2 V/nm²) the absorption behavior resembles that of bare P25, likely caused by the increased amount of vanadia participating in d-d transitions. The latter contribution further increases for the 2.5 V/nm² sample. Overall, the intensity of d-d transitions correlates well with the observed conversions, indicating the participation of vanadia in the reaction mechanism.

To obtain a more detailed understanding of surface adsorbates and the contribution of different vanadia species, quasi in situ DRIFTS was performed, following the procedure as in case of the XRD measurements (see Figure 5). Figure

7a depicts the DRIFT spectra of P25+1.2 V/nm², while Figure 7b shows the difference spectra for all five samples. Figures 7c and d summarize the quantification results of the V=O and Ti-OH regions, respectively. The DRIFT spectra of the remaining P25-based samples and the ALD-based samples are given in the Si (see Figures S12 and S13).
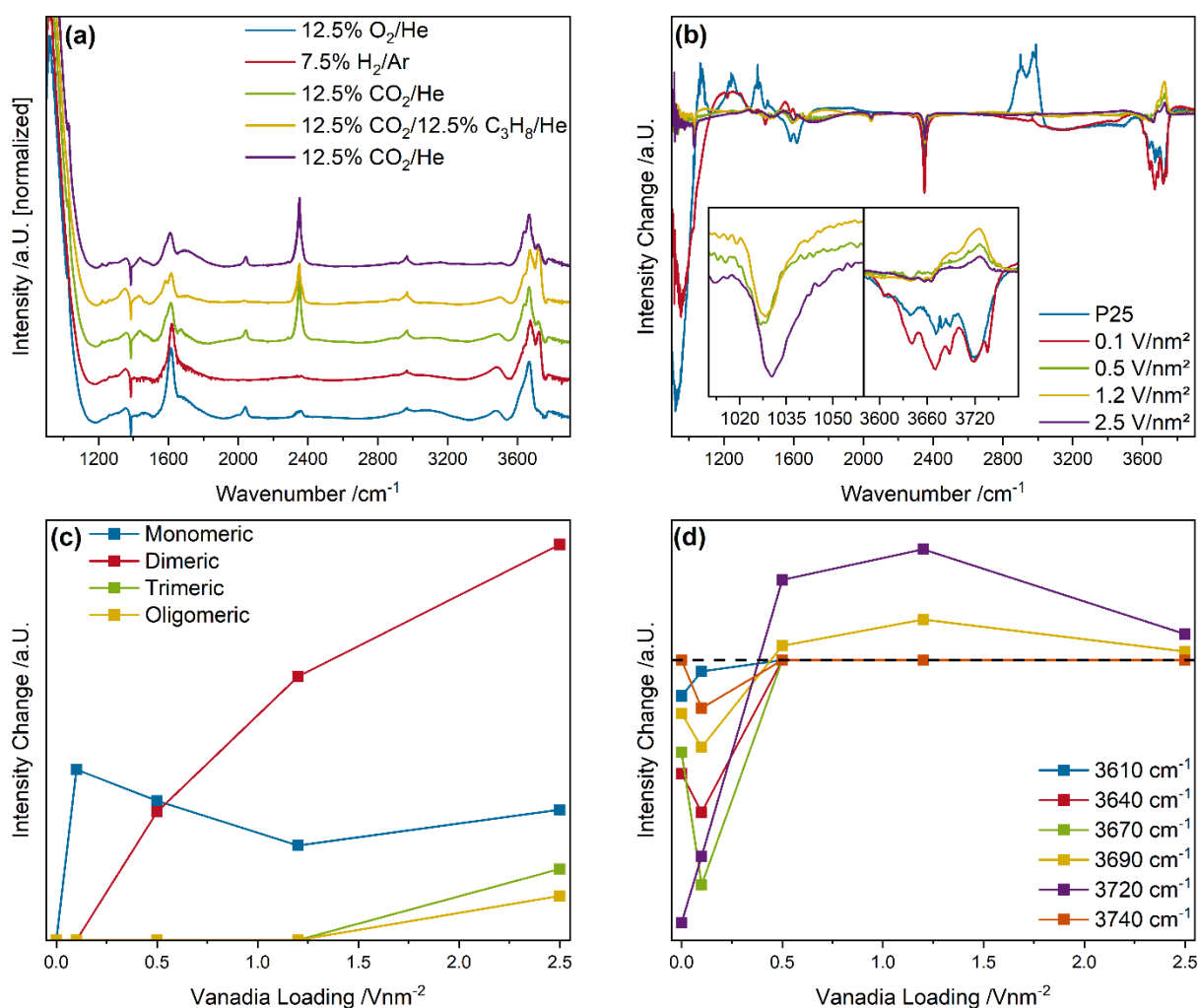
Figure 7: (a) Quasi in-situ DRIFT spectra of the 1.2 V/nm² sample recorded after treatment in different gas feeds (see experimental section) at 550 °C and subsequent rapid cooling to room temperature in He. The spectra were normalized and offset for clarity. **(b)** Difference between the spectra recorded in 12.5% CO_2/12.5% C_3H_8/He and 12.5% CO_2/He for P25 and vanadia-loaded samples. The insets highlight the intensity changes in the V=O region (0.5, 1.2, and 2.5 V/nm²) and in the Ti-OH region (all samples). The horizontal dashed line indicates no change in intensity. Loading-dependent quantification of **(c)** the intensities of different nuclearities in the V=O region and **(d)** the different contributions to the Ti-OH region. The quasi in-situ DRIFT spectra of the other P25-based samples are given in the SI (see Figure S12).

As shown in Figure 7a, in the DRIFT spectra of the 1.2 V/nm² sample differences in the V=O and Ti-OH region can be recognized, that are clearly visible in the difference spectra between oxidative (12.5% O_2/He) and reactive (12.5% CO_2/12.5% C_3H_8/He) conditions (see Figure 7b). Here, in agreement with the previous spectroscopic data on the TiO_2 reducibility, the P25 and P25+0.1 V/nm² samples show a strong intensity decrease in the feature at ~925 cm^{-1}, originating from the Ti-O vibration of Ti-OH species, which indicates strong surface reduction compared to oxidative conditions. The samples with higher vanadia loadings do not show these differences, but rather a pronounced decrease in the vanadyl region (see left inset). In the carbonate region almost no changes are observed, indicative of the absence of surface adsorbates (based on DRIFTS), while different Ti-OH species participate in the reaction for all samples (see right inset). The intensity changes in the vanadyl and Ti-OH region are summarized in Figure 7c and d, respectively.

Starting with the vanadyl contributions in Figure 7c, the 0.1 V/nm² sample shows only one highly symmetric contribution that was previously attributed to a monomeric species.[28] For the samples loaded with 0.5 and 1.2 V/nm², an asymmetric vanadyl feature with an additional contribution at higher wavenumbers is observed, which was previously assigned to dimeric species.[28,66–68] For the P25+2.5 V/nm² sample, additional peaks at higher wavenumbers are observed that can be attributed to trimeric and oligomeric species, which is in agreement with the increased vanadia d-d absorption (see Figure 6).[28,66–68] The contribution of monomers drops with increasing vanadium loading in favor of a significantly increased contribution of dimers, while all species show an increased contribution for the highest loading. As the quantification is performed on the basis of difference spectra, it is assumed that all of these species are either reduced or participating in the reaction mechanism leading to the ODH or PDR reaction. The participation of monomeric vanadia can be observed both in the increase in CO_2 and propane conversion (see Figure 2). Furthermore, it reduces the deep reduction of titania (see Figure 6) compared to P25, while still being heavily reduced to the low amount of VO_x. In comparison, no deep reduction of titania is observed for the 0.5 V/nm² sample, higher vanadium loading. However, at even higher loadings, an increasing amount of dimeric and oligomeric species is present on the catalyst surface. For these loadings, the PDR rate increases again, which seems to indicate that dimeric and oligomeric species are more active in the PDR rate, even

though the reduction of titania is even further reduced. For the 2.5 V/nm² sample, this is likely caused by the presence of highly reducible linear V-O-V bonds of oligomeric vanadia,[28,67,68] that may be prone to the PDR reaction but also further increase the amount of converted propane and CO_2 compared to the 1.2 V/nm² sample, despite the similar PDR rate. These highly reducible vanadia bonds might also be responsible for the initial jumps in the CO_2 and C_3H_8 conversions as well as the PDR rate (see Figure 2), which in the course of the reaction decrease towards a lower level, indicating that these bonds might not be regenerated after the initial reaction. In total, the sum of monomeric and dimeric species correlates well with the observed increase in conversion (see Figure 2), indicating their participation in propane conversion.

Figure 7d summarizes the loading-dependent quantification of the Ti-OH related intensity changes. Bare P25 and the P25+0.1 V/nm² sample show a strong decrease in the intensity of all Ti-OH signals present, as the surface of the catalyst is heavily reduced and most Ti-OH bonds are consumed during reactive conditions. This is emphasized by the DRIFT spectra for the reactive and last regenerative gas phase (see Figure S12). Therefore, the decrease in Ti-OH species for these samples is not related to the reaction mechanism, but rather to catalyst deactivation. In comparison, the samples with higher vanadium loadings show an increase in the intensity of Ti-OH species located at 3690 and 3720 cm^{-1}, which are assigned to bridged and isolated Ti-OH species, respectively.[69–72] Bridged Ti-OH species have previously been associated with hydrogen storage during ODH reaction, thus acting as observer species, while isolated Ti-OH species were reported to be actively involved in the hydrogen transfer from propane to the catalyst.[28] Notably, no intensity change at the position associated with V-OH species is detected, indicating either a very fast or no involvement in the reaction mechanism. The intensity changes of both Ti-OH correlate with the conversion for the 0.5 and 1.2 V/nm² samples. However, for the 2.5 V/nm² sample, only smaller changes are observed, which might be explained by the presence of different vanadia nuclearities, that is oligomers, changing the reaction mechanism and increasing the PDR rate.

Finally, to further elucidate the main route of deactivation for the catalysts, a long-term catalytic experiment during reaction conditions with different CO_2 concentrations was performed (see Figure 8). This was motivated by the fact that the samples with higher vanadium loadings, which are not being as heavily reduced as bare P25, still show a decrease in propane conversion while staying constant in their

CO_2 consumption, indicating that they might be reduced very slowly. For these experiments, the 0.5 V/nm^2 sample was chosen, as it shows less reduction than the lower loadings without the PDR influence of the higher loadings. The results are normalized to the initial propane conversion to emphasize the decrease observed over time (see Figure 8).
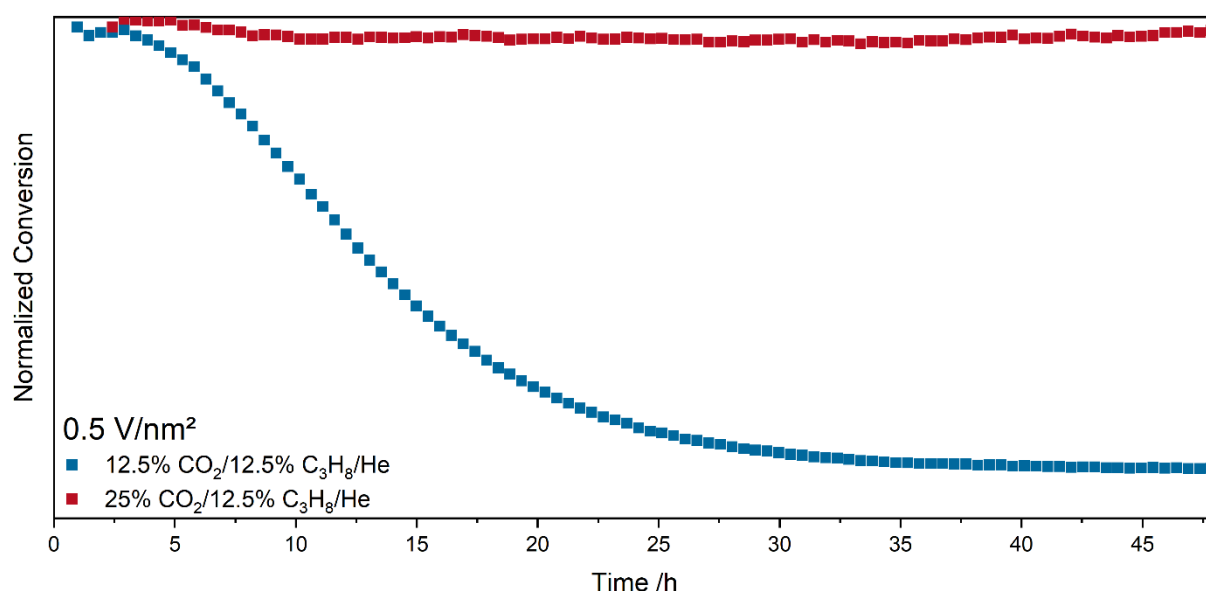
Figure 8: Long-term analysis of the propane conversion of the 0.5 V/nm^2 sample with CO_2/C_3H_8 gas-phase ratios of 1:1 (blue) and 2:1 (red) at 550 °C. The initial conversions were normalized for better comparability.

For a 1:1 ratio of CO_2/C_3H_8, the conversion ratio stays constant for the first 3 h before decreasing continuously to 10% of the initial conversion. In contrast, when increeasing the CO_2/C_3H_8 ratio to 2:1, the conversion stays constant over the full duration of the run (48 h). This behavior indicates that, first, catalyst deactivation also occurs for the higher loadings but at a lower rate, which is outside the range of our spectroscopic experiments, and second, that an increase in CO_2 conversion can stop the catalyst deactivation. Three main deactivation routes were observed in our spectroscopic experiments, that is, carbon deposition on the surface, deep reduction of the catalyst, and V^{4+} integration into titania. The first two might be impeded by the increased amount of CO_2 due to either an increased rate of regeneration or increased reaction of deposited carbon with CO_2 towards CO. The integration of vanadia into titania seems to be an important path, at least for the 1.2 and 2.5 V/nm^2 samples, since the decrease in propane conversion accelerates towards these loadings and might be caused by CO_2 being unable to reoxidize V^{4+} states, which can then only migrate into the titania

lattice.[27] However, the conversion behavior might also be caused by the reduction of different vanadia speices as discussed above (see Figure 7). In addition, bare titania and the samples loaded with 0.1 and 0.5 V/nm² also show a decrease in propane conversion where the most likely deactivation mechanism occurs to be the deep reduction of the catalyst, since the ALD-based samples show no dynamics in the titania phonons or their band gap (see Figures S6, S9, and S11) and had a constant conversion during the catalytic test. However, these samples show significant amounts of carbon during reaction conditions (see Figure S6), which may indicate that carbon deposition is a less important deactivation mechanism. In addition, due to the different titania structure, titania does not seem to transform from anatase to rutile and to incorporate vanadia, as vanadyl dynamics can be observed for these samples (see Figure S6). Overall, the deactivation due to deep reduction seems to be the main deactivation route for the studied VO_x/TiO_2 catalysts, which can be impeded by an increase in the gas concentration of CO_2 leading to an increased rate of regeneration.

Mechanistic Discussion

The reaction mechanism of the CO_2-assisted propane ODH over VO_x/TiO_2 can be categorized according to the vanadium loading, that is, behavior at (near)zero loading (0 and 0.1 V/nm²), at medium loadings (0.5 and 1.2 V/nm²), and at high loading (2.5 V/nm²). As first step, hydrogen transfer is proposed to precede from propane to the titania surface for all samples (see Figure 7), followed byformation of water and an oxygen vacancy in the titania lattice. This is regenerated by oxygen diffusion from the subsurface/bulk for the bare P25 and 0.1 V/nm² samples, leading to a deep reduction of the catalyst, which especially favors the PDR reaction as already observed for the bare support of the VO_x/In_2O_3 system. No adsorbed intermediates are observed for any of the samples, indicating that the reaction occurs with a very high selectivity towards propylene. The deep reduction of titania seems to be the main deactivation mechanism due to a reduced rate of regeneration (see Figure 8). Since there is no selectivity difference between the samples expect for the observed PDR rate, only the identified structures responsible for the ODH rate are discussed.

The vanadia-loaded samples are proposed to undergo a similar hydrogen transfer but are heavily reduced themselves (see Figures 3, 6, and 7), indicating their participation in the reaction mechanism by delivering oxygen to drive the reaction. In

addition, the rate of surface reoxidation by gas-phase activation of CO_2 is significantly increased due to the presence of vanadia, which is confirmed by the increased CO_2 conversion with increasing vanadium loading, despite the reduced PDR rate (see Figure 2). This is further supported by the conversion behavior, which increases linearly with the vanadium loading, emphasizing its importance for the conversion. The presence of vanadia may facilitate the CO_2 activation in two ways: First, the reduced vanadyl peak can activate CO_2 itself, regenerating the catalyst, and second, vanadia reduced to oxidation state V^{4+}, can catalyze the transformation of anatase into rutile (see Figure 5), which is much more active towards CO_2 and might thereby regenerate titania much faster. This is emphasized by the point that the titania reduction decreases with increasing vanadium loading. In fact, for the 2.5 V/nm^2 sample, even the surface of the catalyst is barely reduced. The integration of V^{4+} into the lattice is further supported by the fact, that for the samples with a notable formation of rutile during reaction conditions, no vanadia-related signals are observed (see Figure 3), while for the ALD-based samples, the structural dynamics of the vanadyl peak is clearly visible but no dynamics in the titania lattice due to the highly amorphous nature of the film, is observed.

Regarding the nuclearity dependence of the reactivity behavior, the increase in conversion correlates well with the sum of monomeric and dimeric vanadia species (see Figure 7), as previously observed for the reaction with O_2, indicating its importance as the oxygen site for the reaction. Therefore, a transfer of hydrogen from the titania lattice to vanadia is likely, followed by its integration into the lattice or a fast reduction to water due to the elevated temperatures. This is indicated by the clear reduction of vanadia (see Figures 6 and 7) while no V-OH species are present (see Figure 7d). The higher nuclearities, especially the linear V-O-V bonds of oligomeric vanadia species seem to favor the PDR significantly and react quickly at the beginning of the reaction (see Figures 2 and 7). The sample with 0.5 V/nm^2 shows almost no PDR, while showing a selectivity of close to 100% with a very small contribution from cracking. This sample contains no vanadia species with higher nuclearity and is not deeply reduced, with the ability to form rutile during the reaction. These properties seem to be most important for pushing the selectivity towards the ODH reaction.

4. Conclusion

In this study, we addressed the CO_2-assisted ODH of propane over VO_x/TiO_2 catalysts and elucidated important structural features relevant to the catalytic performance and the catalyst deactivation, by using multiple operando and quasi in situ methods. To unravel the role of the catalyst properties, we varied the vanadium loadings (0-2.5 V/nm^2) and used two different types of titania support material, that is bulk P25 and ALD-prepared thin film titania on silica.

The catalytic performance of the catalysts depends strongly on the vanadium loading. Bare P25 shows a lower conversion, with a contribution of significant amounts of PDR. With increasing in vanadium loading, there is an increase in the conversion of propane and CO_2, but over time, the propane conversion decreases, while the CO_2 conversion stays constant. The PDR rate decreases to zero for the 0.1 and 0.5 V/nm^2 samples, but increases again for the samples loaded with 1.2 and 2.5 V/nm^2, while staying significantly lower than that of bare P25. Besides dehydrogenation and PDR, no significant side reactions were observed, except for some cracking, which is mostly caused by the reactor.

As a result of the mechanistic analysis, three main reaction paths were identified. Titania lattice oxygen is an important oxygen site for the reaction, which is heavily reduced in bare P25 during reaction conditions, leading to a deep reduction of titania. As a result, the catalyst gradually deactivates, leading to a significant increase in PDR as the main side reaction. The introduction of vanadia leads to a better activation of CO_2, enabling faster catalyst regeneration, which may occur via two routes. First, hydrogen can be transferred from the titania lattice to vanadia, where it forms water and reduces the vanadia species, leaving an oxygen vacancy. Since vanadium activates CO_2 better than titania, it can be regenerated more easily by gas phase CO_2, which impedes titania deep reduction and increases the overall reaction rate, while also decreasing the PDR route. Second, one hydrogen can be abstracted from titania to vanadia, reducing it to V^{4+}, which can then catalyze the anatase to rutile transformation, whereby the vanadium is integrated into the titania bulk. The higher activation rate of CO_2 over rutile compared to anatase enables the titania to be less reduced and to achieve a higher oxidation rate.

The nuclearity-dependence of the reaction shows that both monomeric and dimeric species increase the reaction rate and decrease the PDR route, while being actively reduced. However, higher nuclearities (e.g. oligomers in the sample loaded

with 2.5 V/nm²) exhibit highly reducible oxygen atoms, that increase the contribution of the PDR route. Therefore, a selectivity maximum for the ODH route and therefore for propylene is achieved at a medium vanadium loading between 0.1 and 1.2 V/nm², where almost 100 % propylene selectivity is achieved.

The main deactivation route is the catalysts deep reduction, which depletes the active oxygen sites, leading to a continuous decrease in propane conversion, while the CO_2 conversion stays constant. Further deactivation mechanisms include the depletion of vanadia surface species, as they become integrated into the newly formed rutile phase as well as the formation of carbon. However, the ALD-based samples exhibit strong carbon deposition, while no strong titania lattice reduction is observed and the conversion stays constant, indicating carbon deposition to be of lower importance. The deactivation of the catalyst can be avoided by increasing the CO_2 gas phase concentration.

Our results highlight the potential of combining multiple operando and quasi in situ approaches to investigate the reaction mechanism of CO_2 activation during propane ODH, which is a highly relevant reaction with the potential of technical application. The VO_x/TiO_2 catalysts showed a highly promising performance that is more selective than that of most other oxide-based systems and comparable to CrO_x catalysts. For the first time, the reaction mechanism including the complex interplay between surface vanadia and multi-phase TiO_2 was elucidated. With this knowledge the catalyst performance can be improved. Our approach is readily transferable to other systems that are still missing from the literature, e.g. VO_x/CeO_2, to understand the important support contribution to the performance of vanadia-based catalysts in CO_2 activation.

Declaration of Competing Interest

The authors declare that they have no known competing financial interests or personal relationships that could have appeared to influence the work reported in this paper.

Supporting Information

The supporting information contains additional information about the reactivity behavior and additional results from operando spectroscopic analysis.

Acknowledgements

References

(1) Amghizar, I.; Vandewalle, L. A.; van Geem, K. M.; Marin, G. B. New Trends in Olefin Production. *Engineering* **2017**, *3* (2), 171–178. DOI: 10.1016/j.eng.2017.02.006.

(2) Cavani, F.; Ballarini, N.; Cericola, A. Oxidative dehydrogenation of ethane and propane: How far from commercial implementation? *Catal. Today* **2007**, *127* (1-4), 113–131. DOI: 10.1016/j.cattod.2007.05.009.

(3) Lavrenov, A. V.; Saifulina, L. F.; Buluchevskii, E. A.; Bogdanets, E. N. Propylene production technology: Today and tomorrow. *Catal. Ind.* **2015**, *7* (3), 175–187. DOI: 10.1134/S2070050415030083.

(4) Phung, T. K.; Le Pham, T. M.; Vu, K. B.; Busca, G. (Bio)Propylene production processes: A critical review. *J. Environ. Chem. Eng.* **2021**, *9* (4), 105673. DOI: 10.1016/j.jece.2021.105673.

(5) Carrero, C. A.; Schloegl, R.; Wachs, I. E.; Schomaecker, R. Critical Literature Review of the Kinetics for the Oxidative Dehydrogenation of Propane over Well-Defined Supported Vanadium Oxide Catalysts. *ACS Catal.* **2014**, *4* (10), 3357–3380. DOI: 10.1021/cs5003417.

(6) Carter, J. H.; Bere, T.; Pitchers, J. R.; Hewes, D. G.; Vandegehuchte, B. D.; Kiely, C. J.; Taylor, S. H.; Hutchings, G. J. Direct and oxidative dehydrogenation of propane: from catalyst design to industrial application. *Green Chem.* **2021**, *23* (24), 9747–9799. DOI: 10.1039/D1GC03700E.

(7) Baek, J.; Yun, H. J.; Yun, D.; Choi, Y.; Yi, J. Preparation of Highly Dispersed Chromium Oxide Catalysts Supported on Mesoporous Silica for the Oxidative Dehydrogenation of Propane Using CO_2 : Insight into the Nature of Catalytically Active Chromium Sites. *ACS Catal.* **2012**, *2* (9), 1893–1903. DOI: 10.1021/cs300198u.

(8) Kätelhön, A.; Meys, R.; Deutz, S.; Suh, S.; Bardow, A. Climate change mitigation potential of carbon capture and utilization in the chemical industry. *Proc. Natl. Acad. Sci. USA* **2019**, *116* (23), 11187–11194. DOI: 10.1073/pnas.1821029116. Published Online: May. 13, 2019.

(9) Baena-Moreno, F. M.; Rodríguez-Galán, M.; Vega, F.; Alonso-Fariñas, B.; Vilches Arenas, L. F.; Navarrete, B. Carbon capture and utilization technologies: a literature

review and recent advances. *Energ. Source A: Recovery, Util. Environ. Effects* **2019**, *41* (12), 1403–1433. DOI: 10.1080/15567036.2018.1548518.

(10) Al-Mamoori, A.; Krishnamurthy, A.; Rownaghi, A. A.; Rezaei, F. Carbon Capture and Utilization Update. *Energy Technol.* **2017**, *5* (6), 834–849. DOI: 10.1002/ente.201600747.

(11) Álvarez, A.; Borges, M.; Corral-Pérez, J. J.; Olcina, J. G.; Hu, L.; Cornu, D.; Huang, R.; Stoian, D.; Urakawa, A. CO2 Activation over Catalytic Surfaces. *Chem. Phys. Chem.* **2017**, *18* (22), 3135–3141. DOI: 10.1002/cphc.201700782. Published Online: Oct. 5, 2017.

(12) Jacquemin, M.; Beuls, A.; Ruiz, P. Catalytic production of methane from CO_2 and H_2 at low temperature: Insight on the reaction mechanism. *Catal. Today* **2010**, *157* (1-4), 462–466. DOI: 10.1016/j.cattod.2010.06.016.

(13) Lei, T.-q.; Cheng, Y.-h.; Miao, C.-x.; Hua, W.-m.; Yue, Y.-h.; Gao, Z. Silica-doped TiO_2 as support of gallium oxide for dehydrogenation of ethane with CO_2. *Fuel Process. Technol.* **2018**, *177*, 246–254. DOI: 10.1016/j.fuproc.2018.04.037.

(14) Atanga, M. A.; Rezaei, F.; Jawad, A.; Fitch, M.; Rownaghi, A. A. Oxidative dehydrogenation of propane to propylene with carbon dioxide. *Appl. Catal. B: Environ.* **2018**, *220*, 429–445. DOI: 10.1016/j.apcatb.2017.08.052.

(15) Gambo, Y.; Adamu, S.; Tanimu, G.; Abdullahi, I. M.; Lucky, R. A.; Ba-Shammakh, M. S.; Hossain, M. M. CO_2-mediated oxidative dehydrogenation of light alkanes to olefins: Advances and perspectives in catalyst design and process improvement. *Appl. Catal. A: Gen.* **2021**, *623*, 118273. DOI: 10.1016/j.apcata.2021.118273.

(16) Jiang, X.; Sharma, L.; Fung, V.; Park, S. J.; Jones, C. W.; Sumpter, B. G.; Baltrusaitis, J.; Wu, Z. Oxidative Dehydrogenation of Propane to Propylene with Soft Oxidants via Heterogeneous Catalysis. *ACS Catal.* **2021**, *11* (4), 2182–2234. DOI: 10.1021/acscatal.0c03999.

(17) Rigamonti, M. G.; Shah, M.; Gambu, T. G.; Saeys, M.; Dusselier, M. Reshaping the Role of CO_2 in Propane Dehydrogenation: From Waste Gas to Platform Chemical. *ACS Catal.* **2022**, *12* (15), 9339–9358. DOI: 10.1021/acscatal.2c01374.

(18) Botavina, M. A.; Martra, G.; Agafonov, Y.A.; Gaidai, N. A.; Nekrasov, N. V.; Trushin, D. V.; Coluccia, S.; Lapidus, A. L. Oxidative dehydrogenation of C3–C4

paraffins in the presence of CO_2 over CrO_x/SiO_2 catalysts. *Appl. Catal. A: Gen.* **2008**, *347* (2), 126–132. DOI: 10.1016/j.apcata.2008.05.037.

(19) Gashoul Daresibi, F.; Khodadadi, A. A.; Mortazavi, Y.; Huotari, S.; Ritala, M. Highly dispersed atomic layer deposited CrO_x on SiO_2 catalyst with enhanced yield of propylene for CO_2–mediated oxidative dehydrogenation of propane. *Mol. Catal.* **2022**, *526* (80–), 112396. DOI: 10.1016/j.mcat.2022.112396.

(20) Michorczyk, P.; Pietrzyk, P.; Ogonowski, J. Preparation and characterization of SBA-1–supported chromium oxide catalysts for CO_2 assisted dehydrogenation of propane. *Microporous Mesoporous Mater.* **2012**, *161*, 56–66. DOI: 10.1016/j.micromeso.2012.05.011.

(21) Wang, H.; Nguyen, T. D.; Tsilomelekis, G. Propane oxidative dehydrogenation using CO_2 over CrO_x/Fe–CeO_2 catalysts. *Catal. Sci. Technol.* **2023**, *13* (8), 2360–2369. DOI: 10.1039/D2CY01563C.

(22) Wang, Z.-Y.; He, Z.-H.; Li, L.-Y.; Yang, S.-Y.; He, M.-X.; Sun, Y.-C.; Wang, K.; Chen, J.-G.; Liu, Z.-T. Research progress of CO_2 oxidative dehydrogenation of propane to propylene over Cr-free metal catalysts. *Rare Met.* **2022**, *41* (7), 2129–2152. DOI: 10.1007/s12598-021-01959-y. Published Online: Mar. 11, 2022.

(23) Ascoop, I.; Galvita, V. V.; Alexopoulos, K.; Reyniers, M.-F.; van der Voort, P.; Bliznuk, V.; Marin, G. B. The role of CO_2 in the dehydrogenation of propane over WO_x–VO_x/SiO_2. *J. Catal.* **2016**, *335*, 1–10. DOI: 10.1016/j.jcat.2015.12.015.

(24) Balogun, M. L.; Adamu, S.; Ba-Shammakh, M. S.; Hossain, M. M. Promotional effects of CO_2 on the oxidative dehydrogenation of propane over mesoporous $VO_x/\gamma Al_2O_3$ catalysts. *J. Ind. Eng. Chem.* **2021**, *96* (20), 82–97. DOI: 10.1016/j.jiec.2020.12.022.

(25) Jiang, X.; Lis, B. M.; Purdy, S. C.; Paladugu, S.; Fung, V.; Quan, W.; Bao, Z.; Yang, W.; He, Y.; Sumpter, B. G.; Page, K.; Wachs, I. E.; Wu, Z. CO_2-Assisted Oxidative Dehydrogenation of Propane over VO_x/In_2O_3 Catalysts: Interplay between Redox Property and Acid–Base Interactions. *ACS Catal.* **2022**, *12* (18), 11239–11252. DOI: 10.1021/acscatal.2c02099.

(26) Jiang, X.; Lis, B. M.; Wu, Y.; Wachs, I. E.; Wu, Z. Effect of the Molecular Structure of Surface Vanadia on Activity and Regenerability of VO_x/In_2O_3 Catalysts for CO_2-

Assisted Oxidative Dehydrogenation of Propane. *J. Phys. Chem. C* **2023**, *127* (13), 6311–6320. DOI: 10.1021/acs.jpcc.3c00183.

(27) Rogg, S.; Hess, C. CO_2 as a soft oxidant for propane oxidative dehydrogenation: A mechanistic study using operando UV Raman spectroscopy. *J. CO2 Utiliz.* **2021**, *50* (9), 101604. DOI: 10.1016/j.jcou.2021.101604.

(28) Schumacher, L.; Pfeiffer, J.; Shen, J.; Gutmann, T.; Breitzke, H.; Buntkowsky, G.; Hofmann, K.; Hess, C. Collaborative Mechanistic Effects between Vanadia and Titania during the Oxidative Dehydrogenation of Propane Investigated by Operando and Transient Spectroscopies. *ACS Catal.* **2023**, 8139–8160. DOI: 10.1021/acscatal.3c01404.

(29) Balogun, M. L.; Adamu, S.; Bakare, I. A.; Ba-Shammakh, M. S.; Hossain, M. M. CO_2 Assisted Oxidative Dehydrogenation of Propane to Propylene over Fluidizable MoO_3/La_2O_3-γAl_2O_3 Catalysts. *J. CO2 Utiliz.* **2020**, *42*, 101329. DOI: 10.1016/j.jcou.2020.101329.

(30) Balogun, M. L.; Gambo, Y.; Adamu, S.; Ba-Shammakh, M. S.; Hossain, M. M. Kinetic modeling of oxidative dehydrogenation of propane with CO_2 over MoO_x/La_2O_3-Al_2O_3 in a fluidized bed. *AIChE J.* **2023**, *69* (3). DOI: 10.1002/aic.17903.

(31) Beck, B.; Harth, M.; Hamilton, N. G.; Carrero, C.; Uhlrich, J. J.; Trunschke, A.; Shaikhutdinov, S.; Schubert, H.; Freund, H.-J.; Schlögl, R.; Sauer, J.; Schomäcker, R. Partial oxidation of ethanol on vanadia catalysts on supporting oxides with different redox properties compared to propane. *J. Catal.* **2012**, *296*, 120–131. DOI: 10.1016/j.jcat.2012.09.008.

(32) Dinse, A.; Frank, B.; Hess, C.; Habel, D.; Schomäcker, R. Oxidative dehydrogenation of propane over low-loaded vanadia catalysts: Impact of the support material on kinetics and selectivity. *J. Mol. Catal. A: Chem.* **2008**, *289* (1-2), 28–37. DOI: 10.1016/j.molcata.2008.04.007.

(33) Jiang, X.; Manawan, M.; Feng, T.; Qian, R.; Zhao, T.; Zhou, G.; Kong, F.; Wang, Q.; Dai, S.; Pan, J. H. Anatase and rutile in evonik aeroxide P25: Heterojunctioned or individual nanoparticles? *Catal. Today* **2018**, *300*, 12–17. DOI: 10.1016/j.cattod.2017.06.010.

(34) Christodoulakis, A.; Machli, M.; Lemonidou, A. A.; Boghosian, S. Molecular structure and reactivity of vanadia-based catalysts for propane oxidative dehydrogenation studied by in situ Raman spectroscopy and catalytic activity measurements. *J. Catal.* **2004**, *222* (2), 293–306. DOI: 10.1016/j.jcat.2003.10.007.

(35) Spende, A.; Sobel, N.; Lukas, M.; Zierold, R.; Riedl, J. C.; Gura, L.; Schubert, I.; Moreno, J. M. M.; Nielsch, K.; Stühn, B.; Hess, C.; Trautmann, C.; Toimil-Molares, M. E. TiO_2, SiO_2, and Al_2O_3 coated nanopores and nanotubes produced by ALD in etched ion-track membranes for transport measurements. *Nanotechnol.* **2015**, *26* (33), 335301. DOI: 10.1088/0957-4484/26/33/335301. Published Online: Jul. 30, 2015.

(36) Waleska, P. S.; Hess, C. Oligomerization of Supported Vanadia: Structural Insight Using Surface-Science Models with Chemical Complexity. *J. Phys. Chem. C* **2016**, *120* (33), 18510–18519. DOI: 10.1021/acs.jpcc.6b01672.

(37) Antonov, L.; Nedeltcheva, D. Resolution of overlapping UV–Vis absorption bands and quantitative analysis. *Chem. Soc. Rev.* **2000**, *29* (3), 217–227. DOI: 10.1039/A900007K.

(38) Dolgonos, A.; Mason, T. O.; Poeppelmeier, K. R. Direct optical band gap measurement in polycrystalline semiconductors: A critical look at the Tauc method. *J. Solid State Chem.* **2016**, *240* (11), 43–48. DOI: 10.1016/j.jssc.2016.05.010.

(39) Filtschew, A.; Hofmann, K.; Hess, C. Ceria and Its Defect Structure: New Insights from a Combined Spectroscopic Approach. *J. Phys. Chem. C* **2016**, *120* (12), 6694–6703. DOI: 10.1021/acs.jpcc.6b00959.

(40) Bugrova, T. A.; Dutov, V. V.; Svetlichnyi, V. A.; Cortés Corberán, V.; Mamontov, G. V. Oxidative dehydrogenation of ethane with CO_2 over CrO_x catalysts supported on Al_2O_3, ZrO_2, CeO_2 and $Ce_xZr_{1-x}O_2$. *Catal. Today* **2019**, *333*, 71–80. DOI: 10.1016/j.cattod.2018.04.047.

(41) Buekens, A. G.; Froment, G. F. Thermal Cracking of Propane. Kinetics and Product Distributions. *Ind. Eng. Chem. Proc. Des. Dev.* **1968**, *7* (3), 435–447. DOI: 10.1021/i260027a022.

(42) Gomez, E.; Kattel, S.; Yan, B.; Yao, S.; Liu, P.; Chen, J. G. Combining CO_2 reduction with propane oxidative dehydrogenation over bimetallic catalysts. *Nat.*

Commun. **2018**, *9* (1), 1398. DOI: 10.1038/s41467-018-03793-w. Published Online: Apr. 11, 2018.

(43) Chen, L.; Allec, S. I.; Nguyen, M.-T.; Kovarik, L.; Hoffman, A. S.; Hong, J.; Meira, D.; Shi, H.; Bare, S. R.; Glezakou, V.-A.; Rousseau, R.; Szanyi, J. Dynamic Evolution of Palladium Single Atoms on Anatase Titania Support Determines the Reverse Water-Gas Shift Activity. *J. Am. Chem. Soc.* **2023**, *145* (19), 10847–10860. DOI: 10.1021/jacs.3c02326. Published Online: May. 5, 2023.

(44) Doherty, F.; Goldsmith, B. R. Rhodium Single-Atom Catalysts on Titania for Reverse Water Gas Shift Reaction Explored by First Principles Mechanistic Analysis and Compared to Nanoclusters. *ChemCatChem* **2021**, *13* (13), 3155–3164. DOI: 10.1002/cctc.202100292.

(45) Siahvashi, A.; Adesina, A. A. Hydrogen production via propane dry reforming: Carbon deposition and reaction-deactivation study. *Int. J. Hydrog. Energ.* **2018**, *43* (36), 17195–17204. DOI: 10.1016/j.ijhydene.2018.07.118.

(46) Balachandran, U.; Eror, N. G. Raman spectra of titanium dioxide. *J. Solid State Chem.* **1982**, *42* (3), 276–282. DOI: 10.1016/0022-4596(82)90006-8.

(47) Zhang, J.; Chen, X.; Shen, Y.; Li, Y.; Hu, Z.; Chu, J. Synthesis, surface morphology, and photoluminescence properties of anatase iron-doped titanium dioxide nano-crystalline films. *Phys. Chem. Chem. Phys.* **2011**, *13* (28), 13096–13105. DOI: 10.1039/c0cp02924f. Published Online: Jun. 21, 2011.

(48) Ishioka, K.; Petek, H. Raman generation of coherent phonons of anatase and rutile TiO_2 photoexcited at fundamental absorption edges. *Phys. Rev. B* **2012**, *86* (20). DOI: 10.1103/PhysRevB.86.205201.

(49) Martínez-Huerta, M. V.; Fierro, J.L.G.; Bañares, M. A. Monitoring the states of vanadium oxide during the transformation of TiO_2 anatase-to-rutile under reactive environments: H_2 reduction and oxidative dehydrogenation of ethane. *Catal. Commun.* **2009**, *11* (1), 15–19. DOI: 10.1016/j.catcom.2009.08.002.

(50) Glassford, K. M.; Chelikowsky, JR. Optical properties of titanium dioxide in the rutile structure. *Phys. Rev. B Condens. Matter* **1992**, *45* (7), 3874–3877. DOI: 10.1103/physrevb.45.3874.

(51) Daude, N.; Gout, C.; Jouanin, C. Electronic band structure of titanium dioxide. *Phys. Rev. B* **1977**, *15* (6), 3229–3235. DOI: 10.1103/PhysRevB.15.3229.

(52) Tang, H.; Berger, H.; Schmid, P. E.; Lévy, F. Optical properties of anatase (TiO_2). *Solid State Commun.* **1994**, *92* (3), 267–271. DOI: 10.1016/0038-1098(94)90889-3.

(53) Burcham, L. J. In situ IR, Raman, and UV-Vis DRS spectroscopy of supported vanadium oxide catalysts during methanol oxidation. *Top. Catal.* **2000**, *11/12* (1/4), 85–100. DOI: 10.1023/A:1027275225668.

(54) Kryukova, G. N.; Zenkovets, G. A.; Mestl, G.; Schlögl, R. Structural study of titanium doped vanadia and vanadium doped titania catalysts. *React. Kin. Catal. Lett.* **2003**, *80* (1), 161–169. DOI: 10.1023/A:1026000829726.

(55) Lejon, C.; Österlund, L. Influence of phonon confinement, surface stress, and zirconium doping on the Raman vibrational properties of anatase TiO_2 nanoparticles. *J. Raman Spectrosc.* **2011**, *42* (11), 2026–2035. DOI: 10.1002/jrs.2956.

(56) Hearne, G. R.; Zhao, J.; Dawe, A. M.; Pischedda, V.; Maaza, M.; Nieuwoudt, M. K.; Kibasomba, P.; Nemraoui, O.; Comins, J. D.; Witcomb, M. J. Effect of grain size on structural transitions in anatase TiO_2 : A Raman spectroscopy study at high pressure. *Phys. Rev. B* **2004**, *70* (13), 717. DOI: 10.1103/PhysRevB.70.134102.

(57) Tobaldi, D. M.; Pullar, R. C.; Seabra, M. P.; Labrincha, J. A. Fully quantitative X-ray characterisation of Evonik Aeroxide TiO_2 P25®. *Mater. Lett.* **2014**, *122*, 345–347. DOI: 10.1016/j.matlet.2014.02.055.

(58) Liu, L.; Zhao, H.; Andino, J. M.; Li, Y. Photocatalytic CO_2 Reduction with H_2O on TiO_2 Nanocrystals: Comparison of Anatase, Rutile, and Brookite Polymorphs and Exploration of Surface Chemistry. *ACS Catal.* **2012**, *2* (8), 1817–1828. DOI: 10.1021/cs300273q.

(59) Kovačič, Ž.; Likozar, B.; Huš, M. Electronic properties of rutile and anatase TiO_2 and their effect on CO_2 adsorption: A comparison of first principle approaches. *Fuel* **2022**, *328* (19), 125322. DOI: 10.1016/j.fuel.2022.125322.

(60) Amore Bonapasta, A.; Filippone, F.; Mattioli, G.; Alippi, P. Oxygen vacancies and OH species in rutile and anatase TiO_2 polymorphs. *Catal. Today* **2009**, *144* (1-2), 177–182. DOI: 10.1016/j.cattod.2009.01.047.

(61) Kuriechen, S. K.; Murugesan, S.; Paul Raj, S. Mineralization of Azo Dye Using Combined Photo-Fenton and Photocatalytic Processes under Visible Light. *J. Catal.* **2013**, *2013* (4), 1–6. DOI: 10.1155/2013/104019.

(62) Yang, J.; Bai, H.; Tan, X.; Lian, J. IR and XPS investigation of visible-light photocatalysis—Nitrogen–carbon-doped TiO_2 film. *Appl. Surf. Sci.* **2006**, *253* (4), 1988–1994. DOI: 10.1016/j.apsusc.2006.03.078.

(63) Lamoureux, B.; Singh, V. R.; Jovic, V.; Kuyyalil, J.; Su, T.-Y.; Smith, K. E. Structural and electronic properties of thermally evaporated V_2O_5 epitaxial thin films. *Thin Solid Films* **2016**, *615*, 409–414. DOI: 10.1016/j.tsf.2016.07.062.

(64) Choudhury, B.; Choudhury, A. Oxygen defect dependent variation of band gap, Urbach energy and luminescence property of anatase, anatase–rutile mixed phase and of rutile phases of TiO2 nanoparticles. *Phys. E* **2014**, *56*, 364–371. DOI: 10.1016/j.physe.2013.10.014.

(65) Landmann, M.; Rauls, E.; Schmidt, W. G. The electronic structure and optical response of rutile, anatase and brookite TiO_2. *J. Phys. Condens. Matter.* **2012**, *24* (19), 195503. DOI: 10.1088/0953-8984/24/19/195503. Published Online: Apr. 19, 2012.

(66) Lian, Z.; Deng, H.; Xin, S.; Shan, W.; Wang, Q.; Xu, J.; He, H. Significant promotion effect of the rutile phase on V_2O_5/TiO_2 catalysts for NH_3-SCR. *Chem. Commun.* **2021**, *57* (3), 355–358. DOI: 10.1039/d0cc05938b.

(67) Jaegers, N. R.; Lai, J.-K.; He, Y.; Walter, E.; Dixon, D. A.; Vasiliu, M.; Chen, Y.; Wang, C.; Hu, M. Y.; Mueller, K. T.; Wachs, I. E.; Wang, Y.; Hu, J. Z. Mechanism by which Tungsten Oxide Promotes the Activity of Supported V_2O_5/TiO_2 Catalysts for NO_x Abatement: Structural Effects Revealed by [51]V MAS NMR Spectroscopy. *Angew. Chem. Int. Ed.* **2019**, *58* (36), 12609–12616. DOI: 10.1002/anie.201904503. Published Online: Aug. 1, 2019.

(68) Hu, J. Z.; Xu, S.; Li, W.-Z.; Hu, M. Y.; Deng, X.; Dixon, D. A.; Vasiliu, M.; Craciun, R.; Wang, Y.; Bao, X.; Peden, C. H. F. Investigation of the Structure and Active Sites of TiO_2 Nanorod Supported VO_x Catalysts by High-Field and Fast-Spinning [51]V MAS NMR. *ACS Catal.* **2015**, *5* (7), 3945–3952. DOI: 10.1021/acscatal.5b00286.

(69) Primet, M.; Pichat, P.; Mathieu, M. V. Infrared study of the surface of titanium dioxides. I. Hydroxyl groups. *J. Phys. Chem.* **1971**, *75* (9), 1216–1220. DOI: 10.1021/j100679a007.

(70) Tanaka, K.; White, J. M. Characterization of species adsorbed on oxidized and reduced anatase. *J. Phys. Chem.* **1982**, *86* (24), 4708–4714. DOI: 10.1021/j100221a014.

(71) Hadjiivanov, K. I.; Klissurski, D. G. Surface chemistry of titania (anatase) and titania-supported catalysts. *Chem. Soc. Rev.* **1996**, *25* (1), 61. DOI: 10.1039/cs9962500061.

(72) Mathieu, M. V.; Primet, M.; Pichat, P. Infrared study of the surface of titanium dioxides. II. Acidic and basic properties. *J. Phys. Chem.* **1971**, *75* (9), 1221–1226. DOI: 10.1021/j100679a008.

4.3 Rational Design of Vanadia-Based Propane ODH Catalysts: A Multiple Operando Spectroscopic Investigation of VO$_x$/TiO$_2$/CeO$_2$

The third part of this work deals with rational design of a three-oxide VO$_x$/TiO$_x$/CeO$_2$ catalyst for propane ODH based on the obtained knowledge and previously developed methical approaches for the two oxide VO$_x$/CeO$_2$ and VO$_x$/TiO$_2$ systems.

As described in the nineth overall publication, this was achieved by coating CeO$_2$ with variable amounts of TiO$_x$ using ALD and loading the new supports with 1.2 V/nm^2. These new catalysts showed similar conversion compared to the two component systems while exhibiting significantly increased selectivities. To understand this behaviour, the catalysts' structure after synthesis was extensively characterized and operando spectroscopic investigations were used to understand their mode of operation under reaction conditions. For that, operando multi-wavelength Raman (385 and 514 nm) and UV-Vis spectroscopy, as well as XRD, XPS and DRIFTS were used. The most important characterization results indicate that titania is present as islands on the ceria surface and increases the average oxidation state of ceria with increasing titania loading. The vanadia anchors to the titania in proximity to the three oxide interface. Furthermore, a detailed mechanistic picture could be obtained. Two reaction pathways occur on the surface and employ all three oxides. This is in contrast to the two oxide systems and emphasizes the rational design aspect, where the introduction of the TiO$_x$ layer based on the mechanistic understanding of the other systems enabled the increased catalytic performance. This study emphasizes the importance of understanding reaction mechanisms over heterogeneous catalysts to enhance their properties for future applications.

Rational design of vanadia-based propane ODH catalysts: A multiple operando spectroscopic investigation of $VO_x/TiO_2/CeO_2$

Leon Schumacher, Jun Shen, Kathrin Hofmann, Christian Hess [*]

Technical University of Darmstadt, Department of Chemistry, Eduard-Zintl-Institut für Anorganische und Physikalische Chemie, Peter-Grünberg-Str. 8, 64287 Darmstadt, Germany

ABSTRACT

The understanding of reaction mechanisms of supported metal oxide catalysts has significantly increased over the last years due to new methods being applied. This increased knowledge allows to develop approaches towards catalytic materials for reactions with low selectivities by rational design, such as the oxidative dehydrogenation (ODH) of propane, which is of great technical importance. Vanadia (VO_x) supported on reducible oxides (TiO_2, CeO_2, etc.) has shown promising catalytic properties in propane ODH. In this study, we followed a rational-design approach employing atomic layer deposition (ALD) to synthesize a $VO_x/TiO_x/CeO_2$ catalyst with superior selectivity, by combining favourable properties of the individual catalysts (VO_x/TiO_2, VO_x/CeO_2). By applying multiple spectroscopies, including multi-wavelength Raman, UV-Vis, DRIFT, and XP spectroscopy as well as XRD, we were able to identify the functions of each oxide and develop a mechanistic picture. The increased selectivity is the result of distinct interactions between the oxides that slow down the oxygen dynamics in the catalyst and favour reaction pathways beneficial to propylene formation. Our findings highlight the use of rational design to develop improved catalysts based on previously established mechanistic knowledge.

1. Introduction

Propylene is an important basis chemical with a significant demand from industry, which cannot be fully met by current production methods like steam cracking and fluid catalytic cracking. Therefore, additional production methods are required [1,2]. One of the most promising reactions to close the 'propylene gap' is the oxidative dehydrogenation (ODH) of propane, which directly oxidizes propane with oxygen to propylene and water. In comparison to the established production processes like steam cracking, this reaction requires lower temperatures, shows less catalyst leaching and is exothermic, allowing for better heat integration in the plant, but is prone to overoxidation of propylene to CO_x [1–3]. Therefore, for propane ODH to be of interest to commercial applications, the reaction needs to be suitably catalysed to exhibit sufficient propylene yields.

A promising class of catalysts for propane ODH is supported vanadia (VO_x), which has been shown to be highly active with good selectivities in short alkane oxidation [4–9]. However, the properties of vanadia heavily depend on the choice of the support material, as it may actively participate in the redox cycle of the reaction or influence the nuclearity and/or geometry of the vanadia phase [4,6,10–16]. It is therefore

difficult to predict the performance of new vanadia-based catalysts due to the complex interplay between the active phase and the support. To understand these systems on a more detailed level, operando and transient spectroscopy have proven to be powerful tools for the mechanistic investigation of propane ODH over vanadia catalysts on different support materials (SiO_2, Al_2O_3, ZrO_2, TiO_2, and CeO_2) [8,9,17–19].

Focussing on reducible support materials such as TiO_2 and CeO_2, the recent application of combined operando and transient spectroscopic methods (including transient IR spectroscopy) has enabled detailed insight into the VO_x/TiO_2 and VO_x/CeO_2 systems [8,9]. Interestingly, in these studies the two support materials have shown different properties regarding their interaction with surface vanadia. For VO_x/CeO_2 catalysts, ceria lattice oxygen was identified to facilitate the oxidation reaction behind the conversion of propane, while vanadia was important for the initial hydrogen transfer, resulting in the formation of a transient V-OH group, but otherwise shows no structural dynamics. In case of VO_x/TiO_2 catalysts, on the other hand, the oxygen atoms of the V=O and V-O-V groups are driving the conversion, while the titania support catalyses the initial hydrogen abstraction via a transient Ti-OH group, indicating that the more reducible oxygen atoms are the ones responsible for the conversion, while the selectivity is determined by the type

---

of hydrogen transfer and surface adsorbates.

Based on these mechanisms, a rational-design approach towards a catalyst combining the activities of VO_x, TiO_2, and CeO_2 was performed, by introducing a TiO_x layer with varying thickness between ceria and vanadia via atomic layer deposition (ALD). As ALD-deposited titania mostly crystallizes in islands [8,20–22], some of the ceria is likely to be still exposed to the gas-phase and redox active as in the VO_x/CeO_2 system, but in addition vanadia supported on titania can also be redox active, by catalysing the initial hydrogen abstraction, while also blocking some of the ceria surface oxygen sites that are highly relevant for the overoxidation reaction. With this approach, we expect to facilitate a higher catalyst selectivity compared to the two-component systems.

Therefore, in this study, we present the synthesis, structural characterization, and operando spectroscopic investigation of ALD-synthesized $VO_x/TiO_x/CeO_2$ catalysts for propane ODH, designed to combine the properties of CeO_2 and TiO_2 supports. First, we determine the catalysts' performance to validate their superior catalytic performance. ALD is employed to precisely control the TiO_x layer thickness, isolating its influence on the catalyst. By combining multi-wavelength Raman, UV-Vis, DRIFT, and X-ray photoemission spectroscopy (XPS) together with X-ray diffraction (XRD) and the previous mechanistic knowledge of the VO_x/TiO_2 and VO_x/CeO_2 systems [8,9], the structure of the catalyst as well as the function of each oxide during the reaction is investigated, leading to a mechanistic understanding of the new three-component catalyst for propane ODH.

2. Experimental section

2.1. Catalyst preparation

Bulk ceria [7,9,23] and titania (P25) [8] were used as references to the newly synthesized ALD system and were prepared as previously described in detail. In short, P25 was used as a commercially available mixed phase TiO_2 system [24] and ceria was synthesized by two-fold calcination of cerium (III) nitrate hexahydrate (Sigma Aldrich) at 600 °C for 12 h [25]. Ceria was loaded by incipient wetness impregnation using a vanadium(V) oxytriisopropoxide solution diluted in 2-propanol (0.51 mol/l), while titania was loaded using an aqueous solution containing a 1:2 ratio of ammonium metavanadate (AMV) and oxalic acid (0.59 mol/l), resulting in a vanadium surface density of 1.2 V/nm^2 for each sample (61.4 m^2/g and 73 m^2/g for ceria and titania, respectively, as determined by nitrogen physisorption and BET analysis).

Ceria was coated with TiO_2 by ALD in a custom-built setup described elsewhere [22]. For each sample, 1 g of ceria was placed in the ALD reactor and the reactor temperature was set to 120 °C (pressure: 1.3 Torr). $TiCl_4$ was used as the titanium precursor where the feeding system was set to 40 °C to ensure sufficient evaporation, while H_2O was used as the oxidant. It was then coated with 15, 30, 45, 60, 90, and 120 ALD cycles of TiO_x, where one cycle consisted of three half cycles of $TiCl_4$ and three half cycles of H_2O [26]. During each half cycle, the sample was exposed to $TiCl_4/H_2O$ for 60 s and then flushed for 60 s with nitrogen [27]. The theoretical thicknesses of the resulting TiO_x thin films correspond to 2, 4, 6, 8, 12, and 16 nm on a silicon wafer as determined by ellipsometry [28]. The coated samples were calcined in air at 600 °C for 12 h to crystallize the deposited titania and will be referred to as $nTiO_x$ $+CeO_2$ + 1.2 V/nm^2 (n for the number of cycles applied). In the following, the number of cycles applied will be referred to as layers, since theoretically each full cycle represents a layer of TiO_2 during the ALD process. However, during the calcination process TiO_x islands will be formed on the surface. The specific surface area of the $nTiOx+CeO_2$ samples was determined to be ~40 m^2/g (varying by 1–2 m^2/g) by using nitrogen physisorption and subsequent BET analysis. The samples were then loaded with vanadia in the same way as the P25 samples and the precursor concentration was adjusted for the different surface area, resulting in an aqueous solution with a 1:2 ratio of AMV and oxalic acid with a concentration of 0.33 mol/l, yielding a vanadium surface density

of 1.2 V/nm^2 for all samples. The surface areas, used precursor concentrations and resulting vanadia surface densities are summarized in Table 1.

2.2. Catalytic testing

Catalytic testing was performed in a CCR 1000 reaction cell (Linkam Scientific Instruments) operated in a fluidized-bed mode, using 70 mg of catalyst for the bulk CeO_2- and ALD-based samples and, due to its lower density, 60 mg of the bulk P25-based sample. The samples were first dehydrated in 12.5% O_2/He for 1 h at 455 °C, subsequently cooled to 50 °C, exposed to 12.5% O_2/12.5% C_3H_8/He with a total flow rate of 40 ml$_n$/min, and then heated in 45 °C steps up to 550 °C, and held at each temperature for 1 h. The gas-phase composition was analyzed continuously using a gas chromatograph (GC, Agilent Technologies 7890B) equipped with a PoraPlotQ and a Molsieve column as well as a thermal conductivity detector (TCD) and a flame-ionization detector (FID) in series. The setup is connected through a twelve-way valve. One chromatogram is measured every 29 min, resulting in two chromatograms for each temperature, which were averaged. The pressure before and after the GC was monitored to correct the detected areas for pressure fluctuations. For each measurement, the gas phase was gathered for 30 s in a 0.25 ml loop before it was dosed onto the columns, resulting in a fixed amount of gas entering the analysis. The determined areas were normalized to a pressure of 1000 mbar to account for e.g. volumetric expansion during CO_x formation from propane. The products that were observed in the chromatograms were CO, CO_2, and propylene. The selectivity was computed as follows:

$$S = \frac{n_{C3H6}}{n_{C3H6} + \frac{1}{3}n_{CO2} + \frac{1}{3}n_{CO}}$$

The obtained conversions were normalized to the surface area of the catalyst, due to the different sample masses and surface areas used for the bulk and ALD-synthesized catalysts.

2.3. UV-Raman spectroscopy

UV-Raman spectroscopy was performed at an excitation wavelength of 385 nm generated by a laser system based on a Ti:Sapphire solid-state laser pumped by a frequency-doubled Nd:YAG laser (Coherent, Indigo). The fundamental wavelength is frequency doubled to 385 nm using a LiB_3O_5 crystal. The light is focused onto the sample, and the scattered light is collected by a confocal mirror setup and focused into a triple-stage spectrometer (Princeton Instruments, TriVista 555) [29]. Finally, the Raman contribution is detected by a charge-coupled device (CCD, 2048 × 512 pixels) cooled to −120 °C. The spectral resolution of the spectrometer is 1 cm^{-1}. For Raman experiments, 70 mg of catalyst for

Table 1
Summary of the surface areas, precursor solutions and resulting vanadia surface densities of the samples used in this study.

Sample	Surface Area /m^{2}g^{-1}	Precursor Concentration /molL^{-1}	Surface Density /Vnm^{-2}
CeO_2	61.4	0.51	1.21
15TiO$_x$ +CeO$_2$	41.3	0.33	1.17
30TiO$_x$ +CeO$_2$	40.6	0.33	1.18
45TiO$_x$ +CeO$_2$	38.9	0.33	1.23
60TiO$_x$ +CeO$_2$	39.3	0.33	1.22
90TiO$_x$ +CeO$_2$	40.1	0.33	1.20
120TiO$_x$ +CeO$_2$	38.3	0.33	1.25
TiO_2	73.1	0.59	1.19

the CeO_2- and the ALD-based samples and 60 mg for the P25-based sample were placed in a CCR 1000 reactor (Linkam Scientific Instruments) equipped with a CaF_2 window (Korth Kristalle GmbH). A fluidized bed reactor was employed to avoid laser-induced damage, allowing the use of a laser power of 7 mW at the location of the sample. Data processing included cosmic ray removal and background subtraction. Spectra for the structural characterization were recorded at room temperature after 1 h of dehydration under 12.5% O_2/He at 455 °C and subsequent cooling, while operando spectra were measured after dehydration for 1 h in 12.5% O_2/He and subsequent switching to reactive conditions (12.5% O_2/12.5% C_3H_8/He) at 455 °C. The total flow rate was 40 ml_n/min and the resulting spectra were normalized to the F_{2g} peak.

2.4. Vis-Raman spectroscopy

Visible (Vis) Raman spectroscopy was performed at 514 nm excitation, emitted from an argon ion gas laser (Melles Griot). The light was focused onto the sample, gathered by an optical fiber, and dispersed by a transmission spectrometer (Kaiser Optical, HL5R). The dispersed Raman radiation was subsequently detected by an electronically cooled CCD detector (–40 °C, 1024 × 256 pixels). The spectral resolution was 5 cm^{-1} with a wavelength stability of better than 0.5 cm^{-1}. For Raman experiments, 70 mg of catalyst for the CeO_2- and the ALD-based samples and 60 mg for the P25-based sample were placed in a CCR 1000 reactor (Linkam Scientific Instruments) equipped with a quartz window. A fluidized-bed reactor was employed to avoid laser-induced damage, allowing the use of a laser power of 5 mW at the location of the sample. Data analysis of the Raman spectra included cosmic ray removal and an auto new dark correction. Spectra for the structural characterization were recorded at room temperature after 1 h of dehydration under 12.5% O_2/He at 455 °C and subsequent cooling, while operando spectra were measured after dehydration for 1 h in 12.5% O_2/He and subsequent switching to reactive conditions (12.5% O_2/12.5% C_3H_8/He) at 455 °C. The total flow rate was 40 ml_n/min and the resulting spectra were normalized to the F_{2g} peak.

2.5. Diffuse reflection UV-Vis spectroscopy

Diffuse reflectance (DR) UV-Vis spectra were recorded on a Jasco V-770 UV-Vis spectrometer. Dehydrated $BaSO_4$ was used as the white standard and 70 mg of catalyst for the CeO_2- and the ALD-based samples and 60 mg for the P25-based sample were placed in the commercially available reaction cell (Praying Mantis High Temperature Reaction Chamber, Harrick Scientific Products) equipped with transparent quartz glass windows for each experiment. Spectra for the structural characterization were recorded at room temperature after 1 h of dehydration under 12.5% O_2/He at 455 °C and subsequent cooling, while operando spectra were measured after dehydration for 1 h in 12.5% O_2/He and subsequent switching to reactive conditions (12.5% O_2/12.5% C_3H_8/He) at 455 °C. The total flow rate was 40 ml_n/min. The spectra were further analyzed by a least-squares fitting analysis using Gaussian-Lorentzian (70/30) product functions (Voigt). Product functions were used to account for the large contribution of natural line broadening to the overall line-shape, caused by the short lifetime of the electronically excited states.

2.6. X-ray photoelectron spectroscopy

XP spectra were recorded on a modified LHS/SPECS EA200 MCD system described previously [30–32]. The XPS system was equipped with a Mg Kα source (1253.6 eV, 168 W), and the calibration of the binding energy scale was performed with Au $4f_{7/2}$ = 84.0 eV and Cu $2p_{3/2}$ = 932.67 eV signals from foil samples. The samples were dehydrated for 1 h in 12.5% O_2/He at 455 °C in the CCR1000 reactor (Linkam Scientific Instruments) and subsequently cooled rapidly to

room temperature in pure He, each with a total flow rate of 40 ml_n/min.

The subsequent transfer of the sample to the analysis chamber was performed without exposure to air (quasi in situ). Sample charging was taken into account by setting the u''' peak of the Ce 3d signal to 916.7 eV [33]. Detailed spectra were recorded at a resolution of 0.05 eV. The X-ray satellite peaks due to the use of a non-monochromatic source were subtracted from the spectra. The deconvolution of the spectra was performed analogously for all measurements using Gauss–Lorentzian product functions (30/70), whereby the background was subtracted by the Shirley method.

O/(Ce+Ti) and V/(Ce+Ti) ratios were obtained from a least-squares fit analysis by integrating the Ce 3d, O 1s, V $2p_{3/2}$, and the Ti 2p signal after a Shirley background subtraction from the detailed spectra and by applying the same integration boundaries. The resulting areas were corrected with the corresponding relative sensitivity factors (RSFs), as shown in Table 2 [34,35].

2.7. X-ray diffraction

Powder X-ray diffraction (XRD) patterns were recorded on a Stadi-P (Stoe & Cie) diffractometer with a Ge(111)-monochromator, Cu Kα₁ radiation (λ = 1.54060 Å), and a MYTHEN-1 K (Dectris) detector, using a flat sample holder in transmission geometry. For quasi in situ XRD measurements the samples were measured in pristine condition after dehydration in 12.5% O_2/He for 1 h at 455 °C and subsequent rapid cooling to room temperature in pure helium in the CCR 1000 reactor (Linkam Scientific Instruments) and an inert transfer to the XRD sample holder.

2.8. Diffuse reflectance infrared Fourier transform spectroscopy

Diffuse reflectance infrared Fourier transform spectroscopy (DRIFTS) was performed using a Vertex 70 spectrometer (Bruker). A liquid nitrogen-cooled mercury cadmium telluride (MCT) detector was used, operating at a resolution of 1 cm^{-1}. Dehydrated potassium bromide was employed as an infrared transparent sample for the background spectrum. For each experiment, 70 mg of catalyst for the CeO_2- and ALD-based samples and 60 mg for the P25-based sample were placed in the commercially available reaction cell (Praying Mantis High Temperature Reaction Chamber, Harrick Scientific Products) equipped with transparent KBr windows.

For quasi in situ measurements the samples were treated in 12.5% O_2/He, 12.5% O_2/12.5% C_3H_8/He, and was finally regenerated in 12.5% O_2/He for 1 h at 455 °C, respectively and for each gas-phase the sample was cooled rapidly to room temperature in pure helium for one measurement before heating it back to 455 °C. For isotopic exchange experiments, the samples were treated in 12.5% O_2/12.5% C_3D_8/He after the regular reaction gas-phase and before regeneration. The total flow rate for each experiment was 40 ml_n/min.

Data processing consisted of background removal by subtracting a baseline formed by 12 anchor points and removal of the spectrum recorded in 12.5% O_2/He to subtract the contributions from the pristine catalyst and to obtain surface species formed during the reaction only. Finally, to quantify the adsorbate peaks in the vanadyl, carbonate, and hydroxide regions, the spectra were fitted using Lorentzian functions employing the Levenberg-Marquardt algorithm implemented in OriginLab 2022b.

Table 2
Relative sensitivity factors (RSFs) used for the quantitative analysis of XP spectra.

Element	Ce 3d	O 1s	V $2p_{3/2}$	Ti 2p	C 1s
RSF	8.808	0.711	1.411	2.001	1

3. Results and discussion

The mechanistic findings of our previous studies on VO_x/CeO_2 and VO_x/TiO_2 during the ODH of propane are highly important for the following study and are therefore briefly summarized in the following [7–9].

Starting with the reaction mechanism of propane ODH over VO_x/CeO_2 catalysts, the route leading to the selective oxidation products occurs in proximity to the vanadia surface species. The first hydrogen atom is abstracted from propane via the V=O group of either dimeric or oligomeric vanadia species, resulting in the presence of a transient V-OH group, which quickly transfers the hydrogen to the ceria surface, forming a Ce-OH group. Propane is adsorbed onto the ceria surface in an acrylate-like geometry, which is coordinated by the vanadia. The second hydrogen atom is also abstracted via a V=O group and transferred to the ceria surface, resulting in the formation of water, leading to the creation of an oxygen vacancy in the ceria lattice, and formation of propylene. Dimeric and higher oligomeric species have been proposed as active species, while monomeric vanadia can interact with the vacancy, irreversibly blocking it, and trimeric vanadia was determined to be an observer species.

The reaction mechanism over VO_x/TiO_2 catalysts occurs by the abstraction of the first hydrogen atom from propane via a monodentate transient Ti-OH group on the anatase surface, which then quickly transfers the hydrogen atom to the V=O or the V-O-V group of monomeric and dimeric vanadia species. The second hydrogen atom is also transferred via the titania surface to the vanadia species, where water and propylene are formed. The reduced catalyst can then be regenerated by gas-phase oxygen. The linear V-O-V bonds of oligomeric vanadia were the most active but least selective oxygen site for the reaction, while the doubly bridged V-O-V bonds of dimeric vanadia were much more selective.

3.1. Catalytic activity

To verify the successful rational design of $VO_x/TiO_x/CeO_2$ catalysts, the catalytic activity of the samples coated with 0–120 layers of TiO_x was determined between room temperature and 550 °C. Furthermore, we chose a temperature of 455 °C for operando spectroscopy to investigate structure-function relationships of the three-component catalyst and to develop a mechanistic picture. Fig. 1 shows the temperature-dependent conversions and selectivities of the catalysts. For the data shown in Fig. 1, the background activity of the Linkam reactor was already subtracted and for the TiO_x layer-dependent data the conversion of the ceria catalyst was normalized to the same surface area as the $VO_x/TiO_x/CeO_2$ samples. The raw catalytic data together with data for the empty Linkam reactor and bulk titania loaded with 1.2 V/nm^2 are given

in the SI (see Figs. S1 and S2).

Fig. 1a depicts the conversions of CeO_2 coated with 0–120 layers of TiO_x and loaded with vanadium (1.2 V/nm^2) between room temperature and 550 °C. The sample without TiO_x coating is the most active and starts to show propane conversion at 185 °C, with a significant conversion being measured from 230 °C on, increasing exponentially with temperature up to 34% at 550 °C. In comparison, the samples loaded with 15–120 layers of TiO_x show their onset of propane conversion at 320 °C, followed by an exponential increase in conversion with temperature up to 550 °C. The propene selectivity behaviour of the catalysts differs significantly at higher conversions, where the selectivity of the TiO_x-free sample (VO_x/TiO_2) sample decreases rapidly towards a selectivity of 10% between 455 and 550 °C. On the other hand, the selectivity of the catalyst samples with 15–120 TiO_x layers reaches an early maximum in propylene selectivity at 230 °C, which then decreases first towards 275 °C but then increases again starting at around 320 °C (except for the 15 TiO_x sample) and stays on a similar level up to 455 °C before also significantly decreasing again towards 18–55% at 550 °C. The second maximum in selectivity might be caused by titania activation for initial H abstraction from propane [8]. This also explains the absence of this behaviour for the 0 TiO_x sample as well as its weaker characteristic for the 15 TiO_x sample, as crystalline anatase is required for the initial C-H bond activation over titania. The observed behaviour agrees with the activity data for P25 + 1.2 V/nm^2 (see Fig. S2), which shows significant conversions over 275 °C only, increasing exponentially between 320 and 365 °C, indicating activation of titania at this temperature, and plateaus in the end. While the initial selectivities of the three-component catalysts at 230 °C are disregarded here due to low level of conversion (<0.1%), the second selectivity maximum is considered as suitable for further investigation. Therefore, for the operando spectroscopic analysis, a temperature of 455 °C is chosen to represent a balance between the conversion and selectivity behaviour.

Fig. 1c summarizes the propane conversion and propylene selectivity of the catalysts coated with 0–120 TiO_x layers and loaded with 1.2 V/nm^2 at 455 °C after normalization to their surface areas. The background activity of the Linkam reactor was subtracted (see Fig. S1). The TiO_x layer-dependent propane conversion shows a strong decrease from 15.1% to 3.4% for the 0 TiO_x and 15 TiO_x sample, respectively, and further decreases to 2.6% for the 30 TiO_x sample. After that, the conversion increases gradually towards the 90 TiO_x sample (3.9% conversion), before decreasing again. In comparison, the selectivity towards propylene shows an overall increase with increasing TiO_x coating from 10.1% to 80% for the 90 TiO_x sample. The conversion goes through a minimum, while the selectivity constantly increases, resulting in a maximum propylene yield for the catalyst coated with 90 layers of TiO_x. In the following, the sample coated with 120 layers of TiO_x will not be considered further due to its inferior catalytic properties. The propane
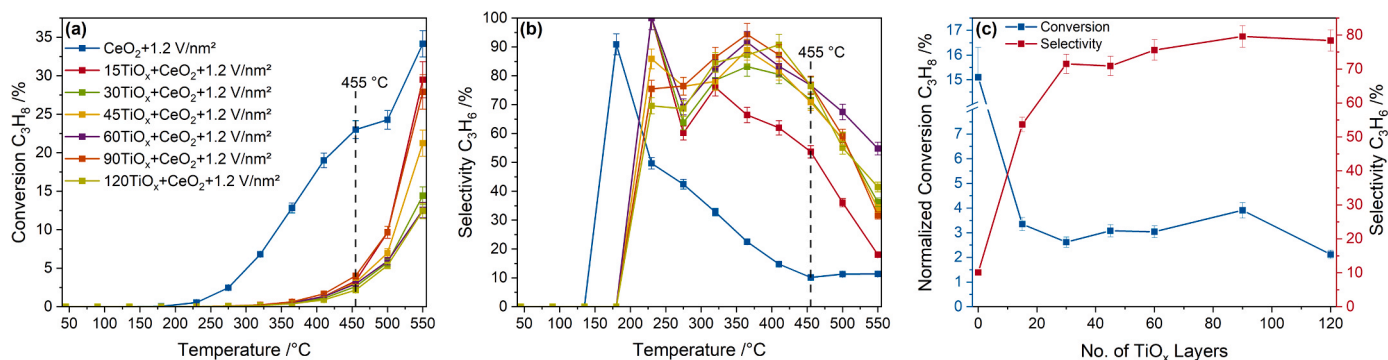
Fig. 1. Temperature-dependent catalytic performance of $VO_x/TiO_x/CeO_2$ catalysts (with 1.2 V/nm^2): **(a)** Propane conversions, **(b)** propylene selectivities, and **(c)** propane conversion normalized to the surface area of the catalysts to correct for varying surface areas and propylene selectivities as a function of the number of TiO_x layers at 455 °C. The reactor background activity was subtracted for all data points (see Fig. S1). As indicated, a temperature of 455 °C was chosen for the operando analysis.

conversions for the samples coated with ≥ 15 layers of TiO_x vary between 2.6% and 3.9%, while the propylene selectivities increase steadily and much more significantly from 54% to 80%, indicating that the selectivity increase is not only caused by the changes in conversion, but also by differences in the reaction pathway. This is most clearly seen for the samples coated with 60 and 90 layers of TiO_x, where both the propane conversion and the propylene selectivity increase.

In comparison to performance data in the literature, our results for the bulk samples are in agreement with fixed-bed reactor results previously described for titania and ceria at different temperatures, indicating the suitability of the Linkam reactor for operando spectroscopic analysis [4,6,10,13,36]. The newly synthesized ALD-based catalysts show conversions between 2.5% and 4% at 455 °C, which is lower than for most other catalysts based on supported vanadia but exhibit selectivities that are higher than those of the single oxide-based supported catalysts, resulting in higher yields with much less CO_x formation compared to other supported VO_x systems [3,6,8,9]. This would make a process based on looping of not converted propane much more viable, as the propane is not lost to CO_x formation.

3.2. Catalyst characterization

The bulk ceria and titania samples, loaded with $1.2\ V/nm^2$ each, were extensively characterized in our previous studies and are used here only as reference materials [7–9,23]. Fig. 2 shows room temperature results from the Vis-Raman and UV-Vis spectroscopic characterization of the $VO_x/TiO_x/CeO_2$ samples after dehydration in 12.5% O_2/He at 455 °C for 1 h. Based on the spectra, the area of the anatase E_g phonon band, the F_{2g} position, and the absorption band gap energy were determined.

As can be seen in the Vis-Raman spectra in Fig. 2a, besides the ceria F_{2g} band at ~459 cm^{-1}, three phonon bands start to appear at 397, 510, and 633 cm^{-1}, which are assigned to B_{1g}, B_{1g}/A_{1g}, and E_g phonons of anatase, respectively [37], and are caused by the gradual increase in titania content confirming that crystalline anatase is present on the ceria surface after the coating by ALD and calcination. Since the phonons at 397 and 510 cm^{-1} overlap significantly with ceria-related features, the peak at 633 cm^{-1} is chosen for quantification of the crystallization of the titania layer by integration (see Fig. 2b). Notably, no peaks of the rutile phase are detected. Since rutile has a lower Raman intensity compared to anatase [37], especially at 514 nm excitation due to a lack of resonance enhancement, it is either possible that rutile is absent, or that the rutile signal is dominated by the ceria and anatase signals. The position of the F_{2g} peak is a good indicator for the state of ceria in the presence of the titania phase, showing a red-shift in case of reduction, or a blue-shift in case of oxidation [38] and was therefore quantified using a Lorentzian function (see Fig. 2b).

As shown in Fig. 2b, the intensity of the anatase E_g phonon as a function of the number of TiO_x layers follows a sigmoidal function indicating that a minimum amount of titania needs to be present to result in its crystallization on the ceria surface, while there is saturation for 60 TiO_x layers with no additional crystallization (at least not as anatase). Additional formation of small amounts of rutile might still occur. For comparison, quasi in situ XRD measurements were performed for the samples coated with 0, 15, and 90 TiO_x layers, pre-treated under the same conditions as for the Raman and UV-Vis spectra (see Fig. S3), indicating that for 15 layers of TiO_x, the diffraction pattern stays unchanged compared to that of the sample without TiO_x. However, a small
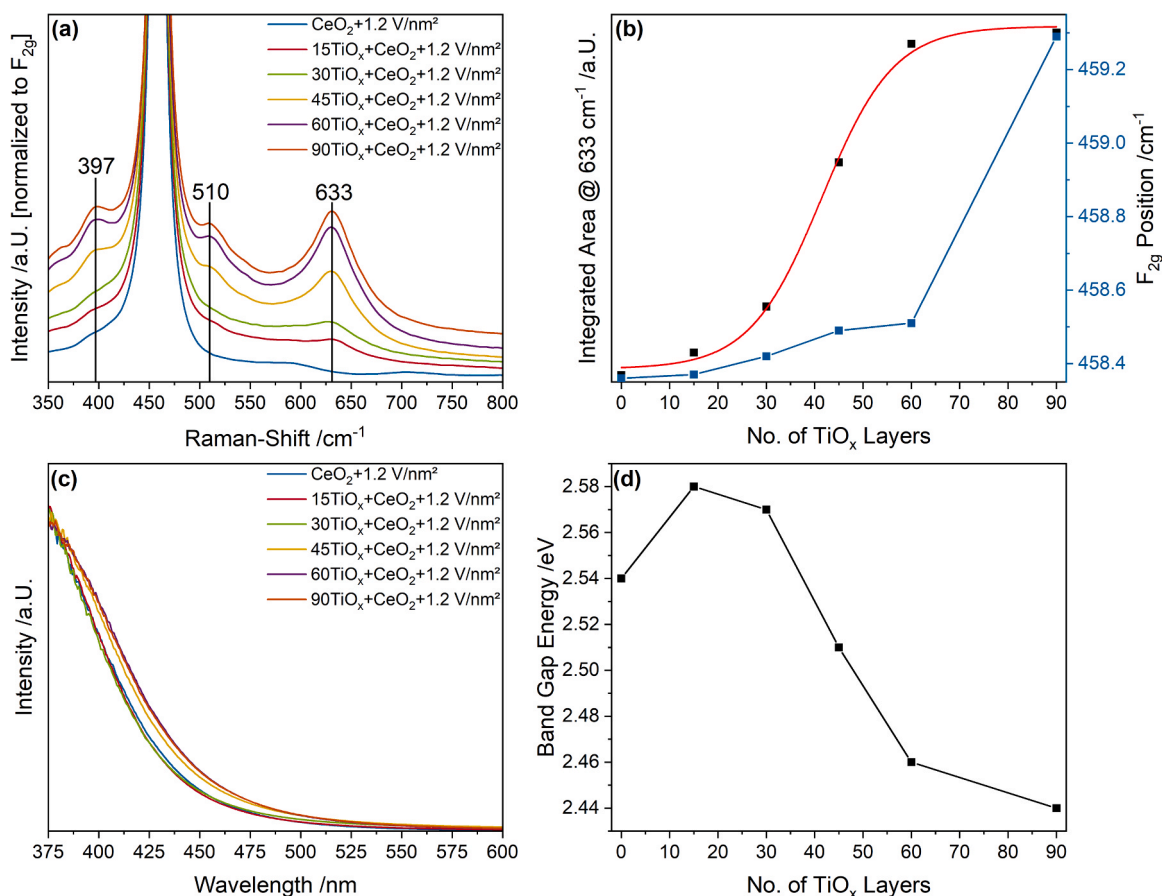
Fig. 2. Catalyst characterization data of $VO_x/TiO_x/CeO_2$ (with $1.2\ V/nm^2$): **(a)** Vis-Raman spectra using 514 nm excitation. **(b)** Anatase phonon intensities and F_{2g} positions determined from the Vis-Raman spectra. **(c)** UV-Vis spectra. **(d)** Band gap energies determined from UV-Vis spectra using Tauc plots. Raman and UV-Vis spectra were recorded at room temperature after dehydration for 1 h in 12.5% O_2/He at 455 °C.

reflex due to the presence of crystalline anatase becomes apparent at ~25° 2θ for 90 TiO_x layers, indicating tiny crystalline particles of TiO_2 [39]. Together with the Vis-Raman data, this hints at the presence of a nanocrystalline anatase phase dispersed in amorphous titania on the surface of ceria. To acquire information about the anchor point of the titania layer on the surface of the ceria, UV-Raman spectra (385 nm excitation) were recorded after the same pre-treatment as described before (see Fig. S4), showing increased intensities at the anatase phonon positions, which is in good agreement with the Vis-Raman spectra. The intensity of the defect region decreases in comparison to the bare material, except at ~505 and ~635 cm^{-1}, where the phonons of the anatase phase are located. This indicates a smaller number of oxygen vacancies and Ce^{3+} ions [40,41]. However, the most significant change in intensity is observed at around 400 cm^{-1}, where despite the intensity increase due to the presence of the anatase A_{1g} phonon band there is still an overall intensity decrease of the transversal Ce-O surface phonon, indicating that the titania layer binds to ceria via Ce-O surface lattice oxygen species [37]. This is further emphasized by the much sharper peroxide signal at around 820 cm^{-1} compared to the rather broad signal on the uncoated sample, which is indicative of the consumption of different ceria surface sites to bind the titania layer (see Fig. S4). The F_{2g} position continuously blue-shifts with increasing titania coating up to 60 layers of TiO_x before jumping significantly by almost 1 cm^{-1}, suggesting less Ce^{3+} ions being present in the ceria, which is in agreement with the UV-Raman data for the defect region as discussed above [38]. In summary, these changes in the defect region of the UV-Raman spectra and the observed blue-shift of the F_{2g} position may indicate the regeneration of the ceria surface due to the binding of titania to its topmost Ce-O layer, and a reduced number of surface oxygen vacancies (resulting in a lower intensity at 590 cm^{-1}) [40,41] which require the transfer of electrons from Ce^{3+} ions to the oxygen atoms to be integrated into the CeO_2-TiO_2 interface as O^{2-}, decreasing the overall amount of Ce^{3+} in the subsurface/bulk and, as a consequence, leading to a F_{2g} blue-shift. Furthermore, the deposition of titania on the ceria surface might remove some of the most reactive surface oxygen species, which decreases the amount of oxygen that ceria is able to transfer to the gas-phase.

Fig. 2c depicts the UV-Vis spectra of the samples coated with 0–90 TiO_x layers after dehydration within 375–600 nm, while the absorption behaviour at lower/higher wavelengths does not show any detectable changes with increasing titania coverage. As main change in the series of spectra, a change in band gap energy is identified, which was quantified using Tauc plots [25], as summarized in Fig. 2d. Starting at a value of 2.54 eV for CeO_2 + 1.2 V/nm^2 the band gap energy goes through a maximum of 2.58 eV for the 15 TiO_x sample before continually decreasing up to a value of 2.44 eV for the 90 TiO_x sample. Comparing Fig. 2b and d, the band gap energies of VO_x/TiO_x/CeO_2 samples show an inverted behaviour of the anatase phonon intensity, whereas the initial increase in the band gap can be explained by the oxidation of ceria, which removes states created within the band gap by reduction, which is consistent with the observed F_{2g} position [38,42,43]. Starting at 30 layers of TiO_x, titania crystallizes into a highly defective anatase phase with a lower band gap in agreement with the observed A_{1g} phonon intensity in Fig. 2b [44,45], which slows down between 60 and 90 layers of TiO_x.

To identify the support material to which vanadia is primarily anchored, DRIFT spectra were recorded after dehydration at 455 °C in 12.5% O_2/He for 1 h and subsequent cooling to room temperature (see Fig. S5). In case of VO_x/CeO_2, the vanadyl region shows the expected fine structure, with peaks located at 1008, 1018, 1024, 1032, and 1040 cm^{-1}, corresponding to monomeric, dimeric, trimeric, tetrameric, and different oligomeric species, respectively [7,9,46,47]. The observed blue-shift of higher nuclearities is attributed to dipole-dipole coupling of vanadyl groups oriented in parallel to each other [48]. For titania coatings with more than 30 layers, the fine structure of the vanadyl region disappears almost completely, showing only a single peak with a

slight asymmetry towards higher wavenumbers and a maximum at 1032 cm^{-1}, which is more typical for the VO_x/TiO_2 system, which contains monomeric and dimeric species at this loading [8]. Only the spectrum of the 15 TiO_x sample shows slightly more structure, with the maximum of the main peak red-shifted to 1025 cm^{-1} and a broad shoulder to higher wavenumbers with a local maximum at ~1040 cm^{-1}. This behaviour suggests that vanadia may be located on either of the supports for low titania loadings but shifts from the ceria to the titania support for larger titania loadings and the formation of the anatase phase.

To gain further insight into the surface composition and the titania crystallization process, XP spectroscopy was applied to the VO_x/TiO_x/CeO_2 samples (see Table 3 and Fig. 3). The results shown in Table 3 reveal that the amount of Ce detected on the surface of the catalyst decreases continuously with an increase in the number of TiO_x layers. The changes between 0 and 30 layers of titania are more significant than those between the other samples, indicating a convergence towards a minimum cerium value. Hence it seems likely, that titania is not present as a uniform and even layer, but forms titania islands upon crystallization, with part of the ceria being exposed and therefore detectable by XPS. This behaviour is in good agreement with ALD-synthesized titania on other supports (SiO_2, Al_2O_3), as demonstrated previously [8,20–22]. The relative concentration of Ti also increases more sharply during the first 30 layers of titania coating, but then increases slower, following the inverse trend of Ce. The amount of surface vanadium expressed by the V/(Ce+Ti) ratio, stays constant within the margin of error, which is in agreement with the constant loading of the samples and indicates that vanadium atoms are not confined by the ALD titania, as observed for other systems [8,27]. At last, the amount of oxygen exposed to the surface layer constantly increases with increasing number of TiO_x layers. This might be caused by the fact that ceria is less reduced in the presence of titania in agreement with the blue-shifted F_{2g} mode (see above). Besides, vanadia might be present in a higher oxidation state when located on titania. Finally, the titania layer consists of both amorphous and nanocrystalline anatase. The interface between both phases with each other and with ceria may lead to the formation of new surface structures with an increased amount of oxygen. This hypothesis is supported by the O/(Ce+Ti) ratio, which should have a value of 2 for stoichiometric titania and ceria but stays below that value for the vanadia loaded ceria sample (due to the presence of surface defects) and then increases up to 3 due to the aforementioned reasons.

For a more detailed understanding, Fig. 3 depicts the Ce 3d, O 1s, Ti 2p, and V 2p photoemission, whereas the results of the fitting analysis (for details see Experimental Section) of the Ce 3d and the V $2p_{3/2}$ regions are shown in Table 3. Starting with the Ce 3d photoemission shown in Fig. 3a, a decrease in the overall intensity is observed with increasing titania loading, which agrees with the results from the elemental compositions, while at the highest loading, there is still some Ce 3d photoemission confirming the presence of titania islands not fully covering the ceria support. To emphasize this point, the Ce 3d area was plotted against the TiO_x thickness (see Fig. S6a), demonstrating that at a theoretical TiO_x thickness of 16 nm, ceria is still observable in XP spectra. Furthermore, the OH stretching region of all samples reveals that Ce-OH species are visible even after a coating with 90 TiO_x layers, further indicating that part of the ceria is exposed to the gas phase (see

Table 3

Surface composition of the VO_x/TiO_x/CeO_2 samples determined from their photoemissions using the RSFs shown in Table 2.

	Ce	O	V	Ti	O/ (Ce+Ti)	V/ (Ce+Ti)
0 TiO_x	30.6	56.9	3.7	0	1.86	0.12
15 TiO_x	19.4	63.3	2.7	8.4	2.27	0.10
30 TiO_x	9.6	67	2.9	15	2.73	0.12
45 TiO_x	6.3	67	3.3	16.8	2.90	0.14
60 TiO_x	4.6	68.9	2.8	18.6	2.97	0.12
90 TiO_x	4.4	65.2	3.1	17.3	3.00	0.15
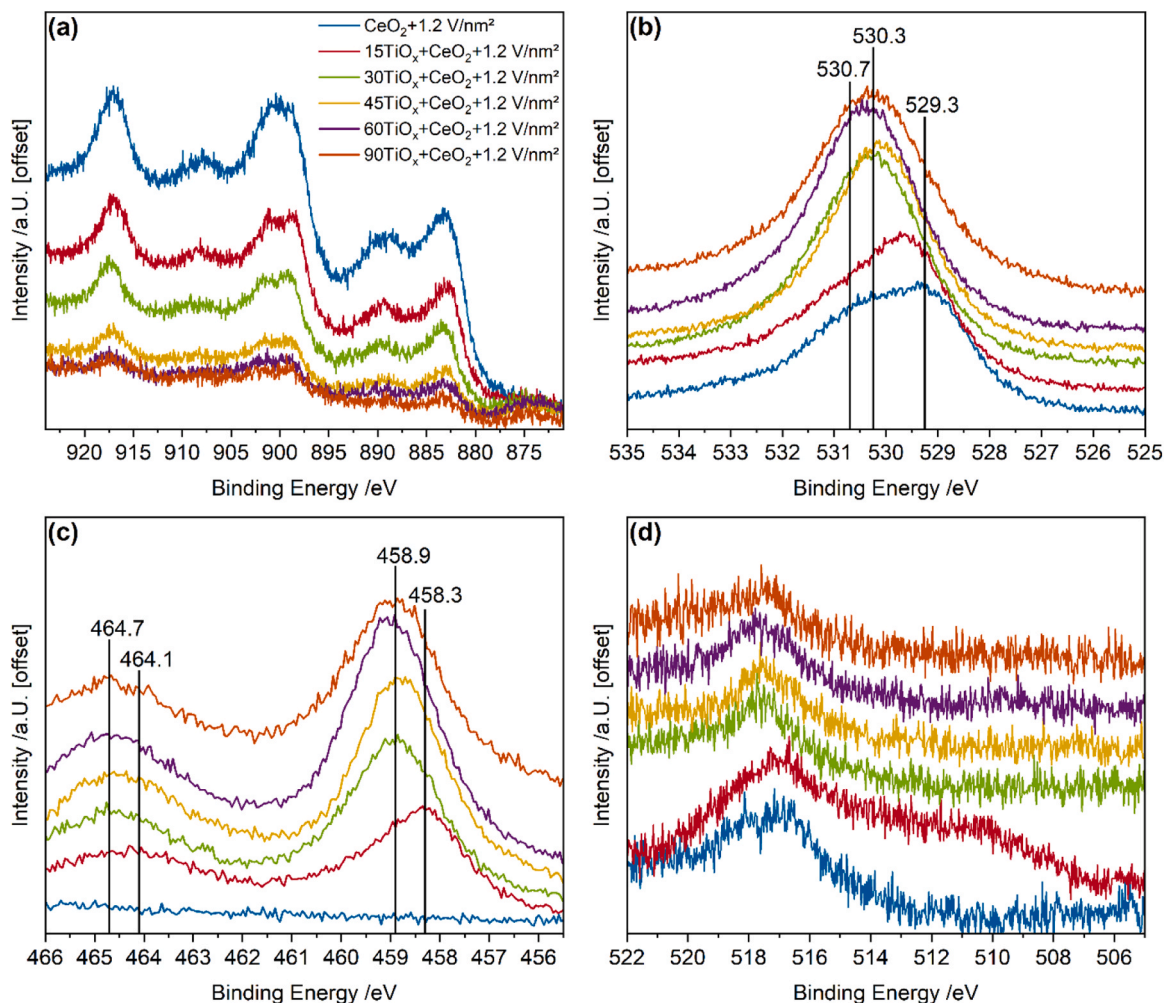
Fig. 3. XP spectra of the $VO_x/TiO_x/CeO_2$ samples (1.2 V/nm^2) after dehydration for 1 h in 12.5% O_2/He at 455 °C, cooling to room temperature, and inert transfer into the XPS chamber: **(a)** Ce 3d, **(b)** O 1s, **(c)** Ti 2p, and **(d)** V 2p photoemissions.

Fig. S6b). The Ce 3d photoemission was fitted as described in the literature and the u_0, u′, v_0, and v′ peaks were used to quantify the amount of surface Ce^{3+} defects in the ceria (see Table 4) [49,50]. The amount of Ce^{3+} amounts to 15.2% in the VO_x/CeO_2 sample and then sharply increases to 25.6% for the 15 TiO_x sample. With an increasing number of TiO_x layers, the relative amount of Ce^{3+} continuously decreases, down to a much more oxidized state of ceria for the 90 TiO_x sample with 4.3% of Ce^{3+}, indicating that ceria is almost fully oxidized at the catalyst surface. This overall trend agrees with the observed F_{2g} shifts, indicating that the oxidation of ceria is not limited to the surface. However, the amount of reduced ceria at low titania loadings deviates from that trend as ceria is more reduced in these samples than in the sample without titania.

Fig. 3b depicts the O 1s photoemission, which for the VO_x/CeO_2 sample is characterized by two signals at 529.3 and 530.7 eV due to

oxidized (Ce^{4+}-) and reduced (Ce^{3+}-) ceria, respectively [50]. For samples with $\geq$ 30 layers of TiO_x, the O 1s signal consists of only one band with a maximum at 530.3 eV, which is indicative of oxidized titania containing Ti^{4+} states, as the surface becomes dominated by the titania contribution [51,52]. The peak might be overlapped by ceria contributions (mainly Ce^{4+} containing ceria at higher titania loadings) but the titania signal dominates. For the 15 TiO_x sample, an intermediate state between the ceria- and titania-dominated regimes is observed. Here, the signals from Ce^{3+} and Ce^{4+} containing ceria are still present, but the peak maximum is blue-shifted to 529.6 eV, due to the presence of titania.

Fig. 3c shows the Ti 2p photoemission, which is largely dominated by two peaks at 464.7 and 458.9 eV, which are indicative of highly oxidized titania in good agreement with the results from O 1s photoemission [51–53]. In contrast, the signal of the 15 TiO_x sample is

Table 4

Distribution of vanadium and cerium oxidation states and their averages based on a least-square fitting analysis of the corresponding Ce 3d and V 2p$_{3/2}$ photoemissions shown in Fig. 3.

	V^{5+}	V^{4+}	V^{3+}	V^0	V Average	Ce^{3+}	Ce^{4+}	Ce Average
0 TiO_x	23.5	62.4	14.1	0	4.10	15.2	84.8	3.85
15 TiO_x	20.1	8.1	44.1	27.7	2.66	25.6	74.4	3.74
30 TiO_x	75.8	23.5	0.7	0	4.75	18.2	81.8	3.82
45 TiO_x	62.4	32.6	5.0	0	4.58	13.4	86.6	3.87
60 TiO_x	59.6	37.0	3.4	0	4.56	7.9	92.1	3.92
90 TiO_x	50.7	38.7	10.6	0	4.40	4.3	95.7	3.96

characterized by significantly red-shifted Ti $2p_{1/2}$ and Ti $2p_{3/2}$ signals at 464.1 and 458.3 eV, which indicate the presence of a titania layer that is dominated by reduced Ti^{3+} species [53] and may explain the lacking crystallization, which only starts to occur at ≥ 30 layers of TiO_x. This might further explain the significantly more reduced state of ceria, since ceria is much more easily reduced than titania during the process of titania oxidation.

At last, Fig. 3d depicts the V $2p_{3/2}$ photoemission, which was fitted to determine the distribution of oxidation states (see Table 4). For the VO_x/CeO_2 sample, 62.4% of the vanadium is present as V^{4+}, which is not detectable in the Raman spectra, 23.5% is present as V^{5+}, and 14.1% is present as reduced V^{3+}. In comparison, for the samples with ≥ 30 layers of TiO_x, the average oxidation state increases significantly from a value of 4.1 to values between 4.4 and 4.75 depending on the exact loading. This behaviour is in good agreement with a shift of the vanadia from ceria to titania [8,23], supporting the DRIFTS results (see Fig. S5). The average vanadium oxidation state is highest for the 30 TiO_x sample and then continuously decreases, which might be related to the state of titania transforming from highly amorphous to more crystalline. For the 15 TiO_x sample, a heavily reduced phase of vanadia is present, where most of the vanadium atoms are present as V^{3+}, while the next most frequent oxidation state is 0, indicative of surface metallic vanadium. The formation of metallic vanadium was previously observed during interaction with reduced titania [53], the presence of which is evidenced by the Ti 2p emission. The strong degree of reduction on the surface containing ceria, titania, and vanadia might be a reason for the initially low propylene yield, that only starts to increase at higher titania loadings.

To summarize the characterization results for VO_x/TiO_x/CeO_2, ceria was successfully coated with nanocrystalline titania, which was anchored to the topmost Ce-O surface oxygen atoms, consuming highly active ceria surface oxygen prone to propane oxidation. Titania is present in the form of islands keeping part of the ceria surface exposed. With increasing titania loading the supported vanadia shifts from ceria to titania. The oxidation states of ceria and vanadia are strongly influenced by the amount of titania present, while the 15 TiO_x sample represents an intermediate state between the samples dominated by ceria or titania, which is characterized by heavy reduction of all three oxides.

Overall, using an ALD-assisted synthesis approach, a new TiO_x/CeO_2 support for vanadia could be engineered, leading to an interaction of all three oxides. The propylene yield of the three-component catalyst was significantly improved in comparison to the two-component systems (VO_x/CeO_2 and VO_x/TiO_2) due to a sharp increase in selectivity, while the conversion is lower. Initial indicators for the improved catalytic performance were proposed during the discussion of the characterization results, but to verify their relevance and gain insight into the reaction mechanism, operando spectroscopic investigations were performed at 455 °C.

3.3. Operando and quasi in situ spectroscopy

To obtain an initial overview of the functions of the different oxides, operando Vis-Raman spectra during propane ODH at 455 °C were recorded. Fig. 4 depicts the results for the samples coated with 0, 15, and
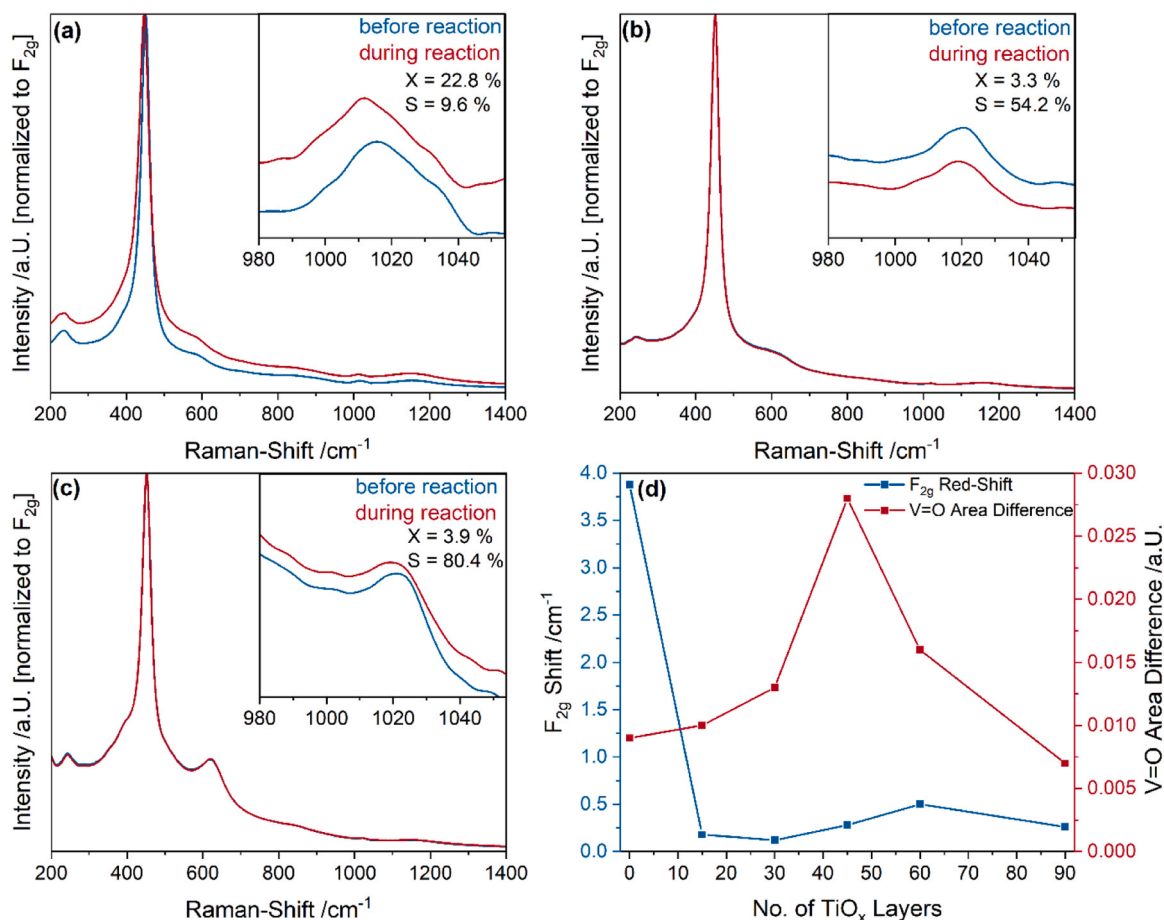
Fig. 4. Operando Vis-Raman spectra (514 nm excitation) of **(a)** CeO_2, **(b)** $15TiO_x+CeO_2$, and **(c)** 90 TiO_x+CeO_2 loaded with 1.2 V/nm^2, respectively, recorded under reactive (12.5% O_2/12.5% C_3H_8/He) and oxidative (12.5% O_2/He) conditions at 455 °C. The spectra were normalized to the F_{2g} mode and the insets give an enlarged view of the vanadyl region for clarity, together with the measured conversions and selectivities. **(d)** F_{2g} red-shift and V=O area difference between reactive and oxidative conditions determined from operando Vis-Raman spectra for CeO_2 coated with 0–90 TiO_x layers and loaded with 1.2 V/nm^2.

90 layers of TiO_x, as well as the quantification of the different structural dynamics. The operando Vis-Raman results for the samples coated with 30, 45, and 60 layers of TiO_x as well as P25 + 1.2 V/nm^2 as reference are given in the SI (see Fig. S7). The conversions given in the Figures were corrected for the activity of the (empty) Linkam reactor and deviate from the conversions discussed above (see Fig. 1) only within the margin of error, providing no indication for laser-induced reactions.

Fig. 4a depicts operando Vis-Raman spectra (514 nm excitation) of VO_x/CeO_2 under oxidative (12.5% O_2/He) and reactive (12.5% O_2/ 12.5% C_3H_8/He) conditions at 455 °C. There is no obvious structural dynamics except for an increase in the background over the entire spectral region. However, upon closer inspection, two types of structural changes become apparent. First, the F_{2g} mode shows a significant red-shift of ~4 cm^{-1} upon switching from oxidative to reactive conditions. Secondly, while the profile of the vanadyl vibration stays largely unchanged (see inset of Fig. 4a), the intensity of the vanadyl peak slightly decreases, which might be owed to the high reaction rate at a propane conversion of 22.8%, preventing ceria from regenerating the supported vanadia fast enough. This is further underlined by the high selectivity towards CO_x products (90.4%), where the reaction uses much more oxygen from the catalyst than the selective oxidation route towards propylene. In comparison, the 15 TiO_x sample (see Fig. 4b), which is characterized by a propane conversion of 3.3% and a propylene selectivity of 54.2%, uses much less oxygen and shows very similar spectra under oxidative and reactive conditions. This behaviour is also resembled by the 90 TiO_x sample (conversion: 3.9%; selectivity: 80.4%). To better differentiate the spectral behaviour of the samples and to identify the reason for their different selectivities, we quantified the F_{2g} red-shift and the area difference in the vanadyl region between oxidizing and reactive conditions, as shown in Fig. 4d.

Starting with the F_{2g} position, the observed red-shift of the VO_x/CeO_2 sample upon exposure to reaction conditions indicates a significant involvement of ceria lattice oxygen from the subsurface in the reaction. Therefore, a diffusion of lattice oxygen atoms from the bulk/ subsurface to the catalyst surface seems important to facilitate the propane oxidation. When the titania coating is applied, the participation of ceria lattice oxygen strongly decreases, as expressed by the 0.2 cm^{-1} red-shift of the F_{2g} position for the 15 TiO_x sample. At higher TiO_2 loadings, the F_{2g} shift correlates with the observed propane conversion, indicating that the most reducible ceria lattice oxygen atoms drive the propane oxidation [23,54–56]. The anchoring of the TiO_x layer to ceria surface lattice oxygen, as observed by UV-Raman spectroscopy (see Fig. S4), therefore consumes some of these active species, decreasing the conversion significantly. This strongly supports the initial supposition, that the formation of titania islands and the re-emergence of ceria lattice oxygen to the catalyst surface might enable the participation of ceria. This decrease in conversion between 0 and 15 layers of TiO_x might also be partly responsible for the increase in propylene selectivity due to the consumption of very active oxygen sites, similar to the consumption of those sites by vanadia monomers observed during propane ODH over VO_x/CeO_2 catalysts [7,46,57]. Only for the 90 TiO_x sample the F_{2g} red-shift does not perfectly correlate with the conversion. The additional conversion of this sample may be caused by other effects, such as the formation of larger crystallites where titania starts to dominate the catalyst's behaviour. This would be in agreement with the Vis-Raman spectrum of bulk P25, which also lacks structural dynamics within the support material, whereas in the UV-Raman spectrum (not shown in this study) [8] a phase transition from anatase to rutile was observed under operando conditions. However, it is not clear if any rutile is present in the 90 TiO_x sample, as the UV-Raman spectrum under operando conditions is dominated by the spectral behaviour of ceria (see Fig. S8). Nevertheless, the UV-Raman spectra of the 90 TiO_x sample show no carbon formation on the catalyst surface, which may have been expected due to the reduced oxygen mobility compared to the VO_x/CeO_2 sample, thus indicating that the propane conversion leads to propylene and CO_x only.

As can be seen in Fig. 4d, all samples show a decrease in the vanadyl intensity (integrated band area) upon exposure to reaction conditions. However, the difference between the samples coated with 0, 15, and 90 layers of TiO_x is small (within the margin of error) and therefore assumed to be similar. On the other hand, the area difference for the samples coated with 30, 45, and 60 layers of TiO_x shows a significant increase (see Fig. S7) and goes through a maximum for the 45 TiO_x sample. This behaviour indicates that vanadia participates in the reaction, confirming that the addition of TiO_x to the catalyst leads to an active participation of the support and the active phase, while previously only one component was observed during static operando experiments and the other showed activity only under transient conditions during the oxidation of short alkanes [8,9]. Furthermore, much less of the vanadium on the 0 and 15 TiO_x samples is present as V^{5+}, which has the most significant Raman scattering cross-section and is therefore observable in the spectra [58–60]. The samples with ≥ 30 layers of TiO_x exhibit much more significant V^{5+} contributions, with the maximum exhibited by the 30 TiO_x sample. Thus, the decreasing V=O dynamics might also be partly caused by the decreasing amount of V^{5+} species when the coating is increased from 30 to 90 TiO_x layers. The participation of vanadia is nevertheless increased by the TiO_x layer, enabling the participation of the active phase and the support. However, the exact influence of vanadia on the observed catalytic activity cannot be conclusively assessed here, but will be discussed later. Please note that a nuclearity-dependent analysis of titania supported vanadia was not possible to the same extent as before [8], since ^{51}V ssNMR could not be performed on ALD-synthesized titania, due to the presence of Ti^{3+} and V^{4+}/V^{3+} states, leading to paramagnetic bleaching [61].

In order to study the reduction of titania and vanadia (e.g. from V^{4+} to V^{3+}), which cannot be observed by Raman spectroscopy due to the small Raman scattering cross-section of reduced vanadia, operando UV-Vis spectra were recorded. Fig. 5 depicts the spectra for the samples coated with 0, 15, and 90 layers of TiO_x as well as the results from the quantification of the observed structural dynamics, while the operando spectra of the samples coated with 30, 45, and 60 layers of TiO_x as well as for VO_x/P25 are given in the Supporting Information (see Fig. S9).

Fig. 5a depicts operando UV-Vis spectra of VO_x/CeO_2 during oxidative and reactive conditions recorded at 455 °C. Upon switching from oxidative to reactive conditions there is an increase in the absorption between 500 and 800 nm, that can either be caused by the presence of a charge transfer transition from Ce^{3+} to Ce^{4+} located at 633 nm [62,63] or by d-d transitions of reduced vanadia [64,65]. Here, the Ce^{3+} to Ce^{4+} transition is less likely, as the reduction of ceria and formation of Ce^{3+} is typically associated with a red-shift of the band gap due to the creation of additional states [66]. However, such a behaviour cannot be observed for the present spectra. In addition, the absorption shows an increase at 800 nm instead of a decline, which indicates that the observed absorption is more likely caused by vanadia d-d transitions, as the transition maximum is located towards > 750 nm [65]. This agrees with the small reduction of the vanadyl peak intensity for this sample in the Vis-Raman spectra (see Fig. 4). Reduced ceria, as evidenced by the F_{2g} red-shift, might be regenerated quickly at the elevated temperature, which significantly increases the oxygen transport rate through the lattice, thus leading to no detectable reduction on an integral level, but only in the subsurface. When titania is added to the catalyst (with 15 TiO_x layers), a red-shift of the band gap energy is observed, while the absorption between 500 and 800 nm still decreases, further evidencing that the increased absorption for the VO_x/CeO_2 sample is caused by vanadia d-d transitions. The band gap energy shift might be caused by the poisoning of ceria surface lattice oxygen by anchoring of titania, while titania itself is not yet crystallized and present in a significantly reduced state (see Section 3.2). Therefore, regeneration of ceria by gas-phase oxygen and oxygen transport from the bulk might be inhibited, leading to an observable degree of reduction. In comparison, the 90 TiO_x sample shows no red-shift of the band gap energy anymore, while the absorption caused by vanadia d-d
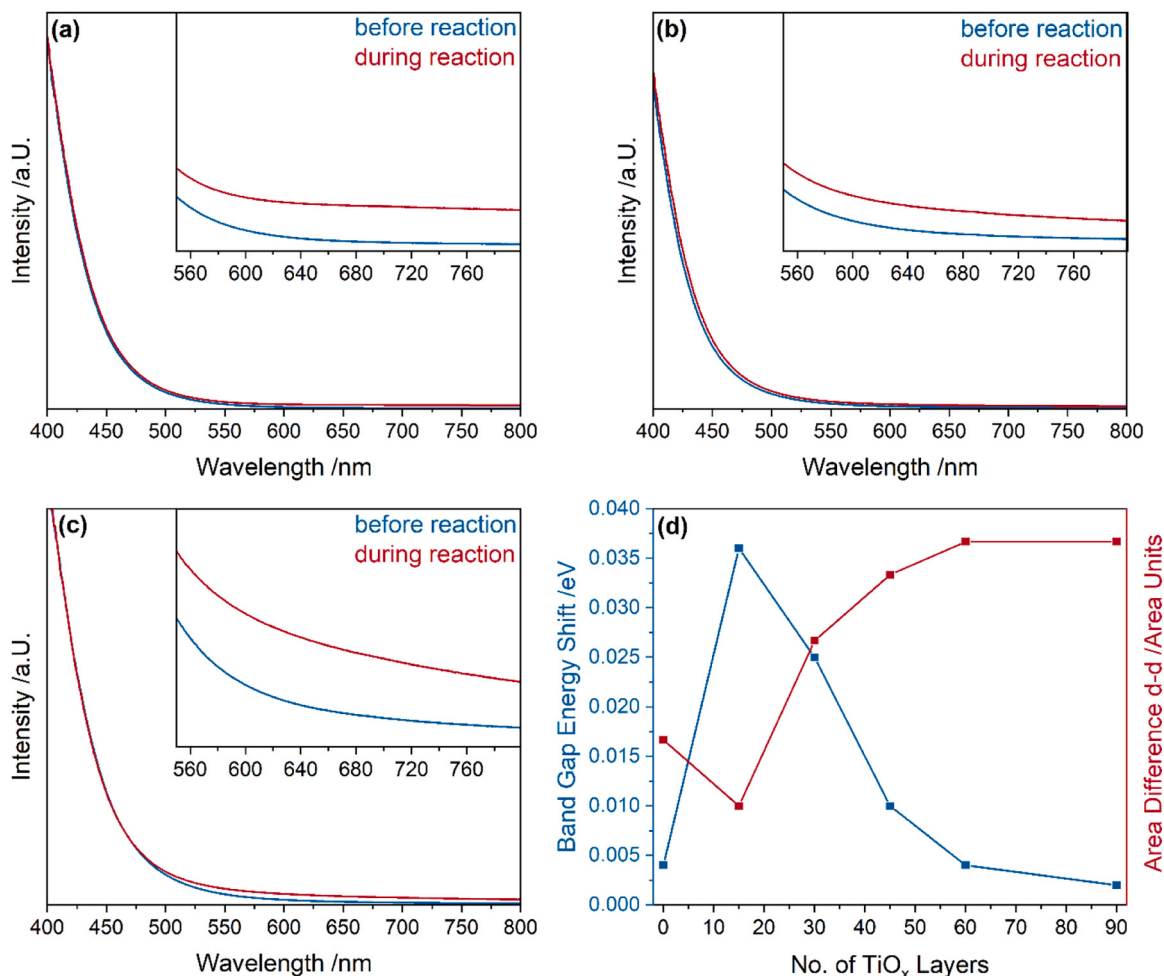
Fig. 5. Operando UV-Vis spectra of **(a)** CeO_2, **(b)** $15TiO_x + CeO_2$, and **(c)** 90 $TiO_x + CeO_2$ loaded with 1.2 V/nm^2, respectively, recorded under reactive (12.5% O_2/ 12.5% C_3H_8/He) and oxidative (12.5% O_2/He) conditions at 455 °C. The insets give an enlarged view of the visible region for clarity. **(d)** Band gap energy shifts and d-d transition area difference between reactive and oxidative conditions determined from operando UV-Vis spectra for CeO_2 coated with 0–90TiO_x layers and loaded with 1.2 V/nm^2.

transitions is increased significantly compared to the other two samples, which would be in agreement with our previous results regarding the VO_x/TiO_2 system, where titania lattice oxygen stays unchanged during the reaction and only facilitates hydrogen transfers, while vanadia delivers the oxygen atoms driving the oxidation reaction. However, we already described the participation of ceria lattice oxygen in the reaction, indicating the participation of all oxides in the reaction due to the introduced and, at this coating thickness, crystallized titania layer.

The detected changes in the band gap energy and the vanadia d-d transitions were quantified by using Tauc plots [25] and a least-square fitting analysis (see Experimental Section) of the UV-Vis spectra (see Fig. 5d). The band gap energy goes through a maximum for the 15 TiO_x sample, following an inverted trend of the crystallization of titania (see Fig. 2). The observed behaviour can be explained by a transition from a ceria- to a titania-dominated behaviour. For VO_x/CeO_2, regeneration is fast due to the high oxygen mobility in the ceria lattice compared to the titania lattice. The introduction of reduced and non-crystalline titania results in a strong reduction of the oxygen mobility due to the consumption of reactive surface oxygen sites, as indicated by the F_{2g} red-shift (see Fig. 4), leading to a decrease in conversion. The increase in the titania content facilitates crystallization into the anatase phase, starting at 30 layers of TiO_x, fully shifting the vanadia onto the titania, towards a titania-dominated behaviour. As a result, the band gap shifts decrease, as titania is not significantly reduced, fully reverting the band gap shift caused by ceria reduction at 90 layers of TiO_x, where titania

starts to appear in larger crystals as evidenced by quasi in situ XRD. Here, the F_{2g} red-shift is also decreased compared to the 60 TiO_x sample despite an increasing conversion, which is likely also caused by the now dominating behaviour of the VO_x/TiO_2 system, where only small amounts of ceria lattice oxygen still participate.

The vanadia d-d transitions show an inverted behaviour of the bandgap energy shifts, that is, increasingly more vanadia d-d transitions are observed when more of the titania crystallized and vanadia is supported by anatase rather than ceria. This also indicates that the described properties are in particular related to those of crystallized titania, as the more amorphous systems at 15, 30, 45, and 60 TiO_x layers do not show these properties to the same extent as the fully crystallized 90 TiO_x sample (see Fig. 2b). Importantly, the intensity of the vanadia d-d transitions does not go through a maximum, in contrast to the Vis-Raman results on the vanadyl area. This indicates that vanadia is more strongly reduced on the samples with more layers of TiO_x coating but is still participating in the reaction, as the trend of the vanadia d-d transitions correlates well with the observed selectivities. The only sample deviating from this trend is the 15 TiO_x sample, as the vanadia participation decreases compared to the VO_x/CeO_2 sample. This is explained by the strong presence of reduced and metallic vanadium species on this sample (see above). Therefore, almost none of the vanadium can be further reduced and the strong increase in selectivity between 0 and 15 layers of TiO_x can mostly be explained by the decreased conversions (see Fig. 1).

To investigate the formation of surface adsorbates and to follow the hydrogen dynamics during the reaction, quasi in situ and isotopic quasi in situ DRIFT spectra were recorded at room temperature (see Fig. 6). In addition, difference spectra between the spectra recorded after pre-treatment in oxidizing and reactive conditions and subsequent cooling to room temperature in pure helium are given, together with a quantification of the resulting area changes in the vanadyl, carbonate, and hydroxyl regions (see Fig. 6d-f).

Fig. 6a depicts exemplary DRIFT spectra of the 90 TiO_x sample after pre-treatment in oxidative and reactive conditions at 455 °C and subsequent cooling to room temperature in pure helium. An increase of the signals in the carbonate and hydroxyl regions at 1630, 3690, and 3745 cm^{-1} is observed. To facilitate identifying, which of these peaks can be related to the reaction and which to a hydrogen transfer, Fig. 6b shows the results of isotopic-exchange experiments, which reveal that all three peaks undergo a shift when the gas-phase is switched from reactive to isotopic conditions, while there is some intensity remaining at the peak located at 1630 cm^{-1}. To further quantify the observed changes, we used difference spectra between those recorded under oxidative and reactive conditions in comparison to VO_x/TiO_2 (see Fig. 6c). The most important changes are observed in the vanadyl region, while two significant peaks are observed in the carbonate region at 1575 and 1630 cm^{-1}, which are caused by adsorbates on the ceria surface, as their signals are already present for the VO_x/CeO_2 sample, while they are shifted compared to the bulk titania sample. The carbonate region exhibits much less intensity than that detected for VO_x/CeO_2 at 275 °C during the ODH of propane [7,9]. This is likely caused by the fact, that many of the adsorbates are not stable enough to withstand a temperature of 455 °C applied in this study and, as a consequence, only the most stable adsorbates in the carbonate region are detected [7,9]. In the hydroxyl region, the peaks at 3660 and 3745 cm^{-1} decrease in intensity,

while the peak at 3690 cm^{-1} increases in intensity with increasing amount of titania. The latter increase at 3690 cm^{-1} suggests this peak to be a titania-related feature, while the decrease at 3660 cm^{-1} almost disappears for the 90 TiO_x sample but is also present for bare ceria, indicating this to be a ceria-related hydroxyl group. A change in peak intensity at 3745 cm^{-1} is neither present for the bulk titania nor the bulk ceria sample, but was previously shown to be due to transient monodentate Ti-OH species on anatase or transient monodentate Ce-OH species, formed on the corresponding two-component systems [9]. Notably, water is formed during the reaction that is not fully purged during the spectra measurement and can be observed as a broad signal between 3300 and 3600 cm^{-1}, which may interact with OH groups and, as a result, lead to a shift in the OH positions. However, the positions observed in the difference spectra are all located at known positions for Ce-OH and Ti-OH groups, indicating that this influence appears to be negligible. The rate at which water was formed and lattice oxygen was regenerated was crucial for propane conversion and overoxidation reactions. As the intensity change is negative and the reducibility of the ceria is decreased significantly upon coating with titania, it seems more likely, that these species are not only observable under transient conditions but may also be observed in static experiments due to the slowed oxygen dynamics and the lower availability of ceria surface sites. Based on these arguments, the peak is attributed to a ceria-related species. Table 5 summarizes the assignments of the relevant peaks detected in the DRIFT spectra.

The results of the quantification of the six afore-mentioned peaks are shown in Fig. 6d-f. The quantification of the vanadyl peaks was performed via integration of the V=O overtone region between 1990 and 2150 cm^{-1}, as the V=O fundamental region is overlapped by the vibrations of either Ce-O [67–69] or Ti-O [8].

Starting with the quantification of the vanadyl region, the VO_x/CeO_2
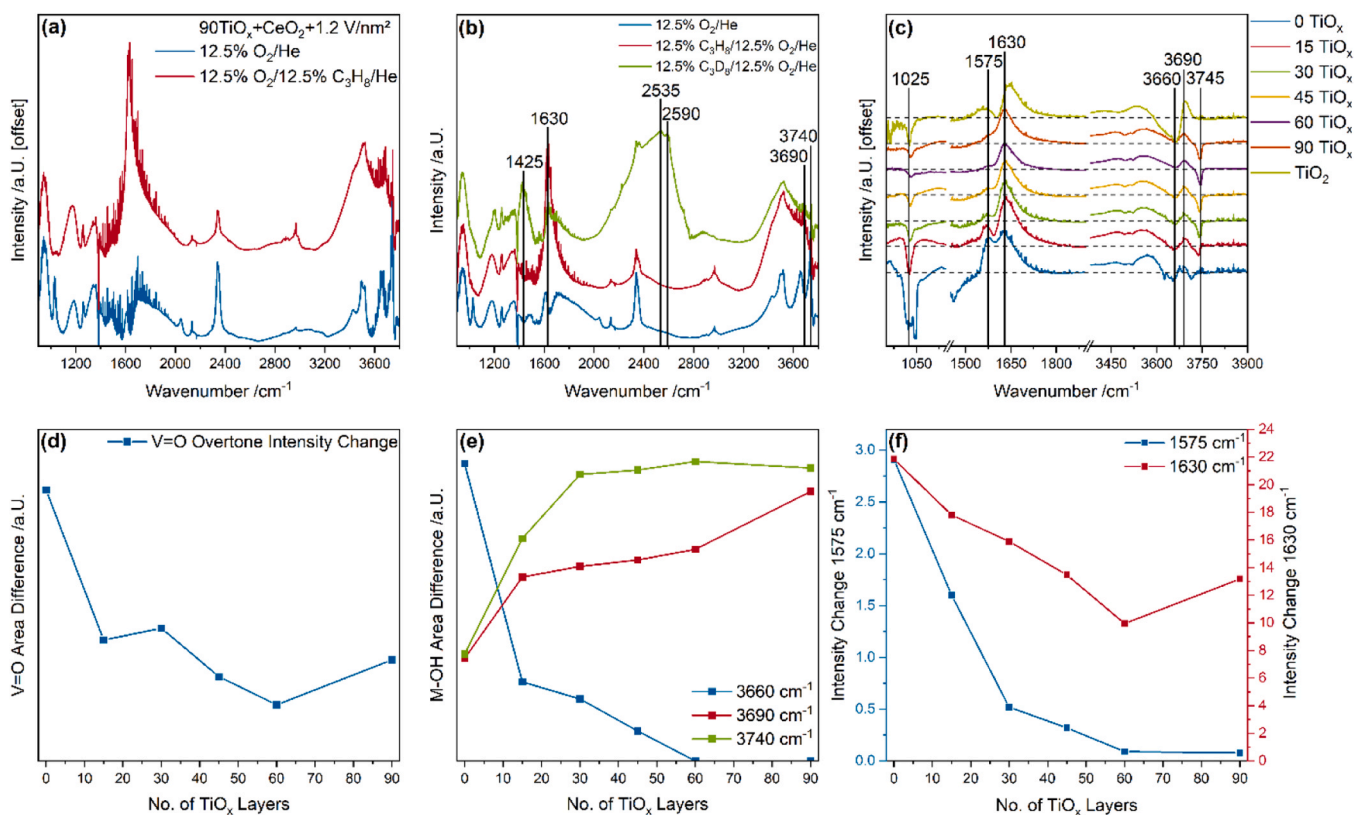
Fig. 6. Quasi in situ DRIFT spectra of $VO_x/TiO_x/CeO_2$ (1.2 V/nm^2) recorded at room temperature after treatment under **(a)** reactive (12.5% O_2/12.5% C_3H_8/He) and oxidative (12.5% O_2/He) and **(b)** isotopic (12.5% O_2/12.5% C_3D_8/He) conditions. **(c)** Difference spectra between reactive and oxidative conditions for $VO_x/TiO_x/CeO_2$ compared to VO_x/TiO_2. Relevant peaks in the vanadyl, carbonate, and hydroxyl regions are marked. Quantification of **(d)** the vanadyl area difference, **(e)** the hydroxyl area differences, and **(f)** the area difference in the carbonate region.

Table 5
Assignments of the relevant peaks detected in the quasi in situ DRIFT spectra of the $VO_x/TiO_x/CeO_2$ samples.

Wavenumber /cm^{-1}	Assignment	Reference
1025	Terminal V=O	[70]
1575	ν_{as} COO	[71]
1630	ν_{as} C=C	[71]
3660	Ce-OH II-B	[67]
3690	Bridged Ti-OH	[72]
3745	Ce-OH I-A	[67]

sample shows the most significant change of the vanadyl group between oxidizing and reactive conditions. This seems to contradict the operando Vis-Raman results at first sight, but it is possible that on the amorphous titania layer (especially at low amounts of TiO_x layers), some of the V=O groups might not be oriented towards the gas-phase, as they are integrated into the amorphous surface titania so that they are still detectable by XPS. This was previously observed for reduced V^{4+} species on titania under reductive and ODH conditions [73]. The vanadyl contribution then further decreases down to a minimum at a coating of 60 TiO_x layers. This is inverse to the Vis-Raman results, possibly indicating that the Vis-Raman spectra might detect the participation of species integrated into the amorphous surface titania layer before it fully crystallizes (see Fig. 2), which would be especially relevant below 60 layers of TiO_x. At $\geq$ 60 layers of TiO_x, the layer is mostly crystallized and the low participation of the V=O group is similar for the Vis-Raman and DRIFT spectra. Then, for the 90 TiO_x sample, the participation of the V=O group increases again, which might be caused by the formation of larger anatase crystallites, shifting the oxidation activity from ceria lattice oxygen towards vanadia, which is fully located on the anatase phase, while the amorphous amounts of titania further decrease. This would also be in agreement with the increasing conversion of the 90 TiO_x sample, despite the decrease in the F_{2g} red-shift (see Fig. 4), since the oxidation activity shifts to the vanadia. Furthermore, the overall degree of vanadia reduction (including strong vanadia reduction; see Fig. 5) correlates very well with the selectivity, indicating that vanadia is important for both the conversion and the selectivity of the 90 TiO_x sample, depending on its oxidation state (that is, the $V^{5+}{\rightarrow}V^{4+}$ transition is important for the conversion, while the $V^{4+}{\rightarrow}V^{3+}$ transition is important for the selectivity). Considering the total vanadia reduction, the amount of reduced vanadia increases with increasing titania coating and correlates with the observed selectivity. Besides, vanadia might still be regenerated by ceria, even when larger amounts of titania are introduced. This might occur when vanadia is anchored to titania but is still located in the proximity of ceria. With increasing titania loading, a regeneration will be less likely, leading to a smaller amount of V^{5+}, that is, a smaller number of vanadyl groups. Vanadia still participates in the reaction despite its strong reduction.

The quantification of the hydroxyl region shows that the Ce-OH peak at 3660 cm^{-1} participates less in the reaction when the amount of titania is increased, whereas the Ti-OH and the Ce-OH peaks at 3690 and 3745 cm^{-1} participate more strongly. However, only the peak at 3690 cm^{-1} increases in intensity. The bridged Ti-OH and Ce-OH species at 3660 and 3690 cm^{-1} that were suggested to allow for hydrogen storage due to their stable nature as bidentate species, were formed only after the ODH reaction [9,10]. On the other hand, the hydroxyl group located at 3740 cm^{-1} was previously determined to be highly relevant for the conversion of propane, as it was involved with the initial C-H bond breakage and the hydrogen transfer via V-OH towards the ceria surface. However, the transfer functions can also be performed by the anatase phase via a transient Ti-OH species, which is likely still the case for the present samples, but the temperatures required for the reaction to occur are too high for the application of transient IR spectroscopy. Therefore, the catalysis of this initial C-H bond breaking step via Ti-OH of anatase is somewhat speculative. However, since vanadia is present on the titania where it was previously shown to facilitate the reaction

instead of transferring the hydrogen (in contrast to VO_x/CeO_2) [8,9], it is still very likely for the anatase phase to facilitate the initial C-H bond breakage. It can therefore be expected that with increasing titania loading from 0 to 30 layers of TiO_x, this initial activation step is facilitated, explaining the increase in catalytic activity. The hydrogen is then transferred to the monodentate Ce-OH group at 3740 cm^{-1}, which leads to the formation of water and would be expected to be also transient for VO_x/CeO_2 due to the very fast regeneration of ceria surface lattice oxygen. However, because due the introduction of titania the oxygen mobility is strongly reduced, the group cannot be regenerated that quickly anymore. This is the reason, why it is absent for the VO_x/CeO_2 sample but then becomes more observable. The intensity decreases from oxidative to reactive conditions indicates that the hydroxyl groups at 3660 and 3745 cm^{-1} are consumed during the reaction. Since this transfer is highly important for the conversion of propane to either CO_x or propylene, the slow-down of the transfer rate to the Ce-OH group significantly increases the propylene selectivity compared to the CO_x formation. This is further highlighted by the perfect correlation between the intensity behaviour of the Ce-OH group at 3740 cm^{-1} and the observed selectivities.

Finally, the two most relevant peaks in the carbonate region were quantified, which are assigned to a carbonate vibration (1575 cm^{-1}), which was previously shown to be an important intermediate for CO_x formation [9], and to C=C stretching (1630 cm^{-1}) of formed propylene, which is adsorbed to the catalyst surface. The peak at 1630 cm^{-1} may also be assigned to deformation vibrations of water. However, the isotopic shift experiments showed that part of the peak shifts (indeed indicating that some water overlaps with this signal), while a significant peak intensity remains at this position, consistent with the C=C assignment. The peak at 1575 cm^{-1} decreases significantly when the amount of titania is increased. This might be caused by two different effects. First, ceria surface sites are blocked by titania, which is anchored to the surface via ceria surface oxygen. Secondly, the introduction of titania almost fully oxidizes the ceria surface, regenerating almost all oxygen vacancies, which would be beneficial to the formation of carbonate species. Therefore, the formation of adsorbates that lead to the formation of CO_x products is suppressed, increasing the selectivity again. The peak at 1630 cm^{-1} correlates to the propylene yield, as it is associated with propylene adsorbed in an acrylate-like geometry on the ceria surface, for which it needs to be in proximity to a vanadia species. This peak first decreases due to the decreasing conversion, but to a lesser extent than the carbonate peak due to the increased propylene selectivity. It increases again, when the amount of titania is increased from 60 to 90 layers, which might be caused by the yield of propylene that is increasing again, or the more crystallized anatase, that seems to locate more V^{5+} species on the surface (see discussion of Fig. 5d). Overall, multiple surface adsorbates were identified to participate in the reaction and to be of importance for the observed selectivity behaviour.

3.4. Structural and mechanistic summary

The most important mechanistic findings regarding selective propane conversion are summarized in Fig. 7 and will be discussed in the following. The ceria- and vanadia-based routes are shown in red and blue, respectively, which occur in parallel but not from the same propane molecule. Intermediates occurring in both routes are coloured in green. All hydrogen atoms involved in both reaction pathways are transferred via the initial transient Ti-OH group (green). The coloured dashed arrows indicate the direction of the hydrogen transfer, that is, the hydrogen atom initially transferred to the Ti-OH group is first transferred to the V-O-Ti/Ce-OH, before a second hydrogen atom is then abstracted to the titania surface again and a second Ti-OH group is formed at the same spot (see Fig. 7).

In the following, the results presented in the operando spectroscopic section will be summarized and discussed, and a mechanistic picture for $VO_x/TiO_x/CeO_2$ catalysts during propane ODH will be developed, based
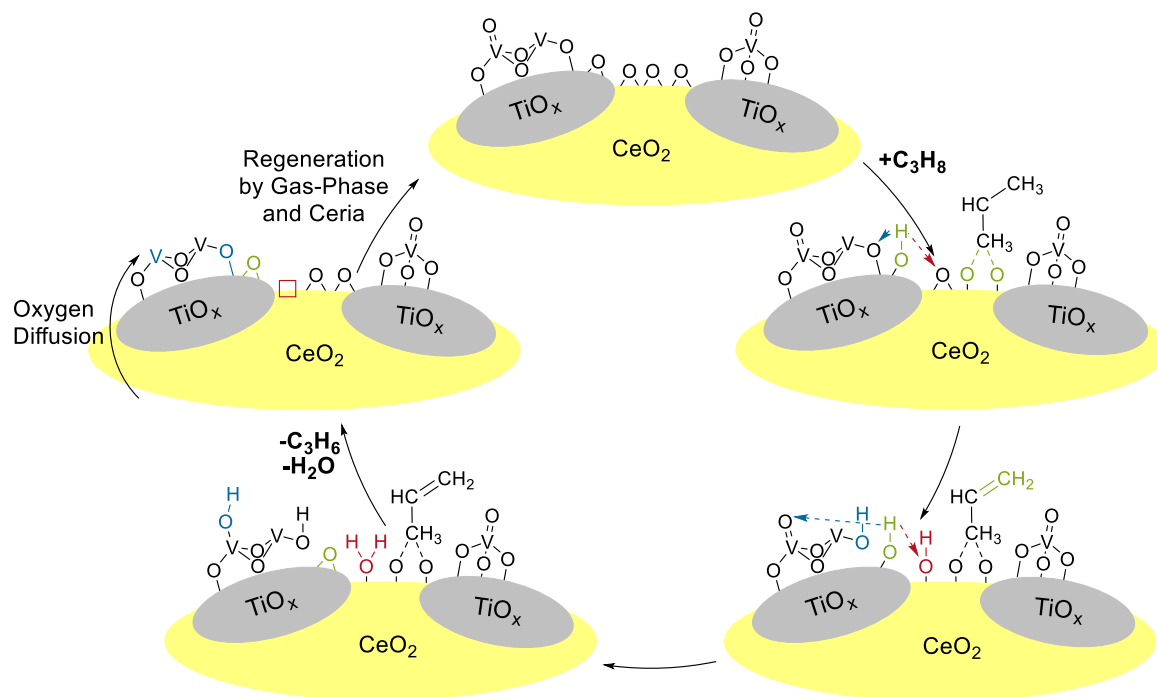
Fig. 7. Mechanistic scheme for $VO_x/TiO_x/CeO_2$ catalysts during propane ODH showing the most important interactions between VO_x, TiO_2, and CeO_2. For details see text.

on previous findings for the VO_x/CeO_2 and VO_x/TiO_2 systems [7–9], combined with the new operando spectroscopic results shown above, elucidating the interactions between vanadia, titania, and ceria. For clarity, we will focus on the most selective sample coated with 90 layers of TiO_x, whereas differences in comparison to the other samples were discussed above (see Sections 3.2 and 3.3).

The core of the investigated catalysts consists of a ceria particle, that is coated with (0−90) TiO_x layers anchored to ceria via surface oxygen atoms (see Fig. S4). The titania coating consists of amorphous or nanocrystalline anatase particles that begin to form larger particles at a coating of 90 TiO_x layers but start to crystallize at much lower loadings (see Fig. 2 and S4). Titania forms islands on the catalyst surface, leading to an exposure of part of the ceria surface to the gas phase, whereby the supported vanadia shifts increasingly from ceria to titania (see Fig. 2 and S5), thereby increasing its average oxidation state towards + 5. In this process, the ceria surface is almost fully oxidized, as the amount of Ce^{3+} detected in the (sub)surface decreases significantly while the amount of surface oxygen increases (see Figs. 2 and 3 as well as Tables 3 and 4). Some of the vanadia species might be encapsulated close to the catalyst surface in the amorphous or not fully crystallized titania (see Figs. 4 and 6).

The propane ODH mechanism starts by the initial hydrogen abstraction, which is likely to occur via a transient monodentate anatase Ti-OH group (first green Ti-OH). The V═O group is unlikely to transfer the initial hydrogen atom, as observed for the VO_x/CeO_2 system, since vanadia is not present on the ceria for $VO_x/TiO_x/CeO_2$ and shows structural dynamics participating in the redox process, like vanadia anchored to titania on VO_x/TiO_2. In a first scenario, the hydrogen atom can then either be transferred to the ceria surface forming a monodentate Ce-OH group (first red Ce-OH) or to vanadia located on the titania (first blue V-OH). Propane adsorbs in an acrylate-like geometry on the ceria surface, where it can be more strongly adsorbed than on titania. For the acrylate-like geometry to occur, the proximity to vanadia was previously observed to be necessary [9], which in this case is located on the titania, indicating that the adsorption site is close to the interface of all three oxides. The formed Ce-OH group reacts and regenerates more slowly than on bare ceria as the introduced titania reduces the oxygen

mobility in ceria. This leads to a reduction of the overoxidation potential of the Ce-OH group (see Fig. 6), showing changes in intensity between the samples, which strongly correlate with the observed selectivity behaviour. The formation of CO_x is further suppressed by the partial blocking of ceria surface oxygen by the anchored titania, and a reduction of the amount of carbonate species, which are crucial for the formation of CO_x.

A second reaction route may occur via vanadia, which is fully anchored to titania, but might be located in the proximity to the ceria surface. The initially abstracted hydrogen atom is transferred to the vanadia species (first blue V-OH), expected to be present mainly as monomeric and dimeric species [8]. For these species, the dimeric V-O-V and the monomeric V═O groups were shown to be of high importance to the overall conversion. Since only some of the titania supporting the vanadia species is present in the anatase phase and is therefore capable of the initial hydrogen transfer, the transfer rate of hydrogen to vanadia is slowed down, which decreases the conversion and, in turn, increases the selectivity.

The second hydrogen abstraction is proposed to be catalysed by the transient anatase Ti-OH group (green Ti-OH) again and can either be transferred to vanadia (blue V-OH) or ceria (red Ce-OH) again, where water is formed. The regeneration of ceria and vanadia is slowed down, because anchored titania is blocking ceria oxygen sites, which is evidenced by e.g., the vanadia reduction from V^{4+} to V^{3+} observed in UV-Vis spectra, which also correlates with the selectivity. The participation of titania supported V^{5+}, on the other hand, shows a varying behaviour, indicating that only some of the V═O species are directly exposed to the gas-phase. The V^{5+} contribution (see Figs. 4 and 6) is shown to contribute to the conversion and provides an explanation for the increased conversion of the 90 TiO_x sample, which shows less ceria lattice oxygen participation (see Fig. 4), but still higher conversion (see Fig. 1). This change might be caused by a further switch from ceria to titania dominated properties, due to the presence of larger anatase crystallites (see Fig. S3). The slowed regeneration rate of the vanadia species might either be caused by the presence of amorphous titania, changing its geometry, or due to the preferred regeneration by ceria, which is the most reducible oxide in the system, but only few vanadia

species might be close enough to the exposed ceria surface. This also explains the differing behaviour observed for oxidized V^{5+} and reduced $V^{3+/4+}$ species. The already reduced V^{4+} species (possibly V-OH formed from V=O) are still able to participate in the reaction but since the most reactive V=O group is already reduced (compare V=O trends in Figs. 4 and 6 correlated more with the conversion), hydrogen might be transferred to dimeric V-O-V or V-O-Ti interface bonds of already reduced species, which are likely more selective due to their lesser reducibility (compare vanadium d-d trend in Fig. 5 correlating with the selectivity behaviour). Since this bond is slowly regenerated (see Figs. 4–6), the hydrogen transfer is shifted away from the V=O group onto more selective bonds. The difference between the V=O trends in Figs. 4 and 6 is likely caused by the integration of some V^{4+} species into titania [73], making it inaccessible for DRIFTS, while the Vis-Raman spectra also probe the subsurface.

The above discussion shows that the additional interactions introduced by titania as a third oxygen component are complex. The presence of ceria and vanadia enables the hydrogen atom initially abstracted to the anatase to be transferred to different sites. The most active oxygen atoms of ceria are partly blocked by the anchored titania, and defects, that are beneficial to carbonate and eventually CO_x formation, are regenerated as titania almost fully oxidizes the ceria. The Ce-OH site used for the oxidation and water formation is also more slowly regenerated as titania decreases the overall oxygen dynamics of the system, thereby increasing the selectivity for the ceria route. On the vanadia route, hydrogen is expected to be transferred either to the titania supported monomeric or dimeric species, as no evidence for the presence of oligomers was found, but the regeneration of vanadia is slowed down, due to the reduced availability of ceria lattice oxygen. Due to this slowdown, the strong reduction of vanadia becomes more pronounced and the oxidation shifts from the V=O bond to more selective V-O-V and interface bonds, as they are more difficult to reduce, which is supported by the correlation of the surface exposed V^{5+} species with the conversion, while the strong reduction correlates with the observed selectivity for the catalyst.

4. Conclusions

In this work, we present a rational-design approach using an ALD-assisted synthesis of three oxide-component $VO_x/TiO_x/CeO_2$ catalysts for propane ODH. To identify the catalysts' structure and to investigate the oxide interactions under reaction conditions, the catalytic performance was determined and related to an extensive structural characterization, including operando multi-wavelength Raman and UV-Vis spectroscopy, as well as XRD, XPS, and DRIFTS.

A superior catalytic performance of the $VO_x/TiO_x/CeO_2$ catalyst, compared to the two-component oxides was found, showing selectivities of up to 80% at 3.9% conversion, which compares favourably with most literature-known catalysts at this conversion [3,4,6]. Based on the performed spectroscopy, we were able to identify key interactions between the three oxides that lead to the increased selectivities. First, titania forms islands on the ceria and nanocrystalline anatase particles are present mixed with amorphous titania. The titania layer anchors to ceria surface oxygen and oxidizes the ceria to a point where almost no Ce^{3+} states can be detected. The vanadia species are located on the titania and the titania islands still leave some ceria exposed to the gas phase. This structure enables the propane oxidation to occur via new reaction pathways, which facilitate the selective conversion of propane to propylene. As a starting point for both reaction pathways, the initial C-H bond breakage is proposed to be catalyzed by an previously identified transient Ti-OH group on anatase [8], while propane adsorbs in an acrylate-like geometry on the ceria surface in proximity to vanadia [9, 71]. Further hydrogen transfer may then proceed either via a ceria- or a vanadia-based route. The ceria-based route consists of a transfer to the remaining active surface lattice oxygen, forming Ce-OH and eventually water, while the vanadia-based route involves a transfer to either V=O,

V-O-V, or interface V-O-Ti species, whereby the transfer to V=O drives the conversion but might be less selective and produce some of the CO_x, while the shift towards a transfer to V-O-V and V-O-Ti leads to strong vanadia reduction and a more selective conversion.

Multiple interactions between the three oxides were identified by operando spectroscopy, which can be related to the increased selectivity of the catalyst. First, anchoring of titania blocks the most active ceria surface oxygen sites, while the consumption of ceria defects reduces the formation of C1 adsorbates on the ceria surface, which are crucial for CO_x formation. Second, the regeneration of ceria is slowed down by the presence of titania, decreasing the overall oxygen mobility, thus leading to a decrease in conversion and increase in selectivity. On the vanadia-based route, the regeneration of vanadia (V=O) by ceria is slowed down, as ceria is not always in proximity. Therefore, additional hydrogen may be transferred to more selective V-O-V and V-O-Ti sites, increasing the selectivity.

Based on our results, we were able to combine the three oxides in a synergetic way to increase the catalysts' selectivity. We identified important interactions between the oxides, leading to a mechanistic understanding mainly based on operando spectroscopic results and previous mechanistic knowledge of the two-component systems. The introduction of new methods to the mechanistic analysis of catalytic reactions, especially the use of transient IR spectroscopy, has led to a detailed understanding of the two-component systems, and has paved the way towards a rational-design approach as well as a mechanistic understanding of this more complex system.

Our approach may be transferable to other catalyst systems and reactions, (e.g. supported metal oxide systems) and highlight the level of understanding, which is currently available by applying state-of-the-art operando and transient spectroscopic methods.

Additional information

The supporting information to this article contains additional catalytic and structural characterization data as well as operando Raman, UV-Vis and XRD data, and results from further analyses.

CRediT authorship contribution statement

Leon Schumacher: Investigation, Methodology, Validation, Formal analysis, Writing – original draft, Visualization **Jun Shen:** Investigation, Formal analysis **Kathrin Hofmann:** Investigation, Formal analysis **Christian Hess:** Conceptualization, Writing – review & editing, Supervision, Project administration, Funding acquisition.

Declaration of Competing Interest

The authors declare that they have no known competing financial interests or personal relationships that could have appeared to influence the work reported in this paper.

Data availability

Data will be made available on request.

Acknowledgements

Appendix A. Supporting information

Supplementary data associated with this article can be found in the online version at doi:10.1016/j.cattod.2023.114387.

References

[1] F. Cavani, N. Ballarini, A. Cericola, Oxidative dehydrogenation of ethane and propane: how far from commercial implementation? Catal. Today 127 (2007) 113–131, https://doi.org/10.1016/j.cattod.2007.05.009.

[2] I. Amghizar, L.A. Vandewalle, K.M. van Geem, G.B. Marin, New trends in olefin production, Engineering 3 (2017) 171–178, https://doi.org/10.1016/j.eng.2017.02.006.

[3] C.A. Carrero, R. Schloegl, I.E. Wachs, R. Schomaecker, Critical literature review of the kinetics for the oxidative dehydrogenation of propane over well-defined supported vanadium oxide catalysts, ACS Catal. 4 (2014) 3357–3380, https://doi.org/10.1021/cs5003417.

[4] B. Beck, M. Harth, N.G. Hamilton, C. Carrero, J.J. Uhlrich, A. Trunschke, S. Shaikhutdinov, H. Schubert, H.-J. Freund, R. Schlögl, J. Sauer, R. Schomäcker, Partial oxidation of ethanol on vanadia catalysts on supporting oxides with different redox properties compared to propane, J. Catal. 296 (2012) 120–131, https://doi.org/10.1016/j.jcat.2012.09.008.

[5] K. Chen, A.T. Bell, E. Iglesia, Kinetics and mechanism of oxidative dehydrogenation of propane on vanadium, molybdenum, and tungsten oxides, J. Phys. Chem. B 104 (2000) 1292–1299, https://doi.org/10.1021/jp9933875.

[6] A. Dinse, B. Frank, C. Hess, D. Habel, R. Schomäcker, Oxidative dehydrogenation of propane over low-loaded vanadia catalysts: impact of the support material on kinetics and selectivity, J. Mol. Catal. A: Chem. 289 (2008) 28–37, https://doi.org/10.1016/j.molcata.2008.04.007.

[7] L. Schumacher, C. Hess, The active role of the support in propane ODH over VOx/CeO2 catalysts studied using multiple operando spectroscopies, J. Catal. 398 (2021) 29–43, https://doi.org/10.1016/j.jcat.2021.04.006.

[8] L. Schumacher, J. Pfeiffer, J. Shen, T. Gutmann, H. Breitzke, G. Buntkowsky, K. Hofmann, C. Hess, Collaborative mechanistic effects between vanadia and titania during the oxidative dehydrogenation of propane investigated by operando and transient spectroscopies, ACS Catal. (2023) 8139–8160, https://doi.org/10.1021/acscatal.3c01404.

[9] L. Schumacher, J. Weyel, C. Hess, Unraveling the active vanadium sites and adsorbate dynamics in VOx/CeO2 oxidation catalysts using transient IR spectroscopy, J. Am. Chem. Soc. 144 (2022) 14874–14887, https://doi.org/10.1021/jacs.2c06303.

[10] F. Arena, F. Frusteri, A. Parmaliana, How oxide carriers affect the reactivity of V2O5 catalysts in the oxidative dehydrogenation of propane, Catal. Lett. 60 (1999) 59–63, https://doi.org/10.1023/A:1019074016773.

[11] A. Christodoulakis, M. Machli, A.A. Lemonidou, S. Boghosian, Molecular structure and reactivity of vanadia-based catalysts for propane oxidative dehydrogenation studied by in situ Raman spectroscopy and catalytic activity measurements, J. Catal. 222 (2004) 293–306, https://doi.org/10.1016/j.jcat.2003.10.007.

[12] A. Kohdakov, J. Yang, S. Su, E. Iglesia, A. Bell, Structure and properties of vanadium oxide-zirconia catalysts for propane oxidative dehydrogenation, J. Catal. 177 (1998) 343–351, https://doi.org/10.1006/jcat.1998.2143.

[13] A.A. Lemonidou, L. Nalbandian, I.A. Vasalos, Oxidative dehydrogenation of propane over vanadium oxide based catalysts, Catal. Today 61 (2000) 333–341, https://doi.org/10.1016/S0920-5861(00)00393-X.

[14] G. Martra, F. Arena, S. Coluccia, F. Frusteri, A. Parmaliana, Factors controlling the selectivity of V2O5 supported catalysts in the oxidative dehydrogenation of propane, Catal. Today 63 (2000) 197–207, https://doi.org/10.1016/S0920-5861(00)00460-0.

[15] M. Puglisi, F. Arena, F. Frusteri, V. Sokolovskii, A. Parmaliana, Effect of vanadia loading in propane oxidative dehydrogenation on V2O5/SiO2 catalysts, Catal. Lett. 41 (1996) 41–43, https://doi.org/10.1007/BF00811710.

[16] D. Shee, T. Rao, G. Deo, Kinetic parameter estimation for supported vanadium oxide catalysts for propane ODH reaction: effect of loading and support, Catal. Today 118 (2006) 288–297, https://doi.org/10.1016/j.cattod.2006.07.017.

[17] G.G. Cortez, M.A. Bañares, A Raman spectroscopy study of alumina-supported vanadium oxide catalyst during propane oxidative dehydrogenation with online activity measurement, J. Catal. 209 (2002) 197–201, https://doi.org/10.1006/jcat.2002.3600.

[18] R. Bulánek, P. Čičmanec, M. Setnička, Possibility of VOx/SiO2 complexes speciation: comparative multi-wavelength Raman and DR UV–vis study, Phys. Proc. 44 (2013) 195–205, https://doi.org/10.1016/j.phpro.2013.04.024.

[19] S. Benomar, A. Massó, B. Solsona, R. Issaadi, J. López Nieto, Vanadium supported on alumina and/or zirconia catalysts for the selective transformation of ethane and methanol, Catalysts 8 (2018) 126, https://doi.org/10.3390/catal8040126.

[20] G. Triani, P.J. Evans, D.R.G. Mitchell, D.J. Attard, K.S. Finnie, M. James, T. Hanley, B. Latella, K.E. Prince, J. Bartlett, Atomic layer deposition of TiO2/Al2O3 films for optical applications, in: M.L. Fulton, J.D.T. Kruschwitz (Eds.), Advances in Thin-Film Coatings for Optical Applications II, SPIE, 2005, 587009.

[21] J. Lu, K.M. Kosuda, R.P. van Duyne, P.C. Stair, Surface Acidity and Properties of TiO2/SiO2 Catalysts Prepared by Atomic Layer Deposition: UV−visible Diffuse Reflectance, DRIFTS, and Visible Raman Spectroscopy Studies, J. Phys. Chem. C. 113 (2009) 12412–12418, https://doi.org/10.1021/jp902200c.

[22] N. Sobel, C. Hess, M. Lukas, A. Spende, B. Stühn, M.E. Toimil-Molares, C. Trautmann, Conformal SiO2 coating of sub-100 nm diameter channels of polycarbonate etched ion-track channels by atomic layer deposition, Beilstein J. Nanotechnol. 6 (2015) 472–479, https://doi.org/10.3762/bjnano.6.48.

[23] L. Schumacher, M. Ziemba, K. Brunnengräber, L. Totzauer, K. Hofmann, B.J.M. Etzold, B. Albert, C. Hess, Understanding the reduction behavior of VOx/CeO2 on a molecular level: combining temperature-programmed reduction with multiple in-situ spectroscopies and x-ray diffraction, J. Phys. Chem. C. 127 (2023) 5810–5824, https://doi.org/10.1021/acs.jpcc.3c00622.

[24] X. Jiang, M. Manawan, T. Feng, R. Qian, T. Zhao, G. Zhou, F. Kong, Q. Wang, S. Dai, J.H. Pan, Anatase and rutile in evonik aeroxide P25: Heterojunctioned or individual nanoparticles? Catal. Today 300 (2018) 12–17, https://doi.org/10.1016/j.cattod.2017.06.010.

[25] A. Filtschew, K. Hofmann, C. Hess, Ceria and its defect structure: new insights from a combined spectroscopic approach, J. Phys. Chem. C. 120 (2016) 6694–6703, https://doi.org/10.1021/acs.jpcc.6b00959.

[26] J. Shen, C. Hess, High Surface Area VOx/TiO2/SBA-15 Model Catalysts for Ammonia SCR Prepared by Atomic Layer Deposition, Catalysts 10 (2020) 1386, https://doi.org/10.3390/catal10121386.

[27] P. Ruff, L. Schumacher, S. Rogg, C. Hess, Atomic layer deposition-assisted synthesis of embedded vanadia catalysts, ACS Catal. 9 (2019) 6349–6361, https://doi.org/10.1021/acscatal.9b01385.

[28] A. Spende, N. Sobel, M. Lukas, R. Zierold, J.C. Riedl, L. Gura, I. Schubert, J.M.M. Moreno, K. Nielsch, B. Stühn, C. Hess, C. Trautmann, M.E. Toimil-Molares, TiO2, SiO2, and Al2O3 coated nanopores and nanotubes produced by ALD in etched ion-track membranes for transport measurements, Nanotechnology 26 (2015) 335301, https://doi.org/10.1088/0957-4484/26/33/335301.

[29] P.S. Waleska, C. Hess, Oligomerization of supported vanadia: structural insight using surface-science models with chemical complexity, J. Phys. Chem. C. 120 (2016) 18510–18519, https://doi.org/10.1021/acs.jpcc.6b01672.

[30] C. Hess, Direct correlation of the dispersion and structure in vanadium oxide supported on silica SBA-15, J. Catal. 248 (2007) 120–123, https://doi.org/10.1016/j.jcat.2007.02.024.

[31] C.T. Nottbohm, C. Hess, Investigation of ceria by combined Raman, UV–vis and X-ray photoelectron spectroscopy, Catal. Commun. 22 (2012) 39–42, https://doi.org/10.1016/j.catcom.2012.02.009.

[32] M. Ziemba, L. Schumacher, C. Hess, Reduction behavior of cubic In2O3 nanoparticles by combined multiple in situ spectroscopy and DFT, J. Phys. Chem. Lett. 12 (2021) 3749–3754, https://doi.org/10.1021/acs.jpclett.1c00892.

[33] A. Laachir, V. Perrichon, A. Badri, J. Lamotte, E. Catherine, J.C. Lavalley, J. El Fallah, L. Hilaire, F. Le Normand, E. Quéméré, G.N. Sauvion, O. Touret, Reduction of CeO2 by hydrogen. Magnetic susceptibility and Fourier-transform infrared, ultraviolet and X-ray photoelectron spectroscopy measurements, J. Chem. Soc., Faraday Trans. 87 (1991) 1601–1609, https://doi.org/10.1039/FT9918701601.

[34] Handbook of X-ray photoelectron spectroscopy: A reference book of standard spectra for identification and interpretation of XPS data, Perkin-Elmer Corporation, Eden Prairie, Minn., 1992.

[35] P. Oelhafen, Practical surface analysis by auger and X-ray photoelectron spectroscopy, J. Electron Spectrosc. Relat. Phenom. 34 (1984) 203, https://doi.org/10.1016/0368-2048(84)80044-4.

[36] P. Viparelli, P. Ciambelli, L. Lisi, G. Ruoppolo, G. Russo, J.C. Volta, Oxidative dehydrogenation of propane over vanadium and niobium oxides supported catalysts, Appl. Catal. A: Gen. 184 (1999) 291–301, https://doi.org/10.1016/S0926-860X(99)00104-0.

[37] U. Balachandran, N.G. Eror, Raman spectra of titanium dioxide, J. Solid State Chem. 42 (1982) 276–282, https://doi.org/10.1016/0022-4596(82)90006-8.

[38] C. Schilling, C. Hess, Real-Time Observation of the Defect Dynamics in Working Au/CeO2 Catalysts by Combined Operando Raman/UV–Vis Spectroscopy, J. Phys. Chem. C. 122 (2018) 2909–2917, https://doi.org/10.1021/acs.jpcc.8b00027.

[39] C.S. Campos, E.R. Spada, F.R. Paula, F.T. Reis, R.M. Faria, M.L. Sartorelli, Raman and XRD study on brookite-anatase coexistence in cathodic electrosynthesized titania, J. Raman Spectrosc. 43 (2012) 433–438, https://doi.org/10.1002/jrs.3048.

[40] A. Iglesias-Juez, M.V. Martínez-Huerta, E. Rojas-García, J.-M. Jehng, M.A. Bañares, On the Nature of the Unusual Redox Cycle at the Vanadia Ceria Interface, J. Phys. Chem. C. 122 (2018) 1197–1205, https://doi.org/10.1021/acs.jpcc.7b09832.

[41] C. Schilling, A. Hofmann, C. Hess, M.V. Ganduglia-Pirovano, Raman spectra of polycrystalline CeO2 a density functional theory study, J. Phys. Chem. C. 121 (2017) 20834–20849, https://doi.org/10.1021/acs.jpcc.7b06643.

[42] M. Lohrenscheit, C. Hess, Direct evidence for the participation of oxygen vacancies in the oxidation of carbon monoxide over ceria-supported gold catalysts by using operando Raman spectroscopy, ChemCatChem 8 (2016) 523–526, https://doi.org/10.1002/cctc.201501129.

[43] B. Huang, R. Gillen, J. Robertson, Study of CeO2 and its native defects by density functional theory with repulsive potential, J. Phys. Chem. C. 118 (2014) 24248–24256, https://doi.org/10.1021/jp506625h.

[44] M. Landmann, E. Rauls, W.G. Schmidt, The electronic structure and optical response of rutile, anatase and brookite TiO2, J. Phys. Condens. Matter 24 (2012) 195503, https://doi.org/10.1088/0953-8984/24/19/195503.

[45] B. Choudhury, A. Choudhury, Oxygen defect dependent variation of band gap, Urbach energy and luminescence property of anatase, anatase–rutile mixed phase and of rutile phases of TiO2 nanoparticles, Phys. E 56 (2014) 364–371, https://doi.org/10.1016/j.physe.2013.10.014.

[46] Z. Wu, A.J. Rondinone, I.N. Ivanov, S.H. Overbury, Structure of vanadium oxide supported on ceria by multiwavelength Raman spectroscopy, J. Phys. Chem. C. 115 (2011) 25368–25378, https://doi.org/10.1021/jp2084605.

[47] M. Baron, H. Abbott, O. Bondarchuk, D. Stacchiola, A. Uhl, S. Shaikhutdinov, H.-J. Freund, C. Popa, M.V. Ganduglia-Pirovano, J. Sauer, Resolving the atomic structure of vanadia monolayer catalysts: monomers, trimers, and oligomers on ceria, Angew. Chem. Int. Ed. 121 (2009) 8150–8153, https://doi.org/10.1002/ange.200903085.

[48] T. Kropp, J. Paier, J. Sauer, Support effect in oxide catalysis: methanol oxidation on vanadia/ceria, J. Am. Chem. Soc. 136 (2014) 14616–14625, https://doi.org/10.1021/ja508657c.

[49] J.I. Flege, B. Kaemena, S. Gevers, F. Bertram, T. Wilkens, D. Bruns, J. Bätjer, T. Schmidt, J. Wollschläger, J. Falta, Silicate-free growth of high-quality ultrathin cerium oxide films on Si(111), Phys. Rev. B 84 (2011), https://doi.org/10.1103/PhysRevB.84.235418.

[50] A. Allahgholi, J.I. Flege, S. Thieß, W. Drube, J. Falta, Oxidation-state analysis of ceria by X-ray photoelectron spectroscopy, ChemPhysChem 16 (2015) 1083–1091, https://doi.org/10.1002/cphc.201402729.

[51] W. Göpel, J.A. Anderson, D. Frankel, M. Jaehnig, K. Phillips, J.A. Schäfer, G. Rocker, Surface defects of TiO$_2$(110): a combined XPS, XAES and ELS study, Surf. Sci. 139 (1984) 333–346, https://doi.org/10.1016/0039-6028(84)90054-2.

[52] R. Nawaz, C.F. Kait, H.Y. Chia, M.H. Isa, L.W. Huei, Glycerol-mediated facile synthesis of colored titania nanoparticles for visible light photodegradation of phenolic compounds, Nanomater 9 (2019), https://doi.org/10.3390/nano9111586.

[53] Z. Zhang, V.E. Henrich, Electronic interactions in the vanadium/TiO$_2$(110) and vanadia/TiO$_2$(110) model catalyst systems, Surf. Sci. 277 (1992) 263–272, https://doi.org/10.1016/0039-6028(92)90767-Z.

[54] J.M. Won, M.S. Kim, S.C. Hong, Effect of vanadium surface density and structure in VO$_x$/TiO$_2$ on selective catalytic reduction by NH$_3$, Korean J. Chem. Eng. 35 (2018) 2365–2378, https://doi.org/10.1007/s11814-018-0158-x.

[55] D.W. Kwon, K.H. Park, S.C. Hong, Influence of VO$_x$ surface density and vanadyl species on the selective catalytic reduction of NO by NH$_3$ over VO$_x$/TiO$_2$ for superior catalytic activity, Appl. Catal. A: Gen. 499 (2015) 1–12, https://doi.org/10.1016/j.apcata.2015.04.005.

[56] L. Arnarson, H. Falsig, S.B. Rasmussen, J.V. Lauritsen, P.G. Moses, A complete reaction mechanism for standard and fast selective catalytic reduction of nitrogen oxides on low coverage VO$_x$/TiO$_2$(001) catalysts, J. Catal. 346 (2017) 188–197, https://doi.org/10.1016/j.jcat.2016.12.017.

[57] C. Penschke, J. Paier, J. Sauer, Oligomeric vanadium oxide species supported on the CeO$_2$(111) surface: structure and reactivity studied by density functional theory, J. Phys. Chem. C. 117 (2013) 5274–5285, https://doi.org/10.1021/jp400520j.

[58] L.J. Burcham, G. Deo, X. Gao, I.E. Wachs, In situ IR, Raman, and UV-Vis DRS spectroscopy of supported vanadium oxide catalysts during methanol oxidation, Top. Catal. 11/12 (2000) 85–100, https://doi.org/10.1023/A:1027275225668.

[59] P. Shvets, O. Dikaya, K. Maksimova, A. Goikhman, A review of Raman spectroscopy of vanadium oxides, J. Raman Spectrosc. 50 (2019) 1226–1244, https://doi.org/10.1002/jrs.5616.

[60] Z. Wu, H.-S. Kim, P.C. Stair, S. Rugmini, S.D. Jackson, On the structure of vanadium oxide supported on aluminas: UV and visible raman spectroscopy, UV–visible diffuse reflectance spectroscopy, and temperature-programmed reduction studies, J. Phys. Chem. B 109 (2005) 2793–2800, https://doi.org/10.1021/jp046011m.

[61] M. de Oliveira, D. Seeburg, J. Weiß, S. Wohlrab, G. Buntkowsky, U. Bentrup, T. Gutmann, Structural characterization of vanadium environments in MCM-41 molecular sieve catalysts by solid state ^{51}V NMR, Catal. Sci. Technol. 9 (2019) 6180–6190, https://doi.org/10.1039/C9CY01410A.

[62] C.W.M. Castleton, J. Kullgren, K. Hermansson, Tuning LDA+U for electron localization and structure at oxygen vacancies in ceria, J. Chem. Phys. 127 (2007), 244704, https://doi.org/10.1063/1.2800015.

[63] C. Binet, A. Badri, J.-C. Lavalley, A spectroscopic characterization of the reduction of ceria from electronic transitions of intrinsic point defects, J. Phys. Chem. 98 (1994) 6392–6398, https://doi.org/10.1021/j100076a025.

[64] B. Lamoureux, V.R. Singh, V. Jovic, J. Kuyyalil, T.-Y. Su, K.E. Smith, Structural and electronic properties of thermally evaporated V$_2$O$_5$ epitaxial thin films, Thin Solid Films 615 (2016) 409–414, https://doi.org/10.1016/j.tsf.2016.07.062.

[65] A. Brückner, Killing three birds with one stone: simultaneous operando EPR/UV–vis/Raman spectroscopy for monitoring catalytic reactions, Chem. Commun. (2005) 1761–1763, https://doi.org/10.1039/b418790c.

[66] N.V. Skorodumova, R. Ahuja, S.I. Simak, I.A. Abrikosov, B. Johansson, B. I. Lundqvist, Electronic, bonding, and optical properties of CeO$_2$ and Ce$_2$O$_3$ from first principles, Phys. Rev. B 6411 (2001), 115108.

[67] A. Badri, C. Binet, J.-C. Lavalley, An FTIR study of surface ceria hydroxy groups during a redox process with H$_2$, J. Chem. Soc., Faraday Trans. 92 (1996) 4669, https://doi.org/10.1039/FT9969204669.

[68] Y. Ji, T.J. Toops, U.M. Graham, G. Jacobs, M. Crocker, A kinetic and DRIFTS study of supported Pt catalysts for NO oxidation, Catal. Lett. 110 (2006) 29–37, https://doi.org/10.1007/s10562-006-0100-4.

[69] C. Li, Y. Sakata, T. Arai, K. Domen, K.-i Maruya, T. Onishi, Carbon monoxide and carbon dioxide adsorption on cerium oxide studied by Fourier-transform infrared spectroscopy. Part 1. - Formation of carbonate species on dehydroxylated CeO$_2$, at room temperature, J. Chem. Soc., Faraday Trans. 185 (1989) 929, https://doi.org/10.1039/f19898500929.

[70] D. Nitsche, C. Hess, Structure of isolated vanadia and titania: a deep UV Raman, UV–Vis, and IR spectroscopic study, J. Phys. Chem. C. 120 (2016) 1025–1037, https://doi.org/10.1021/acs.jpcc.5b10317.

[71] Z. Hu, Z. Wang, Y. Guo, L. Wang, Y. Guo, J. Zhang, W. Zhan, Total oxidation of propane over a Ru/CeO$_2$ catalyst at low temperature, Environ. Sci. Technol. 52 (2018) 9531–9541, https://doi.org/10.1021/acs.est.8b03448.

[72] M.I. Zaki, H. Knözinger, Carbon monoxide - A low temperature infrared probe for the characterization of hydroxyl group properties on metal oxide surfaces, Mater. Chem. Phys. 17 (1987) 201–215, https://doi.org/10.1016/0254-0584(87)90056-3.

[73] M.V. Martínez-Huerta, J.L.G. Fierro, M.A. Bañares, Monitoring the states of vanadium oxide during the transformation of TiO$_2$ anatase-to-rutile under reactive environments: H$_2$ reduction and oxidative dehydrogenation of ethane, Catal. Commun. 11 (2009) 15–19, https://doi.org/10.1016/j.catcom.2009.08.002.

4.4 Investigation of Fe$_2$(MoO$_4$)$_3$ during Alcohol and Alkane ODH Reactions

The fourth part of this work deals with the investigation of bulk oxides compared to supported oxides as catalysts for the ODH of different substrates using O$_2$ as the oxidizing agent. This catalyst is of relevance due to its high activity and selectivity during methanol ODH, which can be attributed to its unique structure. However, due to the complex behavior of bulk oxide catalysts, a detailed mechanistic understanding of Fe$_2$(MoO$_4$)$_3$ under ODH conditions has not yet been obtained. To contribute to the catalysts understanding, methods developed during this work, applied to supported vanadia catalysts, were transferred to Fe$_2$(MoO$_4$)$_3$ to understand the its properties and and reaction mechanism during propane ODH on a molecular level.

4.4.1 Activity, Selectivity and Initial Degradation of Iron Molybdate in the Oxidative Dehydrogenation of Ethanol

The tenth overall publication aims to investigate the reaction behavior of differently synthesized iron molybdates (ball milling and co-precipitation) during ethanol ODH and to characterize their structure using Mössbauer, XPS and Raman spectroscopy, as well as XRD and SEM imaging. For this work, Raman and XP spectroscopic investigations of Fe$_2$(MoO$_4$)$_3$ before and after ethanol ODH were contributed to understand the catalysts behavior. This work was part of the CRC 1487 and was an important basis for further mechanistic investigations of the material under propane ODH conditions. Both materials are highly active and stable under reaction conditions, while the ball milled sample shows lower activities and a lower Mo-content on its surface. Therefore, the Mo/Fe ratio was identified as an important descriptor for the activity and selectivity towards acetaldehyde during the ethanol ODH. Analogue to the methanol ODH, the depletion of surface molybdenum was identified as a main deactivation route of the catalyst. This study acts as an important basis in regard to synthesis and characterization of iron molybdates.

Activity, Selectivity and Initial Degradation of Iron Molybdate in the Oxidative Dehydrogenation of Ethanol

Niklas Oefner,[a] Franziska Heck,[b] Marcel Dürl,[c] Leon Schumacher,[d]
Humera Khatoon Siddiqui,[e] Ulrike I. Kramm,[e] Christian Hess,[d] Angela Möller,[c]
Barbara Albert,[b] and Bastian J. M. Etzold*[a]

Iron molybdate catalysts are applied in the industrial *FormOx* process to produce formaldehyde by oxidative dehydrogenation (ODH) of methanol. Only few studies are available about the applicability of iron molybdate catalysts for the ODH of ethanol to produce acetaldehyde. Herein, an iron molybdate synthesized by co-precipitation (p) and an iron molybdate prepared by a ball-milling solid-state synthesis (bm) are applied as ethanol ODH catalysts. Both materials show attractive acetaldehyde selectivites of $>90\%$ (280 °C: p-Fe$_2$(MoO$_4$)$_3$: $Y_{AcH} = 90.3\%$; bm-Fe$_2$(MoO$_4$)$_3$: $Y_{AcH} = 60.4\%$) and a stable performance.

The bulk composition and crystal structure could be confirmed by various characterization techniques and is maintained during ethanol ODH. XPS reveals an enrichment of Mo on the catalyst surface which is slightly decreasing after the catalytic tests. This observation could be a first sign of long-term deactivation like known from methanol ODH. Comparing the performance of both materials, p-Fe$_2$(MoO$_4$)$_3$ shows higher activity and aldehyde selectivity. We propose the higher Mo/Fe surface ratio and the lower acidity to be the reasons for these differences.

Introduction

In 2020, fossil resources like crude oil, natural gas and coal represented 85% of feedstocks in the global carbon-based chemical industry.[1] For the aspired defossilization of the chemical industry it is indispensable to provide strategies in order to substitute these fossil resources. In such a circular economy, these substitutes can be either waste streams or renewable resources. A commodity that is already produced in large scale based on renewable resources is ethanol. In 2019, 109 billion liters of ethanol were globally produced from sugar or starch containing resources like corn, sugar cane and sugar beets, and the production is predicted to increase to 130 billion liters in 2024.[2,3] Besides the production of bioethanol from sugar containing raw materials, a second-generation bioethanol production is rising. These new techniques are able to convert cellulosic plant parts like straw or residues into so-called cellulosic ethanol.[4]

Most of the produced bioethanol is added to gasoline to produce biofuels but bioethanol is also used as a feedstock in the chemical industry. There are several plants, for example by Braskem, Chematur, British petroleum or Axens which produce ethylene by dehydration of bioethanol on an industrial scale.[4] The Braskem ethylene plant in Brazil, which started operation in 2010, produces 200 000 t a^{-1}. This so-called bioethylene is further used to produce bio-based polymers like polyethylene.

Besides ethylene, bioethanol can be used as a sustainable feedstock to produce other important platform chemicals like acetaldehyde, acetic acid, ethyl acetate, ETBE etc.[5] The selective oxidation of ethanol leads to acetaldehyde:

$$CH_3CH_2OH\,(g) + 0.5\,O_2\,(g) \rightarrow CH_3CHO\,(g) + H_2O\,(g)$$
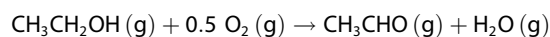
$$\Delta_R H = -177\,kJ\,mol^{-1}$$

Today, acetaldehyde is produced by the Wacker-Hoechst process through oxidation of ethylene.[6] Here, ethylene is oxidized in aqueous solution at 100–130 °C using a PdCl$_2$/CuCl$_2$ catalyst.[6] The low reaction temperature in the Wacker-Hoechst process hinders efficient usage of the heat of reaction. In contrast, a gas-phase conversion like the ethanol ODH operating at higher temperatures would allow employing the heat of reaction more efficiently, leading to a decrease of the overall energy and CO$_2$ footprint of the process.[7] Besides this energetic aspect and the clear advantage of using bioethanol as a

[a] N. Oefner, Prof. B. J. M. Etzold
Ernst-Berl-Institut für Makromolekulare und Technische Chemie
Technische Universität Darmstadt
Alarich-Weiß-Straße 8, 64287 Darmstadt (Germany)
E-mail: bastian.etzold@tu-darmstadt.de
[b] F. Heck, Prof. B. Albert
Eduard-Zintl-Institut für Anorganische und Physikalische Chemie
Technische Universität Darmstadt
Alarich-Weiß-Straße 12, 64287 Darmstadt (Germany)
[c] M. Dürl, Prof. A. Möller
Department of Chemistry
Johannes Gutenberg-University Mainz
Duesbergweg 10–14, 55128 Mainz
(Germany)
[d] L. Schumacher, Prof. C. Hess
Eduard-Zintl-Institut für Anorganische und Physikalische Chemie
Technische Universität Darmstadt
Alarich-Weiß-Straße 12, 64287 Darmstadt (Germany)
[e] H. Khatoon Siddiqui, Prof. U. I. Kramm
Eduard-Zintl-Institut für Anorganische und Physikalische Chemie
Technische Universität Darmstadt
Alarich-Weiß-Straße 12, 64287 Darmstadt (Germany)

sustainable feedstock, the ODH of ethanol can be applied to many catalyst systems, preventing the usage of critical raw materials like palladium that is used in the Wacker-Hoechst process.

Due to this attractiveness, different catalyst systems have been studied for ethanol ODH. The main classes of investigated catalysts are supported metal oxides, mainly supported VO_x,[7–24] mixed metal oxides,[25,26] supported metal catalysts[27–30] or carbon-based catalysts.[31–33] Supported vanadium oxide catalysts show high activity in the ODH of ethanol. Activity and selectivity strongly depend on the nature of the support material, where the activity increases with increasing metal-support-interaction.[7,23] High acetaldehyde selectivity and a yield of around 90% could be reached with a VO_x/TiO_2 catalyst.[13] Besides supported metal oxides, supported metal catalysts, especially the coinage metals, have been investigated as ethanol dehydrogenation catalysts. For example, Liu et al. used gold nanoparticles supported on $(Mg,Cu)Cr_2O_4$ spinel as ethanol ODH catalyst with an acetaldehyde yield of 95%.[30]

Only few studies used mixed metal oxides as ethanol ODH catalysts. $MoVO_x$ catalysts, which are applied industrially in the oxidation of acrolein to acrylic acid, also show promising results in the selective oxidation of ethanol.[26] By doping $MoVO_x$ mixed oxides with tellurium, Sobolev et al. performed temperature programmed reactions with 2 vol% ethanol and 18 vol% oxygen on a $MoV_{0.3}Te_{0.2}O_x$ catalyst and reached nearly quantitative yield of acetaldehyde at 220 °C.[26]

Another mixed oxide system that is employed industrially on a large scale within the *FormOx* process is iron molybdate.[34–36] In this case, methanol is directly oxidized with oxygen to formaldehyde at temperatures between 260 and 400 °C.

$$CH_3OH\ (g) + 0.5\ O_2\ (g) \rightarrow CH_2O\ (g) + H_2O\ (g)$$
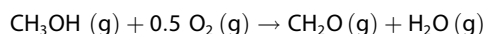
$$\Delta_R H = -147\ kJ\ mol^{-1}$$

At nearly full conversion, the selectivity to formaldehyde still exceeds 90%, leading to overall plant yields of 88–91%.[34] Besides the attractive activity and selectivity of iron molybdates in methanol ODH, the catalytic system suffers from deactivation through molybdenum depletion. Under reaction conditions, volatile molybdenum-oxy-methoxy or molybdenum-oxy-hydroxy species are formed and sublimated from the surface leaving behind a molybdenum depleted catalyst.[37–40] These volatile species decompose in colder zones of the reactor and deposit between the catalyst pellets, blocking the reactor and causing increased pressure drops.[41]

Nevertheless, iron molybdate catalysts show great performance in methanol ODH and are available on large scale. Concerning the applicability of iron molybdates as catalysts for the ethanol ODH reaction only few studies are available.[42–45] These studies had either a different intention (e.g. application in planar ethanol sensors;[42] direct 1,1-diethoxyethane production[44]) or operated at low degree of conversion (<30%) and time on streams[45] or at very high temperatures (350 °C)[43],

thus making an assessment of the applicability of iron molybdate catalysts for ethanol ODH difficult.

In this work, the suitability of $Fe_2(MoO_4)_3$ as catalyst for ethanol ODH is studied. In addition to a classical precipitation-based synthesis route, iron molybdate stemming from a modified ball-milling solid-state synthesis is employed. The catalysts are benchmarked in methanol ODH, since a substantial amount of literature data is available for comparison. The activity, selectivity, and stability of the catalyst in ethanol ODH is investigated in detail. Extensive characterization prior and after catalysis is carried out, employing SEM-EDX, N_2-physisorption, ICP-OES, XRD, XPS, Raman and Mössbauer spectroscopy to investigate reaction-induced changes in structure and composition of the materials. Due to the strong interlink of characterization prior and after catalysis and catalytic performance itself, all results are presented first and afterwards the discussion is based on the full holistic picture.

Results

In the following sections, iron molybdate prepared by the classical co-precipitation method from iron nitrate and ammonium heptamolybdate is referred to as $p-Fe_2(MoO_4)_3$ and iron molybdate synthesized by ball-milling solid-state reaction from Fe_2O_3 and MoO_3 is labelled $bm-Fe_2(MoO_4)_3$. The material that was used for the ethanol ODH temperature cycling experiments is extensively characterized and labelled "spent" material.

Ethanol ODH. Both iron molybdate catalysts were tested for ethanol ODH in a continuous flow tube reactor. First, the catalysts were pre-treated with the reaction mixture at 280 °C till steady-state behavior was reached (see Figure S1, supporting information). After this induction period of approximately 20 h isothermal catalytic experiments between 200 and 300 °C were carried out. The carbon mole balance during temperature cycling was 98.5–100%. The resulting degree of conversion of ethanol and the acetaldehyde selectivity are shown in Figure 1a and b. Besides the desired product acetaldehyde, formation of ethylene and CO was detected. Over two hours at 200 °C, $p-Fe_2(MoO_4)_3$ shows an increase in degree of conversion from 12 to 17%. For all other temperatures and both materials steady-state could be reached and stable degrees of conversion and selectivity were observed. The steady-state values of degree of conversion and selectivities to the reaction products are shown in Figure 1c and d. Below 280 °C, both catalysts show a high acetaldehyde selectivity of >95%. Only at high conversions ($X > 90\%$) formation of ethylene and small amounts of CO_x are detected for $p-Fe_2(MoO_4)_3$. At 280 °C $p-Fe_2(MoO_4)_3$ shows an activity of 6.71 $mmol_{AcH}\,s^{-1}\,kg_{cat}^{-1}$ and a degree of conversion of 93.5% with an acetaldehyde selectivity of 96.5% ($Y_{AcH} = 90.3\%$).

The iron molybdate prepared by solid-state synthesis shows a lower activity. At 280 °C, an activity of 3.0 $mmol_{AcH}\,s^{-1}\,kg_{cat}^{-1}$ is observed and the yield of acetaldehyde is 60.4% ($X_{EtOH} = 63\%$ and $S_{AcH} = 96\%$). After increasing the temperature gradually to 280 °C, the temperature was lowered step by step to study a

ChemCatChem

Full Papers
doi.org/10.1002/cctc.202101219

Chemistry Europe
European Chemical
Societies Publishing
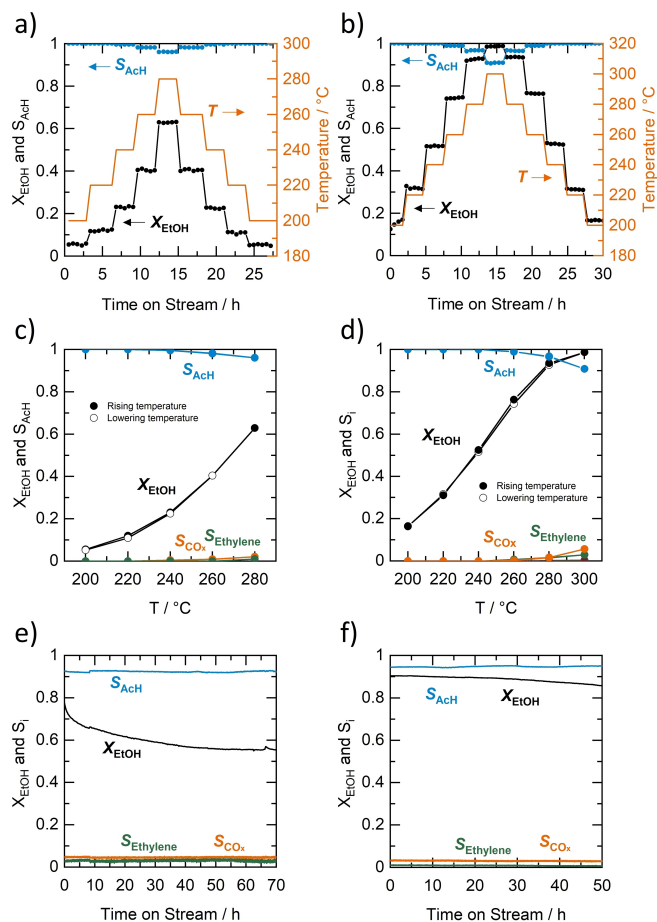
Figure 1. Conversion of ethanol (EtOH) and selectivity to acetaldehyde (AcH) during temperature variation against time on stream for a) 150 mg bm-$Fe_2(MoO_4)_3$ and b) 100 mg p-$Fe_2(MoO_4)_3$; Steady-state values for the conversion of ethanol and the selectivities to acetaldehyde, CO_x and ethylene against reaction temperature for c) 150 mg bm-$Fe_2(MoO_4)_3$ and d) 100 mg p-$Fe_2(MoO_4)_3$; Conversion of ethanol and selectivity to products at 280 °C for 70 h for e) 150 mg bm-$Fe_2(MoO_4)_3$ and f) 100 mg p-$Fe_2(MoO_4)_3$. Feed-flow characteristics in all measurements: 5 vol% EtOH, 10 vol% O_2, 85 vol% He, total volume flow: 20 ml_{STP} min^{-1}.

potential temperature hysteresis. The averaged steady-state values of the degree of conversion and the selectivities in Figure 1c and d show that for both materials no temperature hysteresis is observed (raising temperature: closed symbols, lowering temperature: open symbols). Figure 1e and f depict long-term measurements of both materials at 280 °C (including the described induction period). bm-$Fe_2(MoO_4)_3$ shows a decrease in the degree of conversion from 78% at the beginning to 56% after 70 h time on stream, while the acetaldehyde selectivity remains constant at 93%. For p-$Fe_2(MoO_4)_3$, starting at a degree of conversion of 93%, a slow decline to 86% is observed over 70 h. The selectivity to acetaldehyde is slightly increasing from 93 to 95%.

Methanol ODH. To compare the results of this study to literature findings, the activity and selectivity in the methanol ODH was also assessed since most work on ODH catalysis with iron molybdates was done with methanol as substrate. For

methanol ODH, after reaching steady-state conditions at 300 °C, the temperature was varied within 240–340 °C. The carbon mole balance during temperature cycling was 98–100%. The time on stream resolved results are presented in Figure S3 and show a slight deactivation of the materials. Figure 2 depicts the conversion of methanol and the selectivities to the products after holding each temperature for 2 h. For both materials, besides the desired product formaldehyde, dimethoxymethane and dimethyl ether, as well as traces of carbon monoxide are detected. At temperatures below 240 °C, dimethoxymethane (DMM) is the main side product with selectivities of 10–20%. With increasing temperature, the formaldehyde selectivity increases, and dimethyl ether (DME) becomes the main side product. At 320 °C, p-$Fe_2(MoO_4)_3$ shows high formaldehyde yields of 84.7% at a degree of conversion of 87% with an activity of 12.6 $mmol_{FAld}$ s^{-1} kg_{cat}^{-1}. The methanol ODH activity and selectivity of that catalyst is comparable to the literature data (320 °C: 6.7 $mmol_{FAld}$ s^{-1} kg_{cat}^{-1}, $X_{MeOH} = 91\%$, $Y_{FAld} = 86\%$).[46] bm-$Fe_2(MoO_4)_3$ shows a lower activity and at 320 °C a degree of conversion of 56% (4.6 $mmol_{FAld}$ s^{-1} kg_{cat}^{-1}). Different to p-$Fe_2(MoO_4)_3$, the DME selectivity does not drop at higher temperatures and ranges within 14–17%. Thus, for bm-$Fe_2(MoO_4)_3$ a lower formaldehyde yield of 45.9% results at 320 °C.

Catalyst Characterization. To study the morphology and texture of the synthesized materials, SEM images were taken and N_2-physisorption measurements were performed. SEM images of both materials prior and after catalytic testing are shown in Figure 3. The precipitated p-$Fe_2(MoO_4)_3$ consists of rough particles in the range of 2–8 μm. The morphology is preserved during ODH experiments. The ball-milled bm-$Fe_2(MoO_4)_3$ shows crushed particles which are predominantly < 10 μm in size. The morphology of bm-$Fe_2(MoO_4)_3$ also seems to be unaltered after catalysis.

Nitrogen physisorption experiments reveal specific surface areas of 2.9 $m^2 g^{-1}$ for p-$Fe_2(MoO_4)_3$ and 2.6 $m^2 g^{-1}$ for bm-$Fe_2(MoO_4)_3$, which do not significantly change during the ODH experiments (spent p-$Fe_2(MoO_4)_3$: 2.8 $m^2 g^{-1}$ and spent bm-$Fe_2(MoO4)_3$: 2.6 $m^2 g^{-1}$).
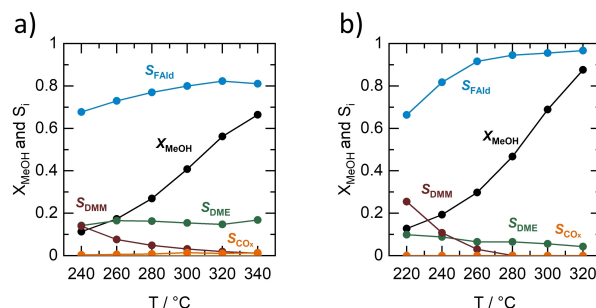
Figure 2. Conversion of methanol (MeOH) and selectivity to formaldehyde (FAld), dimethyl ether (DME), dimethoxymethane (DMM) and CO_x for different reaction temperatures for a) 100 mg bm-$Fe_2(MoO_4)_3$ and b) 100 mg p-$Fe_2(MoO_4)_3$. Feed-flow characteristics: 10 vol% MeOH, 10 vol% O_2, 80 vol% He, total volume flow: 20 ml_{STP} min^{-1}.

ChemCatChem

Full Papers
doi.org/10.1002/cctc.202101219

Chemistry Europe
European Chemical
Societies Publishing

Table 1. Summary of elemental compositions measured by ICP-OES, SEM-EDX and XPS.

Sample	ICP-OES Mo/Fe	Stoichiometry	SEM-EDX Mo [at %]	Fe [at %]	O [at %]	Mo/Fe	Stoichiometry	XPS Fe [at %]	Mo [at %]	O [at %]	Mo/Fe
p-Fe$_2$(MoO$_4$)$_3$	1.53	Fe$_2$Mo$_{3.06}$O$_{12.09}$	17.0	11.4	71.7	1.50	Fe$_2$Mo$_{3.0}$O$_{12.5}$	4.5	15.8	61.4	3.51
Spent p-Fe$_2$(MoO$_4$)$_3$	1.55	Fe$_2$Mo$_{3.09}$O$_{13.04}$	14.6	9.5	75.9	1.53	Fe$_2$Mo$_{3.1}$O$_{15.9}$	4.2	13.6	60.1	3.24
bm-Fe$_2$(MoO$_4$)$_3$	1.48	Fe$_2$Mo$_{2.96}$O$_{12.19}$	17.2	12.2	70.5	1.41	Fe$_2$Mo$_{2.9}$O$_{11.5}$	4.8	15.0	59.1	3.13
Spent bm-Fe$_2$(MoO$_4$)$_3$	1.51	Fe$_2$Mo$_{3.02}$O$_{11.83}$	17.3	11.8	71.0	1.47	Fe$_2$Mo$_{2.9}$O$_{12.0}$	5.0	12.6	54.8	2.52

ICP-OES analysis of both materials was carried out to determine the composition of the materials. The atomic ratios of molybdenum and iron and the calculated stoichiometries of the pristine and spent materials are summarized in Table 1. The Mo/Fe ratio is detected to be close to 1.5 for all materials confirming the theoretical stoichiometry of Fe$_2$(MoO$_4$)$_3$. There is no significant change in the elemental composition observable after the catalytic tests.

The elemental composition is further confirmed by SEM/EDX. In the margin of error, the theoretical Mo/Fe ratio of 1.5 is verified for all samples prior and after catalytic testing. For the spent catalysts a slight increase in oxygen content can be observed.

X-ray photoelectron spectroscopy was performed to determine the surface composition of the catalysts and the resulting elemental compositions are summarized in Table 1. The pristine materials show a surface Mo/Fe ratio of 3.51 (p-Fe$_2$(MoO$_4$)$_3$) and 3.13 (bm-Fe$_2$(MoO$_4$)$_3$), which is significantly higher than the theoretical value of 1.5 determined with the bulk characterization methods. These higher Mo/Fe ratios indicate an enrichment of molybdenum on the catalyst surface. After ODH experiments the Mo/Fe ratios are slightly decreasing to 3.24 for p-Fe$_2$(MoO$_4$)$_3$ and more pronounced to 2.52 for bm-Fe$_3$(MoO$_4$)$_3$, respectively. Besides an enrichment of molybdenum, the oxygen content O/(Mo+Fe) measured by XPS is higher for p-Fe$_2$(MoO$_4$)$_3$ (3.02) and bm-Fe$_2$(MoO$_4$)$_3$ (2.98), as compared to the theoretical value of 2.4 for Fe$_2$(MoO$_4$)$_3$. During ethanol ODH, the O/(Mo+Fe) ratio is slightly increasing to 3.34 (p-Fe$_2$(MoO$_4$)$_3$) and 3.11 (bm-Fe$_2$(MoO$_4$)$_3$).

Raman spectroscopy was used for further characterization of the materials. The Raman spectra of the pristine and the spent catalysts are shown in Figure 4. The Raman bands can be assigned to bulk Fe$_2$(MoO$_4$)$_3$, in good agreement with literature data.[47,48] The triplet of bands between 930 and 1000 cm^{-1} is caused by MoO$_4$ symmetric and the bands at 785 and 823 cm^{-1} by MoO$_4$ antisymmetric stretching modes.[48] The Raman features around 350 cm^{-1} and within 117–258 cm^{-1} can be assigned to MoO$_4$ bending and lattice modes, respectively.[48] The spectra of the spent materials show the same Raman features as the pristine materials. In addition, a slight increase of the background is observed for the spent materials.

Mössbauer spectroscopy was employed to validate the oxidation state of iron in Fe$_2$(MoO$_4$)$_3$. Mössbauer spectra of the pristine and spent catalysts are shown Figure 5. Mössbauer hyperfine parameters are summarized Table 2 and indicate the iron to be in a +3 oxidation state (high spin) in agreement with literature data for phase pure Fe$_2$(MoO$_4$)$_3$.[49,50]
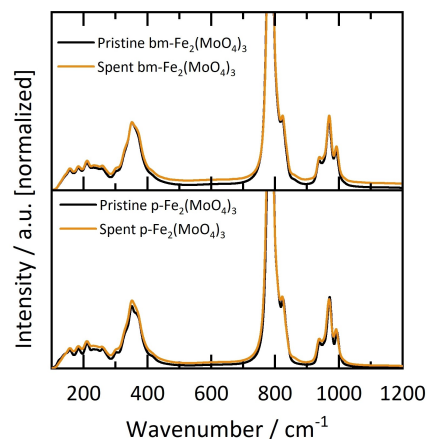
Figure 4. Raman spectra (514.5 nm) of pristine and spent iron molybdate samples; top: bm-Fe$_2$(MoO$_4$)$_3$ and bottom: p-Fe$_2$(MoO$_4$)$_3$.

Figure 3. SEM images of iron molybdate samples: a) pristine bm-Fe$_2$(MoO$_4$)$_3$, b) pristine p-Fe$_2$(MoO$_4$)$_3$, c) spent bm-Fe$_2$(MoO$_4$)$_3$ and d) spent p-Fe$_2$(MoO$_4$)$_3$.

Table 2. Mössbauer hyperfine parameters: Isomer shift (IS), quadrupole splitting (QS).

Sample	IS [mm s^{-1}]	QS [mm s^{-1}]	FWHM [mm s^{-1}]
p-Fe$_2$(MoO$_4$)$_3$	0.42	0.15	0.40
Spent p-Fe$_2$(MoO$_4$)$_3$	0.41	0.16	0.38
bm-Fe$_2$(MoO$_4$)$_3$	0.41	0.17	0.19
Spent bm-Fe$_2$(MoO$_4$)$_3$	0.41	0.19	0.17
Literature[49,50]	0.42–0.44	0.20–0.21	0.27–0.32
	0.42	0.18	0.27

ChemCatChem

Full Papers
doi.org/10.1002/cctc.202101219

Chemistry Europe
European Chemical
Societies Publishing
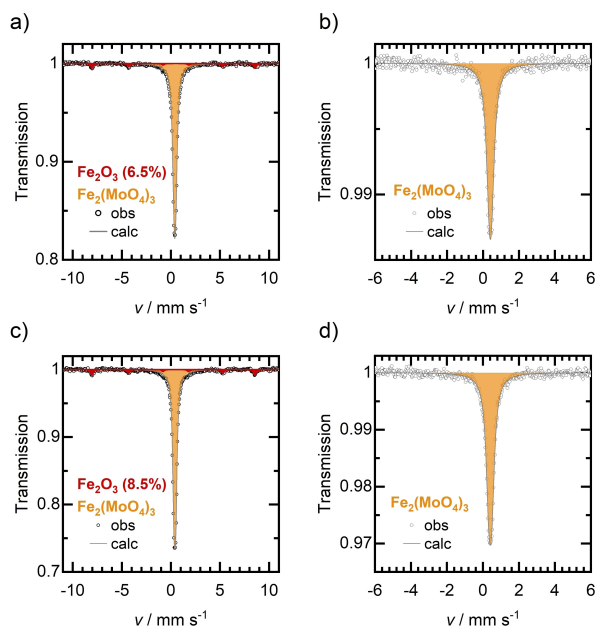
Figure 5. Mössbauer spectra of iron molybdate samples. a) bm-Fe$_2$(MoO$_4$)$_3$, b) p-Fe$_2$(MoO$_4$)$_3$, c) spent bm-Fe$_2$(MoO$_4$)$_3$ and d) spent p-Fe$_2$(MoO$_4$)$_3$.

Figure 6. X-ray diffraction patterns and Rietveld refinements of a) pristine and spent bm-Fe$_2$(MoO$_4$)$_3$ and b) pristine and spent p-Fe$_2$(MoO$_4$)$_3$. (black: measured, orange: calculated, grey: difference curve).

In addition, Fe$_2$O$_3$ (hematite) is detected as an impurity in the bm-Fe$_2$(MoO$_4$)$_3$ samples and its amount is determined to be 6.5% in the pristine sample and 8.5% in the sample after catalytic testing. In contrast, the material prepared by precipitation shows no signs of Fe$_2$O$_3$ impurities neither prior nor after catalysis. The identical Mössbauer spectra of p-Fe$_2$(MoO$_4$)$_3$ before and after catalysis indicate its good structural stability and purity. The rather small values of quadrupole splitting indicate only minor distortions in FeO$_6$ octahedra.

The structure of Fe$_2$(MoO$_4$)$_3$ could be confirmed by Rietveld-refinement of the XRD powder data based on literature known structure model.[51] For bm-Fe$_2$(MoO$_4$)$_3$, the Fe$_2$O$_3$ impurity is determined to be less than 1.5 wt%. The results are shown in Figure 6.

Discussion

Regarding methanol ODH the precipitated catalyst shows a reactivity very similar to iron molybdate catalysts reported in literature.[46] It seems to be justified to draw parallels between the ethanol ODH studied in this work and the earlier investigated methanol ODH. Interestingly, in methanol ODH slight differences in activity and selectivity were observable between bm-Fe$_2$(MoO$_4$)$_3$ and p-Fe$_2$(MoO$_4$)$_3$. The formation of DME during methanol ODH is believed to take place on acidic sites. NH$_3$-TPD measurements are shown in Figure S6 and confirm a higher acidity of bm-Fe$_2$(MoO$_4$)$_3$. The total amount of desorbed NH$_3$ is determined to be 22.7 mmol$_{NH3}$ kg$_{cat}^{-1}$ for bm-Fe$_2$(MoO$_4$)$_3$ and only 13.1 mmol$_{NH3}$ kg$_{cat}^{-1}$ for p-Fe$_2$(MoO$_4$)$_3$. The higher overall acidity of bm-Fe$_2$(MoO$_4$)$_3$ could be the reason for the higher DME selectivity of this material. The origin of the higher acidity of bm-Fe$_2$(MoO$_4$)$_3$ could not be clarified yet.

The activity differences between both materials in the ODH of ethanol could originate from the different Mo/Fe ratios on the catalyst surface. While the elemental composition and the Fe$_2$(MoO$_4$)$_3$ structure was confirmed by ICP-OES, SEM/EDX, Raman spectroscopy and XRD for both materials, the XPS characterization proved a higher surface Mo/Fe ratio for the more active p-Fe$_2$(MoO$_4$)$_3$ (XPS: p-Fe$_2$(MoO$_4$)$_3$: Mo/Fe = 3.51, bm-Fe$_2$(MoO$_4$)$_3$: Mo/Fe = 3.13). This molybdenum enriched surface layer has been stated to be indispensable for an active and selective methanol ODH catalyst.[46,52] The lower Mo/Fe ratio of bm-Fe$_2$(MoO$_4$)$_3$ in comparison to p-Fe$_2$(MoO$_4$)$_3$ could offer an explanation for the lower activity in ethanol ODH and could originate from the high synthesis/calcination temperature (850 °C) of bm-Fe$_2$(MoO$_4$)$_3$. At this temperature, MoO$_3$ may evaporate from the catalyst surface leading to a lower Mo/Fe ratio compared to p-Fe$_2$(MoO$_4$)$_3$ calcined at 500 °C.

Regarding ethanol ODH an Y_{AcH}/X_{EtOH} diagram is given in Figure S4. It shows that the selectivity of bm-Fe$_2$(MoO$_4$)$_3$ is lower than that of the material synthesized by precipitation, but the differences are minor compared to methanol ODH. The reason

ChemCatChem

Full Papers
doi.org/10.1002/cctc.202101219

Chemistry
Europe
European Chemical
Societies Publishing

for the slightly lower selectivity is expected to be the same as in methanol ODH. The acidic catalyst side reaction in ethanol ODH is the ethylene production, which is nevertheless less pronounced compared to the DME pathway in methanol ODH. Thus, the selectivity drop in ethanol ODH is lower and both materials show high selectivities to acetaldehyde.

Activity differences between the two materials are clearly observable for both reactions. These seem not to originate from different specific surface areas but rather the overall lower surface Mo/Fe ratio of bm-$Fe_2(MoO_4)_3$, which shows that less MoO_x is exposed for the solid-state synthesis stemming material.

In ethanol ODH no catalyst deactivation is observable during temperature cycling (30 h time on stream). While most of the bulk characterization techniques showed no reaction-induced changes, especially the surface sensitive XPS measurements revealed a drop of the Mo/Fe ratio for both catalyst systems. This surface depletion of molybdenum could be a first indication for long-term deactivation of the catalyst. From methanol ODH it is known, that MoO_x from the catalyst may sublimate leading to a deactivation of the catalyst. Molybdenum-oxy-methoxy or molybdenum–oxy-hydroxy species are formed from surface MoO_3 under reaction conditions and are believed to be the volatile compounds that lead to a loss of molybdenum.[37–40] Interestingly, Mössbauer spectroscopy also showed an enrichment of Fe_2O_3 during testing, which is a second indication for a slight molybdenum loss during the stability testing. It seems, that in ethanol ODH a similar deactivation mechanism applies as for the methanol ODH. Nevertheless, for steady-state experiments with 70 h time on stream at 280 °C (including the induction period) a deactivation is observable (bm-$Fe_2(MoO_4)_3$: from 3.56 to 2.55 $mmol_{AcH} s^{-1} kg_{cat}^{-1}$; p-$Fe_2(MoO_4)_3$ from 6.43 to 6.07 $mmol_{AcH} s^{-1} kg_{cat}^{-1}$) supporting the described assumptions concerning catalyst deactivation. Nevertheless, more detailed studies are necessary to corroborate these initial findings.

Conclusion

Two stoichiometric iron molybdate catalysts, one prepared by co-precipitation and one synthesized by a ball-milled solid-state reaction route, were applied as catalysts in the ODH of ethanol. Both materials show attractive activity and selectivity towards acetaldehyde and a stable performance under the conditions applied in this study. The catalyst synthesized by the solid-state method is slightly less active and selective than the precipitated one. The higher acidity and lower Mo content on the catalyst surface are proposed to be the reason for the lower activity and selectivity. Further approaches based on this modified synthesis method could be attractive especially in terms of controlling the Fe_2O_3 content and the Mo/Fe ratio on the catalyst surface and the impact on ODH activity and selectivity.

Similar to previous observations for methanol ODH, a depletion of surface molybdenum during ethanol ODH could be observed for both catalysts. Further studies on catalyst long-term stability and stability under higher temperatures and

ethanol concentrations together with extensive ex-situ and in-situ characterization need to be carried out in the future to deepen the insights on a possible long-term deactivation.

Experimental Section

Catalyst Preparation

Solid-State Synthesis. bm-$Fe_2(MoO_4)_3$ was synthesized from Fe_2O_3 (*Chempur*, 99.9%) and MoO_3 (*Chempur*, >99.9%) powders (stoichiometric ratio 1:3). The powders where mixed with acetone (*Fisher Chemicals*, ≥99.8%) and ball-milled for 15 minutes at 650 rpm in corundum crucibles using 9 corundum balls for batches between 10 to 15 g (Retsch PM 100 ball mill). After drying the ball-milled sample for at least 12 h, the mixture was transferred to a corundum crucible and then heated in a box furnace under ambient atmosphere up to 850 °C (200 °C h^{-1}, hold: 15 h). After cooling to room temperature, the material was ball milled twice for 10 and 15 minutes at 650 rpm.

Precipitation. p-$Fe_2(MoO_4)_3$ was prepared using a co-precipitation synthesis procedure according to ref. [49] Iron nitrate nonahydrate (14.9 mmol, $Fe(NO_3)_3 \cdot 9\ H_2O$, *Merck*, ≥98%) and ammonium heptamolybdate tetrahydrate (22.3 mmol, $(NH_4)_6Mo_7O_{24} \cdot 7\ H_2O$, *Merck*, ≥99%) were dissolved separately in demineralized water (100 resp. 200 mL). Afterwards, the aqueous iron nitrate solution was added dropwise to the molybdate solution under vigorous stirring, which instantly led to the formation of a precipitate. In order to complete the precipitation process, the solution was stirred at 100 °C for three more hours. The precipitate was isolated by filtering off and washed with demineralized water and ethanol (*Brentag BCD*, Technical Grade) before it was dried overnight at 100 °C in air. Finally, the powder was calcined in air at 500 °C for 10 h, using a corundum crucible and a tube furnace (Carbolite Gero CWF1200).

Catalyst Characterization

Vis-Raman Spectroscopy. Vis-Raman spectroscopy was performed at an excitation wavelength of 514.5 nm using an argon ion gas laser (Melles Griot). The light was focused onto the sample, gathered by an optic fibre and dispersed by a transmission spectrometer (Kaiser Optical, HL5R). The dispersed Raman radiation was subsequently detected by an electronically cooled CCD detector (−40 °C, 1024×256 pixels). The spectral resolution was 5 cm^{-1} with a wavelength stability of better than 0.5 cm^{-1}. A laser power of 4 mW at the sample location was applied. Data analysis of the Raman spectra included a cosmic ray removal and an auto new dark correction.

X-ray Photoelectron Spectroscopy. X-ray photo-electron spectroscopy (XPS) was carried out on an SSX 100 ESCA spectrometer (Surface Science Laboratories Inc.) employing a monochromatic Al K$_\alpha$ X-ray source (1486.6 eV) operated at 9 kV and 10 mA; the spot size was approximately 1 mm×0.25 mm. The base pressure of the analysis chamber was <10^{-8} Torr. Survey spectra (eight measurements) were recorded between 0 and 1100 eV with 0.5 eV resolution, whereas detailed spectra (30 measurements) were recorded with 0.05 eV resolution. To account for sample charging, the C 1s peak of ubiquitous carbon at 284.4 eV was used to correct the binding-energy shifts in the spectra. Atomic concentrations were calculated using the relative sensitivity factors (RSFs) given in Table 3.

Table 3. Relative sensitivity factors used for the calculation of elemental concentrations from XPS data.

	C 1s	O 1s	Mo 3d	Fe 2p$_{3/2}$	Si 2p
RSF	1.00	2.50	9.79	7.96	0.90

^{57}Fe Mössbauer Spectroscopy. The spectra of bm-Fe$_2$(MoO$_4$)$_3$ were acquired in transmission mode with a custom build setup at 294 K. An α-Fe foil was used for the calibration of the velocity. Mössbauer spectra of p-Fe$_2$(MoO$_4$)$_3$ were acquired in a custom build setup having a ^{57}Co/Rh radiation source equipped with a proportional counter. Velocity values are referenced to an α-Fe foil. The spectra were fitted by Lorentzian Lineshape Analysis using the software *Recoil*.[53]

SEM/EDX. Scanning electron microscopy (Philips XL30 FEG, 20 kV) and energy-dispersive spectroscopy (EDAX Si detector, liquid nitrogen-cooled) was used to check for homogeneity, particle size and composition. Small amounts (~3 mg) of finely ground powder were transferred onto a double-sided carbon tape fixed on an aluminium specimen holder.

X-ray powder diffraction. X-ray powder diffraction of bm-Fe$_2$(MoO$_4$)$_3$ was performed using a Stoe STADI P diffractometer with Mo K$_{\alpha1}$ radiation in transmission mode. Rietveld refinements were performed using the software TOPAS.[54]

p-Fe$_2$(MoO$_4$)$_3$ was analysed in transmission geometry (Stoe & Cie GmbH, StadiP, Cu K$_{\alpha1}$ radiation, Ge(111) monochromator, Dectris/Mythen 1 K). Small amounts of the powder samples were placed on acetate foil. Rietveld refinements were performed using the software TOPAS.[54]

ICP-OES. Inductive coupled plasma optical emission spectrometry (ICP-OES) was carried out using a PerkinElmer OPTIMA 2000DV spectrometer. For sample preparation the materials were dissolved in aqua regia and diluted with deionized water.

N$_2$-Physisorption. Physisorption measurements were carried out using the volumetric measuring system Quadrasorb evo from Quantachrome GmbH & Co. KG (Odelzhausen, Germany). Specific surface areas were calculated using the MBET method.

Catalytic Measurements

The catalytic reactions were performed in a continuous flow apparatus with quartz glass tube reactor with an internal diameter of 4 mm (see Scheme S1). The catalyst was placed between two glass wool plugs. Liquid reactants (methanol >99.95%, *Carl Roth* and ethanol >99%, *Fisher Scientific*) were fed to the reactor by using a saturator system and gases (Helium 5.0, *Westfalen*; Oxygen 4.8, *Air Liquid*) were dosed by mass flow controllers. The total volume flow was 20 ml min^{-1} (STP) with helium as inert gas. Off-gas analytic was performed by an online quadrupole mass spectrometer (GAM 400, InProcess Instruments) and an online gas chromatograph (Shimadzu GC 2010) equipped with a FID and a TCD detector.

Methanol ODH. For the methanol ODH reference measurements, the feed consisted of 10 vol% methanol and 10 vol% O$_2$. 100 mg of catalyst were used and pre-treated with the reaction mixture at 320°C until steady state conditions were reached. Afterwards the temperature was varied within 220–320°C in steps of 20 K. The spent catalyst corresponds to the material after the temperature variation.

Ethanol ODH. For the ethanol ODH measurements, the feed consisted of 5 vol% ethanol and 10 vol% O$_2$. 100 mg p-Fe$_2$(MoO$_4$)$_3$ and 150 mg bm-Fe$_2$(MoO$_4$)$_3$ were used and pre-treated with the reaction mixture at 280°C until steady-state conditions were reached. Afterwards the temperature was varied within 200–280°C in steps of 20 K. The spent catalyst corresponds to the material after the temperature variation. For the long-term measurements, the as prepared catalysts (p-Fe$_2$(MoO$_4$)$_3$: 100 mg; bm-Fe$_2$(MoO$_4$)$_3$: 150 mg) were heated to 280°C and stationary measurements were performed for 70 h.

All data can be found via TUDatalib (DOIs and links in supporting information).

Conflict of Interest

The authors declare no conflict of interest.

[1] M. Carus, F. Kähler, O. Porc, "Global Carbon Demand for Chemicals and Derived Materials," **2021**.
[2] P. Bajpai, *Developments in Bioethanol*, Springer Singapore, Singapore, **2021**.
[3] FAO, OECD, *OECD-FAO Agric. Outlook* **2015**, 145.
[4] A. Mohsenzadeh, A. Zamani, M. J. Taherzadeh, *ChemBioEng Rev.* **2017**, *4*, 75–91.
[5] M. Cozzolino, R. Tesser, M. Di Serio, P. D'Onofrio, E. Santacesaria, *Catal. Today* **2007**, *128*, 191–200.
[6] M. Eckert, G. Fleischmann, R. Jira, H. M. Bolt, K. Golka, *Ullmann's Encyclopedia of Industrial Chemistry*, Wiley-VCH Verlag GmbH & Co. KGaA., Weinheim, **2006**.
[7] T. V. Andrushkevich, V. V. Kaichev, Y. A. Chesalov, A. A. Saraev, V. I. Buktiyarov, *Catal. Today* **2017**, *279*, 95–106.
[8] R. Bulánek, P. Čičmanec, J. Kotera, I. Boldog, *Catal. Today* **2019**, *324*, 106–114.
[9] B. Kilos, A. T. Bell, E. Iglesia, *J. Phys. Chem. C* **2009**, *113*, 2830–2836.
[10] R. Tesser, V. Maradei, M. Di Serio, E. Santacesaria, *Ind. Eng. Chem. Res.* **2004**, *43*, 1623–1633.
[11] E. Santacesaria, A. Sorrentino, R. Tesser, M. Di Serio, A. Ruggiero, *J. Mol. Catal. A* **2003**, *204–205*, 617–627.
[12] J. L. Lakshmi, N. J. Ihasz, J. M. Miller, *J. Mol. Catal. A* **2001**, *165*, 199–209.
[13] V. I. Sobolev, E. V. Danilevich, K. Y. Koltunov, *Kinet. Catal.* **2013**, *54*, 730–734.
[14] P. Ober, S. Rogg, C. Hess, *ACS Catal.* **2020**, *10*, 2999–3008.
[15] P. Waleska, S. Rupp, C. Hess, *J. Phys. Chem. C* **2018**, *122*, 3386–3400.
[16] P. Waleska, C. Hess, *Catal. Lett.* **2018**, *148*, 2537–2547.
[17] P. Čičmanec, Y. Ganjkhanlou, J. Kotera, J. M. Hidalgo, Z. Tišler, R. Bulánek, *Appl. Catal. A* **2018**, *564*, 208–217.
[18] J. M. Hidalgo-Herrador, Z. Tišler, *Period. Polytech. Chem. Eng.* **2018**, *62*, 345–350.

ChemCatChem

Full Papers
doi.org/10.1002/cctc.202101219

Chemistry Europe
European Chemical
Societies Publishing

[19] I. Boldog, P. Čičmanec, Y. Ganjkhanlou, R. Bulánek, *Catal. Today* **2018**, *304*, 64–71.

[20] Y. Ganjkhanlou, Z. Tišler, J. M. Hidalgo, K. Frolich, J. Kotera, P. Čičmanec, R. Bulánek, *Chem. Pap.* **2018**, *72*, 937–946.

[21] J. M. Hidalgo, Z. Tišler, D. Kubička, K. Raabova, R. Bulanek, *J. Mol. Catal. A* **2016**, *420*, 178–189.

[22] V. V. Kaichev, Y. A. Chesalov, A. A. Saraev, A. Y. Klyushin, A. Knop-Gericke, T. V. Andrushkevich, V. I. Bukhtiyarov, *J. Catal.* **2016**, *338*, 82–93.

[23] B. Beck, M. Harth, N. G. Hamilton, C. Carrero, J. J. Uhlrich, A. Trunschke, S. Shaikhutdinov, H. Schubert, H. J. Freund, R. Schlögl, J. Sauer, R. Schomäcker, *J. Catal.* **2012**, *296*, 120–131.

[24] H. Nair, J. E. Gatt, J. T. Miller, C. D. Baertsch, *J. Catal.* **2011**, *279*, 144–154.

[25] A. Malmusi, J. Velasquez Ochoa, T. Tabanelli, F. Basile, C. Lucarelli, S. Agnoli, F. Carraro, G. Granozzi, F. Cavani, *Appl. Catal. A* **2019**, *570*, 139–147.

[26] V. I. Sobolev, K. Y. Koltunov, *ChemCatChem* **2011**, *3*, 1143–1145.

[27] G. V. Mamontov, M. V. Grabchenko, V. I. Sobolev, V. I. Zaikovskii, O. V. Vodyankina, *Appl. Catal. A* **2016**, *528*, 161–167.

[28] V. V. Dutov, G. V. Mamontov, V. I. Sobolev, O. V. Vodyankina, *Catal. Today* **2016**, *278*, 164–173.

[29] A. S. Blokhina, I. A. Kurzina, V. I. Sobolev, K. Y. Koltunov, G. V. Mamontov, O. V. Vodyankina, *Kinet. Catal.* **2012**, *53*, 477–481.

[30] P. Liu, E. J. M. Hensen, *J. Am. Chem. Soc.* **2013**, *135*, 14032–14035.

[31] F. Herold, S. Prosch, N. Oefner, K. Brunnengräber, O. Leubner, Y. Hermans, K. Hofmann, A. Drochner, J. P. Hofmann, W. Qi, B. J. M. Etzold, *Angew. Chem. Int. Ed.* **2021**, *60*, 5898–5906; *Angew. Chem.* **2021**, *133*, 5962–5971.

[32] R. D. Weinstein, A. R. Ferens, R. J. Orange, P. Lemaire, *Carbon N. Y.* **2011**, *49*, 701–707.

[33] I. Abdullahi, T. J. Davis, D. M. Yun, J. E. Herrera, *Appl. Catal. A* **2014**, *469*, 8–17.

[34] A. W. Franz, H. Kronemayer, D. Pfeiffer, R. D. Pilz, G. Reuss, W. Disteldorf, A. O. Gamer, A. Hilt, *Ullmann's Encyclopedia of Industrial Chemistry*, Wiley-VCH Verlag GmbH & Co. KGaA, Weinheim, **2016**.

[35] A. P. Vieira Soares, M. Farinha Portela, A. Kiennemann, *Catal. Rev. Sci. Eng.* **2005**, *47*, 125–174.

[36] C. Brookes, M. Bowker, P. P. Wells, *Catalysts* **2016**, *6*, 92–118.

[37] K. I. Ivanov, D. Y. Dimitrov, *Catal. Today* **2010**, *154*, 250–255.

[38] A. Andersson, M. Hernelind, O. Augustsson, *Catal. Today* **2006**, *112*, 40–44.

[39] A. Gaur, M. Stehle, K. V. Raun, J. Thrane, A. D. Jensen, J. D. Grunwaldt, M. Høj, *Phys. Chem. Chem. Phys.* **2020**, *22*, 11713–11723.

[40] A. Gaur, M. Schumann, K. V. Raun, M. Stehle, P. Beato, A. D. Jensen, J. D. Grunwaldt, M. Høj, *ChemCatChem* **2019**, *11*, 4871–4883.

[41] K. V. Raun, J. Johannessen, K. McCormack, C. C. Appel, S. Baier, M. Thorhauge, M. Høj, A. D. Jensen, *Chem. Eng. J.* **2019**, *361*, 1285–1295.

[42] J. E. Gatt, H. Nair, C. D. Baertsch, *Appl. Catal. B* **2010**, *99*, 127–134.

[43] Y. L. Xiong, R. Castillo, C. Papadopoulou, L. Daza, J. Ladrière, P. Ruiz, B. Delmon, *Stud. Surf. Sci. Catal.* **1991**, *68*, 425–432.

[44] K. A. Thavornprasert, B. De La Goublaye De Ménorval, M. Capron, J. Gornay, L. Jalowiecki-Duhamel, X. Sécordel, S. Cristol, J. L. Dubois, F. Dumeignil, *Biofuels* **2012**, *3*, 25–34.

[45] V. Srihari, D. S. Viswanath, *J. Chem. Technol. Biotechnol.* **1982**, *32*, 868–876.

[46] B. R. Yeo, G. J. F. Pudge, K. G. Bugler, A. V. Rushby, S. Kondrat, J. Bartley, S. Golunski, S. H. Taylor, E. Gibson, P. P. Wells, C. Brookes, M. Bowker, G. J. Hutchings, *Surf. Sci.* **2016**, *648*, 163–169.

[47] H. Tian, I. E. Wachs, L. E. Briand, *J. Phys. Chem. B* **2005**, *109*, 23491–23499.

[48] J. Sejkora, J. Čejka, R. Malíková, A. López, Y. Xi, R. L. Frost, *Spectrochim. Acta Part A* **2014**, *130*, 83–89.

[49] A. P. V. Soares, M. F. Portela, A. Kiennemann, *Catal. Commun.* **2001**, *2*, 159–164.

[50] P. D. Battle, A. K. Cheetham, G. J. Long, G. Longworth, *Inorg. Chem.* **1982**, *21*, 4223–4228.

[51] H.-Y. Cheng, *Mater. Res. Bull.* **1979**, *14*, 1583–1590.

[52] S. Zhang, M. Han, *Molecules* **2020**, *25*, 2410–2420.

[53] K. Lagarec and D.G. Rancourt, Recoil, **1998**.

[54] TOPAS-Academic V6 Brisbane, Australie, **2016** .

4.4.2 Unraveling Surface and Bulk Dynamics of $Fe_2(MoO_4)_3$ during Oxidative Dehydrogenation using Operando and Transient Spectroscopies

The eleventh overall publication elucidates fundamental properties of iron molybdates under propane ODH conditions, which exhibit a lower conversion and allow for the understanding of the materials based on spectroscopy. The methods used include operando multi-wavelength Raman (385 and 514 nm excitation), UV-Vis and EI spectroscopy, as well as ME-DRIFTS. These showed that the molybdate forms amorphous MoO_x layers on its surface, which can act as a hydrogen transfer site that rapidly transfers hydrogen from propane to the catalyst surface, catalyzing the rate-determining step. Multiple effects occuring in the subsurface/the bulk are involved in the further reaction. The first is the percolation of hydrogen in the subsurface and the formation of water and an oxygen vacancy. The water leaves the lattice, while the vacancy can either be regenerated by bulk oxygen or a phase transformation to $FeMoO_4$ can occur, which shows a significantly increased oxygen mobility. By comparing these results to those of reference samples (MoO_3 and MoO_x/Fe_2O_3), the iron content was identified as the key indicator for the oxygen mobility within the bulk and therefore the reaction rate. The iron molybdate combines the beneficial properties of the MoO_3 and Fe_2O_3. This study therefore allows for the detailed understanding of fundamental processes occuring in bulk oxides under ODH conditions by applying and combining new and advanced methods, enhancing the catalytic understanding.

Unraveling Surface and Bulk Dynamics of $Fe_2(MoO_4)_3$ during Oxidative Dehydrogenation using Operando and Transient Spectroscopies

Leon Schumacher, Mariusz Radtke, Jan Welzenbach, Christian Hess*

Technical University of Darmstadt, Department of Chemistry, Eduard-Zintl-Institut für Anorganische und Physikalische Chemie, Peter-Grünberg-Str. 8, 64287 Darmstadt, Germany

*Corresponding Author (E-Mail: christian.hess@tu-darmstadt.de)

TOC

Abstract

Iron(III) molybdate ($Fe_2(MoO_4)_3$) is a commercial catalyst for the oxidative dehydrogenation (ODH) of methanol, but it has recently been shown to be relevant for other substrates as well. Despite its commercial use, a detailed mechanistic understanding of $Fe_2(MoO_4)_3$ catalysts at the surface and in the bulk has been lacking, largely hampered by the lack of suitable spectroscopic methods, directly applicable under reaction conditions. Using propane ODH as an example, we highlight the potential of operando Raman and impedance spectroscopy combined with transient IR spectroscopy, to identify surface active sites and monitor the hydrogen transfer and oxygen dynamics. By comparison with the behavior of reference compounds (MoO_3, MoO_x/Fe_2O_3) a mechanistic model is proposed. The presence of iron greatly influences the reactivity behavior via oxygen diffusion but is moderated in its oxidative capacity by surface MoO_x. Our approach directly elucidates fundamental properties of $Fe_2(MoO_4)_3$ of general importance to selective oxidation catalysis.

Introduction

Fe$_2$(MoO$_4$)$_3$ is a well-known catalyst used commercially for the oxidative dehydrogenation (ODH) of methanol to formaldehyde[1,2] but it has recently been shown to have also potential for other oxidation reactions, such as ethanol ODH.[3–5] In these reactions, Fe$_2$(MoO$_4$)$_3$ shows even higher activities than the commonly used supported vanadia (VO$_x$) catalysts[6] and is therefore very promising. However, the mode of operation of Fe$_2$(MoO$_4$)$_3$ catalysts has been the subject of numerous kinetic and structural studies[7,8] as summarized in excellent reviews.[5,9,10] More recently, there has been renewed interest in Fe$_2$(MoO$_4$)$_3$ catalysts, and new insights into the bulk dynamics were provided by operando X-ray diffraction (XRD) and X-ray absorption spectroscopy (XAS).[11,12] Despite the progress made there is still a distinct lack of mechanistic understanding of the (sub)surface processes in Fe$_2$(MoO$_4$)$_3$ catalysts under reaction conditions and their relation to bulk properties, including the role of iron.[5,7,9,13–16] A problem commonly encountered with such catalysts is that the conversion, even at low temperatures, is very high, leading to additional effects (such as mass transport) that make the mechanistic analysis more complex. One way to approach this is to consider alkane oxidation reactions, such as propane ODH, which in addition to being of great interest for technical applications, might also facilitate the evaluation of fundamental and transferable properties of Fe$_2$(MoO$_4$)$_3$, because the reaction has lower conversions than alcohol ODH at similar temperatures.[6,17] For a detailed mechanistic understanding, it will be of particular importance to further define the role of molybdenum and iron, which is facilitated by the use of reference materials, including MoO$_3$ (characterized by low conversions and high selectivities) and Fe$_2$O$_3$ (shown to be a total oxidation catalyst with high conversions and CO$_x$ yields).[14,18,19]

In this contribution, we present a combined operando and transient spectroscopic study on the reaction mechanism of propane ODH over Fe$_2$(MoO$_4$)$_3$ catalysts. Our focus is on combining methodological approaches of general applicability to selective oxidation reactions, such as modulation excitation (ME-) IR spectroscopy,[20] operando impedance spectroscopy on powder samples,[21] and dedicated resonance enhancement using multi-wavelength Raman spectroscopy,[22] aiming at a profound understanding of the (sub)surface and the bulk processes, as well as their relevance for catalysis. Our findings serve as a fundamental basis for the mechanisitic investigation of oxidation reactions with much higher conversions.

Results

Catalytic Activity

The $Fe_2(MoO_4)_3$ was synthesized using co-precipitation and extensive structural characterization was performed, as described elsewhere.[3] A brief summary of important characterization data for this study is given in the Supporting Information SI, see Table S1). Additional X-ray photoelectron spectroscopy (XPS) data for our $Fe_2(MoO_4)_3$ batch is provided in the SI (see Figure S1 and Table S2), showing a higher surface concentration of molybdenum (Mo/Fe ratio of 2.52) than would be expected from the stoichiometry, which is in good agreement with previous studies.[4,5,13,16] Analysis of the Fe $2p_{3/2}$ photoemission (see Figure S2) reveals that most of the iron is present as Fe^{3+} (711 eV). Besides, a small shoulder due to Fe^{2+} (709 eV) is detected,[23] which may be indicative of some $FeMoO_4$ being present as a side phase in addition to the already detected Fe_2O_3 by Mössbauer spectroscopy.[3]

The reactivity behavior of $Fe_2(MoO_4)_3$ in propane ODH was determined within the temperature range 25–550 °C (see Figure 1a). The corresponding consumption of oxygen is given in the SI (see Figure S3) and shows that oxygen is never fully consumed.
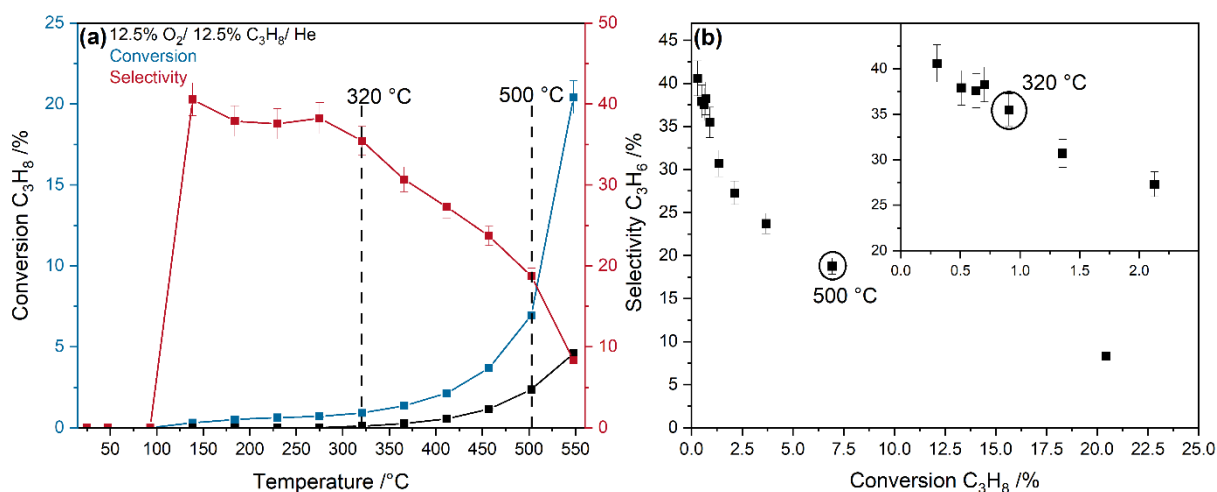
Figure 1: (a) Temperature-dependent reactivity behavior of $Fe_2(MoO_4)_3$ in a feed of 12.5% O_2/12.5% C_3H_8/He (total flow: 40 ml/min). The temperatures chosen for the operando experiments are indicated and the background conversion caused by the reactor is indicated by the black line. **(b)** Propylene selectivity as a function of conversion. The inset shows an enlarged view of the low conversion region for clarity. The temperatures at which spectroscopic experiments were performed are indicated.

The conversion of propane increases exponentially with increasing temperature and constantly stays above that of the empty reactor, while the selectivity is initially around 40%, showing a plateau, and then starts to decline continuously at around 320 °C, following the increase in conversion. To understand the reaction mechanism, two temperatures were chosen for operando measurements, i.e., 320 and 500 °C. At 320 °C the conversion is 0.91% with a selectivity of 35.5% while at 500 °C the conversion significantly increases to 6.94% but the selectivity decreases to 18.8%. The conversions at both temperatures are significantly below those during the ODH of methanol or ethanol,[3,24,25] which eliminates additional kinetic effects such as mass transport, enabling a detailed mechanistic investigation of the reaction mechanism and fundamental surface/bulk properties of the material transferable to other reactions. While the chosen temperatures represent different aspects of the reactivity behavior, the exponential decay of the selectivity–conversion plot (see Figure 1b) indicates that the reaction mechanism stays similar within the temperature range covered in this study. The selectivity-conversion plot for a sequence reaction (like the selective/total oxidation of propane is proposed to be) shows an exponential behavior, while its exact shape depends on the ratio of the rate constants. A switch in reaction mechanisms usually leads to a disruption of this exponential course, which can not be observed here.[26] Furthermore, the temperature-dependent molar product distributions (see Figure S4) show that all products produced at 500 °C (C_3H_6, CO, and CO_2) increase exponentially with the temperature, as expected for similar pathways leading to their formation. The amount of CO_2 increases the most, indicating a significant increase in oxygen mobility necessary for this amount of total oxidation of propane. This is in contrast to methanol oxidation,[3,9,27,28] for example, where not all side products show an exponential increase with increasing temperature, but rather go through maxima, indicating a change of the underlying reaction mechanism, which is not detected for our propane data. The observed behavior strongly suggests a similar ODH reaction mechanism at 320 and 500 °C, allowing operando experiments to be performed at low conversion with higher selectivity and at high conversion.

Transient Spectroscopy

Starting with the structural dynamics at the surface, transient IR spectroscopy was applied during reaction conditions by using modulation-excitation (ME-) DRIFTS

coupled with phase-sensitive detection (PSD), which allows active species to be discriminated from spectator species, as described in detail in the SI. A general description of the MES/PSD procedure and how the results described here were obtained based on time resolved spectra is also given in the SI (see Figures S5, S6, and discussion).[20,29,30] Figure 2 shows the PSD spectra in a constant propane and pulsed oxygen flow at 320 °C with a 30° phase resolution. The assignment to the propane gas phase over KBr after PSD treatment are given in the SI (Figure S6). There are no ME-IR spectra for 500 °C due to increased thermal emission, which leads to very noisy spectra.
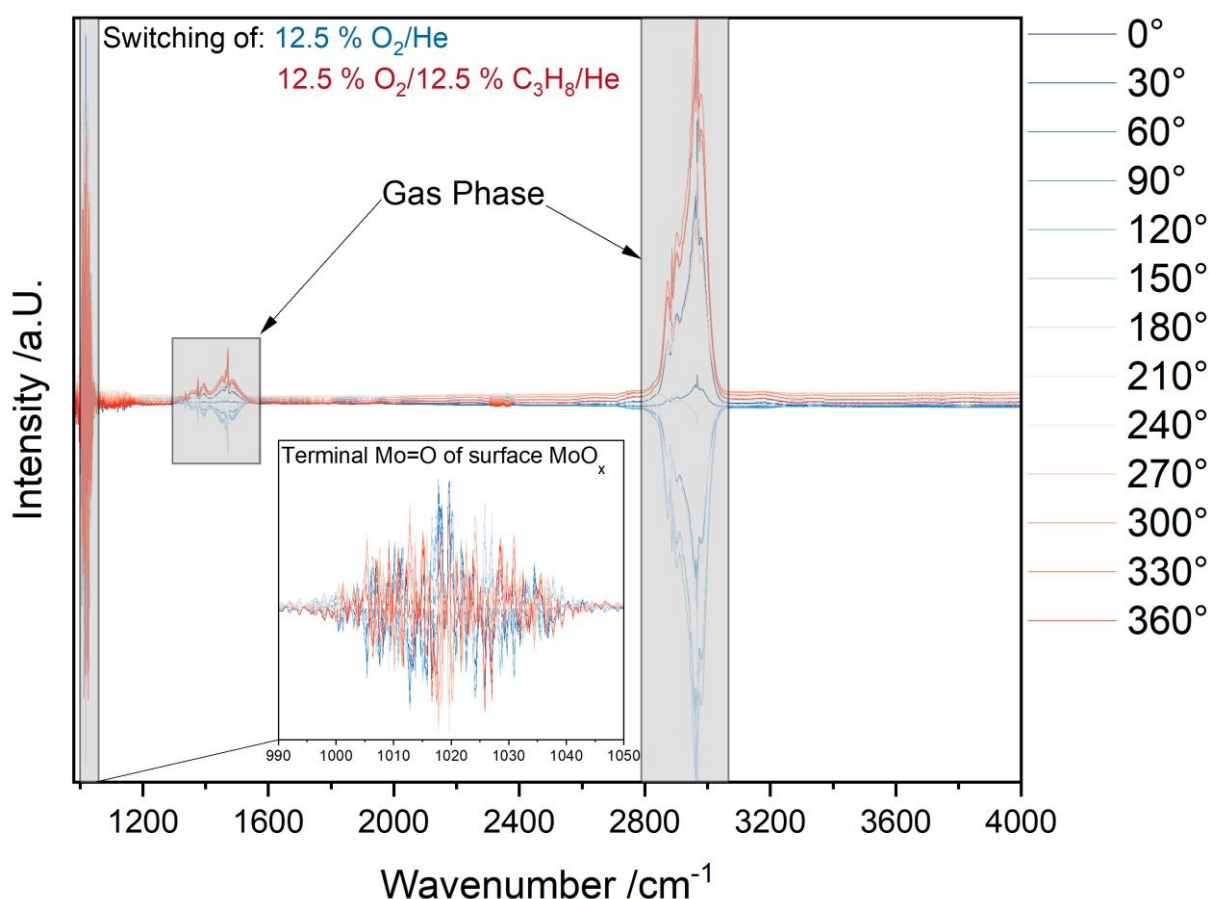
Figure 2: Transient IR spectroscopic behavior of $Fe_2(MoO_4)_3$ based on PSD spectra with a 30° phase resolution during constant propane and pulsed oxygen flow at 320 °C. The gas-phase contributions from propane are highlighted and the inset shows an enlarged view of the terminal Mo=O stretching region. For details see text.

The PSD spectra of $Fe_2(MoO_4)_3$ show mostly gas-phase contributions from propane and one additional peak between 990 and 1050 cm^{-1} with a maximum at

1020 cm^{-1}. This peak was previously assigned to the terminal Mo=O stretching vibration of amorphous molybdenum oxide (MoO$_x$) supported on SiO$_2$ and in reduced MoO$_3$,[31–33] indicating the presence of a molybdenum-rich surface layer in Fe$_2$(MoO$_4$)$_3$. Note that this feature has not been observed previously in Raman spectra of bulk oxides, and its participation in the reaction is accessible here only due to the increased sensitivity of the modulation excitation spectroscopy (MES)/PSD approach as a change in the Mo=O signal cannot be observed in the time domain (see Figure S5).[29,30] The presence of amorphous MoO$_x$ on the surface of Fe$_2$(MoO$_4$)$_3$ was previously proposed based on ex situ scanning transmission electron microscopy (STEM) and electron energy loss spectroscopy (EELS) analysis[13] and is consistent with our XPS results (see Table S2), but was not measured directly under reaction conditions and evidenced an actively participating species in ODH reactions. The small concentration of surface MoO$_x$ (likely less than a couple of monolyers[5,34,35]) in combination with the low conversion explains the small intensity of the Mo=O signal and underlines the need for a highly sensitive approach as provided by ME-DRIFTS coupled with PSD. A transient V=O signal was observed previously in supported vanadia catalysts as a result of a fast hydrogen transfer from propane to the catalyst surface and subsequent regeneration.[20] As there is no indication of a change in mechanism with temperature (see Figure 1), a similar behavior may also be operative in the case of the (supported) molybdenum surface layer of iron molybdate catalysts.

In addition to the ME-DRIFTS results, operando UV-Vis spectra (see Figure S7) reveal small contributions from d–d transitions between 600 and 800 nm caused by the presence of reduced Mo$^{4/5+}$ species under reactive conditions, which are in good agreement with the reduction of Mo=O groups during the hydrogen transfer from propane to MoO$_x$, further indicating the reduction and participation of Mo=O groups during the reaction.[32] The amount of d–d transitions also increases concurrently with the increase in conversion between 320 and 500 °C while no additional structural dynamics is detected, further underlining the occurance of the same reaction mechanism.

Operando Spectroscopy

The two wavelengths at which Raman spectroscopy was performed are highlighted in the UV-Vis spectra (see Figure S7), as the choice of the excitation wavelength can greatly influence the Raman intensity and the depth of information. At

514 nm, the absorption is small and is expected to be mostly caused by oligomerized MoO_x on the catalyst surface,[32] which may undergo a selective resonance enhancement. However, this is not observed in the Vis-Raman (514 nm excitation) spectra (see Figure S8 and Table S3 for assignments), which can be explained by the high depth of penetration of the visible laser, thus gathering information from the bulk and thereby covering the small contribution from surface MoO_x species. Hence, no structural dynamics can be detected at this wavelength for $Fe_2(MoO_4)_3$, indicating that the bulk structure is not significantly changed during the reaction at either temperature. In contrast, in the case of the UV-Raman spectra (at 385 nm excitation) the absorption is much higher (see Figure S7), giving rise to resonance enhancements mainly caused by transitions in the molybdate.[36] Figure 3 depicts operando Raman spectra of $Fe_2(MoO_4)_3$ at 320 and 500 °C recorded in a feed of 12.5% O_2/12.5% C_3H_8/He compared to oxidative conditions (12.5% O_2/He). Based on the increased absorption, the UV wavelength has a smaller depth of penetration compared to the Vis, leading to a difference in the depth over which information is gathered by UV-Raman compared to Vis-Raman spectroscopy, which is more focused on the subsurface of the material.
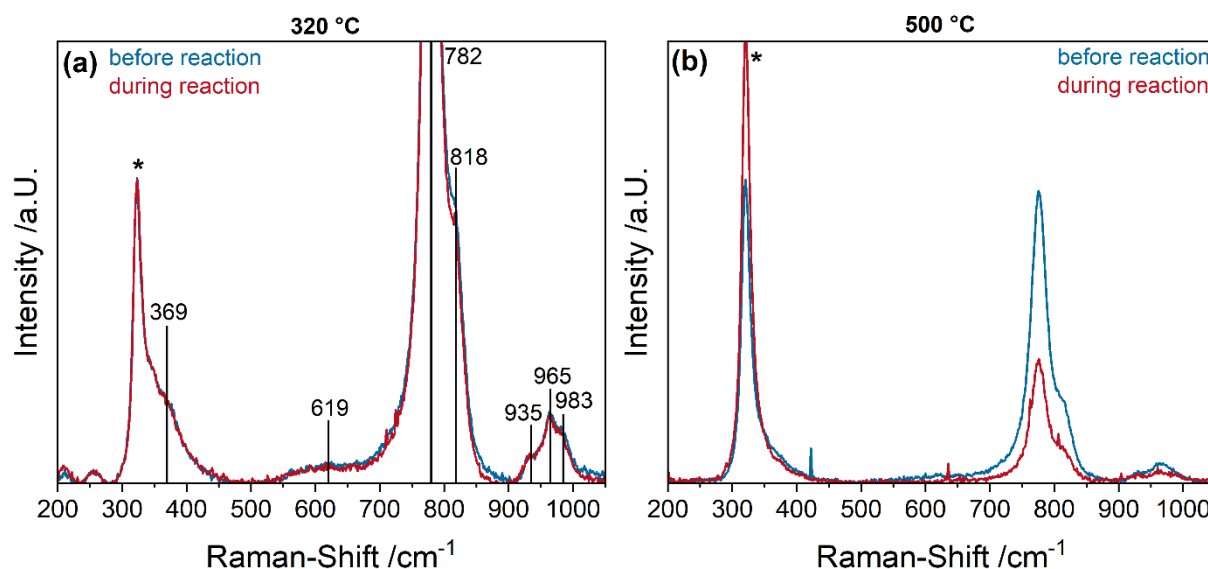
Figure 3: Operando UV-Raman spectra (at 385 nm excitation) of $Fe_2(MoO_4)_3$ recorded in a feed of 12.5% O_2/12.5% C_3H_8/He compared to oxidative conditions (12.5% O_2/He) at **(a)** 320 °C and **(b)** 500 °C. The asterisk (*) marks a peak resulting from the CaF_2 window used.

The spectra measured at 320 °C show only very slight but reproducible changes in the intensity of the antisymmetric MoO_4 stretching modes at 782 and 818 cm^{-1} (see

Figure 3a), indicating that the MoO_4 in the $Fe_2(MoO_4)_3$ lattice is reduced during the reaction. At 500 °C these changes are much more pronounced (see Figure 3b), consistent with the increase in conversion, indicating a significant transport of oxygen from the $Fe_2(MoO_4)_3$ subsurface lattice to the surface of the catalyst, facilitating the ODH reaction. This is also in good agreement with the proposition that the mechanism is the same over the investigated temperature range, as higher temperatures facilitate the formation of oxygen vacancies in the $Fe_2(MoO_4)_3$ lattice and subsequent oxygen diffusion to the surface. As a consequence, there is more oxygen available for the reaction, thus increasing the reaction rate including the over-oxidation of propane to CO_x, which is in good agreement with the observed selectivities. The results from operando/transient ME-DRIFT, UV-Vis spectroscopy, and Raman spectroscopy indicate that surface MoO_x facilitates the initial hydrogen transfer from propane to the catalyst, which is the rate-determining step, while lattice oxygen of $Fe_2(MoO_4)_3$ acts as the oxidizing agent. So far, the discussion has focused on the role of surface MoO_x and the involvement of lattice oxygen. However, the influence of iron and oxygen transport properties is likely to be important, all the more so as the catalyst is characterized by a very small surface area and large particles (as shown previously for this sample)[3], emphasizing the importance of the bulk properties.

To enhance the understanding of the transport properties within $Fe_2(MoO_4)_3$, we applied our newly developed operando powder impedance spectroscopic approach.[21] For comparison, MoO_3 and Fe_2O_3 loaded with MoO_x (1Mo/nm²) were measured as reference samples, to better determine the influence of the Fe and Mo concentration on the catalytic activity. For best possible comparability, the Fe_2O_3 sample had a similar particle size and surface area to the $Fe_2(MoO_4)_3$ one.[3] Operando impedance spectra of the three samples at 320 °C and of MoO_3 at 500 °C are shown in the SI (see Figures S9 and S10).
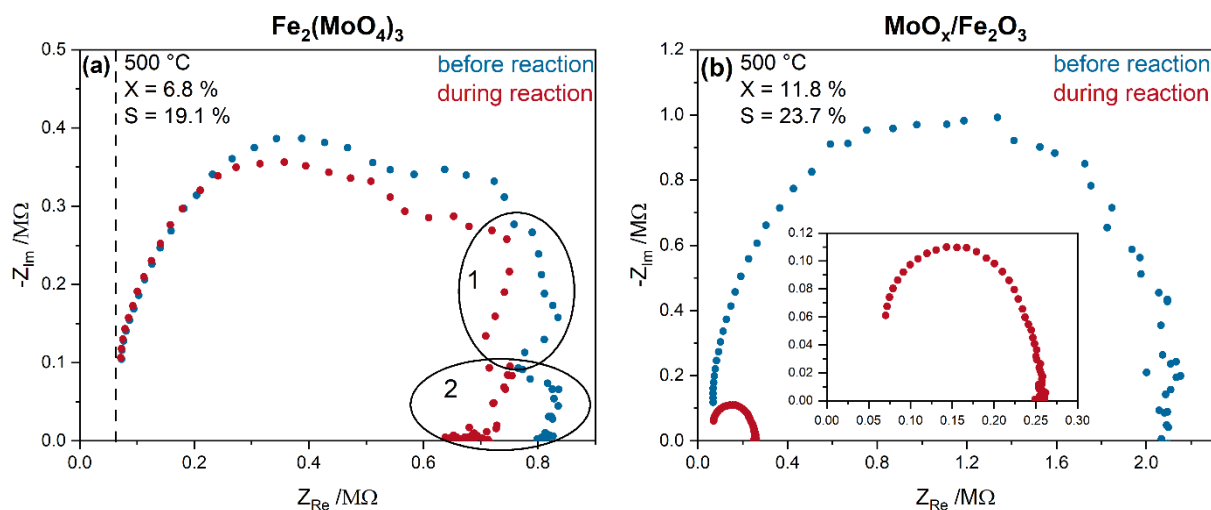
Figure 4: Operando impedance spectroscopic results for **(a)** $Fe_2(MoO_4)_3$ and (b) MoO_x/Fe_2O_3 at 500 °C in a feed of 12.5% O_2/12.5% C_3H_8/He compared to oxidative conditions (12.5% O_2/He). The dashed line marks the region of bulk electrode resistance and the numbered circles highlight the regions in which the $Fe_2(MoO_4)_3$ impedance spectrum differs from that of the MoO_x/Fe_2O_3. The operando impedance spectroscopic results for MoO_3, $Fe_2(MoO_4)_3$, and $1.0MoO_x+Fe_2O_3$ at 320 °C and MoO_3 at 500 °C are shown in the SI (see Figures S9 and S10).

Since the conversions are low at 320 °C for all three samples, the degree of reduction is also small, and due to the low temperatures, the conductivity of the material is not sufficient for good-quality impedance spectra. This leads to a high degree of noise, which makes the interpretation of the spectra difficult (see Figure S9). Therefore, we focused on the 500 °C impedance spectra, which allow access to mechanistic information due to the much higher oxygen mobility and hence conductivity of the materials. Based on all the previous evidence in the kinetic and spectroscopic results, it seems likely that the reaction mechanism stays the same between both temperatures and the effects detected only increase concurrently with the conversion, the assumption that we can focus on the 500 °C impedance spectra seems justified. Based on the impedance data of $Fe_2(MoO_4)_3$ at 500 °C under oxidative and reactive conditions (see Figure 4a), a detailed equivalent circuit model analysis was performed, enabling a physical interpretation of each electric component (see Figures S11 and S12, and discussion). The region left of the dashed line is not shown as it is composed of electrode resistance and inductance due to the material skin effect (see discussion in the SI). When the gas-phase is switched from oxidative to reactive conditions, the overall conductivity of the material increases, which is in good agreement with its reaction-induced reduction (compare Figures 3 and S7) and the

11

increased mass transport of oxygen ions. As explained in detail in the SI, the impedance data suggests oxygen ion mass transport from additional phases (Fe_2O_3, MoO_x, $FeMoO_4$) to be too small to be detected by XRD, as well as hydrogen and water transport in the molybdenum-rich and more defective/porous surface regions of $Fe_2(MoO_4)_3$.[5,21,37] This is in good agreement with the operando UV-Raman and UV-Vis data, providing a clear indication of the relevance of oxygen transport through the material. Furthermore, the resistance element R5 (compare Figure S11) indicates hydrogen transport through the $Fe_2(MoO_4)_3$ surface layer in agreement with ME-DRIFTS data. In addition, taking into account water reduction (in the sub-circuit containing R3, R4, C4, and W), significantly increases the quality of the equivalent-circuit fit compared to a fit based on oxygen transport phenomena only (compare Figure S12). In comparison, the impedance spectra of MoO_x/Fe_2O_3 shown in Figure 4b depict none of the additional features displayed by $Fe_2(MoO_4)_3$ but behave close to an ideal R-C equivalent-circuit, indicating the importance of oxygen ion transport only, without any additional phases. A contribution of MoO_x is not detected for the MoO_x/Fe_2O_3 sample, as the surface loading of MoO_x is expected to be much smaller (1 Mo/nm²) compared to the near stoichiometric presence of Mo close to the $Fe_2(MoO_4)_3$ surface. The MoO_3 impedance spectrum (see Figure S10) shows a poor signal-to-noise ratio with very significant resistances, indicating low conductance.

Comparing the conductance of the three samples to their conversion reveals a correlation. Importantly, the resistance of all samples decreases when the gas phase is switched from oxidative to reactive conditions, indicating an increased oxygen mobility due to the reducing gas atmosphere.[38] The lowest conversion of 0.4% is observed for crystalline MoO_3, which is accompanied by a resistance in the megohm region, but cannot be quantified further due to the high noise. $Fe_2(MoO_4)_3$ and MoO_x/Fe_2O_3 show lower resistances of ~700 and ~250 kΩ and higher conversions of 6.8% and 11.8%, respectively, exhibiting a clear correlation between iron content, oxygen mobility and conversion. This suggests that a higher concentration of iron is the driving factor for higher conversions, while the presence of molybdenum seems to be important for C-H bond breakage, which is supported by the similar selectivities of $Fe_2(MoO_4)_3$ and MoO_x/Fe_2O_3, despite their differences in conversion.

In summary, applying the newly developed operando impedance spectroscopic approach to the $Fe_2(MoO_4)_3$ system allowed direct investigation of the influence of the catalyst composition on the oxygen transport properties and therefore conversion.

Discussion

Based on the operando and transient spectroscopic results presented above, a reaction mechanism is proposed (see Figure 5). First, a hydrogen atom is abstracted from propane via a Mo=O group (shown by ME-DRIFTS, see Figures 2, S5 and S6) of the molybdenum-rich surface and transferred quickly to the catalyst surface. The reduced molybdenum can then be seen in the d-d transitions observable in the operando UV-Vis spectra (Figure S7). The hydrogen atom then diffuses through the surface layer of the catalyst, where hydroxyl and/or water can be formed, as shown by the equivalence cirquit of operando impedance spectroscopy (see Figure S11 and discussion). Similarly, the second hydrogen atom is abstracted and bound to lattice oxygen, eventually leading to the formation of water, which desorbs from the catalyst into the gas phase (see Figure S11, S12 and discussion), thereby leaving an oxygen vacancy, which can then be replenished by subsurface oxygen via oxygen transport to the surface (seen by the conductivity and oxygen transport increase in the impedance spectra) and gas-phase oxygen. As a result of the reaction, there is an overall reduction of the material, both at the molybdenum-enriched surface (ME-DRIFTS, UV-Vis) and in the subsurface (UV-Raman, impedance; see Figures 2, 3, 4, S8, S9 and S11), which facilitates the formation of $FeMoO_4$, which is more conductive and can be seen cleary in the operando impedance spectra (Figure S11). Additionally, an increased amount of iron in the lattice increases the oxygen mobility and therefore the conversion but due to the high oxygen mobility, Fe_2O_3-based catalysts often lead to total oxidation,[5] which was also shown by the significant increase in conductivity in the impedance spectra (Figure 4b) due to the quick transport of oxygen. In contrary, MoO_3 has been demonstrated to be an excellent selective oxidation catalyst but shows low conversion in ODH reactions,[15] which could be explained by its low oxygen mobility (see Figure 4). $Fe_2(MoO_4)_3$ combines these two properties effectively by increasing the oxygen mobility compared to MoO_3, and in addition, by forming a thin layer of amorphous MoO_x on the surface of the catalyst, greatly increasing the selectivity for ODH in comparison to Fe_2O_3. The green and red triangles indicate an increase or decrease of the respective value mentioned, this is, it describes the influence of an increase of the iron or molybdenum content on the conversion and selectivity.
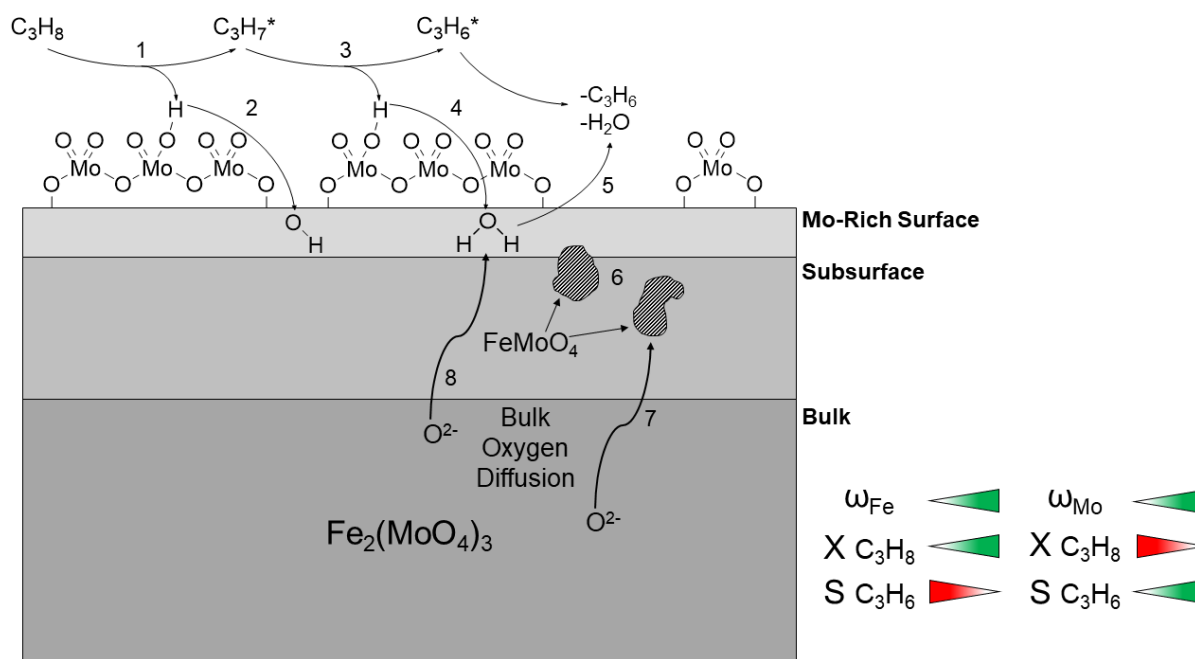
Figure 5: Mechanistic scheme of the ODH of propane over $Fe_2(MoO_4)_3$ catalysts, illustrating the respective influence of iron and molybdenum on the catalytic performance. The hydrogen transfer arrows 2 and 4 indicates oxygen-mediated diffusion. For details see text.

In summary, we applied multiple operando and transient spectroscopies to investigate the mechanism of propane ODH over $Fe_2(MoO_4)_3$. Our findings suggest the M=O groups of MoO_x to be an active site that is responsible for the abstraction of hydrogen from C-H bonds, which is commonly described as the rate-determining step in propane ODH.[6] Multiple effects within the subsurface/bulk contribute to a further enhancement of the catalytic activity, including percolation of hydrogen in the subsurface, the formation of water, subsequent phase transformation and regeneration by oxygen diffusion and gas-phase oxygen. Hereby, the concentration of iron is crucial for the oxygen mobility within the material and can influence the catalytic activity substantially. Owing to the structure of $Fe_2(MoO_4)_3$, both high conversion, due to copious amounts of iron, and good selectivity, due to the interaction of surface MoO_x with the gas phase, can be achieved. By applying novel operando and transient spectroscopic approaches under working conditions, we were able to directly access fundamental properties of $Fe_2(MoO_4)_3$ catalysts that were previously a matter of debate or only observed indirectly. The method of our approach is readily transferable to other oxide catalysts and reactions, while our findings are expected to serve as a basis for a

detailed mechanistic understanding of the mode of operation of selective oxidation catalysts.

Methods

Catalyst Preparation

The synthesis of $Fe_2(MoO_4)_3$ by co-precipitation has been described previously.[3] Briefly, iron nitrate nonahydrate (Merck, ≥98%) and ammonium heptamolybdate (Merck, ≥99%) were dissolved separately in demineralized water. The aqueous iron solution was then added dropwise to the molybdate solution while it was stirred. The mixed solutions were stirred for three more hours to complete the precipitation process. The precipitate was first filtered and washed with demineralized water and ethanol, and then dried over night at 100 °C in air. Finally, the powder was calcined in air at 500 °C for 10 h.

For the reference samples, iron (III) oxide (Sigma Aldrich, particle size <5µm, >96%) was loaded by incipient wetness impregnation with ammonium heptamolybdate tetrahydrate. For that, the iron(III) oxide was dispersed in an aqueous solution of ammonium heptamolybdate tetrahydrate (Fluka, puriss. p. a. >99%) under continuous stirring. The dispersion was dried at 90 °C overnight, followed by calcination at 600 °C for 12 h.

MoO_3 was synthesized by calcination of recrystallized ammonium heptamolybdate tetrahydrate (Fluka, puriss. p. a. >99%) at 600 °C for 12 h.

Catalytic Testing

Catalytic testing was performed in a CCR 1000 reaction cell using 120 mg of catalyst. The sample was first dehydrated for 1 h at 365 °C in 12.5% O_2/He (40 ml_n/min). The catalyst was then cooled to 25 °C, exposed to 12.5% O_2/12.5% C_3H_8/He with a total flow rate of 40 ml_n/min, and then heated to 550 °C in 45 °C steps, staying at each temperature for 1 h. The gas-phase composition was analyzed continuously using gas chromatography (GC, Agilent Technologies 7890B). The GC is equipped with a PoraPlotQ and a Molsieve column as well as a thermal conductivity detector (TCD) and a flame ionization detector (FID) in series. The setup is connected through a twelve-way valve. One chromatogram is measured every 29 min, resulting in two chromatograms for each temperature, which were averaged. The pressure before and after the GC was monitored to correct the detected areas for pressure fluctuations.

X-ray Photoelectron Spectroscopy

X-ray photoelectron spectroscopy (XPS) was carried out on an SSX 100 ESCA spectrometer (Surface Science Laboratories Inc.) employing a monochromatic Al Kα X-ray source (1486.6 eV) operated at 9 kV and 10 mA; the spot size was approximately 1mm×0.25 mm. The base pressure of the analysis chamber was $<10^{-8}$ Torr. Survey spectra (eight measurements) were recorded between 0 and 1100 eV with 0.5 eV resolution, whereas detailed spectra (30 measurements) were recorded with 0.05 eV resolution. To account for sample charging, the C 1s peak of ubiquitous carbon at 284.4 eV was used to correct the binding-energy shifts in the spectra. Atomic concentrations were calculated using the relative sensitivity factors (RSFs) given in Table 1.

Table 1: Relative sensitivity factors (RSFs) for quantification of elemental concentrations from XP spectra.

Element and level	Fe 2p$_{3/2}$	Mo 3d	O 1s	C 1s
RSF	7.96	9.79	2.50	1.00

Diffuse Reflectance UV-Vis Spectroscopy

Diffuse reflectance (DR) UV-Vis spectra were recorded on a Jasco V-770 UV-Vis spectrometer. Dehydrated $BaSO_4$ was used as the white standard. For each experiment, 120 mg of catalyst was put in the commercially available reaction cell (Praying Mantis High Temperature Reaction Chamber, Harrick Scientific) equipped with transparent quartz glass windows. The Harrick cell was calibrated separately to ensure the same temperatures in both reaction cells used. Operando spectra were measured at 320 and 500 °C under oxidizing (12.5% O_2/He) and reactive (12.5% C_3H_8/12.5% O_2/He) conditions, after 1 h of dehydration in 12.5% O_2/He at 365 °C (total flow rate: 40 ml$_n$/min). Before measuring each spectrum, the samples were pretreated in the respective gas phase for 30 minutes, to ensure a steady state.

Visible Raman Spectroscopy

Visible (Vis) Raman spectroscopy was performed at 514 nm excitation, emitted from a Cobolt Fandango diode laser (Hübner Photonics). The light was focused onto the sample, gathered by an optical fiber and dispersed by a transmission spectrometer (Kaiser Optical, HL5R). The dispersed Raman radiation was subsequently detected by an electronically cooled charge-coupled devise (CCD) detector (–40 °C, 1024 × 256 pixels). The spectral resolution was 5 cm^{-1} with a wavelength stability of better than 0.5 cm^{-1}. For Raman experiments, 120 mg of catalyst was filled into a CCR 1000 reactor (Linkam Scientific Instruments) equipped with a quartz window (Linkam Scientific Instruments). The laser power at the sample location was 4 mW. Data analysis of the Raman spectra included cosmic ray removal and an auto new dark correction. Operando spectra were measured at 320 and 500 °C under oxidizing (12.5% O_2/He) and reactive (12.5% C_3H_8/12.5% O_2/He) conditions, after 1 h of dehydration in 12.5% O_2/He at 365 °C (total flow rate: 40 ml_n/min). Before measuring each spectrum, the samples were pretreated in the respective gas phase for 30 minutes, to ensure a steady state.

UV-Raman Spectroscopy

UV-Raman spectroscopy was performed at an excitation wavelength of 385 nm generated by a laser system based on a titanium sapphire (Ti:Sa) solid-state laser pumped by a frequency-doubled Nd:YAG laser (Coherent, Indigo). The fundamental wavelength is frequency doubled to 385 nm using a LiB_3O_5 crystal. The light is focused onto the sample, and the scattered light is collected by a confocal mirror setup and focused into a triple-stage spectrometer (Princeton Instruments, TriVista 555).[39] Finally, the Raman contribution is detected by a CCD (2048 × 512 pixels) cooled to –120 °C. The spectral resolution of the spectrometer is 1 cm^{-1}. For Raman experiments, 120 mg of catalyst was placed in a CCR 1000 reactor (Linkam Scientific Instruments) equipped with a CaF_2 window (Korth Kristalle GmbH). The laser power at the location of the sample was 5 mW. Data processing included cosmic ray removal and background subtraction. Operando spectra were measured at 320 and 500 °C under oxidizing (12.5% O_2/He) and reactive (12.5% C_3H_8/12.5% O_2/He) conditions, after 1 h

of dehydration in 12.5% O_2/He at 365 °C (total flow rate: 40 ml_n/min). Before measuring each spectrum, the samples were pretreated in the respective gas phase for 30 minutes, to ensure a steady state.

Modulation Excitation (ME)-DRIFTS

ME-DRIFT spectroscopy was performed using the same apparatus as for steady-state DRIFTS experiments; a more detailed description of our basic DRIFTS setup and the modifications made for recording ME-DRIFT spectra have already been published.[40,41] For each experiment, 120 mg of catalyst was used.

We used the rapid scan mode of Bruker's spectrometer software OPUS 7.2. Spectra were measured from 850 to 3800 cm^{-1} with a resolution of 0.5 cm^{-1}, an aperture of 8 mm, and a mirror speed of 40 kHz. A Valco Instruments 4/2 valve (Model E2CA, version ED), communicating with the Vertex 70, is used to rapidly switch between different gas feeds, which are controlled *via* digital mass flow controllers (Bronkhorst).

As gases we used C_3H_8 (Westfalen, 3.5), O_2 (Westfalen, 5.0), and helium (Westfalen, 5.0). One measurement series consisted of 20 periods (20 gas-phase switches), each of which had a duration of 360 s and consisted of 240 spectra. For one spectrum, five consecutive interferograms were averaged, so that a new spectrum was acquired every 1.5 s.

As background the catalyst spectrum itself was used, after 1 h of dehydration at 365 °C in 12.5% O_2/helium atmosphere and a 10 min treatment at 320 °C in one of the reaction gases for conventional ME-DRIFTS (12.5% O_2 or 12.5% C_3H_8 in helium). The flow was kept constant at 100 mL_n/min during the pretreatment and experiment.

During ME-DRIFTS, a flow of either 12.5% C_3H_8 or 12.5% O_2 in helium was kept constant over the sample, while the other feed gas was pulsed over the sample. The temperature during all modulation excitation experiments was kept at 320 °C. To remove the gas-phase contribution, we subtracted gas-phase spectra over KBr from each recorded DRIFT spectrum. To exclude the possibility of intensity fluctuations over multiple periods, we checked the intensity profile at three distinct wavenumbers, representative of the background, an adsorbate peak, and a gas-phase peak, but detected no absolute intensity changes over multiple periods that could influence the Fourier transformation.

To obtain phase-sensitive spectra, the time-resolved 3D spectral data was converted from the time to the phase domain. For an overview, the resolution of phase spectra was chosen to be 30°, whereas mechanistic insights were obtained using a resolution of 1°. The main operation of phase-sensitive detection (PSD) is a Fourier transformation according to[42]

$$I_{\tilde{v}}(\varphi) = \frac{2}{T} \int_{0}^{T} I_{\tilde{v}}(t) \cdot \sin(2\pi f t + \varphi) \, dt$$

where $I(t)$ is the time-dependent intensity at one specified wavenumber ($\tilde{v}$) that is convoluted with the sine function, representing the modulation of the external parameter (e.g., the gas-phase concentration), thus forming $I(\varphi)$, the phase-resolved intensity. The frequency of the external modulation is f, and 0 and T represent the times at which the considered dataset begins and ends, respectively. To obtain a complete phase-resolved spectrum, this procedure is repeated for every wavenumber. By varying φ from 0 to 360° with a chosen resolution and repeating the steps above, the complete phase-resolved dataset is created.

The strong noise in the signal of the ME-DRIFT spectra (see Figure 2) is caused by the low MoO_x concentration and low conversion as the intensity after the Fourier transform depends on the intensity change when switching the gas-phases.

Impedance Spectroscopy

Potentiostatic electrochemical impedance spectra (p-EIS) were acquired in a two-electrode system using a BioLogic VSP potentiostat/galvanostat operated in the 1 MHz to 1 Hz range with 60 mV amplitude and 20 measurement points per decade acquired in triplicate with a potential of 0.05 V versus a reference of +0.771 V (Fe^{3+} to Fe^{2+}). The positive reduction potential was referenced against the standard hydrogen electrode (SHE). Impedance spectra were recorded after placing 120 mg of the catalyst in a commercial CCR1000 cell (Linkam Scientific Instruments, UK), equipped with a PTFE (polytetrafluoroethylene) plate with two holes for the copper electrodes, as described previously.[21] In this context, we also performed experiments with gold electrodes (Alfa Aesar, UK, 99.999 %), where no influence of the electrode material on the electrochemical output was observed with the exception of a parasitic potential iR drop, arising from the peculiarities of the cell assembly. Its compensation was

performed manually in the EC-Lab v. 11.33 (BioLogic, France) acquisition software prior to the actual measurement. Before each measurement, to allow for equilibration, the sample was kept at 320/500 °C for about 30 min under oxidative (12.5% O_2/He) or reactive (12.5% O_2/12.5% C_3H_8/He) conditions, respectively (total flow rate: 40 ml_n/min). This procedure ensures that the measurements take place in a stationary state as verified by considering the temporal evolution, which did not show any significant changes during the measurement. Raw spectra were validated by applying the Kramers–Kronig relations, which deviate from an ideal behavior by ca. 8%, with 11% being the benchmark for discarding the measurement, meaning that the real and imaginary parts of the experimental spectra overlap with say, the imaginary spectral points calculated from the real part by applying Hilbert transforms. Before measuring each spectrum, the samples were pretreated in the respective gas phase for 30 minutes, to ensure a steady state.

Associated Content

The supporting information is available free of charge at………

Declaration of Competing Interests

The authors declare that they have no known competing financial interests or personal relationships that could have appeared to influence the work reported in this paper.

Acknowledgements

References

1. Hess, C. & Schlögl, R. *Nanostructured Catalysts. Selective Oxidations* (Royal Society of Chemistry, 2011).

2. Adkins, H. & Peterson, W. R. The Oxidation of Methanol with Air over Iron, Molybdenum, and Iron-Molybdenum Oxides. *J. Am. Chem. Soc.* **53,** 1512–1520; 10.1021/ja01355a050 (1931).

3. Oefner, N. *et al.* Activity, Selectivity and Initial Degradation of Iron Molybdate in the Oxidative Dehydrogenation of Ethanol. *ChemCatChem* **14**; 10.1002/cctc.202101219 (2022).

4. Malik, M. I., Abatzoglou, N. & Achouri, I. E. Methanol to Formaldehyde: An Overview of Surface Studies and Performance of an Iron Molybdate Catalyst. *Catalysts* **11,** 893; 10.3390/catal11080893 (2021).

5. Bowker, M. Rules for Selective Oxidation Exemplified by Methanol Selective Oxidation on Iron Molybdate Catalysts. *Top. Catal.* **58,** 606–612; 10.1007/s11244-015-0399-4 (2015).

6. Beck, B. *et al.* Partial oxidation of ethanol on vanadia catalysts on supporting oxides with different redox properties compared to propane. *J. Catal.* **296,** 120–131; 10.1016/j.jcat.2012.09.008 (2012).

7. Söderhjelm, E. *et al.* On the Synergy Effect in MoO_3–$Fe_2(MoO_4)_3$ Catalysts for Methanol Oxidation to Formaldehyde. *Top. Catal.* **50,** 145–155; 10.1007/s11244-008-9112-1 (2008).

8. Routray, K., Zhou, W., Kiely, C. J., Grünert, W. & Wachs, I. E. Origin of the synergistic interaction between MoO_3 and iron molybdate for the selective oxidation of methanol to formaldehyde. *J. Catal.* **275,** 84–98; 10.1016/j.jcat.2010.07.023 (2010).

9. Soares, A. P. V., Portela, M. F. & Kiennemann, A. Methanol Selective Oxidation to Formaldehyde over Iron-Molybdate Catalysts. *Catal. Rev.* **47,** 125–174; 10.1081/cr-200049088 (2005).

10. Yeo, B. R. *et al.* The surface of iron molybdate catalysts used for the selective oxidation of methanol. *Surf. Sci.* **648,** 163–169; 10.1016/j.susc.2015.11.010 (2016).

11. Gaur, A. *et al.* Operando XAS/XRD and Raman Spectroscopic Study of Structural Changes of the Iron Molybdate Catalyst during Selective Oxidation of Methanol. *ChemCatChem* **11,** 4871–4883; 10.1002/cctc.201901025 (2019).

12. O'Brien, M. G., Beale, A. M., Jacques, S. D. M. & Weckhuysen, B. M. A Combined Multi-Technique In Situ Approach Used to Probe the Stability of Iron Molybdate Catalysts During Redox Cycling. *Top. Catal.* **52,** 1400–1409; 10.1007/s11244-009-9324-z (2009).

13. House, M. P., Shannon, M. D. & Bowker, M. Surface Segregation in Iron Molybdate Catalysts. *Catal. Lett.* **122,** 210–213; 10.1007/s10562-008-9467-8 (2008).

14. House, M. P., Carley, A. F., Echeverria-Valda, R. & Bowker, M. Effect of Varying the Cation Ratio within Iron Molybdate Catalysts for the Selective Oxidation of Methanol. *J. Phys. Chem. C* **112,** 4333–4341; 10.1021/jp711251b (2008).

15. Bowker, M., Carley, A. F. & House, M. Contrasting the Behaviour of MoO_3 and MoO_2 for the Oxidation of Methanol. *Catal. Lett.* **120,** 34–39; 10.1007/s10562-007-9255-x (2007).

16. Soares, A. P. V., Portela, M. F., Kiennemann, A. & Hilaire, L. Mechanism of deactivation of iron-molybdate catalysts prepared by coprecipitation and sol-gel techniques in methanol to formaldehyde oxidation. *Chem. Eng. Sci.* **58,** 5; 10.1016/S0009-2509(02)00573-0 (2003).

17. Carrero, C. A., Schloegl, R., Wachs, I. E. & Schomaecker, R. Critical Literature Review of the Kinetics for the Oxidative Dehydrogenation of Propane over Well-Defined Supported Vanadium Oxide Catalysts. *ACS Catal.* **4,** 3357–3380; 10.1021/cs5003417 (2014).

18. Kristian Viegaard Raun *et al.* Deactivation behavior of an iron-molybdate catalyst during selective oxidation of methanol to formaldehyde. *Catal. Sci. Technol.* **8,** 4626–4637; 10.1039/C8CY01109E (2018).

19. Bowker, M. *et al.* Selectivity determinants for dual function catalysts: applied to methanol selective oxidation on iron molybdate. *Catal. Struct. React.* **1,** 95–100; 10.1179/2055075815Y.0000000002 (2015).

20. Schumacher, L., Weyel, J. & Hess, C. Unraveling the Active Vanadium Sites and Adsorbate Dynamics in VO_x/CeO_2 Oxidation Catalysts Using Transient IR

Spectroscopy. *J. Am. Chem. Soc.* **144,** 14874–14887; 10.1021/jacs.2c06303 (2022).

21. Ziemba, M., Radtke, M., Schumacher, L. & Hess, C. Elucidating CO_2 Hydrogenation over In_2O_3 Nanoparticles using Operando UV/Vis and Impedance Spectroscopies. *Angew. Chem. Int. Ed.* **61,** e202209388; 10.1002/anie.202209388 (2022).

22. Schumacher, L. & Hess, C. The active role of the support in propane ODH over VO_x/CeO_2 catalysts studied using multiple operando spectroscopies. *J. Catal.* **398,** 29–43; 10.1016/j.jcat.2021.04.006 (2021).

23. Hallam, P. M., Gómez-Mingot, M., Kampouris, D. K. & Banks, C. E. Facile synthetic fabrication of iron oxide particles and novel hydrogen superoxide supercapacitors. *RSC Adv.* **2,** 6672; 10.1039/c2ra01139e (2012).

24. Bowker, M. *et al.* The Selective Oxidation of Methanol on Iron Molybdate Catalysts. *Top. Catal.* **48,** 158–165; 10.1007/s11244-008-9058-3 (2008).

25. Bowker, M. *et al.* The selective oxidation of methanol to formaldehyde on iron molybdate catalysts and on component oxides. *Catal. Lett.* **83,** 165–176; 10.1023/a:1021025828544 (2002).

26. Baerns, M., Hofmann, H. & Renken, A. *Chemische Reaktionstechnik* (Thieme Verlag, Stuttgart, 1992).

27. Dias, A. P. S., Rijo, B., Kiennemann, A. & Portela, M. F. Methanol oxidation over iron molybdate catalysts. Main and side reactions kinetics. *Appl. Catal. A Gen.* **658,** 119118; 10.1016/j.apcata.2023.119118 (2023).

28. Brookes, C., Bowker, M. & Wells, P. Catalysts for the Selective Oxidation of Methanol. *Catalysts* **6,** 92; 10.3390/catal6070092 (2016).

29. Srinivasan, P. D., Patil, B. S., Zhu, H. & Bravo-Suárez, J. J. Application of modulation excitation-phase sensitive detection-DRIFTS for in situ /operando characterization of heterogeneous catalysts. *React. Chem. Eng.* **4,** 862–883; 10.1039/C9RE00011A (2019).

30. Urakawa, A., Bürgi, T. & Baiker, A. Sensitivity enhancement and dynamic behavior analysis by modulation excitation spectroscopy: Principle and application in

heterogeneous catalysis. *Chem. Eng. Sci.* **63,** 4902–4909; 10.1016/j.ces.2007.06.009 (2008).

31. M. Dieterle & G. Mestl. Raman spectroscopy of molybdenum oxides Part II. Resonance Raman spectroscopic characterization of the molybdenum oxides Mo_4O_{11} and MoO_2. *Phys. Chem. Chem. Phys.* **4,** 822–826; 10.1039/B107046K (2002).

32. Dieterle, M., Weinberg, G. & Mestl, G. Raman spectroscopy of molybdenum oxides Part I. Structural characterization of oxygen defects in MoO_{3-x} by DR UV/Vis, Raman spectroscopy and X-Ray diffraction. *Phys. Chem. Chem. Phys.* **4,** 812–821; 10.1039/b107012f (2002).

33. Mojet, B. L., Coulier, L., van Grondelle, J., Niemantsverdriet, J. W. & van Santen, R. A. Potential of UV–Raman Spectroscopy for Characterization of Sub-monolayer MoO_x Model Catalysts at Ambient Pressure. *Catal. Lett.* **96,** 1–4; 10.1023/B:CATL.0000029521.80714.8d (2004).

34. Brookes, C. *et al.* The Nature of the Molybdenum Surface in Iron Molybdate. The Active Phase in Selective Methanol Oxidation. *J. Phys. Chem. C* **118,** 26155–26161; 10.1021/jp5081753 (2014).

35. Brookes, C. *et al.* Molybdenum Oxide on Fe_2O_3 Core–Shell Catalysts: Probing the Nature of the Structural Motifs Responsible for Methanol Oxidation Catalysis. *ACS Catal.* **4,** 243–250; 10.1021/cs400683e (2013).

36. Xu, Q., Jia, G., Zhang, J., Feng, Z. & Li, C. Surface Phase Composition of Iron Molybdate Catalysts Studied by UV Raman Spectroscopy. *J. Phys. Chem. C* **112,** 9387–9393; 10.1021/jp800359p (2008).

37. Balasubramani, V. *et al.* Review—Recent Advances in Electrochemical Impedance Spectroscopy Based Toxic Gas Sensors Using Semiconducting Metal Oxides. *J. Electrochem. Soc.* **167,** 37572; 10.1149/1945-7111/ab77a0 (2020).

38. Forzatti, P., Villa, P. L. & Mari, C. M. Electrical conductivity of polycrystalline $Fe_2(MoO_4)_3$. *Mater. Chem. Phys.* **10,** 385–391; 10.1016/0254-0584(84)90099-3 (1984).

39. Waleska, P. S. & Hess, C. Oligomerization of Supported Vanadia: Structural Insight Using Surface-Science Models with Chemical Complexity. *J. Phys. Chem. C* **120,** 18510–18519; 10.1021/acs.jpcc.6b01672 (2016).

40. Ziemba, M., Weyel, J. & Hess, C. Elucidating the mechanism of the reverse water–gas shift reaction over Au/CeO_2 catalysts using operando and transient spectroscopies. *Appl. Catal. B Environ.* **301,** 120825; 10.1016/j.apcatb.2021.120825 (2022).

41. Weyel, J., Ziemba, M. & Hess, C. Elucidating Active CO–Au Species on $Au/CeO_2(111)$: A Combined Modulation Excitation DRIFTS and Density Functional Theory Study. *Top. Catal.* **65,** 779–787; 10.1007/s11244-022-01599-1 (2022).

42. Baurecht, D. & Fringeli, U. P. Quantitative modulated excitation Fourier transform infrared spectroscopy. *Rev. Sci. Instr.* **72,** 3782–3792; 10.1063/1.1400152 (2001).

Supporting Information

Unraveling Surface and Bulk Dynamics of $Fe_2(MoO_4)_3$ during Oxidative Dehydrogenation using Operando and Transient Spectroscopies

Leon Schumacher, Mariusz Radtke, Jan Welzenbach, Christian Hess*

Technical University of Darmstadt, Department of Chemistry, Eduard-Zintl-Institut für Anorganische und Physikalische Chemie, Peter-Grünberg-Str. 8, 64287 Darmstadt, Germany

*Corresponding Author (E-Mail: christian.hess@tu-darmstadt.de)

1. Additional Spectroscopic Data

Table S1: Characterization data for $Fe_2(MoO_4)_3$, MoO_x/Fe_2O_3, and MoO_3.

Sample	ICP-OES Mo/Fe bulk ratio	N_2 Physisorption Surface Area	SEM Imaging Particle Size
$Fe_2(MoO_4)_3$	1.53	2.9 m²/g	2-8 μm
MoO_x/Fe_2O_3	0	8.7 m²/g	5 μm
MoO_3	0	3.9 m²/g	2-5 μm
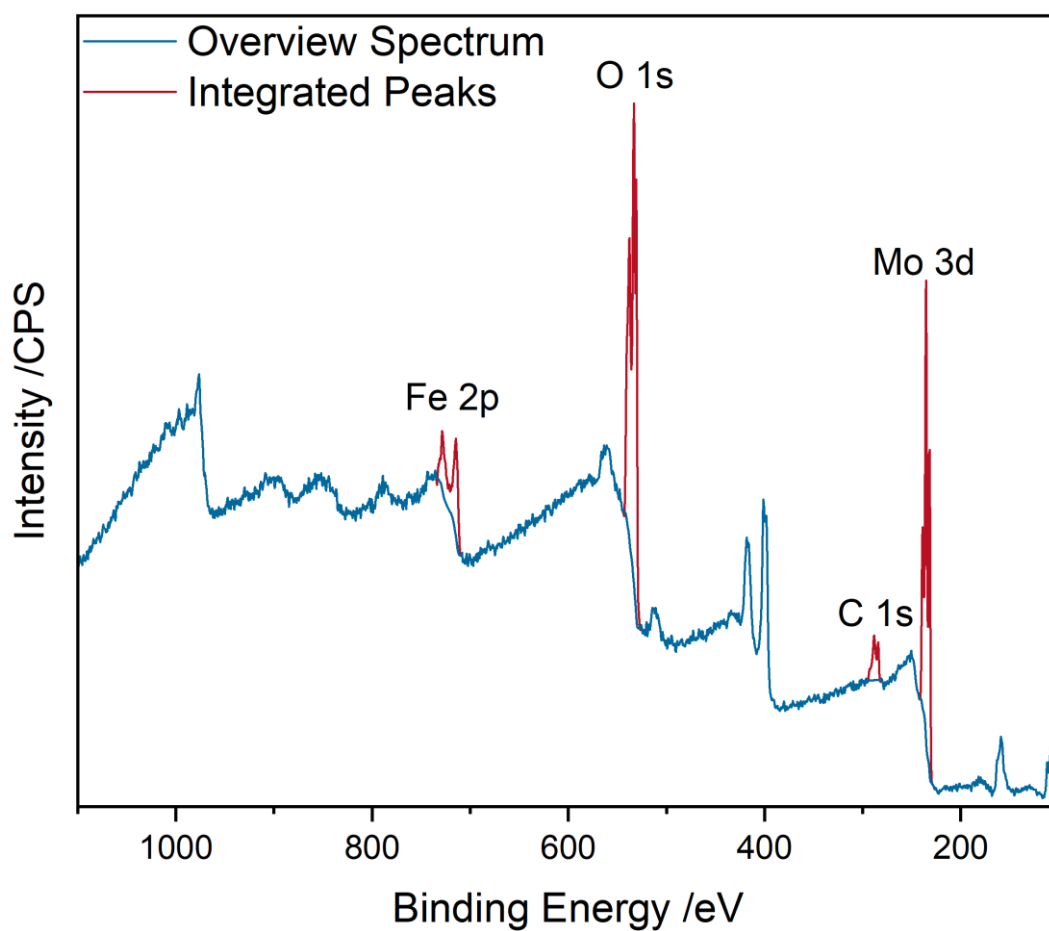
Figure S1: Overview XP spectrum of $Fe_2(MoO_4)_3$. The peaks used for quantification (Table S2) are highlighted in red.

Table S2: Elemental composition of $Fe_2(MoO_4)_3$ based on X-ray photoelectron (XP) survey spectra and the use of the relative sensitivity factor (RSF) values from Table 1.

Fe	Mo	O	C	Mo/Fe
6.2	15.6	60.5	17.7	2.5
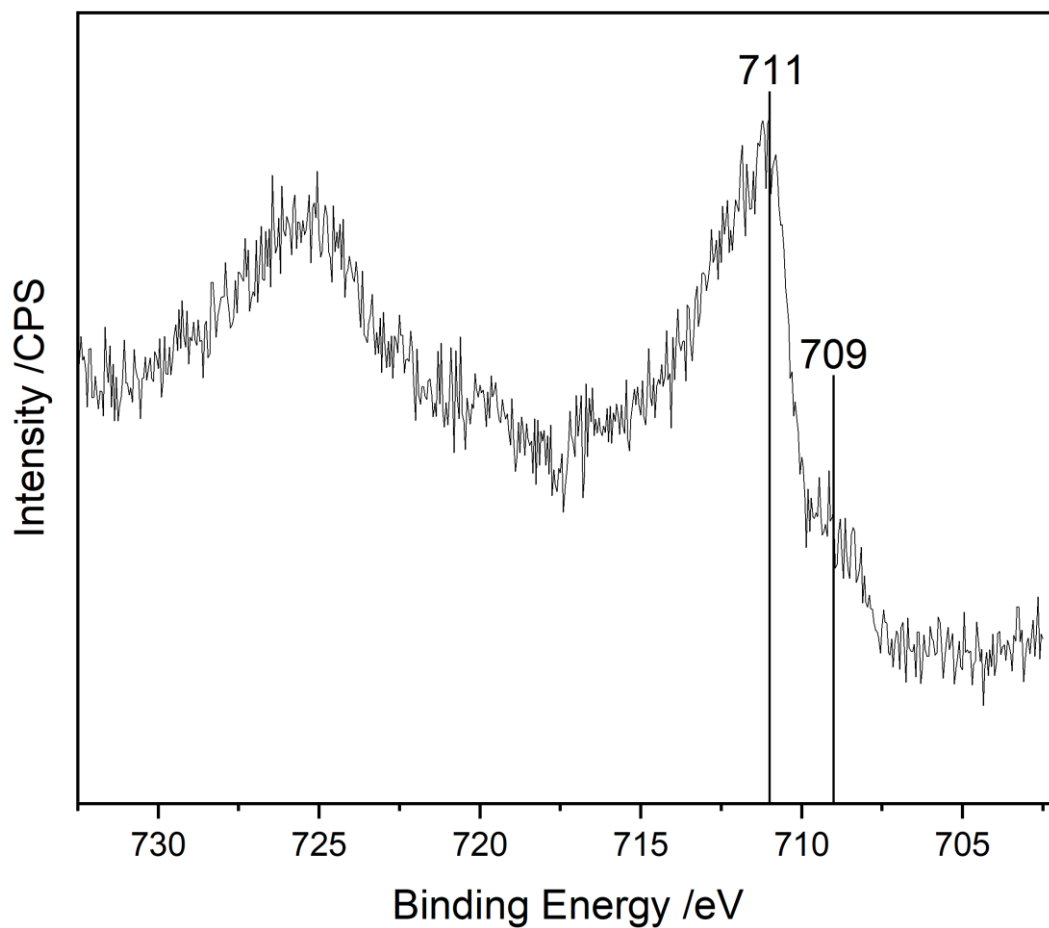
Figure S2: Fe $2p_{3/2}$ photoemission of the $Fe_2(MoO_4)_3$ sample used in this study. The positions of characteristic Fe peaks are marked.
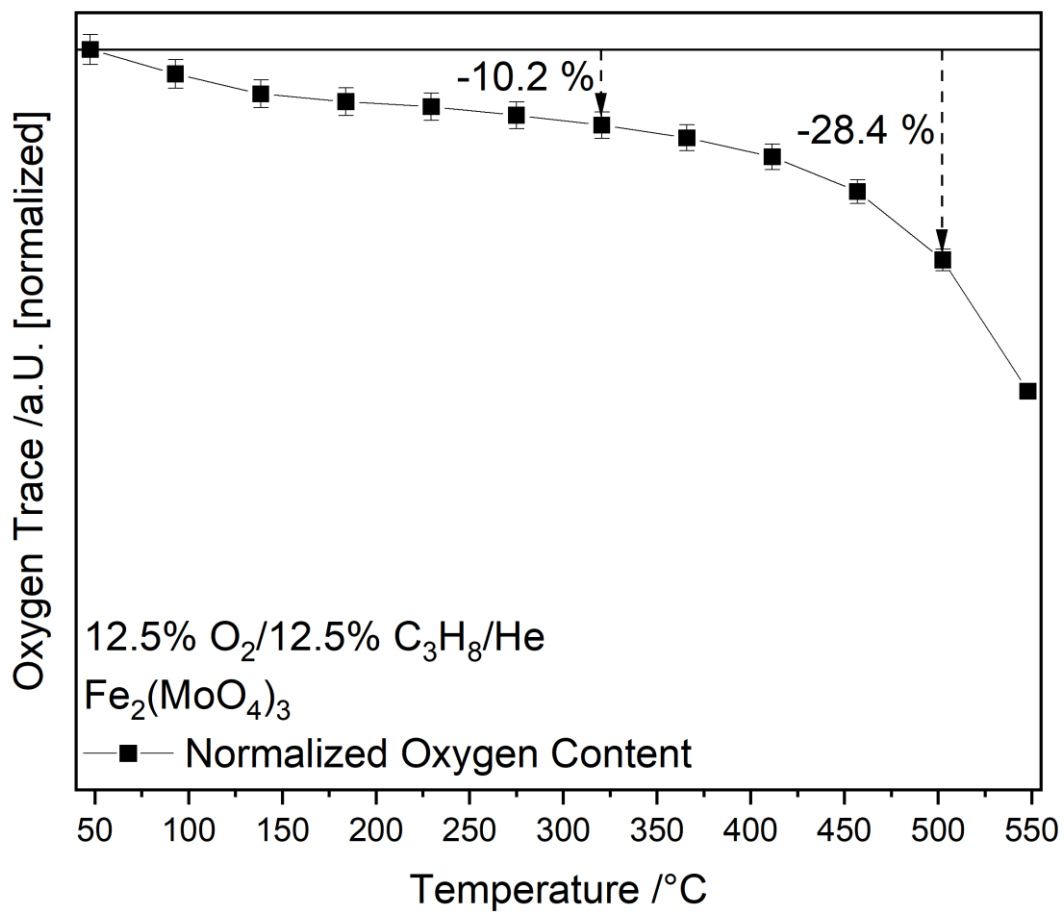
Figure S3: Oxygen consumption of $Fe_2(MoO_4)_3$ during reaction conditions at different temperatures. The temperatures used for operando experiments are highlighted and the percentage of consumed oxygen in regard to the amount where no consumption occurs is indicated by dashed arrows.
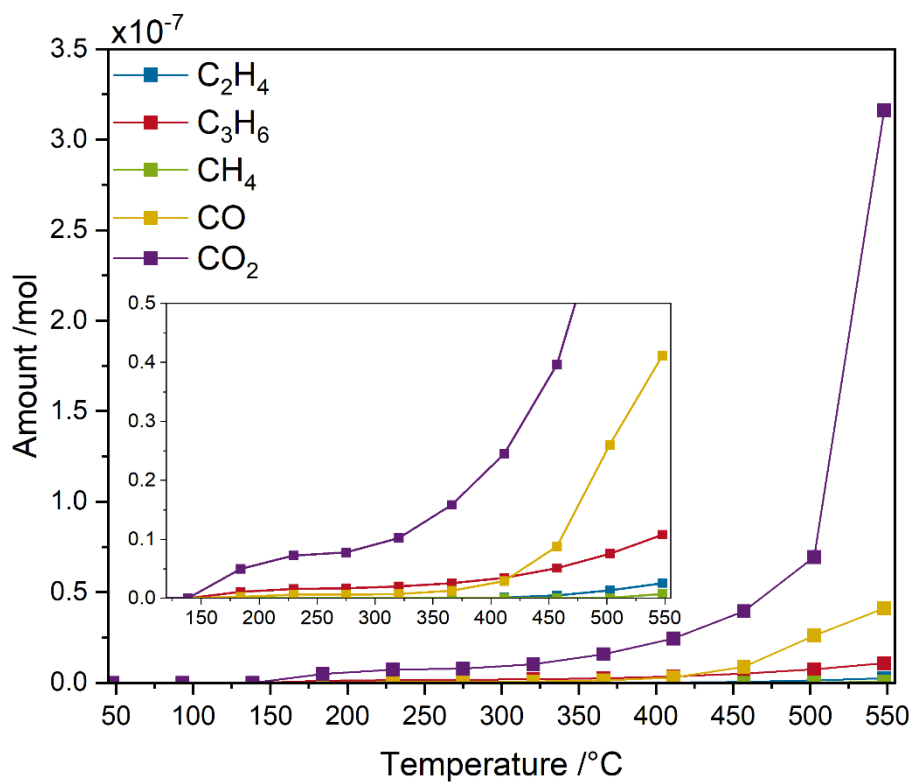
Figure S4: Molar product distribution of all products detected by the gas chromatography (GC) during the treatment of $Fe_2(MoO_4)_3$ in 12.5% O_2/12.5% C_3H_8/He between 50 and 550 °C after initial dehydration in 12.5% O_2/He at 365 °C. The inset gives an enlarged view of the temperature region between 120 and 550 °C.
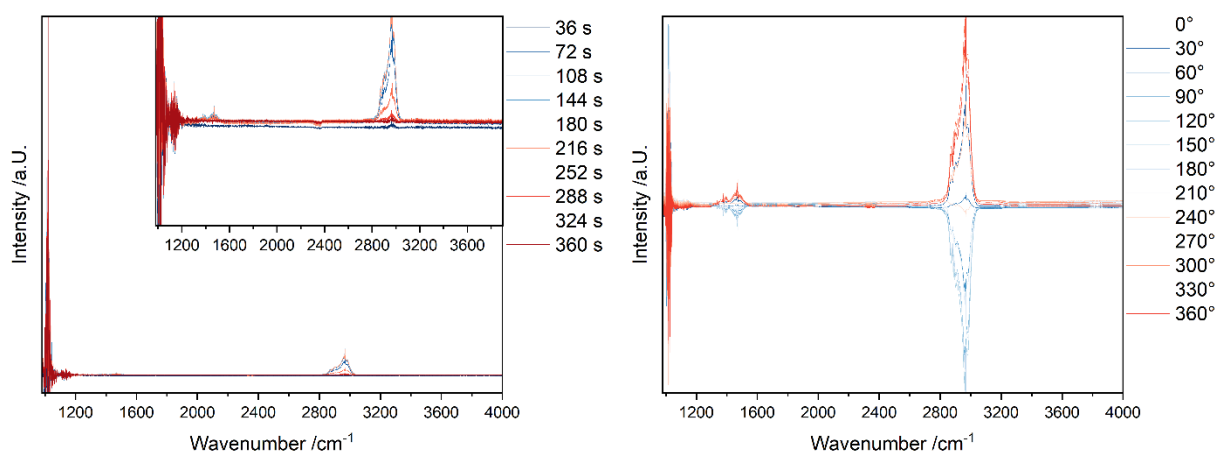
Figure S5: Comparison between the time domain (before PSD, left) and phase domain (after PSD, right) DRIFT spectra of $Fe_2(MoO_4)_3$ recorded under modulation-excitation conditions as described in the experimental section.

The time resolved DRIFT spectra of $Fe_2(MoO_4)_3$ were recorded under a constant propane (12.5% C_3H_8/He) and a pulsed oxygen (12.5% O_2/12.5% C_3H_8/He) flow. A spectrum was measured every 1.54 s while the gas phases were switched according to the experimental section. Due to the reaction conditions being switched on and off, the signal of peaks that participate in the reaction follow the periodic pertubation with a certain phase-shift, while peaks that do not participate in the reaction have no periodic behavior. When the results are Fourier transformed over the entire phase space (phase sensitive detection, PSD), only those peaks following the periodic pertubation due to a concentration modulation remain, while the remaining signals are eliminated, allowing for the discrimination between active and observer species. Due to this, the detection sensitivity towards weak signals that are either heavily overlapped by spectator species/background noise or participate only weakly in the reaction, is significantly enhanced.[1,2]

This is evidenced by Figure S5, where, in the time-resolved spectra (left), a large but noisy signal of the Mo=O region between 950 and 1080 cm^{-1} is observed, but no significant changes between the time resolved spectra can be detected, while a constant background overlaps some of the propane gas phase peaks between 1200 and 1600 cm^{-1}. After PSD, the propane gas phase is more pronounced, but a participation of the Mo=O peak is still observable, indicating its importance in the reaction. To emphasize the assignments to the propane gas phase and to ensure that, besides the gas phase, only the Mo=O peak participates, the same measurement as

in Figure 2 and S5 is performed in the same manner over KBr, which is IR transparent and shows no conversion. The results after the PSD are shown Figure S6.
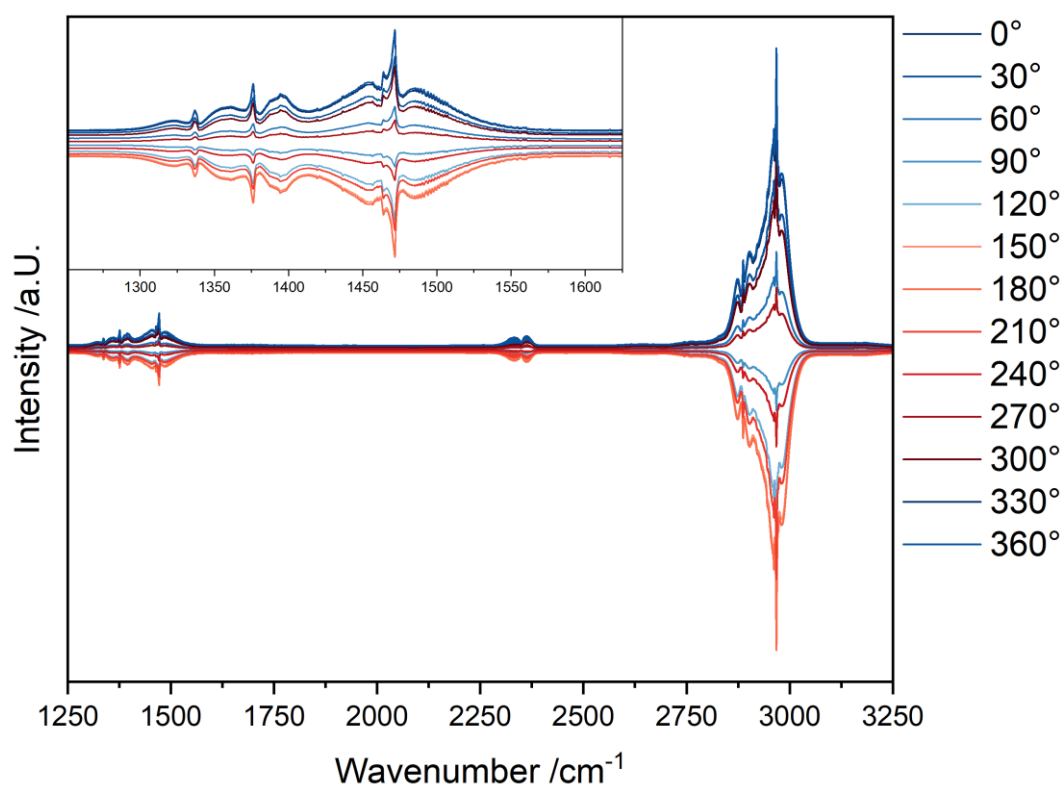
Figure S6: Gas phas contribution from propane to the ME-DRIFT spectra afer PSD.

Comparing the results in Figure S5 and S6, we can deduce that only propane gas phase contributions can be observed beside the Mo=O signal in the ME-DRIFT spectra of $Fe_2(MoO_4)_3$.
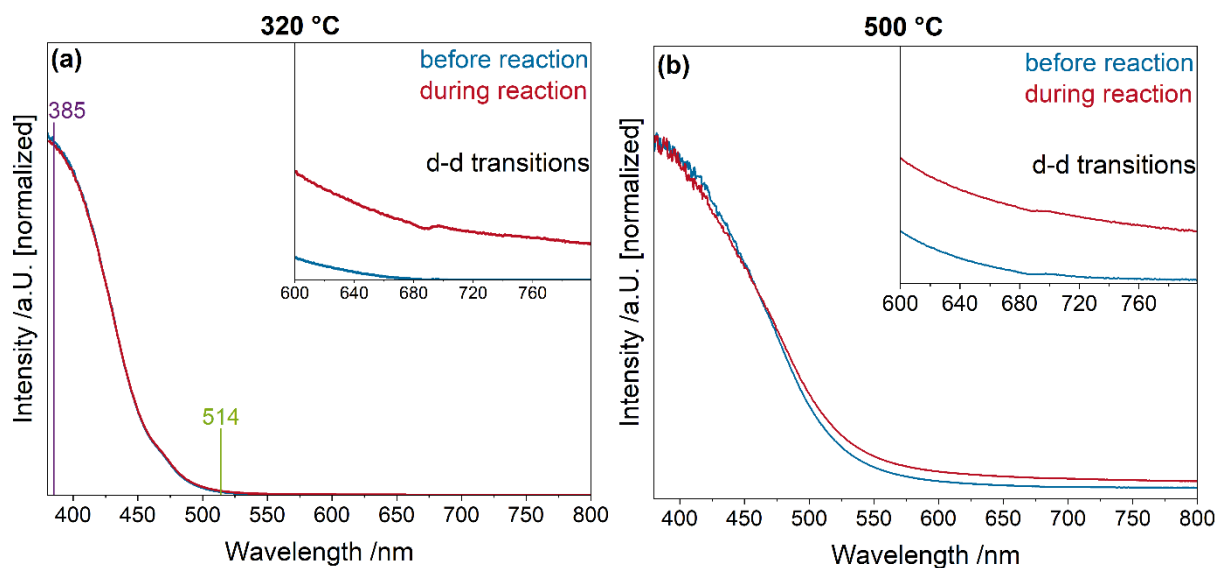
Figure S7: Operando UV-Vis spectra of $Fe_2(MoO_4)_3$ recorded in a feed of 12.5% O_2/12.5% C_3H_8/He, compared to oxidative conditions (12.5% O_2/He) at **(a)** 320 and **(b)** 500 °C. Spectra have been normalized for comparability. The insets give an enlarged view of the absorption between 600 and 800 nm. The wavelengths at which Raman spectroscopy was performed are marked in the left panel.
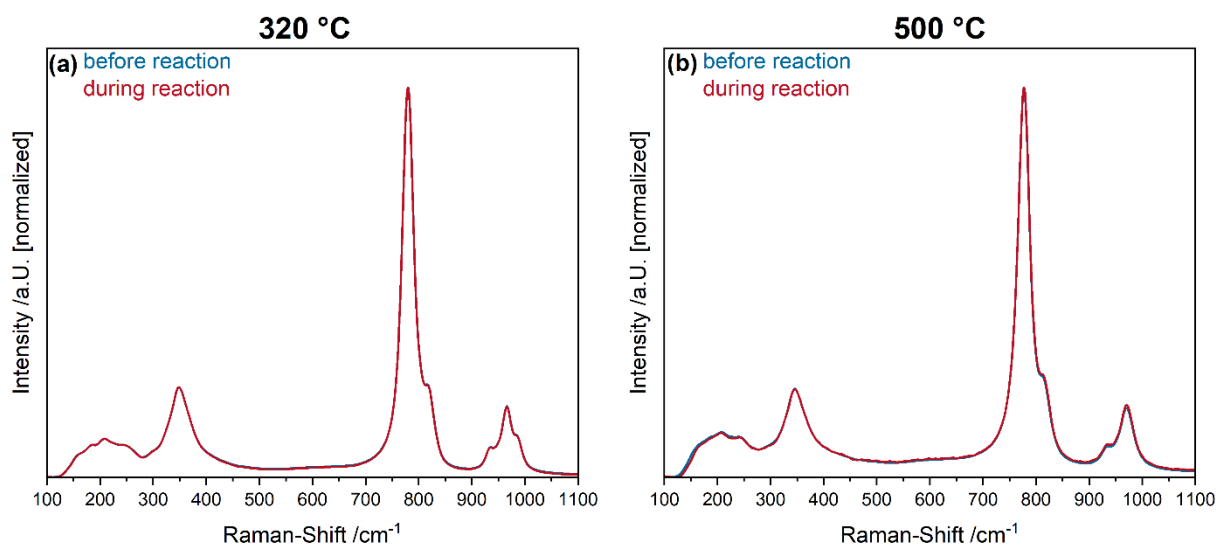
Figure S8: Operando Raman spectra (at 514 nm excitation) of $Fe_2(MoO_4)_3$ recorded in a feed of 12.5% O_2/12.5% C_3H_8/He, compared to oxidative conditions (12.5% O_2/He) at **(a)** 320 °C and **(b)** 500 °C. Spectra have been normalized for comparability.

Table S3: Assignment of the Raman features detected for $Fe_2(MoO_4)_3$.[3]

Wavenumber /cm^{-1}	Assignment
117 – 258	Lattice modes
299 – 370	MoO_4 bending modes
785 – 823	MoO_4 antisymmetric stretching modes
938 – 991	MoO_4 symmetric stretching modes
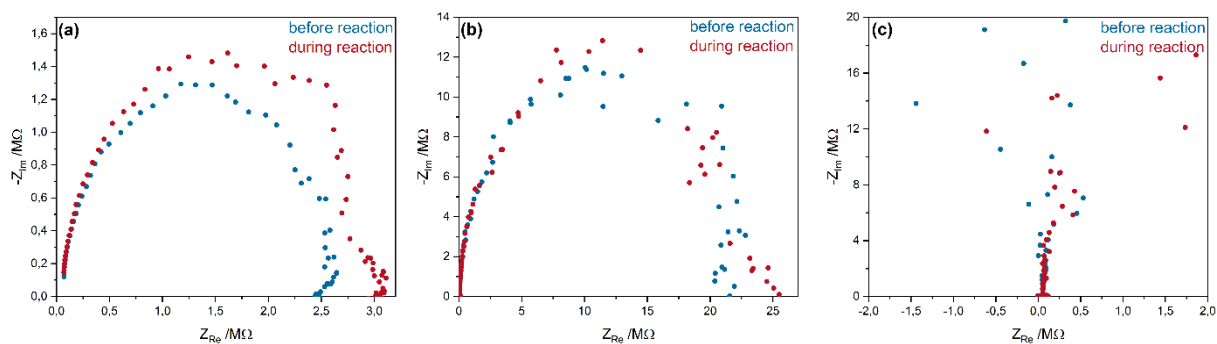
Figure S9: Operando impedance spectra of **(a)** $Fe_2(MoO_4)_3$, **(b)** $1.0MoO_x+Fe_2O_3$, and **(c)** MoO_3 at 320 °C in a feed of 12.5% O_2/12.5% C_3H_8/He, compared to oxidative conditions (12.5% O_2/He).
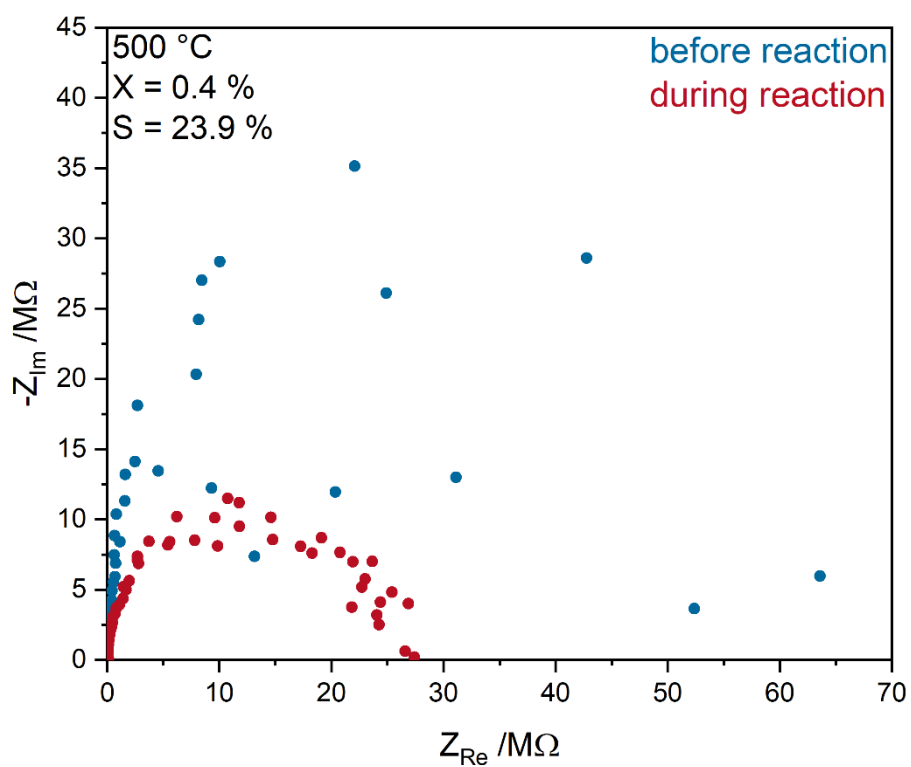
Figure S10: Operando impedance spectra of MoO_3 at 500 °C in a feed of 12.5% O_2/12.5% C_3H_8/He, compared to oxidative conditions (12.5% O_2/He).
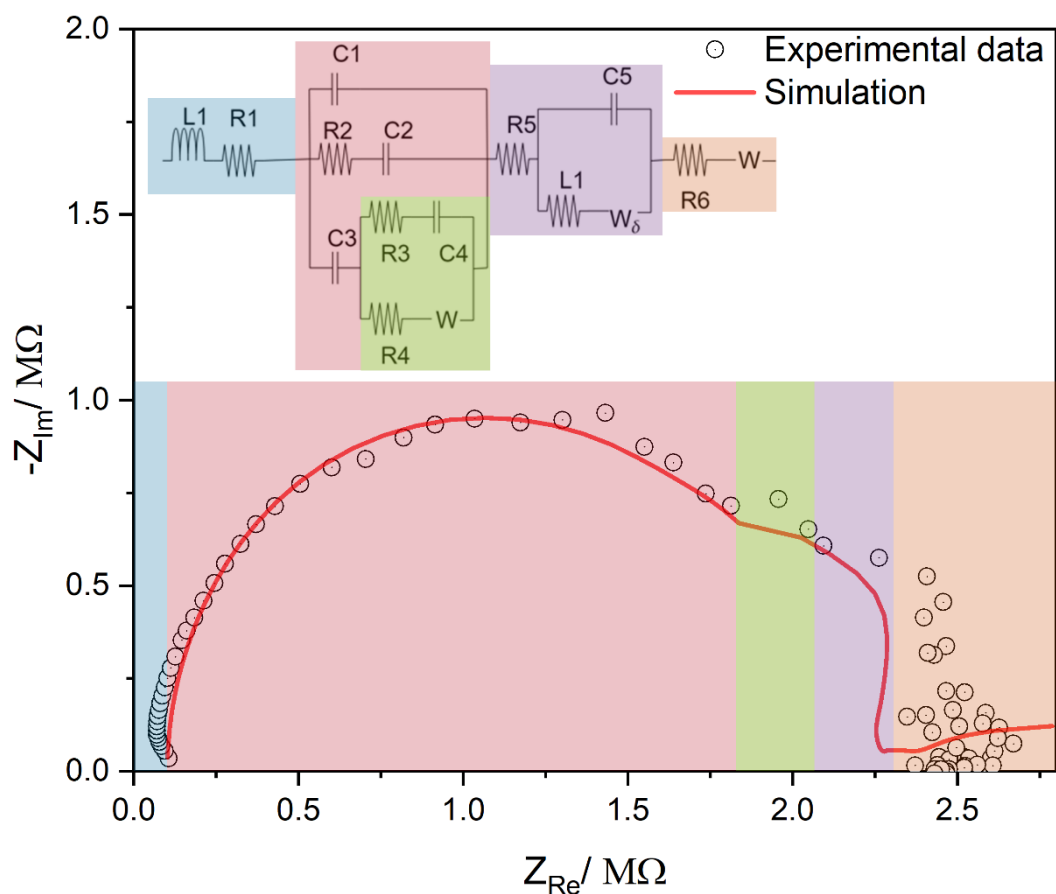
Figure S11: Experimental impedance data (points) of $Fe_2(MoO_4)_3$ recorded under reactive conditions (12.5% O_2/12.5% C_3H_8/He) at 500°C together with the results from equivalent circuit fitting (red line). The parts pf the equivalent circuit corresponding to the skin-effect, water creation, protonation and diffusion, as well as separation of $Fe_2(MoO_4)_3$ are indicated by different colors. For details see text.

The impedance spectrum of $Fe_2(MoO_4)_3$ at 500 °C under reactive conditions is composed of multiple elements separated into four sub-circuits. Each one is divided into ohmic, kinetic and ohmic/kinetic contributions. The ohmic parts represent the materials response, while the kinetic parts describe effects due to the occurring reaction.

The sub-circuit on the left (low impedance/high frequency) is composed of an induction (L) and a resistance (R) element in series (blue). When the indirect band gap of 2.7 eV of $Fe_2(MoO_4)_3$ is considered, the material can be described as a semi-conducting oxide,[4] which therefore implies impaired conductivity at room temperature. This causes the alternating current from the AC-potentiostatic impedance experiment to generate charge at the surface, leading to a high accumulation of current, which is described as the skin effect and is often fitted by L-R elements, even though, in some cases, this part is subtracted from the data.[5] This inductive contribution was minimal in our case, yielding a value of 1.39E-03 H after fitting while the electrode resistance was more significant in comparison, yielding a value of R1=101 kΩ, which is expected for a solid-state system with diminished conductivity.[6]

Following the impedance acquisition path from left (high frequency) to right (low frequency) the measurement time increases for each acquired point. The second sub-circuit of the impedance spectrum (red) is composed of four parts, each of which corresponds to different phases present in addition to $Fe_2(MoO_4)_3$ before and/or due to the reaction, that is, MoO_x, $FeMoO_4$ and Fe_2O_3, as determined by separate measurements (see main text and previous studies).[7,8] MoO_x and $FeMoO_4$ have the largest impact on the spectrum of $Fe_2(MoO_4)_3$; note that the contribution of MoO_x during the reaction has already been observed during transient IR measurements. The exact allocation of each phase to their electrical parts in the second sub-circuit is proposed to be a mixture. This corresponds to the C1-R2 parallel circuit in series with C2, and C2 is in parallel with C3. This C-C element describes the mixed character of MoO_x as Mo(V) and Mo(VI) corresponding to the induced oxygen transport initiated by the reaction and hydrogen transfer upon the first C-H breakage or water reduction.[9]

The third sub-circuit (containing R3, R4, C4, and the Warburg element; green) also describes oxygen transport in compliance with the Mars–van Krevelen mechanism and Frenkel equilibrium: $M_M^x + O_O^x \leftrightarrow M_M^x + O_i^{''} + V_O^{..}$. Here, the Kröger–Vink notation describes the presence of oxygen vacancies within the metal oxide to be responsible for the oxygen conduction. As part of the above-mentioned phase

separation, the more-conductive $FeMoO_4$ is generated, which causes less charge accumulation. Therefore, the second semi-circle in the impedance spectrum is reduced in size since $FeMoO_4$ is more conductive (even at room temperature) than $Fe_2(MoO_4)_3$ at temperatures between 370 and 900 K.[10,11]

The last semi-circle in the lower-frequency region (purple) corresponds to the kinetic/ohmic contribution. Here, the reaction according to the Mars–van Krevelen mechanism occurs. An interesting electrical component, leading to a significantly improved fit (see Figure S7, where only the oxygen transport is regarded), is a proton transport element in the form of R5, which is fully consistent with the transient hydrogen transfer suggested by the ME-DRIFTS data. The impedance data further indicates the diffusion and storage to be mixed according to the analysis performed by Chaparro et al.[12]. This is also the region of mass-transport loss, which indicates the release of compounds from the surface, which were previously diffusing out from the bulk and sub-surface. Here, we propose a mass-transport loss due to water, which is a product of the reaction.[13]

The last part of the spectrum (orange) in the lowest-frequency region corresponds to the mixed mass-transport loss (R) and compensation by the ongoing reaction (Warburg element W). The last R+W contribution (orange) corresponds to a mass-transfer effect, while the previous contribution (purple) describes the kinetic contribution from the reaction itself.

To further support the necessity of the proposed additional effects to oxygen transport, we performed a fit to the same impedance spectrum by taking only oxygen transport into account. The results are shown in Figure S8. If only oxygen transport based on RC-circuits is considered, the fit does not converge completely. This behavior is caused by the lack of diffusive effects, hydrogen transport and the inductive elements arising from the skin effect and vacancy displacement according to the Frenkel equilibrium. For the fit shown in Figure S8, data points strongly deviating from the spectrum were removed, but the quality of the fit is still poor. This behavior strongly indicates that oxygen transport is not the only phenomenon that needs to be taken into account to describe the impedance data of $Fe_2(MoO_4)_3$.
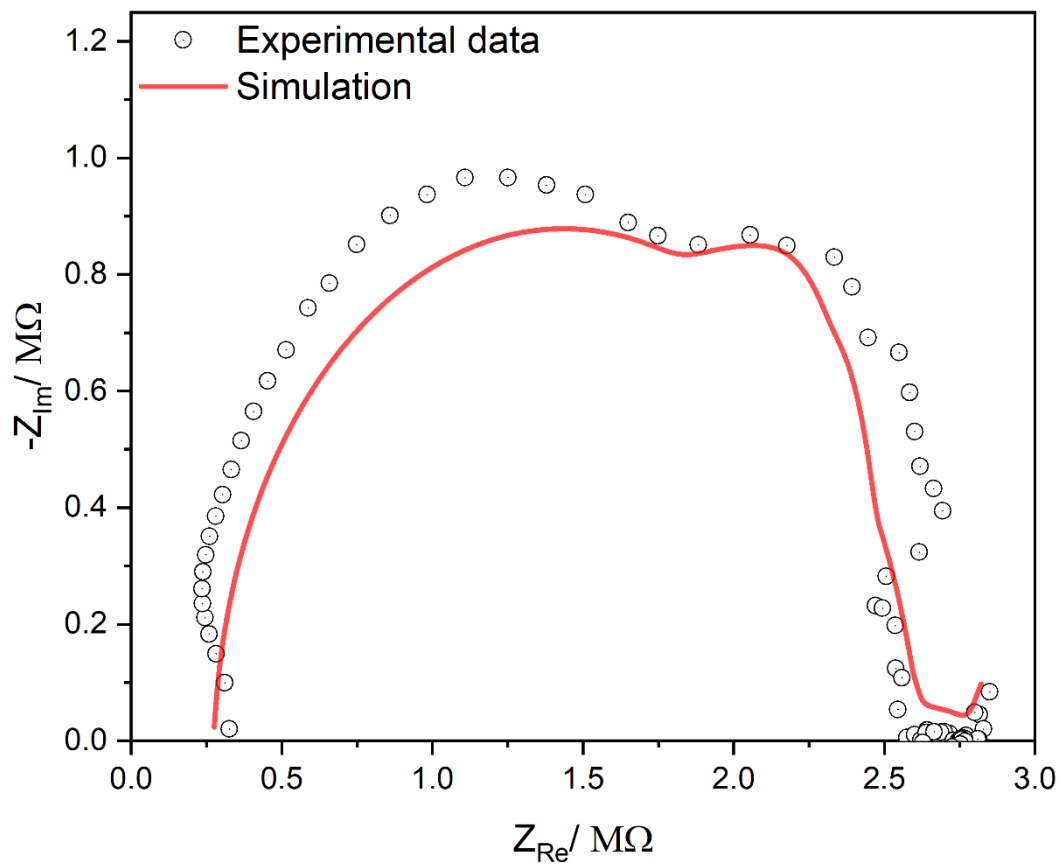
Figure S12: Experimental impedance data (points) of $Fe_2(MoO_4)_3$ recorded under reactive conditions (12.5% O_2/12.5% C_3H_8/He) at 500°C together with the results from equivalent circuit fitting (red line) based on oxygen transport effects only. For details see text.

References

1. Urakawa, A., Bürgi, T. & Baiker, A. Sensitivity enhancement and dynamic behavior analysis by modulation excitation spectroscopy: Principle and application in heterogeneous catalysis. *Chem. Eng. Sci.* **63,** 4902–4909; 10.1016/j.ces.2007.06.009 (2008).

2. Srinivasan, P. D., Patil, B. S., Zhu, H. & Bravo-Suárez, J. J. Application of modulation excitation-phase sensitive detection-DRIFTS for in situ /operando characterization of heterogeneous catalysts. *React. Chem. Eng.* **4,** 862–883; 10.1039/C9RE00011A (2019).

3. Sejkora, J. *et al.* A Raman spectroscopic study of a hydrated molybdate mineral ferrimolybdite, $Fe_2(MoO_4)_3 \cdot 7\text{-}8H_2O$. *Spectrochim. Acta A Mol. Biomol. Spectrosc.* **130,** 83–89; 10.1016/j.saa.2014.03.112 (2014).

4. Parveen, S. *et al.* Synthesis, characterization and photocatalytic performance of iron molybdate ($Fe_2(MoO_4)_3$) for the degradation of endosulfan pesticide. *Mater. Res. Express* **7,** 35016; 10.1088/2053-1591/ab73fa (2020).

5. Boukamp, B. A., Rolle, A., Vannier, R. N., Sharma, R. K. & Djurado, E. Electrostatic spray deposited $Ca_3Co_4O_{9+\delta}$ and $Ca_3Co_4O_{9+\delta}/Ce_{0.9}Gd_{0.1}O_{1.95}$ cathodes for SOFC. *Electrochim. Acta* **362,** 137142; 10.1016/j.electacta.2020.137142 (2020).

6. Laschuk, N. O., Easton, E. B. & Zenkina, O. V. Reducing the resistance for the use of electrochemical impedance spectroscopy analysis in materials chemistry. *RSC Adv.* **11,** 27925–27936; 10.1039/d1ra03785d (2021).

7. Bowker, M. Rules for Selective Oxidation Exemplified by Methanol Selective Oxidation on Iron Molybdate Catalysts. *Top. Catal.* **58,** 606–612; 10.1007/s11244-015-0399-4 (2015).

8. Oefner, N. *et al.* Activity, Selectivity and Initial Degradation of Iron Molybdate in the Oxidative Dehydrogenation of Ethanol. *ChemCatChem* **14**; 10.1002/cctc.202101219 (2022).

9. Bredar, A. R. C., Chown, A. L., Burton, A. R. & Farnum, B. H. Electrochemical Impedance Spectroscopy of Metal Oxide Electrodes for Energy Applications. *ACS Appl. Energy Mater.* **3,** 66–98; 10.1021/acsaem.9b01965 (2020).

10. Suresh babu, G. N., Shakkeel, N. K. & Kalaiselvi, N. $FeMoO_4$ nanorods anchored on graphene sheets as a potential anode for high performance sodium ion batteries. *J. Alloys Compd.* **877,** 160306; 10.1016/j.jallcom.2021.160306 (2021).

11. Forzatti, P., Villa, P. L. & Mari, C. M. Electrical conductivity of polycrystalline $Fe_2(MoO_4)_3$. *Mater. Chem. Phys.* **10,** 385–391; 10.1016/0254-0584(84)90099-3 (1984).

12. Chaparro, A. M., Duque, L. & Folgado, M. A. Analytical Model for the Hydrogen Transport Impedance at a PEMFC Anode. *Meet. Abstr.* **MA2022-02,** 2521; 10.1149/MA2022-02502521mtgabs (2022).

13. Jalani, N. H. *et al.* Performance analysis and impedance spectral signatures of high temperature PBI–phosphoric acid gel membrane fuel cells. *J. Power Sources* **160,** 1096–1103; 10.1016/j.jpowsour.2006.02.094 (2006).

4.5 Additional Related Topics

Lastly, the fifth part of this work deals with additional topics that are related to this work (through vanadia catalysis or CO_2 activation) but do not necessarily overlap fully with the main topics. These include the ethanol ODH over V_4C_3 MXenes, the reduction behavior of In_2O_3 and the investigation of In_2O_3 during the reverse water-gas shift reaction (RWGSr).

4.5.1 MXene Aerogel Derived Ultra-Active Vanadia Catalyst for Selective Conversion of Sustainable Alcohols to Base Chemicals

The twelvth overall publication concerns the synthesis of a new V_4C_3 MXene aerogel phase and its characterization in regards to activity and structure, employing Raman and XP spectroscopy, ICP-OES, temperature-programmed oxidation (TPO), SEM, XRD, HRTEM/EELS, and argon physisorption. Raman and XP spectroscopic investigations before and after ethanol ODH were contributed to this work. The material shows a very high degree of activity and selectivity under reaction conditions, and the in situ formation of mixed valence vanadium oxides (VO_2, V_6O_13, and V_3O_7) as well as V_2O_5 was shown to be highly important for the observed reactivity behavior. Due to the unique 2D structure of the MXene, the entire material on which these highly active vanadia species are supported exhibits a reduced valence state. This, in combination with the nanorod shape of the catalyst, results in an unusually high degree of oxygen mobility and a high density of active sites. The key to obtaining these catalysts was identified to be the MXene precursor, the aerogel arrangement and the soft oxidation conditions under an ODH gas atmosphere. The large number of possible MXenes due to different metal combinations highlights the importance of these results as a new class of mixed metal oxide catalysts.

MXene Aerogel Derived Ultra-Active Vanadia Catalyst for Selective Conversion of Sustainable Alcohols to Base Chemicals

Niklas Oefner, Christopher E. Shuck, Leon Schumacher, Franziska Heck, Kathrin Hofmann, Jana Schmidpeter, Weiqun Li, Mounib Bahri, B. Layla Mehdi, Alfons Drochner, Barbara Albert, Christian Hess, Yury Gogotsi, and Bastian J. M. Etzold*

Cite This: *ACS Appl. Mater. Interfaces* 2023, 15, 16714−16722

Read Online

ACCESS | Metrics & More | Article Recommendations | Supporting Information

ABSTRACT: Selective oxidation reactions are an important class of the current chemical industry and will be highly important for future sustainable chemical production. Especially, the selective oxidation of primary alcohols is expected to be of high future interest, as alcohols can be obtained on technical scales from biomass fermentation. The oxidation of primary alcohols produces aldehydes, which are important intermediates. While selective methanol oxidation is industrially established, the commercial catalyst suffers from deactivation. Ethanol selective oxidation is not commercialized but would give access to sustainable acetaldehyde production when using renewable ethanol. In this work, it is shown that employing 2D MXenes as building blocks allows one to design a nanostructured oxide catalyst composed of mixed valence vanadium oxides, which outperforms on both reactions known materials by nearly an order of magnitude in activity, while showing high selectivity and stability. The study shows that the synthesis route employing 2D materials is key to obtain these attractive catalysts. $V_4C_3T_x$ MXene structured as an aerogel precursor needs to be employed and mildly oxidized in an alcohol and oxygen atmosphere to result in the aspired nanostructured catalyst composed of mixed valence VO_2, V_6O_{13}, and V_3O_7. Very likely, the bulk stable reduced valence state of the material together coupled with the nanorod arrangement allows for unprecedented oxygen mobility as well as active sites and results in an ultra-active catalyst.

KEYWORDS: MXenes, aerogels, heterogeneous catalysis, oxidative dehydrogenation, formaldehyde, acetaldehyde
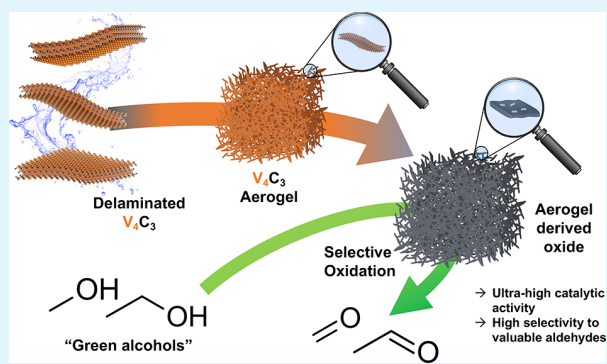
1. INTRODUCTION

Oxidative dehydrogenation (ODH) of primary alcohols, like methanol and ethanol, is a highly sought after heterogeneously catalyzed gas-phase reaction. The alcohol ODH leads to the corresponding aldehydes, which are important intermediates in the chemical industry.[1−4] ODH of methanol is industrially applied within the *FormOx* process on large scales with high selectivity and an overall plant yield of 89−90%.[5] However, the *FormOx* catalyst, an iron molybdate, suffers from deactivation, which is why the search for new, selective, active, and stable catalysts is of great interest.[6]

The ODH of ethanol for the production of acetaldehyde is currently not applied industrially. Presently, acetaldehyde is produced in the *Wacker-Hoechst* process by oxidation of fossil oil-based ethylene in the aqueous phase on noble-metal catalysts containing $PdCl_2/CuCl_2$.[7] Ethanol ODH represents a possibility to substitute fossil oil resources with ethanol as a renewable, green feedstock. It needs to be noted that ethanol is already a commodity that is produced at large scale based on renewable resources in a cost competitive manner. Due to this attractiveness, different catalyst systems have been studied for ethanol ODH.[8] So far, the main classes of investigated catalysts have been supported metal oxides, mainly supported VO_x,[9−13] supported metal catalysts,[14,15] carbon-based catalysts,[1] and mixed metal oxides.[4,16,17]

In 2011, a large class of 2D materials, MXenes, was discovered.[18] MXenes are two-dimensional transition metal carbides or nitrides with the general formula $M_{n+1}X_nT_x$, where M is an early transition metal, X is carbon and/or nitrogen, T_x represents the surface terminations (commonly O, OH, F, or Cl), and $n = 1−4$.[19,20] 2D MXene sheets can be processed into films, coatings or 3D macrostructures like aerogels or crumpled particles, resulting in increased specific surface area and surface accessibility.[21]
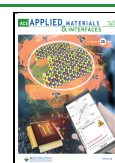
MXenes have been explored as photocatalysts and electro-catalysts (e.g., for hydrogen evolution reaction, oxygen evolution reaction, oxygen reduction reaction), along with many other applications.[22] Despite their high surface area and presence of catalytically active metals in the structure, the use of MXenes in heterogeneous gas-phase catalysis is still at an early stage. Worldwide, more than 90% of all chemicals are produced using heterogeneous catalysts, which underlines the enormous importance of heterogeneously catalyzed processes and thus research on new, active, selective, and stable catalysts.[23] In heterogeneously catalyzed reactions, MXenes have been mostly investigated as support materials, for example, in CO oxidation,[24−28] in the conversion of methane to methanol,[29] or in the dehydrogenation of light alkanes.[30] A few MXenes, such as $Ti_3C_2T_x$, Mo_2CT_x, and V_2CT_x were applied as catalysts in different reactions, including the direct dehydrogenation of ethylbenzene to styrene,[31] the water−gas shift reaction,[32] and methane dry reforming.[33,34]

Zhou et al. used $Ti_3C_2T_x$ as a precursor to produce a defect-rich TiO_2 catalyst under ethane oxidative dehydrogenation conditions.[35] The Ti and oxygen vacancies in the MXene derived oxide are believed to decrease the activation energy barrier of ethane and increase the rate of reoxidation of the catalyst.[35] It is important to note that oxidation of MXenes allows synthesis of oxides with unusual 2D morphology that may not be achieved by other methods.[36,37] These studies indicate the potential for the use of MXenes as heterogeneous catalysts and as precursors to produce metal oxide catalysts with unique morphology and properties.

In general, (mixed) transition metal oxides can be regarded as important catalysts that show promising performance in methanol and ethanol ODH. Because these can be obtained from oxidation of MXene precursors,[36,38−40] the scope of this work is to study if the unique 2D properties of the precursors can lead to metal oxides with special morphology and properties in terms of defects or oxidation state of the metal, which has an enormous influence on the catalytic activity.

Herein, we synthesized $V_4C_3T_x$, produced a MXene aerogel, and oxidized the aerogel to obtain a nanostructured vanadium oxide. Mild oxidation in an alcohol/oxygen atmosphere resulted in a partially oxidized vanadium oxide containing VO_2, V_6O_{13}, and V_3O_7. This in situ activated MXene derived oxide showed outstanding catalytic activity, high selectivity toward the corresponding aldehydes, and stability for more than 10 days on stream for ODH of methanol and ethanol.

2. MATERIAL AND METHODS

2.1. Synthesis of V_4AlC_3 MAX Phase. V_4AlC_3 MAX phase was synthesized by using a mixture of vanadium (99.5%, −325 mesh, Alfa Aesar), aluminum (99.5%, −325 mesh, Alfa Aesar), and graphite (99%, −325 mesh, Alfa Aesar) powders. The powders were mixed in a 4:1.5:3 V:Al:C atomic ratio and added to a polypropylene bottle. A 2:1 mass ratio of 5 mm zirconia balls was added to this mixture. The powders were ball-milled at 60 rpm for 18 h. Afterward, the powder mixture was placed into an alumina crucible and placed into a high temperature furnace (Carbolite Gero). Ar gas was flown continually through the furnace at 200 SCCM for 1 h prior to heating and then throughout the heating/cooling process. The furnace was heated to 1500 °C for 2 h at a heating/cooling rate of 3 °C min⁻¹. After cooling, the sintered compact was crushed with a mortar and pestle and then was placed into 9 M HCl for 24 h to dissolve residual metals and intermetallics. The powders were sieved to <40 μm.

2.2. Synthesis of Multilayer $V_4C_3T_x$ MXene. To synthesize $V_4C_3T_x$, the V_4AlC_3 MAX phase was slowly added to 50 wt % HF (Acros Organics, 48−51 wt %); a ratio of 1 g of MAX to 20 mL of HF was used. *Caution: Working with HF is dangerous; special safety procedures need to be followed to ensure no harm occurs to the researcher.*[41] The mixture was stirred at 300 rpm at 35 °C for 96 h. Afterward, this mixture was transferred to polypropylene centrifuge tubes. Deionized (DI) water was added to the etchant solution, followed by centrifugation (10 min, 3,500 rpm). The acidic supernatant was decanted, and then, fresh DI water was added with the sediment shaken until fully redispersed. This procedure was repeated until >6 pH.

2.3. Manufacturing of the $V_4C_3T_x$ MXene Aerogel. 1 g of multilayer $V_4C_3T_x$ MXene was dispersed in 15 mL of 10 wt % tetramethylammonium hydroxide solution (Sigma-Aldrich) and stirred overnight at 35 °C and 300 rpm. The dispersion was centrifuged at 10,000 rpm until the supernatant became clear. The clear supernatant was decanted, and DI water was added to redisperse the sediment. The dispersion was centrifuged again at 10,000 rpm, and this washing step was repeated until pH 8 was reached. Once the pH was 8, the sample was redispersed again and bath-sonicated for 1 h. After centrifugation at 3,500 rpm for 10 min, the dark black supernatant was collected. This supernatant was centrifuged again at 3,500 rpm for 10 min to make sure that all multilayer MXene and MAX was removed. The supernatant was centrifuged at 10,000 rpm, and the clear supernatant was decanted and redispersed in 15 mL of DI water. The dispersion was frozen in liquid nitrogen and freeze-dried for 48 h using a Christ Alpha 1−2 LD.

2.4. Activation of the $V_4C_3T_x$ Aerogel. The $V_4C_3T_x$ aerogel was activated/partially oxidized in two different ways.

2.4.1. Synthetic Air Activation (SAA). In case of synthetic air activation, the aerogel was placed between two glass wool plugs in a quartz glass reactor with an internal diameter of 4 mm. Synthetic air (20 vol % O_2/80 vol % He) with a total volume flow of 20 mL min⁻¹ (STP) was fed to the reactor and heated to 300 °C for 5 h. Afterward, the reactor was cooled to room temperature in a helium atmosphere.

2.4.2. In Situ Activation (ISA). In case of the in situ activation, the aerogel was placed between two glass wool plugs in a quartz glass reactor. A mixture of 10 vol % methanol and 10 vol % O_2 (balance: He) with a total volume flow of 20 mL min⁻¹ (STP) was fed to the reactor and heated to 300 °C for 5 h. Afterward, the reactor was cooled to room temperature under helium flow.

2.5. Synthesis of Reference Materials. *2.5.1. Iron Molybdate.* Stoichiometric $Fe_2(MoO_4)_3$ was prepared using a coprecipitation synthesis procedure according to ref 42. Iron nitrate nonahydrate (14.9 mmol, $Fe(NO_3)_3$·9 H_2O, Merck, ≥98%) and ammonium heptamolybdate tetrahydrate (22.3 mmol, $(NH_4)_6Mo_7O_{24}$·4 H_2O, Merck, ≥99%) were dissolved separately in DI water (100 and 200 mL, respectively). Afterward, the aqueous iron nitrate solution was added dropwise to the molybdate solution under vigorous stirring, which instantly led to the formation of a precipitate. In order to complete the precipitation process, the solution was stirred at 100 °C for 3 h. The precipitate was isolated by filtering off and washed with DI water and ethanol (Brenntag BCD, Technical grade) before it was dried overnight at 100 °C in air. Finally, the powder was calcined in air at 500 °C for 10 h, using a corundum crucible and a tube furnace (Carbolite Gero CWF1200).

2.5.2. Vanadium Pentoxide. Bulk V_2O_5 was purchased from Acros Organics (>99.6%).

2.5.3. Vanadium(V)oxide. Bulk VO_2 was purchased from Thermo Scientific Alfa Aesar (99%).

2.5.4. Supported Vanadium Oxide. For synthesis of the SBA-15 support, 4.0 g of Pluronic P123 ($EO_{20}PO_{70}EO_{20}$, BASF) was mixed with 120 mL of 2 M HCl and 30 mL of DI water in a polypropylene bottle and stirred at 35 °C until a clear solution was obtained. Subsequently, 8.5 g of tetraethyl orthosilicate (TEOS, Sigma-Aldrich, ≥99%), which served as the precursor for SiO_2, was added under stirring, which was maintained for a further 20 h at 35 °C. The bottle was placed in a furnace at 85 °C for 24 h. Afterward, the suspension was filtered by a glass frit, and the powder was calcined at 550 °C for 12 h in ambient air with a heating rate of 1.5 °C min⁻¹. Incipient wetness impregnation was performed to load the SBA-15 with 1 V

nm^{-2}. Vanadium(V) oxytriisopropoxide ($\geq$97%, Sigma-Aldrich) was mixed with anhydrous 2-propanol (99.5%) in a glovebox and added to the samples while mixing in a mortar. Subsequently, the yellow powder was calcined in air at 600 °C for 12 h with a heating rate of 1.5 °C min^{-1}.

2.6. Characterization. *2.6.1. Raman Spectroscopy.* Raman spectroscopy analysis was performed at an excitation wavelength of 514.5 nm, using an argon ion gas laser (Melles Griot). The light was focused onto the sample, gathered by an optic fiber, and dispersed by a transmission spectrometer (Kaiser Optical, HL5R). The dispersed Raman radiation was subsequently detected by an electronically cooled CCD detector (-40 °C, 1024 × 256 pixels). The spectral resolution was 5 cm^{-1} with a wavelength stability of better than 0.5 cm^{-1}. A laser power of 5 mW at the sample location was applied. Data analysis of the Raman spectra included cosmic ray removal and an auto new dark correction.

2.6.2. XPS. X-ray photoelectron spectroscopy analysis was carried out on an SSX 100 ESCA spectrometer (Surface Science Laboratories Inc.), employing a monochromatic Al Kα X-ray source (1486.6 eV) operated at 9 kV and 10 mA; the spot size was approximately 1 mm × 0.25 mm. The base pressure of the analysis chamber was <10^{-8} Torr. Survey spectra (eight measurements) were recorded between 0 and 1100 eV with 0.5 eV resolution, whereas detailed spectra (30 measurements) were recorded with 0.05 eV resolution. To account for sample charging, the C 1s peak of ubiquitous carbon at 284.4 eV was used to correct the binding-energy shifts in the spectra. Atomic concentrations were calculated using the relative sensitivity factors (RSFs) given in Table 1.

Table 1. Relative Sensitivity Factors Used for the Calculations of Elemental Concentrations from XPS Data

	C 1s	O 1s	N 1s	F 1s	V 2p
RSF	1.00	2.50	1.68	1.33	5.48

2.6.3. Ar Physisorption. Textural properties of the $V_4C_3T_x$ aerogel and the ISA aerogel derived oxide were studied via argon physisorption analysis at 189.3 °C using a 3Flex analyzer (Micromeritics) after degassing of the samples under vacuum at 200 °C for 18 h. Specific surface areas (SSAs) were calculated using the Brunauer–Emmett–Teller (BET) method.

2.6.4. ICP-OES. The vanadium and aluminum content in the multilayer $V_4C_3T_x$ MXene and the produced $V_4C_3T_x$ aerogel were determined by inductively coupled plasma optical emission spectrometry (ICP-OES). ICP-OES was carried out using a PerkinElmer OPTIMA 2000DV spectrometer. For sample preparation, the materials were dissolved in aqua regia and diluted with DI water.

2.6.5. TPO. Temperature programmed oxidation (TPO) of the $V_4C_3T_x$ aerogel was performed using a NETZSCH STA 449 C Jupiter thermo-microbalance. The sample was placed in a corundum crucible and heated to 600 °C in synthetic air with a heating rate of 2 °C min^{-1}.

2.6.6. SEM. Field emission scanning electron microscopy (SEM) images were taken using a Philips XL30 FEG electron microscope. Pictures of the $V_4C_3T_x$ aerogel and the ISA aerogel derived oxide were taken at an acceleration voltage of 30 kV.

2.6.7. XRD. X-ray powder diffraction patterns were collected at room temperature by a Stoe StadiP powder diffractometer with Cu Kα_1 radiation (Ge[111]-monochromator, λ = 1.54060 pm, MYTHEN-1K detector (Dectris)) in transmission geometry. The samples were placed between two X-ray amorphous polymer films.

2.6.8. HRTEM/EELS. The samples ($V_4C_3T_x$ MXene Aerogel or ISA aerogel derived oxide) were ground, and the powder was dispersed onto a lacy-carbon copper grid from TedPella INC. The HRTEM images were taken using a LaB$_6$ JEOL JEM2100+ TEM in low dose conditions at 200 kV. The EELS data was collected using JEOL 2100F Cs corrected scanning transmission electron microscopy at 200 kV. The EELS spectrum imaging acquisition of the vanadium L-edge was done using a Gatan Imaging Filter GIF QuantumSE series post column filter with an energy dispersion of 0.1 eV/channel.

2.7. Catalytic Experiments. *2.7.1. Temperature Cycling and Long-Term ODH Experiments.* The catalytic reactions were performed in a continuous flow apparatus with a quartz glass tube reactor with an internal diameter of 4 mm. The catalyst was placed between two glass wool plugs. Liquid reactants were fed to the reactor by using a two-stage saturator system, and gases were dosed by mass flow controllers. The total volume flow was 20 mL min^{-1} (STP) with helium as inert gas. Off-gas analytic was performed by an online quadrupole mass spectrometer (GAM 400, InProcess Instruments) and an online gas chromatograph (Shimadzu GC 2010) equipped with a flame ionization detector (FID) and a thermal conductivity detector (TCD).

2.7.2. Methanol ODH. For the MeOH ODH measurements, the feed consisted of 10 vol% MeOH and 10 vol% O$_2$. 5 mg of the $V_4C_3T_x$ aerogel was used and activated with the reaction mixture at 300 °C until steady-state conditions were reached (6 h). Afterward, the temperature was varied within 240−320 °C in steps of 20 °C. For the reference measurements, 25 mg of V$_2$O$_5$, 100 mg of Fe$_2$(MoO$_4$)$_3$, 56 mg of VO$_x$/SBA-15, and 100 mg of the multilayer $V_4C_3T_x$ MXene were used.

2.7.3. Ethanol ODH. For the EtOH ODH measurements, the feed consisted of 5 vol% EtOH and 10 vol% O$_2$. 5 mg of the $V_4C_3T_x$ aerogel was used and pretreated with the reaction mixture at 280 °C until steady-state conditions were reached. Afterward, the temperature was varied within 200−280 °C in steps of 20 °C. For the reference measurements, 25 mg of V$_2$O$_5$, 100 mg of Fe$_2$(MoO$_4$)$_3$, 56 mg of
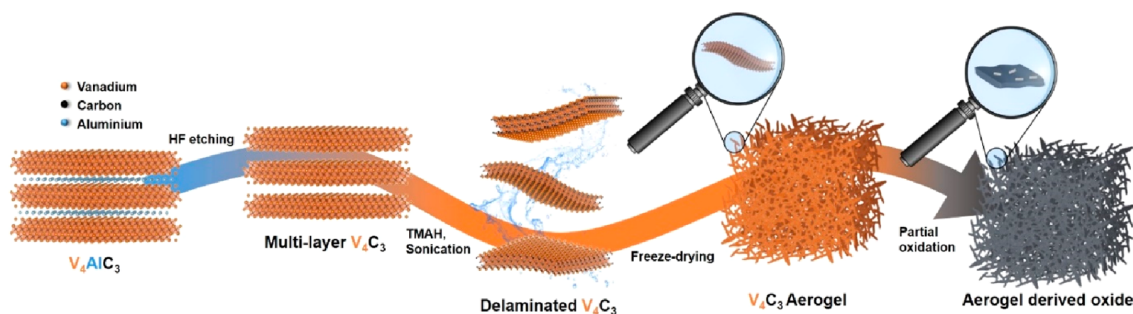

Figure 1. Schematic illustration of MXene aerogel synthesis procedure. $V_4C_3T_x$ multilayer MXene was obtained by selective etching of the aluminum phase from the parent MAX phase V_4AlC_3 with hydrofluoric acid. The multilayer MXene was delaminated in an aqueous solution using tetramethylammonium hydroxide as an intercalant and subsequent sonication. Freeze-drying of the MXene colloidal suspension led to the formation of an aerogel with a random 3D arrangement of MXene sheets. The MXene aerogel was partially oxidized to obtain the aerogel derived oxide catalyst.
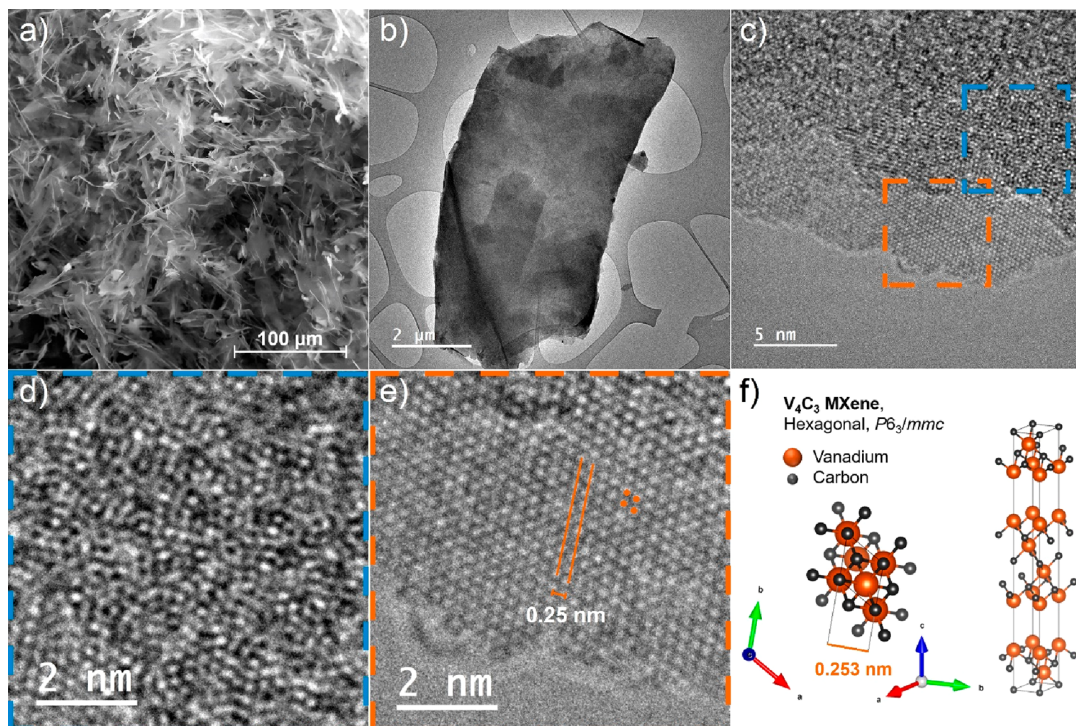
Figure 2. Characterization of $V_4C_3T_x$ MXene aerogel. (a) SEM image of $V_4C_3T_x$ MXene aerogel. (b) Low magnification image of a $V_4C_3T_x$ flake. (c) HRTEM image of $V_4C_3T_x$ showing a mixture of single and multidomain flakes. (d, e) HRTEM image multidomain area (blue) and single domain area (orange) and (f) illustration of the hexagonal MXene structure.

VO_x/SBA-15, and 100 mg of the multilayer $V_4C_3T_x$ MXene were used.

2.7.4. Methanol and Ethanol TPD. MeOH and EtOH temperature programmed desorption (TPD) experiments were performed using the same reaction setup which was described before. 15 mg of the material was treated with 10 vol% alcohol and 10 vol% O_2 at 300 °C for 6 h until steady-state behavior was reached. Afterward, the temperature was lowered to 100 °C. Alcohol desorption at 100 °C was performed for 10 min (10 vol% alcohol in He). After flushing with helium for 2 h, the temperature was raised with a specific heating rate (7.5, 10, 15, and 20 °C min^{-1}) and the off-gas was analyzed by a calibrated online mass spectrometer (GAM 400, InProcess Instruments). The total volume flow was constant at 20 mL min^{-1} (STP).

2.7.5. Methanol and Ethanol Pulse Experiments. MeOH and EtOH pulse experiments were performed using the same reaction setup, which was described before. 15 mg of the catalyst was treated with 10 vol% alcohol and 10 vol% O_2 at 300 °C for 6 h until steady-state behavior was observed and then oxidized with synthetic air at 300 °C for 1 h. During the pulse experiments, the total volume flow was constant at 20 mL min^{-1} (STP) He. Pulses were generated by an automated 6 port valve with a sample loop. By switching the 6 port valve, 50 MeOH/EtOH reduction pulses were generated. The time between the pulses was varied within 1, 2, and 3 min.

3. RESULTS AND DISCUSSION

3.1. Synthesis and Characterization of $V_4C_3T_x$ Aerogel.
A simplified scheme of the synthesis procedure is shown in Figure 1. The starting material, multilayer $V_4C_3T_x$ MXene, was synthesized by etching the V_4AlC_3 MAX phase with hydrofluoric acid (HF). The multilayer MXene was delaminated in aqueous solution by using tetramethylammonium hydroxide (TMAOH) as the intercalant, followed by sonication. The $V_4C_3T_x$ aerogel was obtained by freeze-drying the delaminated MXene dispersion. The freeze-drying step prevented restacking of the MXene sheets, leading to a random

arrangement of the sheets, resulting in a disordered 3D macrostructure, as shown in Figure 2a. Figure 2b shows a transmission electron microscopy (TEM) image of a MXene sheet. The specific surface area (SSA) was determined by argon physisorption and is calculated to be 16 m^2 g^{-1} (Figure S2). Since Ar adsorbs weakly on MXenes and cannot penetrate between MXene sheets, the reported SSA is underestimated.

X-ray powder diffraction (XRD) of the aerogel (Figure S1) showed pronounced (002) and (110) reflections at 5.2°(2θ) and 63.5°(2θ), respectively, confirming the existence of a $V_4C_3T_x$ MXene.[43] In comparison to the starting material, reflections in the 2θ region from 35° to 45° decreased significantly, indicating an increasing loss of crystallinity (or structural order) during delamination and aerogel manufacturing. Additionally, the (002) reflection of the initial MAX phase at 7.8°(2θ) vanished, indicating a removal of the residual MAX phase. Inductively coupled plasma optical emission spectroscopy (ICP-OES) confirmed this observation by a decrease of the Al/V ratio from 0.17 in the starting material to 0.02 in the $V_4C_3T_x$ aerogel, indicating a very low amount of residual Al in the aerogel.

The hexagonal structure of the MXene sheets was also confirmed by high-resolution transmission electron microscopy (HRTEM), as shown in Figure 2c−e. The HRTEM image of the single domain MXene (Figure 2e) clearly showed its hexagonal $P6_3$/mmc symmetry.

The composition of the aerogel was analyzed by X-ray photoelectron spectroscopy (XPS). XPS spectra shown in Figure S3 revealed oxygen (30.5 at. %) and fluorine (9.9 at. %) surface functionalization originating from the HF etching during MXene synthesis. The V 2p XPS revealed that 54 at. % of the vanadium was bound to carbon and 46 at. % was bound
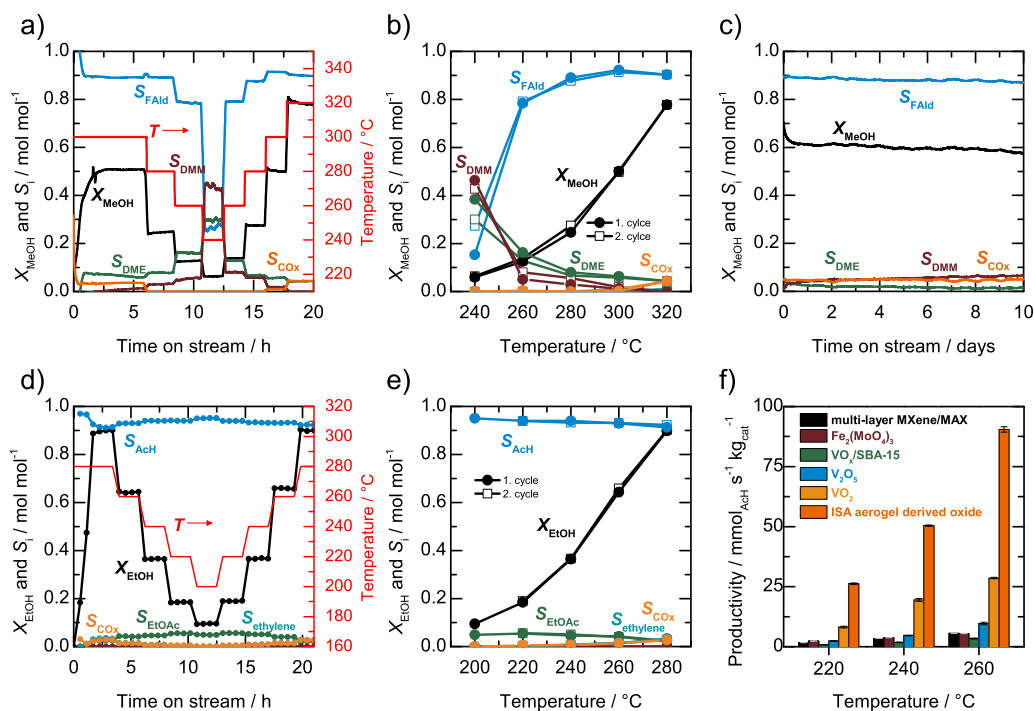
Figure 3. Methanol and ethanol ODH on *in situ* activated $V_4C_3T_x$ aerogel derived oxide. (a) Conversion of methanol (MeOH) and selectivities to formaldehyde (FAld), dimethyl ether (DME), dimethoxymethane (DMM), and CO_x during temperature cycling against time on stream. (b) Steady-state values of conversion of methanol and selectivity to reaction products for different reaction temperatures, (c) long-term methanol ODH measurement, indicating high stability, (d) conversion of ethanol (EtOH) and selectivities to acetaldehyde (AcH), ethyl acetate (EtOAc), ethylene, and CO_x during temperature cycling against time on stream, (e) steady-state values of conversion of ethanol and selectivities to reaction products for different reaction temperatures, and (f) comparison of acetaldehyde productivity of the ISA aerogel derived catalyst compared to VO_2, V_2O_5, VO_x/SBA-15, and $Fe_2(MoO_4)_3$ and the initial multilayer MXene/MAX as reference materials (error bars indicate the standard variation during the measurements).

to oxygen. The averaged oxidation state of the vanadium bound to oxygen could be determined to be +3.8.

3.2. Activation and Catalytic Performance. An oxidative treatment is necessary to convert the $V_4C_3T_x$ aerogel precursor into an active oxide catalyst. To study the temperature range for the oxidation of the $V_4C_3T_x$ aerogel, temperature programmed oxidation (TPO) in synthetic air was performed (Figure S6a). The relative mass increased between 200 and 350 °C, indicating an oxidation of the aerogel in this temperature range. As these temperatures were within the range of the aimed catalytic reactions, two ways of activation of the MXene aerogel were studied: (1) the MXene aerogel was used as prepared and activated *in situ* under methanol ODH conditions, hence with 10 vol% methanol and 10 vol% oxygen at 300 °C (named: ISA, *in situ* activation), and (2) the MXene aerogel was oxidized in synthetic air at 300 °C (named: SAA, synthetic air activation) prior to testing in the ODH of methanol.

The synthetic air activation led to a highly active ODH catalyst. For methanol ODH, this resulted in a productivity to formaldehyde (FAld) of 82 $mmol_{Fald}$ s^{-1} kg_{cat}^{-1} at 300 °C (Figure S6). During temperature cycling between 240 and 320 °C, deactivation was observed at each temperature, indicating a lower catalytic stability or an induction period of the catalyst. Raman spectroscopy of the SAA aerogel derived oxide (Figure S6) revealed features of crystalline V_2O_5, indicating a high oxidation state of the material.[44] The XRD pattern of the SSA aerogel derived oxide is given in Figure S1 and shows weak

reflexes at 7.5°, 25°, and 51°(2θ) that cannot be clearly assigned to a known crystal structure.

The results for the ISA catalyst are shown in Figure 3a, which depicts the time-resolved conversion of methanol (MeOH) and the selectivities to the reaction product formaldehyde and the byproducts dimethyl ether (DME), dimethoxymethane (DMM), and CO_x. In the first 3 h at 300 °C, the degree of conversion increased from 0 to 50% and then reached steady-state behavior. After 5 h, the ISA aerogel derived oxide showed an ultrahigh catalytic activity with a formaldehyde productivity of 134 $mmol_{Fald}$ s^{-1} kg_{cat}^{-1}. Besides the higher activity compared to the SAA aerogel derived oxide, the ISA aerogel derived oxide showed stable performance during temperature cycling between 240 and 320 °C.

At 240 °C, the methanol degree of conversion was 6% and the formaldehyde selectivity decreased to 26% while the dimethoxymethane selectivity and dimethyl ether selectivity increased to 43% and 34%, respectively. With increasing temperature and conversion, the selectivity to formaldehyde increased and was still 90% at 320 °C (X_{MeOH} = 78%). Besides high selectivity, the material showed an outstanding activity of 217 $mmol_{Fald}$ s^{-1} kg_{cat}^{-1} at 320 °C. The averaged steady-state values of methanol conversion and the selectivities during the temperature cycling experiment are shown in Figure 3b and reveal that no significant temperature hysteresis was observed. Figure 3c shows the conversion and the selectivities to the reaction products for a long-term measurement with the ISA aerogel derived oxide at 320 °C. The catalyst showed only a
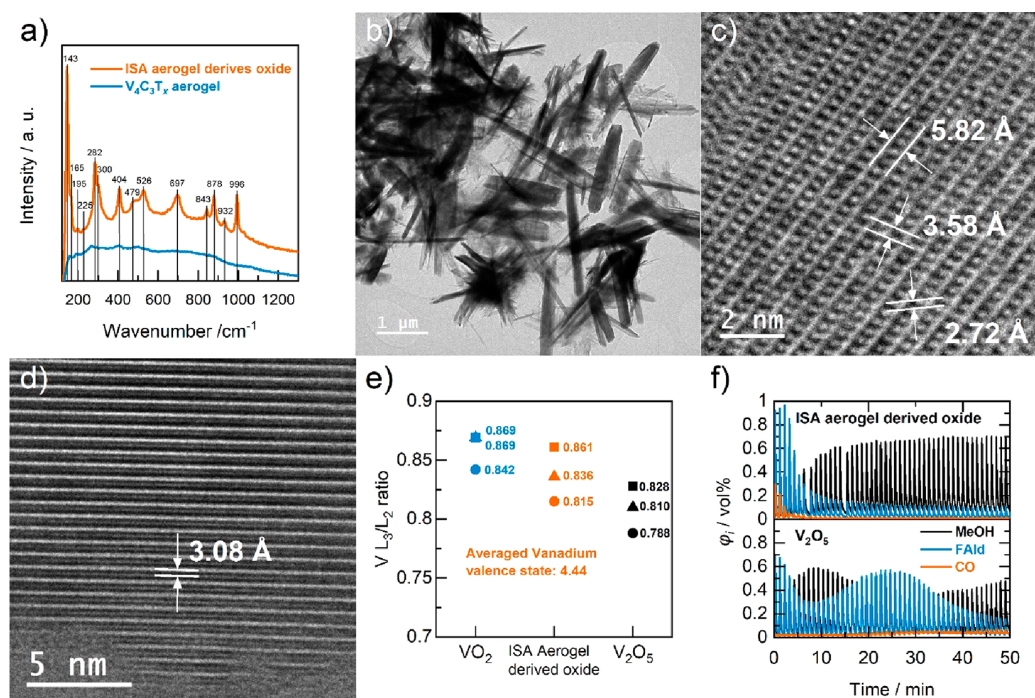
Figure 4. *Post-mortem* characterization of ISA aerogel derived oxide. (a) Raman spectra ($\lambda = 514.5$ nm) of $V_4C_3T_x$ aerogel (blue) and ISA aerogel derived oxide (orange), (b) TEM survey image of ISA aerogel derived oxide nanorods, (c and d) HRTEM images of ISA aerogel derived oxide, indicating V_6O_{13} (c) and V_3O_7 (d), (e) vanadium L_3/L_2 ratios on three different spots in comparison to VO_2 and V_2O_5 as reference materials, and (f) volume fractions of methanol (MeOH), formaldehyde (FAld), and CO during methanol pulse experiments on the ISA aerogel derived oxide (top) and V_2O_5 (bottom) with a pulse interval of 1 min.

slight decrease in degree of conversion from 63% to 58% after 10 days on stream, indicating its high stability.

Besides methanol ODH, the $V_4C_3T_x$ aerogel was also used as catalyst precursor for ethanol ODH. To convert the aerogel to an active catalyst, the aerogel was activated *in situ* at 280 °C under ethanol ODH conditions (5 vol% ethanol, 10 vol% O_2). The degree of conversion of ethanol (EtOH) and the selectivity to the desired product acetaldehyde (AcH) as well as the selectivities to the byproducts, ethyl acetate (EtOAc), ethylene, acetic acid (AcOH), and CO_x, against time on stream are shown in Figure 3d. After an increase of the conversion in the first 2 h, indicating active species formation, the catalyst reached steady-state behavior with a degree of conversion of 90% and an acetaldehyde selectivity of 91%.

The main side products at 280 °C were ethylene, ethyl acetate, and CO_x (all around 3%). At lower temperatures, e.g., at 220 °C, and a degree of conversion of 18%, the selectivity to acetaldehyde increased to 94% and ethyl acetate became the main side product (5%). Figure 3e depicts the steady–state conversion and selectivities during temperature cycling. Again, no temperature hysteresis was observed, demonstrating the stability of the ISA aerogel derived catalyst, which also showed an outstanding acetaldehyde productivity of 123 $mmol_{AcH}$ s^{-1} kg_{cat}^{-1} at 280 °C with a yield of 83%.

Three commonly employed reference oxidation catalysts were prepared and tested to compare their performance with the MXene derived catalyst. The reference materials were bulk V_2O_5, supported VO_x, and $Fe_2(MoO_4)_3$, which is used as catalyst within the industrial *FormOx* process. Figure 3f compares the resulting mass-based productivities at different temperatures to the new ISA MXene aerogel derived oxide of this study. At all temperatures, the productivity of the new

catalyst exceeded the productivity of all reference materials by a factor of 3.2 to 16.7. Additionally, a comparison was made to a catalyst which was obtained by direct *in situ* activation of the starting precursor (multilayer MXene with residues of MAX phase) and thus without the aerogel structuring step. Here, a catalyst with an activity similar to those of the reference catalysts resulted, underpinning the importance of forming an aerogel precursor. The productivities during methanol ODH are shown in Figure S11 and show the same trend concerning the ultrahigh activity of the ISA aerogel derived oxide.

3.3. *Post-mortem* Characterization of ISA Aerogel Derived Oxide. After activation and temperature cycling in methanol ODH, extensive *post-mortem* characterization of the ISA aerogel derived oxide was performed to understand its high catalytic activity and to establish structure−activity relationships. The XRD pattern of the ISA aerogel derived oxide (Figure S1) showed reflections that can be assigned to metastable VO_2 (B) (space group $C/2m$).[45]

VIS-Raman spectroscopy of the pristine $V_4C_3T_x$ aerogel and the ISA aerogel derived oxide after ODH reaction was performed (Figure 4a). The pristine aerogel only showed weak Raman features at 158, 195, 263, 404, and 501 cm^{-1}. In comparison, the ISA aerogel derived oxide showed intensive Raman bands at 996, 697, 526, 497, 404, 300, 282, 195, and 143 cm^{-1} and additional bands at 843, 878, and 932 cm^{-1}. Zhang et al. assigned these features to a mixture of VO_2, V_6O_{13}, and V_2O_5.[46] The VO_2 characteristic Raman band at ~600 cm^{-1} appeared to occur as an enhancement of the background in this case. It should be noted that the formation of V_3O_7 could also lead to bands in the range between 840 and 940 cm^{-1}.[44] Since V_3O_7 is not well documented, the formation of that mixed valence oxide cannot be excluded.

The ISA aerogel derived oxide was *post-mortem* subjected to analysis by HRTEM and electron energy loss spectroscopy (EELS). Figure 4b shows a TEM image of the ISA aerogel derived oxide, which indicated the formation of nanorods. HRTEM images of the nanorods shown in Figure 4c,d confirmed the assumption of the presence of the mixed valence oxides V_6O_{13} and V_3O_7. More HRTEM images, assigned to V_3O_7 and V_6O_{13}, are shown in Figures S4 and S5. EELS analysis of three different particles was performed to estimate the averaged vanadium valence state. The L_3/L_2 intensity ratios for the ISA aerogel derived oxide as well as for V^{4+} and V^{5+} references are shown in Figure 4e. The averaged oxidation state was 4.44, being in good agreement with the observations made by Raman spectroscopy and HRTEM.

The surface composition of the ISA aerogel derived oxide after ODH reaction was determined by XPS (Figure S3). In comparison to the pristine $V_4C_3T_x$ aerogel, the ISA aerogel derived oxide had no fluorine functionalization on the surface. The O/V ratio increased from 1.72 to 2.82 after reaction, confirming oxidation of the material. Fitting the high resolution V 2p spectrum showed a decrease of carbidic vanadium from 54 to 0 at. %. The ratio of V^{4+} to V^{5+} was determined to be 0.52, in good agreement with the observation of the formation of V_3O_7 (V^{4+}/V^{5+} = 0.5) or a mixture of V_6O_{13} and V_2O_5 on the surface.

In summary, the MXene aerogel was *in situ* oxidized, leading to the metastable VO_2 (B) phase in the bulk of the material, while the formation of V_6O_{13}, V_3O_7, and V_2O_5, which appear either amorphous or as a thin film on the surface, could not be detected by XRD.

In addition to the detailed characterization of the ISA aerogel derived oxide, kinetic studies (including variation of oxygen concentration, alcohol concentrations, and temperature) and transient response experiments (including methanol/ethanol pulse experiments and methanol/ethanol temperature programmed desorption (TPD)) were carried out on ISA aerogel derived oxide and the less active highly oxidized bulk V_2O_5 to unravel the cause of the ultrahigh activity of the new catalyst.

3.4. Mechanistic Investigations of the Alcohol ODH on ISA Aerogel Derived Oxide. Kinetics of consumption of oxygen and alcohol were found to approximately follow a power-law approach. The reaction orders for methanol/ethanol and oxygen consumption as well as the apparent activation energies for the ODH reaction on ISA aerogel derived oxide and V_2O_5 can be found in Supplementary Section 5. In summary, slight differences in alcohol and oxygen reaction orders could be observed. The clear trend for both ODH reactions toward lower apparent activation energies for the ISA aerogel derived oxide in comparison to V_2O_5 could be a first hint for the higher activity of the MXene aerogel derived catalyst. Methanol and ethanol TPD experiments were used to determine the activation energies of formaldehyde and acetaldehyde desorption and revealed lower desorption energies on the ISA aerogel derived oxide compared to V_2O_5 (see Supplementary Section 6). Following the Sabatier principle, this could be a reason for the observed higher activities.

For the methanol reduction pulse experiments, a fresh ISA activated catalyst was treated at 300 °C for 1 h with 10 vol% O_2 to generate a defined oxidized surface (Figure S16). 50 methanol reduction pulses in helium were applied, and the off-gas was analyzed by a calibrated online mass spectrometer (see Figure 4f). The ISA aerogel derived oxide showed full conversion of methanol in the first four pulses, mainly producing formaldehyde and smaller amounts of CO, indicating the high ODH activity of the ISA aerogel derived oxide surface. With increasing pulse number and therefore increasing degree of reduction of the surface, the amount of CO and formaldehyde decreased, and after seven pulses, the methanol signal exceeded the aldehyde signal. The bulk V_2O_5 showed a completely different behavior. At the beginning, V_2O_5 was less active than the ISA aerogel derived oxide (1st pulse: X_{MeOH} = 77%) and the conversion decreased to 40% after 8 methanol pulses. Interestingly, the conversion of methanol and therefore the amount of formaldehyde increased again to be 62% after 26 methanol pulses. Afterward, the activity decreased to a degree of conversion of 45% after 50 pulses. This wave-like behavior of the bulk V_2O_5 clearly indicated the presence and participation of bulk oxygen. During the first pulses, the surface was highly oxidized, leading to a high activity. With an increasing degree of reduction of the surface, fewer active sites were available, leading to a decrease in activity. In a bulk metal oxide system, lattice oxygen can be dynamic and can diffuse from the oxide's bulk to the surface, causing a reoxidation of surface sites, thus regenerating active ODH sites.[47] Nevertheless, this bulk oxygen diffusion has different (lower) time constants compared to the surface processes. Thus, the observed wave-like behavior results. This experiment revealed that the methanol ODH activity of V_2O_5 at 300 °C was limited by the oxygen bulk dynamic. This was further corroborated by variation of the time between the pulses as given in Supplementary Section 7. Interestingly, the involvement of bulk oxygen and the limitation of the ODH by bulk oxygen dynamics observed for V_2O_5 was not observed for the ISA aerogel derived oxide.

4. CONCLUSION

From the materials characterization and kinetic studies, it can be posited that under ODH conditions the precursor $V_4C_3T_x$ MXene aerogel was partially oxidized, leading to the formation of nanorods consisting of an unusually high degree of active and selective mixture of vanadium oxides, consisting of VO_2, V_6O_{13}, and V_3O_7 (and V_2O_5). Due to the unique 2D starting material, it was possible to obtain a catalyst where not only the surface consists of mixed valence vanadium oxide "supported" on a fully oxidized bulk but also the full material is in a stable reduced valence state.[48] Very likely, this together with the nanorod arrangement allowed for unprecedented high oxygen mobilities as well as active site numbers, leading to an ultrahigh activity of ISA MXene aerogel derived oxide in alcohol ODH, which is accompanied by high selectivity and stability. The observed lowered desorption energy for the products could also stem from the enrichment of mixed valence states. The MXene starting precursor and aerogel arrangement as well as the softer *in situ* oxidation were the key to obtain these catalysts. In combination with the large variety of possible MXenes in terms of the choice of metals or metal combinations, this approach of MXene derived oxides paves the way for a completely new field of research toward mixed metal oxide catalysts.

■ ASSOCIATED CONTENT

Ⓢⓘ Supporting Information

The Supporting Information is available free of charge at https://pubs.acs.org/doi/10.1021/acsami.2c22720.

Characterization of $V_4C_3T_x$ aerogel, ISA aerogel derived oxide, and SSA aerogel derived oxide; catalytic results of reference catalysts; kinetic investigation of ISA aerogel derived oxide and V_2O_5; temperature programmed desorption; pulse experiments (PDF)

◼ AUTHOR INFORMATION

Corresponding Author

Bastian J. M. Etzold − *Technical University of Darmstadt, Department of Chemistry, Ernst-Berl-Institut für Technische und Makromolekulare Chemie, 64287 Darmstadt, Germany;* ⊙ orcid.org/0000-0001-6530-4978; Email: bastian.etzold@tu-darmstadt.de

Authors

Niklas Oefner − *Technical University of Darmstadt, Department of Chemistry, Ernst-Berl-Institut für Technische und Makromolekulare Chemie, 64287 Darmstadt, Germany*

Christopher E. Shuck − *A.J. Drexel Nanomaterials Institute and Department of Materials Science and Engineering, Drexel University, Philadelphia, Pennsylvania 19104, United States;* ⊙ orcid.org/0000-0002-1274-8484

Leon Schumacher − *Technical University of Darmstadt, Department of Chemistry, Eduard-Zintl-Institut für Anorganische und Physikalische Chemie, 64287 Darmstadt, Germany*

Franziska Heck − *Technical University of Darmstadt, Department of Chemistry, Eduard-Zintl-Institut für Anorganische und Physikalische Chemie, 64287 Darmstadt, Germany*

Kathrin Hofmann − *Technical University of Darmstadt, Department of Chemistry, Eduard-Zintl-Institut für Anorganische und Physikalische Chemie, 64287 Darmstadt, Germany*

Jana Schmidpeter − *Technical University of Darmstadt, Department of Chemistry, Ernst-Berl-Institut für Technische und Makromolekulare Chemie, 64287 Darmstadt, Germany*

Weiqun Li − *Department of Mechanical, Materials and Aerospace Engineering, University of Liverpool, Liverpool L69 3GH, United Kingdom*

Mounib Bahri − *Department of Mechanical, Materials and Aerospace Engineering, University of Liverpool, Liverpool L69 3GH, United Kingdom*

B. Layla Mehdi − *Department of Mechanical, Materials and Aerospace Engineering, University of Liverpool, Liverpool L69 3GH, United Kingdom;* ⊙ orcid.org/0000-0002-8281-9524

Alfons Drochner − *Technical University of Darmstadt, Department of Chemistry, Ernst-Berl-Institut für Technische und Makromolekulare Chemie, 64287 Darmstadt, Germany*

Barbara Albert − *Technical University of Darmstadt, Department of Chemistry, Eduard-Zintl-Institut für Anorganische und Physikalische Chemie, 64287 Darmstadt, Germany*

Christian Hess − *Technical University of Darmstadt, Department of Chemistry, Eduard-Zintl-Institut für Anorganische und Physikalische Chemie, 64287 Darmstadt, Germany;* ⊙ orcid.org/0000-0002-4738-7674

Yury Gogotsi − *A.J. Drexel Nanomaterials Institute and Department of Materials Science and Engineering, Drexel University, Philadelphia, Pennsylvania 19104, United States;* ⊙ orcid.org/0000-0001-9423-4032

Complete contact information is available at:

https://pubs.acs.org/10.1021/acsami.2c22720

Notes

The authors declare no competing financial interest.

◼ REFERENCES

(1) Herold, F.; Prosch, S.; Oefner, N.; Brunnengräber, K.; Leubner, O.; Hermans, Y.; Hofmann, K.; Drochner, A.; Hofmann, J. P.; Qi, W.; Etzold, B. J. M. Nanoscale Hybrid Amorphous/Graphitic Carbon as Key Towards Next-Generation Carbon-Based Oxidative Dehydrogenation Catalysts. *Angew. Chemie Int. Ed.* **2021**, *60* (11), 5898−5906.

(2) Zhang, X.; Yan, P.; Xu, J.; Li, F.; Herold, F.; Etzold, B. J. M.; Wang, P.; Su, D. S.; Lin, S.; Qi, W.; Xie, Z. Methanol Conversion on Borocarbonitride Catalysts: Identification and Quantification of Active Sites. *Sci. Adv.* **2020**, *6* (26), 1−10.

(3) Yan, P.; Zhang, X.; Herold, F.; Li, F.; Dai, X.; Cao, T.; Etzold, B. J. M.; Qi, W. Methanol Oxidative Dehydrogenation and Dehydration on Carbon Nanotubes: Active Sites and Basic Reaction Kinetics. *Catal. Sci. Technol.* **2020**, *10* (15), 4952−4959.

(4) Oefner, N.; Heck, F.; Dürl, M.; Schumacher, L.; Siddiqui, H. K.; Kramm, U. I.; Hess, C.; Möller, A.; Albert, B.; Etzold, B. J. M. Activity, Selectivity and Initial Degradation of Iron Molybdate in the Oxidative Dehydrogenation of Ethanol. *ChemCatChem* **2022**, *14*, e202101219.

(5) Reuss, G.; Disteldorf, W.; Gamer, A. O.; Hilt, A. Formaldehyde. In *Ullmann's Encyclopedia of Industrial Chemistry*; Wiley-VCH Verlag GmbH & Co. KGaA: Weinheim, 2012.

(6) Raun, K. V.; Johannessen, J.; McCormack, K.; Appel, C. C.; Baier, S.; Thorhauge, M.; Høj, M.; Jensen, A. D. Modeling of the Molybdenum Loss in Iron Molybdate Catalyst Pellets for Selective Oxidation of Methanol to Formaldehyde. *Chem. Eng. J.* **2019**, *361* (August 2018), 1285−1295.

(7) Eckert, M.; Fleischmann, G.; Jira, R.; Bolt, H. M.; Golka, K. Acetaldehyde. In *Ullmann's Encyclopedia of Industrial Chemistry*; Wiley-VCH Verlag GmbH & Co. KGaA: Weinheim, 2012; pp 192−207.

(8) Pang, J.; Yin, M.; Wu, P.; Li, X.; Li, H.; Zheng, M.; Zhang, T. Advances in Catalytic Dehydrogenation of Ethanol to Acetaldehyde. *Green Chem.* **2021**, *23* (20), 7902−7916.

(9) Ober, P.; Rogg, S.; Hess, C. Direct Evidence for Active Support Participation in Oxide Catalysis: Multiple Operando Spectroscopy of VO_x/Ceria. *ACS Catal.* **2020**, *10* (5), 2999−3008.

(10) Waleska, P.; Rupp, S.; Hess, C. Operando Multiwavelength and Time-Resolved Raman Spectroscopy: Structural Dynamics of a Supported Vanadia Catalyst at Work. *J. Phys. Chem. C* **2018**, *122* (6), 3386−3400.

(11) Kaichev, V. V.; Chesalov, Y. A.; Saraev, A. A.; Klyushin, A. Y.; Knop-Gericke, A.; Andrushkevich, T. V.; Bukhtiyarov, V. I. Redox Mechanism for Selective Oxidation of Ethanol over Monolayer V_2O_5/TiO_2 Catalysts. *J. Catal.* **2016**, *338*, 82−93.

(12) Beck, B.; Harth, M.; Hamilton, N. G.; Carrero, C.; Uhlrich, J. J.; Trunschke, A.; Shaikhutdinov, S.; Schubert, H.; Freund, H. J.; Schlögl, R.; Sauer, J.; Schomäcker, R. Partial Oxidation of Ethanol on Vanadia Catalysts on Supporting Oxides with Different Redox Properties Compared to Propane. *J. Catal.* **2012**, *296*, 120−131.

(13) Nair, H.; Gatt, J. E.; Miller, J. T.; Baertsch, C. D. Mechanistic Insights into the Formation of Acetaldehyde and Diethyl Ether from

Ethanol over Supported VO$_x$, MoO$_x$, and WO$_x$ Catalysts. *J. Catal.* **2011**, *279* (1), 144−154.

(14) Dutov, V. V.; Mamontov, G. V.; Sobolev, V. I.; Vodyankina, O. V. Silica-Supported Silver-Containing OMS-2 Catalysts for Ethanol Oxidative Dehydrogenation. *Catal. Today* **2016**, *278*, 164−173.

(15) Liu, P.; Hensen, E. J. M. Highly Efficient and Robust Au/MgCuCr$_2$O$_4$ Catalyst for Gas-Phase Oxidation of Ethanol to Acetaldehyde. *J. Am. Chem. Soc.* **2013**, *135* (38), 14032−14035.

(16) Malmusi, A.; Velasquez Ochoa, J.; Tabanelli, T.; Basile, F.; Lucarelli, C.; Agnoli, S.; Carraro, F.; Granozzi, G.; Cavani, F. Ethanol Aerobic and Anaerobic Oxidation with FeVO$_4$ and V$_2$O$_5$ Catalysts. *Appl. Catal. A Gen.* **2019**, *570*, 139−147.

(17) Sobolev, V. I.; Koltunov, K. Y. MoVNbTe Mixed Oxides as Efficient Catalyst for Selective Oxidation of Ethanol to Acetic Acid. *ChemCatChem.* **2011**, *3* (7), 1143−1145.

(18) Naguib, M.; Kurtoglu, M.; Presser, V.; Lu, J.; Niu, J.; Heon, M.; Hultman, L.; Gogotsi, Y.; Barsoum, M. W. Two-Dimensional Nanocrystals Produced by Exfoliation of Ti$_3$AlC$_2$. *Adv. Mater.* **2011**, *23* (37), 4248−4253.

(19) Gogotsi, Y.; Anasori, B. The Rise of MXenes. *ACS Nano* **2019**, *13* (8), 8491−8494.

(20) Deysher, G.; Shuck, C. E.; Hantanasirisakul, K.; Frey, N. C.; Foucher, A. C.; Maleski, K.; Sarycheva, A.; Shenoy, V. B.; Stach, E. A.; Anasori, B.; Gogotsi, Y. Synthesis of Mo$_4$VAlC$_4$ MAX Phase and Two-Dimensional Mo$_4$VC$_4$ MXene with Five Atomic Layers of Transition Metals. *ACS Nano* **2020**, *14* (1), 204−217.

(21) VahidMohammadi, A.; Rosen, J.; Gogotsi, Y. The World of Two-Dimensional Carbides and Nitrides (MXenes). *Science* **2021**, *372*, 1165−1179.

(22) Morales-Garciá, Á.; Calle-Vallejo, F.; Illas, F. MXenes: New Horizons in Catalysis. *ACS Catal.* **2020**, *10* (22), 13487−13503.

(23) Rothenberg, G. *Catalysis - Concepts and Green Applications*; WILEY-VCH Verlag GmbH & Co. KFaA: Weinheim, 2008; Vol. 22.

(24) Zhang, X.; Lei, J.; Wu, D.; Zhao, X.; Jing, Y.; Zhou, Z. A Ti-Anchored Ti$_2$CO$_2$ Monolayer (MXene) as a Single-Atom Catalyst for CO Oxidation. *J. Mater. Chem. A* **2016**, *4* (13), 4871−4876.

(25) Cheng, C.; Zhang, X.; Yang, Z.; Zhou, Z. Cu$_3$-Cluster-Doped Monolayer Mo$_2$CO$_2$ (MXene) as an Electron Reservoir for Catalyzing a CO Oxidation Reaction. *ACS Appl. Mater. Interfaces* **2018**, *10* (38), 32903−32912.

(26) Cheng, C.; Zhang, X.; Yang, Z.; Hermansson, K. Identification of High-Performance Single-Atom MXenes Catalysts for Low-Temperature CO Oxidation. *Adv. Theory Simulations* **2019**, *2* (8), 1900006.

(27) Cheng, C.; Zhang, X.; Wang, M.; Wang, S.; Yang, Z. Single Pd Atomic Catalyst on Mo$_2$CO$_2$ Monolayer (MXene): Unusual Activity for CO Oxidation by Trimolecular Eley-Rideal Mechanism. *Phys. Chem. Chem. Phys.* **2018**, *20* (5), 3504−3513.

(28) Yang, X.; Lu, Z.; Cheng, C.; Wang, Y.; Zhang, X.; Yang, Z.; Lu, W. Identification of Efficient Single-Atom Catalysts Based on V$_2$CO$_2$ MXene by Ab Initio Simulations. *J. Phys. Chem. C* **2020**, *124* (7), 4090−4100.

(29) Sun, X.; Gao, Y.; Zhao, C.; Deng, S.; Zhong, X.; Zhuang, G.; Wei, Z.; Wang, J. G. Palladium Dimer Supported on Mo$_2$CO$_2$(MXene) for Direct Methane to Methanol Conversion. *Adv. Theory Simulations* **2019**, *2* (2), 1800158.

(30) Li, Z.; Yu, L.; Milligan, C.; Ma, T.; Zhou, L.; Cui, Y.; Qi, Z.; Libretto, N.; Xu, B.; Luo, J.; Shi, E.; Wu, Z.; Xin, H.; Delgass, W. N.; Miller, J. T.; Wu, Y. Two-Dimensional Transition Metal Carbides as Supports for Tuning the Chemistry of Catalytic Nanoparticles. *Nat. Commun.* **2018**, *9* (1), 1−8.

(31) Diao, J.; Hu, M.; Lian, Z.; Li, Z.; Zhang, H.; Huang, F.; Li, B.; Wang, X.; Su, D. S.; Liu, H. Ti$_3$C$_2$T$_x$ MXene Catalyzed Ethylbenzene Dehydrogenation: Active Sites and Mechanism Exploration from Both Experimental and Theoretical Aspects. *ACS Catal.* **2018**, *8* (11), 10051−10057.

(32) Deeva, E. B.; Kurlov, A.; Abdala, P. M.; Lebedev, D.; Kim, S. M.; Gordon, C. P.; Tsoukalou, A.; Fedorov, A.; Müller, C. R. *In Situ* XANES/XRD Study of the Structural Stability of Two-Dimensional Molybdenum Carbide Mo$_2$CT$_x$: Implications for the Catalytic Activity in the Water-Gas Shift Reaction. *Chem. Mater.* **2019**, *31* (12), 4505−4513.

(33) Kurlov, A.; Deeva, E. B.; Abdala, P. M.; Lebedev, D.; Tsoukalou, A.; Comas-Vives, A.; Fedorov, A.; Müller, C. R. Exploiting Two-Dimensional Morphology of Molybdenum Oxycarbide to Enable Efficient Catalytic Dry Reforming of Methane. *Nat. Commun.* **2020**, *11* (1), 1−11.

(34) Thakur, R.; Vahidmohammadi, A.; Smith, J.; Hoffman, M.; Moncada, J.; Beidaghi, M.; Carrero, C. A. Insights into the Genesis of a Selective and Coke-Resistant MXene-Based Catalyst for the Dry Reforming of Methane. *ACS Catal.* **2020**, *10* (9), 5124−5134.

(35) Zhou, Y.; Li, X.; Chai, Y.; Wu, Z.; Lin, J.; Pan, X.; Han, Y.; Li, L.; Qi, H.; Su, Y.; Kang, L.; Wang, X. Defect-Rich TiO$_2$ in Situ Evolved from MXene for Efficiently Oxidative Dehydrogenation of Ethane. Preprint at https://www.researchsquare.com/article/rs-85939/v1; 2020; DOI: 10.21203/rs.3.rs-85939/v1.

(36) Ridley, P.; Gallano, C.; Andris, R.; Shuck, C. E.; Gogotsi, Y.; Pomerantseva, E. MXene-Derived Bilayered Vanadium Oxides with Enhanced Stability in Li-Ion Batteries. *ACS Appl. Energy Mater.* **2020**, *3* (11), 10892−10901.

(37) Ghassemi, H.; Harlow, W.; Mashtalir, O.; Beidaghi, M.; Lukatskaya, M. R.; Gogotsi, Y.; Taheri, M. L. *In Situ* Environmental Transmission Electron Microscopy Study of Oxidation of Two-Dimensional Ti$_3$C$_2$ and Formation of Carbon-Supported TiO$_2$. *J. Mater. Chem. A* **2014**, *2* (35), 14339−14343.

(38) Su, T.; Peng, R.; Hood, Z. D.; Naguib, M.; Ivanov, I. N.; Keum, J. K.; Qin, Z.; Guo, Z.; Wu, Z. One-Step Synthesis of Nb$_2$O$_5$/C/Nb$_2$C (MXene) Composites and Their Use as Photocatalysts for Hydrogen Evolution. *ChemSusChem* **2018**, *11* (4), 688−699.

(39) Seredych, M.; Shuck, C. E.; Pinto, D.; Alhabeb, M.; Precetti, E.; Deysher, G.; Anasori, B.; Kurra, N.; Gogotsi, Y. High-Temperature Behavior and Surface Chemistry of Carbide MXenes Studied by Thermal Analysis. *Chem. Mater.* **2019**, *31* (9), 3324−3332.

(40) Naguib, M.; Mashtalir, O.; Lukatskaya, M. R.; Dyatkin, B.; Zhang, C.; Presser, V.; Gogotsi, Y.; Barsoum, M. W. One-Step Synthesis of Nanocrystalline Transition Metal Oxides on Thin Sheets of Disordered Graphitic Carbon by Oxidation of MXenes. *Chem. Commun.* **2014**, *50* (56), 7420−7423.

(41) Shuck, C. E.; Ventura-Martinez, K.; Goad, A.; Uzun, S.; Shekhirev, M.; Gogotsi, Y. Safe Synthesis of MAX and MXene: Guidelines to Reduce Risk During Synthesis. *ACS Chem. Heal. Saf.* **2021**, *28* (5), 326−338.

(42) Vieira Soares, A.P.; Farinha Portela, M.; Kiennemann, A. Iron Molybdates for Selective Oxidation of Methanol: Mo Excess Effects on the Deactivation Behaviour. *Catal. Commun.* **2001**, *2* (5), 159−164.

(43) Tran, M. H.; Schäfer, T.; Shahraei, A.; Dürrschnabel, M.; Molina-Luna, L.; Kramm, U. I.; Birkel, C. S. Adding a New Member to the MXene Family: Synthesis, Structure, and Electrocatalytic Activity for the Hydrogen Evolution Reaction of V$_4$C$_3$T$_x$. *ACS Appl. Energy Mater.* **2018**, *1* (8), 3908−3914.

(44) Shvets, P.; Dikaya, O.; Maksimova, K.; Goikhman, A. A Review of Raman Spectroscopy of Vanadium Oxides. *J. Raman Spectrosc.* **2019**, *50* (8), 1226−1244.

(45) Oka, Y.; Yao, T.; Yamamoto, N.; Ueda, Y.; Hayashi, A. Phase Transition and V^{4+}-V^{4+} Pairing in VO$_2$(B). *J. Solid State Chem.* **1993**, *105*, 271−278.

(46) Zhang, C.; Yang, Q.; Koughia, C.; Ye, F.; Sanayei, M.; Wen, S. J.; Kasap, S. Characterization of Vanadium Oxide Thin Films with Different Stoichiometry Using Raman Spectroscopy. *Thin Solid Films* **2016**, *620*, 64−69.

(47) Heid, M.; Knoche, S.; Gora, N.; Ohlig, D.; Drochner, A.; Etzold, B. J. M.; Vogel, H. Dynamics of Bulk Oxygen in the Selective Oxidation of Acrolein. *ChemCatChem* **2017**, *9* (12), 2390−2398.

(48) Schlögl, R.; Hess, C. Characteristics of Selective Oxidation Reactions. In *Nanostructured catalysts: Selective Oxidations*; RSC Publishing: Cambridge, 2011.

4.5.2 Reduction Behavior of Cubic In$_2$O$_3$ Nanoparticles by Combined Multiple In Situ Spectroscopy and DFT

The thirteenth overall publication elucidates the reduction behavior of cubic In$_2$O$_3$ on a molecular level as an important basis for the ever growing applications of In$_2$O$_3$ in CO$_2$ reduction applications. In situ UV-Raman measurements were contributed to this work. In situ multi-wavelength Raman (385 and 514 nm excitation), UV-Vis and XP spectroscopy under a hydrogen containing gas feed were employed. In addition, DFT calculations were used to assign Raman features of reduced In$_2$O$_3$ to understand the reduction behavior. The results included that bulk defects are favored over surface defects. In addition, the excellent agreement of Raman features and DFT predictions was demonstrated and new features in reduced In$_2$O$_{3-x}$ were assigned, which were only accessible through the exploitation of resonance Raman effects combined with DFT calculations.

Letter

Reduction Behavior of Cubic In$_2$O$_3$ Nanoparticles by Combined Multiple *In Situ* Spectroscopy and DFT

Marc Ziemba, Leon Schumacher, and Christian Hess*

Cite This: *J. Phys. Chem. Lett.* 2021, 12, 3749−3754

Read Online

ACCESS | 📊 Metrics & More | 📄 Article Recommendations | 🆂🅸 Supporting Information

ABSTRACT: Indium oxide (In$_2$O$_3$) has emerged as a highly active catalyst for methanol synthesis by CO$_2$ hydrogenation. In this work we elucidate the reduction behavior and oxygen dynamics of cubic In$_2$O$_3$ nanoparticles by *in situ* Raman and UV−vis spectra in combination with density functional theory (DFT) calculations. We demonstrate that application of UV and visible Raman spectroscopy enables, first, a complete description of the In$_2$O$_3$ vibrational structure fully consistent with theory and, second, the first theoretical identification of the nature of defect-related bands in reduced In$_2$O$_3$. Combining these findings with quasi *in situ* XPS and *in situ* UV−vis measurements allows the temperature-dependent structural dynamics of In$_2$O$_3$ to be unraveled. While the surface of a particle is not in equilibrium with its bulk at room temperature, oxygen exchange between the bulk and the surface occurs at elevated temperatures, leading to an oxidation of the surface and an increase in oxygen defects in the bulk. Our results demonstrate the potential of combining different *in situ* spectroscopic methods with DFT to elucidate the complex redox behavior of In$_2$O$_3$ nanoparticles.
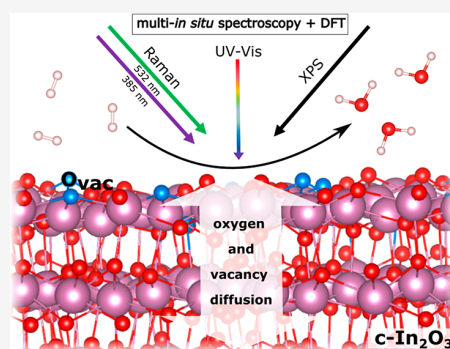
Cubic indium oxide (In$_2$O$_3$, $Ia\overline{3}$) shows high catalytic activity for a variety of reactions, such as CO$_2$ hydrogenation to methanol or the reverse water gas shift reaction.[1−6] To gain insight into the mode of operation of In$_2$O$_3$ catalysts, a detailed understanding of their redox behavior, including the associated oxygen dynamics and the In$_2$O$_3$ defect structure, will be required. In this context, oxygen vacancies could be identified as active sites during methanol synthesis or the reverse water gas shift reaction, since CO$_2$ is activated over In$_2$O$_{3-x}$ sites formed by H$_2$.[2,7−9] Furthermore, selective hydrogen combustion by In$_2$O$_3$ has recently been shown to be an essential part of tandem catalysts for propane to propylene conversion.[10] Since both processes involve oxygen vacancies, there is a need for a detailed understanding of their formation and dynamics. In this context, previous studies have shown that at elevated temperatures (300 °C) and under reducing conditions metallic indium is formed and defect-related Raman bands occur.[11,12] However, the nature of these bands and the interplay of surface and subsurface/bulk processes, which is of great importance for catalysis, are still not clarified, despite previous work on the vibrational analysis of In$_2$O$_3$.[13−19]

In this study, we investigate catalytically interesting In$_2$O$_3$ nanoparticles with respect to their structural behavior under oxidative and reductive conditions, both experimentally and theoretically. By use of multiwavelength *in situ* Raman spectroscopy and, in particular, selective resonance enhancement at 385 nm excitation, a profound description of In$_2$O$_3$-related vibrational modes is provided. Furthermore, we explore the oxygen dynamics at the surface and in the bulk, using a
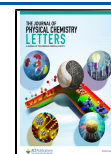
combination of UV−vis and X-ray photoelectron (XP) spectroscopy, as well as X-ray diffraction (XRD).

After synthesis by precipitation of indium(III) nitrate hydrate, the In$_2$O$_3$ particles were first characterized by N$_2$ adsorption at 77 K, XRD, transmission electron microscopy (TEM), and XPS (for details see Supporting Information). By use of N$_2$ adsorption and the Brunauer−Emmett−Teller (BET) model, the specific surface area was determined as 39 m^2/g (for isotherms see Figure S1). The XRD results show that only cubic ($Ia\overline{3}$) In$_2$O$_3$ is present (see Figure S2) and, by means of the Scherrer equation, the size of the particles was calculated to be 19 nm. These results are consistent with the TEM images (see Figure S3), which additionally show that the particles are present as sheets terminating with a In$_2$O$_3$(222) surface, based on the observed distances between the lattice planes of 0.29 nm.[20] XPS analysis reveals an O:In ratio of 1.47 (see Table S1; see Supporting Information for details on the calculation), indicating that oxygen defects are already present in the as-prepared state. However, it should be noted that detailed analysis of the C 1s photoemission reveals a shoulder at higher binding energies (∼289 eV), indicating the presence of oxygen containing adsorbates, e.g., carbonates (see Figure

Downloaded via UNIV DARMSTADT on September 8, 2023 at 12:01:40 (UTC).
See https://pubs.acs.org/sharingguidelines for options on how to legitimately share published articles.

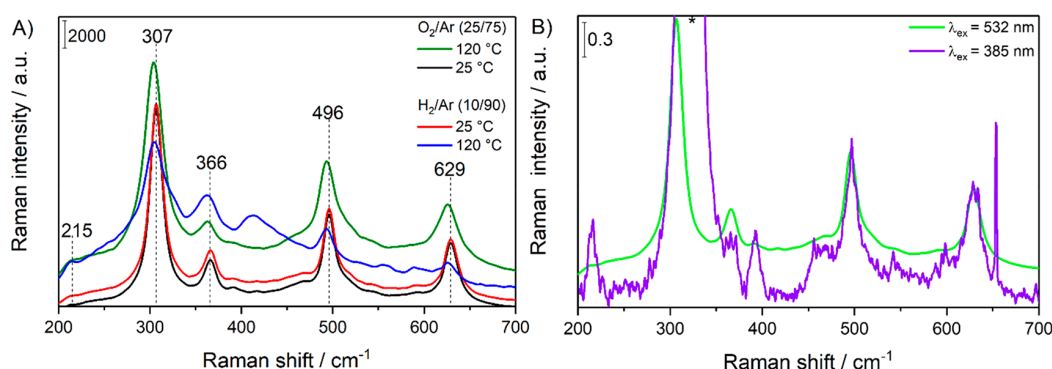**Figure 1.** (A) *In situ* Raman spectra (λ_{ex} = 532 nm) of In_2O_3 nanoparticles. Spectra were recorded at the indicated temperatures at a total flow rate of 100 mL/min and by applying a feed of 25% O_2/Ar for oxidative and of 10% H_2/Ar for reductive conditions. (B) Comparison of two *in situ* Raman spectra, at 532 nm (green) and 385 nm (violet) excitation. Both spectra were recorded at 25 °C after pretreatment in O_2/Ar at 120 °C for 1 h. For better comparability, both spectra were normalized to the band at 629 cm^{-1}. The asterisk (∗) marks a band originating from the CaF_2 window (λ_{ex} = 385 nm), while the sharp feature at 650 cm^{-1} results from cosmic rays.
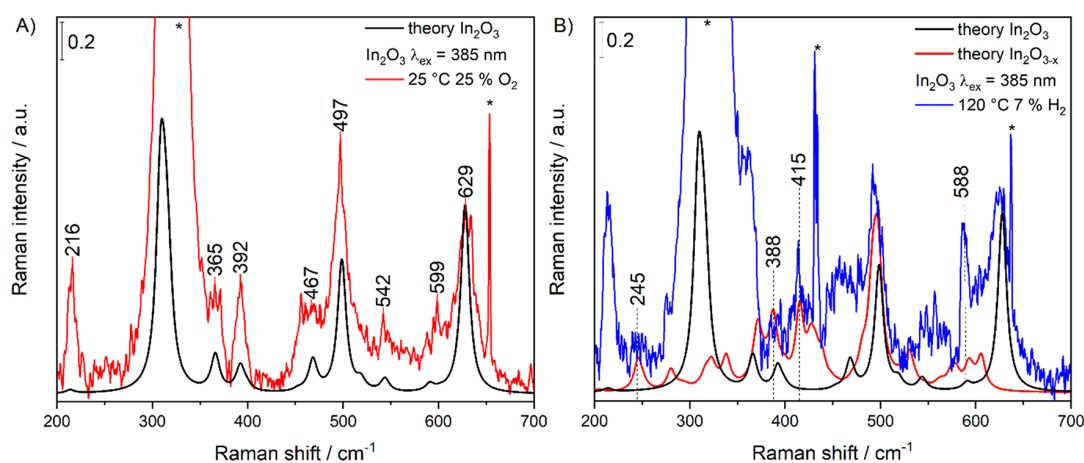
Figure 2. (A) Theoretical (DFT) Raman spectrum of a nondefective primitive In_2O_3 ($Ia\bar{3}$) cell (black) compared to the *in situ* 385 nm Raman spectrum (red) of In_2O_3 recorded at 25 °C in 25% O_2/He (pretreatment: 1 h, 120 °C, 25% O_2/He, 50 mL/min). (B) Theoretical (DFT) Raman spectrum of a defective primitive In_2O_{3-x} ($Ia\bar{3}$) cell (red) compared to the *in situ* 385 nm Raman spectrum (blue) of In_2O_3 recorded at 120 °C in 7% H_2/He (for more details see Supporting Information). The total flow rate was always 50 mL/min. The asterisks (∗) mark bands originating from the CaF_2 window, while the sharp feature at around 430 and 650 cm^{-1} results from cosmic rays. For better comparability, all spectra except the theoretical In_2O_{3-x} spectrum are normalized to the 628 cm^{-1} band. The theoretical In_2O_{3-x} spectrum was normalized and scaled (factor: 1.05) to the band at 495 cm^{-1}.

S4),[21] which increase the O:In ratio. We can therefore conclude that there are significantly more defects present on the surface than *ex situ* XPS reveals.

In the following, we will first discuss the results from multiwavelength Raman spectroscopy. Figure 1A shows *in situ* Raman spectra of In_2O_3 at 532 nm laser excitation. Under O_2/Ar flow the Raman spectra are characterized by four strong bands at 307, 366, 496, and 629 cm^{-1}, which can readily be assigned to $\delta(InO_6)$, $\nu(InO_6)$, In−O−In, and $\nu(InO_6)$ vibrations of cubic In_2O_3, in accordance with the literature.[16,22] Comparison of the temperature-dependent O_2/Ar spectra (black and green) reveals a red shift and a change in full width at half-maximum (fwhm) at 120 °C, which originate from a temperature effect, as the spectra of reduced In_2O_3 (blue) show the same positions. In summary, it can be said that a low degree of reduction has no influence on the Raman positions, just the temperature does, since at 120 °C the spectra in O_2/Ar and H_2/Ar show the same positions. After oxygen treatment at 25 °C, hydrogen was passed over the sample at 25 °C but did

not lead to detectable changes in the Raman spectrum. In contrast, at 120 °C in H_2/Ar flow, the overall intensity decreased and the phonon ratios changed significantly. Furthermore, new Raman features appeared at 254, 413, 555, and 589 cm^{-1}; the broad band at 413 cm^{-1} had already been observed in earlier studies, but its exact nature has not been clarified yet.[11] As part of this study, measurements were also performed at 250 °C, but under these conditions Raman spectra are hampered by increased absorption (see Figure 3) and fluorescence and are therefore not shown. For this reason, the sample was subsequently cooled to 25 °C under argon and another spectrum was recorded (see Figure S6). Again, the spectrum is dominated by the increased absorption (see yellow spectrum in Figure 3A), but the In_2O_3 phonons are visible; however defect-related features remain hidden by the higher background. A significant feature of the band positions is that they exhibit a red shift in contrast to the spectra at 120 °C under H_2. This highlights the fact that the bands shift red at higher defect concentrations. In addition, we see bands at 1499
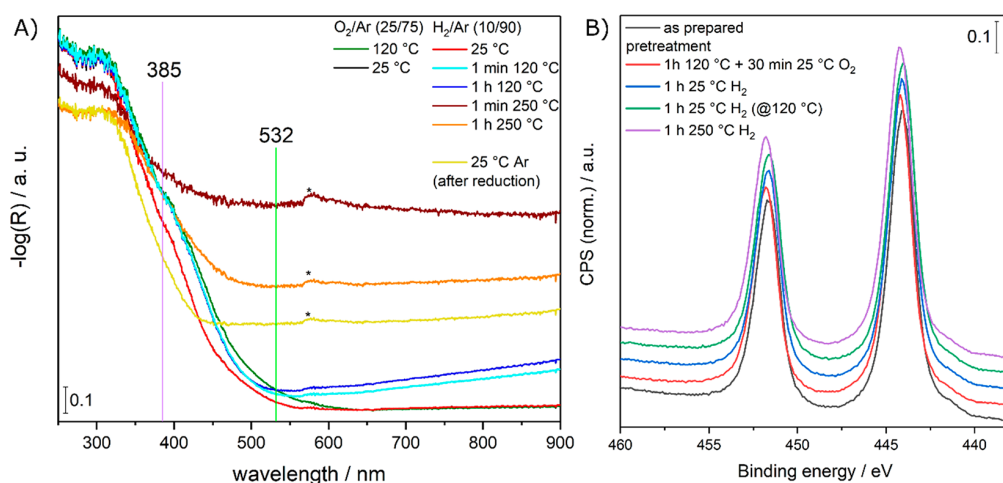
Figure 3. (A) *In situ* UV/vis spectra of In_2O_3 nanoparticles. Spectra were recorded at the indicated temperatures at a total flow rate of 100 mL/min and by applying a feed of 25% O_2/Ar for oxidative and 10% H_2/Ar for reductive conditions. After reduction at 250 °C, the sample was cooled down to 25 °C in Ar (yellow). Spectra were recorded after about 1 h of equilibration. In addition, for H_2/Ar flow at higher temperatures (>25 °C), spectra are shown after 1 min of equilibration. The asterisks (∗) mark a measurement artifact of the spectrometer. Note that the spectra under O_2 and H_2 at 25 °C overlap. Note that no changes between the spectra at 25 °C in O_2 (black) and H_2 (red) occur. (B) In 3d photoemission of In_2O_3 nanoparticles. Spectra were normalized to the In $3d_{5/2}$ signal. Spectra were recorded directly after synthesis (black), after O_2 (25%) pretreatment (red), after H_2 (10%) pretreatment at 25 °C (blue, green), and after H_2 pretreatment at 250 °C (violet). All spectra were recorded at 25 °C except the green one, which was recorded at 120 °C. Spectra in (B) are offset for clarity.

and 1554 cm^{-1} (see Figure S7), which may be attributed to In–H vibrations.[23−26] The intensity ratio of these bands changes with the gas-phase composition; i.e., the band at 1499 cm^{-1} increases upon exposure to hydrogen, indicating the activation of H_2. The chemical environment appears to have a strong influence on the band position, as for example In–H species on CHA zeolites have been shown to exhibit bands within 1700−1800 cm^{-1}.[27] In contrast, OH-related Raman bands show only temperature-related changes and completely disappear upon treatment at 250 °C in H_2 flow (see Figure S8).

As an additional laser wavelength for Raman spectroscopy, we used 385 nm excitation, which minimizes fluorescence and, due to an electronic resonance with In_2O_3, enables selective resonance enhancement of In_2O_3-related modes. A comparison of the two excitation wavelengths shows (see Figure 1B) that the 385 nm Raman spectrum reveals additional phonons, which were not detectable or only very difficult to detect with 532 nm excitation.

In order to understand the nature of these bands, we employed DFT to calculate Raman spectra (for details see Supporting Information). Figure 2A shows a comparison of a calculated Raman spectrum of a primitive In_2O_3 cell with an experimental spectrum (385 nm) recorded in O_2/Ar at 25 °C. The theoretical spectrum was scaled to the band at 629 cm^{-1} (factor 1.09). It is noticeable that the theoretical band positions are in excellent agreement with experiment. Furthermore, the Raman spectrum of the unit cell shows the same positions as that of the primitive cell for symmetry reasons (see Figure S11). In addition to the bands detected at 532 nm excitation, new features appear at 392, 467, 542, and 599 cm^{-1}, which can be assigned to vibrations with F_{2g}/E_g (392 cm^{-1}), F_{2g} (467 cm^{-1}), F_{2g} (542 cm^{-1}), and E_g (599 cm^{-1}) symmetry, based on our DFT results and in accordance with the literature.[14]

In summary, the above results show that Raman spectra of In_2O_3 can be fully described by DFT. Since a combined

experimental and theoretical approach may thus be expected to facilitate the understanding of more complex systems, it was applied to bulk oxygen vacancies in defective In_2O_3. The defect formation in bulk In_2O_3 corresponds to 3.58 eV in the primitive cell and 3.40 eV in the unit cell, which can be attributed to a 50% lower defect concentration in the unit cell, in agreement with the literature.[28−30] In the following, only the primitive cell will be discussed. In this case, our DFT calculations show that the oxygen defect formation energy and the Raman active modes do not differ between the removed oxygen atoms, since all oxygen atoms are equal and possess C_1 symmetry. Thus, no particular oxygen defect is preferred in bulk In_2O_3.

Figure 2B shows a theoretically calculated Raman spectrum of a defective primitive cell ($In_2O_{3−x}$; red), which is compared with a nondefective cell (black), and an experimental Raman spectrum (λ_{ex} = 385 nm; blue), which was recorded in hydrogen at 120 °C. Again, the theoretical spectrum is in good agreement with the experimental results. In fact, it can be clearly seen by comparison of the two theoretical spectra that the Raman features at 245 cm^{-1}, at around 400 cm^{-1}, and at 588 cm^{-1} are defect-related. To this end, a direct comparison of the experimental spectra of In_2O_3 and reduced In_2O_3 is shown in Figure S9 for clarity. In addition, theory also shows that the spectrum of $In_2O_{3−x}$ is dominated by accumulations of closely spaced bands. As a consequence, an exact assignment of the symmetry of the individual bands is difficult and of no use experimentally, since the symmetry is lost due to the presence of the defect in the crystal lattice. Hence the detected bands are composed of several nondegenerate vibrations with similar energy, which explains their width, as illustrated for the broad band at around 413 cm^{-1} (see Figure 1A). This feature can be better resolved at 385 nm excitation due to resonance effects, as shown in Figure 2B. The experimental band shape agrees well with that obtained by DFT calculations. According to theory, its width originates from more than 10 nondegenerate vibrations with similar symmetry (mostly $\delta(InO_5)$ character).

In summary, unlike defect-free In_2O_3, no degeneracy occurs in defect-rich In_2O_3.

A comparison of the two experimental Raman spectra in Figure 2 reveals that in reduced indium oxide the band at 392 cm^{-1} loses its intensity, new bands appear in the region around 400 cm^{-1}, the band at around 550 cm^{-1} loses its asymmetry and becomes wider, and the band at 587 cm^{-1} is more intense. The observed vibrational signature of reduced indium oxide is fully consistent with the simultaneous presence of In_2O_3 and In_2O_{3-x}, based on the combination of the corresponding theoretical spectra (see black and red spectra in Figure 2B). Therefore, hydrogen treatment at 120 °C does not lead to complete reduction. Similar to reduced In_2O_3, the oxygen-treated In_2O_3 shows a feature at 245 cm^{-1} (see Figure 2A,B), which originates from a $\delta(InO_5)$ vibration of In_2O_{3-x} (see Figure 2B), revealing that the oxygen-pretreated In_2O_3 contains oxygen defects.

At 250 °C in H_2/Ar flow, acceptable Raman spectra were not accessible at either excitation wavelength. Therefore, we recorded a spectrum at 25 °C in helium after treatment at 250 °C in H_2 flow (see Figure S9), which shows that the defect-related bands become more intense. The aspects that are responsible for the difficult accessibility of the spectra at 250 °C and H_2 will now be considered in more detail, since in contrast to 532 nm, at 385 nm only small changes in the absorption and hence the electronic structure of the particles were detected (see Figure 3A). The observed Raman behavior must therefore be related to other effects. In this context, XRD measurements (see Figure S2) show that during reduction with hydrogen at 250 °C metallic indium (particle size: 67 nm) is formed and that the particle size of the In_2O_3 particles increases from 19 to 29 nm. To understand this behavior in more detail, we explored the changes in the electronic structure and the properties of the surface and bulk by using XP and UV–vis spectroscopy. Note that by means of XPS, only surface properties are detected. In contrast, all other methods used in this study probe properties of the whole particle, based on the penetration depth and the size of the particles, which will be referred to as bulk in the following.

Figure 3A depicts *in situ* UV–vis spectra of indium oxide, which were recorded analogously to the Raman spectra in Figure 1. These spectra clearly show that the sample undergoes significant changes during reduction and oxidation. First, it is noticeable that all spectra are characterized by strong absorption in the UV range, originating from directly allowed transitions into O 2p valence bands.[31,32] In O_2 atmosphere, the absorption between 250 and 450 nm is observed to increase and broaden at 120 °C compared to 25 °C. This behavior is related to an increase of the band gap with rising temperature, as a result of the increased carrier density caused by the Burstein–Moss effect.[33,34] Upon exposure to hydrogen at 25 °C, no changes are detected, consistent with the 532 nm Raman spectra (see Figure 1A). Subsequent heating to 120 °C leads again to a broadening of the absorption within 250–450 nm, indicative of a band-gap increase. In contrast to the spectrum recorded in oxygen (120 °C), the absorption is somewhat lower, suggesting a slightly lower band gap. This behavior can be explained by the formation of defects, which can act as donors, thus creating new energy levels in the near-band-gap region.[35] Furthermore, Figure 3A shows an increase in absorption in the visible range (>500 nm). In contrast to lower temperatures (<120 °C), the absorption continues to grow after 1 h of treatment. Upon switching to 250 °C, it

reaches a maximum after 1 min and decreases during the following 59 min. The origin of these changes in vis absorption can be explained by the presence of defects located at or near the surface.[35] Besides, at 250 °C in hydrogen, the formation of metallic indium is conceivable, as evidenced by XRD measurements after treatment (see Figure S2). However, the absorption of indium surface plasmons is not as broad as the defect-induced absorption.[36,37] We therefore attribute the observed changes in absorption to a combination of the two effects.

The time-dependent dynamics can be explained by a balance between bulk oxygen and surface vacancies. As a consequence, at a high concentration of surface defects a transfer of oxygen from the bulk to the surface takes place until an equilibrium state is reached. Such a scenario is supported by quasi *in situ* XPS measurements (for details see Supporting Information), which show that, despite indium oxide reduction, the oxygen concentration on the surface slightly increases (see O:In ratios in Table S1). Thus, starting at 120 °C, there is an exchange of oxygen between the bulk and defects at the surface. This can also be demonstrated by heating the sample to 120 °C in the XPS analysis chamber after the same H_2 pretreatment at 25 °C as mentioned before (see Figure 1A) while simultaneously recording mass spectra showing the release of CO_2 and H_2O. The XP spectrum recorded at 120 °C reveals an increase in the surface O:In ratio compared to 25 °C, despite desorption of CO_2 and H_2O (see Table S1).

Returning to the XRD results, which showed formation of metallic indium, we performed XPS measurements of the sample after the same pretreatment (250 °C, 10% H_2). These spectra show a higher amount of oxygen than during reduction at lower temperatures. On the other hand, there is no evidence of metallic indium or indium in oxidation states other than In^{3+} (see Figure 3B). This clearly demonstrates that at higher temperatures (>120 °C) oxygen is transported from the bulk to the surface. Thus, despite the lower defect energy on the surface,[38] defects in the bulk seem to be preferred. In this context, it has previously been shown that oxygen vacancies are the predominant donor in In_2O_3 and are responsible for the oxygen self-diffusion process.[39] These results are also underlined by theoretical studies that propose that oxygen vacancies are already mobile at temperatures of about 400 K.[40]

Summarizing, in this study we elucidated the oxygen dynamics of oxidized and reduced cubic In_2O_3 nanoparticles by a combination of spectroscopic techniques supported by theoretical calculations. We have shown that surface oxygen defects are in equilibrium with the bulk at temperatures above 120 °C and that in the equilibrium state bulk defects are preferred over surface defects, resulting in a lower defect formation on the surface. We furthermore demonstrated that experimental vibrational Raman spectra of In_2O_3 and In_2O_{3-x} are in excellent agreement with those calculated by DFT. By exploitation of resonance effects, for example, at 385 nm excitation, and facilitation by theoretical calculations, new insight into the nature of vibrational bands was provided, such as the band at 245 cm^{-1}, which was assigned to a $\delta(InO_5)$ vibration in defective In_2O_3. Finally, while our findings highlight the potential of combining multiple *in situ* spectroscopic and theoretical analyses to unravel the redox dynamics of cubic In_2O_3, such an approach may be of great interest for other reducible oxide materials as well for their structural characterization under catalytic conditions.

■ ASSOCIATED CONTENT

Ⓢ Supporting Information

The Supporting Information is available free of charge at https://pubs.acs.org/doi/10.1021/acs.jpclett.1c00892.

> Detailed information on experimental and theoretical methods as well as additional experimental data (PDF)

■ AUTHOR INFORMATION

Corresponding Author

Christian Hess − *Eduard Zintl Institute of Inorganic and Physical Chemistry, Technical University of Darmstadt, 64287 Darmstadt, Germany;* ⓘ orcid.org/0000-0002-4738-7674; Email: christian.hess@tu-darmstadt.de

Authors

Marc Ziemba − *Eduard Zintl Institute of Inorganic and Physical Chemistry, Technical University of Darmstadt, 64287 Darmstadt, Germany*

Leon Schumacher − *Eduard Zintl Institute of Inorganic and Physical Chemistry, Technical University of Darmstadt, 64287 Darmstadt, Germany*

Complete contact information is available at:
https://pubs.acs.org/10.1021/acs.jpclett.1c00892

Notes

The authors declare no competing financial interest.

■ ACKNOWLEDGMENTS

■ REFERENCES

(1) Sun, Q.; Ye, J.; Liu, C.; Ge, Q. In_2O_3 as a Promising Catalyst for CO_2 Utilization: A Case Study with Reverse Water Gas Shift over In_2O_3. *Greenhouse Gases: Sci. Technol.* **2014**, *4* (1), 140−144.

(2) Wang, J.; Liu, C.-Y.; Senftle, T. P.; Zhu, J.; Zhang, G.; Guo, X.; Song, C. Variation in the In_2O_3 Crystal Phase Alters Catalytic Performance toward the Reverse Water Gas Shift Reaction. *ACS Catal.* **2020**, *10* (5), 3264−3273.

(3) Wang, W.; Zhang, Y.; Wang, Z.; Yan, J.; Ge, Q.; Liu, C. Reverse Water Gas Shift over $In_2O_3 − CeO_2$ Catalysts. *Catal. Today* **2016**, *259* (Part 2), 402−408.

(4) Tsoukalou, A.; Abdala, P. M.; Stoian, D.; Huang, X.; Willinger, M. G.; Fedorov, A.; Müller, C. R. Structural Evolution and Dynamics of an In_2O_3 Catalyst for CO_2 Hydrogenation to Methanol: An Operando XAS-XRD and in Situ TEM Study. *J. Am. Chem. Soc.* **2019**, *141* (34), 13497−13505.

(5) Frei, M. S.; Capdevila-Cortada, M.; García-Muelas, R.; Mondelli, C.; López, N.; Stewart, J. A.; Curulla Ferré, D.; Pérez-Ramírez, J. Mechanism and Microkinetics of Methanol Synthesis via CO_2 Hydrogenation on Indium Oxide. *J. Catal.* **2018**, *361* (1), 313−321.

(6) Ye, J.; Liu, C.; Mei, D.; Ge, Q. Active Oxygen Vacancy Site for Methanol Synthesis from CO_2 Hydrogenation on $In_2O_3(110)$: A DFT Study. *ACS Catal.* **2013**, *3* (6), 1296−1306.

(7) Wang, J.; Zhang, G.; Zhu, J.; Zhang, X.; Ding, F.; Zhang, A.; Guo, X.; Song, C. CO_2 Hydrogenation to Methanol over In_2O_3 - Based Catalysts: From Mechanism to Catalyst Development. *ACS Catal.* **2021**, *11* (3), 1406−1423.

(8) Qin, B.; Li, S. First Principles Investigation of Dissociative Adsorption of H_2 during CO_2 Hydrogenation over Cubic and Hexagonal In_2O_3 Catalysts. *Phys. Chem. Chem. Phys.* **2020**, *22*, 3390−3399.

(9) Rui, N.; Zhang, F.; Sun, K.; Liu, Z.; Xu, W.; Stavitski, E.; Senanayake, S. D.; Rodriguez, J. A.; Liu, C.-J. Hydrogenation of CO_2 to Methanol on a $Au^{δ+}−In_2O_{3−x}$ Catalyst. *ACS Catal.* **2020**, *10* (19), 11307−11317.

(10) Yan, H.; He, K.; Samek, I. A.; Jing, D.; Nanda, M. G.; Stair, P. C.; Notestein, J. M. Tandem In_2O_3-Pt/Al_2O_3 Catalyst for Coupling of Propane Dehydrogenation to Selective H_2 Combustion. *Science* **2021**, *371* (6535), 1257−1260.

(11) Bielz, T.; Lorenz, H.; Jochum, W.; Kaindl, R.; Klauser, F.; Klötzer, B.; Penner, S. Hydrogen on In_2O_3: Reducibility, Bonding, Defect Formation, and Reactivity. *J. Phys. Chem. C* **2010**, *114* (19), 9022−9029.

(12) Gervasini, A.; Perdigon-Melon, J. A.; Guimon, C.; Auroux, A. An In-Depth Study of Supported In_2O_3 Catalysts for the Selective Catalytic Reduction of NO_x: The Influence of the Oxide Support. *J. Phys. Chem. B* **2006**, *110* (1), 240−249.

(13) Garcia-Domene, B.; Ortiz, H. M.; Gomis, O.; Sans, J. A.; Manjón, F. J.; Muñoz, A.; Rodríguez-Hernández, P.; Achary, S. N.; Errandonea, D.; Martínez-García, D.; Romero, A. H.; Singhal, A.; Tyagi, A. K. High-Pressure Lattice Dynamical Study of Bulk and Nanocrystalline In_2O_3. *J. Appl. Phys.* **2012**, *112* (12), 123511.

(14) Kranert, C.; Schmidt-Grund, R.; Grundmann, M. Raman Active Phonon Modes of Cubic In_2O_3. *Phys. Status Solidi RRL* **2014**, *8* (6), 554−559.

(15) Berengue, O. M.; Rodrigues, A. D.; Dalmaschio, C. J.; Lanfredi, A. J. C.; Leite, E. R.; Chiquito, A. J. Structural Characterization of Indium Oxide Nanostructures: A Raman Analysis. *J. Phys. D: Appl. Phys.* **2010**, *43* (4), No. 045401.

(16) Wang, C. Y.; Dai, Y.; Pezoldt, J.; Lu, B.; Kups, T.; Cimalla, V.; Ambacher, O. Phase Stabilization and Phonon Properties of Single Crystalline Rhombohedral Indium Oxide. *Cryst. Growth Des.* **2008**, *8* (4), 1257−1260.

(17) Panneerdoss, I. J.; Jeyakumar, S. J.; Ramalingam, S.; Jothibas, M. Characterization of Prepared In_2O_3 Thin Films: The FT-IR, FT-Raman, UV−Visible Investigation and Optical Analysis. *Spectrochim. Acta, Part A* **2015**, *147*, 1−13.

(18) Ramsteiner, M.; Feldl, J.; Galazka, Z. Signatures of Free Carriers in Raman Spectra of Cubic In_2O_3. *Semicond. Sci. Technol.* **2020**, *35* (1), No. 015017.

(19) Gan, J.; Lu, X.; Wu, J.; Xie, S.; Zhai, T.; Yu, M.; Zhang, Z.; Mao, Y.; Wang, S. C. I.; Shen, Y.; Tong, Y. Oxygen Vacancies Promoting Photoelectrochemical Performance of In_2O_3 Nanocubes. *Sci. Rep.* **2013**, *3* (1), 1021.

(20) Wang, X.; Zhang, M.; Liu, J.; Luo, T.; Qian, Y. Shape- and Phase-Controlled Synthesis of In_2O_3 with Various Morphologies and Their Gas-Sensing Properties. *Sens. Actuators, B* **2009**, *137* (1), 103−110.

(21) Sun, Y.; Murphy, C. J.; Reyes-Gil, K. R.; Reyes-Garcia, E. A.; Lilly, J. P.; Raftery, D. Carbon-Doped In_2O_3 Films for Photoelectrochemical Hydrogen Production. *Int. J. Hydrogen Energy* **2008**, *33* (21), 5967−5974.

(22) Elouali, S.; Bloor, L. G.; Binions, R.; Parkin, I. P.; Carmalt, C. J.; Darr, J. A. Gas Sensing with Nano-Indium Oxides (In_2O_3) Prepared via Continuous Hydrothermal Flow Synthesis. *Langmuir* **2012**, *28* (3), 1879−1885.

(23) Andrews, L.; Wang, X. Infrared Spectra of Indium Hydrides in Solid Hydrogen and of Solid Indane. *Angew. Chem.* **2004**, *116* (13), 1738−1741.

(24) Wang, X.; Andrews, L. Infrared Spectra of Indium Hydrides in Solid Hydrogen and Neon. *J. Phys. Chem. A* **2004**, *108* (20), 4440−4448.

(25) Fontcuberta i Morral, A.; Zahler, J. M.; Griggs, M. J.; Atwater, H. A.; Chabal, Y. J. Spectroscopic Studies of the Mechanism for Hydrogen-Induced Exfoliation of InP. *Phys. Rev. B: Condens. Matter Mater. Phys.* **2005**, *72* (8), No. 085219.

(26) Liu, N.; Kuech, T. F. Interfacial Chemistry of InP/GaAs Bonded Pairs. *J. Electron. Mater.* **2007**, *36* (3), 179−190.

(27) Maeno, Z.; Yasumura, S.; Wu, X.; Huang, M.; Liu, C.; Toyao, T.; Shimizu, K. Isolated Indium Hydrides in CHA Zeolites: Speciation and Catalysis for Nonoxidative Dehydrogenation of Ethane. *J. Am. Chem. Soc.* **2020**, *142* (10), 4820−4832.

(28) Walsh, A.; Catlow, C. R. A.; Sokol, A. A.; Woodley, S. M. Physical Properties, Intrinsic Defects, and Phase Stability of Indium Sesquioxide. *Chem. Mater.* **2009**, *21* (20), 4962−4969.

(29) Walsh, A.; Sokol, A. A.; Catlow, C. R. A. Free Energy of Defect Formation: Thermodynamics of Anion Frenkel Pairs in Indium Oxide. *Phys. Rev. B: Condens. Matter Mater. Phys.* **2011**, *83* (22), 224105.

(30) Ágoston, P.; Erhart, P.; Klein, A.; Albe, K. Geometry, Electronic Structure and Thermodynamic Stability of Intrinsic Point Defects in Indium Oxide. *J. Phys.: Condens. Matter* **2009**, *21* (45), 455801.

(31) Novkovski, N.; Tanuševski, A. Origin of the Optical Absorption of In_2O_3 Thin Films in the Visible Range. *Semicond. Sci. Technol.* **2008**, *23* (9), No. 095012.

(32) Schleife, A.; Neumann, M. D.; Esser, N.; Galazka, Z.; Gottwald, A.; Nixdorf, J.; Goldhahn, R.; Feneberg, M. Optical Properties of In_2O_3 from Experiment and First-Principles Theory: Influence of Lattice Screening. *New J. Phys.* **2018**, *20* (5), No. 053016.

(33) Burstein, E. Anomalous Optical Absorption Limit in InSb. *Phys. Rev.* **1954**, *93* (3), 632−633.

(34) Moss, T. S. The Interpretation of the Properties of Indium Antimonide. *Proc. Phys. Soc., London, Sect. B* **1954**, *67* (10), 775−782.

(35) Gu, F.; Li, C.; Han, D.; Wang, Z. Manipulating the Defect Structure (V_O) of In_2O_3 Nanoparticles for Enhancement of Formaldehyde Detection. *ACS Appl. Mater. Interfaces* **2018**, *10* (1), 933−942.

(36) Cingarapu, S.; Yang, Z.; Sorensen, C. M.; Klabunde, K. J. Synthesis of Indium Nanoparticles: Digestive Ripening under Mild Conditions. *Inorg. Chem.* **2011**, *50* (11), 5000−5005.

(37) Khanna, P. K.; Jun, K.-W.; Hong, K. B.; Baeg, J.-O.; Chikate, R. C.; Das, B. K. Colloidal Synthesis of Indium Nanoparticles by Sodium Reduction Method. *Mater. Lett.* **2005**, *59* (8−9), 1032−1036.

(38) Walsh, A. Surface Oxygen Vacancy Origin of Electron Accumulation in Indium Oxide. *Appl. Phys. Lett.* **2011**, *98* (26), 261910.

(39) Tang, A.; Mei, Z.; Huo, W.; Du, X. Self-Diffusion Measurements in In_2O_3 Isotopic Heterostructures: Oxygen Vacancy Energetics. *Sci. China: Phys., Mech. Astron.* **2018**, *61* (11), 117321.

(40) Ágoston, P.; Albe, K. Ab Initio Modeling of Diffusion in Indium Oxide. *Phys. Rev. B: Condens. Matter Mater. Phys.* **2010**, *81* (19), 195205.

4.5.3 Elucidating CO$_2$ Hydrogenation over In$_2$O$_3$ Nanoparticles using Operando UV/Vis and Impedance Spectroscopies

The fourteenth overall publication addresses the reaction mechanism of the RWGSr over cubic In$_2$O$_3$. For that, operando UV-Vis and EI spectroscopy, (which was newly developed in the context of thermal catalysis) were combined and complemented by quasi in situ Raman, XP and UP spectroscopy. Parts of the developement of the operando impedance spectroscopic set-up were contributed to this work. The mechanistic investigation was supported by understanding reduction and oxidation processes occuring on the catalyst under different conditions. Surface reduction of the catalyst leads to bulk reduction through oxygen diffusion, while CO$_2$ can re-oxidize the surface. This is not possible for the bulk unless O$_2$ is used. Catalyst re-oxidation was identified as the rate-determining step in the catalytic cycle, indicating a redox behavior. However, catalyst activites are increased under reaction conditions compared to subsequent treatments in only CO$_2$ or H$_2$, indicating that the presence of hydrogen containing surface adsorbates may promote the CO$_2$ conversion. The study highlights the importance of developing new methods for the mechanistic investigation of highly relevant materials for CO$_2$ hydrogenation like In$_2$O$_3$.

GDCh

Research Articles

Angewandte
Chemie
International Edition
www.angewandte.org

Check for updates

CO₂ Hydrogenation

Elucidating CO₂ Hydrogenation over In₂O₃ Nanoparticles using Operando UV/Vis and Impedance Spectroscopies

Marc Ziemba, Mariusz Radtke, Leon Schumacher, and Christian Hess*

Abstract: In_2O_3 has emerged as a promising catalyst for CO_2 activation, but a fundamental understanding of its mode of operation in CO_2 hydrogenation is still missing, as the application of operando vibrational spectroscopy is challenging due to absorption effects. In this mechanistic study, we systematically address the redox processes related to the reverse water-gas shift reaction (rWGSR) over In_2O_3 nanoparticles, both at the surface and in the bulk. Based on temperature-dependent operando UV/Vis spectra and a novel operando impedance approach for thermal powder catalysts, we propose oxidation by CO_2 as the rate-determining step for the rWGSR. The results are consistent with redox processes, whereby hydrogen-containing surface species are shown to exhibit a promoting effect. Our findings demonstrate that oxygen/hydrogen dynamics, in addition to surface processes, are important for the activity, which is expected to be of relevance not only for In_2O_3 but also for other reducible oxide catalysts.

Introduction

Catalysts based on cubic In_2O_3 (c-In_2O_3, $Ia\bar{3}$) are known for their excellent properties in the context of CO_2 activation, such as for methanol synthesis,[1–6] direct liquid fuel production using bifunctional catalysts,[7] or the reverse water-gas shift reaction (rWGSR).[8–12] The latter reaction is of great relevance for the energy sector and the chemical industry, since CO_2 can be converted to CO, which can then be hydrogenated to liquid fuels (via the Fischer–Tropsch process) or used as feedstock for chemical processes. Such an approach would allow the increasing energy demand to be met while reducing the large amounts of CO_2 emitted by burning fossil fuels.

Theoretical studies have addressed CO_2 hydrogenation over In_2O_3, highlighting the importance of oxygen vacancies,[8] where H_2 dissociation is thermodynamically and kinetically favored.[13] More specifically, a frustrated Lewis pair (FLP) on the $In_2O_{3-x}(OH)_y(111)$ surface has been proposed to be responsible for H_2 dissociation as well as for CO_2 reduction, with the latter being the rate-limiting step.[14,15] Another theoretical (density functional theory, DFT) study[6] on possible reaction pathways reports that the protonation of a bent CO_2 adsorbate (bt-CO_2*) to a carboxylate intermediate (COOH*) is the rate-limiting step for CO formation, which is followed by COOH* decomposition into CO and hydroxide on the surface.[6] In a combined in situ spectroscopic and DFT study, the temperature-dependent reduction behavior of c-In_2O_3 was investigated.[16]

On the experimental side, surface indium oxo species have been proposed to be responsible for the heterolytic dissociation of hydrogen on alumina-supported c-In_2O_3, which is associated with the formation of surface indium hydrides and hydroxyl groups.[17] Other studies on In_2O_3-CeO_2 catalysts highlight the importance of oxygen vacancies in In_2O_3 for CO_2 conversion.[9] Cubic In_2O_3 has been shown to be more suitable for rWGSR than hexagonal In_2O_3, by enhancing the dissociative adsorption of H_2, facilitating the formation of oxygen vacancies and increasing the ability to adsorb and activate CO_2.[8] Defect-rich In_2O_3 has been employed as a photocatalyst for rWGSR,[18–20] exhibiting high activities at $\leq 200\,°C$, whereas at higher temperatures the difference between photochemical and thermal activities became smaller.[18]

Mechanistic data on In_2O_3 during the thermal rWGSR ($\geq 200\,°C$) is still very limited, in particular on the surface chemistry and subsurface/bulk dynamics, which may be related to experimental challenges for IR and Raman spectroscopy resulting from the In_2O_3 absorption properties.[16,21,22] In fact, to the best of our knowledge, so far no operando studies on the rWGSR over In_2O_3 catalysts have been reported. Nevertheless, (sub)surface/bulk processes seem to play an important role in c-In_2O_3 catalysts, as our previous study[16] has shown an exchange of oxygen vacancies between bulk and (sub)surface at elevated temperatures. Besides, diffusion of hydrogen may be of relevance by affecting the electronic structure[23–25] or the formation of hydrogenated intermediates (e.g. COOH*),[6,26] thereby influencing the catalytic activity. Impedance measurements were employed to gain mechanistic insight in the context of methanol steam reforming and (r)WGS,[12] but further analysis using equivalent-circuit fitting or operando monitoring was not performed. In summary, it appears that in the literature both a regenerative redox mechanism

[*] M. Ziemba, M. Radtke, L. Schumacher, C. Hess
Eduard Zintl Institute of Inorganic and Physical Chemistry,
Technical University of Darmstadt
Alarich-Weiss-Str. 8, 64287 Darmstadt (Germany)
E-mail: christian.hess@tu-darmstadt.de

(without the occurrence of reaction intermediates like e.g., carbonates, COOH*) and the reaction via intermediates are postulated, whereby the simultaneous occurrence is also conceivable.[3,6,8,21,26]

In this mechanistic study, we employ (quasi) in situ and operando spectroscopies (Raman, UV/Vis, X-ray photoelectron spectroscopy (XPS)) to explore the surface and subsurface dynamics of In_2O_3 during rWGSR. Bulk properties are directly probed by operando impedance spectroscopy supported by ex situ X-ray diffraction (XRD) analysis. We demonstrate, on one hand, the readiness of the In_2O_3 surface for reduction by H_2 and oxidation by CO_2, and, on the other, the participation of the subsurface/bulk in the reaction, thus enhancing the understanding of the mechanism, in particular, the CO_2 activation process, the role of oxygen vacancies, and the participation of hydrogen-related adsorbates.

Results and Discussion

Details of the characterization of the In_2O_3 sample used in this study have already been published.[16] Briefly, the particles have a specific surface area of $39\ m^2g^{-1}$ and our ex situ XRD results show that only cubic ($Ia\bar{3}$) In_2O_3 is present. In addition, transmission electron microscopy (TEM) measurements show that the particles are present as sheets terminating with an $In_2O_3(222)$ surface. Contaminations caused by the synthesis, e.g. nitrogen, can be excluded within the sensitivity of our XPS measurements.

First, the In_2O_3 was analyzed for its activity as a function of temperature, while we simultaneously monitored the electronic structure using operando UV/Vis spectroscopy. Our previous UV/Vis studies on In_2O_3 during 10 vol% H_2 exposure have revealed a strong dependence of the absorption in the visible range on the oxygen defect density.[16] The bottom panel of Figure 1 depicts the temporal evolution of the absorbance at 700 nm as an indicator for oxygen defects upon exposure to different gas phases or temperatures. Starting at 130 °C, switching from O_2 to H_2 leads to an increase in absorption in the visible range and H_2O formation in the gas phase, which illustrates that In_2O_3 undergoes reduction even at just 130 °C. Exposure to reaction conditions shows a further increase in absorbance, resulting from the longer residence time under H_2 flow, since CO_2 is not yet activated at this temperature, as evidenced by the absence of CO in the gas phase (not shown).

Increasing the temperature to 160 °C leads to a strong increase in absorption, which continues even after 160 °C is reached. This behavior can be explained by a strong reduction of the catalyst, as supported by the absence of CO but increasing concentration of H_2O in the gas phase. In this context, H_2-temperature programmed desorption (TPD) experiments from previous studies[21] have shown that a large fraction of adsorbed hydrogen is already desorbed at these temperatures thus does not remain on the surface.

Starting at a temperature of 190 °C, the catalyst becomes active towards CO_2 conversion and shows only a weak
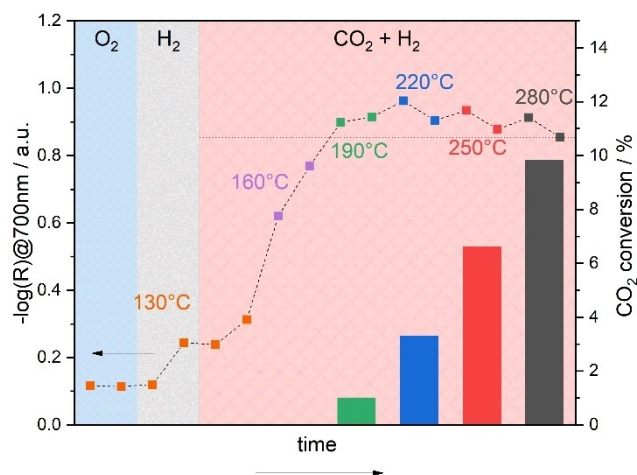

Figure 1. In situ/operando UV/Vis results for In_2O_3 sheets recorded during O_2 and H_2 exposures at 130 °C and reaction conditions (CO_2:H_2, 2:4) ranging from 130 to 280 °C in 30 °C steps. From 190 °C on, the sample becomes active in terms of conversion of CO_2, which is shown by bars (right axis). At lower temperatures, the conversion is within the experimental uncertainty. The exposure time before the conditions were changed was ≈30 min. The horizontal dotted line helps to illustrate the change in absorbance in the reaction phase.

increase or even a decrease in visible absorption. The absorption reaches its maximum during the first measurement at 220 °C and then decreases again over the next 30 min at 220 °C. The changes in absorption behavior can be explained in terms of counteracting contributions to the indium reduction state from temperature-dependent reduction and CO_2 conversion leading to oxidation. At 220 °C the maximum degree of reduction is reached under reaction conditions but at this temperature CO_2 is significantly converted, which oxidizes the surface and thus results in an overall decrease in visible absorption. With time, a stationary state is established by balancing the contributions from reduction by H_2 and oxidation by CO_2. At temperatures >190 °C, a similar absorption behavior is observed, consisting of an initial increase and a subsequent decrease in absorption, which clearly shows that reduction by H_2 is faster than oxidation by CO_2. Comparison of the different equilibrated states reveals that the absorption is at its highest at 190 °C and decreases with temperature, strongly suggesting that the oxidation of the catalyst by CO_2 increases with temperature while the reduction remains at about the same level, because the maximum amount of oxygen vacancies has been reached. This could be a first indication that CO_2 activation with subsequent formation of CO is the rate-determining step. The same experiment was performed with a CO_2 to H_2 ratio of 4:2 (see Figure S1). The results are similar, but the reduction is much slower due to the lower H_2 content, which is why the further reduction of the material ends only after 250 °C. These findings underline our previous results.

The activities we measured compare favorably to those of previous studies on polycrystalline In_2O_3,[9,11] which is likely to terminate with the 111 surface due to the method

of synthesis (thermal decomposition of $In(NO_3)_3$) and the fact that it is the most thermally stable. However, this should be viewed with caution, as previously lower flow rates were used, resulting in higher residence times, and higher reactant concentrations in the gas feed. For this reason, we will refrain from a more detailed comparison of the activities. Other factors leading to higher conversions may be the smaller crystallite size and thus the larger specific surface area of the In_2O_3 particles used here. Besides, the particle shape or the surface termination may have an influence on the activity, as has been shown in the context of CO oxidation,[27] while differences in H_2 or CO_2 activation over $In_2O_3(111)$ or $In_2O_3(110)$ have been demonstrated by theoretical studies (DFT).[6,13,28,29]

Next, we performed operando UV/Vis measurements at 250°C while systematically varying the gas phase between oxidative/reactive and reductive conditions. Figure 2 shows the absorbances at 532 nm and 700 nm (see Figure S2 for the corresponding UV/Vis spectra), where the former mainly resembles the self-absorption in our Raman experi-

ments, which were recorded at 532 nm (see below). In these experiments we first pretreated the catalyst with O_2 to start from an oxidized state. During heating to 250°C under O_2 exposure, desorption of H_2O and CO_2 was observed (not shown), indicating that the surface is being cleaned from adsorbates. Upon exposure to O_2 flow, the absorption at 532 nm increased significantly (see Figure 2). Since this wavelength is located within the absorption edge, the observed behavior can be explained by an increase in the band edge, originating from the temperature increase (Burstein–Moss effect) and/or from oxidation.[16]

On switching to H_2, the absorption at 532 and 700 nm increases significantly, which is mainly attributed to a reduction of the (sub)surface and possibly also to an increase in reflectivity through small metallic indium domains. This is supported by the strong presence of H_2O in the gas phase. Since the same trends in absorption can be observed at both wavelengths (and the entire remaining visible range), only the absorption at 700 nm will be discussed in the following.

Upon exposure to CO_2, there is again a strong decrease in absorption, which is in the range of the absorption in O_2, demonstrating that the sample can be oxidized again by CO_2 and that the process of reduction seems to be completely reversible on the basis of UV/Vis spectra and their penetration depth. At the same time, the gas phase initially shows a small increase in CO (see Figure 2, bottom panel), implying surface oxidation by CO_2, thereby releasing CO. Such a reversibility with respect to the oxidation state in the absence of H_2 could indicate that hydrogen is not required for CO_2 reduction.

On switching to H_2 afterwards, the detected CO signal is significantly lower, which shows that only small amounts of CO_2 in the form of carbonates or other carbonaceous adsorbates remain on the surface in the CO_2 phase. In contrast, the H_2O signal increases, which in turn is associated with the reduction of the surface, as can be seen by the increase in absorbance.

Exposure to reaction conditions (H_2/CO_2) induces a decrease in absorption despite the same H_2 concentration, which, however, does not reach the level detected in CO_2. This behavior confirms the findings of Figure 1, i.e., that the reduction and oxidation processes must be in equilibrium, with the reduction still predominating. Interestingly, the two reaction phases are characterized by the same absorption (see Figure 2, top panel) and CO evolution (see Figure 2, bottom panel), despite the completely different initial states. This clearly demonstrates that the pretreatment has no influence on the reaction and suggests that certain intermediates only form under reaction conditions, since the CO release under reaction conditions is significantly higher than when switching from H_2 to CO_2 or vice versa. In this context, previous photocatalytic studies have shown that the surface hydroxide concentration is also higher under reaction conditions than under pure H_2.[18] As can be seen in Figure 2, switching off CO_2 after reaction conditions leads to a renewed increase in absorption and thus a reduction of the surface.
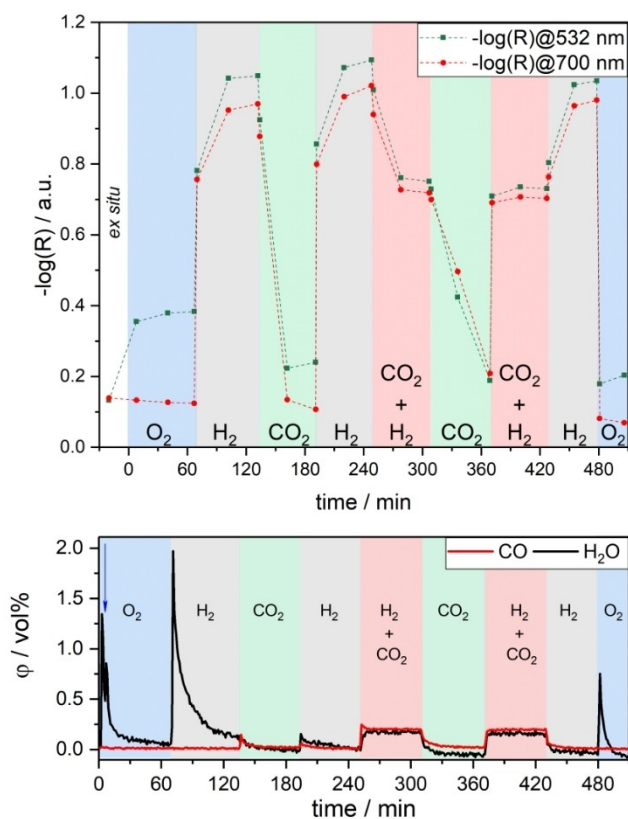

Figure 2. Top: In situ/operando UV/Vis results for In_2O_3 sheets recorded during the indicated gas exposures at 250°C and at a total flow rate of 100 mL min^{-1}, except for the ex situ spectra, which were taken at 25°C. The exposure time in each gas phase was about 1 h with the exception of the last O_2 phase (30 min). Bottom: Gas-phase IR analysis during the UV/Vis measurements. The increased water concentration in the first few minutes is due to the purging of the cell. Starting after 6 min (see blue arrow) the cell was heated to 250°C, leading to water desorption and thus an increase in the H_2O concentration. For details see text.

Finally, In_2O_3 is exposed to O_2 flow to check the reversibility of the system. The gas-phase data reveals a strong H_2O signal decaying with time, which implies the presence/formation of hydroxides/adsorbed hydrogen during H_2 exposure. During this O_2 exposure, the absorbance is lower than during the first O_2 phase, and major differences were detected for 532 nm absorption, which is located in the absorption edge. Since in both cases the experimental conditions were the same, we attribute the observed drop in absorption to a decrease in the band gap resulting from a larger crystallite size. To test this hypothesis, we performed ex situ XRD measurements after different gas exposures until the first reaction phase, which clearly show that the crystallite size increases from 12 nm after the first O_2 phase to 27 nm after the subsequent H_2 (for diffractograms, see Figure S3). Note that all following gas atmospheres have no significant influence on the crystallite size. Notably, after the second H_2 exposure, additional reflections are detected, which originate from metallic indium (JCPDS 85-1409), showing that metallic indium is formed during reduction with 4 vol % H_2 at 250 °C. To this end, it should be noted that small domains of metallic indium, formed during the first H_2 phase and under reaction conditions, may have oxidized back under air exposure and thus cannot be excluded by the present ex situ XRD analysis.

To further probe the reducibility behavior of In_2O_3, we recorded the XRD pattern after CO exposure (4 vol %) after a prior oxygen treatment, analogous to the other measurements. For CO exposure, significantly more metallic indium was formed and the crystallite size grew only to 21 nm, in contrast to the observed 27 nm for H_2. Thus, hydrogen is a weaker reducing agent towards In_2O_3 than CO, which is consistent with the literature.[12] Furthermore, hydrogen must have an additional effect on the sample, since the crystallite size increases significantly more compared to CO. To gain insight into the electronic structure changes during CO reduction, we recorded in situ UV/Vis spectra (see Figure S4), which reveal a higher absorption in the visible region during CO exposure, implying a better reduction by CO. We also highlight the fact that the presence of CO strongly contributes to the enhanced electronic inductive effects in the impedance spectra in the Figure 3B compared to the purely reductive H_2 treatment (Figure S6, Table S2). Interestingly, the sample absorbance almost returns to its original value (measured in O_2) on subsequent exposure to CO_2. Thus, In_2O_3 can be re-oxidized by CO_2, releasing CO regardless of the reducing agent (H_2 or CO). Moreover, no surface hydrogen species are required for the oxidation by CO_2, indicating that no hydrogen-containing intermediates are involved in the re-oxidation process.

To elucidate the charge and mass transport in In_2O_3 nanoparticles, operando potentiostatic electrochemical impedance spectroscopy (p-EIS) spectra were acquired. It should be mentioned that due to the sample shape (no pellet) a Mott–Schottky analysis is disturbed by gas inclusion and an increased number of grain boundaries and is not completely reproducible. For this reason, such an analysis was not performed in this work. The non-uniform sample
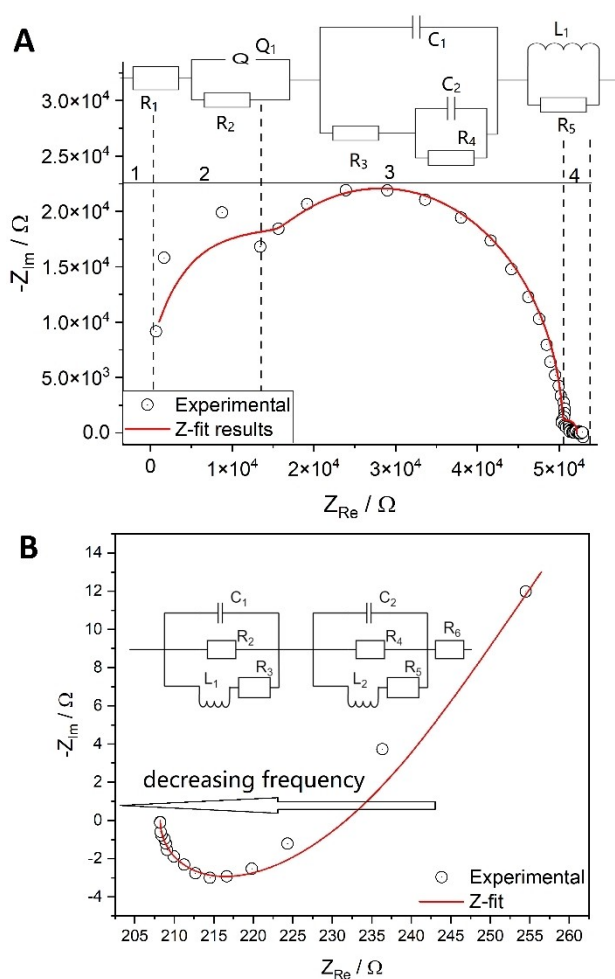

Figure 3. Nyquist plots based on operando p-EIS of In_2O_3, shown together with fits according to the corresponding equivalent circuits. A) During CO_2 gas treatment (2 vol %; total flow: 50 mL min⁻¹) at 250 °C with the different areas in the Nyquist plot and the corresponding assignment in the equivalent circuit. Region 1: electrode bulk resistance; region 2: vacancy reorganization; region 3: capacitive behavior of the non-reduced In_2O_3; region 4: gas diffusion into In_2O_3 nanoparticles. B) During CO_2/H_2 treatment (2 vol % CO_2, 4 vol % H_2; total flow rate: 50 mL min⁻¹) at 250 °C. The experimental data shows a reversed behavior, with high-frequency points located on the right. R: resistance, C: capacitance, L: inductance, Q: non-ideal capacitance. The values resulting from the fit analysis are summarized in Table S2.

distribution also has an impact on the p-EIS spectra, which deviate from ideal behavior by ca. 10 %, as validated by Kramers-Kronig-relations (see Supporting Information). All spectra (see Figure 3 and Figures S5–S11) were recorded under the same gas sequence and composition as in Figure 2. A considerable impact of the gas phase on the impedance spectra was found for all treatments, which is reflected in the profile of the Nyquist plots. However, as there are no fundamental differences between spectra taken under the same gas atmosphere, only the spectra of the first treatment with a specific gas phase will be discussed, starting with the spectrum under O_2 exposure (see Figure S5).

As In_2O_3 is a semiconductor with a band gap of approximately 3 eV,[30] accumulation of charged surface oxygen due to polarization is expected.[31] The polarization manifests itself in a sharp and vertical increase of the impedance in the Nyquist plot, and both imaginary and real parts of the impedance reach values in the megohm range (see Figure S5), which speaks for very limited to no conductivity of In_2O_3 during the oxygen treatment. The spectrum in O_2 atmosphere may therefore be treated as a response of bare In_2O_3 nanoparticles and will serve as a reference for the discussion of changes observed during the following gas treatments.

Regarding surface charging, a similar behavior was previously observed for CeO_2 at room temperature.[32] The presence of a limited diffusion region results from the hindered oxygen accumulation on the In_2O_3 surface. The voltage applied to the sample causes external polarization due to the non-conductive character of In_2O_3 at room temperature, and the activation energy from the temperature dependent conductivity behavior of $137\,kJ\,mol^{-1}$ will not be reached by simple polarization but requires elevated temperatures.[33]

The major reduction of In_2O_3 was observed during the hydrogen treatment (see Figure S6). The pronounced contribution of the inductive part ($L = 2.03 \times 10^{-5}$ H during the first H_2 treatment) observed in the operando p-EIS spectrum is attributed to the percolation of In_2O_3 nanoparticles with hydrogen species,[34] referring here to the penetration of these species into the solid. This is in agreement with previous IR and DFT studies on In_2O_3, which have demonstrated the diffusion of interstitial hydrogen to increase conductivity.[23–25] Thereby, hydrogen percolates into the bulk of a nanoparticle and creates an inductive response of the EIS spectrum, typical for gas diffusion in the bulk of a material.[34] The reduction of the In_2O_3 nanoparticles is proposed to proceed according to the reaction $In_2O_3 + 3\,H_2 \rightarrow 2\,In^0 + 3\,H_2O$. Thus, the first two H_2 phases show a purely resistive behavior at the beginning of the Nyquist plot, indicating the formation of metallic indium. In the third phase, this behavior is less pronounced, but this is also consistent with our UV/Vis results (lowest absorption at 532 nm).

The decomposition of H_2 into protons within In_2O_3 was speculated to occur by a homolytic or a heterolytic splitting process, as discussed by García-Melchor and López.[35] In this context, theoretical studies have shown that both scenarios are conceivable, but strongly depend on the degree of reduction.[13] Under our conditions, owing to the high degree of indium oxide reduction, heterolytic dissociation is more likely.[13] To describe the spectrum in Figure S6, a considerable contribution of the Warburg element is necessary (see Table S2), which speaks for the distribution of hydrogen gas on the surface. The Warburg element is commonly used to describe mass transport processes, therefore, coupling it with inductive parts will deliberately lead to the description of a gaseous contribution to the impedance response.[36]

Following the hydrogen treatment, In_2O_3 was exposed to CO_2 and an operando p-EIS spectrum was recorded (see Figure 3A). The equivalent circuit shown in Figure 3A is divided into four parts. The first part represents the electrode bulk resistance (R_1), which was found to be in the ohm range (see Table S2), speaking for improved conductivity compared to the pristine material (with R_1 in the megohm range); nevertheless, remaining vacancies induced by the H_2 phase remain active, judging by our Raman spectra below. In the second part, the reorganization of vacancies occurs.[37] The third part contributes mostly to the p-EIS spectrum and is assigned to non-reduced In_2O_3, while at low frequencies (L_1R_5 region) gas diffusion takes place, as, for example, observed for polycrystalline tin oxide.[38,39] The regions are assigned based on the frequency domains where impedance data was recorded, starting from the high-frequency region and bulk impedance, followed by the internal electronic structure in the middle-frequency region and ending on the diffusion response within low-frequency regions.[40]

During reaction conditions (see Figure 3B), the hydrogen flow, penetrating the interior of the In_2O_3, carries the CO_2 gas with it, as judged by the inductance contribution ($L = 1.03 \times 10^{-5}$ H), which differs from the value obtained for the first H_2 treatment ($L = 2.03 \times 10^{-5}$ H). The reaction occurs in the bulk due to gas percolation, rather than on the surface as in the case of pure CO_2 exposure. In this context, we propose that the higher inductance is caused by the reaction $CO_2 + H_2 \rightarrow CO + H_2O$ and thus by the presence of CO, which is also detected in the gas phase. Therefore, the respective parts of the triple equivalent circuits of Figure 3B correspond to the interaction of In_2O_3 with H_2 (right part of the circuit) and CO_2 (left part of the circuit). Please note that the EIS spectrum is reversed compared to what it was in the case of H_2 treatment, implying that the high frequency points are in the region of high imaginary and real impedances, originating from gas percolation and the induction of the gas impedance.[34] In contrast to pure hydrogen, there is no pure resistance behavior at the beginning of the spectrum, indicating that no metallic indium is formed under reaction conditions. This is corroborated by our operando UV/Vis results, which show a significantly lower absorption in the visible region than under H_2 atmosphere.

Figure 4 depicts quasi in situ Raman spectra of In_2O_3, recorded under argon at 50 °C after treatment with O_2, H_2, H_2/CO_2, and CO_2. The bands at 306, 366, 495 and 629 cm^{-1} can be assigned to $\delta(InO_6)$, $\nu(InO_6)$, In–O–In, and $\nu(InO_6)$ vibrations of cubic In_2O_3, respectively, which is in accordance with the literature.[16,41] These bands become broader with increasing number of defects (see H_2 and H_2/CO_2 treatment, Figure 4), consistent with previous studies.[42] The feature at 595 cm^{-1} also originates from cubic In_2O_3 and is attributed to a vibration with E_g symmetry.[43] It shows a red-shift under reaction conditions and H_2, as a result of defect formation, consistent with our previous study.[16] All other features (415, 531, and 559 cm^{-1}) are related to oxygen defects, as confirmed by DFT.[16] Notably, the band at 306 cm^{-1} shows a shoulder towards larger wavenumbers, which is caused by reduction and was also observed in previous studies.[21,42,44]
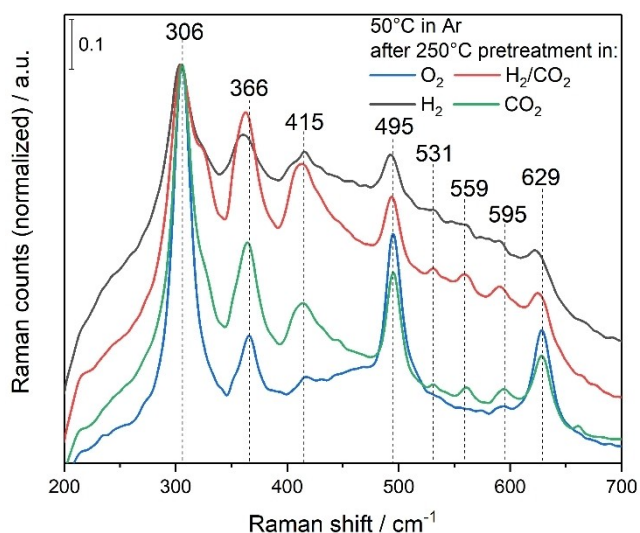
Figure 4. Quasi in situ Raman spectra recorded in argon at 50 °C after the indicated gas exposures at 250 °C and at a total flow rate of 100 mL min^{-1}. The spectra were normalized to the band with the highest intensity at around 306 cm^{-1}. The spectra were recorded sequentially in the order O_2, H_2, H_2/CO_2, and CO_2. The sample was cooled to 50 °C under argon.

Comparison of the different gas phases reveals a significantly higher background for H_2 and reaction conditions, which is caused by fluorescence, self-absorption of the laser, and an increased reflectivity by metallic indium (as also detected by p-EIS, see flat line for Z_{Re} between 240 and 220 Ω in Figure S6). Nevertheless, closer inspection of the spectra recorded after O_2 and CO_2 exposure shows that the 415 cm^{-1} band is less pronounced for O_2, implying that re-oxidation by CO_2 is not as efficient as by oxygen. This behavior is in agreement with previous impedance studies,[12] which show that In_2O_3 is best re-oxidized with O_2, followed by H_2O and CO_2. In the UV/Vis measurements such a difference was not observed due to the lower penetration depth, implying that the surface is completely oxidized, but the bulk is not. Thus, a certain number of defects remain present even under O_2.

The high-wavenumber region of the Raman spectra shows bands at 3647 and 3675 cm^{-1} (see Figure S12), which originate from bridging hydroxyl groups[44,45] and reappear after exposure to reaction conditions after being consumed in the reducing atmosphere. Interestingly, after reaction conditions, a new band is detected at 2867 cm^{-1}, which is assigned to the C–H stretching vibration of a formate-like species.[44] This shows that under reaction conditions a stable adsorbate is formed, which involves atoms from both reactants. However, in this context it is important to note that this observation does not imply the presence of a reaction intermediate, as the detected band may be due to an observer species. At this point it should be noted that we cannot exclude the presence of other intermediates. Future operando Raman experiments may possibly clarify the role of formate or other species, but this is currently hampered by the large background (see introduction).

In order to obtain additional surface information, XPS and ultraviolet photoelectron spectroscopy (UPS) was applied (for XPS data and discussion see Supporting Information). Figure 5 depicts the UP spectra of In_2O_3 using He I radiation after exposure to the different gas atmospheres, analogous to the XP spectra. All UP spectra show the typical valence band features at 4.4, 6.1 and 8.7 eV.[46,47] For all gas atmospheres, the features at 5.7, 8.7, and 10.5 eV increase in intensity compared to the spectrum after O_2 exposure, but most prominently for exposure to CO_2 and reaction conditions. Previous studies have proposed the contributions at 5.7 and 10.5 eV to be determined by modified valence band (VB) states subjected to adsorption of molecules.[46] In our case, in principle, hydroxides and/or carbonaceous adsorbates (e.g., carbonates, formats) may contribute to the spectral changes compared to the O_2 spectrum, but the presence of carbonaceous adsorbates appears to be more likely, considering the increased intensity after exposure to CO_2 and the reaction phase. This is further supported by the IR gas-phase measurements, which show the presence of hydrogen-containing adsorbates on the surface after H_2 treatment (see Figure 2). In this context, in a previous near-ambient-pressure (NAP) UPS study on In_2O_3 during rWGSR, it was shown that the temperature as well as the CO_2:H_2 ratio have a strong influence on the valence region,[48] which is reflected in line broadening. This is in agreement with our findings that the surface is strongly influenced by the gas environment, where a greater CO_2 content leads to greater changes, which indicates the presence of carbonaceous adsorbates.
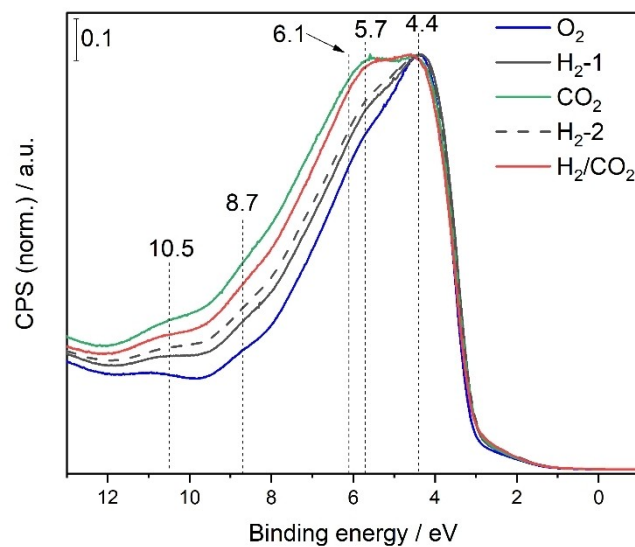

Figure 5. Valence band photoelectron spectra recorded quasi in situ after exposure to the indicated gas atmospheres at 250 °C and at a total flow rate of 100 mL min^{-1}. The blue spectrum was obtained after O_2 (25 %) pretreatment, the gray ones after H_2 (4 %) pretreatment, the green one after CO_2 (2 %) pretreatment, and the red one after H_2/CO_2 (4 %/2 %) pretreatment. The gas sequence corresponds to that of the UV/Vis experiments in Figure 2 up to the first reaction phase and the hyphenated number indicates the order of the gas sequence. The source was He I ($h\nu = 21.2$ eV).

Summarizing the findings from the combined surface analysis by Raman, XP and UP spectroscopies, there is a clear indication of variations in the surface composition, the indium state, and the number of oxygen vacancies when switching between oxidative, reductive, and reactive gas atmospheres. The indium and support surface state after exposure to reaction conditions largely follows a behavior expected within the limits of oxidative (CO_2) and reductive (H_2) atmospheres, while the overall changes in the adsorbate species (e.g. OH, formate) are rather distinct, somewhat resembling the observed subsurface/bulk behavior (see Figure 2). By combining these findings with the operando UV/Vis and impedance results, the active state of the catalyst can be specified as reduced, i.e., oxygen-defect containing (but non-metallic) In_2O_3, percolated with reactant and product gases, and exhibiting surface species, such as hydroxides, hydrides, and carbonaceous adsorbates. Although the redox processes can occur separately, the simultaneous presence of H_2 and CO_2 clearly provides synergetic effects towards CO_2 conversion. Our results emphasize, in particular, the importance of subsurface/bulk dynamics for the activity in reducible oxide catalysts, besides surface processes.

Conclusion

In this study, we have generated a deeper understanding of the mechanism of rWGSR over c-In_2O_3 catalysts by applying operando UV/Vis spectroscopy and (in the context of thermal catalysis) newly developed operando impedance spectroscopy, as well as quasi in situ spectroscopies (Raman, XPS, UPS). The new mechanistic insight into the In_2O_3 mode of operation was supported by a systematic investigation of the related reduction and oxidation processes and their comparison to reaction conditions. For example, our study shows that despite surface reduction, diffusion of oxygen vacancies leads to bulk reduction. While reduced c-In_2O_3 nanoparticles can be re-oxidized by CO_2 on the surface, complete oxidation of the bulk is only possible with O_2. This behavior is independent of the reducing agent (H_2 or CO), although CO leads to stronger In_2O_3 reduction.

Based on temperature-dependent UV/Vis analysis under reaction conditions, oxidation by CO_2 is identified as the rate-determining step for the rWGSR, which is supported by operando impedance spectra, showing a predominance of the hydrogen contribution. The significant evolution of CO and H_2O, also after separate treatment with CO_2 or H_2, is fully consistent with redox processes but because conversions are somewhat higher under reaction conditions, hydrogen-containing surface species (e.g. hydroxides, hydrides) are proposed to have a promoting effect on CO_2 conversion and/or hydrogen containing intermediates (e.g. COOH*) may play an role. Such a behavior would be in accordance with results from theoretical studies, which associate CO_2 conversion with frustrated Lewis pairs.[14,15]

The above analysis of the (sub)surface and bulk properties during the rWGSR demonstrates that the entire In_2O_3 nanoparticle is involved in the reaction, which is only accessible by using complementary in situ/operando techniques. Combining our new experimental findings with results from theory allows us to develop a consistent mechanistic picture of rWGSR over c-In_2O_3. Our findings are of immediate relevance for a detailed understanding of CO_2 hydrogenation and other related catalytic processes over In_2O_3, but they are also expected to be of more general impact, considering the growing importance of catalysts based on reducible oxide materials.

Conflict of Interest

The authors declare no conflict of interest.

Data Availability Statement

The data that support the findings of this study are available from the corresponding author upon reasonable request.

[1] A. Tsoukalou, P. M. Abdala, D. Stoian, X. Huang, M.-G. Willinger, A. Fedorov, C. R. Müller, *J. Am. Chem. Soc.* **2019**, *141*, 13497–13505.

[2] M. S. Frei, M. Capdevila-Cortada, R. García-Muelas, C. Mondelli, N. López, J. A. Stewart, D. Curulla Ferré, J. Pérez-Ramírez, *J. Catal.* **2018**, *361*, 313–321.

[3] J. Wang, G. Zhang, J. Zhu, X. Zhang, F. Ding, A. Zhang, X. Guo, C. Song, *ACS Catal.* **2021**, *11*, 1406–1423.

[4] N. Rui, F. Zhang, K. Sun, Z. Liu, W. Xu, E. Stavitski, S. D. Senanayake, J. A. Rodriguez, C.-J. Liu, *ACS Catal.* **2020**, *10*, 11307–11317.

[5] N. Rui, K. Sun, C. Shen, C. J. Liu, *J. CO2 Util.* **2020**, *42*, 101313.

[6] B. Qin, Z. Zhou, S. Li, P. Gao, *J. CO2 Util.* **2021**, *49*, 101543.

[7] P. Gao, S. Li, X. Bu, S. Dang, Z. Liu, H. Wang, L. Zhong, M. Qiu, C. Yang, J. Cai, et al., *Nat. Chem.* **2017**, *9*, 1019–1024.

[8] J. Wang, C.-Y. Liu, T. P. Senftle, J. Zhu, G. Zhang, X. Guo, C. Song, *ACS Catal.* **2020**, *10*, 3264–3273.

[9] W. Wang, Y. Zhang, Z. Wang, J. Yan, Q. Ge, C. Liu, *Catal. Today* **2016**, *259*, 402–408.

[10] J.-I. Makiura, T. Higo, Y. Kurosawa, K. Murakami, S. Ogo, H. Tsuneki, Y. Hashimoto, Y. Sato, Y. Sekine, *Chem. Sci.* **2021**, *12*, 2108–2113.

[11] Q. Sun, J. Ye, C. Liu, Q. Ge, *Greenhouse Gase Sci. Technol.* **2014**, *4*, 140–144.

[12] T. Bielz, H. Lorenz, P. Amann, B. Klötzer, S. Penner, *J. Phys. Chem. C* **2011**, *115*, 6622–6628.

Angew. Chem. Int. Ed. **2022**, *61*, e202209388 (7 of 8)

© 2022 The Authors. Angewandte Chemie International Edition published by Wiley-VCH GmbH

[13] B. Qin, S. Li, *Phys. Chem. Chem. Phys.* **2020**, *22*, 3390–3399.

[14] M. Ghoussoub, S. Yadav, K. K. Ghuman, G. A. Ozin, C. V. Singh, *ACS Catal.* **2016**, *6*, 7109–7117.

[15] K. K. Ghuman, T. E. Wood, L. B. Hoch, C. A. Mims, G. A. Ozin, C. V. Singh, *Phys. Chem. Chem. Phys.* **2015**, *17*, 14623–14635.

[16] M. Ziemba, L. Schumacher, C. Hess, *J. Phys. Chem. Lett.* **2021**, *12*, 3749–3754.

[17] A. I. Serykh, *J. Phys. Chem. C* **2016**, *120*, 21436–21440.

[18] J. Y. Y. Loh, N. P. Kherani, *Molecules* **2019**, *24*, 3818.

[19] J. Y. Y. Loh, Y. Ye, N. P. Kherani, *ACS Appl. Mater. Interfaces* **2020**, *12*, 2234–2242.

[20] L. Wang, Y. Dong, T. Yan, Z. Hu, A. A. Jelle, D. M. Meira, P. N. Duchesne, J. Y. Y. Loh, C. Qiu, E. E. Storey, et al., *Nat. Commun.* **2020**, *11*, 2432.

[21] T. Bielz, H. Lorenz, W. Jochum, R. Kaindl, F. Klauser, B. Klötzer, S. Penner, *J. Phys. Chem. C* **2010**, *114*, 9022–9029.

[22] N. Siedl, P. Gügel, O. Diwald, *J. Phys. Chem. C* **2013**, *117*, 20722–20729.

[23] Y. Qin, P. Weiser, K. Villalta, M. Stavola, W. B. Fowler, I. Biaggio, L. Boatner, *J. Appl. Phys.* **2018**, *123*, 161506.

[24] S. Limpijumnong, P. Reunchan, A. Janotti, C. G. Van de Walle, *Phys. Rev. B* **2009**, *80*, 193202.

[25] W. Yin, K. Smithe, P. Weiser, M. Stavola, W. B. Fowler, L. Boatner, S. J. Pearton, D. C. Hays, S. G. Koch, *Phys. Rev. B* **2015**, *91*, 075208.

[26] Y. Qi, L. Song, S. Ouyang, X. Liang, S. Ning, Q. Zhang, J. Ye, *Adv. Mater.* **2020**, *32*, 1903915.

[27] W. J. Kim, D. Pradhan, Y. Sohn, *J. Mater. Chem. A* **2013**, *1*, 10193.

[28] A. Posada-Borbón, H. Grönbeck, *Phys. Chem. Chem. Phys.* **2020**, *22*, 16193–16202.

[29] A. Posada-Borbón, H. Grönbeck, *Phys. Chem. Chem. Phys.* **2019**, *21*, 21698–21708.

[30] A. Walsh, J. L. F. Da Silva, S.-H. Wei, C. Körber, A. Klein, L. F. J. Piper, A. DeMasi, K. E. Smith, G. Panaccione, P. Torelli, et al., *Phys. Rev. Lett.* **2008**, *100*, 167402.

[31] V. Balasubramani, S. Chandraleka, T. S. Rao, R. Sasikumar, M. R. Kuppusamy, T. M. Sridhar, *J. Electrochem. Soc.* **2020**, *167*, 037572.

[32] M. M. El-Nahass, A. M. Hassanien, A. A. Atta, E. M. A. Ahmed, A. A. Ward, *J. Mater. Sci. Mater. Electron.* **2017**, *28*, 1501–1507.

[33] M. Radtke, C. Hess, *J. Mater. Eng. Perform.* **2022**, https://doi.org/10.1007/s11665-022-06653-3.

[34] S. Cruz-Manzo, R. Chen, P. Rama, *J. Fuel Cell Sci. Technol.* **2012**, *9*, 051002.

[35] M. García-Melchor, N. López, *J. Phys. Chem. C* **2014**, *118*, 10921–10926.

[36] J. Huang, Y. Gao, J. Luo, S. Wang, C. Li, S. Chen, J. Zhang, *J. Electrochem. Soc.* **2020**, *167*, 166503.

[37] T.-M. Pan, Y.-S. Huang, J.-L. Her, *Sci. Rep.* **2018**, *8*, 12902.

[38] M. Labeau, U. Schmatz, G. Delabouglise, J. Roman, M. Vallet-Regi, A. Gaskov, *Sens. Actuators B* **1995**, *26*, 49–52.

[39] T. Yang, J. Liu, H. Finklea, S. Lee, W. K. Epting, R. Mahbub, T. Hsu, P. A. Salvador, H. W. Abernathy, G. A. Hackett, *Int. J. Hydrogen Energy* **2018**, *43*, 15445–15456.

[40] J. Stankiewicz, M. P. Lozano, F. Villuendas, *Phys. Rev. B* **2012**, *85*, 125306.

[41] S. Elouali, L. G. Bloor, R. Binions, I. P. Parkin, C. J. Carmalt, J. A. Darr, *Langmuir* **2012**, *28*, 1879–1885.

[42] F. Gu, C. Li, D. Han, Z. Wang, *ACS Appl. Mater. Interfaces* **2018**, *10*, 933–942.

[43] C. Kranert, R. Schmidt-Grund, M. Grundmann, *Phys. Status Solidi RRL* **2014**, *8*, 554–559.

[44] S. Sänze, C. Hess, *J. Phys. Chem. C* **2014**, *118*, 25603–25613.

[45] A. N. Kharlanov, O. A. Turakulova, V. V. Lunin, *Kinet. Catal.* **2004**, *45*, 260–265.

[46] V. Brinzari, G. Korotcenkov, M. Ivanov, V. Nehasil, V. Matolin, K. Mašek, M. Kamei, *Surf. Sci.* **2007**, *601*, 5585–5594.

[47] V. Brinzari, G. Korotcenkov, V. Matolin, *Appl. Surf. Sci.* **2005**, *243*, 335–344.

[48] N. B. Mhamane, S. Chetry, R. Ranjan, T. Raja, C. S. Gopinath, *ACS Sustainable Chem. Eng.* **2022**, *10*, 3521–3531.

5 Outlook

In this work, mainly alkane but also alcohol ODH reactions were investigated over differently supported vanadia catalysts and a bulk oxide using O_2 and CO_2 as the oxidzing agents. To this end, the influence of the support materials on the vanadia structure and the ODH reaction mechanisms could be elucidated in great detail. Furthermore, the influence of CO_2 as the oxidizing agent on the reaction network and its mechanism was tested, discovering the high activity of the VO_x/TiO_2 system. The knowledge obtained could be transferred to achieve rational catalyst design with (comparably) high propane ODH selectivities. Subsequently, a bulk oxide was investigated using a combination of methods including operando impedance spectroscopy, which was newly established. However, despite great efforts to contribute to the field of oxidation catalysis, some open questions remain in regard to mechanistic refinement and new oxide systems.

First, the investigation of different titania supports during the ODH of propane with O_2 is of interest due to the influence of its composition on its properties. The exact ratio between anatase and rutile was shown to be important and the interface between the phases is often discussed to be especially sensitive to defect creation. Therefore, the dedicated synthesis of titania, possibly via ALD on SiO_2 to increase its surface area might further increase reaction rates. Furthermore, the usage of modulation-excitation spectroscopy during the CO_2-assisted propane ODH reaction over all catalysts would be of great interest to identify surface active adsorbates, and especially the nuclearity-dependent vanadia contribution under reaction conditions. However, this is not accessible with conventional ME-DRIFTS due to the high temperatures required. Emission IR spectroscopy may be an option which, in theory, enables a spectroscopic investigation at these temperatures. Modulation-excitation Raman spectroscopy is even more promising as it is less sensitive to temperature effects than DRIFTS and enables the more detailed investigation of lattice oxygen dynamics in ceria employing a UV excitation wavelength at which it is resonance enhanced. However, in contrast to ME-DRIFTS, these methods still need to be developed. If this is achieved, a new level of understanding of propane ODH reaction mechanisms is expected. This could enable deeper insights into the interaction of vanadia and ceria at the interface. In the VO_x/TiO_2 system, it might lead to an increased understanding of phase transformations and the

coordination of vanadia by titania.

Besides deeper insights into the already established systems, further support materials can be designed. In_2O_3 has previously been shown to be of high relevance for CO_2 activation and to support VO_x species. A mixed support of In_2O_3/CeO_2 might be designed and investigated. Besides the support, the active phase can be varied. The addition of MoO_x to vanadia in substochiometric amounts was previously described to be benefitial for catalytic performance. The influence of promotor materials, such as MoO_x mixed with VO_x can also be investigated.

For $Fe_2(MoO_4)_3$, the transfer of the obtained knowledge under propane ODH conditions towards the more relevant methanol and ethanol ODH reactions is of great importance. The newly established combination of methods to obtain a detailed picture of bulk oxides can be transferred to understand the other ODH mechanisms. In addition, different iron based oxides could be promising candidates for ODH reactions like $FeVO_4$. At last, additional ODH reactions might be considered that also exhibit great potential for industrial application such as ethane, butane, and ethylbenzene ODH. Further mechanistic understanding will facilitate the developement of improved catalysts for the synthesis of important basis chemicals.

Bibliography

[1]   I. Fechete, Y. Wang, J. C. Védrine, *Catal. Today* **2012**, *189*, 2–27.

[2]   R. Diercks, J.-D. Arndt, S. Freyer, R. Geier, O. Machhammer, J. Schwartze, M. Volland, *Chem. Eng. & Technol.* **2008**, *31*, 631–637.

[3]   A. Kate, L. K. Sahu, J. Pandey, M. Mishra, P. K. Sharma, *CRGSC* **2022**, *5*, 100248.

[4]   A. Kätelhön, R. Meys, S. Deutz, S. Suh, A. Bardow, *Proc. Natl. Acad. Sci. USA* **2019**, *116*, 11187–11194.

[5]   F. M. Baena-Moreno, M. Rodríguez-Galán, F. Vega, B. Alonso-Fariñas, L. F. Vilches Arenas, B. Navarrete, **2019**, *41*, 1403–1433.

[6]   T. K. Phung, T. M. Le Pham, K. B. Vu, G. Busca, *J. Environ. Chem. Eng.* **2021**, *9*, 105673.

[7]   A. V. Lavrenov, L. F. Saifulina, E. A. Buluchevskii, E. N. Bogdanets, *Catal. Ind.* **2015**, *7*, 175–187.

[8]   A. Bottino, G. Capannelli, A. Comite, S. Storace, R. Di Felice, *Chem. Eng. J.* **2003**, *94*, 11–18.

[9]   I. Ascoop, V. V. Galvita, K. Alexopoulos, M.-F. Reyniers, P. van der Voort, V. Bliznuk, G. B. Marin, *J. Catal.* **2016**, *335*, 1–10.

[10] A. G. Buekens, G. F. Froment, *Ind. Eng. Chem. Proc. Des. Dev.* **1968**, *7*, 435–447.

[11] A. Siahvashi, A. A. Adesina, *Int. J. Hydrog. Energ.* **2018**, *43*, 17195–17204.

[12] A. Dinse, B. Frank, C. Hess, D. Habel, R. Schomäcker, *J. Mol. Catal. A Chem.* **2008**, *289*, 28–37.

[13] B. Beck, M. Harth, N. G. Hamilton, C. Carrero, J. J. Uhlrich, A. Trunschke, S. Shaikhutdinov, H. Schubert, H.-J. Freund, R. Schlögl, J. Sauer, R. Schomäcker, *J. Catal.* **2012**, *296*, 120–131.

[14] L.-P. Yuan, W.-J. Jiang, X.-L. Liu, Y.-H. He, C. He, T. Tang, J. Zhang, J.-S. Hu, *ACS Catal.* **2020**, *10*, 13227–13235.

[15] C. Autthanit, W. Chatkaew, P. Praserthdam, B. Jongsomjit, *J. Environ. Chem. Eng.* **2020**, *8*, 103547.

[16] K. Nagaoka, K. Takanabe, K.-i. Aika, *Chem. Commun.* **2002**, 1006–1007.

[17] C. A. Carrero, R. Schloegl, I. E. Wachs, R. Schomaecker, *ACS Catal.* **2014**, *4*, 3357–3380.

[18] E. Aneggi, M. Boaro, C. d. Leitenburg, G. Dolcetti, A. Trovarelli, *J. Alloys Compd.* **2006**, *408-412*, 1096–1102.

[19] A. Filtschew, K. Hofmann, C. Hess, *J. Phys. Chem. C* **2016**, *120*, 6694–6703.

[20] J. Paier, C. Penschke, J. Sauer, *Chem. Rev.* **2013**, *113*, 3949–3985.

[21] M. G. Nobbenhuis, P. Hug, T. Mallat, A. Baiker, *Appl. Catal. A Gen.* **1994**, *108*, 241–260.

[22] A. E. Lewandowska, M. Calatayud, F. Tielens, M. A. Bañares, *J. Phys. Chem. C* **2013**, *117*, 25535–25544.

[23] G. Deo, A. M. Turek, I. E. Wachs, T. Machej, J. Haber, N. Das, H. Eckert, A. M. Hirt, *Appl. Catal. A Gen.* **1992**, *91*, 27–42.

[24] M. Martínez-Huerta, *J. Catal.* **2004**, *225*, 240–248.

[25] M. Baron, H. Abbott, O. Bondarchuk, D. Stacchiola, A. Uhl, S. Shaikhutdinov, H.-J. Freund, C. Popa, M. V. Ganduglia-Pirovano, J. Sauer, *Angew. Chem. Int. Ed.* **2009**, *121*, 8150–8153.

[26] C. Penschke, J. Paier, J. Sauer, *J. Phys. Chem. C* **2013**, *117*, 5274–5285.

[27] Z. Wu, A. J. Rondinone, I. N. Ivanov, S. H. Overbury, *J. Phys. Chem. C* **2011**, *115*, 25368–25378.

[28] P. S. Waleska, C. Hess, *J. Phys. Chem. C* **2016**, *120*, 18510–18519.

[29] D. Nitsche, C. Hess, *J. Phys. Chem. C* **2016**, *120*, 1025–1037.

[30] C. Huang, Z.-Q. Wang, X.-Q. Gong, *Chin. J. Catal.* **2018**, *39*, 1520–1526.

[31] A. Iglesias-Juez, M. V. Martínez-Huerta, E. Rojas-García, J.-M. Jehng, M. A. Bañares, *J. Phys. Chem. C* **2018**, *122*, 1197–1205.

[32] M. V. Martínez-Huerta, G. Deo, J. L. G. Fierro, M. A. Bañares, *J. Phys. Chem. C* **2008**, *112*, 11441–11447.

[33] J. Z. Hu, S. Xu, W.-Z. Li, M. Y. Hu, X. Deng, D. A. Dixon, M. Vasiliu, R. Craciun, Y. Wang, X. Bao, C. H. F. Peden, *ACS Catal.* **2015**, *5*, 3945–3952.

[34] O. V. Safonova, A. Zabilska, M. Zabilskiy, R. J. G. Nuguid, A. H. Clark, M. Nachtegaal, O. Kröcher, *Origin of the volcano-like ethanol oxidative dehydrogenation activity trend for VOx/CeO2 catalysts uncovered by operando time-resolved XAS*, **2022**.

[35] A. Zabilska, M. Zabilskiy, R. J. G. Nuguid, A. H. Clark, I. I. Sadykov, M. Nachtegaal, O. Kröcher, O. V. Safonova, *Angew. Chem. Int. Ed.* **2023**, *135*, 321.

[36] P. Michorczyk, P. Pietrzyk, J. Ogonowski, **2012**, *161*, 56–66.

[37] F. Gashoul Daresibi, A. A. Khodadadi, Y. Mortazavi, S. Huotari, M. Ritala, **2022**, *526*, 112396.

[38] M. L. Balogun, S. Adamu, M. S. Ba-Shammakh, M. M. Hossain, *J. Industr. Eng. Chem.* **2021**, *96*, 82–97.

[39] S. Rogg, C. Hess, **2021**, *50*, 101604.

[40] X. Jiang, B. M. Lis, S. C. Purdy, S. Paladugu, V. Fung, W. Quan, Z. Bao, W. Yang, Y. He, B. G. Sumpter, K. Page, I. E. Wachs, Z. Wu, *ACS Catal.* **2022**, *12*, 11239–11252.

[41] X. Jiang, B. M. Lis, Y. Wu, I. E. Wachs, Z. Wu, *J. Phys. Chem. C* **2023**, *127*, 6311–6320.

[42] A. P. V. Soares, M. F. Portela, A. Kiennemann, *Catal. Rev.* **2005**, *47*, 125–174.

[43] M. Bowker, M. House, A. Alshehri, C. Brookes, E. K. Gibson, P. P. Wells, *Catal. Struct. React.* **2015**, *1*, 95–100.

[44] M. Bowker, *Top. Catal.* **2015**, *58*, 606–612.

[45] M. P. House, M. D. Shannon, M. Bowker, *Catal. Lett.* **2008**, *122*, 210–213.

[46] F. Wang, J. Jiang, B. Wang, **2019**, *9*, 477.

[47] M. A. Bañares, M. O. Guerrero-Pérez, J. L. G. Fierro, G. G. Cortez, **2002**, *12*, 3337–3342.

[48] M. A. Bañares, I. E. Wachs, *J Raman Spectroscopy* **2002**, *33*, 359–380.

[49] M. A. Banares, L. Dauphin, V. Calvoperez, T. P. Fehlner, E. E. Wolf, *J. Catal.* **1995**, *152*, 396–409.

[50] A. Chakrabarti, M. E. Ford, D. Gregory, R. Hu, C. J. Keturakis, S. Lwin, Y. Tang, Z. Yang, M. Zhu, M. A. Bañares, I. E. Wachs, *Catal. Today* **2017**, *283*, 27–53.

[51] C. Hess, *Chem. Soc. Rev.* **2021**, *50*, 3519–3564.

[52] H. Kim, K. M. Kosuda, R. P. van Duyne, P. C. Stair, *Chem. Soc. Rev.* **2010**, *39*, 4820–4844.

[53] P. C. Stair, C. Li, *J. Vac. Sci. Technol. A* **1997**, *15*, 1679–1684.

[54] A. Smekal, *Z. Physik* **1926**, *37*, 319–341.

[55] C. V. Raman, K. S. Krishnan, **1928**, 399–419.

[56] E. Smith, G. Dent, *Modern Raman Spectroscopy: A Practical Approach*, John Wiley & Sons, **2019**.

[57] P. Vandenabeele, *Practical Raman Spectroscopy: An Introduction*, John Wiley & Sons, **2013**.

[58] D. A. Long, *The Raman Effect: A Unified Treatment of the Theory of Raman Scattering by Molecules*, 1st ed., Wiley, **2002**.

[59] D. P. Craig, T. Thirunamachandran, *Molecular Quantum Electrodynamics: An Introduction to Radiation-molecule Interactions*, Courier Corporation, **1998**.

[60] C. Schilling, C. Hess, *J. Phys. Chem. C* **2018**, *122*, 2909–2917.

[61] B. Huang, R. Gillen, J. Robertson, *J. Phys. Chem. C* **2014**, *118*, 24248–24256.

[62] K. M. Glassford, Chelikowsky, *Phys. Rev. B Condens. Matter* **1992**, *45*, 3874–3877.

[63] N. Daude, C. Gout, C. Jouanin, *Phys. Rev. B* **1977**, *15*, 3229–3235.

[64] P. Waleska, S. Rupp, C. Hess, *J. Phys. Chem. C* **2018**, *122*, 3386–3400.

[65] S. K. Kuriechen, S. Murugesan, S. Paul Raj, *J. Catal.* **2013**, *2013*, 1–6.

[66] B. Lamoureux, V. R. Singh, V. Jovic, J. Kuyyalil, T.-Y. Su, K. E. Smith, **2016**, *615*, 409–414.

[67] A. R. C. Bredar, A. L. Chown, A. R. Burton, B. H. Farnum, *ACS Appl. Energy Mater.* **2020**, *3*, 66–98.

[68] M. Höber, P. Wachter, B. Königshofer, F. Mütter, H. Schröttner, C. Hochenauer, V. Subotić, *Int. J. Hydrog. Energ.* **2022**, *324*, 124256.

[69] V. Balasubramani, S. Chandraleka, T. S. Rao, R. Sasikumar, M. R. Kuppusamy, T. M. Sridhar, *J. Electrochem. Soc.* **2020**, *167*, 037572.

[70] N. O. Laschuk, E. B. Easton, O. V. Zenkina, *RSC Adv.* **2021**, *11*, 27925–27936.

[71] Z. Hu, Z. Wang, Y. Guo, L. Wang, Y. Guo, J. Zhang, W. Zhan, *Environ. Sci. Technol.* **2018**, *52*, 9531–9541.

[72] D. Baurecht, U. P. Fringeli, *Rev. Sci. Instr.* **2001**, *72*, 3782–3792.

[73] P. Müller, I. Hermans, *Ind. Eng. Chem. Res.* **2017**, *56*, 1123–1136.

[74] A. Urakawa, T. Bürgi, A. Baiker, *Chem. Eng. Sci.* **2008**, *63*, 4902–4909.

[75] J. Keeler, *Understanding NMR Spectroscopy*, John Wiley & Sons, **2010**.

[76] K. S. W. Sing, *J. Porous. Mater.* **1995**, *2*, 5–8.

[77] W. H. Zachariasen, *Acta. Cryst.* **1967**, *23*, 558–564.

[78] M. Cavalleri, K. Hermann, A. Knop-Gericke, M. Hävecker, R. Herbert, C. Hess, A. Oestereich, J. Döbler, R. Schlögl, *J. Catal.* **2009**, *262*, 215–223.

[79] N. MAGG, *J. Catal.* **2004**, *226*, 88–100.

[80] W. Koch, M. C. Holthausen, *A Chemist's Guide to Density Functional Theory*, John Wiley & Sons, **2015**.

[81] D. Püschner in *Quantitative Rechenverfahren der Theoretischen Chemie*, Springer Spektrum, Wiesbaden, **2017**, pp. 43–51.

[82] D. Püschner, *Quantitative Rechenverfahren der Theoretischen Chemie*, Springer Fachmedien Wiesbaden, Wiesbaden, **2017**.

[83] J. P. Perdew, K. Burke, M. Ernzerhof, *Phys. Rev. Lett.* **1996**, *77*, 3865–3868.

[84] S. L. Dudarev, G. A. Botton, S. Y. Savrasov, C. J. Humphreys, A. P. Sutton, *Phys. Rev. B Condens. Matter* **1998**, *57*, 1505–1509.

[85] J. L. F. Da Silva, M. V. Ganduglia-Pirovano, J. Sauer, V. Bayer, G. Kresse, *Phys. Rev. B* **2007**, *75*, 81.

[86] P. E. Blöchl, *Phys. Rev. B Condens. Matter* **1994**, *50*, 17953–17979.

[87] H. J. Monkhorst, J. D. Pack, *Phys. Rev. B* **1976**, *13*, 5188–5192.

[88] D. Porezag, Pederson, *Phys. Rev. B Condens. Matter* **1996**, *54*, 7830–7836.

[89] M. Lazzeri, F. Mauri, *Phys. Rev. Lett.* **2003**, *90*, 036401.

[90] C. Hess, *J. Catal.* **2007**, *248*, 120–123.

[91] C. T. Nottbohm, C. Hess, *Catal. Commun.* **2012**, *22*, 39–42.

[92] C. Popa, M. V. Ganduglia-Pirovano, J. Sauer, *J. Phys. Chem. C* **2011**, *115*, 7399–7410.

[93] C. Penschke, J. Paier, J. Sauer, *J. Phys. Chem. C* **2018**, *122*, 9101–9110.

List of Figures

List of Abbreviations

Abbreviation	Definition	Unit
ODH	Oxidative dehydrogenation	
DDH	Direct dehydrogenation	
PDR	Propane dry reforming	
RWGSr	reverse water-gas shift reaction	
ME	Modulation-Excitation	
XRD	X-Ray diffraction	
XPS	X-Ray photoelectron spectroscopy	
ssNMR	Solid-state nuclear magnetic resonance spectroscopy	
EIS	Electrical impedance spectroscopy	
DFT	Density functional theory	
ALD	Atomic layer deposition	
TPR	Temperature-programmed reduction	
SMOSI	Strong metal-oxide support interactions	
XANES	X-Ray absorption near edge spectroscopy	
IR	Infrared	
R	Transition dipole moment	$C \cdot m$
Ψ	Wavefunction	
I	Initial state	
F	Finale state	
r	Virtual state	
ρ	Polarization of incident light	$C \cdot m^{-2}$
σ	Polarization of scattered light	$C \cdot m^{-2}$
ω_{rI}	Frequency difference between initial and virtual state	s^{-1}
ω_L	Frequency of the laser	s^{-1}
θ	Electronic contribution to the vibronic wavefunction	
σ	Vibrational contribution to the vibronic wavefunction	
μ	Dipole moment	$C \cdot m$
M_{rI}	Electric dipole moment	$C \cdot m$
α	Transition polarizability	$C^2 \cdot m^2 \cdot J^{-1}$
k	Force constant	$N \cdot m^{-1}$

q	Nuclear distance	m
LMCT	Ligand-to-metal-charge transfer	
PEIS	Potentiostatic electrical impedance spectroscopy	
DRIFTS	Diffuse reflectance infrared Fourier transform spectroscopy	
VASP	Vienna ab-initio simulation package	
DFPT	Density functional pertubation theory	
$\vec{x}_N$	Electron position	
LDA	Local denisty approximation	
ϵ_{XC}	Correlation exchange functional homogeneous electron gas	
GGA	Generalized gradient approximation	
PBE	Perdew, Bukre, and Ernzerhof	
KSO	Kohn-Sham orbitals	
PAW	Projector augmented wave	
μ_s	Frequency of scattered light	s^{-1}
n_i^b	statistical Bose-Einstein factor	
I_{Raman}	Raman intensity	
$\vec{\alpha}_{ij}$	Tensor element of transition polarizability	$C^2 \cdot m^2 \cdot J^{-1}$
R_k	Atomic coordinates	
E^{el}	Electric energy	J
δ_{ij}	Kronecker delta	
Ω_{Cell}	Unit cell volume	m^3
ϵ_{ij}^{inf}	Dielectric tensor element	$F \cdot m^{-1}$
MFC	Mass flow controller	
TCD	Thermal conductivity detector	
FID	Flame ionization detector	
NIR	Near infrared	
BBO	Barium borate	
LBO	Lithium triborate	
SHG	Second harmoinc generation	
THG	Third harmonic generation	
PBC	Periodic boundary conditions	
TPO	Temperature-programmed oxidation	
SEM	Scanning electron microscopy	
HRTEM	High resolution transmission electron microscopy	
EELS	Electron energy loss spectroscopy	
ICP-OES	Ion-coupled plasma optical emission spectroscopy	

Acknowledgement

Meiner Familie und meinen Freunden für die emotionale Unterstützung in allen Situationen die während der Anfertigung dieser Arbeit aufgekommen sind.

Parts of this work have been previously published in peer reviewed journals and at national and international conferences.

Journal Articles:

- <u>Leon Schumacher</u>, Christian Hess, The active role of the support in propane ODH over VO_x/CeO_2 catalysts studied using multiple operando spectroscopies, J. Catal., 398, 29-43 (2021).

- Marc Ziemba, <u>Leon Schumacher</u>, Christian Hess, Reduction Behavior of Cubic In_2O_3 Nanoparticles by Combined Multiple In Situ Spectroscopy and DFT, J. Phys. Chem. Lett, 12, 3749-3754 (2021).

- Niklas Oefner, Franziska Heck, Marcel Dürl, <u>Leon Schumacher</u>, Humera Khatoon Siddiqui, Ulrike I. Kramm, Christian Hess, Angela Möller, Barbara Albert, Bastian J. M. Etzold, Activity, Selectivity and Initial Degradation of Iron Molybdate in the Oxidative Dehydrogenation of Ethanol, ChemCatChem, 14 (2022).

- Marc Ziemba, Mariusz Radtke, <u>Leon Schumacher</u>, Christian Hess, Elucidating CO_2 Hydrogenation over In_2O_3 Nanoparticles using Operando UV/Vis and Impedance Spectroscopies, Angew. Chem. Int. Ed., 61 (2022).

- <u>Leon Schumacher</u>, Jakob Weyel, Christian Hess, Unraveling the Active Vanadium Sites and Adsorbate Dynamics in VO_x/CeO_2 Oxidation Catalysts Using Transient IR Spectroscopy, J. Am. Chem. Soc., 144, 14874-14887 (2022).

- <u>Leon Schumacher</u>, Marc Ziemba, Kai Brunnengräber, Lea Totzauer, Kathrin Hofmann, Bastian J. M. Etzold, Barbara Albert, Christian Hess, Understanding the Reduction Behavior of VO_x/CeO_2 on a Molecular Level: Combining Temperature-Programmed Reduction with Multiple In-Situ Spectroscopies and X-ray Diffraction, J. Phys. Chem. C, 127, 5810-5824 (2023).

- Niklas Oefner, Christopher E. Shuck, <u>Leon Schumacher</u>, Franziska Heck, Kathrin Hofmann, Jana Schmidpeter, Weiqun Li, Mounib Bahri, B. Layla Mehdi, Alfons Drochner, Barbara Alber, Christian Hess, Yury Gogotsi, Bastian J. M. Etzold, MXene Aerogel Derived Ultra-Active Vanadia Catalysts for Selective Conversion of Sustainable Alcohols to Base Chemicals, ACS Appl. Mater. Interfaces, 15, 16714-16722 (2023).

- <u>Leon Schumacher</u>, Johannes Pfeiffer, Jun Shen, Torsten Gutmann, Hergen Breitzke, Gerd Buntkowsky, Kathrin Hofmann, Christian Hess, Collaborative Effects between Vanadia and Titania during the Oxidative Dehydrogenation of Propane Investigated by Operando and Transient Spectroscopies, ACS Catal., 13, 8139-8160 (2023).

- <u>Leon Schumacher</u>, Jun Shen, Kathrin Hofmann, Christian Hess, Rational Design of Vanadia-Based Propane ODH Catalysts: A Multiple Operando Spectroscopic Investigation of $VO_x/TiO_2/CeO_2$, Catal. Today, 426, 114387, (2024).

- <u>Leon Schumacher</u>, Kathrin Hofmann, Christian Hess, Insight into the Reaction Mechanism and Deactivation during CO_2-Assisted Propane ODH over VO_x/TiO_2 Catalysts: An Operando Spectroscopic Study, ChemRxiv (DOI: 10.26434/chemrxiv-2023-rnfrd) (2023).

- <u>Leon Schumacher</u>, Mariusz Radtke, Jan Welzenbach, Christian Hess, Unraveling Surface and Bulk Dynamics of $Fe_2(MoO_4)_3$ during Oxidative Dehydrogenation using Operando and Transient Spectroscopies, Commun. Chem, accepted (2023).

Oral Presentations:
- <u>Schumacher, L.</u>, Hess, C., The Mechanistic Interplay between Vanadia and its Support during Propane ODH Studied by Transient Spectroscopy. 9th World Congress on Oxidation Catalysis, Cardiff, United Kingdom, 2022.

Poster Presentations:

- Schumacher, L., Weyel, J., Hess, C., Unraveling the Active Vanadium Sites and Adsorbate Dynamics in VO_x/CeO_2 Oxidation Catalysts Using Transient IR Spectroscopy, 56. Deutsches Katalytikertreffen, Weimar, 2023.

- Welzenbach, J., Schumacher, L., Hess, C., Structural Dynamics of Iron Molybdate Catalysts for Oxidative Dehydrogenation studied by In-Situ and Operando Spectroscopy, 56. Deutsches Katalytikertreffen, Weimar, 2023.

- Schumacher, L., Hess, C., Operando Spectroscopic Investigation of the Reaction Mechanism of the Propane ODH over VO_x/TiO_2 Catalysts. 55. Deutes Katalytikertreffen, Weimar, 2022.

- Schumacher, L., Hess, C., The Active Role of the Support in Propane ODH over VO_x/CeO_2 Catalysts Studied using Multiple Operando Spectroscopies. ExpReS, Online, 2021.

- Schumacher, L., Rogg, S., Hess, C., CO_2 as a Soft-Oxidant for Propane ODH over VO_x/CeO_2 Catalysts and its Influence on the Reaction Mechanism: an Operando Spectroscopic Study. 54. Deutsches Katalytikertreffen, Weimar, Germany, 2021.

- Schumacher, L., Rogg, S., Hess, C., Direct Spectroscopic Evidence for Ceria Participation in VO_x/CeO_2 Catalysts during the ODH of Propane: an Operando Spectroscopic Study. 53. Deutsches Katalytikertreffen, Weimar, Germany, 2020.

- Schumacher, L., Rogg, S., Hess, C., An Operando Spectroscopic Approach to Investigate the Role of the Support Material in the ODH of Propane for Vanadia Catalysts. Operando Day, Frankfurt, Germany, 2020.

**Erklärung zum Eigenanteil an den Veröffentlichungen
der kumulativen Dissertation**

Im Folgenden ist aufgelistet, mit welchem Anteil ich an den Veröffentlichungen beteiligt war.

Mein Anteil an der folgenden Veröffentlichung beträgt 80 %.

1. Leon Schumacher, Christian Hess, The active role of the support in propane ODH over VO_x/CeO_2 catalysts studied using multiple operando spectroscopies, J. Catal., 398, 29-43 (2021).

Mein Anteil an der folgenden Veröffentlichung beträgt 15 %.

2. Marc Ziemba, Leon Schumacher, Christian Hess, Reduction Behavior of Cubic In_2O_3 Nanoparticles by Combined Multiple In Situ Spectroscopy and DFT, J. Phys. Chem. Lett, 12, 3749-3754 (2021).

Mein Anteil an der folgenden Veröffentlichung beträgt 5 %.

3. Niklas Oefner, Franziska Heck, Marcel Dürl, Leon Schumacher, Humera Khatoon Siddiqui, Ulrike I. Kramm, Christian Hess, Angela Möller, Barbara Albert, Bastian J. M. Etzold, Activity, Selectivity and Initial Degradation of Iron Molybdate in the Oxidative Dehydrogenation of Ethanol, ChemCatChem, 14 (2022).

Mein Anteil an der folgenden Veröffentlichung beträgt 10 %.

4. Marc Ziemba, Mariusz Radtke, Leon Schumacher, Christian Hess, Elucidating CO_2 Hydrogenation over In_2O_3 Nanoparticles using Operando UV/Vis and Impedance Spectroscopies, Angew. Chem. Int. Ed., 61 (2022).

Mein Anteil an der folgenden Veröffentlichung beträgt 70 %.

5. Leon Schumacher, Jakob Weyel, Christian Hess, Unraveling the Active Vanadium Sites and Adsorbate Dynamics in VO_x/CeO_2 Oxidation Catalysts Using Transient IR Spectroscopy, J. Am. Chem. Soc., 144, 14874-14887 (2022).

Mein Anteil an der folgenden Veröffentlichung beträgt 40 %.

6. Leon Schumacher, Marc Ziemba, Kai Brunnengräber, Lea Totzauer, Kathrin Hofmann, Bastian J. M. Etzold, Barbara Albert, Christian Hess, Understanding the Reduction Behavior of VO_x/CeO_2 on a Molecular Level: Combining Temperature-Programmed Reduction with Multiple In-Situ Spectroscopies and X-ray Diffraction, J. Phys. Chem. C, 127, 5810-5824 (2023).

Mein Anteil an der folgenden Veröffentlichung beträgt 10 %.

7. Niklas Oefner, Christopher E. Shuck, Leon Schumacher, Franziska Heck, Kathrin Hofmann, Jana Schmidpeter, Weiqun Li, Mounib Bahri, B. Layla Mehdi, Alfons Drochner, Barbara Alber, Christian Hess, Yury Gogotsi, Bastian J. M. Etzold, MXene Aerogel Derived Ultra-Active Vanadia Catalysts for Selective Conversion of Sustainable Alcohols to Base Chemicals, ACS Appl. Mater. Interfaces, 15, 16714-16722 (2023).

Mein Anteil an der folgenden Veröffentlichung beträgt 45 %.

8. <u>Leon Schumacher</u>, Johannes Pfeiffer, Jun Shen, Torsten Gutmann, Hergen Breitzke, Gerd Buntkowsky, Kathrin Hofmann, Christian Hess, Collaborative Effects between Vanadia and Titania during the Oxidative Dehydrogenation of Propane Investigated by Operando and Transient Spectroscopies, ACS Catal., 13, 8139-8160 (2023).

Mein Anteil an der folgenden Veröffentlichung beträgt 65 %.

9. <u>Leon Schumacher</u>, Jun Shen, Kathrin Hofmann, Christian Hess, Rational Design of Vanadia-Based Propane ODH Catalysts: A Multiple Operando Spectroscopic Investigation of $VO_x/TiO_2/CeO_2$, Catal. Today, 426, 114387, (2024).

Mein Anteil an der folgenden Veröffentlichung beträgt 75 %.

10. <u>Leon Schumacher</u>, Kathrin Hofmann, Christian Hess, Insight into the Reaction Mechanism and Deactivation during CO_2-Assisted Propane ODH over VO_x/TiO_2 Catalysts: An Operando Spectroscopic Study, ChemRxiv (DOI: 10.26434/chemrxiv-2023-rnfrd) (2023).

Mein Anteil an der folgenden Veröffentlichung beträgt 60 %.

11. <u>Leon Schumacher</u>, Mariusz Radtke, Jan Welzenbach, Christian Hess, Unraveling Surface and Bulk Dynamics of $Fe_2(MoO_4)_3$ during Oxidative Dehydrogenation using Operando and Transient Spectroscopies, Commun. Chem, accepted (2023).

Mein Anteil an der folgenden Veröffentlichung beträgt 90 %.

12. <u>Leon Schumacher</u>, Christian Hess, A Detailed Analysis of Vanadias Vibrational Structure in the Raman Spectra of VO_x/CeO_2: A Periodic Density Functional Theory Study, Manuscript.

Mein Anteil an der folgenden Veröffentlichung beträgt 80 %.

13. <u>Leon Schumacher</u>, Marc Ziemba, Christian Hess, The Investigation of the Activation and Regeneration of Reduced VO_x/CeO_2 Catalysts with CO_2 Using Multiple In-Situ Spectroscopies, Manuscript.

Mein Anteil an der folgenden Veröffentlichung beträgt 70 %.

14. <u>Leon Schumacher</u>, Marius Funke, Christian Hess, Unraveling the Mechanism of the CO_2-Assisted Oxidative Dehydrogenation of Propane over VO_x/CeO_2 Catalysts: An Operando Spectroscopic Study, Manuscript.

_____   _____
Ort, Datum   L. Schumacher

Erklärung zur Begutachtung der Veröffentlichung

Referent: Prof. Dr. Christian Hess
Co-Referent: Prof. Dr. Bastian Etzold   Datum _____

Weder Referent (Prof. Dr. Christian Hess) noch Co-Referent (Prof. Dr. Bastian Etzold) der vorliegenden kumulativen Doktorarbeit waren an der Begutachtung nachstehender Veröffentlichungen beteiligt:

1. Leon Schumacher, Christian Hess, The active role of the support in propane ODH over VO_x/CeO_2 catalysts studied using multiple operando spectroscopies, J. Catal., 398, 29-43 (2021).

2. Marc Ziemba, Leon Schumacher, Christian Hess, Reduction Behavior of Cubic In_2O_3 Nanoparticles by Combined Multiple In Situ Spectroscopy and DFT, J. Phys. Chem. Lett, 12, 3749-3754 (2021).

3. Niklas Oefner, Franziska Heck, Marcel Dürl, Leon Schumacher, Humera Khatoon Siddiqui, Ulrike I. Kramm, Christian Hess, Angela Möller, Barbara Albert, Bastian J. M. Etzold, Activity, Selectivity and Initial Degradation of Iron Molybdate in the Oxidative Dehydrogenation of Ethanol, ChemCatChem, 14 (2022).

4. Marc Ziemba, Mariusz Radtke, Leon Schumacher, Christian Hess, Elucidating CO_2 Hydrogenation over In_2O_3 Nanoparticles using Operando UV/Vis and Impedance Spectroscopies, Angew. Chem. Int. Ed., 61 (2022).

5. Leon Schumacher, Jakob Weyel, Christian Hess, Unraveling the Active Vanadium Sites and Adsorbate Dynamics in VO_x/CeO_2 Oxidation Catalysts Using Transient IR Spectroscopy, J. Am. Chem. Soc., 144, 14874-14887 (2022).

6. Leon Schumacher, Marc Ziemba, Kai Brunnengräber, Lea Totzauer, Kathrin Hofmann, Bastian J. M. Etzold, Barbara Albert, Christian Hess, Understanding the Reduction Behavior of VO_x/CeO_2 on a Molecular Level: Combining Temperature-Programmed Reduction with Multiple In-Situ Spectroscopies and X-ray Diffraction, J. Phys. Chem. C, 127, 5810-5824 (2023).

7. Niklas Oefner, Christopher E. Shuck, Leon Schumacher, Franziska Heck, Kathrin Hofmann, Jana Schmidpeter, Weiqun Li, Mounib Bahri, B. Layla Mehdi, Alfons Drochner, Barbara Alber, Christian Hess, Yury Gogotsi, Bastian J. M. Etzold, MXene Aerogel Derived Ultra-Active Vanadia Catalysts for Selective Conversion of Sustainable Alcohols to Base Chemicals, ACS Appl. Mater. Interfaces, 15, 16714-16722 (2023).

8. Leon Schumacher, Johannes Pfeiffer, Jun Shen, Torsten Gutmann, Hergen Breitzke, Gerd Buntkowsky, Kathrin Hofmann, Christian Hess, Collaborative Effects between Vanadia and Titania during the Oxidative Dehydrogenation of Propane Investigated by Operando and Transient Spectroscopies, ACS Catal., 13, 8139-8160 (2023).

9. <u>Leon Schumacher</u>, Jun Shen, Kathrin Hofmann, Christian Hess, Rational Design of Vanadia-Based Propane ODH Catalysts: A Multiple Operando Spectroscopic Investigation of $VO_x/TiO_2/CeO_2$, Catal. Today, 426, 114387, (2024).

10. <u>Leon Schumacher</u>, Kathrin Hofmann, Christian Hess, Insight into the Reaction Mechanism and Deactivation during CO_2-Assisted Propane ODH over VO_x/TiO_2 Catalysts: An Operando Spectroscopic Study, ChemRxiv (DOI: 10.26434/chemrxiv-2023-rnfrd) (2023).

11. <u>Leon Schumacher</u>, Mariusz Radtke, Jan Welzenbach, Christian Hess, Unraveling Surface and Bulk Dynamics of $Fe_2(MoO_4)_3$ during Oxidative Dehydrogenation using Operando and Transient Spectroscopies, Commun. Chem, accepted (2023).

_____   _____

Referent   Co-Referent
(Prof. Dr. Christian Hess)   (Prof. Dr. Bastian J.M. Etzold)